



**UNIVERSITY OF IOANNINA  
SCHOOL OF ENGINEERING  
DEPARTMENT OF MATERIALS  
SCIENCE & ENGINEERING**

**Strongly correlated Transition Metal Oxides: Synthesis, Structure, Magnetic,  
Dielectric and Dynamical properties**

**Eleni Aza**

**PhD Thesis**

Ioannina

2019





**UNIVERSITY OF IOANNINA  
SCHOOL OF ENGINEERING  
DEPARTMENT OF MATERIALS  
SCIENCE & ENGINEERING**

**Strongly correlated Transition Metal Oxides: Synthesis, Structure, Magnetic,  
Dielectric and Dynamical properties**

**Eleni Aza**

**PhD Thesis**

Ioannina

2019





**ΕΛΛΗΝΙΚΗ ΔΗΜΟΚΡΑΤΙΑ  
ΠΑΝΕΠΙΣΤΗΜΙΟ ΙΩΑΝΝΙΝΩΝ  
ΠΟΛΥΤΕΧΝΙΚΗ ΣΧΟΛΗ  
ΤΜΗΜΑ ΜΗΧΑΝΙΚΩΝ ΕΠΙΣΤΗΜΗΣ ΥΛΙΚΩΝ**

**Ισχυρά συσχετιζόμενα οξειδία μεταβατικών μετάλλων: Σύνθεση, Δομικές,  
Μαγνητικές, Διηλεκτρικές και Δυναμικές ιδιότητες**

**Ελένη Αζά**

**Διδακτορική διατριβή**

Ιωάννινα

2019

*«Η έγκριση της διδακτορικής διατριβής από το Τμήμα Μηχανικών Επιστήμης Υλικών της Πολυτεχνικής Σχολής του Πανεπιστημίου Ιωαννίνων δεν υποδηλώνει αποδοχή των γνώμων του συγγραφέα Ν. 5343/32, άρθρο 202, παράγραφος 2».*

**Date of application of Ms. ....Eleni Aza .....**: 16 January 2013  
**Designation date of the three-membered Advisory committee:** 16 January 2013  
**Members of the Advisory Committee:**

Supervisor: **Panagiotopoylos Ioannis**, Professor, Department of materials science and engineering, University of Ioannina

Members: **Lappas Alexandros**, Research Director, Institute of Electronic Structure and Laser, Foundation for Research and Technology-Hellas

**Douvalis Alexios**, Associate Professor, Department of Physics, University of Ioannina

**Date of Subject determination:** 16 January 2013  
*“Strongly correlated Transition Metal Oxides: Synthesis, Structure, Magnetic, Dielectric and Dynamical properties”*

**Designation of the 7-membered Committee:**

**Panagiotopoulos Ioannis,**

Professor, Department of materials science and engineering,  
University of Ioannina

**Alexandros Lappas**

Research Director, Institute of Electronic Structure and Laser,  
Foundation for Research and Technology-Hellas

**Douvalis Alexios**

Associate Professor, Department of Physics,  
University of Ioannina

**Karakasidis Michail**

Professor, Department of materials science and engineering,  
University of Ioannina

**Agathopoulos Symeon**

Professor, Department of materials science and engineering,  
University of Ioannina

**Lidorikis Eleftherios**

Professor, Department of materials science and engineering,  
University of Ioannina

**Papageorgiou Dimitrios**

Associate Professor, Department of materials science and  
engineering, University of Ioannina

Approval of the PhD thesis marked with “.....” at 6 June 2019

**Chair of the department**

**Department secretary**

**Alkiviadis Paypetis**  
**Professor**

**Maria Kontou**



**Ημερομηνία αίτησης της/του κ. ....Ελένης Αζά.....:** 16 Ιανουαρίου 2013  
**Ημερομηνία ορισμού Τριμελούς Συμβουλευτικής Επιτροπής:** 16 Ιανουαρίου 2013  
**Μέλη Τριμελούς Συμβουλευτικής Επιτροπής:**

Επιβλέπων/ουσα: **Παναγιωτόπουλος Ιωάννης**, Καθηγητής, Τμήμα Μηχανικών και Επιστήμης υλικών Πολυτεχνικής Σχολής, Πανεπιστήμιο Ιωαννίνων

Μέλη:**Λάμπας Αλέξανδρος**, Ερευνητής Α' βαθμίδας, Ινστιτούτο Ηλεκτρονικής Δομής και Λέιζερ, Ίδρυμα Τεχνολογίας και Έρευνας (ΙΤΕ)

**Δούβαλης Αλέξιος**, Αναπληρωτής Καθηγητής, Τμήμα Φυσικής, Σχολή Θετικών Επιστημών, Πανεπιστήμιο Ιωαννίνων

**Ημερομηνία ορισμού θέματος:** 16 Ιανουαρίου 2013  
*«Ισχυρά συσχετιζόμενα οξειδία μεταβατικών μετάλλων: Σύνθεση, Δομικές, Μαγνητικές, Διηλεκτρικές και Δυναμικές ιδιότητες»*

### **ΔΙΟΡΙΣΜΟΣ ΕΠΤΑΜΕΛΟΥΣ ΕΞΕΤΑΣΤΙΚΗΣ ΕΠΙΤΡΟΠΗΣ :**

**Παναγιωτόπουλος Ιωάννης**

Καθηγητής, Τμήμα Μηχανικών και Επιστήμης υλικών Πολυτεχνικής Σχολής, Πανεπιστήμιο Ιωαννίνων

**Λάμπας Αλέξανδρος**

Ερευνητής Α' βαθμίδας, Ινστιτούτο Ηλεκτρονικής Δομής και Λέιζερ, Ίδρυμα Τεχνολογίας και Έρευνας (ΙΤΕ)

**Δούβαλης Αλέξιος**

Αναπληρωτής Καθηγητής, Τμήμα Φυσικής, Σχολή Θετικών Επιστημών, Πανεπιστήμιο Ιωαννίνων

**Καρακασίδης Μιχαήλ**

Καθηγητής, Τμήμα Μηχανικών και Επιστήμης υλικών Πολυτεχνικής Σχολής, Πανεπιστήμιο Ιωαννίνων

**Αγαθόπουλος Συμεών**

Καθηγητής, Τμήμα Μηχανικών και Επιστήμης υλικών Πολυτεχνικής Σχολής, Πανεπιστήμιο Ιωαννίνων

**Λοιδωρικής Ελευθέριος**

Καθηγητής, Τμήμα Μηχανικών και Επιστήμης υλικών Πολυτεχνικής Σχολής, Πανεπιστήμιο Ιωαννίνων

**Παπαγεωργίου Δημήτριος**

Αναπληρωτής Καθηγητής, Τμήμα Μηχανικών και Επιστήμης υλικών Πολυτεχνικής Σχολής, Πανεπιστήμιο Ιωαννίνων

Έγκριση Διδακτορικής Διατριβής με βαθμό «.....» στις 6 Ιουνίου 2019

**Ο Πρόεδρος του Τμήματος**

**Η Γραμματέας του Τμήματος**

**Αλκιβιάδης Παϊπέτης,  
Καθηγητής**

**Μαρία Κόντου**





The work described in this thesis was performed in the “Functional Nanocrystals and Quantum Magnetism Laboratory” at the Institute of Electronic Structure and Laser, Foundation for Research and Technology-Hellas, Heraklion, Greece, under the guidance and supervision of Dr. Alexandros Lappas.

This research has been co-financed by the Institute of Electronic Structure and Laser through ERC03-ITSSUED and Kripis, project PROENYL (448305) while the training and scientific missions have been partially supported by COST TO-BE action MP1308.



**regions at the centre of development**

Co - financed by the Hellenic Republic and the European Union - European Regional Development Fund, in the context of the O.P. Competitiveness and Entrepreneurship (OPC II) and the R.O.P. Attica, R.O.P. Macedonia - Thrace



UK Research and Innovation





“Science isn’t but a perversion of itself unless it has as its ultimate goal the betterment of humanity”

Nikola Tesla

*To my parents Sissi and Stelios,  
In the memory of Fotini*

## **PREFACE**

Before you, lies the dissertation entitled as “Strongly correlated Transition Metal Oxides: Synthesis, Structure, Magnetic, Dielectric and Dynamical properties” the basis of which is the investigation and study over the field of new single phase multiferroic materials in the category of transition metal oxides. The present dissertation has been written to fulfill the graduation requirements for the degree of Doctor of Philosophy from the department of Materials’ Science and Engineering of the University of Ioannina in cooperation with the Institute of Electronic Structure and Laser (IESL) of Foundation for Research and Technology-Hellas (FORTH) located in Heraklion, Crete.

The present thesis has been motivated by the revival of interest on multiferroic materials where competing magnetic interactions may lead to coupling of electric and magnetic order which further allows the utilization of such fundamental mechanisms to multiple technological applications. The so called “ $d^0$  vs  $d^n$  problem” which makes the simultaneous coexistence of a magnetic moment and charge dipole nearly impossible and as a result, the existence of single phase multiferroics non-trivial, has set the challenge and initiated an investigation over whether multiferroism can rely in d-electron magnetism having ferroelectricity induced through a geometrical route.

The will to uncover such highly sought materials while pursuing fundamental study of the driving mechanisms of magnetoelectricity guided me to focus my research on polymorphs of the geometrically frustrated  $\text{NaMnO}_2$  system in order to answer my queries. My research question and the path to the final results has been formulated together with my supervisors Dr A. Lappas and Prof I. Panagiotopoulos who supported me all the way from the starting point of the material synthesis, the setting up of the experimental station, the organization of the experimental process and the analysis of the results.

## **ACKNOWLEDGEMENTS**

At this point I would like to express my gratitude to the people that have inspired me and helped me pave my path through the PhD adventure as a minimum recognition for their offer.

First and foremost I would like to thank my supervisor Dr. Alexandros Lappas who gave me the opportunity to be a part of his team and pursue high quality research as well as for the continuous guidance, insightful discussions, initiative, patience and encouragement when in need.. and for always correcting the way I pronounce the word “experiment”!

I would also like to express my gratitude to the Department of Materials’ Science and Engineering and my advising committee, Prof. Ioannis Panagiotopoulos and Prof. Alexios Douvalis for accepting me as a PhD candidate.

I am really grateful to Prof. Geetha Balakrishnan for the patient guidance through the single crystal growth challenge at university of Warwick. It wouldn’t have worked without her and Monica C. Hatnean taking care of all the details. My UK room-mates, Marina, Kostas and George deserve a dozen thank you!

The great learning experience of the single crystal neutron diffraction experiment at WISH diffractometer has been greatly supported by brilliant Fabio Orlandi to whom I am deeply grateful.

I was lucky to meet, share my queries and learn from inspiring experimentalists such as Dr Bastian Klemke, Dr Martin Lees, Prof. Denis Arcon, Prof. Martin Green and Dr Bohdan Kundys who owes the quote “never try to repeat good results”.

One of the greatest challenges and a great demand on my time during my PhD research has been the development of the in-house Magnetoelectric Station of FUNL. This enormous thank you goes to Kuriakos Mouratis for working great together towards the accomplishment of this part. At this point I would like to thank also Mr Papadakis, Mr Goussis and Mr Koutsaidis, Makis and Nikos from the machinery workspace for putting “hands and mind” into whatever was needed at this point. Of course I would never forget our glass blower Mpampis for the heartwarming welcome to every enquiry I had.

Part of my everyday life in the lab, office, lunch and dinner, my colleagues, advisors and great friends who I was extremely lucky to work with, Athanasia Kostopoulou, Kostas Mprintakis, Ioanna Bakaimi, Antonio F. Martinez, Kostas Vassilopoulos and George Antonaropoulos.

A great thank you also to my pleasant distractions from my research! Dancing and lindy hopping with a great team of people that form the Cretan Swing Shots and the Jam Rooters and especially Giannis, Alexandra, Maria, Irini, Maira, Vladimiros, Aggeliki, Jo and Marios.

I am really grateful to my loving people who could not really feel the PhD blues but have been patient enough to be by my side and lighten up my days. Thank you Athina, Dimitris, George, Penelope, Klitos and Vassilis.

I deeply thank my parents for their support to my decisions, my sister Venetia and my brother Paschalis.

Ευχαριστώ θερμά τους γονείς μου Σίσσυ και Στέλιο, την αδερφή μου Βενετία και τον αδερφό μου Πασχάλη για την αγάπη και την υποστήριξή τους.

Eleni Aza

ελένη αζά

## ABSTRACT

The discovery of materials with coexisting magnetic and ferroelectric orders, has revived the interest of condensed matter physics and materials' science communities maintaining the great promise of such fundamental mechanisms in devising applications ranging from portable magnetoelectric (ME) sensors and memories to radar technologies.

The present PhD thesis is a study in the field of strongly correlated systems where coupled properties arise from the interplay of charge and spin degrees of freedom over lattice topologies enabling competing magnetic interactions and therefore emergence of coupling of electric and magnetic order. Non-perovskite, two-dimensional (2D) Na-Mn-O oxides are revisited in scope of this in both polycrystalline and large single crystal forms.

Among Na-deficient polymorphs, hexagonal  $\alpha$ -Na<sub>0.7</sub>MnO<sub>2</sub> (single crystals) has been investigated for the first time as a playground of competing interactions due to mixed Mn valence (Mn<sup>4+</sup> / Mn<sup>3+</sup>), fostered by Na vacancies in the structure. The competition of FM (Mn<sup>3+</sup>-Mn<sup>4+</sup>) and AFM (Mn<sup>3+</sup>-Mn<sup>3+</sup>) interactions is believed to be the origin of the magnetic instability leading to a glassy ground state leaving also their footprint in the dielectric permittivity measurements.

Competing FM and AFM interactions are also investigated as the origin of the anisotropic magnetic properties witnessed in  $a$ -Na<sub>x</sub>MnO<sub>2</sub> ( $x= 0.96$ ) single crystals. Neutron single crystal experiments show a well-established AFM long range order which vanishes above 26 K while a coexistent canted antiferromagnetic state persists up to 45 K. In both alpha powders and  $a$ -Na<sub>0.96</sub>MnO<sub>2</sub> single crystals, the dielectric permittivity suggests the onset of the commensurate magnetic long range order ( $T \sim 45$  K) which in the case of the powders allows a magnetocapacitance effect.

Compositional modulations in  $\beta$ -NaMnO<sub>2</sub>, which are depicted as an intergrowth of  $\alpha$ - and  $\beta$ - like oxygen coordinations, are found to trigger a proper-screw magnetic ground state which evolves into collinear commensurate AFM state. Features in the dielectric permittivity coincide with the onset of the commensurate AFM order giving away also the contribution of the  $\alpha$ - structural domains.

Further understanding of the mechanisms that dictate the relief of frustrated interactions and establishment of magnetic order together with the role of structural complexity in the form of domains or domain-walls is a direction that warrants further exploration as it will

help us to resolve whether other coupled electron degrees of freedom are likely to be generated in this family of oxides.

## ΠΕΡΙΛΗΨΗ

Η ανακάλυψη υλικών στα οποία συνυπάρχει μαγνητική και σιδηροηλεκτρική τάξη έχει ανατροφοδοτήσει το ενδιαφέρον στον τομέα της φυσικής συμπεκνωμένης ύλης και στην ευρύτερη κοινότητα της επιστήμης των υλικών ενθαρρύνοντας την έρευνα με σκοπό την αξιοποίηση θεμελιωδών φυσικών μηχανισμών στην επινόηση τεχνολογικών εφαρμογών.

Η παρούσα διδακτορική διατριβή αποτελεί μελέτη στο πεδίο των ισχυρά συσχετιζόμενων συστημάτων όπου οι συζευγμένες ιδιότητες προκύπτουν σαν αλληλεπίδραση των βαθμών ελευθερίας του ηλεκτρονίου (φορτίο, ιδιοστροφομή). Η τοπολογία κρυσταλλικού πλέγματος μπορεί να διαμορφώσει αυτή την αλληλεπίδραση επιτρέποντας ανταγωνιστικές μαγνητικές αλληλεπιδράσεις και πιθανή σύζευξη ηλεκτρικής και μαγνητικής τάξης. Για την παραπάνω μελέτη επιλέχθηκαν διαφορετικές πολυμορφικές φάσεις του συστήματος Na-Mn-O λόγω της ενδογενούς γεωμετρικής (μαγνητικής) όχλησης που προκύπτει από την τρίγωνη τοπολογία του κρυσταλλικού πλέγματος των κατιόντων μαγγανίου.

Μεταξύ των υποστοιχειομετρικών σε Νάτριο πολύμορφων της οικογένειας, μονοκρυστάλλοι του  $\alpha\text{-Na}_{0.7}\text{MnO}_2$  αναπτύχθηκαν με σκοπό την μελέτη των ανταγωνιστικών σιδηρομαγνητικών και αντισιδηρομαγνητικών αλληλεπιδράσεων όπως αυτές προκύπτουν λόγω του μικτού σθένους του μαγγανίου ( $\text{Mn}^{4+} / \text{Mn}^{3+}$ ). Στην ύπαρξη ανταγωνιστικών αλληλεπιδράσεων αποδίδεται η μαγνητική αστάθεια του συστήματος που οδηγεί σε βασική κατάσταση υαλώδους σπιν όπως και οι «ανωμαλίες» που παρατηρούνται στις μετρήσεις διηλεκτρικής σταθεράς.

Οι ίδιες ανταγωνιστικές αλληλεπιδράσεις εξετάζονται ως αιτία της ανισοτροπικής μαγνητικής συμπεριφοράς των κρυστάλλων  $\alpha\text{-Na}_{0.96}\text{MnO}_2$ . Πειράματα σκέδασης νετρονίων αποκαλύπτουν την εγκαθίδρυση σύμμετρης αντισιδηρομαγνητικής τάξης στην θεμελιώδη κατάσταση η οποία εξαφανίζεται πάνω από τους 26 K ενώ συνυπάρχουσα στρεβλωμένη αντισιδηρομαγνητική κατάσταση επιμένει μέχρι τους 45 K. Ασθενή φαινόμενα στην θερμοκρασιακή εξέλιξη της διηλεκτρικής σταθεράς εμφανίζονται στα σημεία μαγνητικής μετάβασης στην σύμμετρη κατάσταση μακράς εμβέλειας ( LRO) επισημαίνοντας σύζευξη μεταξύ ηλεκτρικής και μαγνητικής τάξης.

Στην περίπτωση του στοιχειομετρικού πολύμορφου  $\beta\text{-NaMnO}_2$ , η εναλλαγή στην ύπαρξη μικροδομικών περιοχών που ανήκουν και στα 2 πολύμορφα ( $\alpha$ - ,  $\beta$ -) διαμορφώνει μια θεμελιώδη κατάσταση ελικοειδούς σπιν ενώ και σε αυτή την περίπτωση διηλεκτρικές

«ανωμαλίες» συναντώνται στην θερμοκρασία εγκαθίδρυσης της σύμμετρης αντισιδηρομαγνητικής τάξης.

Περαιτέρω κατανόηση των μηχανισμών που υπαγορεύουν άρση της όχλησης και εγκαθίδρυση μαγνητικής τάξης καθώς και ο ρόλος της κρυσταλλικής ανομοιογένειας αποτελεί πεδίο συνεχιζόμενης έρευνας και μπορεί να οδηγήσει στην κατανόηση του τρόπου σύζευξης βαθμών ελευθερίας συζευγμένων ηλεκτρονίων και πως αυτό μπορεί να οδηγήσει σε σύζευξη ηλεκτρικής και μαγνητικής τάξης σε αυτήν την οικογένεια οξειδίων.

<b>Abstract</b> .....	i
<b>Περίληψη</b> .....	iii
<b>Contents</b> .....	v
<b>List of Figures</b> .....	x

## CONTENTS

<b>1 CHAPTER ONE: INTRODUCTION</b>	<b>1</b>
<b>1.1 Scope</b>	<b>1</b>
1.1.1 Methods	3
<b>1.2 Single Ion interactions</b>	<b>3</b>
1.2.1 Ions in anisotropic environments	3
1.2.1.1 Crystal fields	3
1.2.1.2 Jahn-Teller effect	5
1.2.2 Classification of layered structures	6
<b>1.3 Collective interactions- Magnetism</b>	<b>9</b>
1.3.1 Magnetic Interactions	9
1.3.1.1 Superexchange	10
1.3.1.2 Double-exchange	11
1.3.1.3 Dzyaloshinskii-Moriya	11
1.3.2 Magnetic response to an external field	12
1.3.3 Magnetic order	13
1.3.3.1 Antiferromagnetic order	14
1.3.1 Complex magnetic structures	16
1.3.2 Dimensionality of Magnetic Lattices	17
1.3.2.1 Competing interactions and low dimensionality	17
1.3.2.2 Origin of Spin gap	18
<b>1.4 Frustration</b>	<b>20</b>
1.4.1 Triangular lattice antiferromagnet	22
1.4.2 Magnetic ground state of frustrated systems	23
1.4.2.1 The spin-glass state	23
1.4.2.2 Re-entrant spin-glass	24

<b>1.5 Multiferroicity and Magnetoelectricity</b>	<b>25</b>
1.5.1 Classification of multiferroics	28
1.5.1.1 Type I Multiferroics	28
1.5.1.2 Type II Multiferroics- Improper MFs	28
1.5.1.3 Type III Multiferroics – Disordered MFs	29
1.5.2 Coupling of magnetic and electric degrees of freedom- Requirements	29
1.5.2.1 Electron configuration	29
1.5.2.2 Symmetry	30
1.5.2.3 Ordering	31
1.5.2.4 Geometry of structure	31
1.5.2.5 Electric properties	32
1.5.3 Classification of driving mechanisms based on electrons degrees of freedom	33
1.5.4 Magnetoelectric effect	34
<b>1.6 Structure of Dissertation</b>	<b>35</b>
<b>2 CHAPTER TWO: EXPERIMENTAL METHODS</b>	<b>37</b>
<b>2.1 Solid state synthesis</b>	<b>37</b>
<b>2.2 Single Crystal growth</b>	<b>38</b>
2.2.1 Flux method	39
2.2.2 Floating zone technique	40
<b>2.3 Basic Structural and Chemical characterization techniques</b>	<b>42</b>
2.3.1 X-ray diffraction[93], [94]	42
2.3.1.1 X-Ray Powder Diffraction (XRPD)	47
2.3.1.2 Single Crystal X-Ray Diffraction	49
2.3.1.3 X-ray Laue method	51
2.3.2 Inductively Coupled Plasma Mass Spectroscopy (ICP-MS)	52
2.3.3 X-Ray Photoelectron spectroscopy (XPS)[96]	53
2.3.4 Scanning electron microscopy –Electron dispersive spectroscopy (SEM-EDS)[97]	54
<b>2.4 Macroscopic physical property probing</b>	<b>55</b>
2.4.1 Superconducting Quantum Interference Device (SQUID)[99]	55
2.4.2 Dielectric Constant measurements	58
2.4.3 Custom Magneto-electric Station	62
2.4.3.1 Custom made Sample insert	63
2.4.3.2 Sample preparation and mounting	65
2.4.3.3 Physical Property Measurement System (PPMS)[100]	68
2.4.4 Issues during DE measurements- Standardization and improvement of the set up	70

2.4.4.1	Effect of electrical contacts on capacitance measurements	70
2.4.4.2	Linearity of temperature ramp	71
2.4.4.3	Humidity	73
2.4.4.4	Elimination of electronic noise [105]	76
2.4.5	Nuclear Magnetic Resonance (NMR)	76
2.4.5.1	Solid State NMR	77
2.4.5.2	Types of magnetic relaxation	77
<b>2.5</b>	<b>Studies in International Large-scale Facilities</b>	<b>79</b>
2.5.1	Synchrotron X ray scattering [94]	79
2.5.2	Neutron Diffraction [107]–[109]	80
2.5.2.1	Nuclear Neutron scattering	81
2.5.2.2	Magnetic Neutron diffraction	83
2.5.2.3	Constant wave length (CW)	83
2.5.2.4	Time of flight (TOF)	84
2.5.2.5	Inelastic Neutron scattering[111]	86
2.5.1	Analysis of diffraction Data (Le Bail & Rietveld methods) [93], [112]–[115]	88
2.5.1.1	Least-Squares refinement techniques	89
<b>3</b>	<b>CHAPTER THREE: CHEMICAL SYNTHESIS OF NA-MN-O SYSTEM</b>	<b>93</b>
<b>3.1</b>	<b>Introduction</b>	<b>93</b>
<b>3.2</b>	<b>Sample preparation</b>	<b>95</b>
3.2.1	Polycrystalline specimens	95
3.2.1.1	The alpha polymorph	95
3.2.1.2	The beta polymorph	97
3.2.2	Single crystal growth- The Flux method	98
3.2.2.1	Results and Discussion	101
3.2.3	Single crystal growth- The Floating Zone method	104
3.2.3.1	Crystals grown from $\alpha$ -NaMnO <sub>2</sub> powders	104
3.2.3.2	Crystals grown from $\beta$ -NaMnO <sub>2</sub> powders	108
3.2.3.3	Summary of synthesis results	113
<b>4</b>	<b>CHAPTER FOUR: PROGRESS ON MAGNETIC STRUCTURE AND MAGNETO-ELECTRIC STUDY ON B-NAMNO<sub>2</sub></b>	<b>115</b>
<b>4.1</b>	<b>Introduction</b>	<b>115</b>
4.1.1	What is already known	116
4.1.2	Contribution of the present work	118

<b>4.2 Phase purity and crystallinity</b>	<b>119</b>
4.2.1 X-Ray powder diffraction- phase purity	119
4.2.1.1 XRPD patterns of $\beta$ -NaMnO <sub>2</sub> samples annealed in O <sub>2</sub>	122
<b>4.3 Macroscopic physical properties</b>	<b>123</b>
4.3.1 Magnetic measurements	123
4.3.1.1 Experiment and sample preparation	123
4.3.1.2 Dc susceptibility measurements	123
4.3.2 Heat Capacity	127
4.3.2.1 Experiment and sample preparation	127
4.3.2.2 Heat capacity hints magnetic transitions	127
<b>4.4 Phase transition's impact on the spin dynamics: NMR study</b>	<b>129</b>
4.4.1 Experiment and sample preparation	129
4.4.2 <sup>23</sup> Na Dynamics near the transition	129
<b>4.5 Crystal structure evolution- Neutron powder diffraction study</b>	<b>133</b>
4.5.1 Experiment and sample preparation	133
4.5.2 Determination of crystallographic structure[147]	134
<b>4.6 Magnetic Structure evolution topologically correlated to defected lattice[147]</b>	<b>139</b>
4.6.1 CM and IC magnetic structures	139
4.6.2 Magnetic Spin configurations	141
<b>4.7 Parameterization of Magnetic excitations-INS study [147]</b>	<b>146</b>
4.7.1 Experiment and sample preparation	146
4.7.2 Spin gap and dimensionality of magnetic interactions	146
<b>4.8 Magneto-electric response</b>	<b>148</b>
4.8.1 Experiment and sample preparation	149
4.8.2 Dielectric permittivity of $\beta$ -NaMnO <sub>2</sub> "as made"	151
4.8.2.1 Effect of frequency on the dielectric permittivity	154
4.8.2.2 Ac-electric field effect	157
4.8.2.3 Effect of magnetic field	158
4.8.3 Dielectric permittivity of $\beta$ -NaMnO <sub>2</sub> "annealed in O <sub>2</sub> "	160
4.8.3.1 Effect of magnetic field	162
<b>4.9 Discussion</b>	<b>165</b>
<b>4.10 Summary and Conclusions</b>	<b>169</b>

<b>5</b>	<b>CHAPTER FIVE: QUEST FOR SINGLE CRYSTALS IN 2 D MANGANITES: A- NA<sub>0.7</sub>MNO<sub>2</sub></b>	<b>171</b>
<b>5.1</b>	<b>Introduction</b>	<b>171</b>
5.1.1	Crystal structure and physical properties	172
5.1.2	Contribution of the present work	173
<b>5.2</b>	<b>Crystal structure</b>	<b>174</b>
5.2.1	X-Ray Powder Diffraction	174
5.2.1.1	Experiment and sample preparation	174
5.2.1.2	Phase purity of starting powders and grown crystals	174
5.2.2	Laue Method	177
5.2.3	Single Crystal x-ray Diffraction	179
5.2.3.1	Experiment and sample preparation	179
5.2.3.2	Structure and stacking	179
<b>5.3</b>	<b>Chemical characterization</b>	<b>185</b>
5.3.1	SEM-EDS	185
5.3.1.1	Experiment and sample preparation	185
5.3.1.2	Layered structure and Na:Mn ratio	185
5.3.2	XPS	187
5.3.2.1	Experiment and sample preparation	187
5.3.2.2	Quantification of mixed valence ratio	187
<b>5.4</b>	<b>DC-magnetization study</b>	<b>189</b>
5.4.1	Experiment and sample preparation	189
5.4.2	Spin-Glass behavior and magnetic anisotropy	190
<b>5.5</b>	<b>Dielectric response of h-NMO crystals</b>	<b>195</b>
5.5.1	Experiment and sample preparation	195
5.5.2	Effects on the dielectric permittivity	196
<b>5.6</b>	<b>Results and Discussion</b>	<b>197</b>
<b>5.7</b>	<b>Summary and Conclusions</b>	<b>200</b>
<b>6</b>	<b>CHAPTER SIX: STUDY OF THE TRIANGULAR ANTIFERROMAGNET A- NAMNO<sub>2</sub> – FROM POWDERS TO SINGLE CRYSTALS</b>	<b>202</b>
<b>6.1</b>	<b>Introduction- The <math>\alpha</math>-NaMnO<sub>2</sub> system</b>	<b>202</b>
6.1.1	Structure and polymorphism	203
6.1.2	Magnetic structure and interactions	204

6.1.3	Deviations from stoichiometry and competing interactions	206
6.1.4	The quest for single crystal and contribution of the present work	206
<b>6.2</b>	<b>Phase purity and Crystallinity</b>	<b>207</b>
6.2.1	X-Ray Powder Diffraction	207
6.2.1.1	Experiment and sample preparation	207
6.2.1.2	Polycrystalline specimens of $\alpha$ -Na-Mn-O	208
6.2.1.3	Single crystals of $\alpha$ -Na-Mn-O	209
6.2.2	Laue Method	212
6.2.3	Single crystal X-ray diffraction	214
6.2.3.1	Experiment and sample preparation	214
6.2.3.2	Results and issues	215
<b>6.3</b>	<b>Chemical characterization</b>	<b>219</b>
6.3.1	ICP-MS	219
6.3.1.1	Experiment and sample preparation	219
6.3.1.2	Results and drawbacks	219
6.3.2	SEM-EDS	220
6.3.2.1	Experiment and sample preparation	220
6.3.2.2	Layered crystals and off stoichiometry	220
6.3.3	XPS	223
6.3.3.1	Experiment and sample preparation	223
6.3.3.2	Quantification of mixed valence ratio	224
<b>6.4</b>	<b>Synchrotron X-ray Powder Diffraction (XPD)</b>	<b>226</b>
6.4.1	Experiment and sample preparation	226
6.4.2	Structural considerations	227
<b>6.5</b>	<b>DC-magnetization study</b>	<b>234</b>
6.5.1	Experiment and sample preparation	235
6.5.2	Canting behavior witnessed in magnetization measurements of $\alpha$ -Na <sub>0.96</sub> MnO <sub>2</sub> single crystals	235
6.5.3	Powders versus single crystals	240
<b>6.6</b>	<b>Single crystal neutron diffraction</b>	<b>241</b>
6.6.1	Experiment and sample preparation	241
6.6.2	Evaluation of Single Crystal Neutron Diffraction	242
6.6.3	Possible Spin configuration	249
<b>6.7</b>	<b>Magneto- electric response</b>	<b>252</b>
6.7.1	Experiment and sample preparation	253
6.7.2	Studies on $\alpha$ -NaMnO <sub>2</sub> powders	254

6.7.2.1	Effect of frequency on the dielectric permittivity	256
6.7.2.2	Effect of magnetic field	258
6.7.3	Studies on $\alpha$ - $\text{Na}_{0.96}\text{MnO}_2$ crystals	261
<b>6.8</b>	<b>Effects of deviation from stoichiometry- discussion</b>	<b>263</b>
<b>6.9</b>	<b>Summary and Conclusions</b>	<b>266</b>
<b>7</b>	<b>CHAPTER SEVEN: WAKE &amp; PERSPECTIVES</b>	<b>268</b>
<b>7.1</b>	<b>Literature Studied</b>	<b>272</b>
<b>8</b>	<b>APPENDIX A: MD-STATION OF FUNL</b>	<b>I</b>
<b>9</b>	<b>APPENDIX B: STUDY OF B-NAMNO<sub>2</sub> MODULATIONS THROUGH SUPERSPACE FORMALISM</b>	<b>I</b>
<b>10</b>	<b>APPENDIX C: SINGLE CRYSTAL HOLDER FOR NEUTRON DIFFRACTION EXPERIMENT</b>	<b>I</b>

## TABLE OF FIGURES

Figure 1-1	Crystal field splitting of the d-orbital in an octahedral crystal environment [11] .....	4
Figure 1-2	Magnetic ion (purple sphere) in a (a) non-distorted and a (b) Jahn-Teller distorted octahedral environment of Oxygen ions (red and yellow spheres) .....	5
Figure 1-3	The 3d energy levels of $\text{Mn}^{3+}\text{O}_6$ in an octahedral environment before (left) and after (right) o Jahn Teller distortion .....	6
Figure 1-4	Classification of the different layered structures adopted in Na-Mn-O systems.MeO <sub>6</sub> layers are in blue and Na cation in yellow. [13].....	8
Figure 1-5	Two mangetic atoms interacting with an oxygen atom ,O. (a)Antiferromagnetic alignment is favored by superexchange interaction since it allows movement of the oxygen atom in contrary to (b) and (c).....	10
Figure 1-6	The single state exchange interaction favours hopping if neighbours are (a)FM aligned and does not favor hopping when neighbouring ions are (b) AFM aligned [11] .....	11
Figure 1-7	Top panel: Schematic representation of magnetic ordering in A,C,E and G- type Antiferromagnets. Bottom panel:(a)ferromagnetic (B) antiferromagnetic and (c) ferromagnetic spin alignements .....	15

Figure 1-8 Schematic of cycloid and proper screw type magnetic ordering [18] .....	16
Figure 1-9 Schematics of non-collinear magnetic ordering as presented in reference [19] showing the direction of developing polarization in the cycloidal and transverse conical propagation.....	17
Figure 1-10 Schematic of the geometry of 2-leg and 3-leg spin ladders as crossover between 1D chain and 2D spin system. Reprinted from reference [29].....	20
Figure 1-11 (a) Non-frustrated square lattice where each spin can be antialigned antiferromagnetically with all each neighbors (b) Frustrated Triangular lattice where two neighboring spins are paired AFM while simultaneously the third remains frustrated.....	21
Figure 1-12 Schematics of geometrically frustrated (a) triangular lattice, (b) kagomé lattice, (c) pyrochlore lattice as it is partially reprinted by references [32,35].....	22
Figure 1-13 Illustration of “multiferroism” as a combination of “ferroic” properties related to lattice, spin and charge. In a ferroic material, polarization P, magnetization M and strain $\epsilon$ , are spontaneously formed to produce ferromagnetism, ferroelectricity or ferroelasticity, respectively.	25
Figure 1-14 Venn diagram reprinted from J.F.Scott [2] after Eerenstein et al. [1] with representative oxides after Bibes et al. [62]. .....	27
Figure 1-15 Schematic representation of the effect of spatial inversion and time reversal on (a) ferromagnets, (b) ferroelectrics, (c) multiferroics. Reproduced from reference [1].....	31
Figure 1-16 Multiferroics family tree reprinted by reference [64] Different combinations of ‘root’ magnetic and ferroelectric mechanisms are presented. ....	32
Figure 1-17 Schematic of the three mechanisms( spin-charge, spin-orbit, spin-lattice) behind the magnetoelectric coupling. Charge dipole on the left indication of ferroelectricity a magnetic moment on the right indicative of magnetism.....	33
Figure 2-1 Schematic (internal view) of high temperature box furnace during the Flux growth of single crystals.....	40
Figure 2-2 Schematic of an optical furnace with feed and seed rods mounted. ....	42
Figure 2-2-3 The diffraction processing real space. Parallel monochromatic x-rays (red) are incident on the planes of atoms (purple spheres. The scattered rays that are in phase with one another are shown in blue. Reproduced from Thesis of Dr Wooldridge.....	43
Figure 2-4 Top panel: The incident ( $k_0$ ) and diffracted ( $k_1$ ) wavevectors originating from a common point (left) and the same two vectors overlapped with the two-dimensional reciprocal lattice, which is based on the unit vectors $a^*$ and $b^*$ (right). The origin of the reciprocal lattice is chosen at the end of $k_0$ . Bottom panel: The visualization of diffraction using the Ewald’s sphere	

with radius $1/\lambda$ and the two dimensional reciprocal lattice with unit vectors $a^*$ and $b^*$ . The origin of the reciprocal lattice is located on the surface of the sphere at the end of $k_0$ .	44
Figure 2-5 Two dimensional diffraction pattern of a stationary (left) and rotating (right) single crystal. The incident wavevector is perpendicular to both the detector and the plane of the figure. Dash dotted line show the rotation axis which is collinear with $c^*$ .	45
Figure 2-6 (a) X-rays diffracted by single crystal produce a series of spots in Ewald sphere (b) All orientations are present resulting in continuous Debye rings. This gives the linear diffraction pattern with discrete reflections.	46
Figure 2-7 Incident X-rays are scattered by a polycrystalline sample according to the aforementioned Bragg's law in a Bragg-Brentano topology. Reprinted by " <a href="http://pd.chem.ucl.ac.uk/pdnn/inst1/optics1.htm">http://pd.chem.ucl.ac.uk/pdnn/inst1/optics1.htm</a> "	48
Figure 2-8 Sample holder sealed with Mylar (a) and the base of the same holder where the pulverized powder is placed.	49
Figure 2-9 Left: Schematic of 4-circle diffractometer geometry. The angles between the incident ray, the detector and the sample are noted. Right: Actual picture of Bruker D8 venture geometry used in the present study reproduced from Bruker.com.	50
Figure 2-10 Schematic diagram describing a back-scattered Laue experiment. A white beam (red arrow) is incident to the crystal and diffracted beams are visible as a series of unique spots on the ccd camera.	52
Figure 2-11 Schematic of a Scanning Electron Microscope (SEM) reprinted by the webpage of Diamond industry news. [13]	55
Figure 2-12 Schematic illustration of the SQUID operation reproduced from "MPMS MultiVu Application User's Manual"	57
Figure 2-13 Curie-Weiss susceptibility of different magnetic system above the ordering temperature. The inverse susceptibility is plotted and used to extract the $\theta$ temperature which is $\theta < 0$ for an antiferromagnet, $\theta = 0$ for a paramagnet and $\theta > 0$ for a ferromagnet.	57
Figure 2-14 (a) Ideal, Real and Measured values in a capacitor topology, (b) parallel equivalent circuit mode for capacitor measurements.	59
Figure 2-15 A parallel plate capacitor, where electrodes are separated by (a) vacuum (b) a dielectric material. (c) Schematic of the wiring and connection of the sample insert for dielectric measurements.	60

Figure 2-16 Magnetolectric station (MD) used for the in house magneto dielectric measurements .....	62
Figure 2-17 Initial design of the MD probe (a) length of the sample space from the top hat (b) choice of the suitable temperature sensor (c) Teflon bottom cover for protection and (d) design of the sample space and removable sample holder.....	64
Figure 2-18 (a) MD carbon fiber stick, (b) lower carrier socket on brass frame and 2 detachable sample holders/carriers, (c) 4 wires come down to lower carrier socket from isolated Teflon flange, (d) 4TP wiring sketch, (e) GND according to 4TP and noise shield in the lower carrier socket, (f) sample wired with 4TP as a capacitor, (g) “Sample holder1 – capacitor topology”, no wires on sample, (h) “Sample holder2- Flat multi pin carrier 2 or 4 probe wire connections to the sample, (i) sample connected as a capacitor using paste (sketch of (f)).....	65
Figure 2-19 “Sample holder 1- Capacitor topology” on the left and “Sample holder 2- Flat multipin carrier” on the left side with no samples mounted. ....	66
Figure 2-20 (a) Parallel to H field orientation of the sample carrier- Sample Holder2 (b) Vertical to field orientation of the sample carrier- Sample Holder1 .....	67
Figure 2-21 Exploded view of the plug-in designed puck and sample platform used in PPMS for standard Heat Capacity measurements [15] .....	69
Figure 2-22 BaTiO <sub>3</sub> test measurements using different contact pastes. Details found in the text. ..	71
Figure 2-23 (a) Temperature ramp with a big inertia due to heavy mass of the holder (b) after the correction of the mass but still non-linear in high temperatures where N <sub>2</sub> flow should be less (c) After the control of the N <sub>2</sub> flow into the cryostat.....	73
Figure 2-24 Effect of rapid increase of the dielectric constant above 230 K observed also in the dielectric Loss. ....	74
Figure 2-25 (a) Capacitance measurement after which the sample came out soaked in droplets. (b) modification of the top hat with high vacuum paste. ....	75
Figure 2-26 Top panel: (left) Schematic of a non-guarded topology which exhibits stray capacitance. (right) Insertion of a shielding plate so that all grounds are connected there. Bottom panel: Actual photo of the implementation of the afore mentioned “noise” shielding by addition of a copper plate on the back of the holder.....	76
Figure 2-27 Solid echo pulse sequence .....	77
Figure 2-28 Inversion recovery pulse sequence for measuring T <sub>1</sub> .....	78

Figure 2-29 The scattering triangle relating the incident and final wavevectors to the scattering wavevector .....	81
Figure 2-30 Neutron scattering geometry after Squires [24] .....	82
Figure 2-31 Schematic of layout of the WISH diffractometer in TS2 –ISIS reprinted from science case reference [25] .....	85
Figure 2-32 The scattering triangle for incident and final wave vectors in the case of inelastic scattering. ....	87
Figure 3-1 Solid state synthesis protocol of $\alpha$ -NaMnO <sub>2</sub> polycrystalline powders.....	96
Figure 3-2 Solid state synthesis protocol of $\beta$ -NaMnO <sub>2</sub> polycrystalline powders .....	97
Figure 3-3 Heating protocol followed for both the mixtures using NB and NNB Fluxes. ....	100
Figure 3-4 Topology of the crucible used for the flux growth for NB Flux (a) and NNB Flux (b) after the cool down. Overflow of the solution is obvious. ....	101
Figure 3-5 (a)& (b) Pictures of the result as it came out of the furnace from NB and NNB Fluxes respectively. (c) An amount of needle crystals in the process of diluting the NNB Flux in distilled water and (d) in acetone. (e) An amount of needle crystals free of Flux in a water droplet.....	102
Figure 3-6 A mixture of beta phases is confirmed for the needle crystals grown using the NNB Flux. An amount of pulverized needles had been mixed with grease and placed on a glass. This explains the amorphous picture in the low-angle area. ....	103
Figure 3-7 Left panel- SEM image of 3 different needles mechanically extracted from NNB flux growth. Right panel- zoom in the edge of needle two confirms a layered structure.....	103
Figure 3-8 (a) Shape powder in a cylindrical rod by hand pressing it inside a ballon (b) cut-reveal the rod after being isostatically pressed under 6 tons (c) The drill used in order to drill the sintered feed rod and prepare it for suspension (d) Both feed rod (inside alumina crucible) and seed rod being ready for mounting on the shafts of the mirror furnace.....	105
Figure 3-9 (a) Both feed (top) and seed (bottom) rods mounted and aligned in the 2-mirror furnace and sealed under Ar-pressure inside the quartz tube (b) Well-formed molten zone during the growth of batch #9 (c) The quartz tube coated with thin powder right after the growth while still under Ar atmosphere. ....	105
Figure 3-10 (a-b) Lump-like crystal boule from early growth attempts. The crystal flakes after the lump had been crushed proved useful for primal characterization and further optimization of the protocol (c-d) Long crystal boule with facets of $\alpha$ -Na <sub>0.96</sub> MnO <sub>2</sub> system (d) Cleaved single crystal flakes from the as-grown crystal boule along the b-axis of the monoclinic cell. ....	108

Figure 3-11 X-ray patterns of feed rods that have experienced different sintering conditions. Black star indicates peak of $\alpha$ - $\text{Na}_{0.7}\text{MnO}_2$ , blue star peak of $\alpha$ - $\text{NaMnO}_2$ and blue arrow peak of $\text{Mn}_3\text{O}_4$ . .....	110
Figure 3-12 (a-b) Issues of decomposing while trying to form a molten zone (c-d) 2-phase melt causing drops of melt over the already crystallized sample .....	111
Figure 3-13 Crystal boules grown using beta polymorph as starting powder. Several crystal flakes could only be separated after crushing the as grown boule.....	111
Figure 3-14 (a) Coated quartz tube after the first #1 growth attempt using $\beta$ - $\text{NaMnO}_2$ as starting powder. (b) Coated quartz tube after the #5 growth attempt using $\beta$ - $\text{NaMnO}_2$ as starting powder which resulted in crystal boule of $\text{Na}_{0.7}\text{MnO}_2$ .....	112
Figure 4-1 Schematic representation of the Mn sublattice topology, in the orthorhombic (Pmmn) $\beta$ - $\text{NaMnO}_2$ polymorph. (a) The Mn-Mn distances drawn, depict the possible intra-layer magnetic exchange coupling pathways ( $J_1$ to $J_3$ ). .....	117
Figure 4-2 Sketch of the magnetic structure of the $\beta$ - polymorph. The strong AFM chains run along $\mathbf{a}_0$ and $\mathbf{b}_0$ direction. ....	118
Figure 4-3 X-Ray Powder Diffraction pattern of the polycrystalline $\beta$ - $\text{NaMnO}_2$ at room temperature. The green vertical lines correspond to the orthorhombic cell indexed according to the 16271 file of ICSD database. The blue vertical lines are attributed to the monoclinic C/2m cell of $\alpha$ - $\text{NaMnO}_2$ (ICSD 21028). The red arrows represent the reflections of the mylar film. ....	120
Figure 4-4 Results of the modified protocols as described in table-1 for the $\beta$ - $\text{NaMnO}_2$ . The 4 gr batches have been used as starting powders for the single crystal growth attempts. In the batches eza001, eza003 we note apart from the presence of the 001 peak of $\alpha$ - $\text{Na}_{0.7}\text{MnO}_2$ (vertical line in turquoise).....	121
Figure 4-5 X-Ray Powder Diffraction pattern, taken at room temperature, of polycrystalline $\beta$ - $\text{NaMnO}_2$ samples extra annealed at 300°C under $\text{O}_2$ flow. ....	122
Figure 4-6 Magnetic susceptibility and inverse magnetic susceptibility of beta- $\text{NaMnO}_2$ for under 10 Oe (top panel) and 70 kOe (bottom panel).....	124
Figure 4-7 TRM measurements after cooling under 7T field with 2K increment.....	125
Figure 4-8 Field dependent Hysteresis loops of $\beta$ - $\text{NaMnO}_2$ measured at 5K, 50K, 90K, 170K, 300K.....	126
Figure 4-9 Magnetic susceptibilities of $\alpha$ and $\beta$ $\text{NaMnO}_2$ polymorphs with blue and black patterns, respectively. ....	126

Figure 4-10 Left panel: The measured heat capacity, $C(T)$ of $\beta$ - $\text{NaMnO}_2$ . The red line over the $C(T)$ data is the calculated phonon contribution to the specific heat, $C_{\text{ph}}(T)$ . Right panel: Zoomed in areas of features correlated to magnetic phase transitions .....	127
Figure 4-11 The heat capacity remaining after subtracting the $C_{\text{ph}}(T)$ (black line) contribution from the experimental $C_{\text{exp}}(T)$ depicts two featured peaks assigned as $T_{\text{N1}}$ and $T_{\text{N2}}$ . The calculated $S_{\text{mag}}$ is presented in blue following the pattern of the aforementioned peaks in $C_{\text{mag}}$ .....	128
Figure 4-12 Normalized $^{23}\text{Na}$ NMR powder spectra of $\beta$ - $\text{NaMnO}_2$ revealing two different magnetic regimes that evolve with temperature lowering. The spectra are shifted vertically for clarity. The insets point to a specific part of the spectra, where the quadrupolar frequency is indicated by the vertical dashed line.....	131
Figure 4-13 (a) The temperature dependence of the $^{23}\text{Na}$ NMR central line intensity multiplied by temperature for $\beta$ - $\text{NaMnO}_2$ . The arrows indicate the two transition temperatures $T_{\text{N1}}$ and $T_{\text{N2}}$ . (b) Normalized magnetization-recovery curves at selected temperatures. The datasets are shifted vertically for clarity. The solid lines are fits of a stretched single-component magnetic-relaxation model for $I = 3/2$ (Eq. 4-3; see text), while the dashed line corresponds to the fit with two such components, AFM1 and PM. (c) The temperature dependence of the spin-lattice relaxation rate for $\beta$ - $\text{NaMnO}_2$ . The arrows indicate the two transition temperatures. A double-component fit is needed in the intermediate temperature regime $T_{\text{N2}} < T < T_{\text{N1}}$ . The solid lines indicate a critical type of behavior for $T > T_{\text{N2}}$ and an activated one for $T < T_{\text{N2}}$ (see text for details).....	132
Figure 4-14 Model of the average nuclear structure (Pmnm space group) of $\beta$ - $\text{NaMnO}_2$ obtained from the Rietveld refinement of the main reflections of the WISH powder patterns (see main text): top, highlighting the unusually large anisotropic thermal parameter elongated along the $c$ direction for the oxygen atoms; bottom, the splitting of the oxygen-site position, suggested from the anisotropic thermal parameters. Reprinted from reference 19. ....	135
Figure 4-15 Rietveld plot at 300 K for the $\beta$ - $\text{NaMnO}_2$ structure in the $\text{Pmnm}(\alpha 00)000$ superspace group. Inset: zoom of the low $d$ -spacing region inferring that stacking faults and defects give rise to a peculiarly broadened profile function. In both panels observed (black crosses), calculated (red line) and difference (blue line) pattern are shown. The tick marks indicate the calculated position of the main (black ticks) and satellite reflections (green ticks). The asterisk marks the main reflection of the $\alpha$ - $\text{NaMnO}_2$ impurity, whereas the hash-tags indicate, for example, two satellite peaks that are slightly off with respect to the calculated Bragg position indicating the possibility of the other two components of the modulation vector to be different from zero (see text for details). Reprinted from reference 19.....	136

Figure 4-16 Projection of the structure in the ac-plane, depicting the refined incommensurate compositional modulated structure; two types of stacking changing between the NaMnO<sub>2</sub> polymorphs are shown. The violet atoms represent the Mn, the yellow ones the Na, and the red spheres the oxygen atoms. The small rectangle indicates the unit cell of the average Pmmn structure (Appendix B, Figure I). Reprinted from reference 19..... 138

Figure 4-17 Fourier maps of the observed structure factor ( $F_{\text{obs}}$ ) depicting the crystallographic cation sites (a) and oxygen positions (b). The solid colored lines represent the calculated position of the atoms showing no positional modulation along the  $x_4$  for the Mn/Na but its presence for the oxygen sites (violet Mn, green Na, red oxygen and blue the primed oxygen position). The black continuous lines indicate the positive density iso-surface and the dashed lines the negative iso-surface (the neutron scattering length for the Mn atoms is negative). The iso-surface contours correspond to 2 scattering density units ( $\text{\AA}^{-2}$ ) in all the plots. Reprinted from reference 19..... 139

Figure 4-18 (a) A long d-spacing section of the neutron powder diffraction patterns as a function of temperature, showing the complex nature of the magnetic contribution to the pattern. Color map: the neutron scattering intensity. (b) Integrated intensity versus temperature for the main magnetic reflections with propagation vector  $\mathbf{k} = (\frac{1}{2}, \frac{1}{2}, \frac{1}{2})$ , and for the satellites with propagation vector  $\mathbf{k} + \mathbf{q}$ , where  $\mathbf{q} = (0.077(1), 0, 0)$ . The lines over the data points depict the fit to the critical region (details in text). Reprinted from reference 19 ..... 140

Figure 4-19 (a) Rietveld plot at 100 K of the  $\beta$ -NaMnO<sub>2</sub> structure in  $C_{a2}/c'(\alpha 0\gamma)00$  superspace group, with cell parameters  $a = 5.7108(2) \text{ \AA}$ ,  $b = 12.6394(9) \text{ \AA}$ ,  $c = 5.5397(4) \text{ \AA}$ ,  $\beta = 120.96(7)^\circ$ , and  $\mathbf{q} = (0, 0, 0.078(1))$ . Observed (black crosses), calculated (red line) and difference (blue line) patterns are reported. The tick marks indicate the calculated position of the main (black ticks) and satellite reflections (green ticks). The asterisk marks the main nuclear and magnetic reflections from the  $\alpha$ -NaMnO<sub>2</sub> impurity phase, whereas the diamond indicates the main MnO magnetic reflection. (b-c) Sketch of the magnetic structure below 200 K, (a) along the Mn zig-zag chain typical of the  $\beta$ - polymorph ( $\mathbf{a}_0$  direction) and (b) in the same projection as for Figure 4-11 (top panel). The black rectangle depicts the unit cell of the average Pmmn structure ( $a_0 = 4.7851(2) \text{ \AA}$ ,  $b_0 = 2.85699(8) \text{ \AA}$ ,  $c_0 = 6.3287(4) \text{ \AA}$ ), while the red rectangle indicates the unit cell of the average low temperature monoclinic structure ( $a_m = 5.7112(2) \text{ \AA}$ ,  $b_m = 12.6388(9) \text{ \AA}$ ,  $c_m = 5.5365(4) \text{ \AA}$ ,  $\beta = 120.97(7)^\circ$ ); please note that the  $\mathbf{c}_m$ -axis is inclined by  $\sim 60^\circ$  out of the plane. Reprinted from reference 19..... 143

Figure 4-20 (a) Rietveld plot at 5 K for the  $\beta$ -NaMnO<sub>2</sub> structure in  $C_{a2}/c'(\alpha 0\gamma)00$  superspace group, with cell parameters  $a = 5.7112(2) \text{ \AA}$ ,  $b = 12.6388(9) \text{ \AA}$ ,  $c = 5.5365(4) \text{ \AA}$ ,  $\beta = 120.97(7)^\circ$ , and  $\mathbf{q} = (0, 0, 0.081(1))$ . Observed (black crosses), calculated (red line) and difference (blue line) patterns are shown. The tick marks indicate the calculated position of the main (black ticks) and satellite

reflections (green ticks). (b) Schematic of the  $\beta$ -NaMnO<sub>2</sub> modulated magnetic structure at 5 K, projected at the same plane as the nuclear structure shown in Figure 6 (top panel). (c) Sketch of the incommensurate part of the magnetic structure depicting a proper screw order propagating along the (-110) direction with respect to the average Pmmn unit cell. In both panels the axes directions with subscript '0' indicate the average orthorhombic Pmmn cell (black rectangle), whereas the axes with subscript 'm' indicate the direction of the low-temperature monoclinic structure (red rectangle)..... 145

Figure 4-21 (a) The powdered averaged magnetic scattering in  $\beta$ -NaMnO<sub>2</sub> and (b) the corresponding Single Mode Approximation (SMA) heuristic model, with two-dimensional (2D) interactions. Color map: indicates the powder average scattering intensity  $I(Q, \hbar\omega)$ . Reprinted from reference 19..... 147

Figure 4-22 The temperature dependence of the low-energy magnetic fluctuations in  $\beta$ -NaMnO<sub>2</sub>, measured on the high-resolution DCS spectrometer. All data has been corrected for a temperature independent background using the detailed balance relation. Color map: indicates the powder average scattering intensity. Reprinted from reference 19..... 148

Figure 4-23 Dielectric constant ( $\epsilon'_r$ ) (black symbol-left Y-axis) and dielectric loss (black thin line-right Y-axis) of  $\beta$ -NaMnO<sub>2</sub> measured with a ZFC protocol at 111 Hz, applying 741 V/m upon heating. The inset on the  $\epsilon'_r$  (T) shows the weak feature observed below 50 K assigned to the a-phase..... 152

Figure 4-24 Two different runs of Dielectric constant measured at 1 kHz with  $V_{rms}$ = 1600 V/m. (Top panel) The two different runs are taken with 7 hours distance while measurements in other frequencies were taken. Inset- low temperature effect is almost not changed. (Bottom panel) 1<sup>st</sup> derivative curves calculated from dielectric constant against temperature for run1 (red) and run2 (blue). ..... 153

Figure 4-25 Dielectric constant and dielectric loss of  $\beta$ -NaMnO<sub>2</sub> measured at low and high frequency area. (Top panel) Low frequencies measured are 111 Hz, 1 kHz, 20 kHz and (bottom panel) high frequencies are 100 kHz, 500 kHz and 800 kHz. Inset shows the low temperature feature. The two different frequency ranges were measured using different instrumentation. .... 156

Figure 4-26 f-scan of  $\epsilon'_r(T)$  from 111Hz up to 1 MHz. (a-b) f-scan for low temperatures (a) 111Hz- 20 kHz and on the right panel from (b) 30 kHz- 1 MHz are presented. (c-d) f-scan for high temperatures. The two frequency ranges were taken using different instrumentation and this is reason of the offset on the value of the dielectric constant. Nevertheless, the trend is that the magnitude of the  $\epsilon'_r(T)$  is decreasing with the increase of frequency. .... 157

Figure 4-27 The  $\epsilon'_r(T)$  of a  $\beta$ -NaMnO<sub>2</sub> sample measured at 1 kHz under increasing  $V_{rms}$  of the ac test signal. No significant enhancement of the feature has been observed. .... 158

Figure 4-28 Dielectric constant of  $\epsilon'(T)$  of  $\beta$ -NaMnO<sub>2</sub>, measured upon heating at 1 kHz under applied magnetic fields from 0 T- 14 T. Top panel: The whole temperature range. Bottom panel: low temperature area of the same measurement zoomed in. The measurement under zero (0 T) magnetic field was carried out twice: first before the application of the magnetic fields, represented with the turquoise and second in red, after the magnetic fields have been applied..... 159

Figure 4-29 Left-bottom axes (black):  $\Delta\epsilon'$  (%) calculation against Temperature for H= 14 T showing the maximum change in the values of dielectric constant with the application of the external magnetic field. The MDE is of 0.03 % at 43 K. Right-top axes: shift of the critical temperatures  $T_\alpha$  with respect to the applied magnetic fields.  $T_\alpha$  refer to the temperature where the dielectric constant is maximum..... 160

Figure 4-30 right axis: Dielectric constant and dielectric loss of annealed in O<sub>2</sub>  $\beta$ -NaMnO<sub>2</sub> measured at 111 Hz, 1 kHz, 20 kHz. Left axis: 1<sup>st</sup> derivatives of the  $\epsilon'_r(T)$  against T of the same frequencies. The red arrows point the maxima of the features while the dotted vertical lines are a guide to the eye for the Temperature of the change of slope. .... 161

Figure 4-31 f-scan of  $\epsilon'_r(T)$  from 111Hz up to 1 MHz for low temperatures 20K-120K. The two frequency ranges (111 Hz- 20 kHz and 30 kHz to 1 MHz) were taken using different instrumentation. In this case the offset on the value of the dielectric constant has been corrected. .... 162

Figure 4-32 Dielectric constant of  $\epsilon'(T)$  of annealed  $\beta$ -NaMnO<sub>2</sub> measured upon heating at 1 kHz under applied magnetic fields from 0 T- 4 T. Inset shows a close up to the low are feature developed below 100 K..... 163

Figure 4-33 The powdered averaged magnetic scattering in (a)  $\beta$ -NaMnO<sub>2</sub> and (b)  $\alpha$ -NaMnO<sub>2</sub>. The background subtraction method to remove phonon scattering and instrument back-ground is described in the main text. Both datasets were taken on MARI with  $E_i = 85$  meV at T =5 K. Color map: indicates the powder average scattering intensity ..... 167

Figure 5-1 Layered P2 structure of Na<sub>x</sub>MnO<sub>2</sub> (x=0.7) showing the 2 different Na sites. .... 173

Figure 5-2 X-Ray Powder Diffraction pattern of the polycrystalline  $\beta$ -NaMnO<sub>2</sub> at room temperature. The green vertical lines correspond to the orthorhombic cell indexed according to the 16271 file of ICSD database. The blue star is attributed to the monoclinic C/2m cell of  $\alpha$ -NaMnO<sub>2</sub> (ICSD 21028). The grey star indicated a peak attributed to the sample holder (a part of the sample

holder area has not been fully covered with sample powder). The green arrows represents the reflection 011 as defined by Billaud et.al [7] .....	175
Figure 5-3 X-ray-powder diffraction pattern of the feed rod (black line) and a crashed crystal boule (red line) of #11 single crystal batch (table 3-5). Green ticks represent the 15769 card of $\beta$ -NaMnO <sub>2</sub> and turquoise ticks are attributed to $\alpha$ -Na <sub>0.7</sub> MnO <sub>2</sub> phase. Impurities of $\beta$ -Na <sub>0.7</sub> MnO <sub>2</sub> phase (magenta arrow) are observed in the phase of the grown crystal.....	176
Figure 5-4 X-ray-diffraction patterns of a crystal flake of #5 batch (black line) and of the empty sample holder (gray line). Turquoise ticks represent $\alpha$ -Na <sub>0.7</sub> MnO <sub>2</sub> as presented by Parant et. al [1]. .....	177
Figure 5-5 (a-b) Actual picture of boule and cleaved flakes and Laue photograph of the flat side of flake of batch #5. The Laue photograph match the simulation pattern of (001) plane of hexagonal P6 <sub>3</sub> /mmc cell. ....	178
Figure 5-6 (a) Laue photograph of the flat side of a cleaved flake of batch #5 (b) Laue photograph of the flat side of a cleaved flake of batch #12. Both photographs are identical and match the simulation pattern of (001) plane of hexagonal P6 <sub>3</sub> /mmc cell. ....	178
Figure 5-7 Precision picture of reflections of (a) 0kl plane , (c) h0l plane and (e) hk0 plane and simulation using the P6 <sub>3</sub> /mmc hexagonal cell in view direction (b) [001], (d) [010] and (f) [001]. .....	181
Figure 5-8 Schematic of the P6 <sub>3</sub> /mmc hexagonal structure of the crystals $\alpha$ -Na <sub>0.7</sub> MnO <sub>2</sub> ; projections in the (a) ac plane showing the alternation of layers between the MnO <sub>6</sub> octahedra and the Na cations in a prismatic site revealing the P2 stacking sequence. ....	183
Figure 5-9 Schematic of the P6 <sub>3</sub> /mmc hexagonal structure of the crystals $\alpha$ -Na <sub>0.7</sub> MnO <sub>2</sub> ; projections in the ab plane where the triangular topology of the Mn is clear. The MnO <sub>6</sub> octahedra is non Jahn-Teller distorted. Mn is represented by purple spheres and Oxygen with red. ....	183
Figure 5-10 SEM image depicting (a) the layered morphology of the as-grown crystal flake of $\alpha$ -Na <sub>0.7</sub> MnO <sub>2</sub> , (b) a close-up view of the stacking layers. Inset in (a) is the EDS pattern revealing a Na:Mn= 0.68. ....	186
Figure 5-11 A close up of the surface of a flake with a surface stoichiometry ratio of Na:Mn = 0.696.....	186
Figure 5-12 X-ray photoelectron spectra (XPS) showing the fitted deconvolution of (a) the main Mn 2p <sub>3/2</sub> peak, and (b) the main Na 1s peak for the same crystal flake; for the component curves see main text. Comparing the area ratio of the fitted XPS data provides an estimate of the Mn <sup>4+</sup> :Mn <sup>3+</sup> (ca. 2.5:1) and Na:Mn (ca. 0.56:1) surface elemental ratios.....	188

Figure 5-13 Cleaved crystal flake of $\alpha$ - $\text{Na}_{0.7}\text{MnO}_2$ mounted in two different orientations for magnetization measurements. From left to right are presented: orientation of the flat surface of the crystal flake, mount on holder with H field in parallel with the [001] direction, mount on the holder with the H field perpendicular to the [001] direction (details in text).....	190
Figure 5-14 ZFC-FC susceptibility measurements of a single crystal $\alpha$ - $\text{Na}_{0.7}\text{MnO}_2$ flake at two selected orientations ( $H//c$ left panel in blue and $H\perp c$ right panel in black), at applied field of 100 Oe. The insets in (a), (c) present the zoomed area of susceptibility, where the start of the bifurcation and the broad feature are indicated. The dashed vertical lines from right to left, are indicative of the maxima of the broad hump ( $T_C$ ) and the sharp peak ( $T_f$ ) respectively. Red arrows point at the start of ZFC-FC bifurcation in each orientation.....	191
Figure 5-15 ZFC-FC susceptibility measurements of a single crystal $\alpha$ - $\text{Na}_{0.7}\text{MnO}_2$ flake at two selected orientations ( $H//c$ left panel and $H\perp c$ right panel), at applied fields of 10 kOe. The insets present a zoom of the bifurcation in the low temperature area. ....	192
Figure 5-16 Magnetization measurements of single crystal $\alpha$ - $\text{Na}_{0.7}\text{MnO}_2$ flake at two selected orientations. $M(H)$ , hysteresis loops between applied fields of $-20 \text{ kOe} < H < +20 \text{ kOe}$ . ....	194
Figure 5-17 Top panel: ZFC-FC dc susceptibility measured at 100 Oe in $H//c$ orientation. Middle panel: ZFC-reference and ZFC- $t_w$ curves measured at 5 Oe with the $T_w = 22 \text{ K}$ , Bottom panel: “Ageing” or “memory” curve which is the subtraction of ZFC-reference curve from ZFC- $t_w$ curve. ....	195
Figure 5-18 Dielectric permittivity of the $\alpha$ - $\text{Na}_{0.7}\text{MnO}_2$ crystals measured with the stimulating ac field in parallel to [001] direction (schematic) at frequency of 100 kHz. Several runs were taken starting from a ZFC protocol and a series of FC protocols. ....	197
Figure 5-19 Dielectric permittivity of the $\alpha$ - $\text{Na}_{0.7}\text{MnO}_2$ crystals measured with the stimulating ac field in parallel to [001] direction (schematic) at frequency of 100 kHz. Left panel: ZFC run and 1 <sup>st</sup> derivative, Right panel: FC 10 <sup>th</sup> run and 1 <sup>st</sup> derivative.....	197
Figure 5-20 ZFC-FC susceptibility measurements of a) a single crystal $\alpha$ - $\text{Na}_{0.7}\text{MnO}_2$ flake at $H//c$ left panel and b) of polycrystalline powder of Birnessite $\text{Na}_{0.3}\text{MnO}_2 \times 0.2 \text{ H}_2\text{O}$ right panel, at applied fields of 100 Oe and 200 Oe respectively. The insets present the inverse susceptibility in the case of the crystal $H//c$ orientation. ....	200
Figure 6-1 Schematic of the C2/m monoclinic structure in the stoichiometric $\alpha$ - $\text{NaMnO}_2$ ; projections in the (a) ac plane showing the alternation of layers between the $\text{MnO}_6$ octahedra and the Na cations and (b) ab plane where the triangular topology of the Mn is clear. The green and	

blue lines show inequivalent (J1, J2) magnetic interactions along  $bm$  and  $[110]_m$  (subscript  $m$  for monoclinic). Mn is represented by purple spheres, Na with yellow and Oxygen with red..... 204

Figure 6-2 AFM spin configuration represented in the  $C2/m$  monoclinic cell of  $\alpha\text{-NaMnO}_2$ . The spin arrangement consists of AFM chains running along the monoclinic  $bm$  axis. In the  $ambm$  plane, the chains are stacked ferromagnetically along the  $[1-10]_m$  direction and antiferromagnetically along  $[110]_m$ . Coupling between adjacent  $\text{MnO}_2$  layers along the  $cm$  direction is FM. .... 205

Figure 6-3 X-ray powder diffraction pattern of a polycrystalline sample of  $\alpha\text{-NaMnO}_2$  (black continuous line). The indexing of the Bragg reflections has been done according to the 21028 cif file of the ICSD data base, which corresponds to the blue vertical lines. The magenta vertical line at 15.7 deg correspond to the 002 peak of the sodium deficient  $\text{Na}_{0.7}\text{MnO}_2$ . The red arrows are attributed to reflections of the mylar film. .... 208

Figure 6-4 Examples of 2 different batches. Left panel batch of 1 gr. Right panel batch of 4 gr (scale up). Bragg peaks of  $\beta\text{-NaMnO}_2$  (001),  $\alpha\text{-Na}_{0.7}\text{MnO}_{2+y}$  (002) and  $\beta\text{-Na}_{0.7}\text{MnO}_2$  (002) are detected and represented with green, turquoise and magenta lines respectively. The black arrow point the peak of  $\text{Na}_3\text{MnO}_4$ . .... 209

Figure 6-5 XRPD pattern of a mixed batch of  $\alpha\text{-NaMnO}_2$  used as starting powders (black line) and the same batch sintered (refer to batch #3 in table 3-4) shown in red line. Blue ticks represent the 21028 card of  $\alpha\text{-NaMnO}_2$  and green ticks the 15769 card of  $\beta\text{-NaMnO}_2$ . Impurities of  $\beta\text{-Na}_{0.7}\text{MnO}_2$  (magenta),  $\text{MnO}$  (orange) and  $\text{Mn}_3\text{O}_4$  (grey) are observed both starting powders and sintered rod. The high background in low angles is the contribution of grease which was mixed with the powder as a protective media against moisture and oxygen. .... 210

Figure 6-6 XRPD pattern of a sintered feed rod used for successful growth (black line) (refer to batch #9 in table 3-4). Blue ticks represent the 21028 card of  $\alpha\text{-NaMnO}_2$ . Impurities of  $\beta\text{-NaMnO}_2$  (green arrow),  $\beta\text{-Na}_{0.7}\text{MnO}_2$  (magenta arrow),  $\text{MnO}$  (orange arrow) are observed. The high background in low angles is the contribution of grease which was mixed with the powder as a protective media against moisture and oxygen when there was not available sample holder for air-sensitive samples ..... 211

Figure 6-7 XRPD pattern of a crashed crystal boule of #9. Blue ticks represent the 21028 card of  $\alpha\text{-NaMnO}_2$  and green ticks the 15769 card of  $\beta\text{-NaMnO}_2$ . Impurities  $\beta\text{-Na}_{0.7}\text{MnO}_2$  (magenta arrow),  $\text{MnO}_2$  (black arrow) are observed. Red arrows point out the mylar contribution of the sample holder..... 212

Figure 6-8 a) Laue photograph of the boule facet and b) Laue photo of the flat side of a cleaved flake, both matched with the simulation pattern of (-202) plane of monoclinic C2/m produced with Crystal Maker.....	213
Figure 6-9 (a-b) Laue photograph of the flat side of a cleaved flake of batch#9 and the actual picture of the flake. (c-d) Laue photograph of the flat side of a cleaved flake of batch #8 and the actual picture of the flake. Both photographs are identical and match the simulation pattern of (-202) plane of monoclinic C2/m cell.....	214
Figure 6-10 Precision picture of reflections of (a) 0kl plane , (c) h0l plane and (e) hk0 plane and simulation using the C2/m monoclinic cell in view direction (b) [001], (d) [010] and (f) [001]. The gray arrows point out reflections of weaker intensity that could not be indexed by the C2/m cell, the light blue arrows point systematic absences of the C-centered unit cell while the red arrows point at examples of multiple reflections per site.....	216
Figure 6-11 Precision picture of reflections of 0kl plane and simulation using the (a) C2/m monoclinic cell and (b) Pmmn orthorhombic cell in view direction [100] . The light blue arrows point out reflections of weaker intensity that would either belong to another lattice and have been well indexed with Pmmn or were indexed as systematic absences with a blue x. ....	218
Figure 6-12 SEM image depicting (a) the layered morphology of the as-grown crystal flake of a-Na <sub>0.96</sub> MnO <sub>2</sub> , (b) a close-up view of the stacking layers .....	221
Figure 6-13 A close up of the surface of a flake that initially had a surface stoichiometry ratio of Na/Mn = 0.96/1 taken on 3 different dates having the flake exposed at ambient conditions. (a) 26 <sup>th</sup> April, (b) 27 <sup>th</sup> April, (c) 24 <sup>th</sup> May of the same year. The tables on the top right corners present the EDS results for Na and Mn relative proportions (Atomic %).....	222
Figure 6-14 SEM picture through a developed crack after 1 month of exposure at ambient conditions of the flake with initial Na/Mn = 0.96/ 1 ratio. (a) x2700 zoom and (b) x20000 zoom in the inner part of the crack. EDS spectra reveals reduced amount of Na in the interior of the crack (Atomic %: Mn= 82.11, Na= 6.71, C= 11.18). ....	223
Figure 6-15 SEM image depicting (a) the layered morphology of the as-grown crystal flake of a-Na <sub>0.96</sub> MnO <sub>2</sub> , (b) a close-up view. X-ray photoelectron spectra (XPS) showing the fitted deconvolution of (c) the main Mn 2p <sub>3/2</sub> peak, and (d) the main Na 1s peak for the same crystal flake; for the component curves see main text. Comparing the area ratio of the fitted XPS data provides an estimate of the Mn <sup>4+</sup> :Mn <sup>3+</sup> (ca. 0.14:1) and Na:Mn (ca. 0.96:1) surface elemental ratios. ....	225

Figure 6-16 X-ray photoelectron spectra of three as-grown specimens (Table 6-2), showing the fitted deconvolution of (a-c) the main Mn 2p<sub>3/2</sub> peak for the three chosen crystal flakes and (d-f) the corresponding Na 1s peak for the same crystal flakes. .... 226

Figure 6-17 (a) Two-phase Le Bail refinement of the synchrotron X-ray diffraction data (300 K) from a pulverized  $\alpha$ -Na<sub>0.96</sub>MnO<sub>2</sub> single crystal; observed (circles), calculated (black line) and difference (bottom) profiles are shown. Vertical ticks indicate the predicted reflection positions in the monoclinic P2/m (top set) and orthorhombic Pnmm cell settings (bottom set). .... 227

Figure 6-18 Multi-phase refinements of the synchrotron X-ray diffraction data (300 K) collected on a pulverized single crystal of  $\alpha$ -Na<sub>0.96</sub>MnO<sub>2</sub>; observed (circles), calculated (black line) and difference (thick line at the bottom) profiles are shown. Vertical ticks indicate the predicted reflection positions in (a) two-phase Le Bail model assuming the monoclinic C2/m (top set) and orthorhombic Pnmm cell settings (bottom set) (b) two-phase Le Bail model assuming the monoclinic C2/m (top set) and tetragonal I 41/md of Mn<sub>3</sub>O<sub>4</sub> cell settings (bottom set)..... 228

Figure 6-19 (a) Two-phase model where the monoclinic P2/m (top set) phase is treated by the Rietveld method and the minority orthorhombic Pnmm phase (bottom set) by the Le Bail approach; (b) three-phase Le Bail model assuming a majority, monoclinic C2/m (top row), hexagonal  $\alpha$ -Na<sub>0.7</sub>MnO<sub>2</sub> (P6<sub>3</sub>/mmc; middle row) and orthorhombic  $\beta$ -NaMnO<sub>2</sub> (Pnmm; bottom row) type of polymorphs. Quality of fit factors and lattice parameters are compiled in Table 6.1. .... 229

Figure 6-20 Schematic of the refined P2/m monoclinic structure in  $\alpha$ -Na<sub>0.96</sub>MnO<sub>2</sub>, projected in the ac- (a) and ab- (b) planes. The distorted oxygen coordination environment for neighboring Mn-sites is depicted by alternating color-shading of the MnO<sub>6</sub> octahedra in the [010] direction, while intercalated Na-cations are represented by gold/yellow-colored spheres. The interlayer Mn-Mn separation is marked (a), and the differing Mn-oxygen apical (O<sub>ap</sub>) and equatorial (O<sub>eq</sub>) bonds of the in-plane spatially anisotropic triangular lattice are portrayed (b)..... 230

Figure 6-21 ZFC-FC susceptibility measurements of a single crystal  $\alpha$ -Na<sub>0.96</sub>MnO<sub>2</sub> flake at three selected orientations (a- b- c; top raw of sketches), at applied fields of 100 Oe (left panel) and 10 kOe (right panel). The insets present the 1<sup>st</sup> order derivative of the ZFC susceptibility..... 237

Figure 6-22 Indication of a spin-flop transition in dc-susceptibility of  $\alpha$ -Na<sub>0.96</sub>MnO<sub>2</sub> crystals measured in b and c directions as shown in the inserts. .... 238

Figure 6-23 Magnetization measurements of single crystal  $\alpha$ -Na<sub>0.96</sub>MnO<sub>2</sub> flake at three selected orientations. M(H), hysteresis loops between applied fields of -20 kOe < H < +20 kOe. The small decrease in the saturation magnetization in panel (f) (small red arrow) indicates the evolution of a subtle competing process. .... 239

Figure 6-24 Temperature evolution of the hysteresis loops' parameters for a single crystal $\alpha$ - $\text{Na}_{0.96}\text{MnO}_2$ flake. The saturation magnetization ( $M_S$ ), remnant magnetization ( $M_R$ ) and coercive field ( $H_C$ ) at selected orientations, b (inset, left panel) and c (inset, right panel). The small decrease of the $M_S$ for c orientation (bottom panel) is an indication for the development of competing processes below 26 K.....	240
Figure 6-25 Susceptibility measurements of parent powders and single crystal flake in 3 selected orientations (a), (b)& (c). (a- d) Low temperature plateau (e- h) broad bump around 200 K related to low-dimensional AFM interactions.....	241
Figure 6-26 The red arrow and circle corroborate that the non-zero scattering at $d \sim 2.87 \text{ \AA}$ , while $\alpha$ - $\text{Na}_{0.96}\text{MnO}_2$ is still in the paramagnetic state ( $T > 45 \text{ K}$ ), originates from the nuclear structure; it is indexed as 010 on the basis of the P2/m monoclinic cell.....	243
Figure 6-27 Temperature evolution of the intensity of the $\alpha$ - $\text{Na}_{0.96}\text{MnO}_2$ neutron diffraction peaks in a limited d-spacing section (left panel) and the integrated intensity versus temperature (right panel) for the main scattering features of magnetic origin.] (a), (d): Bragg peak at the (010) lattice position. The intensity of the nuclear reflection is subtracted and only the magnetic contribution is presented. (b), (e): Bragg peak at the $(\frac{1}{2} \frac{1}{2} 0)$ lattice position. (c), (f): The broad asymmetric scattering (diffuse) around the $(\frac{1}{2} \frac{1}{2} 0)$ lattice point indexed as $(\frac{1}{2} \frac{1}{2} 1)$ . Red lines represent the fit to the data (see text). .....	244
Figure 6-28 Reciprocal space intensity maps of $\alpha$ - $\text{Na}_{0.96}\text{MnO}_2$ in the HK0 (a, c) and in the $\frac{1}{2}$ KL (b, d) lattice planes at (a, b), 35 K (c, d) and 1.5 K; x and y axes are presented in reciprocal lattice units (r.l.u.). The 2D character of the coexisting magnetic scattering is depicted by means of the elongation of the diffuse component along the L direction. At the base temperature (b, d), the strong increase in intensity at the $L=0$ position indicates the increase of the spin-correlation length. The subscripts of the Miller indices at the scattering features of the maps, point to either nuclear (n) or magnetic (m) peak contributions. ....	245
Figure 6-29 Magnetic-field dependence of the (010) reflection at 1 K (b) and 50 K (c) respectively. The progressive intensity saturation at 1 K is in line with the weak-ferromagnetic character of the ordered state. ....	247
Figure 6-30 Magnetic field dependence of the scattering features at 1 K and 50 K, for (a, b) a well-shaped sharp peak indexed at the $(\frac{1}{2} \frac{1}{2} 0)$ lattice position in P2/m cell system and (c, d) a diffuse scattering contribution in the vicinity of $(\frac{1}{2} \frac{1}{2} 0)$ Bragg position, described as $(\frac{1}{2} \frac{1}{2} 1)$ .....	248
Figure 6-31 (a) A d- spacing section of the single crystal neutron diffraction patterns as a function of temperature. Intensity of AFM peak with propagation vector $\mathbf{k} = \frac{1}{2} \frac{1}{2} 0$ (contour plot on the left) being at least 1 order of magnitude more intense than the FM peak described by propagation vector	

$\mathbf{k}_1 = 0\ 0\ 0$  (contour plot on the right). Both contributions are indexed in P2/m monoclinic system (b) Temperature evolution of the integrated intensity of the two different magnetic regimes indexed in  $\mathbf{k}_1 = 000$  (FM- black spheres) and  $\mathbf{k} = \frac{1}{2}\ \frac{1}{2}\ 0$  (AFM- red spheres) suggesting a coexistence of both FM and AFM orders as temperature goes below 26 K. The existence of the plateau of the weak FM contribution (gray spheres below 26 K) confirms that only a fraction of the magnetic moments order AFM. .... 249

Figure 6-32 Proposed magnetic models for (a) the  $\mathbf{k}_1 = (000)$  component, (b) the antiferromagnetic  $\mathbf{k}_2 = (\frac{1}{2}\ \frac{1}{2}\ 0)$  state, and (c) a likely low-temperature ferrimagnetic stripe-like structure; plus and minus signs indicate the spin-orientation at adjacent Mn-sites, while the different colors indicate the symmetry in-equivalent magnetic sites. For clarity only one triangular Mn-layer is shown, assuming a ferromagnetic stacking sequence along the c-axis, for both propagation vectors. The magnetic space group and the associated irreducible representations are also given for each spin configuration. .... 251

Figure 6-33 Dielectric constant ( $\epsilon'$ ) (black symbol-left Y-axis) and dielectric loss (black thin line-right Y-axis) of  $\alpha$ -NaMnO<sub>2</sub> measured with a ZFC protocol at 1 kHz, applying 1600 V/m upon heating. The inset on the  $\epsilon'_r$  (T) shows the weak feature observed below 50 K. .... 255

Figure 6-34 Dielectric constant and dielectric loss of  $\alpha$ -NaMnO<sub>2</sub> measured at low frequency area: 111 Hz, 1 kHz, 20 kHz. Inset shows the low temperature feature. .... 256

Figure 6-35 Two different runs of Dielectric constant measured at 1 kHz (left panel) and 100 kHz (right panel) with  $V_{rms} = 1600$  V/m. (Top panel) Dielectric constant against temperature. (Bottom panel) 1<sup>st</sup> derivative curves calculated from dielectric constant against temperature. .... 257

Figure 6-36 Dielectric constant of  $\epsilon'(T)$  of  $\alpha$ -NaMnO<sub>2</sub> measured upon heating at 1 kHz under applied magnetic fields from 0 T- 14 T. Top panel: The whole temperature range. Bottom panel: low temperature area of the same measurement zoomed in. The measurement under zero (0 T) magnetic field was carried out twice: first before the application of the magnetic fields, represented with the turquoise and second in red, after the magnetic fields have been applied. .... 258

Figure 6-37 Left-bottom axes (black):  $\Delta\epsilon'$  (%) calculation against Temperature for  $H = 14$  T showing the maximum change in the values of dielectric constant with the application of the external magnetic field. The MDE is of 0.05 % at 47 K. Right-top axes: shift of the critical temperature  $T_N$  with respect to the applied magnetic fields.  $T_N$  refers to the temperature where the dielectric constant is maximum. .... 259

Figure 6-38 Dielectric permittivity of the  $\alpha$ -Na<sub>0.96</sub>MnO<sub>2</sub> crystals measured parallel to [-202] direction (schematic) at 2 different frequencies of 20 kHz (orange) and 100 kHz (red). The inset show the 1<sup>st</sup> derivative of the dielectric permittivity measured at 20 kHz. .... 261

Figure 6-39 Dielectric permittivity of the $\alpha$ - $\text{Na}_{0.96}\text{MnO}_2$ crystals measured parallel to $[-202]$ direction at $f= 100$ kHz (red). The inset show the 1 <sup>st</sup> derivative of the dielectric permittivity measured at 100 kHz.....	262
Figure 6-40 The thermal evolution of the magnetic scattering at $d\sim 5.05$ Å; the diffuse component precedes the growth of the Bragg contribution at the $(\frac{1}{2} \frac{1}{2} 0)$ commensurate lattice position. ....	264
Figure 6-41 Schematic of Mn-spin canting (ab-plane view), a possibility due to non-negligible hole-concentration ( $n$ ) in the off-stoichiometric $\alpha$ - $\text{Na}_x\text{MnO}_2$ ( $n\approx 1-x$ ). According to Ouyang et al [33] a weak ferromagnetic component is expected to develop along the b-axis of the monoclinic cell.....	266
Figure 8-1 Magneto- electric Station of B009.....	ii
Figure 8-2 Superconducting magnet (7-Tesla) and continuous flow Cryostat.....	iii
Figure 8-3 Instrumentation used to probe physical properties and control external stimuli .....	iv
Figure 8-4 “Sample holder2” Flat carrier. The pellet is mounted with grease on the sapphire substrate. Silver paste is used on a $\text{BaTiO}_3$ pellet. Copper wires are attached with S. Paste on the sample’s surfaces and soldered on the Nickel pins of the sample carrier. ....	vii
Figure 8-5 Standard 4-point topology for low resistivity measurements. ....	viii
Figure 8-6 (a) MD fiber stick, (b) lower carrier socket on brass frame and 2 detachable sample holders/carriers, (c) 4 wires come down to lower carrier socket from isolated Teflon flange, (d) 4TP wiring sketch, (e) GND according to 4TP and noise shield in the lower carrier socket, (f) sample wired with 4TP as a capacitor, (g) “Sample holder1 – capacitor topology”, no wires on sample, (h) “Sample holder2- Flat multi pin carrier 2 or 4 probe wire connections to the sample, (i) sample connected as a capacitor using paste (sketch of (f))......	x
Figure 8-7 (a) Parallel to H field orientation of the sample carrier- Sample Holder2 (b) Vertical to field orientation of the sample carrier- Sample Holder1 .....	xi
Figure 8-8 Dewar and transfer line of cryogenic liquid ( $\text{N}_2$ ) .....	xi
Figure 8-9 (a) Base of the cryogenic liquid transfer line, (b) Liquid $\text{N}_2$ level indicator, (c) Control circuit in box with DC motor, (d) Gear transmission system with metal stopper rod that changes the condition of the two micro switches. ....	xiii
Figure 8-10 “Control_Dewar_Vlave_ver2.vi” .....	xiii
Figure 8-11- “Lakeshore_332.vi” .....	xiv

Figure 8-12 “Show_Indicators.vi” .....	xv
Figure 8-13 “Sequence_Controller_ver2.vi”.....	xvi
Figure 8-14 (a) Ideal, Real and Measured values in a capacitor topology, (b) parallel equivalent circuit mode for capacitor measurements.....	xvii
Figure 8-15 Solo experiment- “07_Ramp_Temperature_Lakeshore_332.vi”- Tab 1 Set the experiment/Save file.....	xix
Figure 8-16 Solo experiment- “07_Ramp_Temperature_Lakeshore_332.vi”- Tab 2-Setting instruments .....	xx
Figure 8-17 “Graphs.vi” .....	xxi
Figure 8-18 “Create_Sequence_ver3.vi”- Tab 1 Add experiments, Save file.....	xxii
Figure 8-19 “07-Ramp_Temperature_Lakeshore332_multifrequencies.vi”- Tab-1- Set temperature and select frequency range. ....	xxiv
Figure 8-20 “07-Ramp_Temperature_Lakeshore332_multifrequencies.vi”- Tab-2- Connect & Set Instruments .....	xxiv
Figure 8-21 Example of resonance peaks in piezoelectric material .....	xxv
Figure 8-22 Frequency dependence of dielectric permittivity .....	xxv
Figure 8-23 “45_Sweep_Frequency_From_File_Agilent_E4980A.vi”, Tab 1-Load point file and save data .....	xxvi
Figure 8-24 “45_Sweep_Frequency_From_File_Agilent_E4980A.vi”, Tab 2-Set temperature, measurement mode and signal level.....	xxvii
Figure 8-25 Wiring for measuring resistivity with the direct 4-probe method. ....	xxvii
Figure 8-26 “07_Ramp_Temperature_Lakeshore_332.vi”- Tab-4 Connect and set current source and nanovoltmeter for Delta function resistivity measurements.....	xxix
Figure 8-27 Determine the resistivity of an insulator.....	xxix
Figure 8-28 “07_Ramp_Temperature_Lakeshore_332.vi”-Tab-3 Keithley 6517B connected.....	xxxi
Figure 8-29 “00_Target_Magnetic_Field_AMI_430.vi” .....	xxxiii
Figure 8-30 Keep AMI430 connected during an experiment that takes place under magnetic field .....	xxxiv
Figure 9-1 The cation-oxygen distances against the fourth coordinate (x04) in the (3+1)D approach (t-plot) for the room temperature crystal structure of $\beta$ -NaMnO <sub>2</sub> . ....	iii

Figure 9-2 Schematic representation of the Mn sublattice topology, in top panel the monoclinic (C2/m)  $\alpha$ -NaMnO<sub>2</sub> and bottom panel the orthorhombic (Pmmn)  $\beta$ -NaMnO<sub>2</sub> polymorphs. The Mn-Mn distances drawn, depict the possible intra-layer magnetic exchange coupling pathways ( $J_1$  to  $J_3$ )..... iv

Figure 10-1 Left to right: As grown single crystal boule, cleaved flakes, Laue photograph. .... ii

Figure 10-2 The base of the holder carrying three crystals in different orientations. .... iii

Figure 10-3 pin holders shaped in 4 different ways in order to accommodate the crystal in different angles..... iii

Figure 10-4 left: actual crystal flake cleaved from boule. The tiny lines on the crystal's surface are indicative b-axis while the flat surface is described by this orientation [-202]. Right: illustration of the desired orientation of the specific crystal in order to have..... iv

# Chapter One: Introduction

---

With the term “Strongly correlated materials” we refer to a wide class of compounds often emerging unique and unusual physical properties while offering a strong technological potential. In such materials the ability to exhibit magnetism, to conduct electricity and heat is fundamentally linked to the electronic dynamics and interactions with the atomic nuclei and other electrons. On the same side, the discovery of materials with coexisting magnetic and ferroelectric orders, namely magnetoelectrics[1] has revived the interest of condensed matter physics in materials science communities. More precisely it challenged the design of systems where electric and magnetic orders could be strongly coupled maintaining the great promise of such fundamental mechanisms in devising applications ranging from portable magnetoelectric (ME) sensors and memories to radar technologies [2]. In view of the broad field of applications, basic research becomes imperative to understand the principles that may produce the appropriate microscopic processes for ferroelectric and magnetic order to coexist and be mutually coupled.

## 1.1 Scope

The present dissertation wishes to uncover such highly sought material-systems where fundamental studies could be pursued. The main research has been evolved in the field of the study/characterization of strongly correlated systems where coupled properties arise from the interplay of charge and spin degrees of freedom over lattice topologies which enable competing magnetic interactions. In particular, the focus has been on the  $A^+M^{3+}O_2$



(A= H, Li, Na; M= 3d transition metal) mixed-metal oxides, from the family of delafossites [3] whose properties have enormous potential for future high-capacity Na-ion re-chargeable batteries [4]–[7] that could meet the needs of intermittent renewable energy sources while offering solutions for information storage and processing technologies. [8] Our work has pointed out that non-perovskite, two-dimensional (2D) Na-Mn-O oxides are good candidates for such a kind of magnetoelectricity so the focus was put on layered polymorphs of  $\text{Na}_x\text{MnO}_2$  ( $0.7 < x < 1$ ) system which in the case of stoichiometric compounds, crystallize in a distorted variant of the 3R polytype  $\alpha\text{-NaFeO}_2$  structure ( $R\bar{3}m$ ) due to the deformation of the  $\text{MnO}_6$  octahedra caused by the Jahn-Teller effect, inherent to the  $\text{Mn}^{3+}$ . Because of this,  $\alpha\text{-NaMnO}_2$  becomes monoclinic ( $C2/m$ ), the  $\beta\text{-NaMnO}_2$ , appears to adopt an orthorhombic cell ( $Pmnn$ ) while the  $\alpha\text{-Na}_{0.7}\text{MnO}_2$  crystallizes in the hexagonal  $P6_3/mmc$  structure.

Geometrical frustration due to triangular lattice together with the existence of mixed valence of Mn ( $\text{Mn}^{3+}/\text{Mn}^{4+}$ ) introduced a palette of competing interactions that frame the anisotropic properties of the systems through lattice distortions. More specifically, Jahn-Teller effect favors the formation of anisotropic structures and consequently of anisotropic transport and magnetic properties while mixed valence of Mn offers the possibility of electronic delocalization over the metal–oxygen framework. In addition to these, the crystal chemistry of  $\text{Na}_x\text{MnO}_2$  allows for polymorphism due to oxygen-layer gliding processes. [6], [9], [10] As a fact, their performance is mediated by phase transitions between nearly degenerate structural types (e.g. designated, as O3- ( $3R$ ;  $R\bar{3}m$ ) and P2- ( $P6_3/mmc$ )), while extended defects (e.g. stacking faults) formed between various crystal domains, render the apparently simple  $\text{Na}_x\text{MnO}_2$  compounds metastable. Therefore, new insights on the impact of their inherent compositional variation are sought in order to explain their complicated sequences of electronic, structural, and magnetic processes.

The structural complexity of the system and the potential emerging of magnetoelectric coupling have been the starting point and motivation for this study which wishes to enlighten the path towards the understanding of processes that relieve frustration in favor of an ordered ground state.

As an introduction, the underlying physics relevant to these compounds will be discussed after a short description of the experimental methods employed for the completion of the present study. A summary of types of multiferroics and the root mechanisms of emergence



and coupling of magnetic and electric degrees of freedom is then presented, leading into an outline of the current thesis.

### 1.1.1 Methods

We intensified training on the Floating zone technique and pursued a quality single crystal growth by controlling the stages of the preparation and sintering of the rods and also the conditions during the growth procedure itself. Starting from the polycrystalline powders of two different polymorphs of our 2D manganese oxide system,  $\alpha$ -NaMnO<sub>2</sub> (monoclinic) and  $\beta$ -NaMnO<sub>2</sub> (orthorhombic), we obtained mm to cm sized crystals.

X-ray diffraction (XRD) approaches (Laue method for single crystals and Bragg-Brentano for powders) together with electron microscopy (SEM / EDX) and XPS experiments allowed for the basic characterization of the structural and chemical characterization, while single crystal xrd and Synchrotron x-ray diffraction has been employed to define the crystal structure.

The magnetic properties have been studied by a Superconducting Quantum Interface Device (SQUID) while dielectric permittivity of the compounds studied in this thesis in a wide temperature range (5- 320 K) and under magnetic fields (up to 14 T) an appropriate in-house set up and a custom made measurement stick were developed. Physical Measurements were also held in a commercial PPMS system which worked as a guide for the development of in house MD station.

For the dynamic properties <sup>23</sup>Na NMR measurements were performed supported by inelastic neutron scattering work performed in MARI direct geometry chopper spectrometer (ISIS, UK) and also on the DCS spectrometer (NIST, USA). The crystal and magnetic structure on temperatures has been studied by Neutron Powder Diffraction Experiments in the ISIS- Rutherford Appleton Laboratory, Oxford, United Kingdom.

## 1.2 Single Ion interactions

### 1.2.1 Ions in anisotropic environments

#### 1.2.1.1 *Crystal fields*

The crystalline environment of a magnetic ion in a solid highly determines some of its properties. The anions and cations in a crystal will generally arrange themselves in such a way as to minimize the effects of electrostatic repulsion. This arrangement is dependent on



the atomic orbitals, and can have a significant influence on the magnetic properties which are exhibited. The effect of Coulomb repulsion between the electron wave functions of the ion and its nearest neighbors, defines the interactions that gives rise to eigenstates with different energy levels. These eigenstates are highly dependent on the symmetry of these wavefunctions and the symmetry of the crystalline environment. The effects of crystal fields are strong for  $d$ -electrons because their wavefunctions extend a relatively long way from the nucleus towards the surrounding ions, whereas  $f$ -electron wavefunctions are smaller and are partly shielded from Coulomb interactions with the surroundings by the  $s$ - and  $p$ -electrons in filled levels.

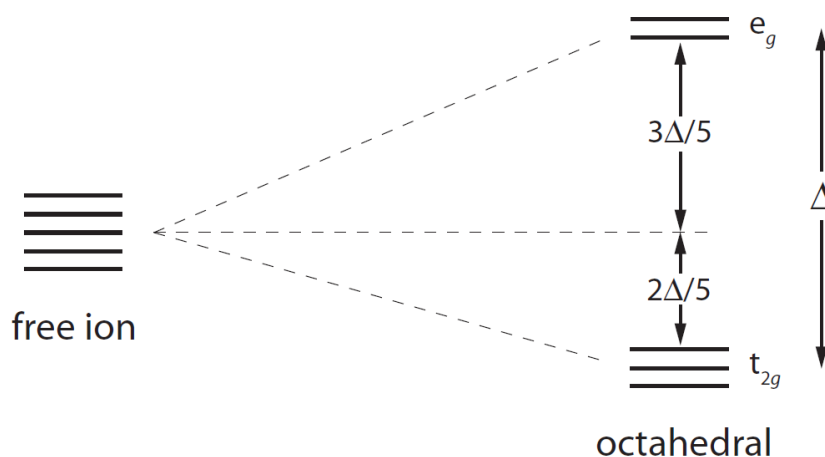


Figure 1-1 Crystal field splitting of the  $d$ -orbital in an octahedral crystal environment [11]

The compounds central to this thesis have a rock-salt crystal structures developed by layers of octahedra with a central  $Mn^{3+}/Mn^{4+}$  ion surrounded by  $O^{2-}$  ions (fig. 1-2). Electrostatic forces in this case occur between the  $d$  orbital of the Mn ion and the  $p$  orbitals of the oxygen ions. The  $d$  orbitals, in the case of  $Mn^{3+}$  ( $3d^4$ ) ions, can take five different forms: the  $e_g$  levels ( $d_z^2$  and  $d_{x^2-y^2}$ ), defined with the orbitals pointing along the  $x$ -,  $y$ - and  $z$ -axes; and the  $t_{2g}$  levels ( $d_{xy}$ ,  $d_{xz}$  and  $d_{yz}$ ) in which the orbitals point between the axes. The three  $p$  orbital types,  $p_x$ ,  $p_y$  and  $p_z$ , point along each respective axis. Therefore, in the octahedral environment the  $e_g$  orbitals will be in a higher energy configuration than the  $t_{2g}$  orbitals. [11]

There is a corresponding splitting of the  $d$  orbital energy levels, as shown in Figure 1-1. The amount of splitting,  $\Delta$ , is dependent on such factors as the geometry of the octahedra, the repulsion between the ions, and the effects of Jahn-Teller distortion, as discussed in the following section.



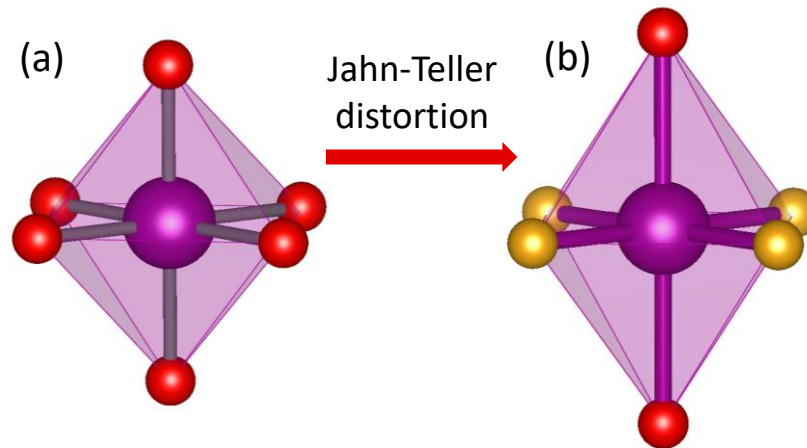


Figure 1-2 Magnetic ion (purple sphere) in a (a) non-distorted and a (b) Jahn-Teller distorted octahedral environment of Oxygen ions (red and yellow spheres)

#### 1.2.1.2 *Jahn-Teller effect*

In a 3d ion, there are six  $t_{2g}$  states and four  $e_g$  states, separated by an energy gap that can be occupied. These are orbitally degenerated, [12] and in cases that these states are partially filled it may be energetically favourable for the lattice to distort spontaneously, thus lowering the degeneracy. This phenomenon is known as the Jahn-Teller effect and it works as balancing mechanism in which the energy gained by the system due to elastic strain is outweighed by the energy lost by a lowering of the energy of the occupied orbitals. An illustration of this effect in a  $\text{Mn}^{3+}\text{O}_6$  environment is shown in figure 1-2b, where the distortion is a stretching of the octahedron along the  $z$ -axis. The preferred spin configuration in this case (according to Hund's first rule) is for the spins to all align parallel, which would give three electrons in the lower energy  $t_{2g}$  levels and the remaining electron in the higher energy  $e_g$  level. By distorting the octahedra via a stretch along the  $z$ -axis and a contraction along the  $x$ - and  $y$ -axes, the  $e_g$  and  $t_{2g}$  levels are split in energy in such way that the lone electron in the  $e_g$  state can now occupy a lower energy level (Figure 1-3). Such distortions of the crystal structure can occur in magnetic systems lowering the overall energy.

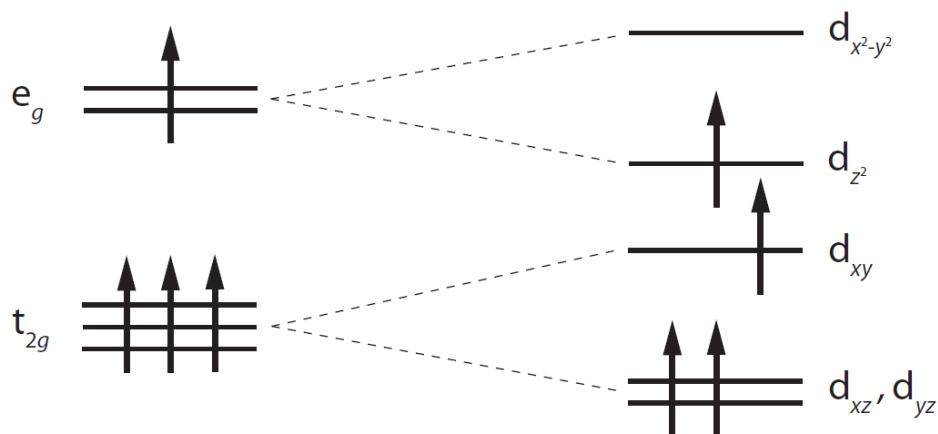


Figure 1-3 The 3d energy levels of  $Mn^{3+}O_6$  in an octahedral environment before (left) and after (right) of Jahn Teller distortion

### 1.2.2 Classification of layered structures

Most common layered structures are built up of layers of  $MeO_6$  (3d transition metals) octahedra sharing edges. Stacking of these layers with different orientation along the c-axis, drives polymorphism modulating interlayer interactions and possible ion orderings. [13]

Early investigation of two-dimensional layer oxides was performed by Delmas and Hagemuller in the early 1980s.[9], [14], [15] They defined the crystal structure of layered compounds depending on the stacking sequence of alkali ions between layers introducing a specific nomenclature to describe them. Sodiated transition metal oxides,  $Na_{1-x}MeO_2$  (Me: transition metal), were representatively classified into two main groups, O3 type and P2 type (Fig. 1-4), by Delmas et al..[15] Those crystal structures consist of edge-sharing  $MO_6$  octahedral layers in alternation with Na ion layers where the Na ion may sit in an octahedral (O) or a prismatic (P) environment. The number (O2, O3, P2, and P3) indicates the packing number of Na ion octahedral or prismatic layers within each unit cell. The O3 type is stable when the Na content is high in  $Na_{1-x}MeO_2$  (x is close to 0), in which the average oxidation state of Me is close to 3+. Reversible structural transformation of  $O3 \leftrightarrow O'3 \leftrightarrow P3 \leftrightarrow P'3$  may happen with the extraction/insertion of  $Na^+$  ion. In cases where  $Na^+$  ions are partly extracted from the crystal structure creating Na vacancies, the prismatic environment is favored for the remaining  $Na^+$ . This extraction induces strong repulsion of oxygen in the Na layers causing expansion of the interlayer distance.  $Na^+$  diffusion occurs

faster in the P'3 phase due to the greater interlayer distance compared to O3. These transitions are followed by

gliding of the  $\text{MeO}_2$  slice without breakage of Me–O bonds, as proposed by Delmas et al..[15]

The P2 type has a different optimal environment for Na compared to the O3 type. In particular, the structure is stable when the Na content is in the range of 0.3–0.7 in  $\text{Na}_{1-x}\text{MO}_2$ , in which the average oxidation state of M is above +3. The presence of vacancies in the structure causes strong repulsion of oxygen in the Na layers, resulting in expansion of the interlayer distance. This leads to  $\text{Na}^+$  ions occupying prismatic (P) sites due to the large Na ionic size.  $\text{Na}^+$  ions occupy two different types of trigonal prismatic sites:  $\text{Na}_f$  ( $\text{Na}_1$ ) contacts the two  $\text{MO}_6$  octahedra of the adjacent slabs along its face, whereas  $\text{Na}_e$  ( $\text{Na}_2$ ) contacts the six surrounding  $\text{MO}_6$  octahedra along its edges. Adjacent  $\text{Na}_f$  and  $\text{Na}_e$  sites are too close together (considering the  $\text{Na}^+$  ionic radius) to be occupied simultaneously.

Phase transition from P2 to O2 or between P3 and O3 types are of low energy cost and can take place at room temperature since they don't demand breakage of the Me-O bonds as mentioned earlier. In contrary to that, P2 to P3 (or O3) transcriptions require breakage of the aforementioned bonds since there not only shifting of the  $\text{MeO}_6$  layers but also a tilt of  $60^\circ$ . [6]



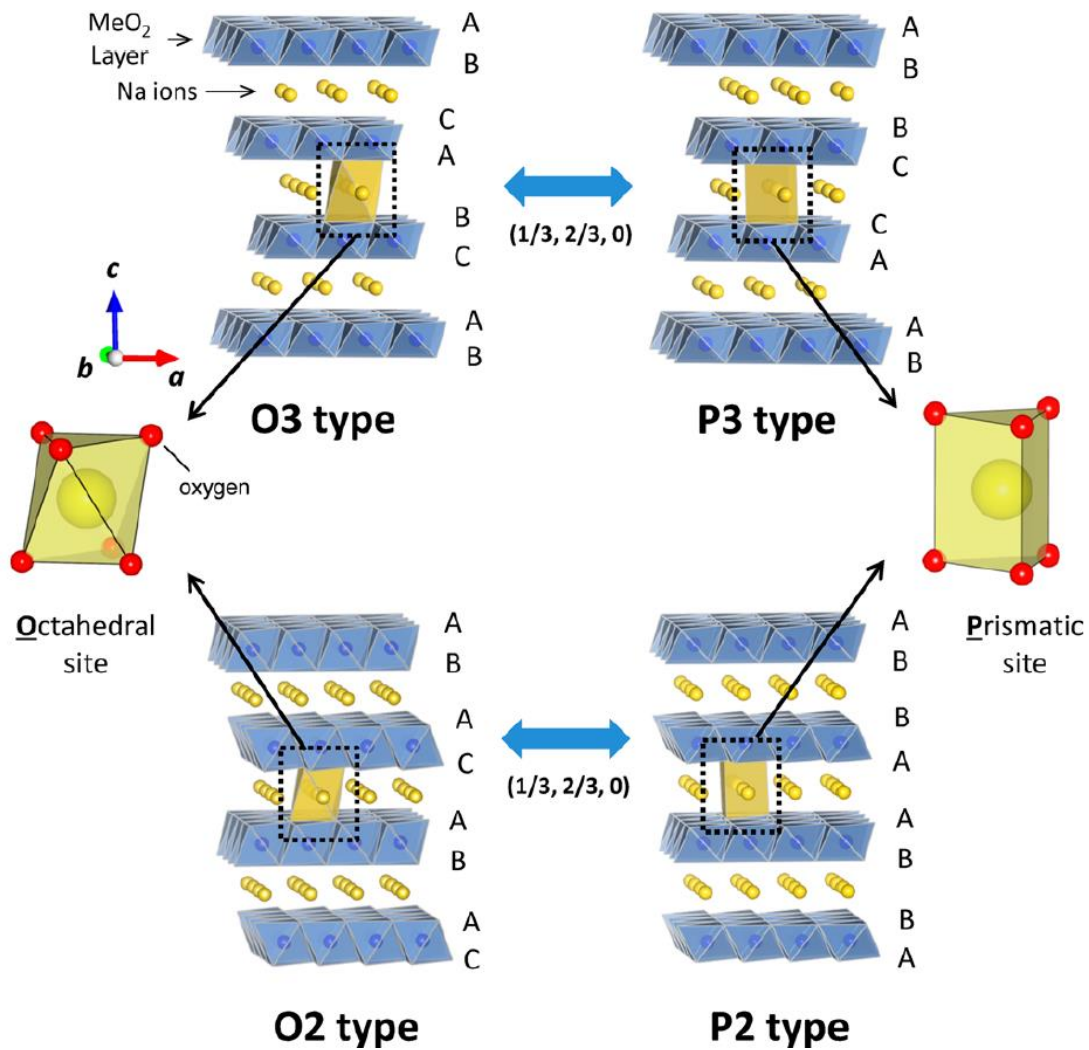


Figure 1-4 Classification of the different layered structures adopted in Na-Mn-O systems. MeO<sub>6</sub> layers are in blue and Na cation in yellow.[13]

Interactions among ions are strongly modulated by gliding of MeO<sub>2</sub> sheets leading to the formation of superstructures. In the cases of low cost transformations the resulting structure unavoidably develops stacking faults. [16]

In the specific case of Mn based layered structures, complexity arises by the coexistence of the active Jahn Teller of Mn<sup>3+</sup> and non-Jahn Teller active Mn<sup>4+</sup>. Jahn Teller distortion results in reduction of the unit cell symmetry while the synthesis conditions tailor the distortion in the cases of the P2 type as they alter slightly the Na content. [6] The fluctuating Mn valence in between +3 and +4 may initiate structural and electronic modifications that have a strong impact on the physical properties of the resulting system.

## 1.3 Collective interactions- Magnetism

Thales of Miletus (625 to 547 BC) is the first person known to have considered magnetism, an account of which appears in Aristotle's *De Anima*. [17] Science has progressed somewhat in the intervening years, however fundamental magnetic phenomena are still providing a means for us to test the limits of our knowledge.

A magnetic moment originates from the angular momentum of a charged particle. In quantum magnetism there are two components that make up the total angular momentum  $J$  and define the magnetism: the orbital angular momentum  $L$ , whose total magnitude is equal to  $\hbar\sqrt{l(l+1)}$ , and the spin angular momentum  $S$  with a magnitude of  $\hbar\sqrt{s(s+1)}$ . The projection of  $L$  and  $S$  along the z-axis is  $\hbar m_l$  and  $\hbar m_s$  respectively. The principal (n), angular (l), magnetic ( $m_l$ ), spin (s) and spin magnetic ( $m_s$ ) quantum numbers define the quantum state of an electron; the Pauli exclusion principle, which states that electrons occupying the same position in space and time must differ by at least one quantum number, is one of the characteristics that defines the electronic properties of solid state materials while the sequence of occupation of localised electrons in an atom is governed by Hund's rules.

### 1.3.1 Magnetic Interactions

The exchange interaction arises due to Coulomb interactions arising from the overlap of electron wavefunctions in a material. [11] The Heisenberg Hamiltonian,  $H$ , for exchange interaction terms is given by:

$$\hat{H} = -\sum_{ij} J_{ij} S_i \cdot S_j \quad (1-1)$$

Where  $J_{ij}$  is the exchange interaction between the  $i^{\text{th}}$  and  $j^{\text{th}}$  spins, having a positive value corresponding to ferromagnetism and a negative value corresponding to antiferromagnetism.

In a ferromagnet adjacent magnetic moments are aligned parallel, whereas in an antiferromagnet they are antiparallel along one or more directions. The periodicity of ferromagnetic order is equal to the separation of the magnetic moments, whereas for antiferromagnetic order the repeat period is doubled. There are many other magnetic structures that can arise, for a variety of reasons, where the periodicity is different. For example the magnetic moments may be helically ordered so that along a particular direction neighboring moments are rotated by a fixed angle relative to their neighbors.



Such order can be commensurate, where the period of the magnetic order is equal to an integer number of lattice units, or incommensurate where it is not.

### 1.3.1.1 *Superexchange*

Direct exchange refers to the interaction between neighboring moments, but if the process occurs via some intermediate process it is termed indirect exchange or superexchange. If we consider a system with two magnetic atoms, each with a single d-orbital electron, separated by an oxygen atom their wavefunctions will not directly overlap. In an ionically bonded system, the oxygen ion will have two electrons in its p-orbital which will overlap with the d-orbitals of the magnetic atoms (Fig. 1-5). The energy of the system is lowered if the magnetic atoms order antiferromagnetically, since the electrons are then free to move from the oxygen ion to either side magnetic ion. Conversely, if the magnetic ions order ferromagnetically, the oxygen electrons will not be able to move due to the Pauli Exclusion Principle.

The Goodenough-Kanamori-Anderson (GKA) rules are a set of guidelines for estimating the sign and relative magnitudes of superexchange interactions.

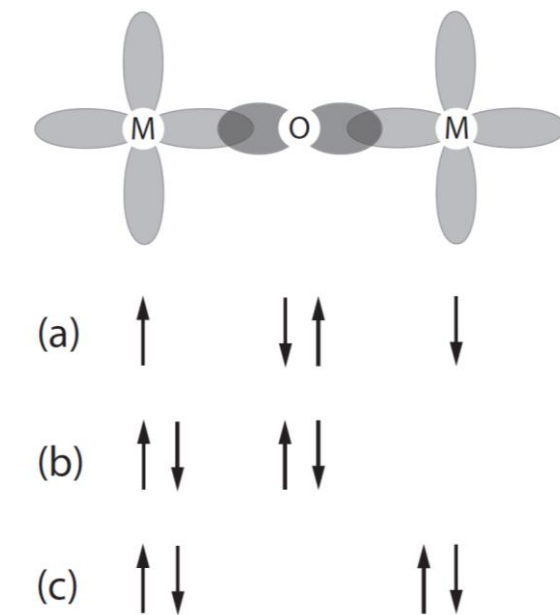


Figure 1-5 Two magnetic atoms interacting with an oxygen atom, O. (a) Antiferromagnetic alignment is favored by superexchange interaction since it allows coupling the spins of magnetic cations indirectly through the intervening oxygen ions in contrast to (b) and (c)

### 1.3.1.2 Double-exchange

Mixed valency of a magnetic ion may be the origin of a ferromagnetic exchange interaction. A strong example is the case of Mn that can exist in +3 and 4+ oxidation states. The ferromagnetic alignment is attributed to the double exchange mechanism as described in figure 1-6. The  $e_g$  electron on a  $Mn^{3+}$  ion can hop to a neighbouring site only if there is a vacancy there of the same spin (since hopping proceeds without spin-flip of the hopping electron). If the neighbour is a  $Mn^{4+}$  which has no electrons in its  $e_g$  shell, this should present no problem. However, there is a strong single-centre (Hund's rule number 1) exchange interaction between the  $e_g$  electron and the three electrons in the  $t_{2g}$  level which wants to keep them all aligned. Thus it is not energetically favourable for an  $e_g$  electron to hop to a neighbouring ion in which the  $t_{2g}$  spins will be antiparallel to the  $e_g$  electron. Ferromagnetic alignment of neighbouring ions is therefore required to maintain the high-spin arrangement on both the donating and receiving ion [11]

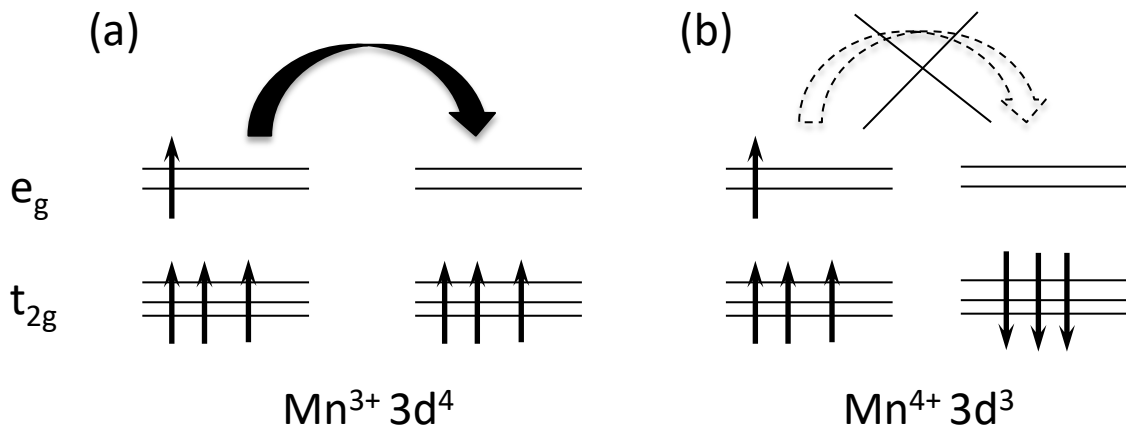


Figure 1-6 The single state exchange interaction favours hopping if neighbours are (a) FM aligned and does not favor hopping when neighbouring ions are (b) AFM aligned [11]

### 1.3.1.3 Dzyaloshinskii-Moriya

Another kind of interaction, the Dzyaloshinskii-Moriya (DM) or anisotropic exchange interaction, arises due to spin-orbit coupling. In the case of superexchange there is a mixing of the ground state and excited state of the system due to the presence of a non-magnetic ion such as oxygen, whereas here the spin-orbit interaction can lead to the ground state of one magnetic ion interacting with the spin-orbit excited state of the other magnetic ion. The form of the DM Hamiltonian is:



$$\hat{H} = D \cdot (S_i \times S_j) \quad (1-2)$$

when acting between the  $i^{\text{th}}$  and  $j^{\text{th}}$  spins. The vector  $D$  is finite provided that the crystal field acting on the two spins does not present inversion symmetry at the half-way point of the vector joining the two spins. The effect of the DM interaction is often to provide a small canting of the moments in an antiferromagnetic structure, resulting in weak ferromagnetism as the spins to lie preferentially at right angles to one another, in a plane perpendicular to  $D$ . If there are other interactions acting on the system then such a situation may not be realized, and instead the DM interaction may result, for example, in spins lying in the same plane and rotating slightly from site to site. The DM interaction favors non-collinear spin ordering, which has important implications for multiferroic properties.

### 1.3.2 Magnetic response to an external field

The response of the moment to the presence of a magnetic field is described by a quantity known as the magnetic susceptibility ( $\chi$ ) which depends on whether the band contributing to the magnetic moment is localized or itinerant as well as the interaction between it and other magnetic particles in the lattice.

Diamagnetism and Paramagnetism describe two types of magnetic response to an applied field characterized by negative and positive susceptibility respectively. Diamagnetism results in the magnetic polarization opposing the applied field and in classical electrodynamics it can be explained by Lenz' rule. According to Lenz' rule, when a magnetic field induces circular currents in a material this responds by a field that opposes the applied field. In quantum electrodynamics the same effect is described by the Larmor theorem; electrons precess around the direction of their spin in the presence of the magnetic field with a frequency equal to  $\omega_L = e\mathbf{H}/2m$  where  $\mathbf{H}$  is the magnitude of the applied field,  $m$  is the mass of the electron and  $e$  the electronic charge. The resulting negative susceptibility is:

$$\chi_{dia} = \frac{-\mu_0 n Z e^2}{6m} \langle r^2 \rangle \quad (1-3)$$

where  $\mu_0$  is the magnetic permeability of free space,  $n$  the number of magnetic atoms in the sample,  $Z$  is the atomic number of the atom and  $\langle r^2 \rangle$  the mean square distance of the electron from the nucleus.

On the other hand, Paramagnetism is a result of already existing unordered magnetic moments in a system aligning with the field. In a set of weakly interacting moments the susceptibility is approximated as follows using the Brillouin function:



$$\chi_{para} = \frac{n\mu_0\mu_{eff}^2}{3k_B T} \quad (1-4)$$

where  $\mu_{eff}$  is the effective magnetic moment on each of the  $n$  sites,  $k_B$  is Boltzmann's constant and  $T$  the temperature. This is known as Curie's Law and enables an estimate of the magnetic moment on each atom to be made from the experimental magnetic susceptibility data. The effective magnetic moment is related to the total angular momentum by:

$$\mu_{eff}^2 = g_J\mu_B\sqrt{J(J+1)} \quad (1-5)$$

where  $g_J$  is the Landé g-factor,  $\mu_B$  the Bohr magneton and  $J$  the magnitude of the total angular momentum, equal to  $L \pm |S|$ .

The response of a real magnetic material to an applied magnetic field  $\mathbf{H}$  is measured by its bulk magnetization  $\mathbf{M}$ . The magnetization  $\mathbf{M}$  is defined as the number density of the magnetic dipole moments aka the magnetic moment ( $m$ ) per unit volume ( $V$ ):

$$\mathbf{M} = \frac{m}{V} \text{ (emu/cm}^3\text{)} \quad (1-3)$$

and it is related to the external magnetic field ( $H$ ) and the magnetic induction within the sample ( $B$ ) by the following relation:

$$B = \mu_0(H + M) \quad (1-4)$$

with the susceptibility defined as  $\chi = M/H$ .

### 1.3.3 Magnetic order

The choice of some materials to display finite magnetism in the absence of applied fields as a result of strong interactions between the magnetic atoms is called magnetic order. The most common ordering patterns for the magnetic moments in a material are termed ferromagnetic (FM) and antiferromagnetic (AFM). The former implies parallel alignment of all the spins along a unique direction and the latter is described by two interpenetrating, opposite-oriented FM lattices which lead to a zero net magnetization. Below a critical ordering temperature (termed the Curie temperature ( $T_C$ ) in FM and the Néel temperature ( $T_N$ ) in AFM), the moments in the sample align as indicated in the figure. Above these ordering temperatures the moments display no long range order but may be aligned with an applied field according to the Curie-Weiss law:

$$\chi = \frac{C}{T - \theta_w} \quad (1-5)$$



Where where  $\theta_w$  is equal to the Curie temperature or the negative of the Néel temperature, and C stands for the Curie constant which equals to  $C = \frac{\mu_B^2}{3k_B} N g^2 J(J+1)$ .

The Curie-Weiss theorem explains phenomenologically the appearance of magnetic order. The introduction of mechanical exchange interaction J by Heisenberg differs to the “mean field” approach of Weiss model describing the interaction between specific magnetic sites. Specific approximations to the Heisenberg model include the Ising model, in which the spin vector operator is one dimensional and has only two states (“spin up” and “spin down” aligned along a particular crystallographic direction) and the XY model, in which the two dimensional spin operator allows the moments to rotate in the (x, y) plane. The onset of magnetic order in any of these approximations may be estimated by examining the behavior of the free energy above and below the transition temperature. How a physical quantity of the system varies around the critical temperature is defined by its critical exponent; the exponents for the magnetization M [and therefore magnetic order parameter  $\Psi$ ],  $M(\Psi) \propto (T_c - T)^\beta$ , and the isothermal susceptibility  $\chi \propto (T - T_c)^{-\gamma}$  are listed in table 1-1. A comparison with experimental data enables the determination of the nature of the phase transition to be made.

Table 1-1 Critical exponents for a variety of magnetic models, after reference[11]

	2D Ising	3D Ising	XY	Heisenberg	Mean Field
Spin Dimensionality (d)	1	1	2	3	-
Crystal Dimensionality (D)	2	3	3	3	-
$\beta$	0.125	0.326	0.345	0.367	0.5
$\gamma$	1.75	1.2378(6)	1.31(6)	1.3888(3)	1

### 1.3.3.1 Antiferromagnetic order

Antiferromagnetism can exist in many forms, with the common theme of sublattices of moments arranged so as to cancel each other out thus giving no net magnetization in the absence of an applied magnetic field. If the sublattices are not equally opposed in a way that a net magnetisation is present, the system is called ferrimagnetic. These different configurations together with the ferromagnetic one are illustrated in Figure 1-7 bottom panel. Antiferromagnetic order can be described as commensurate when the periodicity of



the spins is linked to the crystal structure or incommensurate otherwise. Depending on the configuration of the crystal lattice and the symmetry breaking involved in the magnetic ordering transition, there may be many different ways of arranging an equal number of up and down moments onto a three dimensional set of magnetic atoms. Four types of commensurate AFM ordering that are met orthorhombic crystal settings are shown in figure 1-7 top panel.

In an antiferromagnetic coordination, below the Néel temperature, the magnetization depends on how the applied field is oriented with respect to the moments. In cases where the field is aligned perpendicular to the spin polarization axis, the moments will tilt towards  $H$  leading to a roughly temperature independent susceptibility. When the field is aligned along the magnetization direction of one lattice (and hence antiparallel to the second lattice) the application of a field at zero temperature will have no net effect resulting in zero magnetic susceptibility. Increasing the temperature produces thermal agitations of the spins that will increase the magnetization until the temperature reaches an energy equal to the strength of the exchange integral at  $T_N$ .

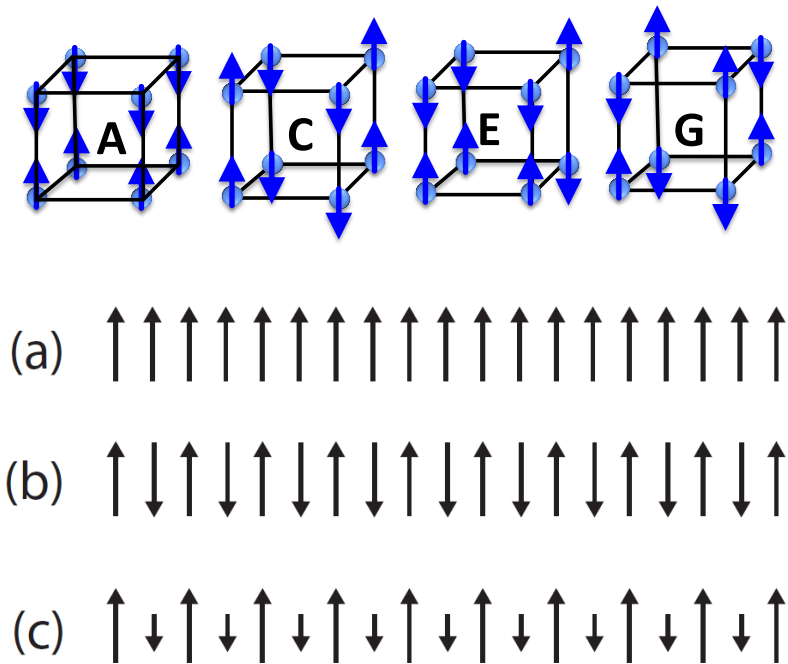


Figure 1-7 Top panel: Schematic representation of magnetic ordering in A,C,E and G- type Antiferromagnets. Bottom panel:(a)ferromagnetic (B) antiferromagnetic and (c) ferromagnetic spin alignments

### 1.3.1 Complex magnetic structures

Noncollinear magnetic orderings, which may arise from competing interactions, have their spins ordered neither parallel nor antiparallel to one another. The spin propagates in the lattice in a way that is determined by the crystal structure and the spin configurations can be classified into two types of spiral structures, *cycloid* and *proper screw* (fig.1-8). [18] Structural modulations are in the base of complex non collinear magnetic orders such as spiral, cycloid and conical magnetic orders. Such noncollinear magnetic ordering is strongly connected with ferroelectricity in magnetoelectric multiferroics explained by mechanisms such as the aforementioned Dzyaloshinsky- Moriya interactions and d-p hybridization mechanism. [18] The potential to break the inversion symmetry and produce a spontaneous (FE) polarization  $P$  is briefed in Figure 1-9. [19]

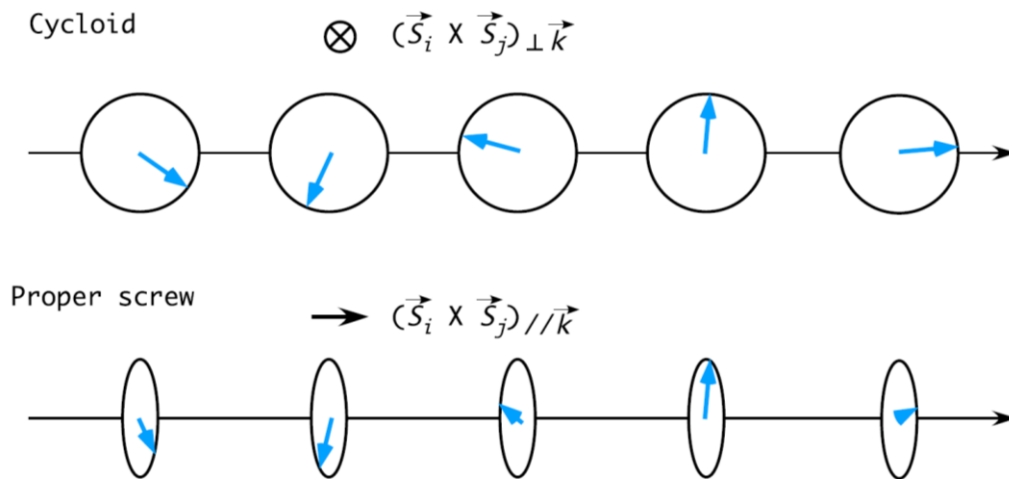


Figure 1-8 Schematic of cycloid and proper screw type magnetic ordering [18]

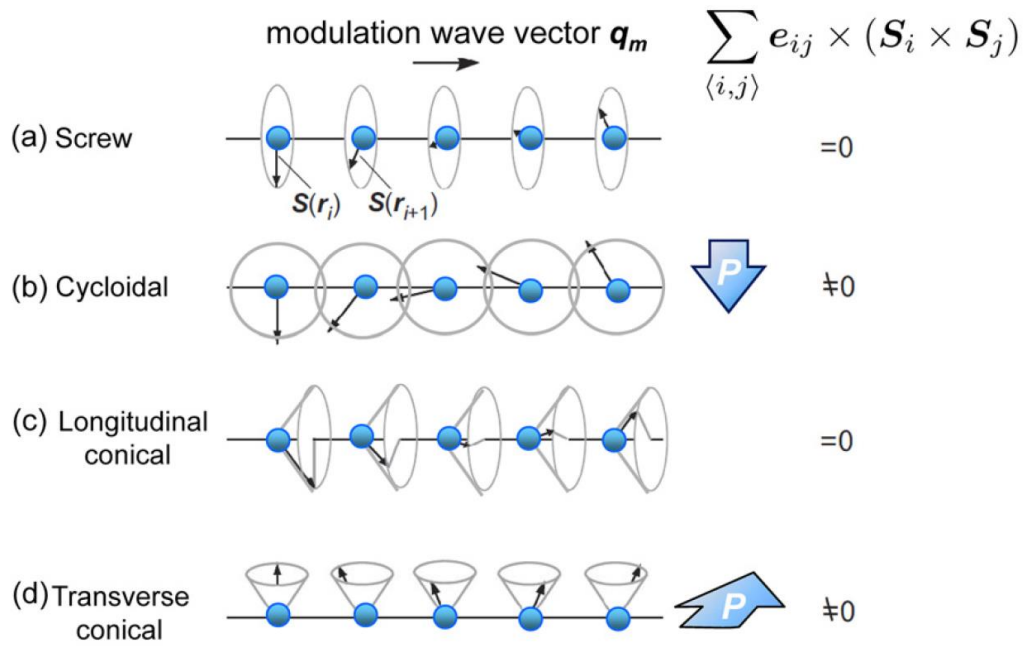


Figure 1-9 Schematics of non-collinear magnetic ordering as presented in reference[19] showing the direction of developing polarization in the cycloidal and transverse conical propagation.

### 1.3.2 Dimensionality of Magnetic Lattices

One way magnetic systems can be categorized is according to the lattice dimensionality  $d$  and the dimensionality of the magnetic moments  $D$ . The  $d$  dimensionality is related to the crystallographic structure and topology of the magnetic sublattice of the system under study and allows the distinction between 1-d (chain like), 2-d (layered) and 3-d (space) networks. The dimensionality  $D$  of the magnetic moments, refers to the geometric restrictions that apply on the magnetic moments. Thus refers to the anisotropy of the magnetic spin system.  $D=1$  refers to Ising spin system with one reference axis (spins point up or down), XY-systems allow the magnetic moment lay in one defined plane and are described by  $D=2$  while  $D=3$  describes the o-called Heisenberg magnets where the spins are allowed to point at any direction in space and so are isotropic. Possible combinations of these dimensionalities are presented in table 1-1.

#### 1.3.2.1 Competing interactions and low dimensionality

When we refer to low dimensionality magnetism we are referring to the reduction of  $d$  dimensionality that is related to the dimension of the magnetic exchange pathways.

Low-dimensional magnetism is a result of specific principles potentially responsible for the reduction of the spin dimension from the three dimensional physical space. The obvious one is enlarged distances because of missing “bridging” ions corresponding to a particular direction or even two directions within the crystal structure. Secondly, the Kanamori-Goodenough’ superexchange rules may reduce the strength of antiferromagnetic interactions in cases where the two interacting magnetic moments define the right angle with the bridging oxygen ion. [20], [21] Compounds that incorporate these structural aspects can be characterized by strong electronic correlation exhibiting a number of unusual magnetic properties that are related to strong quantum fluctuations.

In a Heisenberg system consisting of uniform spin chains with only nearest-neighbor antiferromagnetic coupling, the ground state, according to Haldane, strongly depends on the value of the spin. [22] If the chain consists of half-integer spins it should exhibit long range order. In contrary to that, integer-spin systems are of short-range nature in their ground state with an exponentially vanishing correlation function while expressing robustness to external perturbations. This happens due to an energy gap (Haldane gap) between the ground state and the lowest excited state in the excitation spectrum of an integer system. [23] So the observation of a spin gap in a integer-spin system is strongly related to lowering of dimensionality.

In cases of 2D triangular antiferromagnets, such as the system under study, where the degeneracy of competing magnetic exchange routes is diminished by one, a spatially anisotropic triangular lattice is formed. The triangular lattice as a paradigm of geometrically frustrated spin may be resolved in this way through this lowering of the dimensionality of the magnetic interactions.

#### 1.3.2.2 *Origin of Spin gap*

The spin gap in one and two dimensions can be attributed to the integer nature of spins, a special exchange topology, frustration of the underlying spin lattice or dimerization, which is the consequence of a broken translational symmetry. Lower dimensional interactions may be described by the 1D or linear chain systems, 2D planar systems, and spin ladders.

In a 1D chain, intra and inter chain interactions appear while the later become more dominant as the temperature is lowered. In this case the origin of the spin-gap behavior may be a lattice dimerization, which may set-in in the case of soft lattices in the direction of the chains while the chains are well magnetically separated. This is the case for in spin-



Peierls systems. Another possible mechanism leading to spin-gap behavior in one-dimension (1D) is sufficient frustration due to next-nearest-neighbor antiferromagnetic exchange interaction. It was shown by Majumdar and Ghosh that when the next-nearest exchange accounts for exactly half of the nearest-neighbor exchange, the Heisenberg model is exactly solvable and has a two-fold degenerated singlet ground state [24]. This solution was recently used also as a guide for constructing various more or less artificial spin Hamiltonians with the spin-liquid ground state and gapped magnetic excitations [25]. In two dimensions a route to the gapped excitation spectrum is a modified exchange topology. Such case may be expressed in triangular lattices as well as in the Kagomé lattice, where the antiferromagnetically coupled triangles share corners instead of sites in contrast to the familiar triangular lattice [26], and in the Shastry-Sutherland lattice [27].  $\text{SrCu}_2(\text{BO}_3)_2$  is topologically equivalent to the two-dimensional Shastry-Sutherland lattice. In this case the ground state of the model Hamiltonian takes into account the antiferromagnetic exchange coupling  $J$  with the nearest-neighbor  $\text{Cu}^{2+}$  magnetic moment and the antiferromagnetic exchange  $J'$  to four next-nearest neighbors. [28] In the present study we confirm the existence of correlations

The spin ladder systems serve as a bridge between one- and two-dimensional spin systems (fig. 1-10). They consist of a specific number of strongly magnetically coupled chains of infinite length and finite width. The features associated with ladder systems are dependent to the number of legs of the ladder. In odd-legs ladders there is no spin gap and have a power-law vanish of the spin correlation functions while in even-leg ladders there is a spin gap and a spin liquid ground state. As the number of legs increases we reach two dimensions and the magnitude of the spin gap is reduced to zero and this is why not all two-dimensional systems exhibit a spin gap.



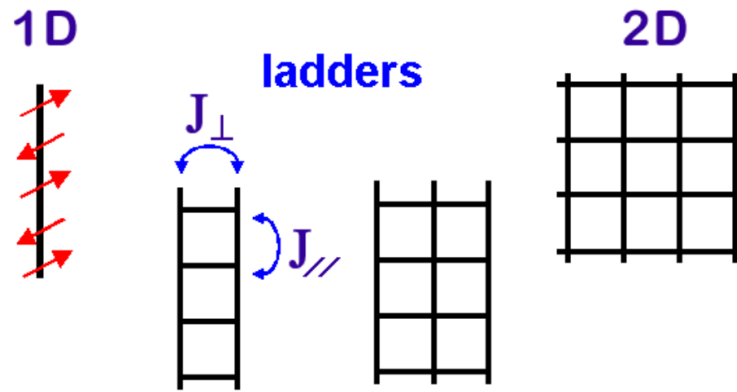


Figure 1-10 Schematic of the geometry of 2-leg and 3-leg spin ladders as crossover between 1D chain and 2D spin system. Reprinted from reference [29]

## 1.4 Frustration

According to the Third Law of Thermodynamics the entropy of a system goes to zero as the temperature approaches zero.[30] This implies that in the absence of any energy present in a closed thermodynamic system that might excite its parts out of their ground energy states, a single macroscopic ground of the lowest overall energy should form. Nevertheless observations prove the existence of systems that have degenerate macroscopic ground states meaning that even when  $T=0$  there is possibility that the system might alternate between different states. If these degenerate ground states are an outcome of the inability of the system to simultaneously minimize all interactions among its constituents, then the system can be classified as frustrated.

In the world of magnetism the term “frustration” was initially introduced in order to express the impossibility of simultaneous satisfaction of all exchange processes in a spin glass. According to Moessner and Ramirez, what is conceived as frustration is a situation where “..interactions between magnetic degrees of freedom in a lattice are incompatible with the underline crystal geometry..” [31] In the case where frustration is related to the lattice geometry it is more specifically described as “geometric frustration” and produces classically degenerate states of matter with a potential for emergent quantum properties. Thus it is a path to “magnetic frustration”. Since geometrical frustration leads to degeneracy of ground states it potentially leads to exotic, macroscopically degenerate spin-liquid ground states for which magnetic order is absent even at zero temperature. [32], [33]

The simplest example of a geometrically frustrated system is the triangular lattice Ising antiferromagnet where not all interactions can be satisfied simultaneously. The Hamiltonian in this case can be described as follows:

$$H = \sum_{(i,j)} J_{ij} S_i S_j, \quad S_i, S_j = \pm 1 \text{ or } \uparrow, \downarrow \quad (1-6)$$

where the spins  $S_{i,j}$  are unit vectors,  $i$  and  $j$  are sites of a periodic lattice and  $J_{ij}$  is assumed to depend only on their relative position. In figure 1-11 a square geometry of lattice with an antiferromagnetic configuration is presented where there is clearly no conflict in the antiferromagnetic exchange paths of the spins. In the triangular topology though, once the two of the three spins are aligned antiferromagnetically, the third one can no longer point in a direction opposite to both other spins. As a result, instead of the two ground states mandated by the Ising symmetry (up and down), there are six ground states. On 2D and 3D lattices, such degeneracies can persist. When they do, fluctuations are enhanced and ordering is suppressed.

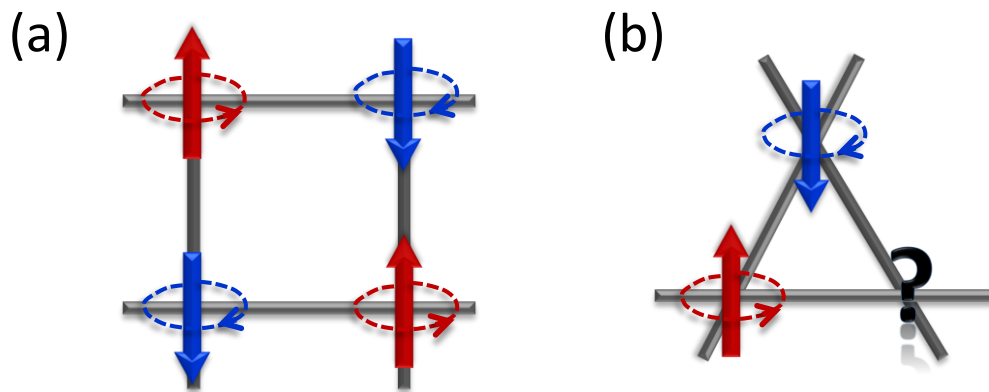


Figure 1-11 (a) Non-frustrated square lattice where each spin can be antialigned antiferromagnetically with all each neighbors (b) Frustrated Triangular lattice where two neighboring spins are paired AFM while simultaneously the third remains frustrated

On the basis of this fact, Ramirez introduced a simple empirical measure of frustration that has become widely used.[34] At high temperatures, the spin (or magnetic) susceptibility of a local-moment magnet generally follows the Curie–Weiss law,  $\chi = \frac{C}{T - \theta_w}$  where  $T$  is temperature and  $C$  is the Curie constant. This allows extraction of the Curie–Weiss temperature,  $\theta_w$ , from a plot of  $1/\chi$  versus  $T$ .  $|\theta_w|$  provides a natural estimate for the strength of magnetic interactions ( $\theta_w < 0$  for an antiferromagnet) and sets the scale for magnetic ordering in a non-frustrated material. By comparing the Curie–Weiss temperature with the temperature at which order freezes,  $T_c$ , the frustration parameter,  $f$ , is obtained:  $f = |\theta_w|/$

$T_c$ . Typically,  $f > 5-10$  indicates a strong suppression of ordering, as a result of frustration. For such values of  $f$ , the temperature range  $T_c < T < |\theta_w|$  may define the spin-liquid regime. If one extends a spatial dimension, the triangular lattice becomes face-centered-cubic (FCC) lattice (fig.1-12 (a)). A simpler but stronger two-dimensional frustrated system is kagomé lattice, with the coordination number 4 (Figure 1-12 (b)) while the three-dimensional version of the kagomé lattice is the known spinel. The pyrochlore lattice as shown in Figure 1-12 (c) is an often visited playground for the study of a novel magnetic ground state called “spin ice”.

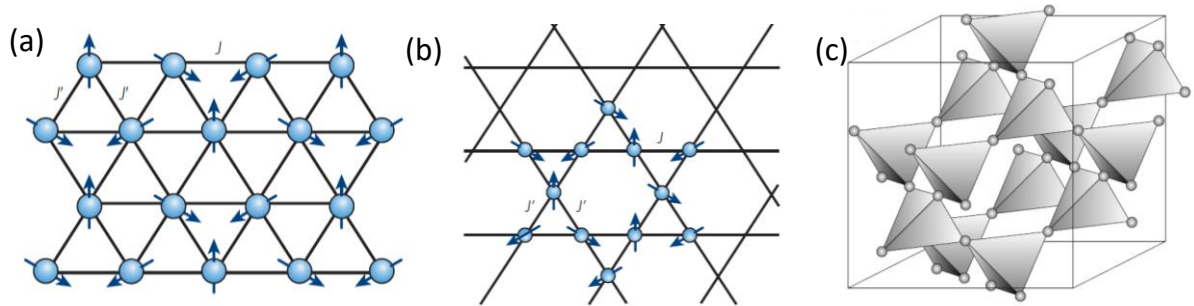


Figure 1-12 Schematics of geometrically frustrated (a) triangular lattice, (b) kagomé lattice, (c) pyrochlore lattice as it is partially reprinted by references [32], [35]

#### 1.4.1 Triangular lattice antiferromagnet

In addition to the low dimensionality, intriguing physics could take place when the symmetry of lattice does not fit with the symmetry of the exchange interaction, such as triangular lattice with antiferromagnetic exchange interaction, simply triangular lattice antiferromagnet (TLAF). [36]–[39] The low temperature magnetic phase diagram of TLAF is determined by many factors because the frustration results in the proximity of a macroscopic number of states in the energy landscape, reminiscent of spin glass.[40] However, a distinct difference between the geometrically frustrated system and the spin glass is that the degenerate ground states are separated by a tiny energy gap or no energy gap for the former, but noticeable energy gaps for the latter.

With the quasi-two-dimensional (2D) triangular-lattice  $\text{MnO}_2$  layers, the compounds  $\text{AMnO}_2$  ( $A=\text{Na}, \text{Cu}$ ) [41], [42] are of great interest as model compounds for the study of geometrically frustrated magnets and motivated the present study.

### 1.4.2 Magnetic ground state of frustrated systems

Magnetic frustration may lead to a variety of possible magnetic ground states. Three are of most interest, magnetic long range order forming a Néel state, spin glass ground state and spin liquid state.

The Néel state is a case of true long range magnetic order as it is described by a compromise between competing interactions. Since an antiferromagnetic alignment in the triangular topology is not possible for obtaining a long range magnetic order, a relief of frustration would result in a configuration in which neighboring spins are oriented by forming  $120^\circ$  deg angles relative with each other. [43] Such reorientation initiates the establishment of non collinear long range magnetic orders with helical or cycloidal spin arrangements.

In the case of spin liquids, instead of minimizing the total energy by relieving frustration through entering one state of compromising interactions a large number of equivalent states is generated. These states are based on spin-pairs that are coupled antiferromagnetically and by carrying a  $180^\circ$  degree flip on such pair a degenerate state is formed.

#### 1.4.2.1 *The spin-glass state*

Spin glasses must contain two basic properties: Disorder (or randomness) and Frustration according to Ramirez [34] Namely, the process of disordering the lattice leads to frustrated interactions. Such a state is best described as a short range magnetic ground state where the overall spin orientation is random and almost static.

The energy topology of a spin glass can be viewed as numerous local energy minima separated by many different large energy barriers, which impede relaxation between the different minima. As a result, a spin glass exists in a metastable state, since its constituents seemingly cannot overcome the large energy barriers and form a global ground state.

Spin glasses have a number of magnetic experimental signatures. However, they share many of these signatures with other magnetic systems, meaning that experiments showing evidence for glassiness do not necessarily indicate that the measured material is a spin glass. To start with, measurements of the magnetization  $M$  as a function of temperature at very low fields first after initially cooling the material in zero applied magnetic field (ZFC) and then after initially cooling the sample in the measurement field (FC). Since the spin glass exists in a metastable state, we will see a bifurcation in the resulting  $M(T)$  data at the



glass temperature created by the different initial states of the ZFC and FC measurement. A process where the spontaneous re-organization of the spin structure in a spin glass occurs is a relaxation experiment. In that, a ZFC magnetization is taken by measuring  $M$  as a function of time at a temperature below the glass transition. Once we apply the field  $M$  will slowly change from  $M = 0$  to the value that would have been obtained if we had used the FC procedure. The time over which this will happen, though, can be paraphrased from Mydosh' book as being, “[greater than] the average lifetime of a graduate student [which] is only about  $10^8$  s. [44] AC magnetic susceptibility experiments also lend great insight in determining if a material is a spin glass. Since we can make these measurements at various frequencies, we can probe the distribution of spin relaxation times in a spin glass. Also, application of even a static magnetic field as small as  $H \sim 0.01$  T can be sufficient to disturb the spin glass state in a way that the peak in the  $\chi(T)$  broadens and shifts to lower temperatures with the increase of the field. As expected, due to the absence of periodic spin structure, no Bragg peaks are expected to be found in the diffraction patterns.

#### 1.4.2.2 *Re-entrant spin-glass*

In mixed valence Mn oxides is met the phenomenon of competing FM (attributed to double exchange, DE)) and AFM (attributed to Superexchange ,SE) interactions. Any lattice distortion in such systems may affect the proportion of these competing interactions and so create various forms of magnetic order. In systems where the DE interaction is dominant in comparison to AFM interaction, there may still be frustration and there is high possibility that the system will show a reentrant spin glass state in low temperature. [45], [46] In these systems as the temperature is lowered a paramagnetic to ferromagnetic (or antiferromagnetic transition happens first and as the cooling proceeds the system re-enters a spin-glass state.

Re-entrant ferromagnets have striking properties and their magnetic response is exceedingly sensitive to the magnitude of the applied magnetic field [45]. Thus, it is a demanding task to reach a regime of linear response to be able to investigate intrinsic (not field-driven) response functions. The low temperature spin-glass state of these systems exhibits a substantially enhanced field regime of linear response compared to the high temperature ferromagnetic phase and exhibits the dynamic characteristics of a pure spin-glass state. In contrast, the frustrated ferromagnetic phase at higher temperature possesses an enhanced ageing behaviour the response function changes dramatically with age ( $t_w$ ).



The dynamics of the ferromagnetic phase show rejuvenation on decreasing temperature, but no memory phenomenon [47]. Thus, there are manifestations of disorder and frustration in the dynamics of the ferromagnetic phase of re-entrant systems; however, the equilibrium spin structures developed are more fragile and susceptible to temperature and field disturbances than the corresponding features in standard spin-glasses.

## 1.5 Multiferroicity and Magnetoelectricity

A multiferroic material is one in which more than one type of ‘ferroic’ order exists simultaneously- spontaneous polarization, magnetization and strain, exhibited individually in ferroelectric, magnetic and ferroelastic materials respectively. A schematic of the coexistence of at least two of the antiferro/ferri/ferromagnetism, ferroelectricity and ferroelasticity, namely multiferroism, is illustrated in figure 1-13. The term “multiferroic” (MF), initially coined by Schmid, [48] is usually applied to materials in which there is a coupling or coexistence of magnetic and ferroelectric (FE) order though.

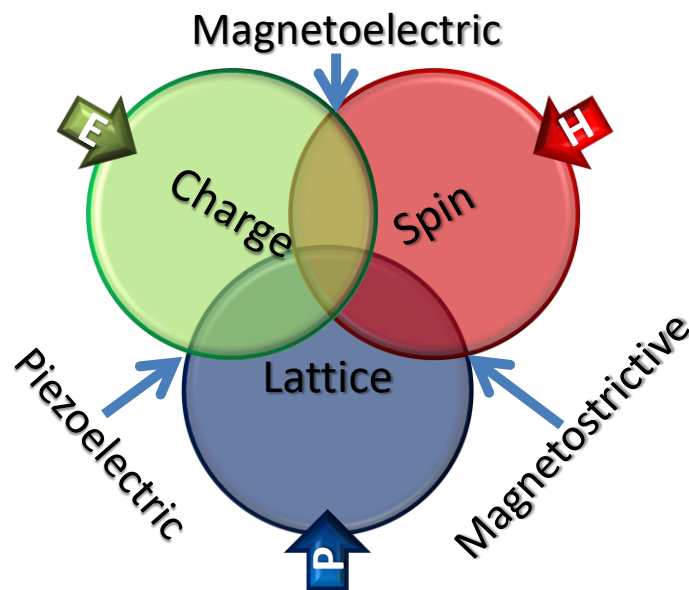


Figure 1-13 Illustration of “multiferroism” as a combination of “ferroic” properties related to lattice, spin and charge. In a ferroic material, polarization  $P$ , magnetization  $M$  and strain  $\epsilon$ , are spontaneously formed to produce ferromagnetism, ferroelectricity or ferroelasticity, respectively.

It is worth to clarify here that there is a tricky overlap of the “multiferroics” and “magnetoelectric” definition which is incomplete. Magnetoelectrics (ME) may be multiferroics but this is not always the case. More precisely, magnetoelectric coupling may

exist whatever the electric or magnetic order parameters are (not necessary that are ferroelectric and ferromagnetic at the same time). [1], [2] Magnetoelectric coupling is the coupling between magnetic and electric degrees of freedom and may arise directly between the two order parameters or indirectly via strain. The result will be an electric (magnetic) polarization induced by a magnetic (electric) field.[49] Although there are MF materials that are not ME and vice versa, the ME effect in single-phase materials is stronger when they are also MFs. For this reason, the development of these classes of materials is motivating although the case of multiferroic which combines both ferromagnetic and ferroelectric order is very rare, due to restrictions imposed by structural, physical and electronic properties[50]

As mentioned earlier, ME/MFs allow the possibility of switching the magnetization with electric field [51]–[54]. Such option opens the door for information storage applications as it could remove the main hindrance in the miniaturization of magnetic random access memory (MRAM), where the write operation requires magnetic fields or large currents [55] as well as setting new threshold for low power logic-memory devices.[2], [56] Another application field is related with the development of memory bits with multiple stable states [57], [58] or mixed memory and logic functions with various applications in the world of spintronics. [59], [60].

In recent years there has been an upsurge in research into such materials, although examples of this behavior have been already known since 1960 where magnetoelectric coupling has been confirmed in antiferromagnets  $\text{Cr}_2\text{O}_3$  by Dzyaloshinskii by the observation of a magnetization being induced by the application of electric field and vice versa. [61]



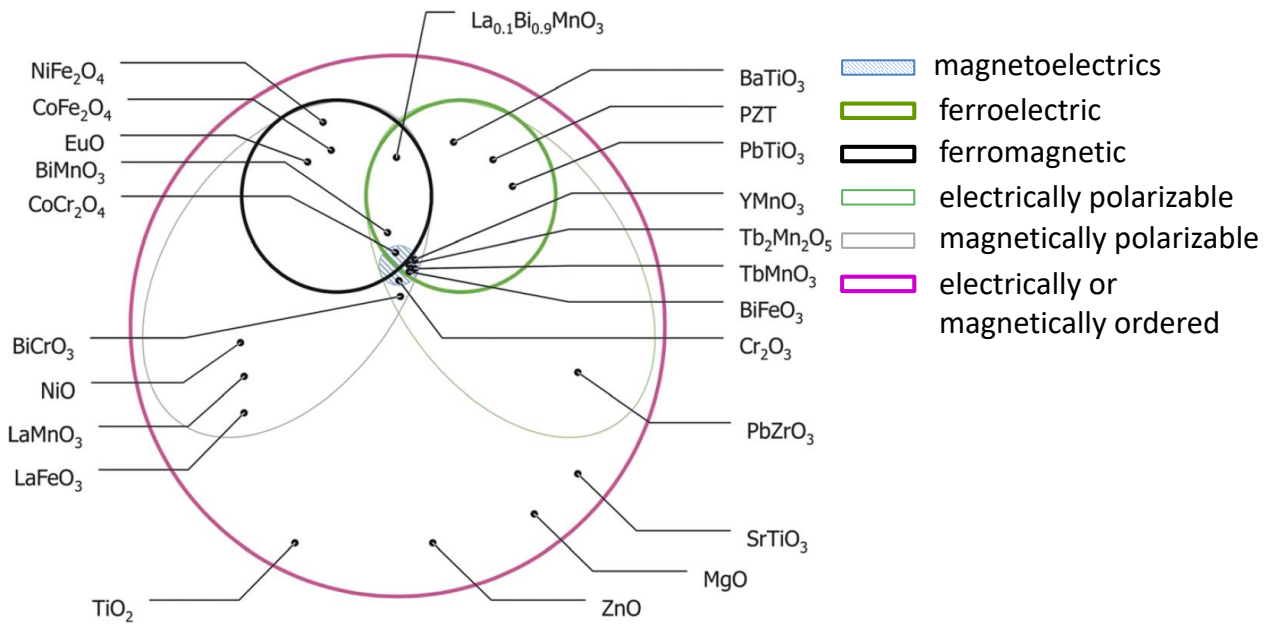


Figure 1-14 Venn diagram reprinted from J.F.Scott[2] after Eerenstein et al. [1] with representative oxides after Bibes et al.[62].

The revival of the magnetoelectric effect led by Fiebig [63] has inspired new paths of exploration into the multiferroic “jungle”. Extensive studies related to the fundamental mechanisms that sculpt the resulting magnetoelectric behavior have followed as well as further improvement in the experimental methods that probe such mechanisms straight to the final point of multiple applications. Recent extended review of Spaldin and Ramesh [64] commenting on the progress on the fundamental understanding of the coupling mechanisms, advances in characterization and modeling tools support that the era of “multiferroic material by design” is within reach while a parallel review of Cheng focuses in cutting-edge technologies of composite ME materials which can be more easily engineered.

Apart from the fact that ME/MFs are of applied interest because they allow various types of novel magnetic and electric device structures the field of multiferroics is very attractive for research also from fundamental point of view. The complexity of ME/MFs makes them of fundamental interest as a playground to study electronic behavior, coupling magnetic interactions and electric dipolar order. In the following section the driving mechanisms behind the magnetoelectric behavior will be briefly presented.

### 1.5.1 Classification of multiferroics

Typically the multiferroic family has been ordered in three main “types” namely Type I, Type II and Type III multiferroics.

#### 1.5.1.1 *Type I Multiferroics*

According to Khomskii [49] Type-I multiferroics are “older” and more numerous. Having critical temperatures of the magnetic and ferroelectric transitions well above room temperature they have been promising for applications if not for the coupling between magnetism and ferroelectricity in these materials has been rather weak. Such examples are ferroelectric perovskites which are of a displacement type or lone pair type such as BaTiO<sub>3</sub>. In the same category lay the geometric ferroelectrics such as hexagonal manganites like the case of YMnO<sub>3</sub> [65], [66] where the ferroelectricity originates from the Mn-O-Mn variation and tilt of the MnO<sub>5</sub> polyhedra due to magnetoelectric coupling[67]. In case of more complex structured boracites and fluorites like BaMnF<sub>4</sub> the ferroelectricity was recently found to have geometric origins and so it is classified to geometric ferroelectric.[2], [68] Charge order has proved to give rise to net electronic polarization in RE manganites with mixed valence transition metal as in the case of R<sub>1-x</sub>Ca<sub>x</sub>MnO<sub>3</sub>[69] as well in triangular lattices like LuFe<sub>2</sub>O<sub>4</sub>.

#### 1.5.1.2 *Type II Multiferroics- Improper MFs*

Multiferroics that are categorized as type II are named as “improper” and express ferroelectricity induced by spin order. The resulting ferroelectricity and hence the ME coupling is typically larger than in type I materials.[70] Breakage of inversion symmetry by magnetic order may happen in various ways that can merely divide this type-II in three subcategories. The first group consists of MFs that have a collinear magnetic order and so ferroelectricity arises by symmetric exchange striction (SE). An example is Ca<sub>3</sub>CoMnO<sub>6</sub> which consists of 1D chains of Co and Mn. [71]. Magnetic order in this case breaks the spatial symmetry by distorting the bonds for the sake of electric polarization. In the second group there are the materials that are non-collinear magnetically ordered described by cycloid or spiral spin arrangements, where anti-symmetric striction (SE) drives the electric polarization. In this case the polarization is driven by weaker spin-orbit coupling interactions. In this case Dzyaloshinskii –Moriya interaction is the driving force. Finally, in the third subgroup the ferroelectricity is induced by the magnetic p-d hybridization.



Most of the type II MFs show magnetic frustration which originates by lattice topology. In principle frustration leads to large degeneracy in the ground state but in cases, after cooling the material down to finite temperature the frustration may be relieved and long range order may be established based on compromising spin configurations which further initiate non-collinear spin arrangements like the ones mentioned earlier.

Some frustrated triangular lattice materials with a delafossites structure ( $ABO_2$ ) that belong to this category are  $AgFeO_2$  [72],  $ACrO_2$  [73],  $NaFeO_2$  [74], in which ICM phases down to base temperature are resulting in admixture of noncollinear arrangements with cycloidal and spiral components generating magnetic field switchable polarization  $P$ , naming  $CuFeO_2$  [75] as the most visited one. The emergence of ferroelectric polarization can be explained by both the extended inverse Dzyaloshinsky–Moriya effect and the  $d - p$  hybridization mechanism. [18]

#### 1.5.1.3 *Type III Multiferroics – Disordered MFs*

Disorder multiferroics as defined by Kleemann [76] escape the conventional schematics of *type-I* and *type-II* multiferroics, where two types of ferroic long-range order are expected to coexist under different interdependences and promise to attain a maximized bilinear ( $\alpha$  or  $EH$ ) magnetoelectric ( $ME$ ) effect under well-defined symmetry conditions. As a consequence a higher order ME response occurs. In this family one can find materials that relax in a glassy ground state. What these have in common is the indication of a strong higher order ME effect where  $\Delta\varepsilon \propto H^2$ . Nevertheless, also the first order EH-type ME effect has been observed specifically in cases where metastable homogeneous parameters are induced by field cooling as in the case of  $EuTiO_3$ . The contribution of the higher – ordered terms of the free energy formula in the understanding of ME effects will be further discussed as it is highly related to the observed results of the systems under study.

### 1.5.2 **Coupling of magnetic and electric degrees of freedom- Requirements**

#### 1.5.2.1 *Electron configuration*

Conceptually the mere existence of multiferroics is highly non trivial. [50] For most magnetic materials, the magnetic moments arise from unpaired electrons in partially occupied  $d$  orbitals and/or  $f$  orbitals. However, the spontaneous formation of a charge dipole usually needs empty  $d$  orbitals as a condition of having a coordinate bond, i.e. the so-called  $d_0$  rule. Thus, the key ions involved in typical magnetic materials and those in



polar materials are different, making these two areas of research nearly isolated from each other. This so-called “ $d^0$  vs  $d^n$  problem” was one of the first to be studied theoretically at the beginning of the recent revival of multiferroics. [49] Towards the solution of this conflict come single phase multiferroics containing two cations, one of which provides the ferroelectricity (stereochemical activity of  $6s^2$  ‘lone pair’ of electrons) while the other induces magnetism from 3d electrons like in the case of  $\text{BiFeO}_3$ . [64] Another case of two-cation materials could offer the combination of  $f$  electrons provide magnetism while the  $d^0$ -ness such as in  $\text{EuTiO}_3$ . [77] Nevertheless multiferroism can rely even in d- electron magnetism having the ferroelectricity induced through a geometrical route by lifting the inversion center through tilting or other mechanism. [64]

#### 1.5.2.2 *Symmetry*

As mentioned earlier, for the majority of materials there is no cross-coupling between electric and magnetic properties. This can be explained also by examining the effect of time and spatial inversion operations on the system. A strong coupling between the magnetic and electric degrees of freedom was observed in an insulator as an intrinsic property of matter, at 1894 by Piere Curie. [78] Curie even then claims that “*it is the symmetry that creates the phenomenon*”, recognizing that the magnetic symmetry is the key ingredient for the existence of magnetoelectricity.

The electric polarization and electric field change sign under spatial inversion, and are invariant under time reversal. Conversely, the magnetization and magnetic field are invariant under spatial inversion and change sign upon time reversal. The magnetoelectric susceptibility tensor is invariant for a material with inversion symmetry. A non-zero value for  $\alpha$  can only occur for a material which breaks both time and spatial inversion symmetry. A representation of the effect of symmetry on the coupling is illustrated in figure 1-15. According to an extended review by Schmid only 13 point groups allow breaking of both time and space symmetry. [79]



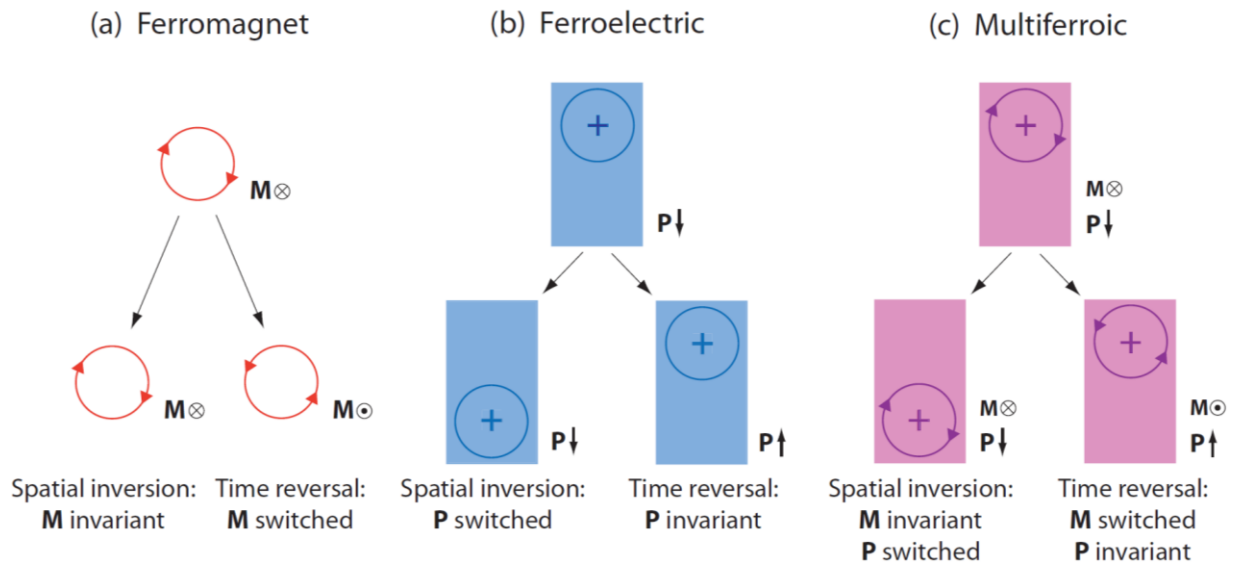


Figure 1-15 Schematic representation of the effect of spatial inversion and time reversal on (a) ferromagnets, (b) ferroelectrics, (c) multiferroics. Reproduced from reference[1]

### 1.5.2.3 Ordering

Either charge ordering or magnetic ordering is often in the roots of a magnetoelectric behaviour. Charge ordering leads to a small band gap, high conductivity and small ferroelectric hysteresis in magnetite  $\text{Fe}_3\text{O}_4$  while in newly discovered metal-organic frameworks allows the coexistence of robust ferroelectricity and magnetic order almost at room temperature. [80] Magnetic ordering as commented earlier and breakage of the inversion symmetry may cause a spontaneous polarization. That puts spin spiral ordering and other non collinear spin arrangements in the spotlight for exploration of possible magnetoelectric coupling in such magnetically ordered materials.

### 1.5.2.4 Geometry of structure

Another contrast between ferroelectric and ferromagnetically ordered systems is the way structure is distorted. While ferroelectrics undergo a phase transition as temperature changes, low temperature phase being non-centrosymmetric, ferromagnetic materials show significant Jahn-Teller distortion arising from partially filled d-shells. The latter is almost absent in most ferroelectrics as it has been postulated that Jahn-Teller distorted structure may have less driving force for off-center displacement of B-ions in the octahedra.

In addition to direct coupling, there may be instances of indirect coupling mediated by strain. This is likely to arise in two phase systems where two components are coupled via

strain. However, more recently, in cubic  $\text{SrMnO}_3$  and  $\text{EuTiO}_3$ , strain mediated ME effect is observed in single phase.

### 1.5.2.5 *Electric properties*

Electrically, while a ferroelectric material must be an insulator, it is not a constraint for a ferromagnetic material. For most ferromagnets, electronically speaking, the conductivity is due to high density of states at the Fermi level while the same is not true for ferroelectrics and insulators. However, there are a few magnetic oxides, such as half metallic magnets and ferrimagnetic oxides which show reasonable spontaneous magnetism while simultaneously being semiconducting or insulating.

In figure 1-5, Reprinted from Spaldin and Ramesh [64], the “root” mechanisms of the interplay between magnetic and ferroelectric mechanisms is beautifully summarized as an attempt to present the complex characteristics that should be met in a compound in order to act as a multiferroic.

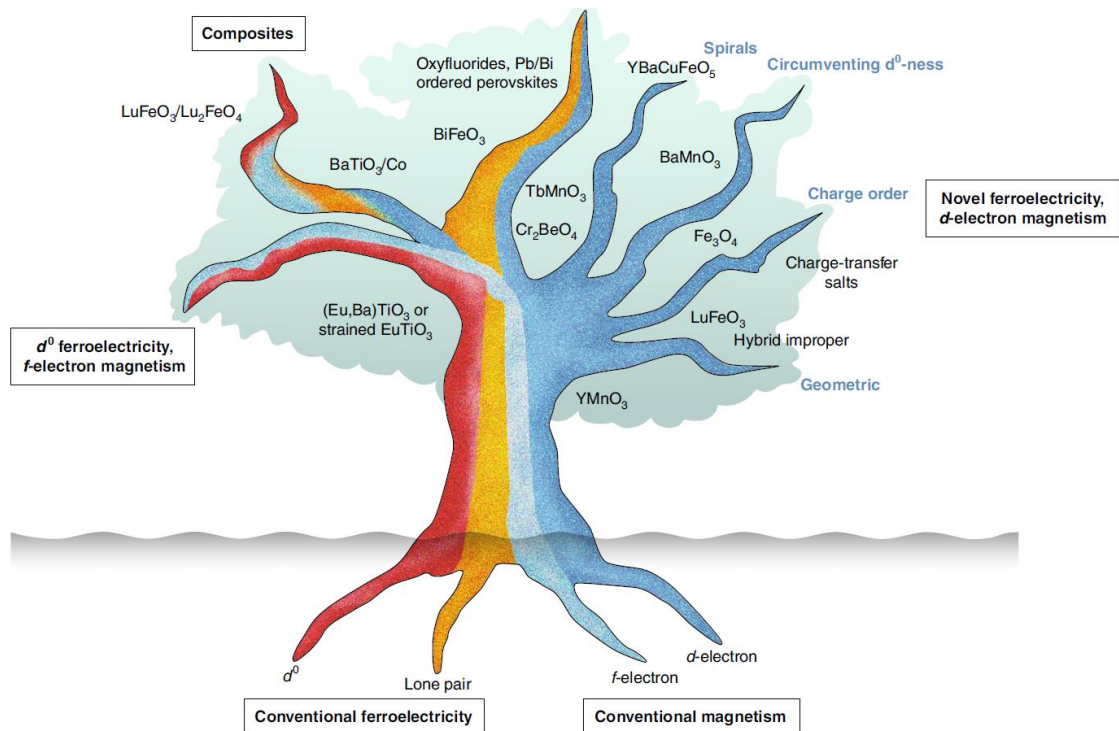


Figure 1-16 Multiferroics family tree reprinted by reference [64] Different combinations of ‘root’ magnetic and ferroelectric mechanisms are presented.

### 1.5.3 Classification of driving mechanisms based on electrons degrees of freedom

Due to their different origins, it is nontrivial to couple magnetism and electric polarity together in solids.[50] In spite of this conceptual complication, research in the past few years have found several “glues” as mentioned by Dong et al., that are hidden behind the symmetry restrictions and ordering, that may link these apparently disjoint phenomena. [81], [82]

The first one is related to the spin-orbit coupling which is a relativistic effect. In principle, a charge dipole breaks the space inversion symmetry, while a spin breaks the time reversal symmetry. Time and space are independent in non-relativistic physics, but the relativistic effect can link time and space. Thus, the spin-orbit coupling may link magnetic moments and charge dipoles. As an example, a non-collinear magnetic order with chirality breaks inversion symmetry which can be translated through the spin orbit coupling into a charge dipole.

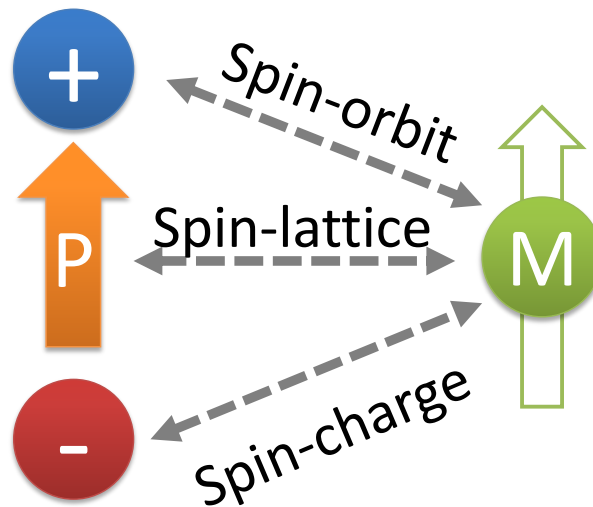


Figure 1-17 Schematic of the three mechanisms( spin-charge, spin-orbit, spin-lattice) behind the magnetoelectric coupling. Charge dipole on the left indication of ferroelectricity a magnetic moment on the right indicative of magnetism.

The second as called “glue” is the spin-lattice coupling. The magnetic interactions between magnetic ions, both the regular symmetric exchanges and the antisymmetric Dzyaloshinskii-Moriya interaction, depend on the details of the electronic exchange paths. Microscopically, the changes of bond angles and lengths seriously affect the overlaps

between wave functions and, thus, the exchanges. On this aspect, crystal distortions may tune the crystalline field in favor of coupling of already existing magnetism and polarity in a material.

The third “glue”- mechanism relates to the spin-charge coupling, mediated by the charge density distribution. [83] Since carriers (electrons or holes) can be spin-polarized in magnetic systems, the local magnetization (or even the magnetic phases) can be tuned by modulating the distribution of the charge density.

In real materials’ world all three glue-mechanisms may cooperate even if one acts as the primary driving force and is crucial to investigate in detail in order to better understand the magnetoelectricity in multiferroics.

#### 1.5.4 Magnetoelectric effect

Landau theory describes the magnetoelectric effect in a single phase material through expansion of the free energy expression in an electric field  $E$  and/or magnetic field  $H$  as:

$$F(\vec{E}, \vec{H}) = F_0 - P_i^s E_i - M_i^s H_i - \frac{1}{2} \varepsilon_0 \varepsilon_{ij} E_i E_j - \frac{1}{2} \mu_0 \mu_{ij} H_i H_j - a_{ij} E_i H_j - \frac{1}{2} \beta_{ijk} E_i H_j H_k - \frac{1}{2} \gamma_{ijk} H_i E_j E_k - \frac{1}{2} \delta E_i E_j H_k H_l \quad (1-7)$$

Here  $\varepsilon$  and  $\mu$  are the dielectric permittivity and magnetic permeability respectively. The second and the third term in Equation (1-7) are the temperature dependent electrical polarization,  $P_i^s$ , and magnetization,  $M_i^s$ . Fourth and fifth terms describe the effect of electrical and magnetic field on the electrical and magnetic behavior respectively, while sixth term consisting of  $a_{ij}$  describes linear magnetoelectric coupling. The next two terms consisting of  $\beta_{ijk}$  and  $\gamma_{ijk}$  are third rank tensors and represent higher order coupling coefficients.

Differentiation of Equation (1-7) with respect to electric and magnetic fields respectively leads to polarization and magnetization expressions as presented below:

$$P_i(\vec{E}, \vec{H}) = \frac{-\partial F}{\partial E_i} = P_i^s + \frac{1}{2} \varepsilon_0 \varepsilon_{ij} E_j + a_{ij} H_j + \frac{1}{2} \gamma_{ijk} H_i E_j E_k - \dots \quad (1-8)$$

$$M_i(\vec{E}, \vec{H}) = \frac{-\partial F}{\partial H_i} = M_i^s + \mu_0 \mu_{ij} H_j + a_{ij} E_i + \beta_{ijk} E_i H_j + \frac{1}{2} \gamma_{ijk} E_j E_k - \dots \quad (1-9)$$



In most cases, we are interested to know about the linear magnetoelectric coefficient,  $\alpha_{ij}$ , as magnetoelectric effect is linear in most compounds. This coefficient basically quantifies the dependence of polarization on magnetic field or of magnetization on the electric field. In case of multiferroics, although many linear magnetoelectric effects are expected because these materials often possess large susceptibility and permeability respectively, this is not a necessary condition as some ferroelectrics and ferromagnets do show small dielectric susceptibility and magnetic permeability.

Increased interest has recently arisen in second-order  $EH^2$  and  $E^2H$ , and third-order  $E^2H^2$  effects, synonymously also referred to as  $\beta$ ,  $\gamma$ , and  $\delta$  effects, respectively. They are very precisely measured, *e. g.*, by *ME* Superconducting Quantum Interference Device (SQUID) susceptometry [12] via the electric field-induced magnetization components of (1-9). It is worth to mention that high-order ME effects have been successfully summarized by Schmid [48]. The tensor  $\beta$  in equation (1-7) parameterizes a magnetic-field-induced ME effect. It was first observed by Hou and Bloembergen, who called it the ‘paramagnetoelectric effect’. [84] It represents the most thoroughly investigated higher-order ME effect. It is allowed in time symmetric media and, thus, in the absence of long-range magnetic order. On the same side, the tensor  $\gamma$  in equation (1-7) parameterizes an electric-field-induced ME effect. It is allowed in centrosymmetric media and was observed by Cardwell. [85]

The magnetoelectric coupling may be experimentally probed either directly or indirectly. Indirect measurements of magnetoelectric coupling include measurement of changes in the magnetization near the magnetic transition temperatures or changes in dielectric constant near the magnetic transition temperature. However, such measurements do not provide any mechanistic insight into the coupling constant. Direct measurements measure magnetic response of material to an applied electric field or electric response to an applied magnetic field.

## 1.6 Structure of Dissertation

In the present thesis we detail the systematical study of layered  $\text{Na}_x\text{MnO}_2$  ( $x= 0.7-1$ ) systems.

In chapter 2, various experimental techniques that have been used for the study of nuclear structure, chemical characterization and several physical properties of the synthesized specimens, are briefly described. These include in-house lab-hosted methods and



instrumentation for measuring dc magnetic susceptibility, dielectric constant. Each technique probes different physical properties of samples and specific phenomena are observed, accordingly, which are described in the same chapter. The detailed description of the experimental procedure of selected techniques is also presented in Appendix A.

The protocols and methods of synthesis of the materials under study are detailed in chapter 3. The growth of quality single crystals of different air-sensitive polymorphs of  $\text{NaMnO}_2$ , progressed by floating zone technique (FZT), utilizing our experience gained during missions in the laboratories of the Physics Department of the University of Warwick and has been an innovation to the field of  $\text{Na}_x\text{MnO}_2$  compounds. The availability of sizable crystals is crucial for experimental techniques that require large volumes of areas, such as neutron scattering, a powerful technique to study nuclear and magnetic structure.

In chapter 4,  $\beta\text{-NaMnO}_2$  has been revisited for a thorough study of the crystallographic and dynamical properties. A single phase nuclear structure model has been used to describe the structural modulations that are strongly connected to the evolution of the magnetic structure from an AFM long range order to a proper screw magnetic state, hinting on possible emerging ME effect.

Starting from polycrystalline powders grown under Ar atmosphere ( $\beta\text{-NaMnO}_2$ ) single crystals of  $\alpha\text{-Na}_{0.7}\text{MnO}_2$  crystallized in hexagonal system have been grown with FZT. In chapter 5, the anisotropic magnetic susceptibility features are commented indicating a glassy behavior at low temperatures as well as a preliminary dielectric characterization.

Finally, single crystals of  $\alpha\text{-Na}_{0.96}\text{MnO}_2$  grown with FZT are presented in chapter 6. An interesting interplay between competing interactions initiated by the  $\text{Mn}^{3+}/\text{Mn}^{4+}$  ratio gives rise to local inhomogeneities allowing the existence of a weak FM component observed in anisotropic magnetic measurements while single crystal neutron experiment confirms the coexistence of short range correlations and AFM long range order. Features in dielectric permittivity measurements in both powders and single crystals suggest the onset of magnetic order while a weak magnetocapacitance effect is observed in powders' detailed dielectric study.

In the end, in chapter 7, the wake of this experimental journey is put into few words together with perspectives inspired by the current study.



## Chapter Two:

# Experimental Methods

---

The main experimental techniques that have been utilized for the investigations and realizations described in this thesis will be presented in this chapter. There will be given details over methods covering sample synthesis and preparation, as well as laboratory measurements using both in-house custom-made experimental installations and standard instrumentation for characterization of physical properties. The underlying physics of X-ray scattering and neutron scattering experiments carried out at central large scale facilities will be also briefly described.

### 2.1 Solid state synthesis

All the polycrystalline samples used for the experiments detailed in the present thesis have been prepared in the Functional NanoCrystals Laboratory (FUN-L) in the Institute of electronic structure and laser (IESL-FORTH), in Crete, using solid state reaction. As solid state reactions, are defined reactions between or within solid reactants to yield a solid product and are prototypical of solvent free reactions. A remarkable difference between solid state reactions and reactions using solvents is that solid state reactions occur within the rigid constraining environment of the crystal lattice. [86], [87] The finite environment of the reactant crystal lattice can control the kinetic features of a reaction and hence the nature of products while high temperatures are necessary to provide the energy for thermal movement of the ions in order to surpass lattice restriction. Nevertheless, however high the



heating temperature, it still remains well below the melting point. The product of such reaction is not necessarily the thermodynamically most stable product available to the system, but is rather the one dictated by the reaction pathway available in the surroundings of the solid. Solid state synthesis is a quite simple and cost efficient method and rather common for preparation of polycrystalline oxides. However simple and cost efficient though, they are intrinsically slow since despite the reactants are well mixed in particle level they are quite inhomogeneous in the atomic level. [88] Other drawbacks of the method is the production of secondary phases that are formed in temperatures lower than the final heating temperature while there is possibility to find unreacted traces of the starting materials in the final product.

For the synthesis of  $\text{NaMnO}_2$  polymorphs, the chosen reacting agents had to be accurately weighted in an appropriate ratio, well mixed and ground to fine powder before being pelletized. Due to volatility of Na and sensitivity to ambient conditions of the final products, the reaction was taking place under continuous flow of specific gas atmosphere and the final product was often “quenched”. Typically, powders were heated 1-3 times for 24-hours sessions (dwelling time) or more, at temperatures up to  $950^\circ\text{C}$  in alumina crucibles without any preheating of the reactants. Details for all used protocols will be presented in chapter 3.

## 2.2 Single Crystal growth

Single crystals have been vital to studies of a plethora of anisotropic systems giving the opportunity to better understand the physical mechanisms behind magnetic and magneto-electric behavior and so offering a boost in the exploration of multiferroic materials. Apart from multiferroicity, the necessity to further explore local magnetic behavior motivated the quest for single crystals of the Na-Mn-O system under study. The thermodynamically stable crystals are a powerful tool in the understanding of challenging Na-Mn-O system in which very similar free-energies of its polymorphs suggest compositional modulation at low energy cost and realization of intermediate phases. Taking into account the demanding nature of the air-sensitive samples in the Na-Mn-O phase space, it is worth noting that only recently we succeeded, for the first time, in having optimized the growth conditions and reached into phase-pure crystal specimens. The crystal growth covers a wide range of study on synthesis, nucleation, growth rates, translation rates, morphological stability, seeding process, segregation, stability, growth interfaces, growth atmosphere and



crystalline defects. As it is expected also the selection of the crystal growth method depends on various parameters of requirement such as the growth kinetics, size, shape, purity and the cost involved in the process of the growth. The 3 general classifications of the numerous methods of crystal growth are: i) growth from solid phase, ii) growth from vapour and iii) growth from liquid phase (growth from melts & growth from solvent).[89] All attempts for crystal growth of the system Na-Mn-O that have been made until now belong in growth from liquid category. The first attempts for single crystal growth of the Na-Mn-O system have been done by Jansen, Hoppe and Brachtel back in the 1970s using sealed crucible technique while the hydrothermal method was later used by Hirano for sub stoichiometric polymorphs of the system. [90]–[92] The hydrothermal technique has the ability to grow crystals which are not stable at the melting point. The crystal growth is achieved in an apparatus consisting of a fused high pressure metal vessel called the autoclave. The result of the first  $\text{NaMnO}_2$  crystals was needle-like crystals of 1-2mm length and  $\varnothing = 0.1$  mm. Since then, the growth of large volume crystals has remained elusive. Among the numerous methods available and under the guidance of Prof. Balakrishnan the methods of Flux and Floating Zone have been explored in the quest of sizable single crystals of Na-Mn-O that were crucial for the large scale experiments and will be further described in the following paragraphs.

### 2.2.1 Flux method

Flux growth is the growth of crystal from molten salt solvent. The principle of the flux-growth is similar to the growth in solution: the temperature is higher and related to the melting temperature of the flux in this case. Flux is defined as a molten solvent in high temperature and allows the growth to carry on well below the melting temperature of the solute material which is the main advantage of the method. Simple metals (Ni, Fe...), oxides ( $\text{B}_2\text{O}_3$ ,  $\text{Bi}_2\text{O}_3$ ), hydroxides (KOH, NaOH), salts (BaO, PbO,  $\text{PbF}_2$  and other halides ...) can be used as solvents. The growths demand high temperature furnace equipment and the crystals grown by this method are free from mechanical and thermal constrains. [89] However, the choice of flux is yet a difficult procedure as it entails various thermodynamical factors. From the solubility point of view, a desirable flux should be chemically similar to the character of bonding to the solute and it should not be a barrier to the solute movement in the flux. Other desirable properties of the ideal solvent are: Low



reactivity with the crucible, ease of separation from the grown crystal by physical or chemical means, low tendency of solvent to creep out of the crucible etc.

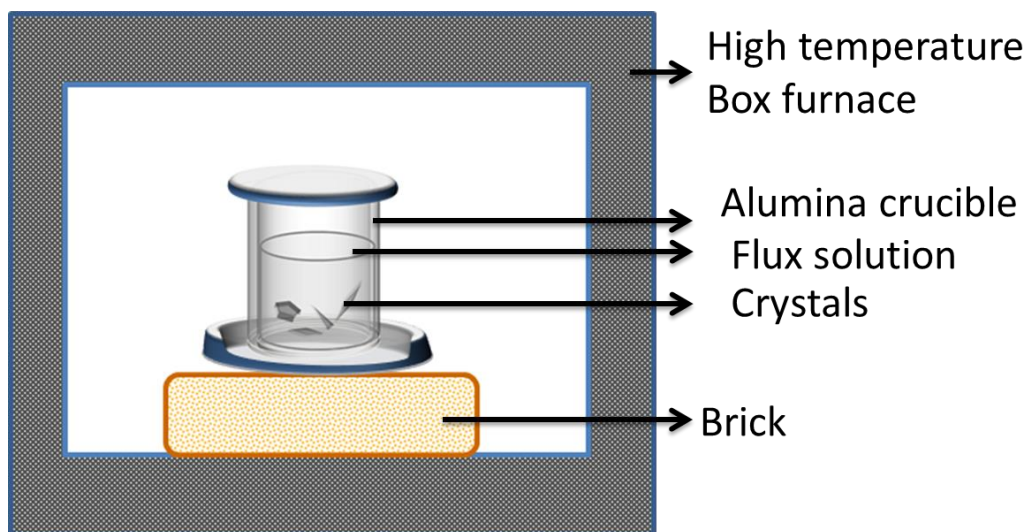


*Figure 2-1 Schematic (internal view) of high temperature box furnace during the Flux growth of single crystals*

In the case of Na-Mn-O system we experimented with 2 different fluxes using of NaCl and  $B_2O_3$  after studying similar system  $Na_xCoO_2$ . The protocols and results will be described in detail in chapter 3 for all systems studied in the present thesis.

### 2.2.2 Floating zone technique

The floating Zone (FZ) method for single crystal growth is based on the zone-melting principle and was invented by Theuerer in 1962. It is a method developed from Bridgman-Stockbarger method. The basic idea in float zone (FZ) crystal growth is to move a liquid zone through the material. If properly seeded, a single crystal may result. It is most broadly utilized in growing crystals of silicon but it proved beneficial for high purity growth of sizable crystal boules of magnetic materials including manganese perovskites, low dimensional compounds, frustrated magnets and superconducting compounds. Its main advantage is the absence of crucible which is one of the sources of contamination in the other methods while it gives the grower the opportunity to control atmosphere, pressure and growth rate. The growths are carried in optical furnaces. There are systems of different geometries (two or four elliptical mirrors) equipped with halogen or xenon lamps that ensure a uniform temperature profile as the light is focused in a well-defined area, creating a narrow region of high temperature which is called the “hot zone”. Direct temperature

measurement in the image furnace by pyrometry is not possible since, by definition, all viewing axes inside the mirrors are focused on the image of the lamps. It is therefore the lamp temperature, rather than the sample temperature that is probed during the growth. The growths of the Na-Mn-O system were carried out using a 2 mirror Canon Machinery SC1-MDH 11020 (University of Warwick) with standard double elliptical mirror geometry equipped with two 1.5 kW lamps, which can reach a maximum operating temperature of 2000 degrees Centigrade. The floating zone technique demands long rods of polycrystalline samples. These polycrystalline rods are prepared by compacting the powder into a waterproof balloon before compressing isostatically by submerging in water and applying high pressure ( $>150 \text{ kg cm}^{-2}$ ). The resulting rods are sintered to reduce the possibility to crumble upon handling. One sintered polycrystalline rod, which is used as a feed, is suspended from a shaft using platinum wire (which is non-reactive and has a high melting point). A second polycrystalline rod or crystal of the same compound is mounted directly underneath and used as a growth “seed”. Both are enclosed inside a sealed quartz tube in the optical floating zone furnace, as shown in Figure 2-2. The shafts of the “feed” and “seed” rods are counter-rotated and are brought close to each other at the center of the furnace. The temperature in the “hot zone” is gradually increased until both rods reach their melting points. At this point they are brought together to create a molten zone which is held together by the surface tension of the material. The counter-rotation movement tends to homogenize both the temperature distribution and composition in the molten zone. Both rods are lowered through the hot region in a way that the feed rod is transformed from solid polycrystalline to molten state and then into a single crystal boule as it leaves the high temperature zone and re-solidifies upon slow cooling. One of the most challenging aspects in this method is the stabilization of the molten zone that ensures a quality crystal. This stability can be maintained by controlling the power of the light bulbs so as to raise/lower the temperature in the zone while controlling the individual rate at which each shaft is lowered. Small adjustments to their positions are usually necessary especially during the initial formation of the molten zone. Crystal growth can be carried out in a variety of atmospheres as air, oxygen, inert gases and combination of these under continues flow or under controlled pressure. Details about the growth protocols followed for the single crystals used in the present thesis will be given in chapter 3.



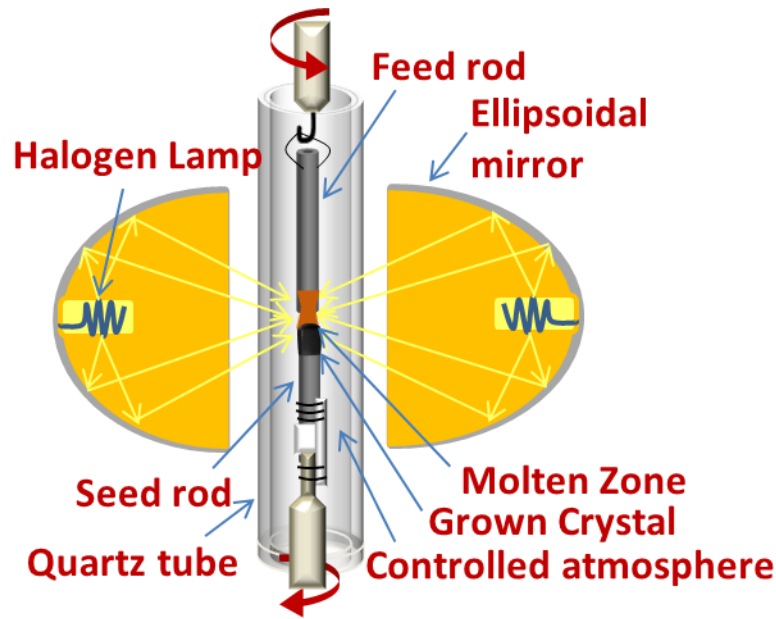


Figure 2-2 Schematic of an optical furnace with feed and seed rods mounted.

## 2.3 Basic Structural and Chemical characterization techniques

### 2.3.1 X-ray diffraction[93], [94]

X-ray diffraction is the principle technique in solid state chemistry used for “fingerprint” characterization of crystalline materials and determination of their nuclear structure. In a preliminary characterization it is used to define the phase and provide the first information about the quality of the synthesized sample.

If a sample is bathed in a parallel beam of monochromatic x-rays, the incident rays will scatter isotropically from the atoms in the sample. If the sample also exhibits crystalline order, the x-rays scattered in certain directions will be in phase, reinforcing one another to produce a measurable signal. As illustrated in figure 2-3 the x-rays hit atoms A and B and scatter in all directions. The path difference between the trajectories of the two waves are reflected at the same angle so as the blue rays are in phase with each other. Path length differences for rays between the first and second layers will be equal to:

$$sC + Ct = D\sin\theta + D\sin\theta \quad (2-1)$$

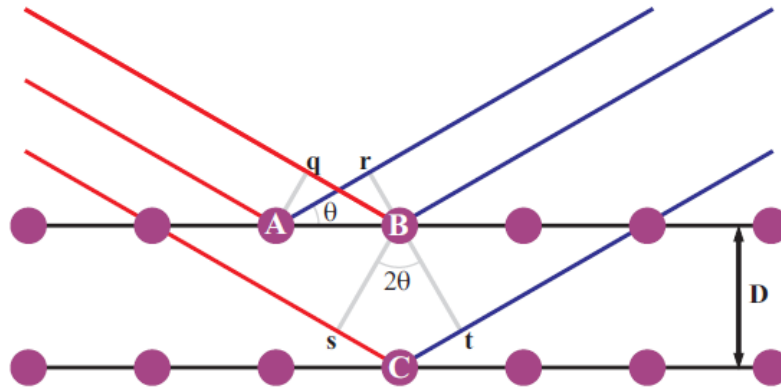


Figure 2-2-3 The diffraction processing real space. Parallel monochromatic x-rays (red) are incident on the planes of atoms (purple spheres). The scattered rays that are in phase with one another are shown in blue. Reproduced from Thesis of Dr Wooldridge.

From which the Bragg law is derived and written as follows:

$$n\lambda = 2D \sin \theta \quad (2-2)$$

where  $\lambda$  is the wavelength of the X-ray beam,  $\theta$  is the incident angle, and  $d$  is the distance between crystal planes. The value for  $D$  is dependent on the Miller indices  $h$ ,  $k$  and  $l$ .

It is clear that diffraction provides a nondestructive technique that determines the spacing between lattice planes in a crystalline sample from which the crystal symmetry and lattice constants may be deduced.

The best visual representation of the phenomenon of diffraction has been introduced by P.P. Ewald. Consider an incident wave with a certain propagation vector,  $k_0$ , and a wavelength,  $\lambda$ . If the length of  $k_0$  is selected as the inverse of the wavelength  $|k_0| = 1/\lambda$  then the entire wave is fully characterized and it is said that  $k_0$  is its wavevector.

When the primary wave is scattered elastically, the wavelength remains constant. Thus, the scattered wave is characterized by a different wavevector,  $k_1$ , which has the same length as  $k_0$ :  $|k_1| = |k_0| = 1/\lambda$ .

The angle between  $k_0$  and  $k_1$  is  $2\theta$  (Fig. 2-4, top panel-left). We now overlap these two wavevectors with a reciprocal lattice (Fig. 2-4, top panel-right) such that the end of  $k_0$  coincides with the origin of the lattice. As shown by Ewald, diffraction in the direction of  $k_1$  occurs only when its end coincides with a point in the reciprocal lattice. Considering that  $k_0$  and  $k_1$  have identical lengths regardless of the direction of  $k_1$  (the direction of  $k_0$  is fixed by the origin of the reciprocal lattice), their ends are equidistant from a common point, and therefore, all possible orientations of  $k_1$  delineate a sphere in three dimensions.

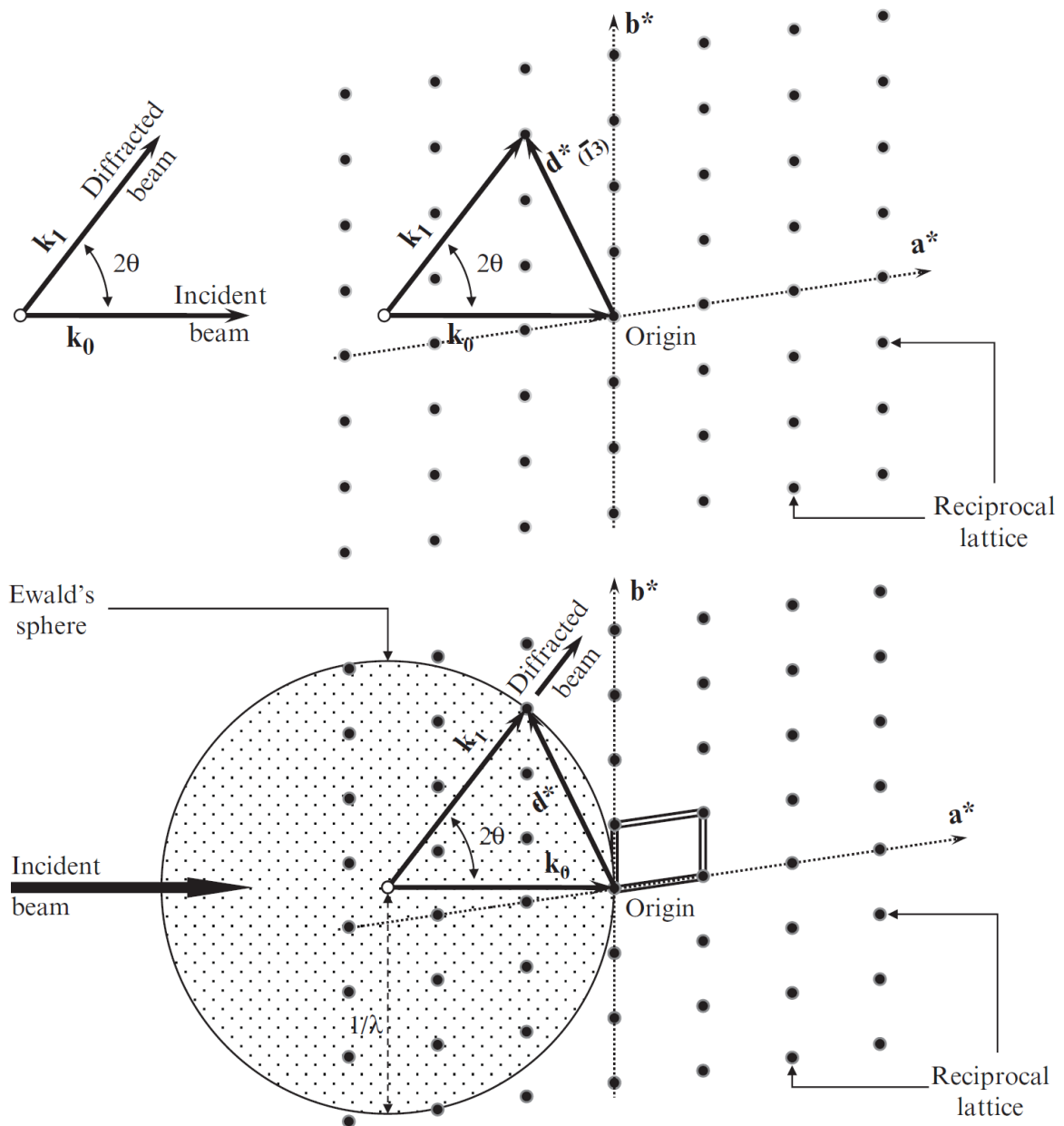


Figure 2-4 Top panel: The incident ( $k_0$ ) and diffracted ( $k_1$ ) wavevectors originating from a common point (left) and the same two vectors overlapped with the two-dimensional reciprocal lattice, which is based on the unit vectors  $a^*$  and  $b^*$  (right). The origin of the reciprocal lattice is chosen at the end of  $k_0$ . Bottom panel: The visualization of diffraction using the Ewald's sphere with radius  $1/\lambda$  and the two dimensional reciprocal lattice with unit vectors  $a^*$  and  $b^*$ . The origin of the reciprocal lattice is located on the surface of the sphere at the end of  $k_0$ .

This sphere is called the Ewald's sphere and it is shown schematically in Fig. 2-4. Obviously, the radius of the Ewald's sphere is the same as the length of  $k_0$ , in other words, it is equal to  $1/\lambda$ . The simple geometrical arrangement of the reciprocal lattice, Ewald's sphere, and three vectors ( $k_0, k_1$ , and  $d_{hkl}^*$ ) in a straightforward and elegant fashion yields Bragg's equation.

The Ewald's sphere and the reciprocal lattice are essential tools in the visualization of the three-dimensional diffraction patterns from single crystals. They are also invaluable in the understanding of the geometry of diffraction from polycrystalline (powder) specimens.

If a stationary single crystal is randomly oriented and irradiated by monochromatic X-rays, only a few, if any points of the reciprocal lattice will coincide with the surface of the Ewald's sphere (fig.2-5 left). This occurs because first, the sphere has a constant radius determined by the wavelength, and second, the distribution of the reciprocal lattice points in three dimensions is fixed by both the lattice parameters and the orientation of the crystal. The resultant diffraction pattern may reveal just a few Bragg peaks. Many more reciprocal lattice points are placed on the surface of the Ewald's sphere when the crystal is set in motion, for example, when it is rotated around an axis. The rotation of the crystal changes the orientation of the reciprocal lattice but the origin of the latter remains aligned with the end of the incident wavevector.

Hence, all reciprocal lattice points with  $|d^*| \leq 2/\lambda$  will coincide with the surface of the Ewald's sphere at different angular positions of the crystal. When the rotation axis is collinear with one of the crystallographic axes and is perpendicular to the incident beam, the reciprocal lattice points form planar intersections with the Ewald's sphere. The planes are mutually parallel and equidistant, and the resultant diffraction pattern is similar to that illustrated in Fig. 2-5 right.

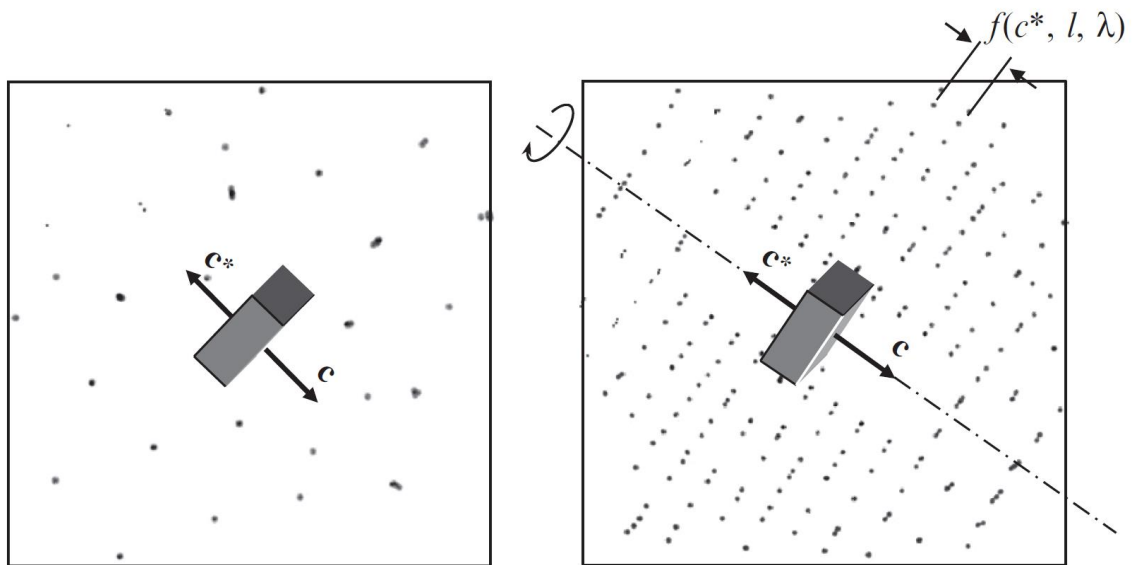


Figure 2-5 Two dimensional diffraction pattern of a stationary (left) and rotating (right) single crystal. The incident wavevector is perpendicular to both the detector and the plane of the figure. Dash dotted line show the rotation axis which is collinear with  $c^*$ .

There are several conventional laboratory techniques for measuring x-ray diffraction, corresponding to the variation of the two independent parameters in Bragg's law and can be divided in three categories summed in Table 2-1:

Table 2-1 Different experimental approaches using x-rays

	<b>POWder</b>	<b>Rotating Crystal</b>	<b>Laue</b>
<b>Probed characteristic</b>	Lattice parameters	Lattice constant	Orientation
<b>Samples</b>	Polycrystalline	Single crystals	Single Crystals
<b>X-ray beam</b>	Monochromatic	Monochromatic	Polychromatic
<b>Geometry</b>	Variable angle	Variable Angle	Fixed angle

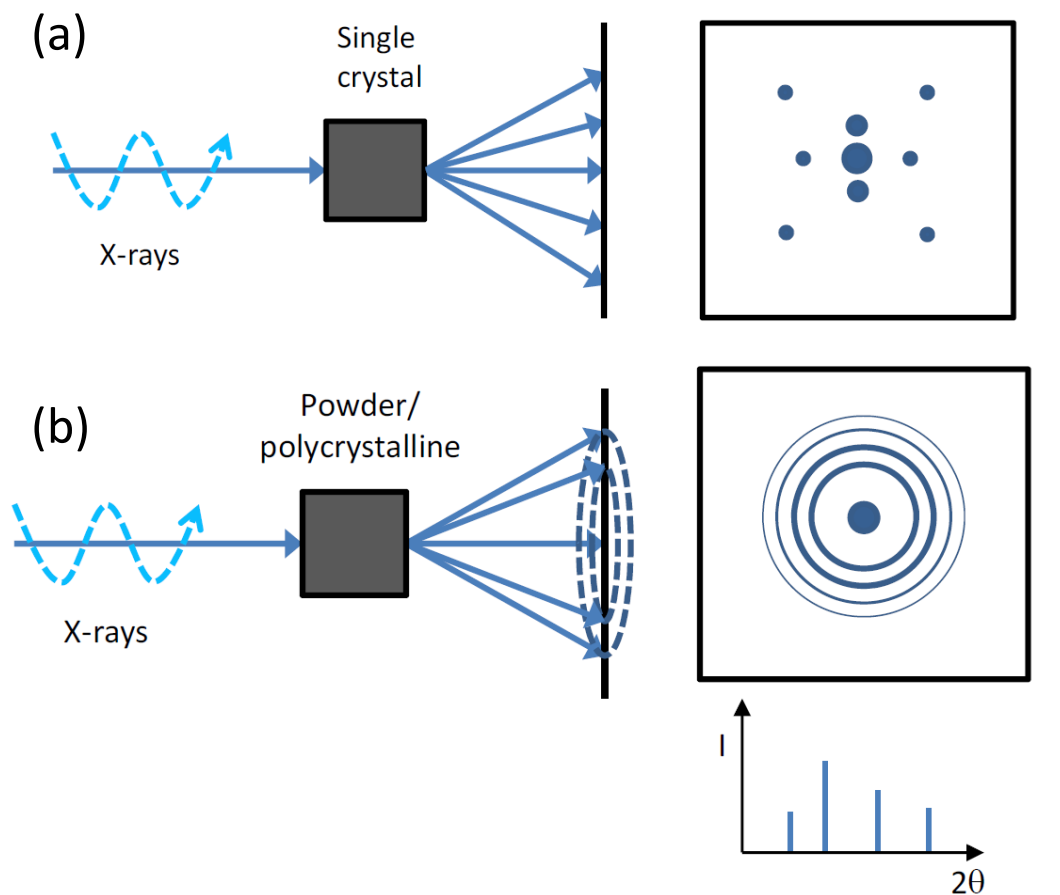


Figure 2-6 (a) X-rays diffracted by single crystal produce a series of spots in Ewald sphere (b) All orientations are present resulting in continuous Debye rings. This gives the line diffraction pattern with discrete reflections.

### 2.3.1.1 *X-Ray Powder Diffraction (XRPD)*

Powder X-ray diffraction was used to check phase formation and determine the crystal structure of synthesized samples. In powder x-ray diffraction, the wavelength of the radiation is kept constant and the diffraction angle  $2\theta$  is varied. The process is that of elastic scattering. A polycrystalline powder sample consists of small crystallites, aligned randomly with respect to one another. The random alignment of the crystallites forces all the possible orientations of the x-ray onto the surface of a cone. According to that, bigger D spacing will create cones with smaller angles and vice versa.

Two different X-ray machines have been used for the experiments presented in this thesis. The first one has been the in house Rigaku D/MAX-2000H rotating anode diffractometer and a (more advanced) Panalytical X'Pert diffractometer Pro multipurpose X-ray diffraction system (MPD), with monochromated Cu  $K_{\alpha 1}$  Radiation (University of Warwick). Both of them are using the Bragg Bretano Geometry ( $\theta$ -  $2\theta$ ) which is illustrated in Figure 2-7. In this geometry, the anode can be fixed and the sample and detector can be rotated by  $\theta$  and  $2\theta$ , respectively. In our case both the x-ray source and the detector are rotated during the measurement.

For interpretation of the diffraction pattern, information of powder diffraction data for most compounds can be obtained from The International Centre for Diffraction Data (ICDD) Powder Diffraction File (PDF) database. The software EVA has been used for search and comparison of the sample's diffraction pattern to the PDF library.

The purity of the sample under study has then been ascertained while a calculation of the volume fraction of any impurities is made possible by comparing the intensity ratios of the strongest peaks in the diffraction patterns.



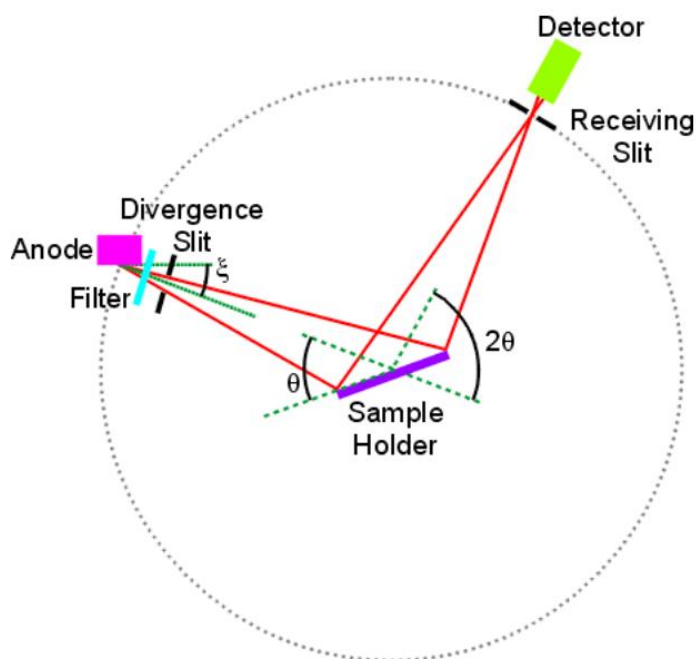


Figure 2-7 Incident X-rays are scattered by a polycrystalline sample according to the aforementioned Bragg's law in a Bragg –Brentano topology. Reprinted by "<http://pd.chem.ucl.ac.uk/pdnn/inst1/optics1.htm>"

Due to the air sensitive nature of the system under study a special sample holder has been designed to keep the powder (or pulverized crystals) sealed with mylar under inert atmosphere and minimize the time of exposure to ambient conditions of humidity and oxygen. A picture of the holder is presented in figure 2-8. As this has been a custom made holder for the specific Rigaku D/MAX-2000H machine, in cases if using a different diffractometer mixing powder with high vacuum grease inside an inert environment (i.e inside an Ar Glove Box) was usually used to protect the sample from oxidation.

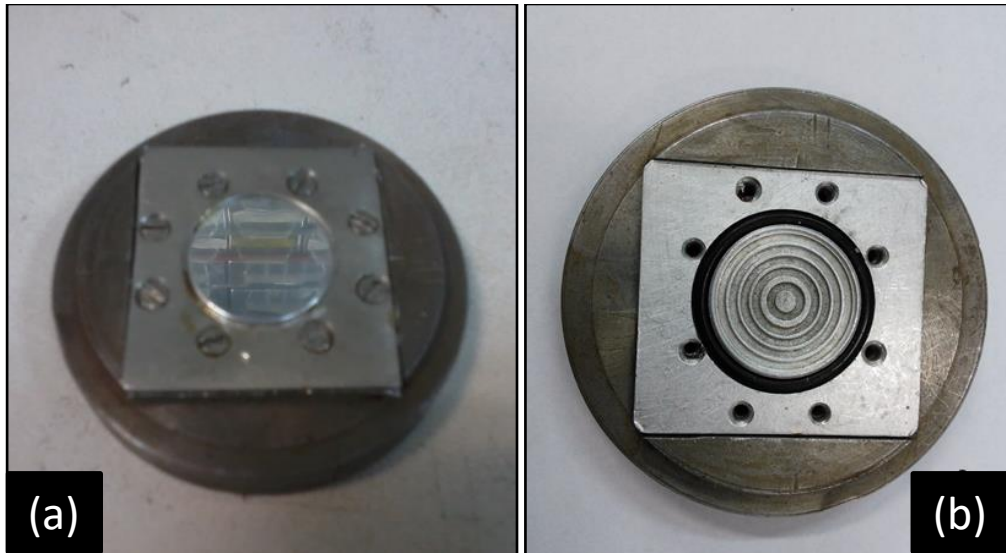


Figure 2-8 Sample holder sealed with Mylar (a) and the base of the same holder where the pulverized powder is placed.

### 2.3.1.2 Single Crystal X-Ray Diffraction

Single-crystal X-ray diffraction is most commonly used for precise determination of a unit cell, including cell dimensions and positions of atoms within the lattice. Bond-lengths and angles are directly related to the atomic positions and so the crystal structure of a material is a characteristic property that is crucial for understanding many of the mechanisms that dictate the structure modulated physical properties.

Usually, crystal structures contain from several hundred to several thousand unique reflections, the spatial arrangement of which is referred to as a diffraction pattern. Indices (hkl) may be assigned to each reflection, indicating its position within the diffraction pattern. This pattern has a reciprocal Fourier transform relationship to the crystal lattice and the unit cell in real space. This step is referred to as the solution of the crystal structure. After the structure is solved, it is further refined using the least-squares techniques.

Molybdenum is the most common radiation source for single crystal diffraction, with  $\text{MoK}\alpha$  radiation =  $0.7107\text{\AA}$ . These X-rays are collimated and directed onto the sample. When the geometry of the incident X-rays impinging the sample satisfies the Bragg's Law, constructive interference occurs. Figure 2-9 represents schematically the set-up of a single crystal X-ray diffractometer. That is a three axis system comprising of fixed-chi stage (chi angle  $\sim 54.74^\circ$ ) and phi drive with  $360^\circ$  rotation. The X-rays which are not diffracted are

either transmitted through the crystal or reflected off the crystal surface. A beam stop is located directly opposite the incident beam to block transmitted rays and prevent burn-out of the detector. Reflected rays are not picked up by the detector due to the different angles involved. Diffracted rays at the correct orientation are then collected by the detector.

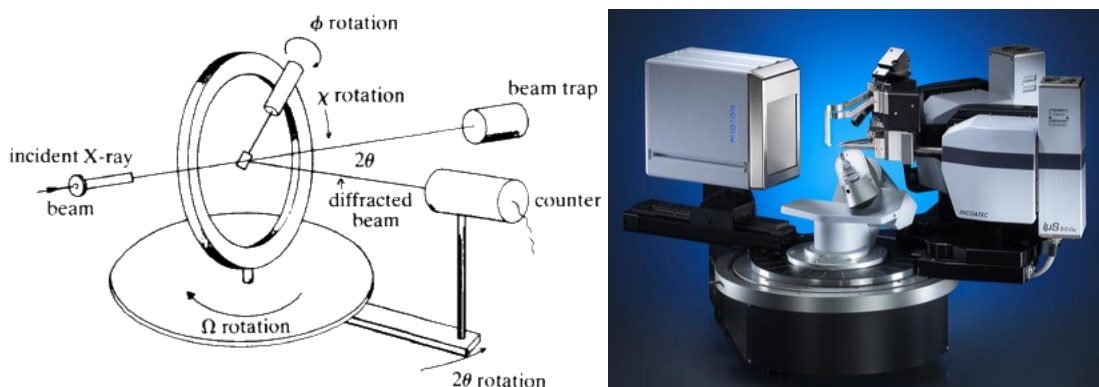


Figure 2-9 Left: Schematic of 4-circle diffractometer geometry. The angles between the incident ray, the detector and the sample are noted. Right: Actual picture of Bruker D8 venture geometry used in the present study reproduced from Bruker.com.

Once the crystal is mounted and centered, a preliminary rotational image is collected to screen the sample quality and to select parameters for later steps. An automatic collection routine can then be used to collect a preliminary set of frames for determination of the unit cell. Reflections from these frames are auto-indexed to select the reduced primitive cell and calculate the orientation matrix which relates the unit cell to the actual crystal position within the beam. The primitive unit cell is refined using least squares and then converted to the appropriate crystal system and Bravais lattice. This new cell is also refined using least squares to determine the final orientation matrix for the sample. After the refined cell and orientation matrix have been determined, intensity data is collected. Generally this is done by collecting a sphere or hemisphere of data using an incremental scan method, collecting frames in  $0.1^\circ$  to  $0.3^\circ$  increments (over certain angles while others are held constant). Data is typically collected between  $4^\circ$  and  $60^\circ$   $2\theta$  for molybdenum radiation. A complete data collection may require anywhere between 6 – 24 hours, depending on the specimen and the diffractometer. Exposure times of 10 – 30 seconds per frame for a hemisphere of data will require total run time of 6 – 13 hours.

The data collection took place at in-house BRUKER D8 VENTURE (Cu  $K_\alpha$ ,  $\lambda=1.54 \text{ \AA}$ , Mo  $K_\alpha$  radiation,  $\lambda = 0.7107 \text{ \AA}$ ) diffractometer (IMBB-FORTH) equipped with PHOTON II

detector and kappa goniometer under the guidance of Prof. K. Petratos and Dr R. Gessmann. The kappa geometry of the goniometer provides true multiplicity and better description of the absorption surface leading to an increased  $I/\sigma I$  (Average intensity / average intensity error) ratio. The PROTEUM2 [95] software has been the software tool used in order to determine the unit cell, prepare the strategy of the data collection and integrate the data collected.

After the data have been collected, corrections for instrumental factors, polarization effects, Xray absorption and (potentially) crystal decomposition must be applied to the entire data set. This integration process also reduces the raw frame data to a smaller set of individual integrated intensities. When the final data set have been produced, the phase problem must be solved to find the unique set of phases that can be combined with the structure factors to determine the electron density and, therefore, the crystal structure. A number of different procedures exist for solving the phase problem, but the most common method is the least squares. Solution of the phase problem leads to the initial electron density map. Elements can be assigned to intensity centers, with heavier elements associated with higher intensities. Distances and angles between intensity 23 centers can also be used for atom assignment based on likely coordination. If the sample is of a known material, a template may be used for the initial solution. Once the initial crystal structure is solved, various steps can be done to attain the best possible fit between the observed and calculated crystal structure. The final structure solution will be presented with an R value, which gives the percent variation between the calculated and observed structures.

The crystals used for data collection in this thesis were investigated under cooled nitrogen. Showering a crystal with cold dry nitrogen during data collection reduces thermal vibrations of atoms so that better data quality is possible. The choice of crystals has been done according to size and well defined edges under a microscope. As soon as the crystal got out of the glove box they were bathed in paraffin oil to prevent any moisture absorption and then captured on the kapton loop.

#### 2.3.1.3 *X-ray Laue method*

A complementary x-ray diffraction technique used for the quality check and orientation definition of single crystal samples, is x-ray Laue photography. In the present study we used the backscattered Laue method as illustrated in figure 2-10. A white beam of x-rays is incident on a crystal, having passed through a hole in a photographic film or CCD camera



and diffracted rays are emitted in all directions in three dimensions in which the Bragg condition is satisfied. The incident beam contains a continuum of wavelengths; in reciprocal space this conforms to a continuous distribution of Ewald spheres so that many diffracting planes satisfy Bragg's law simultaneously. An alternative way of viewing the process is that  $\theta$  is fixed for every diffracting plane, each one selects the particular wavelength for Bragg diffraction producing a spot on the photographic film. The spots on any one curve, as shown in figure 2-10, belong to the same zone (for example  $[00l]$ ) since these reflections lie on the surface of an imaginary cone whose zone axis is coincident with the cone axis. The symmetry of the pattern of spots depends on the symmetry of the crystal as viewed down the camera axis. Analysis of the patterns allows the crystallographic axes of the sample to be identified. In the present thesis the Crystal maker software has been used to simulate and match the produced Laue photographs in order to decide about the orientation of the crystal.

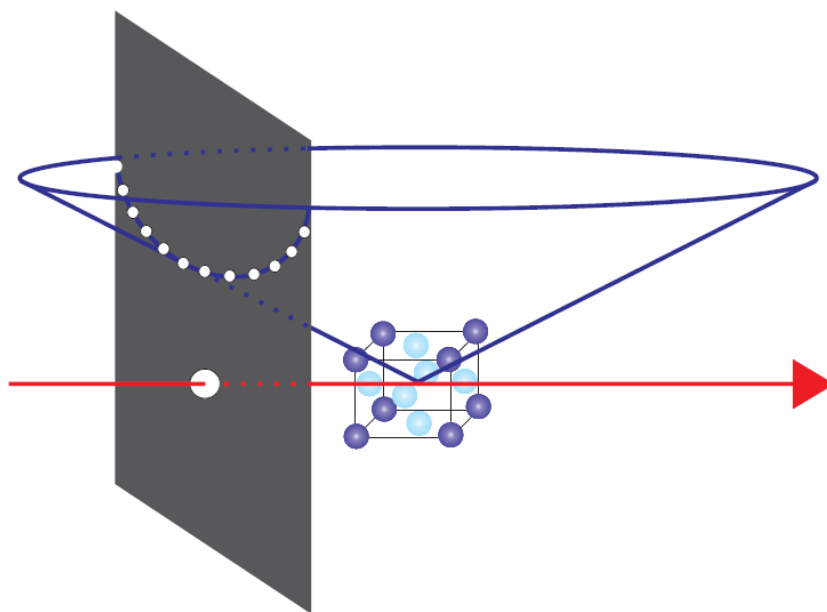


Figure 2-10 Schematic diagram describing a back-scattered Laue experiment. A white beam (red arrow) is incident to the crystal and diffracted beams are visible as a series of unique spots on the ccd camera.

### 2.3.2 Inductively Coupled Plasma Mass Spectroscopy (ICP-MS)

ICP-MS technique has been employed of the quantification of the chemical constituents of the compounds under study.

An ICP-MS combines a high-temperature ICP (Inductively Coupled Plasma) source with a mass spectrometer. The ICP source converts the atoms of the elements in the sample to ions. These ions are then separated and detected by the mass spectrometer.

The samples are dissolved in nitric acid to produce an aqueous solution, before being introduced into the core of an inductively coupled plasma (usually argon at  $> 8000^{\circ}\text{C}$ ). The thermal excitation of each element in the sample results in the emission of light at characteristic wavelengths. The full spectrum is passed through a diffraction grating so that a profile of light intensity as a function of  $\lambda$  may be obtained. The relative intensities for each element produce a mass ratio for all the elements in the sample, when calibrated with a sample of known elemental concentration.

### 2.3.3 X-Ray Photoelectron spectroscopy (XPS)[96]

X-ray Photoelectron Spectroscopy (XPS) is the most widely used surface analysis while the information that provides (elemental analysis in depth of 5-12 nm) about surface layers is important for industrial and surface applications.

XPS is typically accomplished by mono-energetic Al  $K_{\alpha}$  x-rays causing photoelectrons to be emitted from the sample surface. An electron energy analyzer is used to measure the energy of the emitted photoelectrons. From the binding energy and intensity of a photoelectron peak, the elemental identity, chemical state, and quantity of a detected element can be determined. It is based on the kinetic energy analysis of photoelectrons, which originate mainly from the core levels of the atoms in a solid, when this is exposed to x-rays with energy of about 1-1.5 KeV. The exact Kinetic Energy of the peaks in an XPS spectrum characterizes the kind of atoms (*qualitative analysis*) and their chemical environment on the surface (*chemical shifts*). The number of electrons detected at each energy level is analogue to the concentration of the certain kind of atoms at the analyzed area. (*quantitative analysis*).

The surface analysis studies were performed in an Ultra High Vacuum (UHV) chamber ( $P < 10^{-9}$  mbar) equipped with a SPECS LHS-10 hemispherical electron analyzer at the Institute Chemical Engineering Sciences (ICE-HT, FORTH, Greece).



### 2.3.4 Scanning electron microscopy –Electron dispersive spectroscopy (SEM-EDS)[97]

In scanning electron microscopy (SEM), the image is obtained by scanning a finely focused electron probe in a raster pattern over the sample surface in synchrony with writing the detector signals. Strong detector responses result in high brightness in the image. Magnification is determined by the ratio of the area scanned to the display area. One imaging mode makes use of the secondary electrons emitted by the sample surface upon excitation from the incident electron beam. These secondary electrons are low in energy, making it very easy to collect them by an appropriately biased scintillator. The number of electrons emitted depends on the angle of the specimen surface with respect to the electron beam and the detector. The resultant differences in brightness, therefore, reveal the surface topography. Another imaging mode within a SEM makes use of backscattered electrons. These electrons possess much higher energies comparable to those of the incident beam electrons (1-30 keV). Therefore, the signal intensity is less sensitive to surface topography (higher penetration depth of the incident beam) but instead depends on the chemical composition of the specimen. This imaging mode is capable of providing excellent atomic number contrast.

The machine used for the purpose of this work is JEOL JSM-7000F operating at 15 kV accelerated voltage in IMBB-FORTH while some preliminary photographs have been taken in the University of Warwick instrumentation.

Complementary to the XPS technique, energy dispersive x-ray spectroscopy analysis (EDX or EDS), was employed for the determination of the Na:Mn ratio in the  $\text{Na}_x\text{MnO}_2$  compounds of the present study. Although time consuming, this process provides a measure of the elemental mass ratios in an area localized to the finite size of the x-ray beam. Electron excitations caused by the high voltages usually used in microscopes lead to ionization within the sample. The consequent relaxation in energy results in emission of X-rays that can be analyzed by a solid-state energy-dispersive detector. Qualitative analysis by this method is straightforward since each element has a unique pattern of X-ray lines from the K, L, and M shells. EDS method can provide, however, only semi-quantitative analysis.

The spread in sodium concentration across the surface of a sample has therefore been measured. Typically distributions in sodium content were found to be of the order of  $x = 0.7-1$ . Since EDS probes just the sample surface, in order to verify that the crystals were



single phased throughout the layers, several samples were cleaved as thin as possible. The exposure of the samples in ambient conditions was of extra interest since Na was found to form salty compounds on the surface leaving vacancies in between the  $\text{MnO}_6$  layers. Quantification of the elemental ratios at the surface of the crystal flakes for this work was carried with energy dispersive spectroscopy (EDS) by using a JEOL JSM-6390LV scanning electron microscope equipped with an Oxford INCA PentaFET-x3 detector

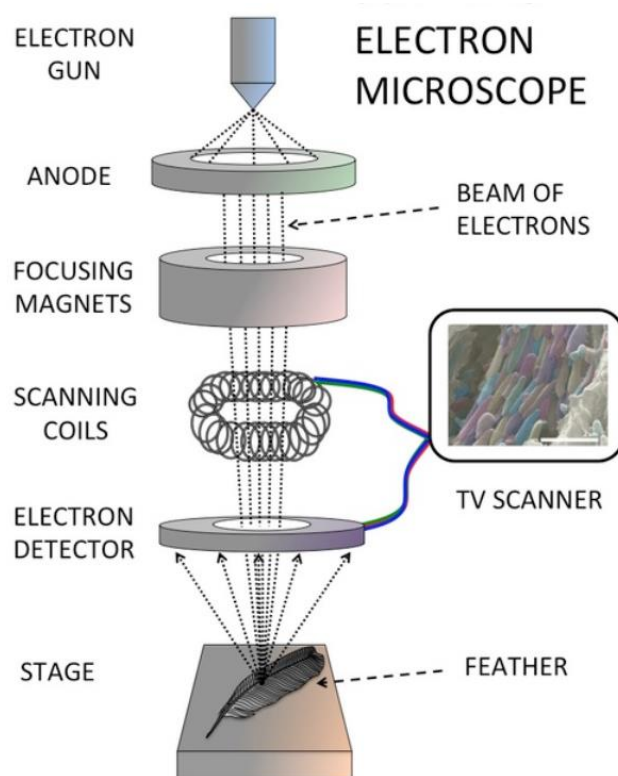


Figure 2-11 Schematic of a Scanning Electron Microscope (SEM) reprinted by the webpage of Diamond industry news.[98]

## 2.4 Macroscopic physical property probing

### 2.4.1 Superconducting Quantum Interference Device (SQUID)[99]

The principle aim of magnetometry is to measure the magnetization (either intrinsic or induced by an applied field) of a material. This can be achieved in a number of ways utilizing various magnetic phenomena.

Magnetometry data in this thesis has been recorded using a SQUID magnetometer. The SQUID magnetometer is an instrument which is very sensitive to magnetic fields, making

it ideal for measuring subtle changes in the magnetic behavior of a sample when it is subjected to different temperatures, magnetic fields or pressures.

A magnetometer uses the principle of Faraday's Law of electromagnetic induction in order to measure the magnetization of a sample using a set of pick-up coils. The detection coil is superconducting itself and wound in the formation of a second-derivative gradiometer. Samples are fixed to non-magnetic holders with and then placed on the end of a non-magnetic sample rod between the pick up coils. During the measurement, the sample is step-scanned through the gradiometer (specified range typically 4 cm) as it is slowly moved through the coils and the change of magnetic flux associated with this movement produces a change in the persistent current. These pick-up coils are inductively coupled via a set of superconducting wires to a Superconducting Quantum Interference Device (SQUID) located inside a magnetic shield below the sample space. A SQUID consists of a superconducting ring with two Josephson junctions in parallel; variations in the current in the detection coils result in proportional variations in the SQUID output voltage. The calibration of this voltage response curve to a sample of known mass and magnetic susceptibility enables the measurement of magnetic moments in other samples. The SQUID essentially acts as an extremely sensitive flux-to-current-to-voltage converter and is capable of resolving moments as small as  $5 \times 10^{-7}$  emu (electromagnetic units).

Liquid helium and liquid nitrogen are used to cool the magnet and control the temperature inside the sample space.

A schematic diagram of the SQUID is shown in Figure 2-12. Two different SQUID magnetometers were utilized to take the measurements presented in this thesis - a Quantum Design MPMS-5S and MPMS-XL. The MPMS-5S can be used to take magnetisation measurements over a temperature range of 1.8–400 K and applied magnetic field range of up to  $\pm 5$  T. The MPMS-XL is able to reach  $\pm 7$  T.

Typical measurements carried out with the SQUID were of DC magnetic susceptibility versus temperature at a rate of  $\sim 1$  K/min when measuring around magnetic transitions, or 2-5 K/min if measuring the paramagnetic behaviour over a large temperature range. Magnetic susceptibility can be measured in both zero-field cooled (ZFC) and field cooled (FC) situations. A zero-field cooled measurement involves the sample being cooled from the high temperature paramagnetic state to base temperature before a magnetic field is applied to the sample, and in a field cooled measurement the field is applied beforehand.



There can be a significant difference between the ZFC and FC data depending on the nature of the magnetic order present in a material. According to the shape of the magnetic susceptibility curve in respect with the scanning temperature we may extract useful information about the magnetic order of the measured material. According to Curie-Weiss law as it has been presented in 1.3.3 section, we can distinguish the basic behaviors as presented in figure 2-13.

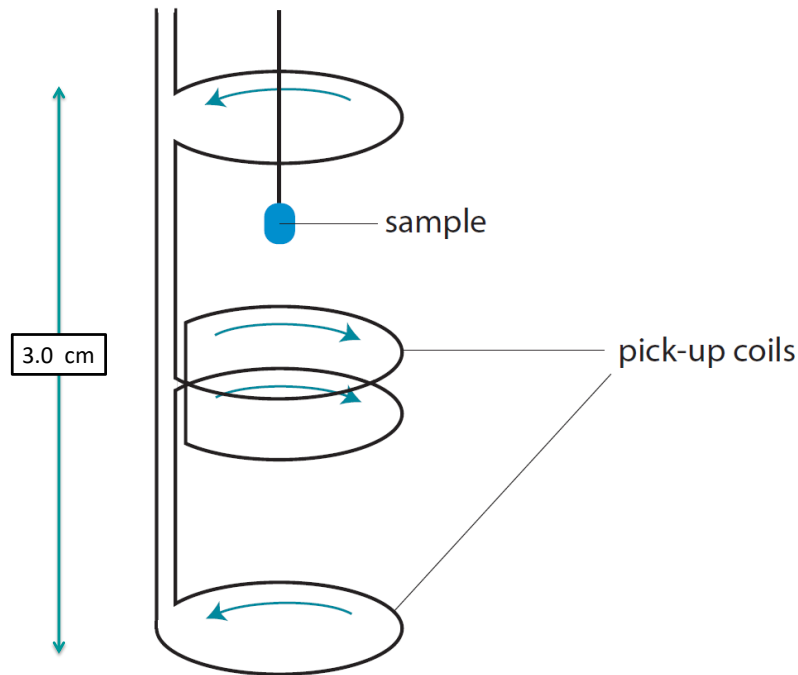


Figure 2-12 Schematic illustration of the SQUID operation reproduced from “MPMS MultiVu Application User’s Manual”

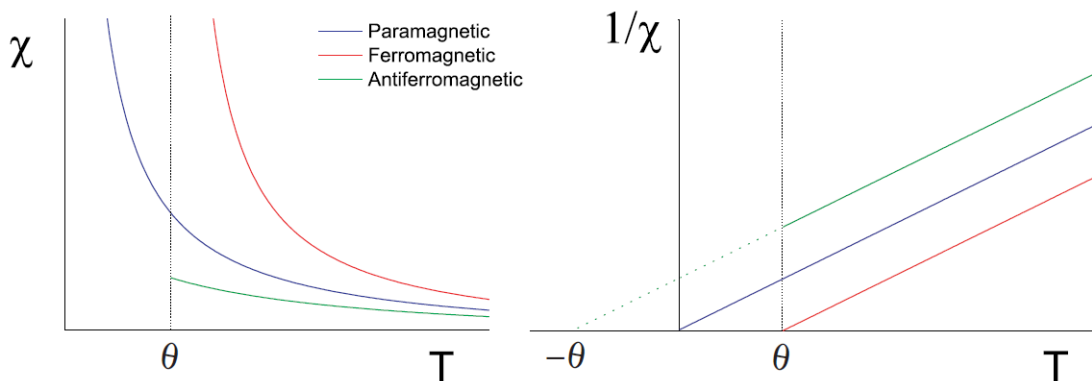


Figure 2-13 Curie-Weiss susceptibility of different magnetic system above the ordering temperature. The inverse susceptibility is plotted and used to extract the  $\theta$  temperature which is  $\theta < 0$  for an antiferromagnet,  $\theta = 0$  for a paramagnet and  $\theta > 0$  for a ferromagnet.

Depending on the needs of the need of the project several functions and protocols may be followed such as ac susceptibility measurements in order to investigate dynamic of the system or M (H) in order to explore hysteresis phenomena.

#### 2.4.2 Dielectric Constant measurements

A material is referred to as a dielectric if it can be electrically polarized upon the application of an electric field. This polarization occurs due to electric dipoles orienting themselves in response to the applied field. An internal electric field within the dielectric is generated (the electric displacement field), and acts to compensate the external field. The electric susceptibility of a dielectric,  $\chi_e$  is a measure of how strongly the polarization, P, is dependent on the applied field, E:

$$P = \chi_e \varepsilon_0 E \quad (2-3)$$

Where  $\varepsilon_0$  is the permittivity of free space ( $\varepsilon_0 = 8.854 \times 10^{-12} \text{ Fm}^{-1}$ ). The electric susceptibility is a dimensionless quantity, and is related to the permittivity,  $\varepsilon$ . For a material with a relative permittivity,  $\varepsilon_r$ :

$$\varepsilon = \varepsilon_0 \varepsilon_r = (1 + \chi_e) \varepsilon_0 \quad (2-4)$$

The relative electric permittivity is also referred to as the dielectric constant. The electric displacement field, D is also directly linked to the electric polarization and the dielectric constant:

$$D = \varepsilon_0 E + P \quad (2-5)$$

Referring to Equations 2-3 and 2-4, this relation can be expressed as

$$D = \varepsilon_0 \varepsilon_r E \quad (2-6)$$

The behavior of dielectric materials in response to external electric field is well illustrated in the case of the parallel plate capacitor. For two electrodes of area A, separated by a distance d across a vacuum (Figure 2-14 a), a capacitance develops when an electric field is applied:

$$C = \varepsilon_0 A / d \quad (2-7)$$

If a dielectric material is then inserted between the two electrodes (Figure 2-14 b), the electric field is reduced, and the capacitance increases:

$$C = \varepsilon_0 \varepsilon_r A / d \quad (2-8)$$



In a homogenous material, the dielectric constant or relative permittivity “  $\epsilon_r$  ” is expressed as fraction of linear permittivity over the permittivity of vacuum. The definition of dielectric constant is described in equation (2-6).

$$\kappa = \frac{\epsilon}{\epsilon_0} = \epsilon_r = \epsilon_r' - j\epsilon_r'' \quad (2-9)$$

Where  $\epsilon_r'$  represents the Storage ability of the material while the imaginary part  $\epsilon_r''$  represents the Losses.

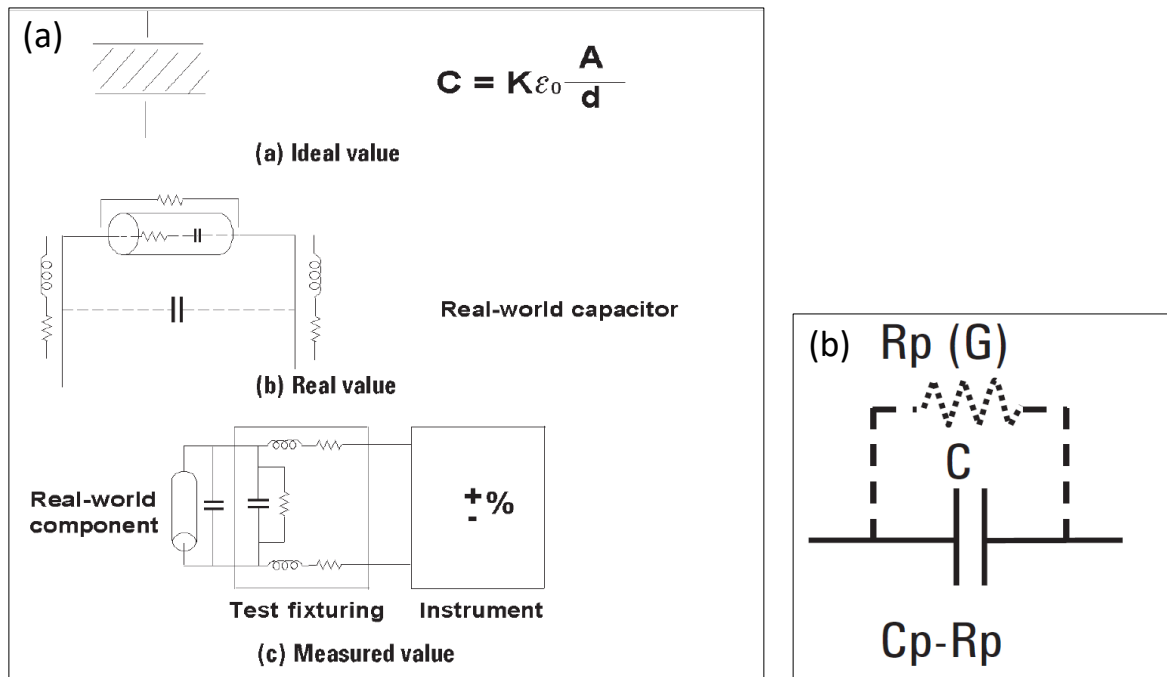


Figure 2-14 (a) Ideal, Real and Measured values in a capacitor topology, (b) parallel equivalent circuit mode for capacitor measurements

Experimentally, the dielectric constant of a material can be determined by measuring its capacitance, assuming its dimensions are well known. So in most cases the capacitance or the impedance of the sample has been measured as a function of temperature, frequency and electric field. In the present study we have performed AC measurements on Agilent LCR meter (or AH capacitance bridge) in a Cp-D (Capacitance-Dissipation Factor) mode. In such case we consider a parasitic Resistance in parallel with the ideal capacitor as pictured in Figure 2-3. We then can calculate the dielectric permittivity by the following formula:

$$\epsilon_r' = \frac{C \cdot d}{\epsilon_0 \cdot A}, D = \tan\delta = \frac{\epsilon_r''}{\epsilon_r'} \quad (2-10)$$

Where  $d$  is the distance between the capacitor plates (thickness of the sample),  $A$  is the conducting area of the plates. If we have an area covered with conductive paint this is the area we should use for our calculations. The Dissipation factor ( $D$ ) measured should be close to zero value for a good dielectric material and is related to the  $C_p$  value as following:

$$D = \frac{1}{2\pi f C_p R_p} = \frac{1}{Q} \quad (2-11)$$

Where  $f$  is the frequency of the  $V_{ac}$  triggering signal,  $R_p$  is the equivalent parallel resistance in the parallel equivalent model circuit (Fig. 2-3 b) and  $Q$  is the Quality factor.  $Q$  serves as a measure of a reactance's purity (how close it is to being a pure reactance, no resistance), and is defined as the ratio of the energy stored in a component to the energy dissipated by the component and is dimensionless.

Along with that the application of an external magnetic field could provide us with the valuable information in respect with a possible magnetoelectric coupling.

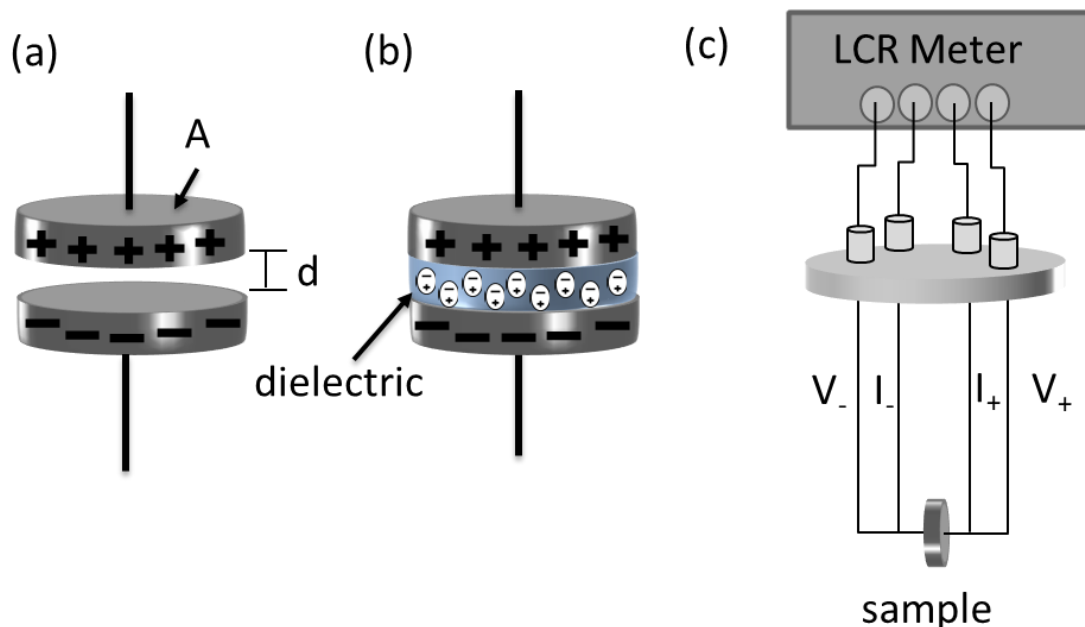


Figure 2-15 A parallel plate capacitor, where electrodes are separated by (a) vacuum (b) a dielectric material. (c) Schematic of the wiring and connection of the sample insert for dielectric measurements

The dielectric and magnetodielectric measurements of the Na-Mn-O system under study have been partially done in Helmholtz Zentrum Berlin, Institute of Complex Magnetic Materials LaMMB MagLab, Department of Samples and Environments using a Physical Properties Measurement System (PPMS) while a number of them has been held in Functional Nanocrystal Laboratory (FUNL) in Institute of Electronic Structure and Laser (IESL), Crete.

In the case of the PPMS system a modified sample insert made by the local team has been used for both measurements of polycrystalline specimens in pellet form and single crystals. Details on this are given in section 2.4.3.2.

For the in-house experiments the custom-made Magnetodielectric Station was employed. The whole set up has been modified while a new sample insert has been designed and manufactured from scratch. This insert allowed the sample to be measured inside a continuous flow cryostat which was placed in the center of a superconducting magnet in a range of temperature from 320 K to 2 K and under magnetic fields up to 7 T.

The sample insert could be connected to an LCR meter, a capacitance bridge, an electrometer or a high voltage power supply as required. This will be described in detail in section 2.4.3.1. A schematic diagram of the wiring and connectivity of the sample insert can be seen in Figure 2-3 (c). A sequential interface designed in LabVIEW has been developed (in cooperation with Mr K. Mouratis as a part of his master thesis), enabling computer control of the operations and communication with all afore mentioned instruments including the superconducting magnet and a control valve that regulates the flow of the cryogenic liquid into the cryostat. Major part of the work carried out for this Ph.D. was involvement into the setting up of the in-house MD station including all necessary modifications and performing trial experiments in order to standardize methods and prove the adequacy of the newly designed features. A detailed user's guide on how the MD Station is programmed for a measurement session is given in Appendix A.



### 2.4.3 Custom Magneto-electric Station

The in house custom-made Magnetodielectric Station of Functional Nanocrystals Laboratory has been installed and programmed to be run remotely and sequentially using a LABview designed interface through which the user can preview and control most of the parameters.

The system uses a continuous flow cryostat by *Janis*, which is placed in the center of 7 Tesla cryogen-free superconducting solenoid magnet, allowing probing evolution of physical properties under controlled temperature and applied magnetic field conditions. It is also equipped with electronic Instrumentation capable to probe temperature and frequency dependent phenomena with externally applied magnetic or electric stimuli and measure physical quantities like Capacitance and Dielectric Loss, Voltage, Electric DC Current and Impedance. The main Instrumentation used to probe physical properties and control external stimuli is presented in figure 2-16 and are mentioned briefly below.

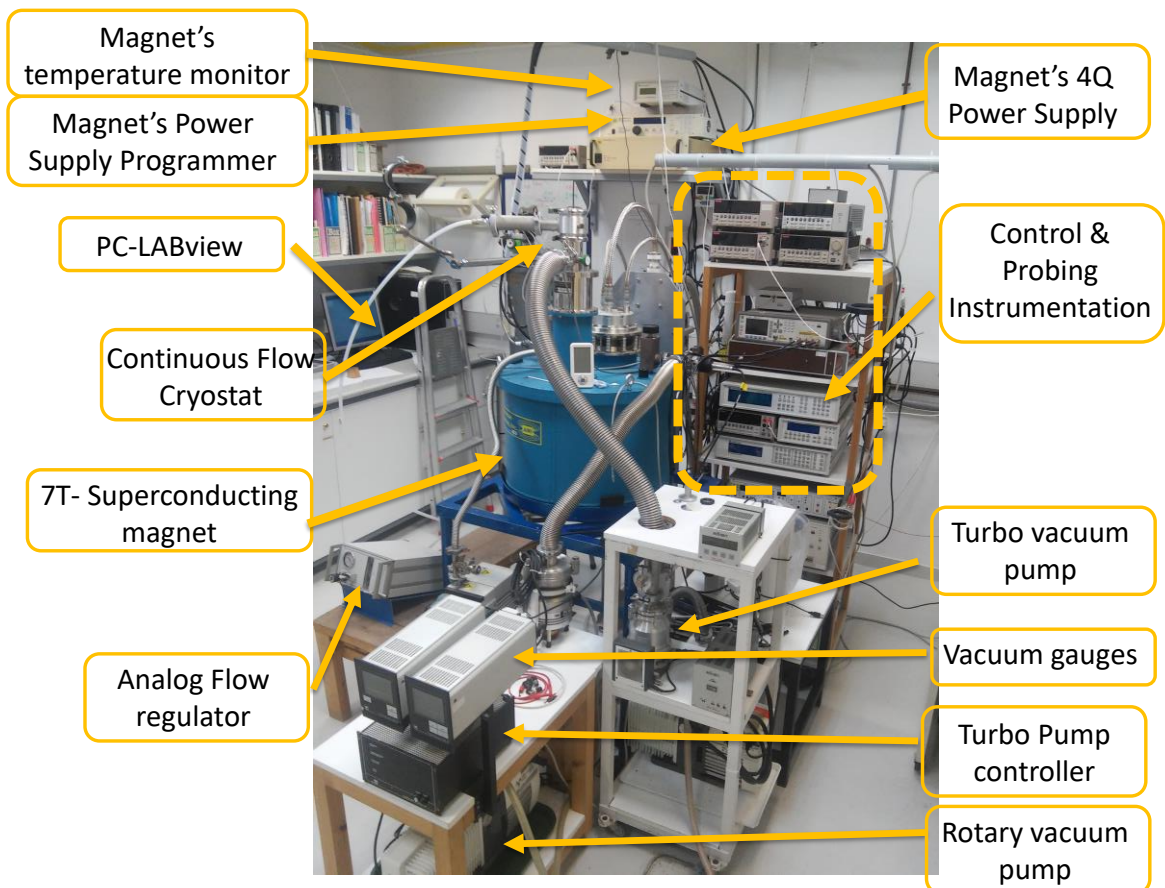


Figure 2-16 Magnetolectric station (MD) used for the in house magneto dielectric measurements

- 1- A 7 Tesla cryogen-free superconducting solenoid Magnet by American Magnetics. The magnet is controlled by an AMI Model 430 programmer and Model 4Q05100 bi-polar power supply and has a persistent switch heater installed with the ability to isolate the magnetic field in the coils and ensure stability of the magnetic field applied during a long lasting experiment with the main magnet leads discharged.
- 2- A continuous flow cryostat by *Janis*, which is placed in the center of the magnet coils allowing probing properties under specified temperature and applied magnetic field conditions at the same time. The continuous flow cryostat is used in order to cool down to cryogenic temperatures (Liquid N<sub>2</sub> down to 77 K). The flow of gas into the Cryostat is maintained with the support of a diaphragm pump.
- 3- The main instrument employed for probing Capacitance or Impedance is precision LCR meter E4980 of Agilent with a frequency range of 20 Hz- 2 MHz. Depending on the sample a 4-probe or a 2-probe connection can be established and a standard correction can be used depending on the length of the wires used. For the lower frequency range (50 Hz- 20 k Hz) an AH 2700 ultra-precision capacitance bridge is used.
- 4- The main temperature control of the sample environment, both Janis Cryostat and the sample space, is in the hands of Lakeshore 332 temperature controller in which channel A is connected with the Cryostat heater of 40 Ohm and CX-1050-SD Cernox #X235263 and channel B is connected with the heater (20 Ohm) placed on the sample holder stick and CX-1050-CU Cernox #X94732.

#### 2.4.3.1 *Custom made Sample insert*

The MD probe used in this set up is suitable for measuring dielectric properties (Capacitance or Impedance) and Pyroelectric current of non-conductive materials in both polycrystalline and single crystal forms. Two different sample holders/carriers are designed in such way so that they can be detachable from the main stick and can be prepared inside an atmosphere controlled Glove box. That makes the construction also suitable for air-sensitive samples (Fig. 2-18 b). This probe is designed to be used in temperature range 2-325 K and is suitable for use under magnetic field up to 7 Tesla.

In order to accomplish an independent probing and control of the temperature on the sample environment we follow a dual- loop control which requires the installation of a heater and a temperature sensor on the probe apart from the ones installed inside the



cryostat. The temperature sensor in the sample area is a Lakeshore CX1050-CU. The heater is a resistance of 20 Ohms constructed by Lakeshore MW-30 wire wrapped around the brass neck of the holder base (Fig. 2-18 e black part on the top). The electrical isolation from the brass base is succeeded with the use of the thinnest rolling paper and varnish so that there is also good temperature conductivity between the heater and the brass part. The heater is electrically isolated with a top coat of STYCAST.

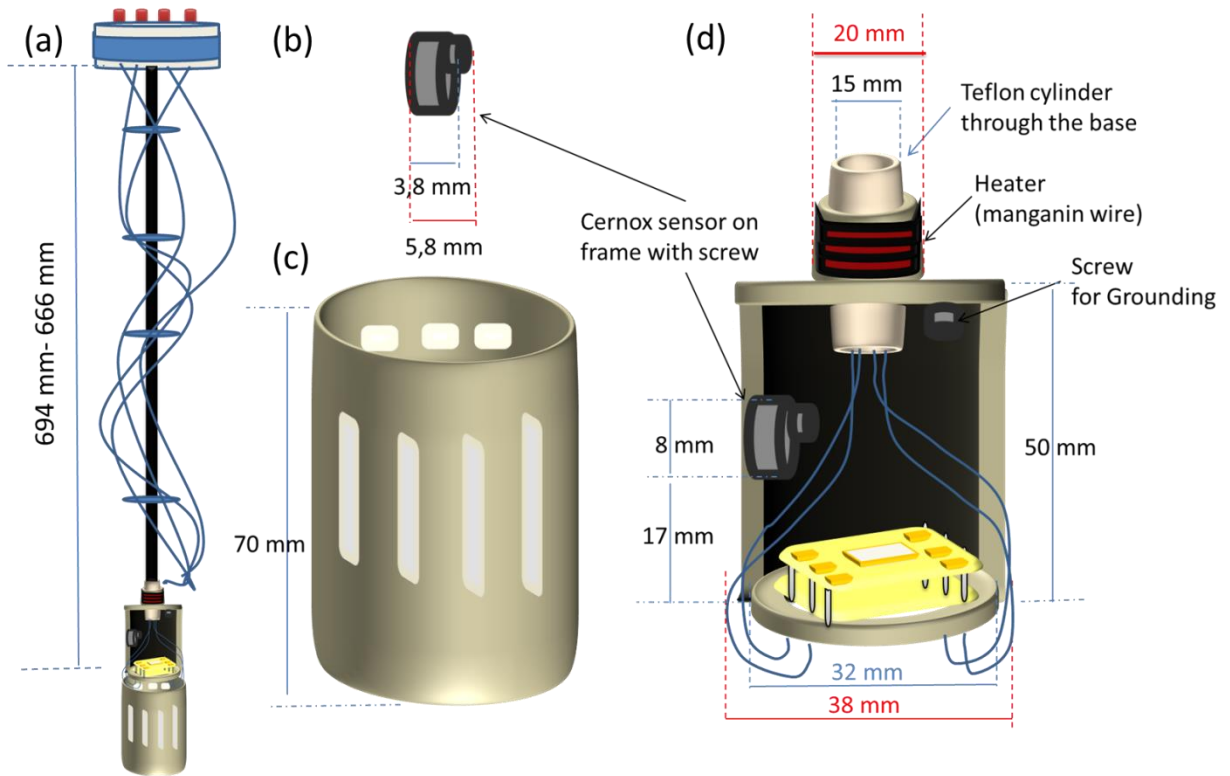


Figure 2-17 Initial design of the MD probe (a) length of the sample space from the top hat (b) choice of the suitable temperature sensor (c) Teflon bottom cover for protection and (d) design of the sample space and removable sample holder.

The wiring allows 2-probe and 4-probe measurements depending on the physical property that is probed. The cables from the BNC connectors to the sample holder base are Lakeshore CC-C cables (solid copper center conductor drain wire and aluminized/polyester shield) since low conductor resistance is prime consideration for measuring low signals. We used the 4-Terminal-Points configuration since our main probing Instrument (LCR-Agilent) which provides 4 terminals ( $V_H$ ,  $V_L$ ,  $I_H$ ,  $I_L$ ) suggests a better probing precision in a wide range of Impedance in this configuration (Fig. 2-18 c, d). We also use a floating GND. All 4 wires' shields are connected together on a noise shield (copper plate)

which is close to the sample (or DUT) at the back side of the lower carrier socket in order to limit the stray capacitance that develops among the 4 leads (Fig. 2-18 e).

The main part of the stick is chosen to be carbon fiber of diameter= 6.4 mm and its length from the bottom of the Teflon flange to the sample space calculated to bring the sample space exactly to the vertical center of the magnet coils (adjustable height from 691-716 mm) (Fig. 2-18 a) where the magnetic field is homogeneous over a certain diameter of spherical volume (DSV) which in our case is 1 cm.

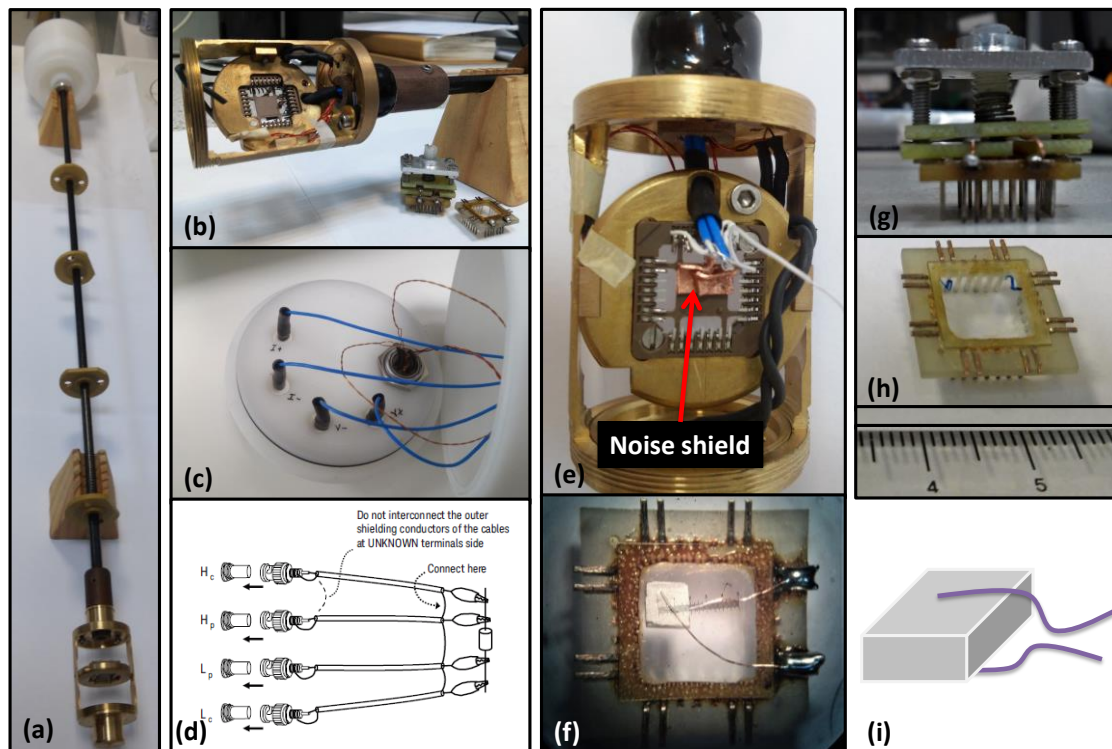
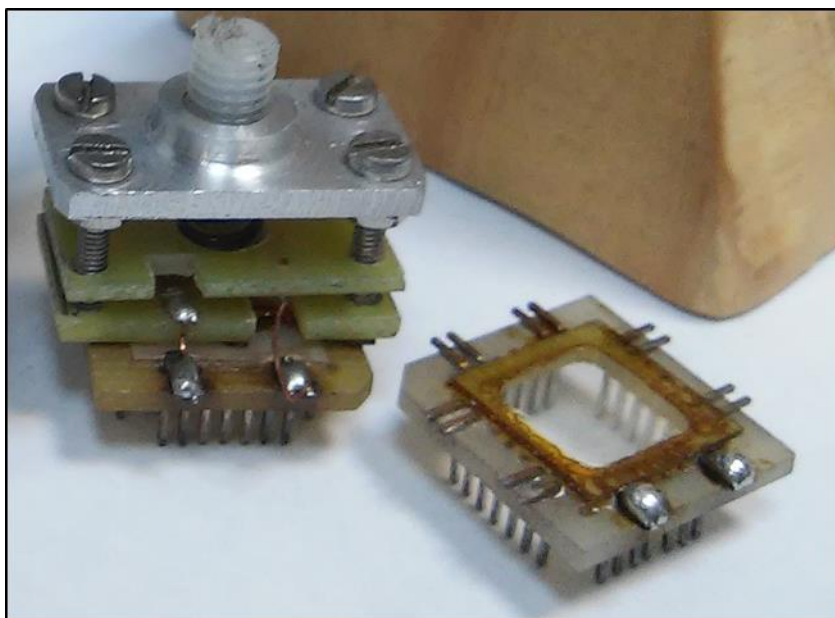


Figure 2-18 (a) MD carbon fiber stick, (b) lower carrier socket on brass frame and 2 detachable sample holders/carriers, (c) 4 wires come down to lower carrier socket from isolated Teflon flange, (d) 4TP wiring sketch, (e) GND according to 4TP and noise shield in the lower carrier socket, (f) sample wired with 4TP as a capacitor, (g) “Sample holder1 – capacitor topology”, no wires on sample, (h) “Sample holder2- Flat multi pin carrier 2 or 4 probe wire connections to the sample, (i) sample connected as a capacitor using paste (sketch of (f)).

### 2.4.3.2 Sample preparation and mounting

For the Impedance or Capacitance measurements of either a single crystal or a polycrystalline sample (in a pellet form), the sample has been measured as a capacitor. In most cases the application of a conductive paste has been used on the flat surfaces that would serve as the capacitors plates. The pastes that have been mainly used were Silver,

Carbon and in a few cases Gold deposition using a custom made Gold evaporator. The design of two different sample carriers would serve all possible needs of a 2 or 4 probe wiring, fast mounting and using extra wiring or not. Both carriers with no sample mounted are depicted in figure 2-119.



*Figure 2-19 “Sample holder 1- Capacitor topology” on the left and “Sample holder 2- Flat multipin carrier” on the right side with no samples mounted.*

1. “Sample holder 1- Capacitor topology” (Fig. 2-19-left): No wires attached to the sample. Depending on the nature of the sample the use or not of a conductive paint on the 2 flat parallel surfaces is possible. The electrodes on the two mica plates of the holder are of solder bulbs to ensure point contact with the sample. Another view with a sample mounted is on Figure 2-20 (b).

Since the mechanical strain induced to the sample from such a holder could affect the measurements especially if the pellets is fragile, the second holder serves as an alternative.

2. “Sample holder2- Flat multi pin carrier” (Fig. 2-19-right): The substrate used in this case is sapphire which is electrically insulating while being a good thermal conductor. In this case, after the sample’s surfaces are covered with a conductive paint copper or gold

wires are attached with conductive paste on both of the surfaces. It should look like figure 2-20 (a) (2 wires on each surface).

### 1- Polycrystalline pellet

For the study of polycrystalline specimens of the Na-Mn-O system the samples have been prepared in pressed pellet form as will be described in Chapter 3. In such case, the orientation of the applied magnetic field should not affect the probing properties and so the vertical orientation of the socket has been preferred (flat surface of the lower carrier socket  $\perp$  to H field) during the measurement to avoid mechanically stabilizing the pellet (Fig. 2-17 b). The choice between the two sample carriers/ holders depends on how fragile the pellet is or how important is a fast mounting.

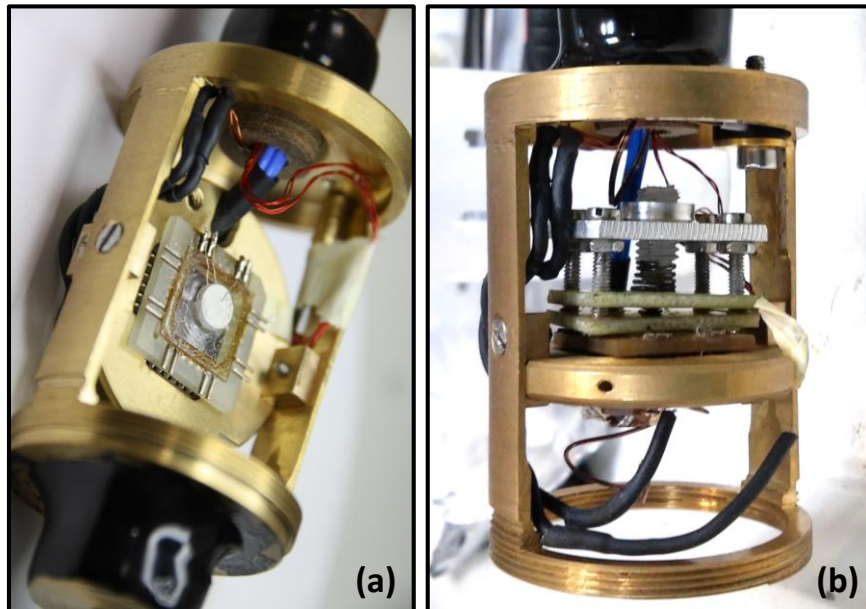


*Figure 2-20 (a) Parallel to H field orientation of the sample carrier- Sample Holder2 (b) Vertical to field orientation of the sample carrier- Sample Holder1*

### 2- Single Crystal

In the case of a single crystal one should take into consideration the proper orientation of mounting the sample itself on the carrier and the orientation of the carrier since the lower carrier socket can be oriented either parallel or vertical to the applied Magnetic field. The orientation of the electric field depends on the experiment and the way you are going to choose your contact areas on the sample under study.

### 2.4.3.3 *Physical Property Measurement System (PPMS)[100]*

The PPMS is a cryogenic platform that is used to carry out temperature (between 1.8 K and 400 K) and magnetic field (up to 14 T) dependent physical measurements. It allows the conduction of transport measurements such as resistivity, Hall effect, Seebeck effect, Heat capacity, magneto resistance and capacitance measurements.

For the magnetoelectric studies that took place in LaMMB - MagLab at the Helmholtz-Zentrum Berlin we utilized a 14 T PPMS system. A custom insert made by the local team, has been used for the measurements of capacitance of both polycrystalline and single crystal specimens of Na-Mn-O. The sample holder here keeps a capacitor topology with golden electrode plates. By means of a sample rotator, it is possible to measure the anisotropic properties of single crystal samples. The temperature is controlled through a single loop system having a temperature sensor only inside the cryostat and not on the sample insert. The temperature ramps were found to ideally respond in a 2K/ min rate having a linear profile. The setup gives the possibility to select between an AH 2700A Ultra-precision Capacitance Bridge, for relatively low-frequencies (50 Hz - 20 kHz) or a Solatron 1260 Impedance/Gain Phase Analyser, for the high-frequency region up to 32 MHz; the latter is being used together with a 1296A Dielectric Interface System in order to cope with ultra-low capacitance levels. A Lakeshore 370 temperature controller was utilized to cover a broad temperature range ( $5 \leq T \leq 180$  K). All measurements were controlled using an interface based in combination of LabView, Python and Visual Basic.

Heat capacity,  $C(T)$ , of beta polymorph ( $\beta$ -NaMnO<sub>2</sub>) has been measured in a similar PPSM system at zero-field on a cold-pressed pelletized powder sample by means of the relaxation technique, utilizing a physical property measurement system (Quantum Design, PPMS). The PPMS is used to measure the heat capacity of a sample, usually as a function of temperature, but also as a function of applied magnetic field. The sample has been placed on a  $3 \times 3$  mm<sup>2</sup> platform in the middle of a “puck”. The platform is suspended by wires, which isolate the platform from thermal contact with the system and are also used for platform heating and temperature measurement. This puck is then placed inside a superconducting magnet which has a temperature range of 2-400 K, and is capable of applying magnetic fields up to  $\pm 9$  T. The heat capacity is then determined at a particular temperature by applying a small increase in temperature (typically ~5% of the current temperature) and measuring how long the sample takes to return to the initial temperature.



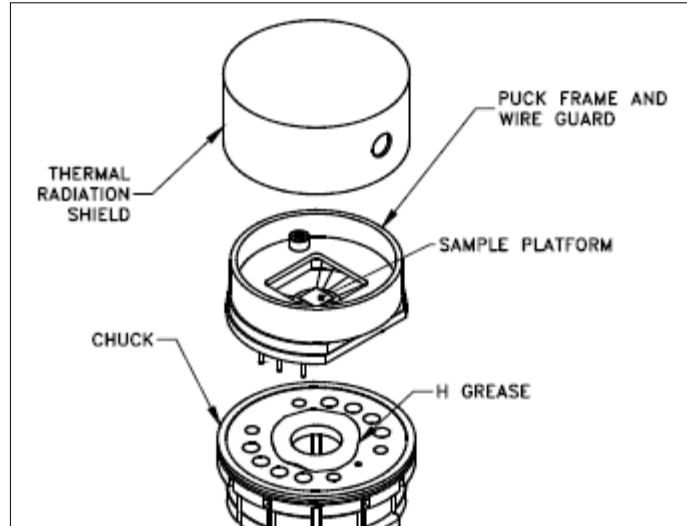


Figure 2-21 Exploded view of the plug-in designed puck and sample platform used in PPMS for standard Heat Capacity measurements [100]

The heat capacity,  $C$ , of a sample at a particular temperature gives information on the entropy,  $S$ , present in the system. [101] At constant pressure, this relationship is given by

$$C_p = T \left( \frac{\partial S}{\partial T} \right)_p \quad (2-12)$$

The entropy of a system is given by the following equation for a fixed volume,  $V$  and magnetic field,  $B$ :

$$S = - \left( \frac{\partial F}{\partial T} \right)_{V,B} \quad (2-13)$$

where  $F$  is the Helmholtz free energy, a portion of the total internal energy,  $E$  of the system defined as:

$$F = U - TS \quad (2-14)$$

From equation 2-11, it can be seen that a change in the energy of the system is associated with a change in entropy and so heat capacity studies are providing useful information for possible phase transitions, which appear as sharp peaks as a function of temperature.

In order to extract the magnetic contribution of the specific heat from measured quantity, phonon contributions need to be subtracted. This can be achieved by by measuring the heat capacity of a non-magnetic analogue of the sample as in the case of  $TbMnO_3$ . [102] This non-magnetic compound is known as a phonon blank, and is chosen to have a molecular weight and crystal structure as close as possible to the magnetic compound in order to have an accurate representation of its lattice contribution to the heat capacity. Another way to

isolate the magnetic part of the measured heat capacity is by subtracting the phonon contribution using the Debye approximation to the phonon spectrum of a crystal lattice. [101]

Debye improved on Einstein's theory by treating the coupled vibrations of the solid in terms of  $3N$  normal modes of vibration of the whole system, each with its own frequency. The lattice vibrations are therefore equivalent to  $3N$  independent harmonic oscillators with these normal mode frequencies. This improved the low temperature behavior of the Debye approximation in comparison to the Einstein more simplified model gave better quantitative description in all range of temperature. The characteristic temperature  $\frac{h\nu_D}{k} = \theta_D$  is known as Debye temperature while the relation for  $C(t)$  derived by Debye is the following:

$$C(T) = \left(\frac{9rNkT^3}{\theta_D^3}\right) \int_0^{\theta/T} \frac{x^4 e^x}{(e^x - 1)^2} dx \quad (2-15)$$

#### 2.4.4 Issues during DE measurements- Standardization and improvement of the set up

##### 2.4.4.1 Effect of electrical contacts on capacitance measurements

In continuation of the BaTiO<sub>3</sub> measurements with different pastes that started in August 2014 in HZB, in order to study the behavior of the pastes and how the choice of paste affects the measurements with this specific set up we measured BaTiO<sub>3</sub> with Carbon Paste to check if there will be any "false" peak around 230-250 K that we could observe in measurements with silver paste contacts. In this range of temperature (230-250 K) there was a peak in almost all previous measurements (NaMnO<sub>2</sub> and BaTiO<sub>3</sub> both with Silver paste contacts). As shown in figure 2-22 the silver paste adds an effect in the area of 230-250 K which is not observed in cases of carbon paste or no paste samples. In panel d the temperature ramp is shown in order to confirm that our measurements can be comparable to one another and the only effect could be attributed to the change of the contacting paste. The case of effects initiated by the different kind of contacts including paste has been commented by Lunkenheimer et al. [103]. According to this study large values of dielectric constant or CDCs (colossal dielectric constants) may originate from the effect of contacts either sputtered or spread on the samples in a way of creating Schottky barriers because of the small metal clusters applied during sputtering for example.



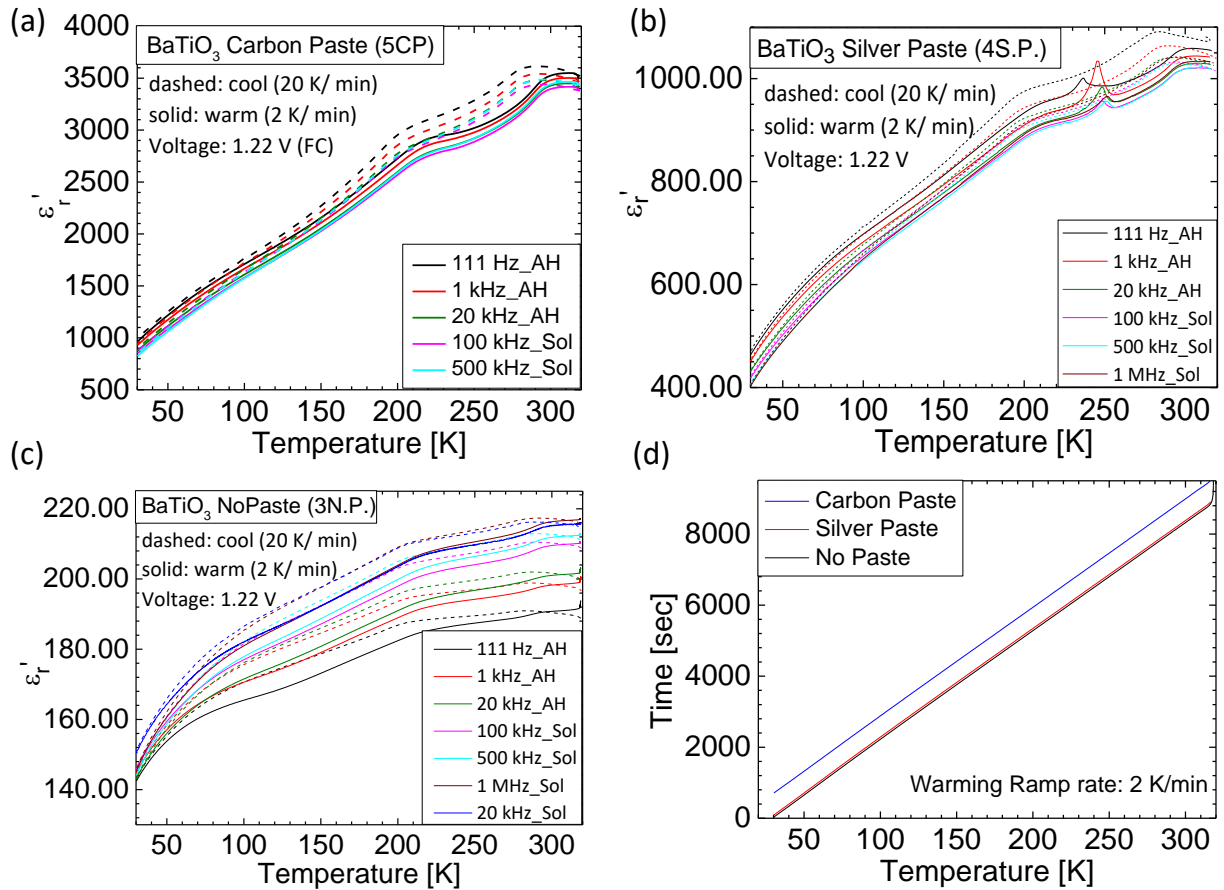


Figure 2-22  $BaTiO_3$  test measurements using different contact pastes. Details found in the text.

Difference in magnitude may be attributed to the different pastes used as electrodes on the pellet as far as the properties of the paste and thickness of the layer are concerned.

It was observed that trying different ramp rates could affect the appearance of the kink (according to August measurements on  $BaTiO_3$ ). However the rate of 2 K/min was chosen while heating/measuring because it seemed to be the most appropriate for the specific set up in HZB.

#### 2.4.4.2 Linearity of temperature ramp

Issues on the temperature control in custom made set ups are an important drawback questioning the results of a study. Learning the hard way we had to face the picture of non-smooth temperature ramp which was affected by factors such as the smooth flow of the cryogenic liquid, the adequate heating of the heater of the set up together with the appropriate control loop system including the set of instrumentation.

In house MD station: The issue of the temperature linearity is a complex one and dependent on various facts. One of them has been the combination of the heater's power used in the sample temperature control loop which was attached on the stick and the mass of the sample holder/ stick itself. Due to the big thermal mass the inertia has grown big and led to a sinusoidal ramp of the temperature (fig.2-23a). Removing the lower part of the sample holder which didn't allow the system to respond to the temperature changes, as shown in figure 2-20, has been a noticeable improvement (fig.2-23b). However we could still not achieve a perfect linear ramp throughout the whole temperature range even if the temperature control has been arranged in two loops with two different heaters (one for the system and one for the sample holder).

The solution to this was brought by a custom made control valve system on the transfer line of the cryogenic liquid that has been developed by Mr Mouratis (MSc). The concept is the opening/ closing of the valve through a DC step motor connected to a transmission gear. This is further powered and controlled by a current source (Keithley 2400). The algorithm compares the set point to the actual temperature point and depending on the error allows different speed modes for the stepper motor resulting to the modulation of the valve. The whole programming once more has been done in LabView. The function of this is further detailed in Appendix A while the details of the design can be found in the Master thesis of Mr Mouratis. It is important to note here that the attempt to use a mass flow controller in order to control the cryogenic flow didn't work for the system.

The temperature ramp in the PPMS system used in HZB facilities was found to work linearly only in the slow ramping rate of 1 K/ min since it was using a single loop temperature control arrangement and we had to adjust to that. It is worth to mention that after the latest tuning of the double loop temperature control system in the in house MD set up the linear ramp could be achieved even with a 4K / min ratio as shown in figure 2-23c.



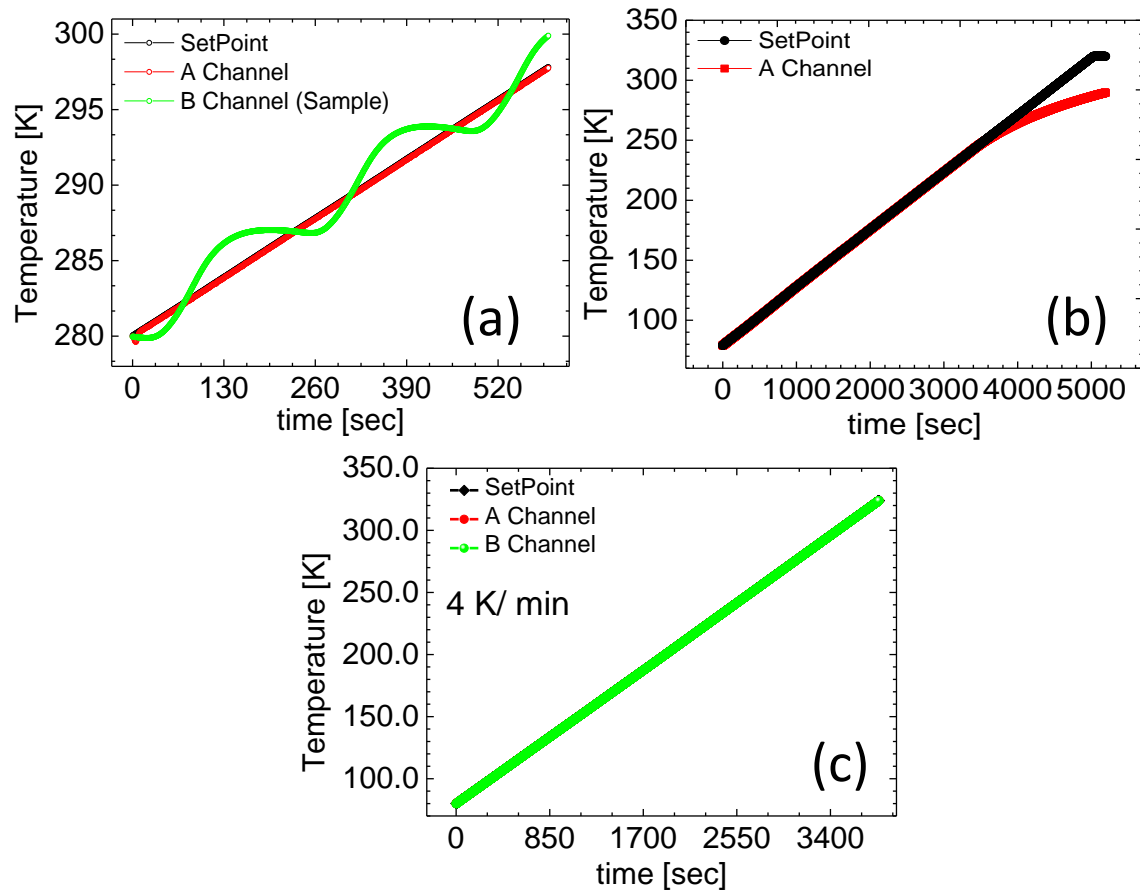


Figure 2-23 (a) Temperature ramp with a big inertia due to heavy mass of the holder (b) after the correction of the mass but still non-linear in high temperatures where  $N_2$  flow should be less (c) After the control of the  $N_2$  flow into the cryostat.

#### 2.4.4.3 Humidity

A feature in high temperature area (235-270 K) has triggered our suspiciousness towards the presence of humidity inside the experimental station of the PPMS while in HZB. It was observed that during the measurements there has been an impressive rise in dielectric constant above 230 K with this feature being affected when the system has been extra pumped and heated (350 K) for 20-30 min (or even more) in order to seal properly. We assume that it could be humidity absorption from sample or parts of the stick, because it is around 250-270 K where we could see some effects. The case of paste contacts causing a false effect of CDCs (colossal dielectric constants) as commented in 2.4.4.1, was taken into consideration but there were also cases where we could see such an increase even when there were no paste contacts on the pellet sample.



To our understanding that effect is not related to any intrinsic property of the system under study but there is good possibility that it is related to a combination of the humidity and the grain boundaries effects due to clustering on the surface or due to paste contacts. [103], [104]

The fact that this effect was also observed in Kapton Foil test measurements supports the scenario of the trapped humidity.

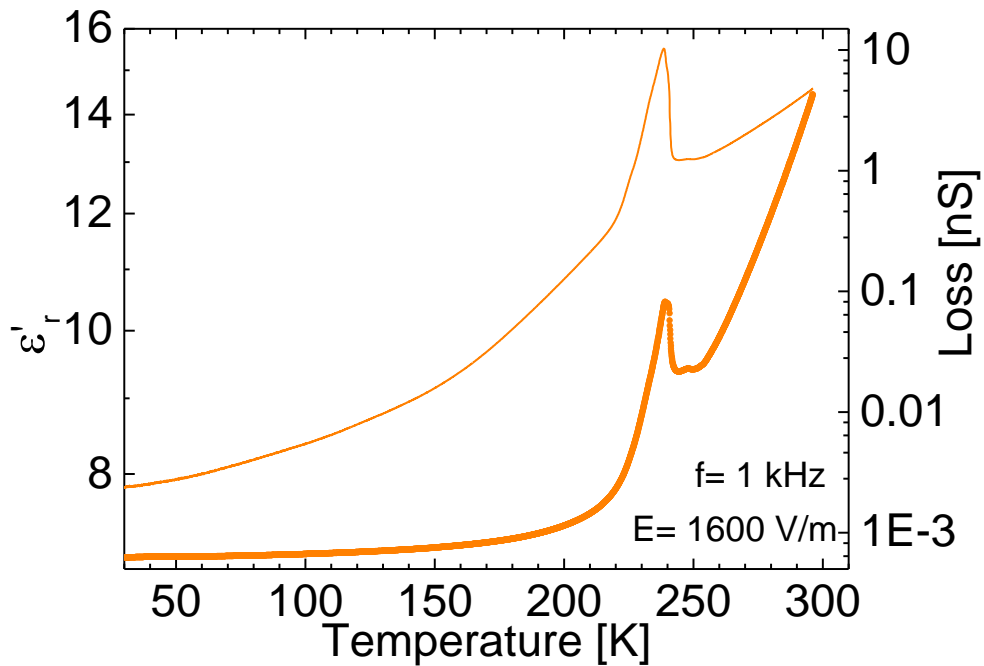


Figure 2-24 Effect of rapid increase of the dielectric constant above 230 K observed also in the dielectric Loss.

Same effects of random features in the temperature area > 250 K hinted the existence of humidity were also met in the in-house MD set up during the use of the new sample insert (figure 2-25a). This was confirmed with droplets found on the sample and around the sample holder when we got the stick out of the cryostat ( $T \approx 298$  K).

The samples that have been exposed to these conditions have been destroyed as they have been air and humidity sensitive. Contacts were checked and found good and solid with no shortcut after measurement.

The first solution we came up with, as an improvement of the custom made MD station, was the opening of several holes on the carbon tube of the MD probe so that during the pumping of the cryostat area the trapped humidity would be pumped as well. This inspiration failed as a solution to our problem since after several runs we would still find

drops on the sample holder. The origin of the humidity was finally found to be the lack of isolation around the signal terminals on the upper part of the stick (figure 2-25 b) which because of the continuous pumping was letting "Air" inside the cryostat which would liquefy when the system was ramped to low temperatures.

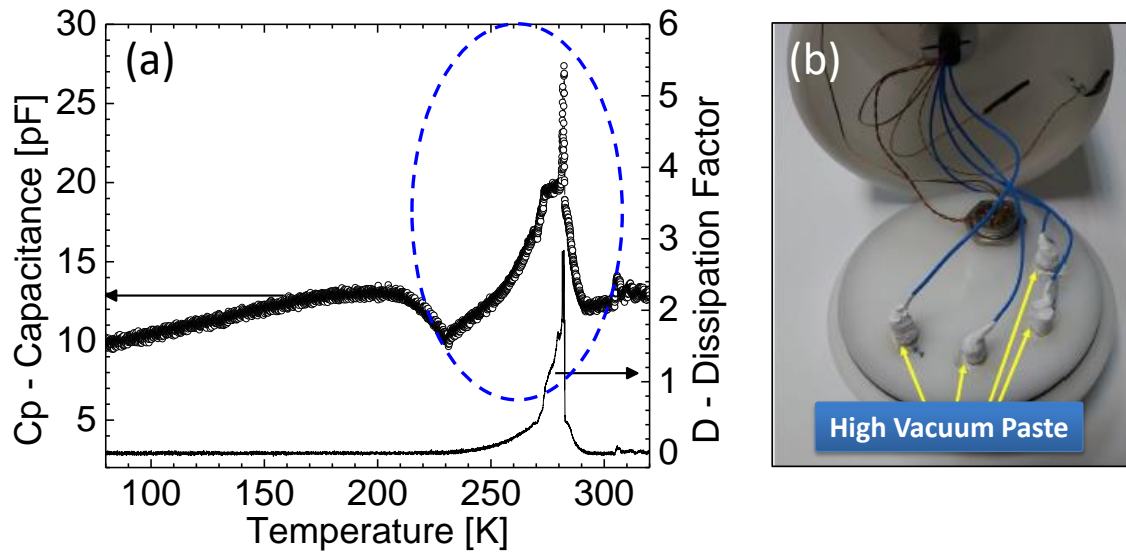


Figure 2-25 (a) Capacitance measurement after which the sample came out soaked in droplets. (b) modification of the top hat with high vacuum paste.

#### 2.4.4.4 Elimination of electronic noise [105]

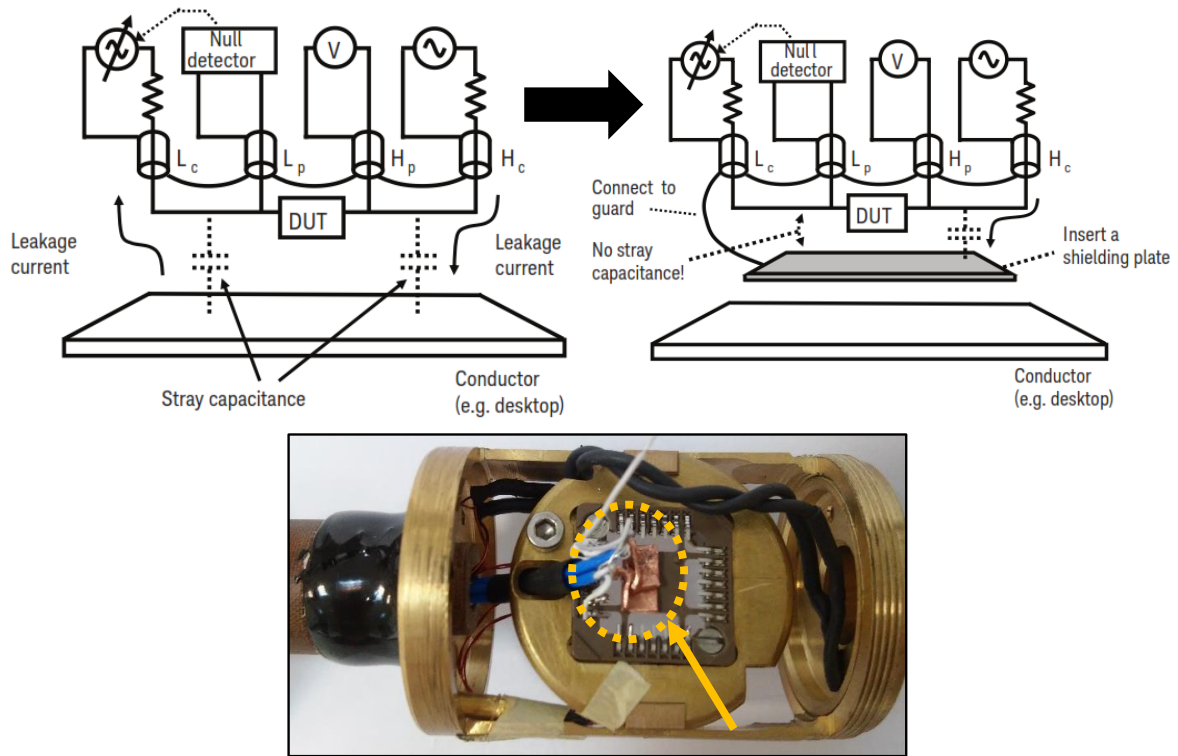


Figure 2-26 Top panel: (left) Schematic of a non-guarded topology which exhibits stray capacitance. (right) Insertion of a shielding plate so that all grounds are connected there. Bottom panel: Actual photo of the implementation of the afore mentioned “noise” shielding by addition of a copper plate on the back of the holder.

The electronic noise developed by the stray capacitance existing between the terminals connected to the device under test and a conducting environment can affect small signal measurements especially in high frequencies. [105] The effect can be eliminated by the addition of a conductive shield surface in the vicinity of the signal. As a second case of stray capacitance is the development of one in parallel with the device under test between the high and low terminals. In this case the shielding plate has to be connected as close as possible to the exposed parts of the terminals and connected to the common ground as illustrated in figure 2-26.

#### 2.4.5 Nuclear Magnetic Resonance (NMR)

The techniques of nuclear magnetic resonance (NMR) can be also successfully applied to the study of the electronic properties of solids. The virtue of this experimental method is that it can provide us with a probe that is only weakly coupled to the electronic system,

allowing for precise determination of the local magnetic fields present in the material under investigation.

Because of the effectively weak coupling, which is usually much weaker than the leading Zeeman term, the NMR results are easy to interpret. Nuclear magnetic resonance is sensitive to the time-averaged local magnetic fields through the position of the absorption lines as well as to certain spectral components of fluctuating fields. The fluctuations affect the linewidth and the relaxation times of nuclei. Consequently, employing different methods like 1D, 2D, solid state NMR, relaxation measurements e.t.c, valuable information can be retrieved about the microscopic dynamics of the system on a local scale.

#### 2.4.5.1 *Solid State NMR*

A solid (quadrupolar) echo refocuses dipolar and quadrupolar couplings. It is generated by a  $90^\circ$  pulse applied at a time  $\tau$  after the  $90^\circ$  excitation pulse (see Fig.2-27). The two  $90^\circ$  pulses must be  $90^\circ$  out of phase. The echo maximum is at a time  $\tau$  after the second pulse. The echo delay  $\tau$  should be smaller than the inverse coupling strength.

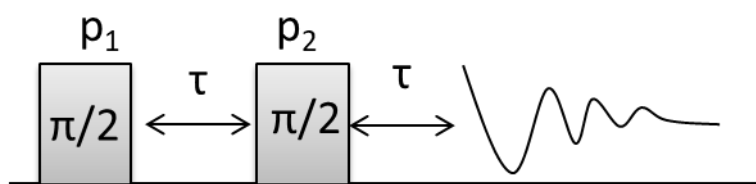


Figure 2-27 Solid echo pulse sequence

In the present study we performed NMR measurements on  $^{23}\text{Na}$  quadrupolar nucleus with  $I=3/2$ . The shape of the central line as well as the satellite line determines the nature of the transitions observed observing changes in the quadrupole frequency  $\nu_Q$ .

#### 2.4.5.2 *Types of magnetic relaxation*

Any excited magnetic moment (generally excited by an RF) relaxes back to equilibrium on the  $z$ -axis. There are two mechanisms involved: spin-lattice and spin-spin mechanism. Spin-spin relaxation is also referred to as transverse relaxation or  $T_2$  and describes the decay of the excited magnetization perpendicular to the applied magnetic field. On the other hand, spin-lattice relaxation is referred to as longitudinal relaxation or  $T_1$  and describes the return to equilibrium in the direction of the magnetic field.



The spin-lattice relaxation ( $T_1$ ) can be measured from the buildup of magnetization along the static applied magnetic field. For this an inversion recovery pulse sequence is used. The inversion recovery ( $T_1$ ) pulse sequence (fig. 2-28) inverts the magnetization on the  $z$ -axis so that the second pulse yields a signal of intensity directly proportional to the relaxing magnetization along that axis: negative for short evolution times and positive for long evolution times. The intensity of the signal is described by the equation:

$$I_0 \left[ 1 - 2 \exp\left(-\frac{\tau}{T_1}\right) \right] \quad (2-15)$$

The intensity is zero at  $T_1 \ln(2)$  ( $0.693T_1$ ) so the value of  $T_1$  can be measured by running single experiments, changing the value of  $\tau$  until a null intensity is found. If the intensity is positive then  $\tau$  needs to be reduced and if it is negative then  $\tau$  needs to be increased. The value of  $T_1$  is  $1.443\tau_{\text{null}}$ .

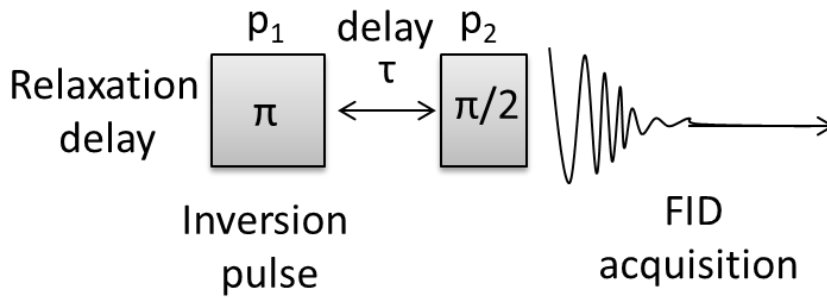


Figure 2-2-28 Inversion recovery pulse sequence for measuring  $T_1$

Spin –lattice relaxation rate  $1/T_1$  can be determined by fitting magnetization recovery curves to the magnetic-relaxation model for  $I=3/2$ :

$$M(t) = M_0 \left[ 1 - s \left( 1/10 e^{-\left(\frac{t}{T_1}\right)^\alpha} + 9/10 e^{-\left(\frac{6t}{T_1}\right)^\alpha} \right) \right] \quad (2-16)$$

Where,  $s < 1$  accounts for imperfect inversion of  $^{23}\text{Na}$  nuclear magnetization after the initial  $\pi$  pulse, while  $\alpha$  stands for a stretching exponent.

The spin-lattice relaxation ( $T_1$ ) is expressed by the following equation for determining the nature of magnetic fluctuations:

$$\frac{1}{T_1} = \frac{2\gamma_n^2 k_B T}{(\gamma_e \eta)^2} \sum_{q\rho} A_q^\rho A_{-q}^\rho \frac{\chi''(q^\rho, \omega)}{\omega} \quad (2-17)$$



where  $A_q$  denotes the hyperfine coupling of the  $^{23}\text{Na}$  nuclei with the electronic magnetic moments,  $\chi''$  is the imaginary part of the dynamical susceptibility and  $\omega$  is the Larmor frequency.

## 2.5 Studies in International Large-scale Facilities

### 2.5.1 Synchrotron X ray scattering [94]

Very high intensity X-ray beams,  $\sim 100$ – $10,000$  times more intense than the  $K\alpha_1$  radiation from X-ray tubes, are generated in a synchrotron, a type of particle accelerator. Highly accelerated electrons are confined to travel in near-circular paths in a ‘storage ring’ by the action of magnets placed at intervals around the ring. The ‘synchrotron radiation’, which arises as a result of the continuous inward radial acceleration of the electrons, is outputted tangentially from the ring and covers a wavelength range from infrared to very short X-ray wavelengths. The radiation then passes to a crystal monochromator, set to reflect the particular wavelength required.

Apart from the high brilliance of the X-ray beam, the advantage of synchrotron radiation is that, unlike X-ray tubes where one is restricted to the particular  $K\alpha_1$  wavelength of the anode element, the monochromator can be ‘tuned’ to reflect X-rays either well away from the absorption edge of (e.g.) a heavy element in the specimen to minimize absorption effects. Duo to the size of the storage ring the nearly parallel beams at distances offer a better resolution compared to conventional X-ray beams. The radiations also differ in their states of polarization; that from an X-ray tube is almost wholly unpolarized whereas that from a synchrotron is wholly polarized in the plane of the storage ring.

In general, there is no principal difference in the diffraction phenomena using the synchrotron and conventional X-ray sources, except for the presence of several highly intense peaks with fixed wavelengths in the conventionally obtained X-ray spectrum and their absence, because of the continuous distribution of photon energies, when using synchrotron sources.

The phase purity of pulverised Na-Mn-O crystals was studied by synchrotron X-ray powder diffraction, performed at the National Synchrotron Light Source (NSLS-II, BNL, USA). The specific measurements were performed at room temperature employing the 28-ID-2 (XPD) beam line at NSLS-II, equipped with an image plate detector and  $\lambda = 0.2354 \text{ \AA}$ . Small Na-Mn-O crystal flakes were ground in fine powder, loaded in  $\varnothing 1 \text{ mm}$  glass



capillaries, which were then flame-sealed and studied at XPD as two separate specimens. The data were analysed by using both the Le Bail and Rietveld refinement options available within the FullProf suite of programs.[106] Le Bail and Rietveld methods will be briefly described in section 2.5.3.

### 2.5.2 Neutron Diffraction [107]–[109]

Neutron scattering is a tool which allows both the nuclear and the magnetic structure of a material to be examined and more specifically Neutron diffraction describes the elastic scattering of a neutron from an atom providing information for determining the crystal structure. Unlike X-rays, neutrons have no electrical charge, and so do not strongly interact with the electron cloud of an atom. The result of this is that neutrons can probe deeper into a material than X-rays, and the effect of absorption does not increase with the size of the atom. These properties are particularly useful for defining the crystal structure of a compound, since the positions of relatively light atoms (e.g. oxygen) can be determined even when alongside much heavier rare earth atoms and transition metal ions.

Neutrons are produced in two different ways, through the fission of  $^{235}\text{U}$  in a nuclear reactor (as used at the Institut Laue Langevin (ILL)) or through a spallation process which involves the collision of high energy protons that have been accelerated in a synchrotron with a heavy metal target (as at ISIS in the UK or the Paul Scherrer Institut (PSI) in Switzerland). Both processes require the use of a room-temperature moderator, in which the neutrons are slowed to thermal velocities via collisions with light atoms such as deuterium.

A disadvantage of using neutrons is that scattering is weak - only a small fraction of the incident neutron beam is scattered by the nuclei in the sample. This, combined with the fact that the incident neutron flux produced by a neutron source will be orders of magnitude smaller than the photon flux from an X-ray source means that, generally, much longer counting times are required in neutron scattering experiments than in X-ray scattering experiments. Also, samples are generally required to be large for magnetic measurements using neutrons, providing a practical problem for single crystal work.



### 2.5.2.1 Nuclear Neutron scattering

In a neutron diffraction experiment (elastic scattering), neutrons fired upon a sample have an incident wavevector  $k_i$ , and scattered wavevector  $k_f$ . The scattering vector,  $Q$ , is then defined as:

$$Q = k_i - k_f \quad (2-18)$$

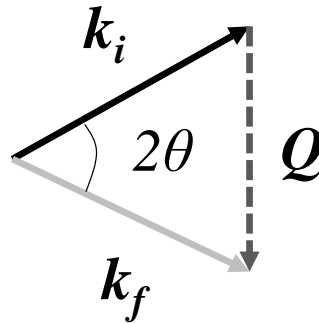


Figure 2-29 The scattering triangle relating the incident and final wavevectors to the scattering wavevector

The effective cross section,  $\sigma$ , seen by the neutron beam is related to the nuclear scattering length,  $b$ , an atom (and isotope) dependent quantity:

$$\sigma = 4\pi b^2 \quad (2-19)$$

The differential cross section,  $\frac{d\sigma}{d\Omega}$ , is defined as the number of neutrons scattered into a solid angle  $d\Omega$  per second, as a fraction of the incident flux (It is assumed that the distance between the sample and detector is large compared with the dimensions of the sample and detector, such that  $d$  is well defined [109]).



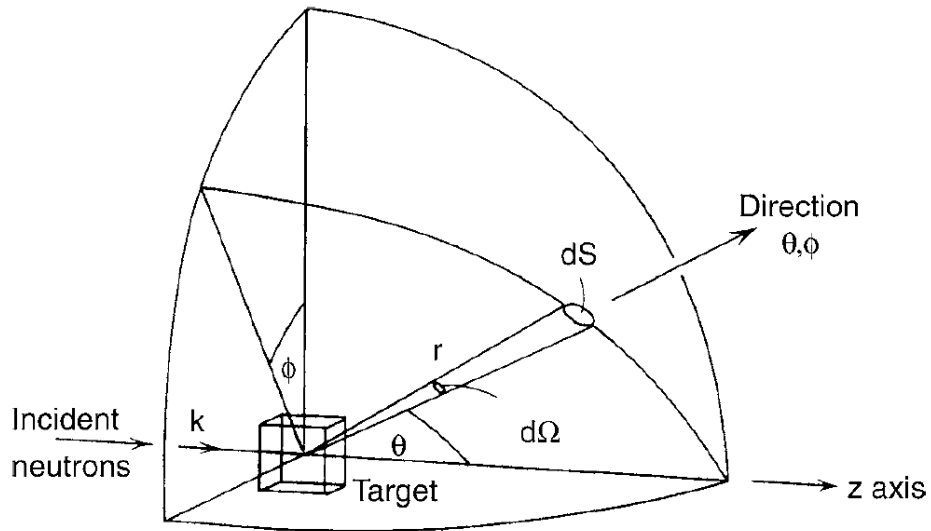


Figure 2-30 Neutron scattering geometry after Squires [109]

This value represents the probability of detecting a neutron over a solid angle range, and is dependent on the values of  $Q$  and  $b$ . For a neutron beam elastically scattered by an array of  $n$  atoms, the differential cross section is given by:

$$\frac{d\sigma}{d\Omega} = |\sum_n b_n \exp(iQ \cdot r_n)|^2 \quad (2-20)$$

where  $r$  is the vector describing the position of the nucleus the neutron interacts with. For a crystal with lattice parameters  $a$ ,  $b$  and  $c$ :

$$r = xa + yb + zc \quad (2-21)$$

Scattering from a crystal occurs when the Laue condition is satisfied:

$$Q = G = ha^* + kb^* + lc^* \quad (2-22)$$

where  $a^*$ ,  $b^*$  and  $c^*$  are the reciprocal space lattice parameters ( $a^* = 2\pi/a$ , etc), and  $h$ ,  $k$  and  $l$  are the crystal Miller indices. The differential cross section in this case is given by:

$$\frac{d\sigma}{d\Omega} = N^2 |F_{hkl}|^2 \quad (2-23)$$

where  $N$  is the number of unit cells in the crystal.  $F_{hkl}$  is the nuclear structure factor, and is given by:

$$F_{hkl} = \sum_n b_n \exp[2\pi i(hx_n + ky_n + lz_n)] \quad (2-24)$$

The intensity,  $I$ , of the scattered beam is related to the nuclear structure factor according to Squires[109]:

$$I \propto |F_{hkl}|^2 \quad (2-25)$$



### 2.5.2.2 *Magnetic Neutron diffraction*

Neutrons have a spin value of 1/2, allowing them to interact with the magnetic moments present in a sample. The interaction between the intrinsic magnetic moment of the neutron,  $\mu_N$ , and the atomic magnetic field,  $B$  (which is due to the resultant spin and orbital angular momenta of the atom) is described by a potential of the form  $-\mu_N \cdot B$ . Neutron scattering can therefore be used to determine the magnetic structure of a compound.

As mentioned above, neutrons are also scattered by the magnetic moments in a crystal. Magnetic scattering only occurs from components of the magnetisation which are perpendicular to the scattering vector  $Q$ . The magnetic structure factor,  $F_M$ , is given by:

$$F_M = \sum_j f_j(Q) \mu_j \exp[iQ \cdot r_j] \quad (2-26)$$

where  $\mu_j$  is the magnetic moment at the  $j$ th site, and  $f_j(Q)$  is the magnetic form factor (as given by the dipole approximation), which gives the  $Q$ -dependence of the magnetic scattering from an atom. The magnetic scattering intensity is dependent on  $F_M$ , as with the nuclear scattering case [109]:

$$I_M \propto |F_M|^2 \quad (2-27)$$

If a neutron powder diffraction experiment utilises measurements of the scattered intensity as a function of the scattering vector,  $Q$  or the crystal  $d$ -spacing, any peaks found can then be related to the magnetic or crystal structure of the compound. In order to distinguish between nuclear peaks and magnetic peaks, measurements can be taken at temperatures in the paramagnetic phase, where no magnetic order (and thus no magnetic Bragg peaks) are expected. Models of the magnetic structure can then be determined by using Rietveld refinement of the data.

### 2.5.2.3 *Constant wave length (CW)*

For diffraction experiments, as is the case for the x-ray diffraction measurements described in section 3.2, the wavelength should be kept constant whilst the diffraction angle is varied. The beams are therefore monochromated by diffraction from high quality crystals or a mechanical rotating device known as a chopper, which permits neutrons that are travelling at the correct velocities to pass through a small window.

In the first case, higher order diffraction with wavelengths of  $\lambda_N/n$  also takes place. These secondary wavelengths must be removed by filters, but monochromation of this kind results in a continuous beam and is the method used at PSI. The second method, employed at ISIS, gives out a pulsed neutron beam with an error in  $\lambda_N$  related to the width of the



chopper window. A pulsed neutron beam necessitates an analysis method known as *time-of-flight*.

#### 2.5.2.4 *Time of flight (TOF)*

The incident neutron energy and direction with respect to the crystal are fixed by the experimenter. The neutron transfers both momentum and energy to the sample and the direction and time of the scattered neutron is then measured. In the detector system of the instrument, the neutrons are counted both as a function of position and time. The time taken ( $t$ ) for the neutron to travel a distance  $L$  from the chopper to the sample to the detector can be used to determine the magnitude of  $k_f$  via the relation  $|k_f| = m_N L / \hbar t$ .

The powders and crystals of this study have been measured using the TOF diffractometer WISH (Wide angle on a single Histogram) in Target Station 2, at ISIS of Rutherford Appleton Laboratory. The general layout of TOF diffractometer is presented in figure 2-27. WISH is a long wavelength magnetic diffractometer suitable for the study of magnetic or large unit cell compounds with wavelengths that vary from 1.5 Å to 15 Å (or d-spacing 0.7 Å -50 Å). Neutrons travel towards the sample with a velocity  $v$ , through a guide of total length  $L$  (for the WISH instrument  $L=50$  m). The time of flight ( $t$ ) for neutrons is related to the wavelength ( $\lambda$ ) by De Broglie equation:

$$\lambda = \frac{h}{p} = \frac{h t}{m L} \quad (2-28)$$

For the case of TOF diffractometer Bragg's law can be re-written as

$$\lambda_{hkl} = 2 d_{hkl} \sin \theta \quad (2-29)$$

where  $\theta$  is the fixed detector angle and each interplanar spacing  $d_{hkl}$  corresponds to a distinct wavelength  $\lambda_{hkl}$ .

The substitution of the wavelength in equation (2-30) with its equivalent from equation (2-28) yields for the interplanar spacing

$$d_{hkl} = \frac{h t}{2 m L \sin \theta} = \frac{t}{505.554 L \sin \theta} \quad (2-30)$$

Data presented in the form of number of neutrons as a function of time of flight (in microseconds) are collected from different detectors (or "banks" as they are usually called) which are placed circularly with respect to the sample covering different d-spacing regions. Backscattering detectors also exist, which in the case of WISH produces the data with the highest resolution.



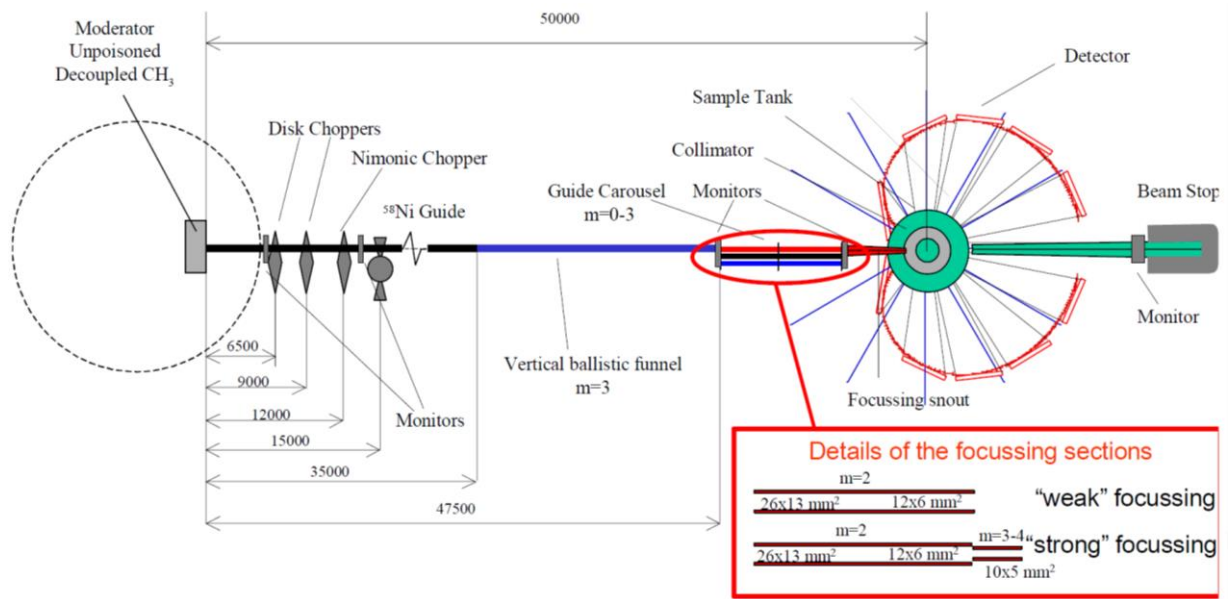


Figure 2-31 Schematic of layout of the WISH diffractometer in TS2 –ISIS reprinted from science case reference [110]

When a neutron enters the detector, the helium gas inside the chamber is ionised via the following reaction:



If a voltage is applied across the gas chamber, the emitted charged He ions result in a measurable electrical pulse. In a powder neutron diffraction experiment, an array of  ${}^3\text{He}$  detectors are placed on an arc, each one equidistant from the sample. Rather than scanning a detector through a range of  $2\theta$  values, data at each angle are collected simultaneously.

In a single crystal diffraction experiment, the sample is rotated through the Bragg condition and a plot of neutron counts versus rotation angle is recorded. The resulting curve is fitted to a Gaussian or Lorentzian distribution and the integrated area used to determine a quantity known as the nuclear structure factor, defined as:

$$F_N(q) = \sum_i \bar{b}_i \exp[iq \cdot R_i - W_i(q)] \quad (2-32)$$

where  $R_i$  represents the position vector of atom  $i$  within the unit cell and the last term in the exponential is known as the Debye-Waller factor which accounts for the thermally induced displacements of the atoms around their mean position.

The structure factor is related to the coherent elastic differential cross section via:

$$\left(\frac{d^2\sigma}{d\Omega}\right) = \frac{(2\pi)^3}{V_0} \sum_{\tau} |F_N(q)|^2 \delta(q - G) \quad (2-33)$$

where  $V_0$  is the volume of the crystallographic unit cell and  $G$  a reciprocal lattice vector. The delta function in the above equation is a restatement of the Bragg condition that diffraction may only occur when the momentum transfer vector equals a reciprocal lattice vector. Of course, in reality a Bragg reflection does not correspond to a delta function. The Bragg peaks are finite in two dimensions due to factors such as crystal mosaic spread and instrumental resolution (because of error in the incident neutron wavelength and/or imperfect collimation).

In three dimensions, the Bragg reflection is contained within a resolution ellipsoid. It is for this reason that the reflection is measured and integrated over an extended range to measure the total intensity of each reflection ( $I_{hkl}$ ). The structure factors are calculated thus:

$$I_{hkl} = \frac{N_{hkl}\omega}{\Phi_0} = \frac{\lambda^3 V}{V_0^2} |F_{hkl}|^2 \quad (2-34)$$

where  $N$  is the number of diffracted neutrons,  $V$  the sample volume and  $\omega$  the rotational angular velocity.

Several corrections need to be made to the data. Firstly, as mentioned above, thermal agitation of the crystal structure is accounted for via the Debye-Waller factor. Secondly, if the sample is highly absorbing a correction for  $\Phi_0$  as a function of sample thickness needs to be made. Thirdly an effect known as extinction should be accounted for. Primary extinction produces a similar effect to absorption; if a large proportion of the incoming neutrons are diffracted by the first part of a crystal, the incident flux further into the crystal is significantly reduced. Secondary extinction relates to the diffraction of beams by misaligned domains within the crystal. Finally, the Lorentz factor incorporates the effect due to the angular rotation of the crystal. Since the Ewald sphere is centered on the origin of  $k_i$  and not the reciprocal lattice, a constant speed of rotation in real space causes different points in reciprocal space to pass through the Ewald sphere with different velocities; each reciprocal lattice point therefore obtains a different period of time with which to satisfy the Bragg condition leading to an alteration in the measured values of  $I_{hkl}$ .

#### 2.5.2.5 *Inelastic Neutron scattering[111]*

Neutrons are also inelastically scattered from atoms, either losing or gaining energy during the collision. A diffraction experiment counts neutrons that satisfy the Bragg condition of



the crystal i.e. when  $|k_i| = |k_f|$ , the scattering processes when this condition is not met are measured in inelastic neutron spectroscopy (INS) and give information on the time dependence of atomic motions. The scattering vector  $q$  is defined as the difference between the incident and final wavevectors  $q = k_i - k_f$ . Applying the cosine rule to the wavevector configuration in figure 2-32 gives:

$$Q^2 = k_i^2 + k_f^2 - 2|k_i||k_f| \cos \theta \quad (2-35)$$

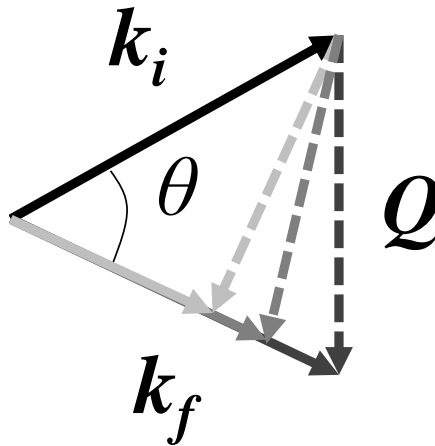


Figure 2-32 The scattering triangle for incident and final wave vectors in the case of inelastic scattering.

which can be written in terms of energy as follows:

$$\frac{\hbar^2 Q^2}{2m_n} = E_i + E_f - 2\sqrt{E_i E_f} \cos \theta \quad (2-36)$$

The neutron transfers both energy ( $\hbar\omega$ ) and momentum ( $Q$ ) to the sample; an inelastic scattering experiment therefore counts neutrons that satisfy equation 2-35 and maps out the scattering function  $S(\vec{Q}, \hbar\omega)$ . The scattering function at nonzero energy contains both inelastically scattered neutrons and quasielastic scattering - scattering due to non-periodic motions of atoms that results in nearly elastic scattering at  $Q$  values between Bragg reflections. The coherent part of this scattering is also known as diffuse scattering and characterizes the deviation of the system from ideal (spatial or temporal) periodic order resulting in a broadening of the elastic line into both positive and negative energy transfer. The techniques for measuring INS are split into two categories, direct and indirect geometry spectrometers. Direct geometry instruments monochromate the incident neutron

beam. Aligning the crystal along a direction of interest with the neutron beam defines  $k_i$  in terms of the reciprocal lattice of the system under study. The neutron scatters from the sample, changing in both energy and momentum and then  $k_f$  is measured. Indirect geometry spectrometers make use of a white beam of neutrons. A crystal analyzer then selects the final neutron energy. Further to this, direct geometry spectrometers are divided into two categories, time of flight spectrometers and triple axis spectrometers.

Inelastic neutron scattering work for the present study was performed on the MARI direct geometry TOF chopper spectrometer (ISIS, UK) and also on the DCS spectrometer (NIST, USA). Experiments on MARI used incident energies  $E_i=85$  and  $150$  meV, with a Gd Fermi chopper spun at  $300$  and  $450$  Hz, respectively. Measurements on DCS were done with an incident energy of  $E_i=14.2$  meV.

As the measured neutron scattering cross section is proportional to the structure factor  $S(\vec{Q}, \hbar\omega)$ , for a powder material, the measured, momentum integrated neutron intensity is proportional to the following average at a fixed  $|\vec{Q}|$ ,  $\bar{I}(\vec{Q}, \hbar\omega) = \int \frac{d\Omega S(\vec{Q}, \hbar\omega)}{d\Omega Q^2}$ . Obtaining microscopic exchange interactions that form the basis of the magnetic Hamiltonian from powder neutron data is rather difficult owing to the averaging over all reciprocal space directions,  $|\vec{Q}|$ . However, applying sum rules allows information to be obtained about the interactions and correlations in a general way which is independent from the microscopic Hamiltonian. This method is outlined in section 4.7.2 in an attempt to parametrize the dispersion of the  $E(\vec{Q})$ . Furthermore, single-mode approximation and parameterization of the dispersion,  $E(\vec{Q})$ , allows us to characterize which correlations are important and also determine the dimensionality of the excitations.

### 2.5.1 Analysis of diffraction Data (Le Bail & Rietveld methods) [93], [112]–[115]

Powder diffraction remains a powerful method even when single crystals are available due to the speed and simplicity of data collection while the profile refinement techniques work in favor of the affinity of this method. Either using X-rays or neutrons the analysis of the data collected leads to the study and determination of crystal structures (by using either x-rays or neutrons) and the determination and analysis of magnetic structures (in case of neutron diffraction), where often complicated magnetic moment configurations are met.



A powder diffraction pattern is the result of the Bragg scattering of x-rays or neutrons from a crystalline material. As mentioned in previous section, in real life a Bragg reflection does not correspond to a delta function as it is ideally described. So, the whole pattern may be thought as a collection of individual reflection profiles, finite in two dimensional space, characterized by peak height, position, width and tails decaying gradually moving away from the peak position. This pattern is a 1-D representation of a 3-D lattice and the characteristics of the observed Bragg reflections depend on a number of factors related both to the specimen (crystal or magnetic properties) but also to the instrument specifications of the diffractometer itself and the measurement technique (CW, TOF). So the diffraction pattern is represented by the scattered intensity usually plotted in Y-axis as a function of an independent variable ( $2\theta$  angles, time of flight, d- spacing, energies).

### 2.5.1.1 *Least-Squares refinement techniques*

The powder diffraction data presented in this thesis have been analysed using both the Le Bail and Rietveld refinement options available within the FullProf Suite of programs.[106] Profile matching or else Le Bail refinement, is just the refinement of the lattice parameters and peak shape while in the Rietveld refinement the crystal structure of the material is refined. It is important to note that Rietveld is a refinement method and not a method of solving structures.

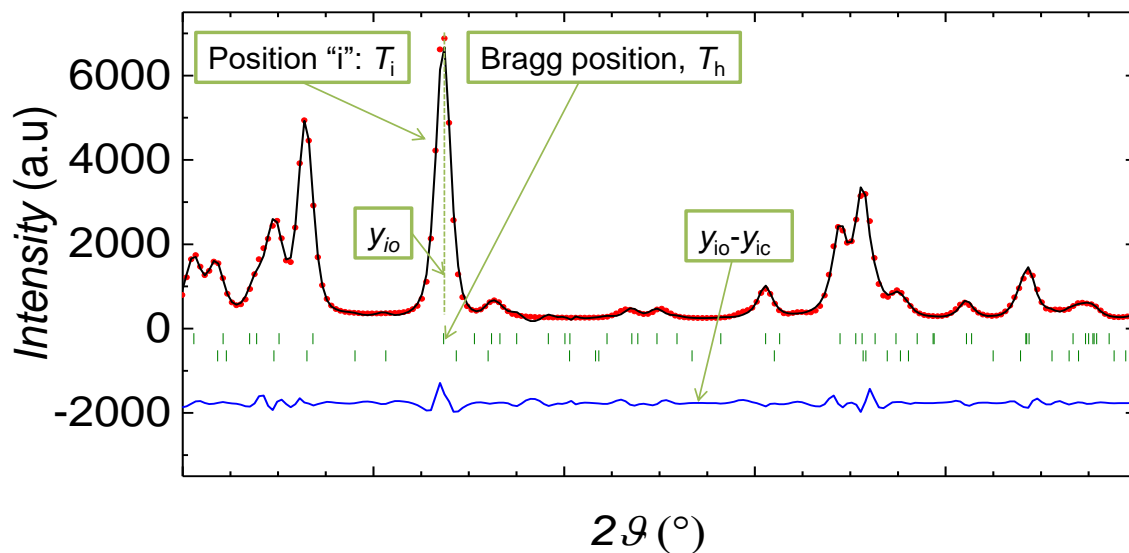


Figure 2-33 Plotted 2-phase Le Bail refinement from x-ray diffraction pattern of  $a\text{-Na}_{0.96}\text{MnO}_2$ . The observed pattern of the experimental data ( $y_i$ ) and the calculated theoretical model ( $y_{ci}$ ) are presented in red and black respectively while the difference of the two is in blue.



In both of these methods, the observed pattern of the experimental data is matched with a calculated pattern and the quality of the match is presented by the difference line of these two patterns as presented in figure 2-33. This is a two phase refinement where the dotted red line represents the experimental data and the black line shows the intensity which is calculated by the model. The green tick marks along the x-axis, below each reflection represent the Bragg peaks of each one of the two phases, as predicted by the model.

More specifically, an intensity profile as a function of scattering angle is measured and the peaks in the pattern are indexed to a particular space-group, from which the unit cell parameters can be determined accurately. Diffraction patterns from structures with large unit cell volumes and relatively low symmetry contain a large number of reflections, the intensities of which may overlap depending on the diffractometer resolution function and the quality of the sample. That makes the process of assigning Miller indices to every reflection nontrivial. This is because the intensity at any particular step in  $2\theta$  is likely to contain contributions from several Bragg reflections not to mention the unknown error in the measured values of  $2\theta$ . However, the Rietveld method overcomes this problem by fitting the diffraction as a whole ( $I_i$ ), rather than a set of individual ( $I_{hkl}$ ) reflections, with a least-squares fit to each value of intensity in the pattern carried out simultaneously. A review of Rietveld refinement method can be found in reference [113] while the process which is also used in the Le Bail refinement will be briefly described right away.

Both of these methods rely on least square refinement techniques using the Rietveld algorithm. Le Bail technique is relied on the Rietveld code and was first introduced by Pawley on 1981 and is usually the first step of the refinement process when the crystal structure is not accurately known. It uses a constant scale factor and the calculated intensities are adjusted to fit the observed intensities in order to obtain initial values for the profile parameters, before the refinement of the crystal structure is attempted. In the Rietveld algorithm the quantity that is being minimized is the weighted sum of squared differences between the observed  $y_{io}$  and calculated  $y_{ic}$  intensities

$$S_y = \sum_i w_i (y_{io} - y_{ic})^2 \quad (2-37)$$

Where  $w_i = \frac{1}{\sigma_i^2} = \frac{1}{\sigma_{ip}^2 + \sigma_{ib}^2}$  is the inverse weighting factor for each intensity and  $\sigma_{ip}$ ,  $\sigma_{ib}$  are the standard deviations associated with the peak value and the background measurement respectively.



As mentioned earlier each calculated intensity value represents a sum of contribution from neighbor Bragg reflections and background contribution. The calculated intensity at each point as determined by the structure factor  $|F_{hkl}|^2$  is presented below:

$$y_{ic} = s \sum_{hkl} L_{hkl} |F_{hkl}|^2 G(\Delta\theta_i) P_{hkl} A + y_{ib} \quad (2-38)$$

Where,

s: scale factor

$L_{hkl}$ : contains the Lorentz, polarization and multiplicity factors for reflection (hkl),

$|F_{hkl}|^2$ : is the structure factor for the reflection (hkl)

$(\Delta\theta_i)$ : is the 2-theta value corrected for the zero point shift of the detector and so, the

$G(\Delta\theta_i)$ : is a reflection profile function,

$P_{hkl}$ : preferred orientation for reflection (hkl)

A: an absorption factor and finally

$y_{ib}$ : is the background intensity at the  $i_{th}$  step

The background term represents the contribution of diffuse scattering, noise in the detector system and insufficient shielding and is often refined to a polynomial function as presented below:

$$y_{ib} = \sum_n b_n (2\theta_i)^n \quad (2-39)$$

where  $b_n$  are refinable coefficients.

In general, a successful profile refinement relies on the knowledge of a reasonably accurate crystal structure and profile parameters which can be obtained by the Le Bail refinement. In the final refinement using Rietveld, the refinable parameters for each phase in the crystal structure include the lattice parameters, the  $(x_i, y_i, z_i)$  atomic positions of each site (unless constrained to high symmetry positions), the atomic thermal parameters  $B_i$  and the site occupancies  $n_i$ . Multiple phases may be refined simultaneously and the whole procedure repeated for patterns taken at different temperatures, magnetic fields and/or pressures in order to characterize the structural (and possibly magnetic) properties of a material across its phase diagram.



In any Le Bail or Rietveld refinement we use some agreement factors that are indicative of the quality of the refinement as they estimate the agreement between the experimental and calculated patterns. The most commonly used factors are the:

“weighted profile”:  $R_{wp} = \left[ \frac{S_y}{\sum_i w_i y_{io}^2} \right]^{1/2}$ , “expected profile”:  $R_{exp} = \left[ \frac{n-p}{\sum_i w_i y_{io}^2} \right]^{1/2}$ , where  $n$  and  $p$  are the number of data points in the profile and the refined parameters respectively.

Finally the known as “goodness of the fit” :  $\chi^2 = \left( \frac{R_{wp}}{R_{exp}} \right)^2 = \left[ \frac{\sum_i w_i (y_{io} - y_{ic})^2}{n-p} \right]$  is the square ration of the previous two values equal to the reduced  $\chi^2$  value having an ideal value of  $\chi^2 = 1$ .



## Chapter Three:

# Chemical Synthesis of Na-Mn-O System

---

### 3.1 Introduction

The early attempts of chemical synthesis of the Na-Mn-O system using the solid state method stand back to the 70s (Scholder et. al, Parant et.al.). [116], [3] In the study of Scholder et.al the reactants in use,  $\text{Mn}_2\text{O}_3$  and NaOH were fired at 700 °C under  $\text{N}_2$  flow while in the extended study of Parant et.al,  $\text{MnO}_2$  or  $\text{Mn}_2\text{O}_3$  oxides were used as Mn source and sodium hydroxide or alkaline oxygenated salt (carbonate, nitrite, manganate etc.) as Sodium source, following a high temperature method under  $\text{O}_2$  pressure. The mixture in the latter case undergoes an initial treatment under oxygen flow at a temperature between 600 and 800°C depending on the basic agent used for removing water, carbon dioxide or nitrous vapours, and then a second treatment at a temperature and oxygen pressure selected. The product of the reaction is then submitted to a quench. Other methods that have been used as synthetic pathways to obtain layered  $\text{Na}_x\text{MnO}_2$  phases have been reduction of  $\text{NaMnO}_4$ [117], hydrothermal synthesis [118] and sol-gel approach[119]. The main disadvantage of the late mentioned solution methods is the poor crystallinity of the obtained particles due to the low temperatures used. In addition to that, the hydrated phases that are the product of these methods present the challenge of successfully removing water without collapsing the layered structure.

Among the different layered structured Na-Mn-O oxides, P2-type  $\text{Na}_{0.7}\text{MnO}_2$  has received significant attention due to its high capacity as a cathode in energy storage systems with



the advantage of the ease of synthesis through the solid state method. [120], [121] More specifically, precursors  $\text{Na}_2\text{CO}_3$  and  $\text{MnCO}_3$  were mixed in a 0.7:1 Na:Mn ratio ball-milled and heated at  $1000^\circ\text{C}$  for 15h in air atmosphere followed by quenching in RT. [121] To our knowledge, Hirano et. al was the first to hydrothermally prepare single crystals of  $\text{Na}_{0.7}\text{MnO}_{2.25}$  in order to study the physical properties of the system [122].  $\beta\text{-MnO}_2$  and NaOH powders were sealed in a gold capsule with NaOH solution and treated in a test tube hydrothermal apparatus at  $1000\text{kg/cm}^2$  up to  $525^\circ\text{C}$ . The result was hexagonal plate-like crystals of  $\alpha\text{-Na}_{0.7}\text{MnO}_{2.25}$  with edge length of 2.5 mm and thickness of 0.5 mm. Since then another attempt has been made by Su & Wang for growing nanoplates of  $\text{Na}_{0.7}\text{MnO}_2$  with wet chemistry methods.[123]

In the cases of the 1:1 Na:Mn stoichiometric compounds of Na-Mn-O system we name two different polymorphs,  $\alpha\text{-NaMnO}_2$  and  $\beta\text{-NaMnO}_2$ . In the study of Parant et. al both allotropic forms have been synthesized with solid state reaction coexisting with  $\text{Na}_3\text{MnO}_4$ . Due to the energy proximity of these two polymorphs [124]–[126] producing a stable single phase has been a challenge in contrast with the stable  $\alpha\text{-Na}_{0.7}\text{MnO}_2$ . These two competing phases ( $\alpha\text{-NaMnO}_2$  and  $\beta\text{-NaMnO}_2$ ) were found to inter-grow in each other as defects, tailoring the physical properties of the system.[126] In literature one can find different modified synthesis protocols compared to the ones presented by Parant, for both alpha and beta polymorphs including different preparation of reactants, atmosphere or number of firing steps while in an attempt to stabilize both formations substitutional doping by Ti & Cu cations has been recently discussed. [127]–[130] In the present thesis the preparation of the polycrystalline powders of both alpha and beta polymorphs is based in the protocol published by Abakumov et. al with small modifications and a scale up and will be further discussed in this chapter.

In a quest for single crystal studies of Na-Mn-O system we can confirm studies on hydrothermal and sealed crucible methods[90], [131], [92] which have permitted the growth of small volume crystals of Na-Mn-O system. More precisely, ochre coloured needle-like single crystals of alpha phase, having a maximum of 2 mm length, have been grown starting from  $\text{Na}_2\text{O}$  and  $\text{MnO}$  sealed in Ag capsule and heated at  $850^\circ\text{C}$  for 10 days. In the case of beta, the crystals form coarse needles with a diameter up to 0.2 mm and length of 1.5 mm maximum having brown to brown-red colour. However, high purity growth of large volume crystals has remained elusive. This is mainly due to the close energetics of the two polymorphs ( $\alpha\text{-NaMnO}_2$  and  $\beta\text{-NaMnO}_2$ ) combined with the



challenge of high volatility of both Na and Mn. The successful growth of crystals of  $\text{Na}_x\text{CoO}_2$  system using both Flux and FZ method has provided useful information on how to handle volatility and provided access to valuable experimental insights and was used as starting point for the present study. [132]–[134]

In the present thesis we present and discuss the successful growth of sizable single crystals of  $\alpha\text{-Na}_{0.96}\text{MnO}_2$  and  $\alpha\text{-Na}_{0.7}\text{MnO}_2$  which were grown by the advanced floating zone (FZ) technique starting from  $\alpha\text{-NaMnO}_2$  and  $\beta\text{-NaMnO}_2$  powders respectively and our parallel efforts using Flux method for crystal growth of the same systems.

## 3.2 Sample preparation

### 3.2.1 Polycrystalline specimens

The Na-Mn-O samples in polycrystalline form that are studied in the present thesis were prepared by means of solid state chemistry following the protocol published earlier [126]. High purity powders of  $\text{Na}_2\text{CO}_3$  (Aldrich, 99.5%) and  $\text{Mn}_2\text{O}_3$  (Aldrich, 99.5%) were used as starting reagents. Enough quantity of these reactants was kept in the drying cabinet (~70 °C) for at least 12 h before the mixing. After the completion of the reaction process both  $\text{NaMnO}_2$  compounds were handled as air-sensitive and were further processed into an Ar-filled Glove box.

#### 3.2.1.1 *The alpha polymorph*

For the synthesis of the  $\alpha\text{-NaMnO}_2$  polymorph, the reactants were mixed in a nominal stoichiometric ratio of 1:1 and ground in an agate mortar to fine powder before being pressed into pellets. For the preparation of 1 gr of  $\alpha\text{-NaMnO}_2$  the quantities to be mixed were 0.4846 gr and 0.7253 gr of  $\text{Na}_2\text{CO}_3$  and  $\text{Mn}_2\text{O}_3$  respectively, taking into account the % purity of the reactants. The resulting mixture was then pressed into pellets using a hydraulic press ( $\varnothing$ 13 mm at 4 tons for 20 min). The pellets placed in an alumina crucible were heated with a constant heating rate of 3 °C/min up to 750 °C for 60 h under continuous Ar flow (60-80 l/h) during which the following reaction took place:



The sintering temperature of 750 °C is far below the melting temperature of the two reactants (851 °C & 940 °C respectively) allowing the diffuse of Na and Mn ions that lead to the formation of  $\alpha\text{-NaMnO}_2$ . The exact heating protocol that has been followed is



depicted in figure 3-1. After the dwell of 60 hs the pellet was cooled down to 160°C with the fastest possible rate (cooling process lasts almost 3.5 hs) and transferred immediately into the Ar filled Glove Box (GB) in order to minimize the possibility of humidity absorption and contact with oxygen since it is oxidized and hydrolyzed easily. The color of  $\alpha$ - $\text{NaMnO}_2$  is light brown while the powder of the mixed reactants has been of dark gray color. In order to better control the stoichiometry of the final product in both mixing and grinding stage as well as the sintering process the “quantity of 1gr” had been the target of the synthesis for all samples that were planned for experiments on the polycrystalline form of the oxide.

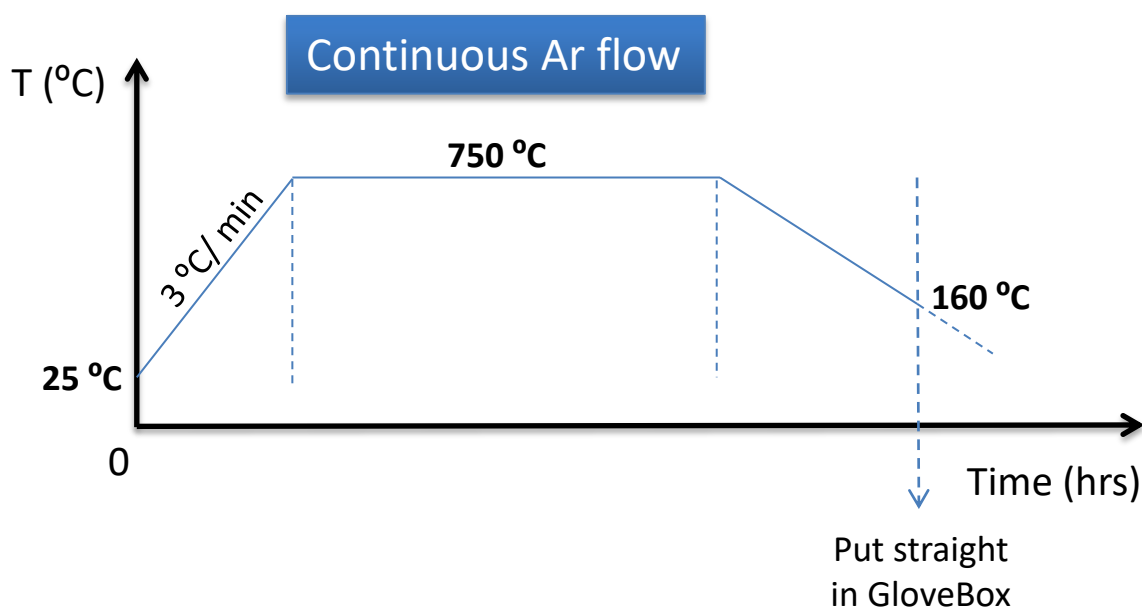


Figure 3-1 Solid state synthesis protocol of  $\alpha$ - $\text{NaMnO}_2$  polycrystalline powders

For further characterization, the 1gr pellets were ground into powder inside the Ar filled GB and either used as powder for magnetization, x-ray and neutron diffraction experiments or re-pelletized with a handhold press in smaller pellets for further dielectric and magneto electric measurements. The optimized conditions for a firm pellet using the handhold  $\varnothing 5$  mm press are pelletizing almost 87-89 mg under 22 Nm for 1h.

Growing single crystals of the system using the floating zone technique demands a large quantity of polycrystalline powder. So, for the first time, we tried a scale up the protocol that had been followed until now. The synthesis target has been 4 gr pellets of  $\alpha$ - $\text{NaMnO}_2$ . The quantities of the reactants that have been calculated are 1.93804 gr and 2.90136 gr for  $\text{Na}_2\text{CO}_3$  and  $\text{Mn}_2\text{O}_3$  respectively. For the 4 gr powder the  $\varnothing 20$  mm press has been used

following a pelletizing protocol of 4 tons for 20 min. There were several cases that the final product had a small percentage of beta-NaMnO<sub>2</sub> polymorph. This was not of great concern, since these quantities would be further sintered and finally melt for the growth of the single crystals. For the needs of the single crystal growth the quantity of 76 gr of  $\alpha$ -NaMnO<sub>2</sub> has been synthesized!

### 3.2.1.2 *The beta polymorph*

Using again the high temperature solid state reaction route, the  $\beta$ -NaMnO<sub>2</sub> polycrystalline specimens had been prepared following a synthesis protocol based on the one published in Abakumov et al..[126] The ratios of the reactants in this case, have been 1.1:1 for Na<sub>2</sub>CO<sub>3</sub> and Mn<sub>2</sub>O<sub>3</sub> respectively. The 10% excess that has been used in the first grinding was to compensate the loss of Na during the reaction. The quantities calculated taking into account the 10% Na<sub>2</sub>CO<sub>3</sub> excess along with the purity of the reactants are 0.5329 gr and 0.72534 gr for Na<sub>2</sub>CO<sub>3</sub> and Mn<sub>2</sub>O<sub>3</sub> respectively for the preparation of 1gr of  $\beta$ -NaMnO<sub>2</sub>. After mixing well in agate mortar, the starting powders were pelletized in  $\varnothing$ 13 mm hydraulic press under 1 ton for 5 min. The pressed pellets placed in alumina crucible had been heated under continuous flow of O<sub>2</sub> following the heating protocol that is shown in figure 3.2.

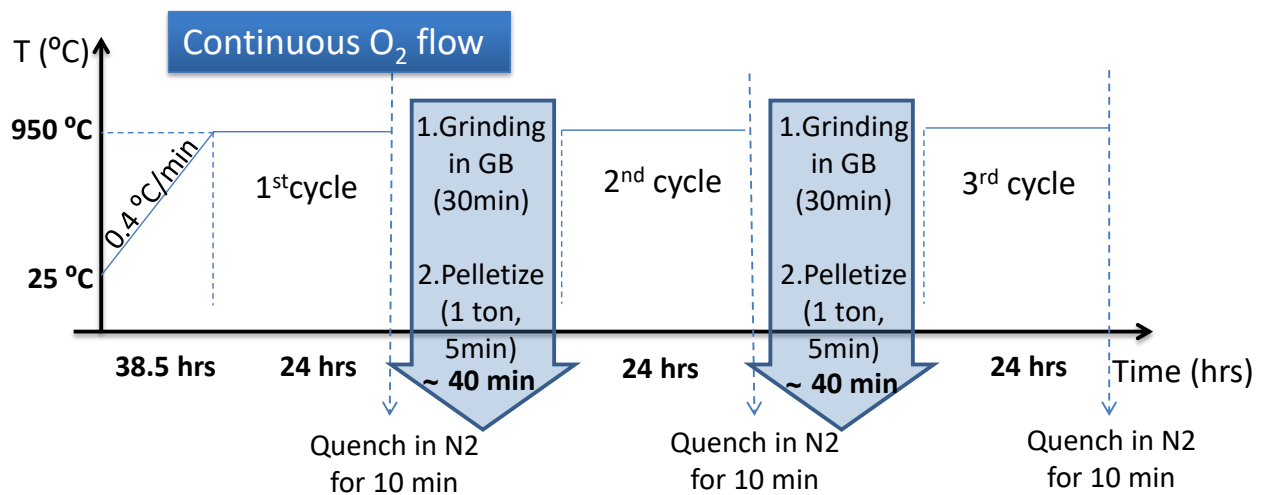


Figure 3-2 Solid state synthesis protocol of  $\beta$ -NaMnO<sub>2</sub> polycrystalline powders

In the case of  $\beta$ -NaMnO<sub>2</sub> 3 firing cycles of 24 h duration have been done. In between each cycle the pellets had been quenched from the 950 °C straight into Liquid N<sub>2</sub> for 10 min and



then transferred into the GB. The quenching intended to reassure absence of intermediate phases that might be formed during a gradual cooling process. Grinding and re-pelletizing before the next cycle adds to the homogeneity of the mixture since it helps fresh surfaces of grains come together speeding up the reaction and has been done inside the Ar-filled Glove box. The reaction that takes place is described below (eq. 3.2).



The protocol described earlier had been scaled up while most of the times the synthesis of 2x 4 gr pellets has been scheduled for a mass production of polycrystalline powder. The process has been very demanding since after the first heating the samples were handled as air sensitive so all grinding and pelletizing had to be done inside the GB for two pellets, instead of one, and be time-efficient in such way so that both pellets enter the furnace for the next heating with no more than 15 min time phase. It has been observed that after the first heating areas of the pellet had greenish color which hints for MnO which can be produced after the reaction of Mn<sub>2</sub>O<sub>3</sub> with CO. This could be attributed to the insufficient mixing of the powders due to the bigger quantity that comes with the scale up, that confirms the necessity of the 3 cycles of grinding and firing in order to achieve a homogeneous product.

### 3.2.2 Single crystal growth- The Flux method

Since the hydrothermal method was the one used for the growth of the first crystals of Na-Mn-O system, approaching the growth of sizable crystals using another method based in the “growth from liquid phase” principle seemed feasible and promising. Studies on Flux growth of the similar to the Na-Mn-O system of Na<sub>x</sub>CoO<sub>2</sub> have been the starting point of this study.[134], [135] In particular, Mikami et. al used two different kind of fluxes using NaCl, Na<sub>2</sub>CO<sub>3</sub> and B<sub>2</sub>O<sub>3</sub> in order to obtain different phases of Na<sub>x</sub>CoO<sub>2</sub> crystals. [134]

In the present study we experimented on growing crystals using also 2 different fluxes. These fluxes were mixtures involving NaCl (99.5%), Na<sub>2</sub>CO<sub>3</sub> (99.5%), and B<sub>2</sub>O<sub>3</sub> (99.9%). Since the flux contained Na<sub>2</sub>CO<sub>3</sub>, there was no reason of adding any excess of Na<sub>2</sub>CO<sub>3</sub> in our starting powders as had been done in the synthesis of the polycrystalline powders. Stoichiometric 1:1 quantities of the reactants Na<sub>2</sub>CO<sub>3</sub> (Aldrich, 99.5-100.05%) and Mn<sub>2</sub>O<sub>3</sub> (99%, Aldrich) have been weighed and mixed with each flux mixture. Both reactions were allowed to happen in air and not in a sealed container as suggested in hydrothermal synthesis but in an alumina crucible, so we were lucky enough to see some



tiny needle crystals grow. According to Mikami et. al several issues came out with the use of boron oxide and so the concentration of  $B_2O_3$  into the solution was eliminated to 10 mol %. Since the preliminary need for crystal growth is the achievement of supersaturation, several techniques are employed in order to achieve this. Among them *slow cooling* has been the one visited in the present study.

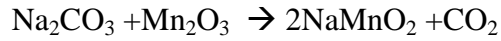
The two fluxes that have been used are the following:  $NaCl : Na_2CO_3 : B_2O_3 = 4 : 4 : 1$  (NNB Flux) and  $Na_2CO_3 : B_2O_3 = 8 : 1$  (NB Flux). As suggested by literature, the percentage of the solute should be 10 mol %  $\Rightarrow x = (n_i / n_{tot}) * 100 = \text{mol } \%$  where  $n_i$  is the diluted quantity and  $n_{tot}$  the solution. So considering stoichiometric ratio of the starting materials, the following calculations were done for each of the two mixtures presented in Tables 3-1 and 2.

Table 3-1 Calculation of the mass of the reactants and the Flux of NNB

<b>NaCl : Na<sub>2</sub>CO<sub>3</sub> : B<sub>2</sub>O<sub>3</sub> = 8 : 8 : 2 (NNB Flux)</b>			
<b>Reactants</b>			
<b>Mn<sub>2</sub>O<sub>3</sub>:</b>	1 mol	157.87429	g
	x		<b>3 g</b>
	x=	0.019002	moles
<b>Na<sub>2</sub>CO<sub>3</sub>:</b>	1 mol	105.98844	g
	0.01900246		Q g
	Q=	<b>2.014041</b>	<b>g</b>
<b>Flux</b>			
<b>NaCl:</b>	Q=	<b>8.884451</b>	<b>g</b>
<b>Na<sub>2</sub>CO<sub>3</sub>:</b>	Q=	<b>16.11233</b>	<b>g</b>
<b>B<sub>2</sub>O<sub>3</sub>:</b>	Q=	<b>2.64591</b>	<b>g</b>
<b>m<sub>tot</sub>=</b>		<b>32.656732</b>	<b>g</b>

The mixture in both cases has been well mixed and placed in 2 different  $Al_2O_3$  crucibles. There was an alumina tray below each Alumina crucible and another tray covering the crucible to prevent the solution from creeping out of the crucible. The reaction taking place for the creation of  $NaMnO_2$  is the following:





The heating took place under air atmosphere with a rate of 2 °C / min until 950 °C and stayed at final point for 24h. After 24 h it was very slowly cooled down to help the growth of crystals. The heating protocol is presented in Figure 3-3. The whole process lasted several days before we could obtain our first results.

Table 3-2 Calculation of the mass of the reactants and the Flux of NB

<b>Na<sub>2</sub>CO<sub>3</sub> : B<sub>2</sub>O<sub>3</sub> = 8 : 1 (NB Flux)</b>			
<b>Reactants</b>			
<b>Mn<sub>2</sub>O<sub>3</sub>:</b>	1 mol	157.87429 g	
	x		<b>3 g</b>
	x=	0.019002 moles	
<b>Na<sub>2</sub>CO<sub>3</sub>:</b>	1 mol	105.98844 g	
	0.01900246		Q g
	Q=	<b>2.014041 g</b>	
<b>Flux</b>			
<b>Na<sub>2</sub>CO<sub>3</sub>:</b>	Q=	<b>32.22466</b>	<b>g</b>
<b>B<sub>2</sub>O<sub>3</sub>:</b>	Q=	<b>2.64591</b>	<b>g</b>
<b>m<sub>tot</sub>=</b>		<b>39.88461</b>	<b>g</b>

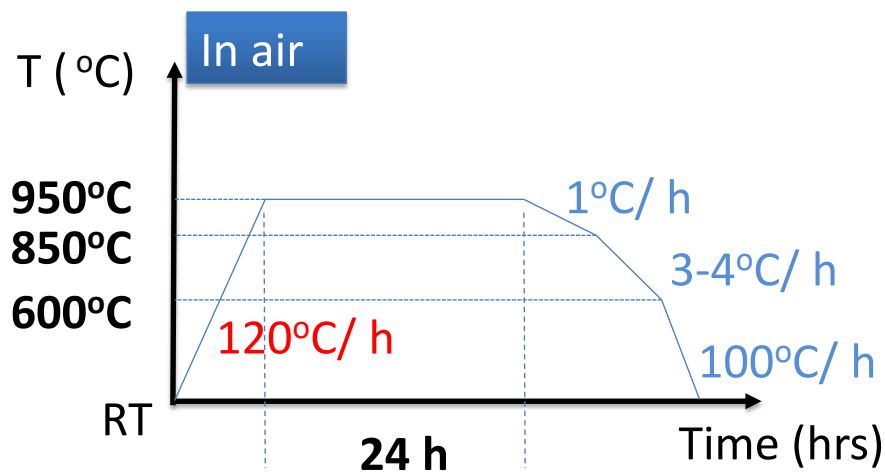


Figure 3-3 Heating protocol followed for both the mixtures using NB and NNB Fluxes.



### 3.2.2.1 *Results and Discussion*

The flux method gave us needle-like crystals that are of maximum 2 mm length and 0.2 mm thickness, comparable sizes that have been mentioned in the literature, although the method we used has been different than the one first followed in 1970s and 1980s. The color of the needle crystal products has been from light to dark brown. The topology of the crucibles in use is pictured in figure 3-4 (a-b) as it ended to be after the growth for NB and NNB flux respectively. During the growth, the solution expanded and the biggest amount of the solution crept out of the crucible.

Especially in the case of NB flux it broke the crucible and spread so an important amount of it has been lost and only a couple of needles could be observed and mechanically extracted from the mass of the final mixture (figure 3-4 b). The issue of expansion has been mentioned in literature for fluxes using  $B_2O_3$  [134] and so a possible modification of the percentage of  $B_2O_3$  in the flux should be taken into consideration. In the case of the NNB flux a satisfying amount of dark needles had crept all over the carrier crucible which was hard to mechanically extract. For this reason distilled water and a great amount of centrifugations were used to harvest an amount of needles for further treatment.

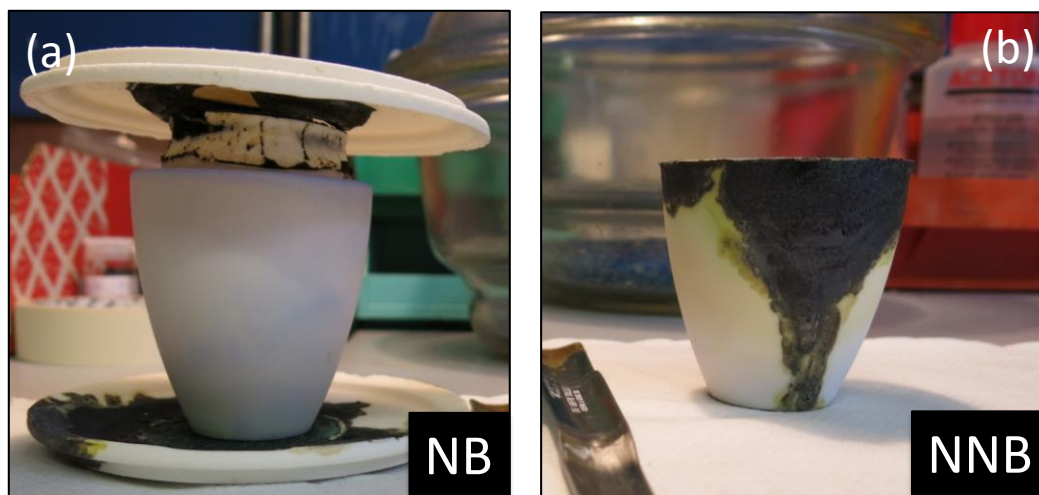


*Figure 3-4 Topology of the crucible used for the flux growth for NB Flux (a) and NNB Flux (b) after the cool down. Overflow of the solution is obvious.*

As observed in figure 3-5 (a)& (b) the very few needles grown by the NB flux had a light brown color and a flat and rectangular shape. The SEM image can show the clear cuts and layered structure (figure 3-7 a). Unfortunately not having enough amount of these it was

impossible to have an xrd pattern but the confirmation of Na deficiency has been confirmed through EDS.

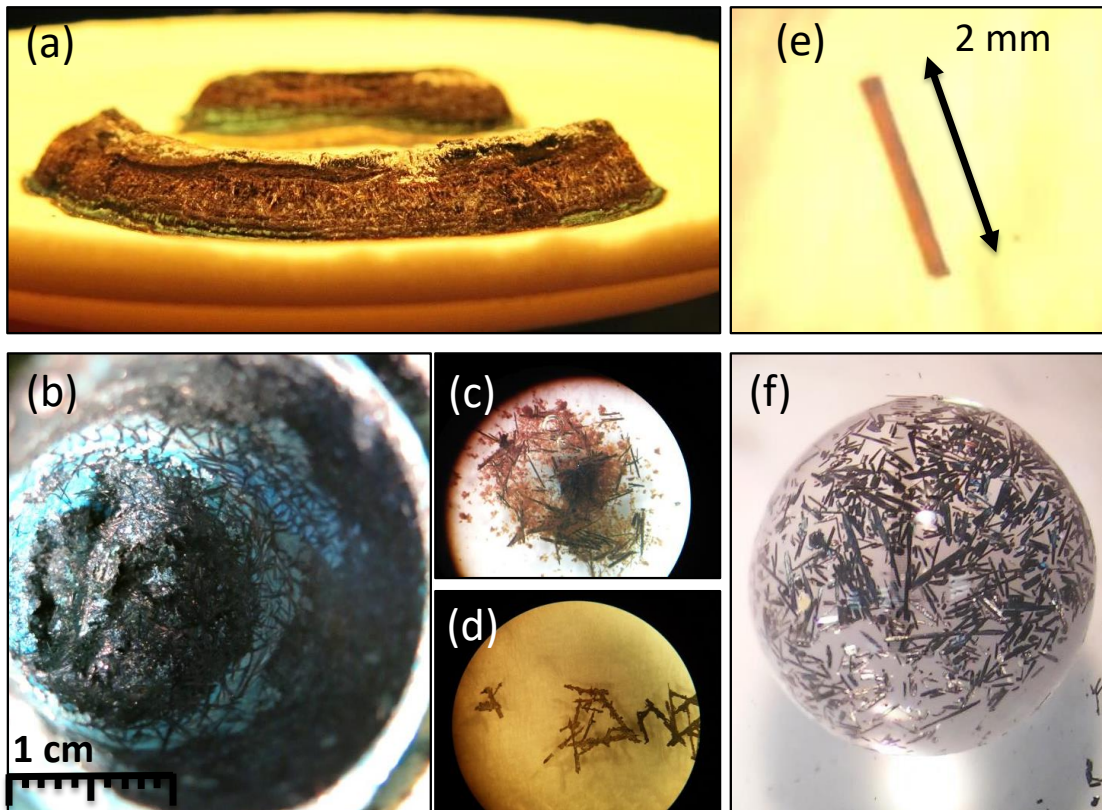


Figure 3-5 (a)& (b) Pictures of the result as it came out of the furnace from NB and NNB Fluxes respectively. (c) An amount of needle crystals in the process of diluting the NNB Flux in distilled water and (d) in acetone. (f) An amount of needle crystals free of Flux in a water droplet.

The NNB Flux gave dark and sharp crystals as described in Hoppe et. al [131]. Since it was impossible to mechanically extract the necessary amount of needles for further measurements, the Flux has been diluted to distilled water and the needles had been extracted after numerous centrifugations (figure 3-5 c, f). Removing the flux using acetone seemed to affect the crystals (figure 3-5 d). An amount of needles has been pulverized for x-ray measurements confirming a mixture of beta phases (figure 3-6) as has been expected by the morphology resembling in the first place the crystals grown by Hoppe et. al.[131] SEM images of the needle crystals revealed a well-defined layered structure which proved to be a low quality crystalline sample when checked with single crystal x-rays measurements.

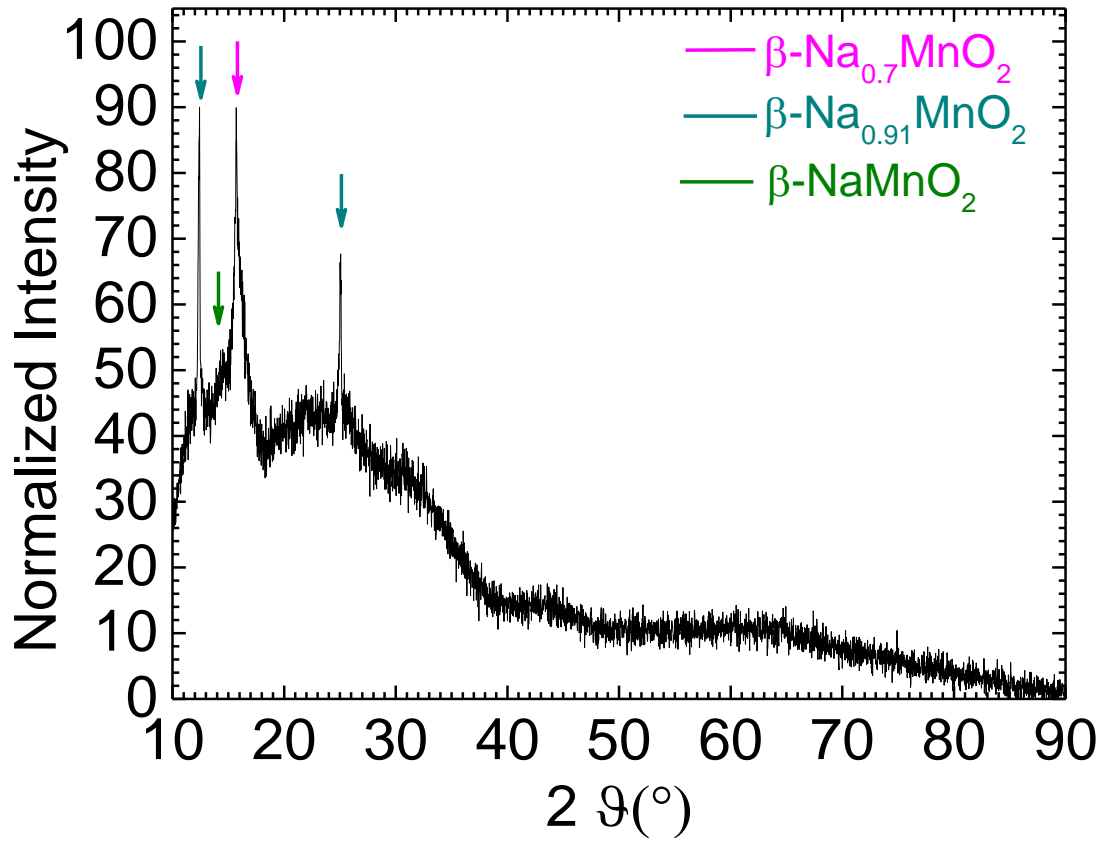


Figure 3-6 A mixture of beta phases is confirmed for the needle crystals grown using the NNB Flux. An amount of pulverized needles had been mixed with grease and placed on a glass. This explains the amorphous picture in the low-angle area.

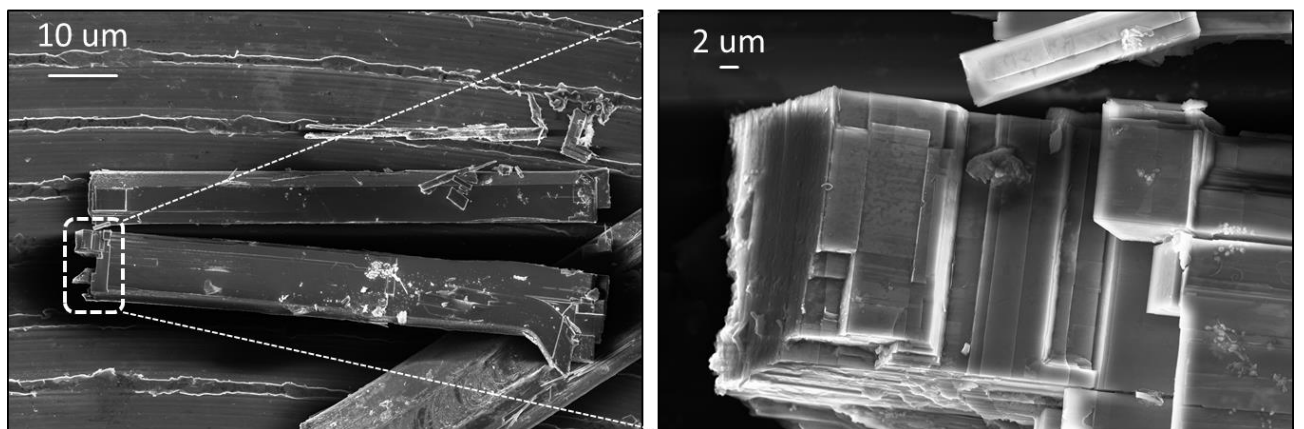


Figure 3-7 Left panel- SEM image of 3 different needles mechanically extracted from NNB flux growth. Right panel- zoom in the edge of needle two confirms a layered structure.

### 3.2.3 Single crystal growth- The Floating Zone method

Since the Flux method seemed to repeat, in the best case, the results already mentioned in early works, the focus has been put on the advanced Floating zone method which advantages are described in section 2.2.2. So, sizable single crystals of the Na-Mn-O system have been grown for the first time by the floating zone (FZ) technique. The growths were carried out using a 2 mirror Canon Machinery SC1-MDH 11020 (University of Warwick) with standard double elliptical mirror geometry equipped with two 1.5 kW lamps, which can reach a maximum operating temperature of 2000 degrees Centigrade. Direct temperature measurement in the image furnace by pyrometry is not possible since, by definition, all viewing axes inside the mirrors are focused on the image of the lamps. It is therefore the lamp temperature, rather than the sample temperature that is probed. Several attempts were performed using different growth conditions. Post-growth handling of the crystal boules was carried out in a glove box. The quality of the as grown crystals was confirmed using Laue x-ray back reflection technique.

#### 3.2.3.1 Crystals grown from $\alpha$ -NaMnO<sub>2</sub> powders

The synthesized powder of  $\alpha$ -NaMnO<sub>2</sub> has been ground well in the glove box and after being shaped inside an elastic sleeve (balloon) it was isostatically pressed under 6 tons for almost 1 min into cylindrical rods approximately 6 mm diameter and 60-70 mm length (Fig. 3-8). The resulting rods were sintered at 750 °C under Ar atmosphere following protocols that differ from those reported in a parallel study. [136] The modification in the growth approach proved to have an impact on the phase purity of the final feed/seed rods, and it will be further explained in this paragraph.

The quartz tube of the FZ furnace was flushed with Ar gas, to be finally compressed up to 8 bars under Ar atmosphere, aiming to suppress the possible evaporation of Na and Mn species. For this reason, the feed and seed rods were weighed before and after the crystal growth to determine the likely material loss due to evaporation. The mass loss of the successfully grown crystal batches was found to be negligible. Subsequently, the acquired crystal boules were immediately transferred into an Ar-circulating glove box for further treatment.





Figure 3-8 (a) Shape powder in a cylindrical rod by hand pressing it inside a ballon (b) cut-reveal the rod after being isostatically pressed under 6 tons (c) The drill used in order to drill the sintered feed rod and prepare it for suspension (d) Both feed rod (inside alumina crucible) and seed rod being ready for mounting on the shafts of the mirror furnace.

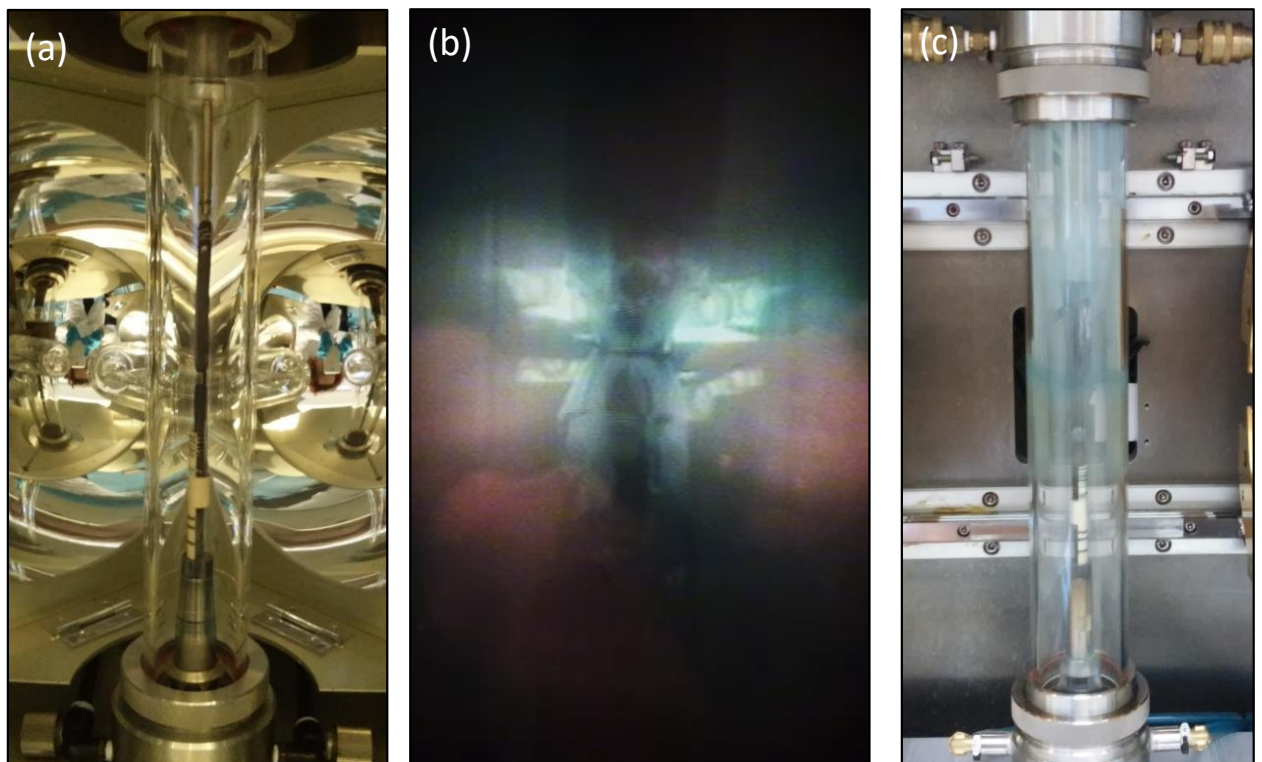


Figure 3-9 (a) Both feed (top) and seed (bottom) rods mounted and aligned in the 2-mirror furnace and sealed under Ar-pressure inside the quartz tube (b) Well-formed molten zone during the growth of batch #9 (c) The quartz tube coated with thin powder right after the growth while still under Ar atmosphere.

Different sintering and growth conditions were tested in order to improve the stability of the molten zone (summarized in Table 3-1). The duration of the sintering step of the feed rod was varied as well as the start temperature of the sintering. The feed rod was introduced in the Ar filled tube furnace at temperatures ranging from room temperature up to 750 °C. The optimum sintering conditions that led to successful growths entailed a  $T_{\text{start}} = 750$  °C and a duration of 16 hours. The sintered rods were allowed to slowly cool down to a temperature above 100 °C in order to avoid the absorption of moisture that could lead to Na-deficiency (via hydrolysis). Following the afore-mentioned sintering protocol, X-ray diffraction of the rods finds that the main  $\alpha$ -NaMnO<sub>2</sub> phase coexists with minority  $\alpha$ -Na<sub>0.7</sub>MnO<sub>2</sub> and  $\beta$ -NaMnO<sub>2</sub> phases, mainly at the surface. Interestingly, the majority phase of the sintered rod in similar study was found to be of the  $\beta$ -NaMnO<sub>2</sub> crystal polytype. [136]

The main challenge while growing crystals in Na-Mn-O system has been to control the formation of a stable molten zone (fig.3-9 b), perturbed by possible decomposition and evaporation processes entailing the metal constituents. After experimenting on the heating power in the hot zone area the milestone in getting an optimized floating zone has been to keep both feed and seed rod out of the hot zone until the temperature (or the indicated lamp operating voltage) would be of certain value. In the successful growths the feed and seed rods remained out of the hot zone until the operating lamp voltage had reached almost 47 V and then brought them (first the feed and then the seed rod) in the “hot zone” to allow melting with the least possible fuming. In figure 3-9 the quartz tube is depicted before (a) and (c) after the growth showing the coat of powder because of the evaporation of material during the growth. The light turquoise color is a hint of possible evaporation of both Na and mixture of Mn (V) or Mn (VI), during the heating of the feed since it appears mostly on the upper part of the tube. Only when the quartz tube was left in air it would turn brownish suggesting creation of Mn<sub>3</sub>O<sub>4</sub> or Mn<sub>2</sub>O<sub>3</sub>. In order to balance the loss of Na due to evaporation while the feed had been heated, we even experimented on preparing a feed rod by mixing 1% excess of Na<sub>2</sub>CO<sub>3</sub> on the starting alpha powder (#6). The result has been even more fuming and a heavily coated quartz tube with white powder which has obviously been caused by the excess of Na<sub>2</sub>CO<sub>3</sub>.

In order to achieve a stable molten-zone various parameters had to be tailored and so the following have been explored: the rotation speed of the feed and seed rods, the growth



speed, the gas pressure inside the quartz tube as long as the timing of bringing the feed and seed rods into the “hot zone”. All these parameter modifications during a number of growth attempts are summarized in table 3-4.

*Table 3-3 Summary of crystal growth conditions, with  $\alpha$ -NaMnO<sub>2</sub> polymorph as a precursor powder.*

Batch	Morphology	Start Temperature of sintering (°C)	Sintering duration @ 750 °C	Atmosphere / Pressure (atm)	Rotation speed (rpm)	Growth rate feed/seed (mm/ h)
#3	melted-edge	25	48 h	Ar/ 5	10-16	4/ 1.5
#4	Lump-like boule	25	48 h	Ar/ 6	20-25	4-10
#6	Spongy edge	25	14 h	Ar/ 6	20-25	--
#7	Lump-like boule	90	14 h	Ar/ 6	20-30	10-40/ 10-40
#8	Elongated lump-like boule	750	16 h	Ar/ 6-7	20-33	15-35/ 15-35
#9	Crystal boule with facets	750	16 h	Ar/ 6- 8	20	30-37/ 30
#10	Crystal boule with facets	750	16 h	Ar/ 6- 7.5	20-23	36-40/ 30

In most of the cases, the protocols suffered from a two-phase growth and evaporation of the material. These growths gave a “lump” like boule (Fig. 3-10 a, b) even when the growth rates were high, as in case #8. Employing a fast growth rate of almost 37 mm/ h, with a rotation speed of 20 rpm for both seed and feed rods led to a longer crystal boule with clear facets after 1 cm of growth. The unwanted evaporation of Na and Mn related products was confirmed by X-ray diffraction pursued of powder specimen deposited on the inner surface of the quartz tube of the optical furnace. Effectively, this led to sensitive lamp-power adjustments during the growth to minimize such a flow. After the growth the crystal boule was cooled-down to room temperature and was transferred back to an Ar-filled glove box for further handling.



As illustrated in Figure 3-10 (c)& (d), the facets that were formed along the crystal boule had been oriented in the (-202) lattice plane, indicating a  $b^*$  growth direction. The edges of the crystal boules usually contained domains misaligned along  $b^*$  and impurities of manganese oxides due to oxidation. So, in order to perform further characterization we needed a bigger amount of high quality grown crystals and even larger amount of good quality of starting  $\alpha$ - $\text{NaMnO}_2$  powders. For the needs of the crystal growth experiments the quantity of 76 gr of  $\alpha$ - $\text{NaMnO}_2$  has been synthesized. The crystal boules have been found hard to cut with the diamond saw but since crystal flakes were grown along the  $b^*$  direction they could be easily cleaved with a thin razor after the boule had been “cracked” with a pestle. Quality and crystal structure of the grown crystal boules starting from  $\alpha$ - $\text{NaMnO}_2$  powders will be further discussed in chapter 6.

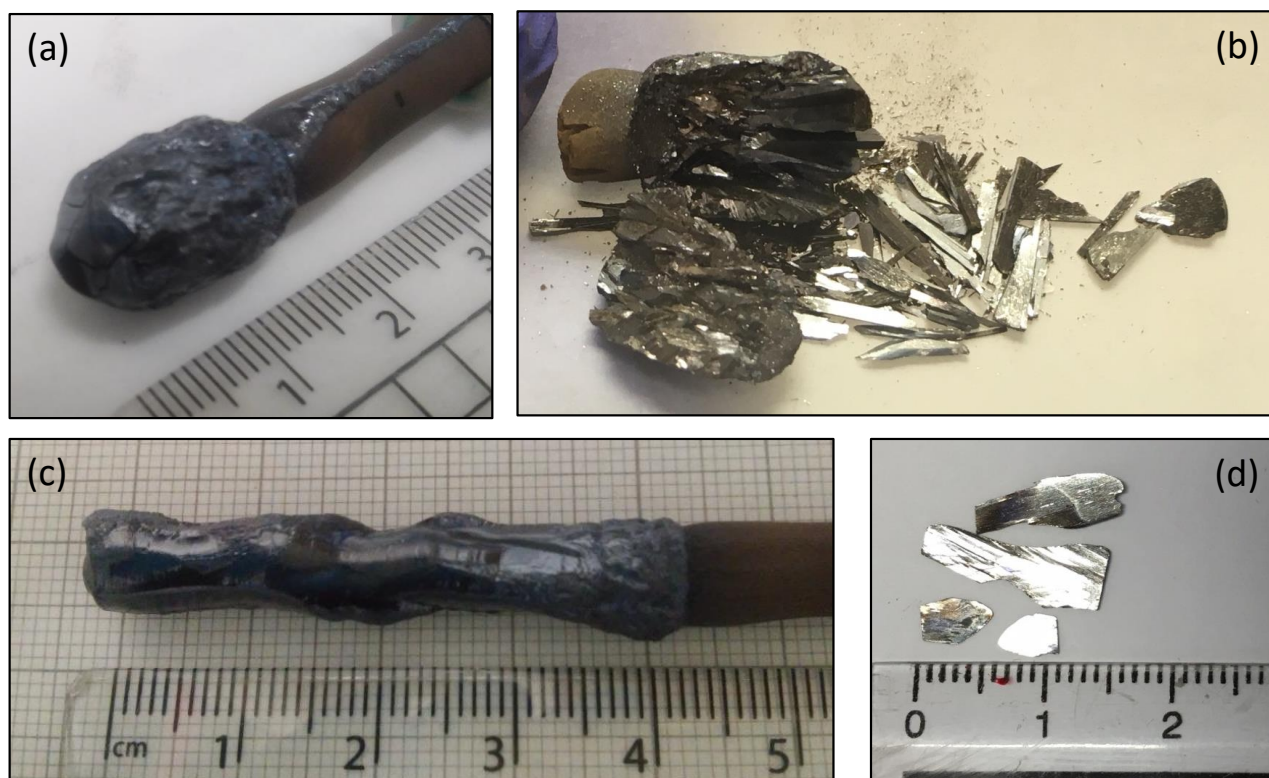


Figure 3-10 (a-b) Lump-like crystal boule from early growth attempts. The crystal flakes after the lump had been crushed proved useful for primal characterization and further optimization of the protocol (c-d) Long crystal boule with facets of  $\alpha$ - $\text{Na}_{0.96}\text{MnO}_2$  system (d) Cleaved single crystal flakes from the as-grown crystal boule along the  $b$ -axis of the monoclinic cell.

### 3.2.3.2 Crystals grown from $\beta$ - $\text{NaMnO}_2$ powders

The single crystal growth attempts using the floating zone method while starting from the  $\beta$ - $\text{NaMnO}_2$  polycrystalline powders proved to be even more challenging. The

polycrystalline powder of beta has been more “sticky” and not easy to handle in order to prepare the feed and seed rods for the growth. The synthesized powder of  $\beta$ -NaMnO<sub>2</sub> has been ground well in the glove box and after being shaped inside an elastic sleeve (balloon) it was isostatically pressed under 6 tons for almost 1 min into cylindrical rods approximately 6 mm diameter and 60-70 mm length in the same way as described in the previous paragraph. The resulting rods were sintered at 950 °C under O<sub>2</sub> atmosphere following the synthesis protocol of the beta powders. The quartz tube of the FZ furnace was flushed with O<sub>2</sub> gas, to be finally compressed up to 7.5 bars under O<sub>2</sub> atmosphere, aiming to eliminate the fuming of material during heating. Subsequently, the acquired crystal boules were immediately transferred into an Ar-circulating glove box for further treatment.

Table 3-4 Summary of crystal growth conditions, with  $\beta$ -NaMnO<sub>2</sub> polymorph as a precursor powder.

Batch	Morphology	Start Temperature of sintering (°C)	Sintering duration @ 950 °C	Atmosphere / Pressure (atm)	Rotation speed (rpm)	Growth rate feed/seed (mm/ h)
#1	Spongy& metallic edge	25	24 h	O <sub>2</sub> / 5-6.5	16	--
#2	Spongy& metallic edge	25	24 h	O <sub>2</sub> / 8	20	--
#5	Crystal boule	100	12 h	O <sub>2</sub> / 6-7.5	25-27	6-20/ 6-20
#11	Dark boule	950	12 h	O <sub>2</sub> / 6-7.5	25-35	20-30/ 20-30
#12	Crystal boule edge	100	12 h	O <sub>2</sub> /6.4-7.6	25-30	10-17/ 10-17

In table 3-4 the summary of the sintering and growth parameters is presented. An attempt to start the sintering process while the furnace has already been at 950°C didn't seem to play a part in the final product of the growth. The x-ray patterns of the feed rods (figure 3-11) that have been used for growths using different sintering protocol show mainly a beta phase with minorities of  $\alpha$ -NaMnO<sub>2</sub> (blue star),  $\alpha$ -Na<sub>0.7</sub>MnO<sub>2</sub> (black star) and even Mn<sub>3</sub>O<sub>4</sub> (blue arrow) which as it will be discussed in chapter 5 will play no part in the phase of the final crystal boule.



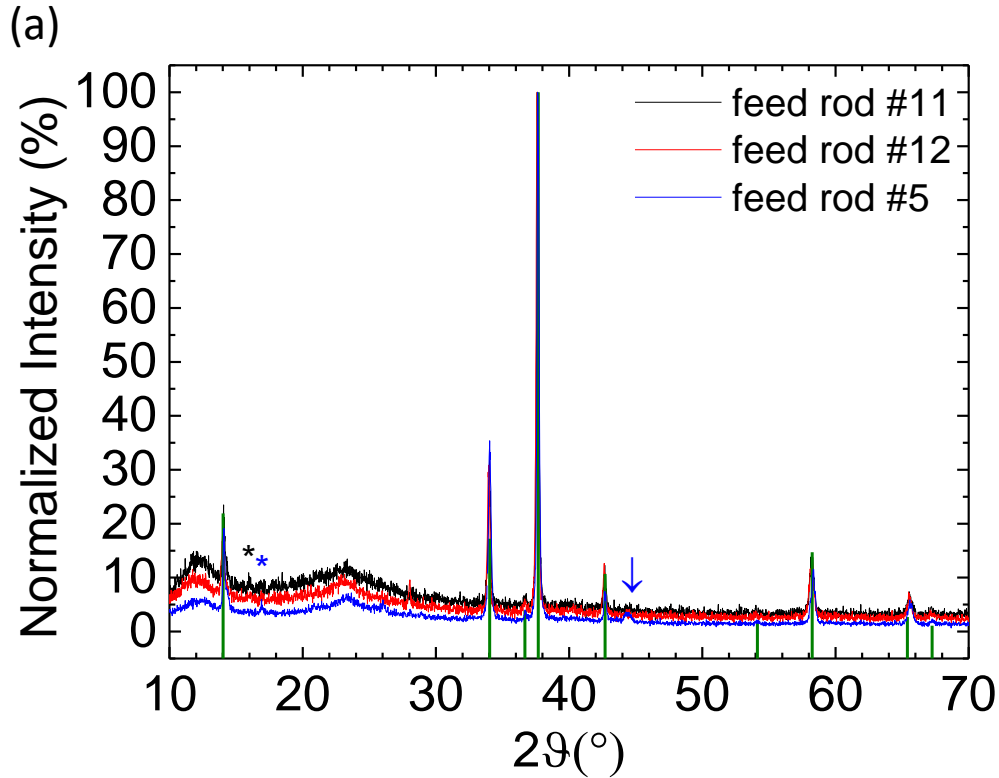


Figure 3-11 X-ray patterns of feed rods that have experienced different sintering conditions. Black star indicates peak of  $\alpha\text{-Na}_{0.7}\text{MnO}_2$ , blue star peak of  $\alpha\text{-NaMnO}_2$  and blue arrow peak of  $\text{Mn}_3\text{O}_4$ .

The high volatility of the starting powders even under  $\text{O}_2$  pressurized atmosphere was the main reason that the first trials have been completely unsuccessful in getting even a melt of the feed rod. The main feature of these first trials has been high fuming and decomposition of the material as pictured in figure 3-12 (a-b). This would lead to a heavily powder coated quartz tube and so minimum visibility which would demand even more lamp power. Once again, bringing the feed rod in the hot zone only after 47 V was reached would help to avoid decomposition and form a first melt. The stabilization of the molten zone had been extra challenging though since we experienced a 2 phase melt in almost every growth as shown in figure 3-12 (c-d). In these cases continuous manual adjustment of the growth parameters would improve the situation. The increased growth rate named as “fast scan” of the floating zone that has been suggested in similar cases as in  $\text{Na}_x\text{CoO}_2$  [132] would not be of any use in contrast with the case of the alpha polymorph. In fact, slower growth rate of 6-20 mm/h together with a high rotation speed (30 rpm) to ensure homogeneity of the coat and internal part of the feed rod, would give the best result of a crystal boule (figure 3-13).



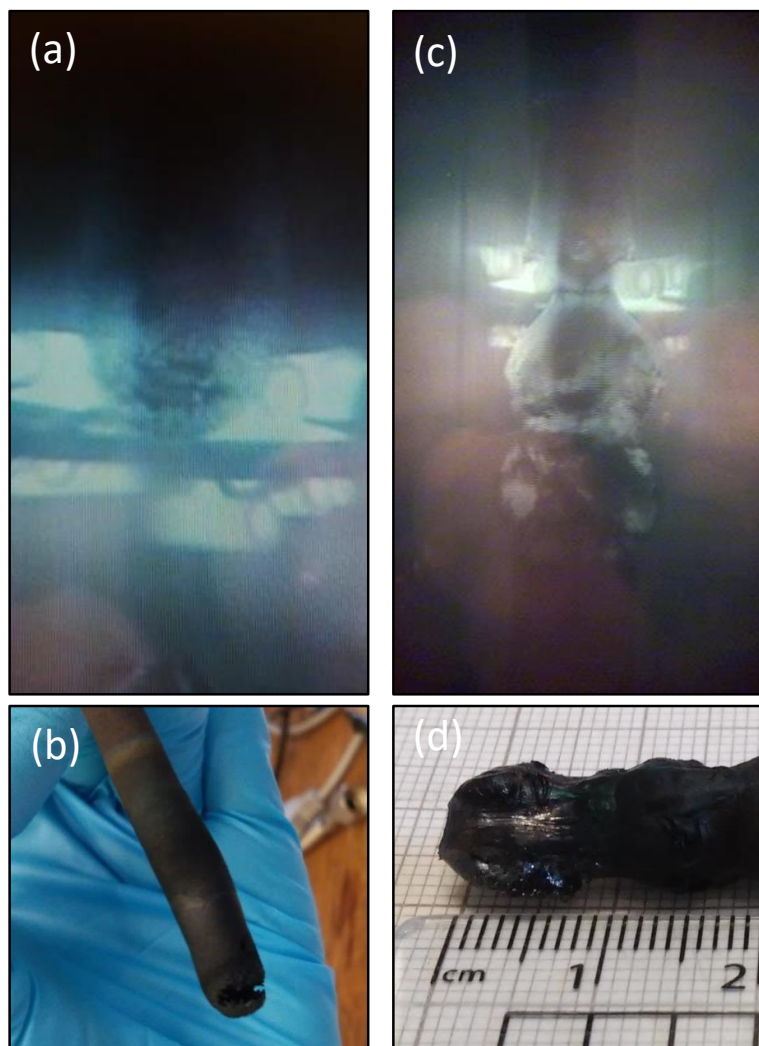


Figure 3-12 (a-b) Issues of decomposing while trying to form a molten zone (c-d) 2-phase melt causing drops of melt over the already crystallized sample



Figure 3-13 Crystal boules grown using beta polymorph as starting powder. Several crystal flakes could only be separated after crushing the as grown boule.

The resulting crystal boule, as illustrated in Figure 3-8 (a)& (b), had visible facets. The boule has been too hard to orient and cut so in order to get some crystal flakes for the study we had to crash it. All flakes were cleaved with (001) crystal plane predominantly exposed. The unwanted evaporation of Na and Mn related products, was confirmed once more by the coated quartz tube as depicted in figure 3-14 as well as the final substoichiometric phase of the crystal boule products which was proved by x-rays. The edges of the crystal boules usually contained impurities of manganese oxides due to oxidation. So in order to perform further characterization we needed a bigger amount of high quality grown crystals and even larger amount of good quality of starting powders. For the needs of the crystal growth experiments the quantity of 52 gr of  $\beta\text{-NaMnO}_2$  has been synthesized. The quality and crystal structure of the grown crystal boules starting from  $\beta\text{-NaMnO}_2$  powders will be further discussed in chapter 5. After the growth the crystal boule was cooled-down to room temperature and was transferred back to an Ar-filled glove box for further handling.



Figure 3-14 (a) Coated quartz tube after the first #1 growth attempt using  $\beta\text{-NaMnO}_2$  as starting powder. (b) Coated quartz tube after the #5 growth attempt using  $\beta\text{-NaMnO}_2$  as starting powder which resulted in crystal boule of  $\text{Na}_{0.7}\text{MnO}_2$

### 3.2.3.3 *Summary of synthesis results*

For the present study both polycrystalline and single crystal specimens have been synthesized aiming to study the correlation of the lattice topology to the magnetic and magneto-dielectric phenomena of the 2D triangular lattice system of Na-Mn-O.

In the case of the polycrystalline specimens solid state synthesis of both stoichiometric polymorphs of  $\alpha$ -NaMnO<sub>2</sub> and  $\beta$ -NaMnO<sub>2</sub> has been done. The modification of protocol published by Abakumov et.al has been the quenching after each firing step in the case of beta. This seemed to eliminate the impurities of small percentage of  $\alpha$ -Na<sub>0.7</sub>MnO<sub>2</sub> in it as it will be further discussed in Chapter 4. The polycrystalline powders were used as made for x-ray measurements, measurements of magnetic susceptibility and neutron diffraction experiments and in pressed pellet forms for magneto-dielectric measurements. The scale up of the synthesis protocol that has been done for the first time allowed the preparation of a big amount of powders to be used for the single crystal growth with the Floating Zone method.

After the first crystal growth trials of Na-Mn-O system in the 70s we managed to prepare single crystals of the system under study for experiments that require large volume of areas (neutron diffraction, anisotropic property measurements), as a way to dig deeper into the understanding of the systems rich phase behavior. We visited two different single crystal growth methods, the flux method which provided us with crystals similar to the ones first prepared in the 70s (table 3-5) and the floating zone method. Using the later method, we managed to grow sizable single crystals of  $\alpha$ -Na<sub>0.96</sub>MnO<sub>2</sub> for the first time and simultaneously with the study of Dally et al. [136] The crystal boules were of 4.5 cm length with definable facets grown towards the b\* direction and were further used for dc magnetic susceptibility measurements, single crystal neutron measurements and dielectric measurements in comparison to the starting powders of alpha. Our findings will be further discussed in chapter 6.

The unstable melt and the uncontrollable fuming during the growth didn't allow the growth of single crystals of the beta polymorph ( $\beta$ -NaMnO<sub>2</sub>). The conditions tested, however, allowed for the growth of sizable substoichiometric crystals of Na<sub>0.7</sub>MnO<sub>2</sub> for the first time. The only reference met in literature has been for "Single Crystalline Na<sub>0.7</sub>MnO<sub>2</sub> Nanoplates" studied as cathode materials [123] while most studies that would focus on the physical properties use polycrystalline specimens. Structural and magnetic characterization of the Na<sub>0.7</sub>MnO<sub>2</sub> single crystals is presented in chapter 5.



Table 3-5 Summary of the calculated and weighted quantities for both Nb and NNB Fluxes used for the growth of Na-Mn-O needle crystals

		<b>NB Flux</b> <b>Na<sub>2</sub>CO<sub>3</sub>: B<sub>2</sub>O<sub>3</sub></b> <b>8: 1</b>	<b>NNB Flux</b> <b>NaCl: Na<sub>2</sub>CO<sub>3</sub>: B<sub>2</sub>O<sub>3</sub></b> <b>4: 4: 1</b>
<b>Starting materials</b>	Mn <sub>2</sub> O <sub>3</sub>	3	3
	Na <sub>2</sub> CO <sub>3</sub>	2.014041	2.014041
<b>Flux</b>	NaCl	0	8.884
	Na <sub>2</sub> CO <sub>3</sub>	32.225	16.112
	B <sub>2</sub> O <sub>3</sub>	2.646	2.646
<b>Heating protocol</b>	<p>The heating protocol graph shows temperature (T in °C) on the y-axis and time (hrs) on the x-axis. The process starts at room temperature (RT) and is conducted in air. The temperature rises at a rate of 120°C/h to 950°C, where it is held for 24 hours. It then cools at 1°C/h to 850°C, followed by a cooling rate of 3-4°C/h to 600°C, and finally at 100°C/h back to RT.</p>		
<b>Final product</b>		Light-brown flat needles ~ 2mm	Dark sharp needles ~2mm



## Chapter Four:

# Progress on Magnetic structure and Magneto-electric study on $\beta$ -NaMnO<sub>2</sub>

---

### 4.1 Introduction

Competing exchange interactions pertaining to magnetic frustration,[76], [137], [138] may promote complex spin arrangements which release symmetry restrictions for the emergence and coupling of ferroelectric and magnetic order. Layered rock-salt-type of oxides (AMnO<sub>2</sub>, A= Na, Cu) are appealing in this respect, as they provide a paradigm where polymorphism [126] and triangular lattice topology [139] have profound implications on their spin-dependent properties. In this context, the non-perovskite, two-dimensional (2D) Na-Mn-O oxides are studied as a testing ground for such a kind of magnetoelectricity. These rock-salt derivatives have been investigated continuously since 1970 [3]. They attract both research and industrial interest for presenting a unique diversity of physical and chemical properties that make them good candidates for studies in a variety of fields ranging from SIBs (sodium ion secondary batteries) applications to CJTE (cooperative Jahn-Teller effect) studies and multiferroics[72]–[74] setting them as a model system for studies of magnetic and electrical properties in a two-dimensional lattice. [6], [140], [141]

Among them, the orthorhombic  $\beta$ -NaMnO<sub>2</sub> was recently found to display a sequence of peculiar phase changes. In exploration of these changes, high-resolution transmission



electron microscopy (HRTEM) observations postulate the presence of compositional modulation that entails a coherent intergrowth of beta and alpha type MnO<sub>6</sub> layer-stacking sequences. The fact that abundant  $\alpha$ - and  $\beta$ - polytype interfaces trigger complex spin arrangements that release symmetry restrictions in favor of topologically correlated, cooperative magnetism, could possibly allow emerging dielectric properties.

The motivation around this project has been the investigation of the subtle balance of competing processes over a triangular lattice topology and how this may stimulate partially ordered states with symmetry-breaking pinning sites and implications beyond magnetism. In this chapter the exploration over unvisited areas of the beta polymorph is presented as a continuation of recent studies on this polymorph in comparison to other polymorphs of the Na-Mn-O system.

#### 4.1.1 What is already known

The beta polymorph of the Na-Mn-O system crystallizes in a distorted variant of the O3-NaFeO<sub>2</sub> structure (3R polytype,  $R-3m$ ). [142] In this layered compound the spontaneous deformation of the MnO<sub>6</sub> octahedra is caused by the Jahn-Teller effect, inherent to the high-spin Mn<sup>3+</sup> cations ( $t_{2g}^3 e_g^1$ ;  $S= 2$ ;  $\mu_{\text{eff}} \cong 4.9 \mu_B$ ).  $\beta$ -NaMnO<sub>2</sub> appears to adopt an orthorhombic cell ( $Pmmn$ ) (Figure 4-1b) [131] entailing zig-zag sheets of MnO<sub>6</sub> octahedra which is similar to the thermodynamically stable lithiated analogue  $\beta$ -LiMnO<sub>2</sub>, [143] an important precursor phase for cathode materials in solid-state Li-ion batteries. [144]

Electron diffraction and high resolution transmission electron microscopy (HRTEM) studies on  $\beta$ -NaMnO<sub>2</sub> polycrystalline powders manifest an abundant quasi-periodic arrangement of defects. [126] The latter is depicted as a coherent intergrowth of two types of NaMnO<sub>2</sub> layers, reflecting the  $\alpha$ - and  $\beta$ - type oxygen coordinations. In support to that, room-temperature <sup>23</sup>Na solid-state nuclear magnetic resonance (NMR) spectra supported by first-principles DFT computations identified a wealth of local structural rearrangements, entailing a trade-off between the majority  $\beta$ -type nanodomains and those of the  $\alpha$ -like phase upon electrochemical cycling of sodium. [145]



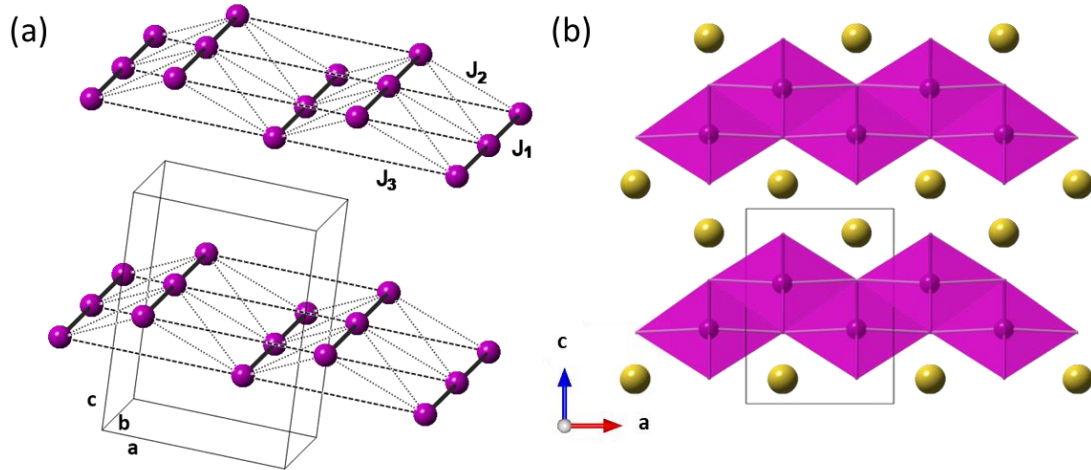


Figure 4-1 Schematic representation of the Mn sublattice topology, in the orthorhombic ( $Pmmn$ )  $\beta$ -NaMnO<sub>2</sub> polymorph. (a) The Mn-Mn distances drawn, depict the possible intra-layer magnetic exchange coupling pathways ( $J_1$  to  $J_3$ ).

On the other hand, the magnetic ground state of  $\beta$ -NaMnO<sub>2</sub> is less well understood from the experimental point of view. Theoretical calculations, though, predict that a spin-model with two-dimensional couplings ( $J_1 \sim 70$  K nearest neighbor and  $J_3 \sim 57$  K next nearest neighbor; Figure 4-1a) and a weaker frustrated interaction ( $J_2 \sim 13$  K) are likely to describe the experimental magnetic susceptibility. [126] The strong AFM couplings  $J_1$  and  $J_3$  that run along the  $b$  and  $a$  directions, respectively (figure 4-2) are triggered by the Mn–O–Mn pathway with a bridging angle of  $166.8^\circ$  (i.e., nearly  $180^\circ$  superexchange). The dimensionality of the magnetic interactions has been confirmed by theoretical calculations in comparison to the experimental DC susceptibility of a  $\beta$ -NaMnO<sub>2</sub> revealing that the spin ladder model describes better the magnetic interactions in comparison with the 2D model which corresponds to the  $\beta$ -NaMnO<sub>2</sub> phase.

The traces of polymorphism detected in nuclear structure in combination with the geometric frustration due to the triangular lattice topology triggered preliminary investigations for coupling mechanisms that could be projected as features on the temperature-dependent dielectric permittivity,  $\epsilon'(T)$ . Evidence for such a type of behavior in  $\beta$ -NaMnO<sub>2</sub> was first reported by Bakaimi et al. [146] who demonstrated that the temperature-dependent dielectric permittivity,  $\epsilon'(T)$ , displays two small anomalies. Such findings confirmed the necessity of determining the crystal and magnetic symmetries which until now have remained unexplored.

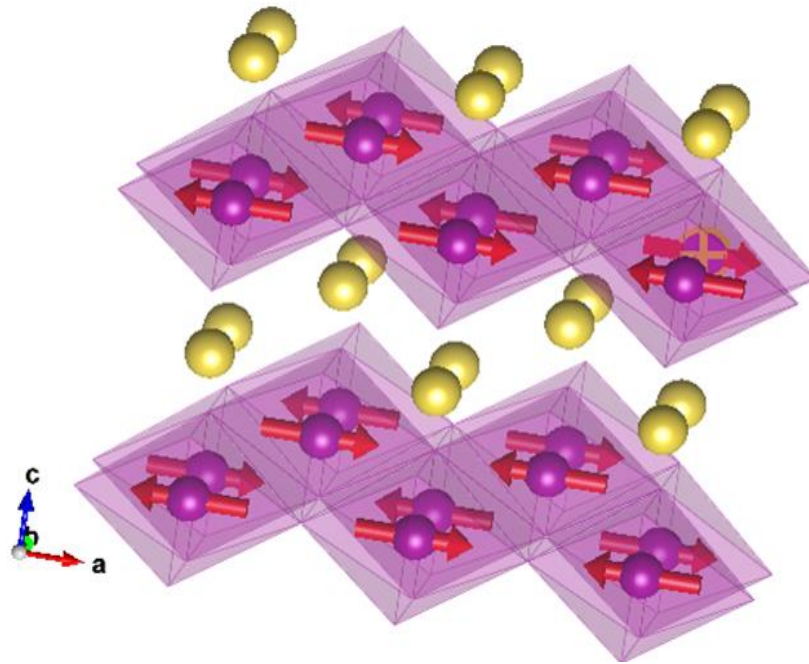


Figure 4-2 Sketch of the magnetic structure of the  $\beta$ - polymorph. The strong AFM chains run along  $a_o$  and  $b_o$  direction.

#### 4.1.2 Contribution of the present work

The principal aim of the work presented in this chapter was to address some of the incomplete areas of research for the layered  $\beta$ -NaMnO<sub>2</sub>.

The present contribution provides unique neutron powder diffraction insights of  $\beta$ -NaMnO<sub>2</sub>, highlighting that this challenging material is stabilized by intermediate phases formed at low energy cost. Compositional modulation that entails coherent intergrowth of two types of NaMnO<sub>2</sub> layers, involving  $\alpha$ - and  $\beta$ - type oxygen coordination, is shown to determine the material's symmetry controlled properties (section 4.6). We illustrate the implications of the modified lattice topology, with its intrinsic extended defects, on the successive magnetic phase transitions. Furthermore, temperature-dependent <sup>23</sup>Na NMR (section 4.3) and inelastic neutron scattering experiments (section 4.7) point that the magnetic dynamics are gapped, while the influence of the magnetic order on the electric dipole order is also discussed through temperature- and field- dependent magnetocapacitance studies (section 4-8).

## 4.2 Phase purity and crystallinity

### 4.2.1 X-Ray powder diffraction- phase purity

X-Ray powder diffraction (XRPD) has been carried out to all synthesized  $\beta$ -NaMnO<sub>2</sub> batches on a Rigaku D/MAX-2000H rotating Cu anode diffractometer ( $\lambda=1.5406 \text{ \AA}$ ). The samples, synthesized with the protocol which is described in paragraph 3.2, are referred to as “As made” in the following sections while a number of them has been extra annealed at 300°C under continuous flow of O<sub>2</sub>. For the X-Rays experiment, the sample, either “As made” or “annealed”, was prepared in powder or pellet form and sealed using a mylar film under argon atmosphere (the whole preparation was taking place inside the glove box) in order to prevent contact with moisture and air. All measurements have been taken with the same step of 0.02 degrees and time per step,  $t=12 \text{ sec}$ .

The synthesized compound has an average structure that fits to that of the  $\beta$ -NaMnO<sub>2</sub> which crystallizes in the orthorhombic Pmnm symmetry ( $a=2.86 \text{ \AA}$ ,  $b=6.33 \text{ \AA}$ ,  $c=4.78 \text{ \AA}$ ,  $\alpha= \beta= \gamma= 90 \text{ deg.}$ ). However, the appearance of secondary phases, in particular those of  $\alpha$ -NaMnO<sub>2</sub> and in smaller percentage  $\alpha$ -Na<sub>0.7</sub>MnO<sub>2</sub>, are evident by their characteristic Bragg peaks in the XRPD patterns and has been observed in most of our results. Variations in the quenching protocol didn't seem to eliminate the appearance of impurities of secondary phases while the scale up in the synthesis protocol confirmed the necessity of the 3 heating cycles without showing a different xrd pattern. Selected examples of the synthesized batches are presented in table 4-1.

In figure 4-3 the pattern of a  $\beta$ -NaMnO<sub>2</sub> batch quenched in liquid N<sub>2</sub> is presented. The green vertical lines correspond to the beta orthorhombic cell Pmnm indexed according to ICSD 16271 cif file while the blue vertical lines are attributed to the monoclinic C/2m cell of  $\alpha$ -NaMnO<sub>2</sub> as given in ICSD 21028. The red arrows point at the main mylar peaks which could not be avoided because of the topology of the sample holder.



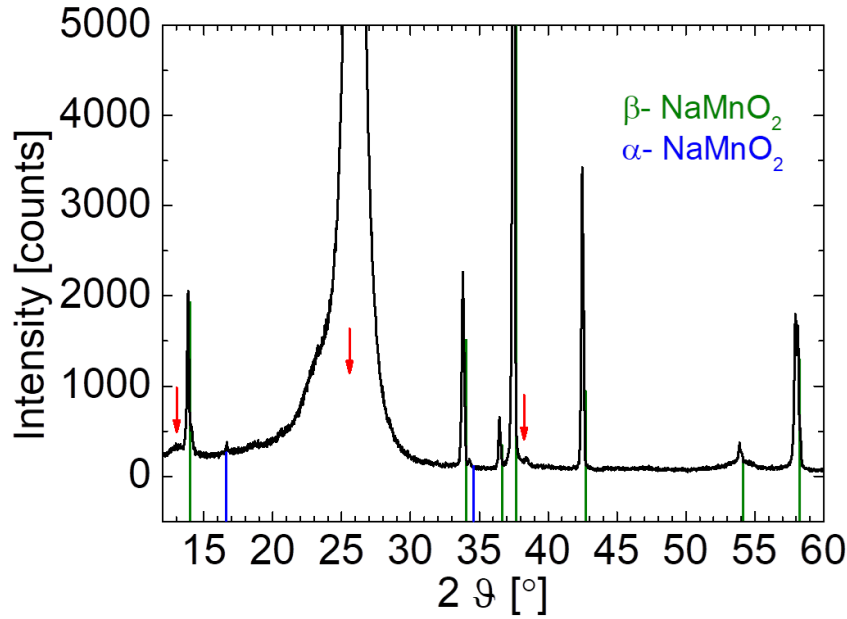


Figure 4-3 X-Ray Powder Diffraction pattern of the polycrystalline  $\beta$ -NaMnO<sub>2</sub> at room temperature. The green vertical lines correspond to the orthorhombic cell indexed according to the 16271 file of ICSD database. The blue vertical lines are attributed to the monoclinic  $C/2m$  cell of  $\alpha$ -NaMnO<sub>2</sub> (ICSD 21028). The red arrows represent the reflections of the mylar film.

Table 4-1 Different quenching methods applied between the heating cycles during the synthesis for the preparation of  $\beta$ -NaMnO<sub>2</sub>

Batch label - m (gr)	Synthesis notes	Xrd results
Eza001- 1 gr	-quench in the edge of the furnace -voltage drop x2 during second heating -last heating 22h	Peak @2-theta=21° (Na <sub>4</sub> Mn <sub>2</sub> O <sub>2</sub> impurity) peak 001 of a-Na <sub>0.7</sub> MnO <sub>2</sub> Peak 001 of a-NaMnO <sub>2</sub> Shoulder in 001 b-NaMnO <sub>2</sub>
Eza002- 1 gr	-quench in liquid N <sub>2</sub>	Peak @2-theta=21° (Na <sub>4</sub> Mn <sub>2</sub> O <sub>2</sub> impurity) Peak 001 of a-NaMnO <sub>2</sub> Shoulder in 001 b-NaMnO <sub>2</sub>
Eza003- 1 gr	-straight in GB	Peak @2-theta=21° (Na <sub>4</sub> Mn <sub>2</sub> O <sub>2</sub> impurity) peak 001 of a-Na <sub>0.7</sub> MnO <sub>2</sub> Peak 001 of a-NaMnO <sub>2</sub> Shoulder in 001 b-NaMnO <sub>2</sub> (more pronounced)
Eza018- 4 gr	-quench in liquid N <sub>2</sub>	Green areas after 1 <sup>st</sup> heating Peak 001 of a-NaMnO <sub>2</sub>
Eza022- 4 gr	-quench in liquid N <sub>2</sub>	darker after 1 <sup>st</sup> heating Peak 001 of a-NaMnO <sub>2</sub> Shoulder in 001 b-NaMnO <sub>2</sub>

Selected XRPD patterns of the batches that are presented in table-1 are shown in figure 4-4. The different quenching between the heating cycles eliminated the appearance of the secondary phase of  $\alpha$ -Na<sub>0.7</sub>MnO<sub>2</sub> as shown for the batches eza002 and eza018. While in the batches that haven't been quenched in Liquid N<sub>2</sub> (eza001, eza003) we note the presence of

the 001 peak of  $\alpha$ -Na<sub>0.7</sub>MnO<sub>2</sub> that crystallizes in the hexagonal P63/mmc system (vertical line in turquoise). The presented  $2\theta$  area is selected because the 001 peaks of alpha, beta and  $\alpha$ -Na<sub>0.7</sub>MnO<sub>2</sub> phases are clearly distinguished from one another.

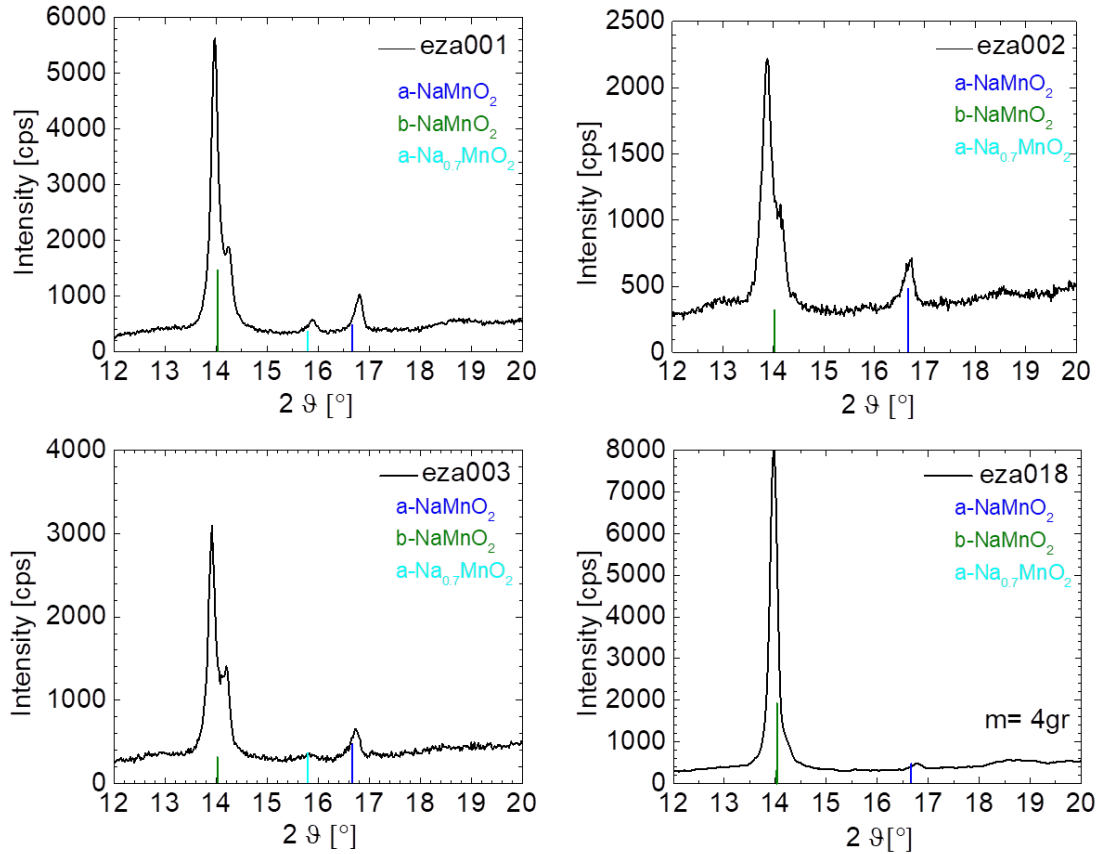


Figure 4-4 Results of the modified protocols as described in table-1 for the  $\beta$ -NaMnO<sub>2</sub>. The 4 gr batches have been used as starting powders for the single crystal growth attempts. In the batches eza001, eza003 we note apart from the presence of the 001 peak of  $\alpha$ -Na<sub>0.7</sub>MnO<sub>2</sub> (vertical line in turquoise).

The detection of the alpha phase as a minority phase in the measured pattern of  $\beta$ -NaMnO<sub>2</sub> seems to be related with the latest electron diffraction (ED) and transmission electron microscopy (HRTEM) investigations that confirm the presence of alpha phase as an intergrowth in the form of stacking sequences inside the  $\beta$ -NaMnO<sub>2</sub> structure. [126] On the basis of these findings, new high resolution neutron powder diffraction measurements have been performed. The complexity of the neutron diffraction pattern was lacking an adequate description until recently and will be further commented in section 4.5. Aiming to a better understanding, the superspace model that has been employed in order to interpret the HRTEM findings[126] has been revisited and modified confirming the existence of



corrugated layer stacking sequences of the  $\beta$ -NaMnO<sub>2</sub> type, which are interrupted by flat sheets of the  $\alpha$ -like oxygen topology. [147]

#### 4.2.1.1 XRPD patterns of $\beta$ -NaMnO<sub>2</sub> samples annealed in O<sub>2</sub>

The extra annealing process came at first as a need to ease the internal stresses of the formed pellets of the original synthesis and make them less brittle. However it proved that studying further the dielectric properties reveal some interesting behavior. In figure 4-5 a selected annealed sample (eza002) is presented in comparison with one synthesized and annealed 1 year earlier (WISH). The increase in the intensity of the  $\alpha$ -Na<sub>0.7</sub>MnO<sub>2</sub> 001 peak is evident in both cases as it became comparable to the intensity of the 001 of  $\beta$ -NaMnO<sub>2</sub> while the secondary alpha phase is still there.

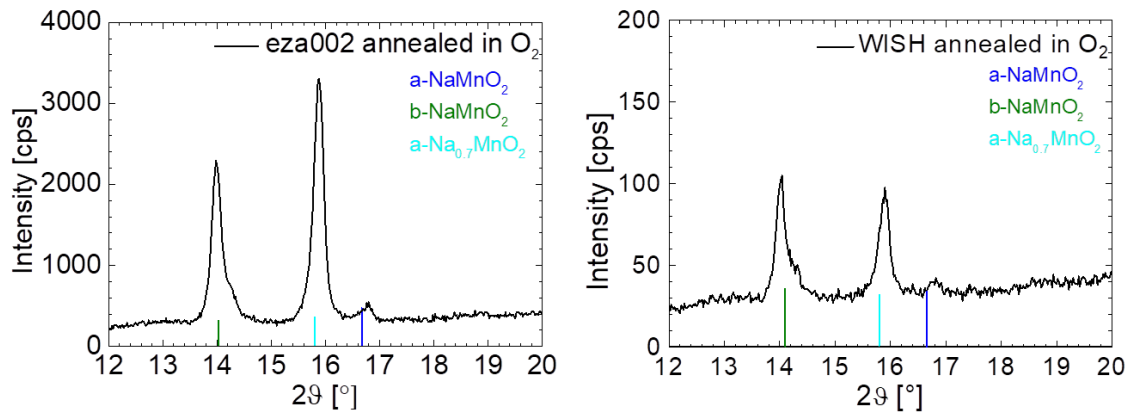


Figure 4-5 X-Ray Powder Diffraction pattern, taken at room temperature, of polycrystalline  $\beta$ -NaMnO<sub>2</sub> samples extra annealed at 300°C under O<sub>2</sub> flow.

As it will be detailed in section 4.8 of the dielectric study the strongest presence of secondary phases which could probably be translated in higher density of intermediate stacking areas inside the average  $\beta$ -NaMnO<sub>2</sub> structure gave rise to the feature in the  $T_N=95$  K critical temperature, where a spatially modulated proper-screw magnetic state is established related to the spin perturbation initiated at the boundary of the two different stacking sequences.



### 4.3 Macroscopic physical properties

#### 4.3.1 Magnetic measurements

##### 4.3.1.1 *Experiment and sample preparation*

The DC susceptibility of  $\beta$ -NaMnO<sub>2</sub> has been revisited again in the present study after the study of Abakumov et. al in 2014 [126]. As a further confirmation to the aforementioned study, temperature dependent dc susceptibility measurements ( $\chi$ ) at moderate and high magnetic field (up to 70 kOe) have been held in the range of 5 K to 300 K. The measurements were performed in a SQUID magnetometer (Quantum Design, MPMS-XL7) using a ZFC-FC protocol. The measurements were made on 20 mg batches of powder samples prepared in gelatin capsules. Pursuing indications of magnetic transition and establishment of magnetic order in the beta polymorph we performed Thermo-Remanent magnetization measurement which confirmed the existence of phase transition at  $T_N \sim 100$  K and encouraged further exploration. Field dependent hysteresis measurements in temperature below and above the transition are also presented in this section.

##### 4.3.1.2 *Dc susceptibility measurements*

In figure 4-6, the ZFC temperature dependent Dc susceptibility ( $\chi$ ) measured at 10 Oe and 7 T with 2K increment is shown. The shape of the curve suggests no profound magnetic transition. However, we can observe a low temperature paramagnetic tail that evolves to a “dip” just below 100 K which as we move to higher temperatures shapes a broad hump in the area above 200 K. This broad maximum at high temperatures is indicative of low – dimensional magnetic correlations while the shift of the maximum towards higher temperatures when compared to the alpha polymorph is a predicted behavior for a stronger AFM.

These observations have been also commented by Dr I. Bakaimi in her PhD thesis and further studied and supported by calculations in Abakumov et. al [126]. According to these calculations, the strong AFM couplings  $J_1 = 70$  K and  $J_3 = 57$  K run along b and a direction respectively and are coupled by a weaker frustrated interaction  $J_2 = 13$  K. Since  $J_1 = 70$  K and  $J_3 = 57$  K are of comparable magnitude a pure beta-NaMnO<sub>2</sub> would be considered a quasi 2D magnet. Despite that, as mentioned in the introductory section of this chapter, the experimental data of the dc susceptibility fit better with a spin ladder topology.



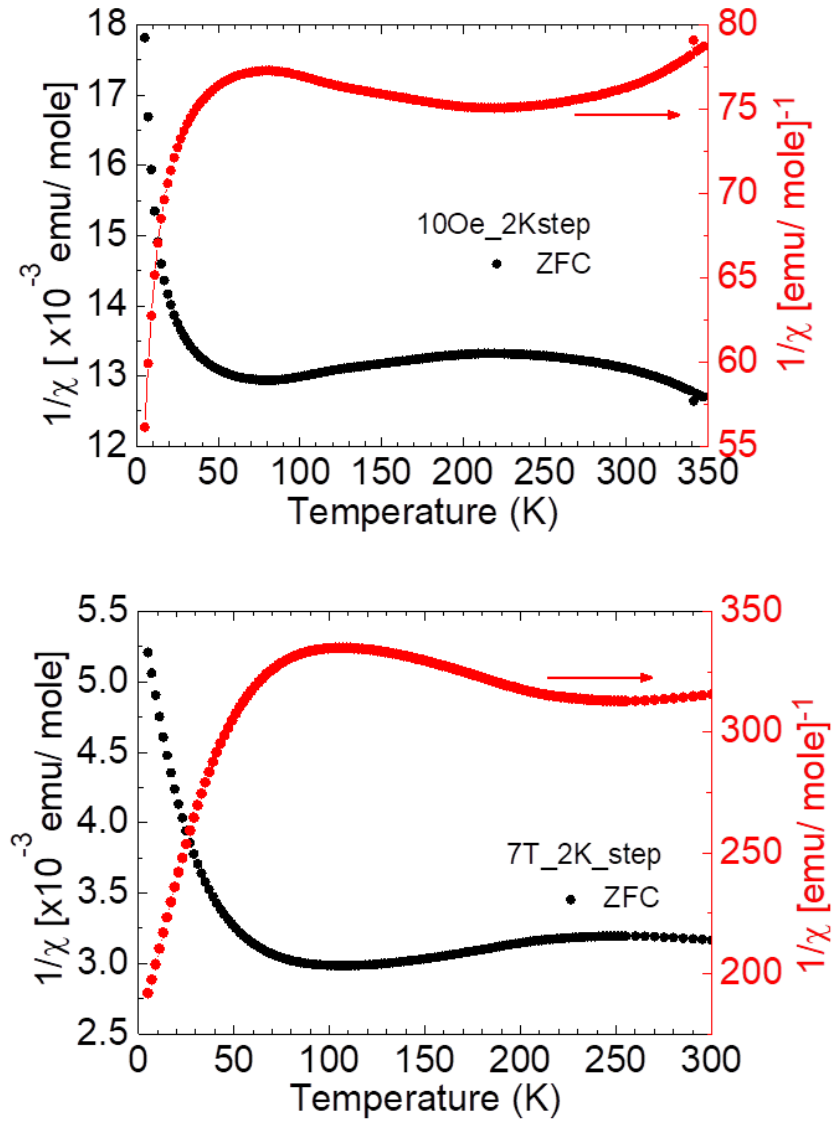


Figure 4-6 Magnetic susceptibility and inverse magnetic susceptibility of  $\beta$ -NaMnO<sub>2</sub> for under 10 Oe (top panel) and 70 kOe (bottom panel)

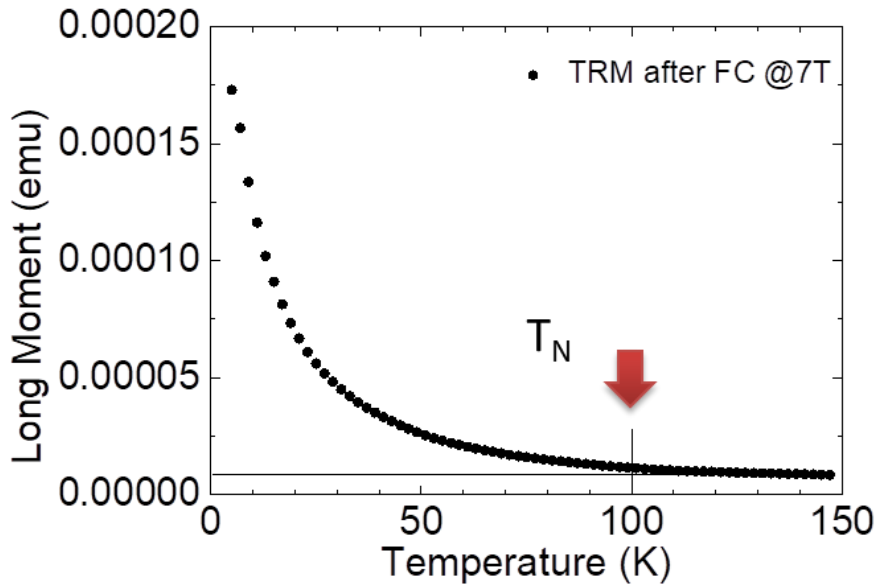


Figure 4-7 TRM measurements after cooling under 7T field with 2K increment

In figure 4-7 the results of the Thermoremanent (TRM) protocol are presented. This protocol has been used in order to locate the temperature where a possible magnetic transition occurs. After field cooling by applying a field of 7 T down to 5 K, the measurement has been taken upon warming with zero field applied. As shown in figure 4-7, the curve meets flat point just below 100 K. This is the indication for a magnetic transition which could not be shown through DC susceptibility ZFC-FC protocols.

In addition to that, field dependent hysteresis loops,  $M(H)$ , have been measured in temperatures below and above the  $T_N \sim 100$  K and up to 300 K, in order to explore possible ferromagnetism. As shown in figure 4-8, there is no hysteresis observed and so, no indication of ferromagnetism in all range of temperatures examined.

In general, the temperature dependent magnetic susceptibility,  $\chi(T)$ , of the different NaMnO<sub>2</sub> polymorphs, qualitatively appears similar. The presence of a broad maximum at  $\sim 200$  K for the  $\alpha$ -polymorph,[41] shifts to higher temperature in the  $\beta$ -polymorph (Figure 4-9). Such a broad feature is a general characteristic of low-dimensional antiferromagnetic systems. However, from  $\chi(T)$  data alone no evidence for a transition to a long-range ordered state is observed.



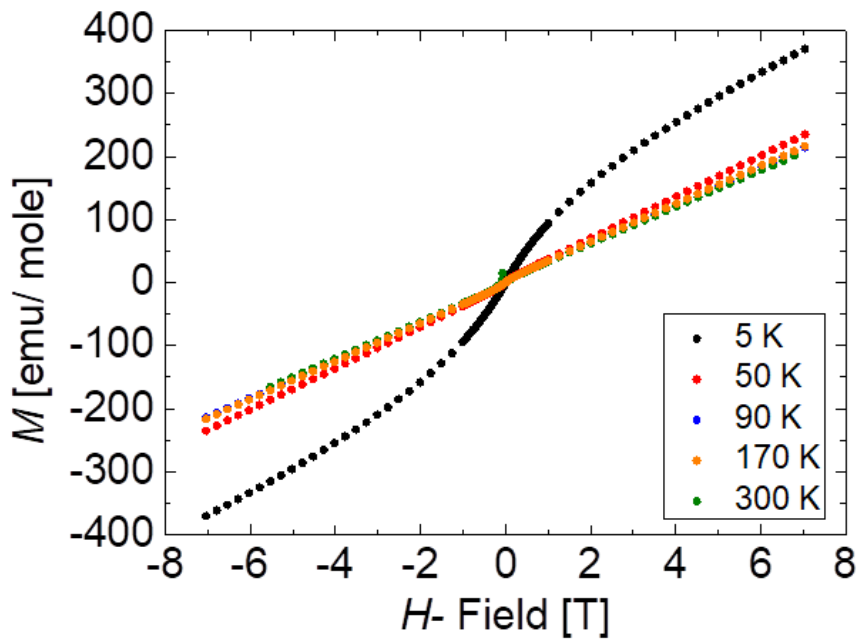


Figure 4-8 Field dependent Hysteresis loops of  $\beta$ -NaMnO<sub>2</sub> measured at 5K, 50K, 90K, 170K, 300K

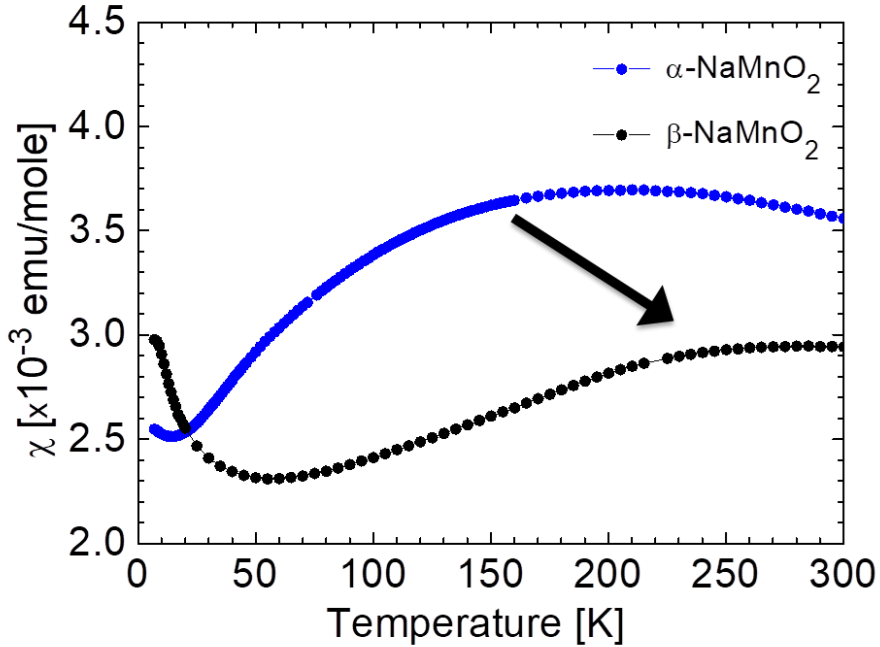


Figure 4-9 Magnetic susceptibilities of  $\alpha$  and  $\beta$  NaMnO<sub>2</sub> polymorphs with blue and black patterns, respectively.

### 4.3.2 Heat Capacity

#### 4.3.2.1 Experiment and sample preparation

For the heat capacity  $C(T)$  measurements, samples were prepared as cold-pressed pellets from  $\beta$ -NaMnO<sub>2</sub> powder synthesized according to the protocol described in chapter 3. The heat capacity  $C$ , has been measured as a function of temperature in zero magnetic field by means of the relaxation technique, utilizing a physical property measurement system (Quantum Design, PPMS).

#### 4.3.2.2 Heat capacity hints magnetic transitions

The measured pattern is completely dominated by phonon excitations especially in the high temperature area. However we can still observe several very weak anomalies, possibly of magnetic origin. In right panel of figure 4-10 we can see features on two temperature areas  $T < 100$  K and  $T \sim 200$  K.

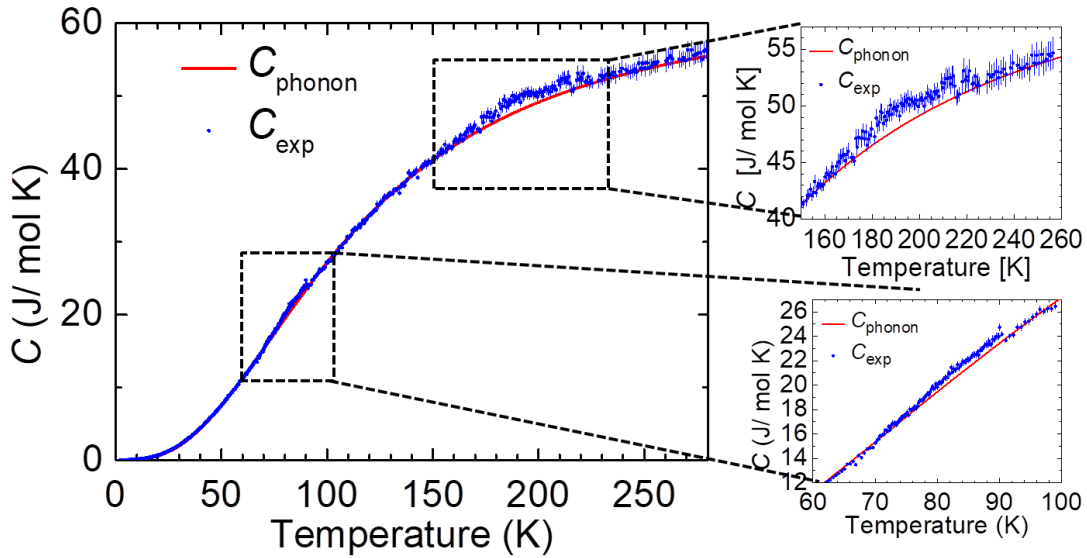


Figure 4-10 Left panel: The measured heat capacity,  $C(T)$  of  $\beta$ -NaMnO<sub>2</sub>. The red line over the  $C(T)$  data is the calculated phonon contribution to the specific heat,  $C_{ph}(T)$ . Right panel: Zoomed in areas of features correlated to magnetic phase transitions

In order to highlight these features, we estimated the phonon contribution to the specific heat,  $C_{ph}(T)$  and subtracted it from the experimentally measured heat capacity data.  $C_{ph}(T)$  in the present study we assume a sum of Debye contributions ( $2 < T < 280$  K), following the procedure used before for other low-dimensional spin systems: [148], [149]



$$C_{ph}(T) = 9R \sum_{i=1}^2 C_i \left( \frac{T}{\theta_D^{(i)}} \right)^3 \int_0^{x_D^{(i)}} \frac{x^4 e^x}{(e^x - 1)^2} dx \quad (4-1)$$

In (4-1) Debye relation,  $R$  ( $=8.314$  J /mol K) is the gas constant,  $\theta_D$  is the Debye temperature and  $x_D^i = \theta_D^i / T$ . For the  $\beta$ -NaMnO<sub>2</sub> system we considered two different Debye functions which account for the two separate contributions of the constituent element coupled vibrations, Na-O and Mn-O. These contribute to the  $C_{ph}(T)$  relation with different atomic masses yielding the fitting parameters,  $C_1 = 0.55(2)$ ,  $C_2 = 2.0(2)$  and  $\theta_D^1 = 287(22)$  K and  $\theta_D^2 = 510(15)$  K (Figure 4-10). The vanishingly small magnitude of  $C(T)$  at very low temperatures, in accord with the  $\beta$ -phase insulating nature, agrees well with the  $\propto T^3$  term that corresponds to phonons (eq. (4-1)). The outcome of the subtraction of  $C_{ph}(T)$  from the total heat capacity is shown in Figure 4-11.

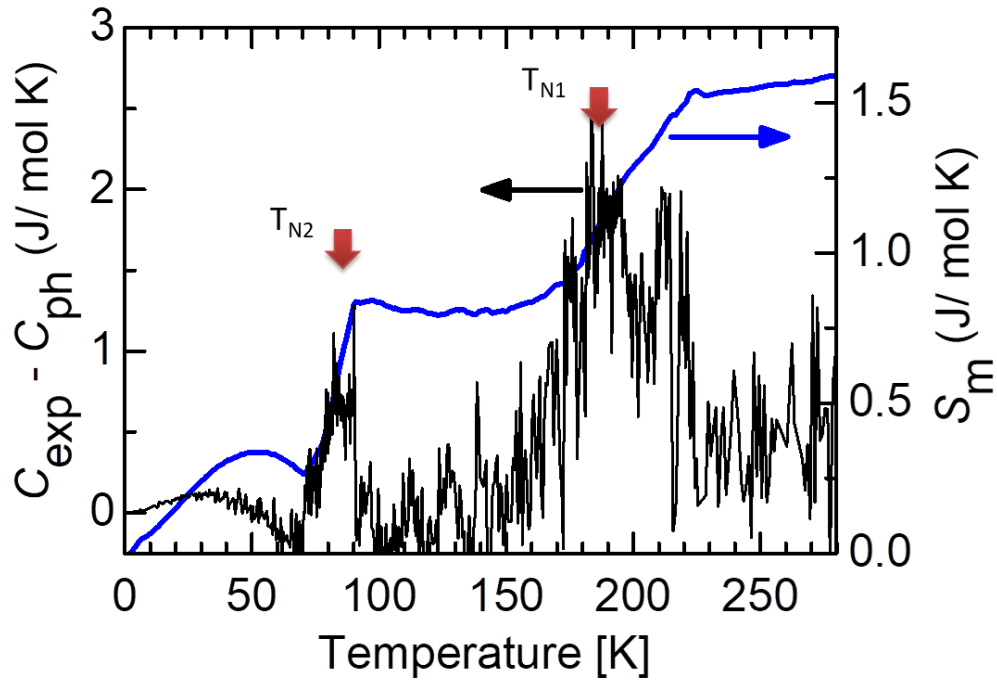


Figure 4-11 The heat capacity remaining after subtracting the  $C_{ph}(T)$  (black line) contribution from the experimental  $C_{exp}(T)$  depicts two featured peaks assigned as  $T_{N1}$  and  $T_{N2}$ . The calculated  $S_{mag}$  is presented in blue following the pattern of the aforementioned peaks in  $C_{mag}$ .

The corresponding peaks observed in the magnetic part of capacity  $C_{mag}(T)$  as it is calculated by the subtraction of  $C_{ph}(T)$  from the  $C_{exp}(T)$ , are quite small. Such a behavior could be pointing to some sensitivity to the defects in the lattice structure (*vide-infra*) which together with high uncertainty of the estimated phonon part, renders further analysis to assess the magnetic contribution. The  $S_{mag}$  is given by the following relation:



$$\Delta S_{\text{mag}} = \int_2^T \frac{C_{\text{mag}}(T)}{T} dT \quad (4-2)$$

and is presented in figure 4-11. On the other hand, the identification of two broad peaks, at  $\sim 95$  K ( $T_{N2}$ ) and  $\sim 200$  K ( $T_{N1}$ ), hints that  $\beta$ -NaMnO<sub>2</sub> undergoes two transitions, therefore motivating a further study on the role of magnetic interactions in the suggested phase transitions.

## 4.4 Phase transition's impact on the spin dynamics: NMR study

### 4.4.1 Experiment and sample preparation

For a deeper understanding of numerous macroscopic thermodynamic properties, the material's microscopic dynamical response is investigated. Techniques, such as solid-state <sup>23</sup>Na NMR, are capable of detecting spin dynamics on a local scale and proved to contribute to the understanding of the complex behavior of  $\beta$ -NaMnO<sub>2</sub>.

NMR measurements on the <sup>23</sup>Na nucleus (nuclear spin  $I = 3/2$ ) were performed on a powder sample sealed in a pyrex sample holder in Jozef Stefan Institute, Ljubljana under the supervision of Dr A. Zorko and Dr D. Arčon. <sup>23</sup>Na NMR spectra and spin-lattice relaxation rate  $1/T_1$  were recorded between 50 and 300 K in a magnetic field of 8.9 T using a solid-echo and inversion recovery pulse sequences, respectively. Wide-line <sup>23</sup>Na NMR powder data were obtained as sums of individual spectra acquired by changing the measurement frequency in 50 kHz steps over  $\pm 3$  MHz around the <sup>23</sup>Na reference frequency,  $\nu_0 = 100.5234$  MHz, which was determined from a 0.1 M NaCl solution. The spin-lattice relaxation rate measurements were also performed at the position of the central line.

### 4.4.2 <sup>23</sup>Na Dynamics near the transition

In Figure 4-12 the <sup>23</sup>Na NMR powder spectra of  $\beta$ -NaMnO<sub>2</sub> between room temperature and 50 K are presented. The spectra become very broad and, consequently, the signal becomes very weak and difficult to measure. At 300 K, the spectrum has a characteristic powder line shape for a quadrupole  $I = 3/2$  nuclei with the quadrupole asymmetry parameter of  $\eta \approx 0$ . We can clearly observe the satellite ( $\pm 3/2 \leftrightarrow \pm 1/2$ ) transitions of the 300 K spectrum terminated around  $\pm \nu_Q = \pm 1.28$  MHz from the narrow central transition ( $1/2 \leftrightarrow -1/2$ ) line (inset to Figure 4-12a) where  $\nu_Q$  is the <sup>23</sup>Na quadrupole frequency. The



indicated observation shows that the expected singularity is rounded, which is consistent with a high-degree of Na local site disorder probably caused by the stacking faults. [126] On cooling down below  $T_{N1} = 200$  K, there is almost no change of the central transition line. However, a close inspection of the  $^{23}\text{Na}$  NMR satellite line reveals that a shoulder starts to gradually broaden well beyond  $\pm\nu_Q$ . This is clearly seen as a growth of the NMR signal intensity on both sides of the satellite line (inset of Figure 4-12b).

Since the positions of the satellite shoulder remain nearly at the same frequency, the quadrupole frequency must also remain the same through the transition at  $T_{N1} \approx 200$  K. This suggests that no structural deformation takes place in the vicinity of the Na. The broadening at the high temperature transition ( $T_{N1}$ ) can thus be magnetic in origin. On further cooling, the broadening on the NMR central line becomes really pronounced below 94 K (figure 4-12c) and the spectrum becomes completely dominated by a broad distribution of internal magnetic fields at certain Mn ion sites. The previously described line shape changes verify that  $\beta$ -NaMnO<sub>2</sub> indeed undergoes two successive transitions to magnetically ordered states, at  $\sim 200$  K and  $\sim 95$  K, in agreement with the subtle peaks in the differential  $C(T)$  assigned as magnetic transitions (section 4.3.2, figure 4-11).

As presented in figure 4-13a, below  $T_{N1}$  the intensity of the sharp central peak multiplied by temperature (to counterbalance the changing Boltzmann population), starts to progressively decrease with decreasing temperature. The gradual wipeout of the central line below  $T_{N1}$  reveals that the high-temperature paramagnetic-like signal vanishes only gradually, as it remains present at all temperatures below  $T_{N1}$ . This leads us to the important conclusion that the magnetic state below  $T_{N1}$  is inhomogeneous.



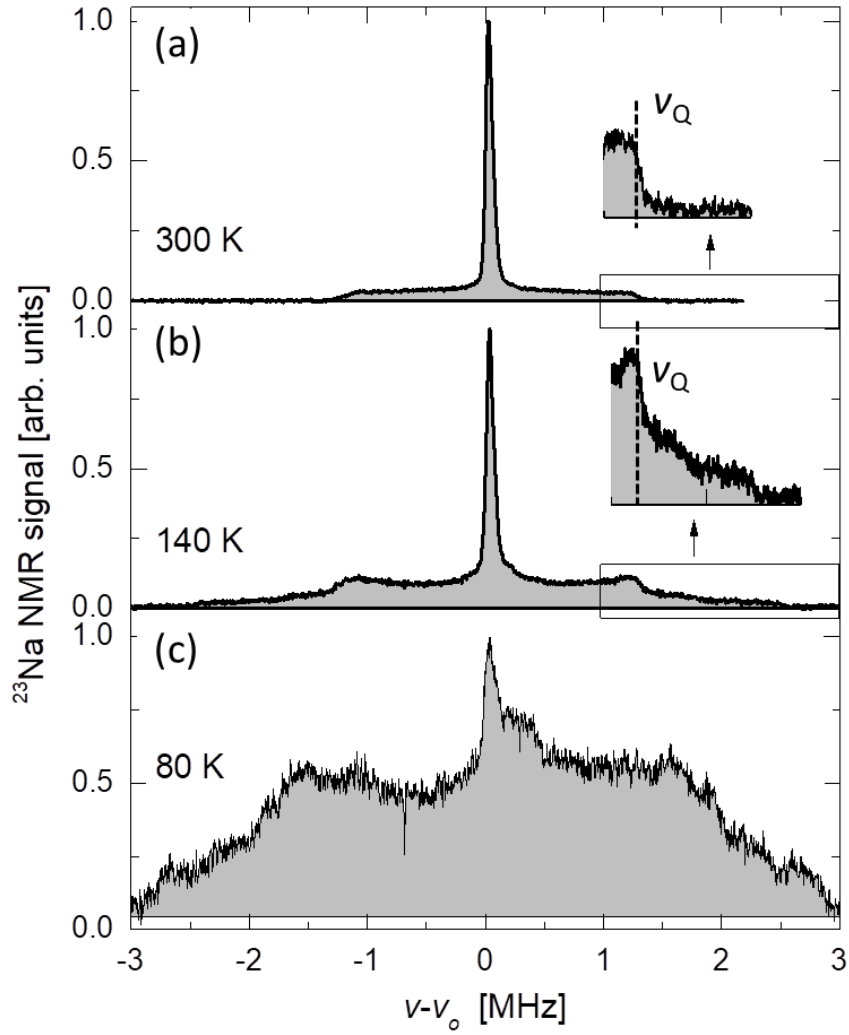


Figure 4-12 Normalized  $^{23}\text{Na}$  NMR powder spectra of  $\beta\text{-NaMnO}_2$  revealing two different magnetic regimes that evolve with temperature lowering. The spectra are shifted vertically for clarity. The insets point to a specific part of the spectra, where the quadrupolar frequency is indicated by the vertical dashed line.

Additional information about the two magnetic transitions is deduced from the  $^{23}\text{Na}$  spin-lattice relaxation rate  $1/T_1$ , which was determined from fitting of  $^{23}\text{Na}$  magnetization recovery curves (Figure 4-8b) to the magnetic-relaxation model for  $I=3/2$ , [150]

$$M(t) = M_0 \left[ 1 - s \left( \frac{1}{10} e^{-\left(\frac{t}{T_1}\right)^\alpha} + \frac{9}{10} e^{-\left(\frac{6t}{T_1}\right)^\alpha} \right) \right] \quad (4-3)$$

Here,  $s < 1$  accounts for imperfect inversion of  $^{23}\text{Na}$  nuclear magnetization after the initial  $\pi$  pulse, while  $\alpha$  stands for a stretching exponent. It is important to note that significantly different stretching exponent  $\alpha$  is found for temperatures above  $T_{N1}$  and below  $T_{N2}$ .



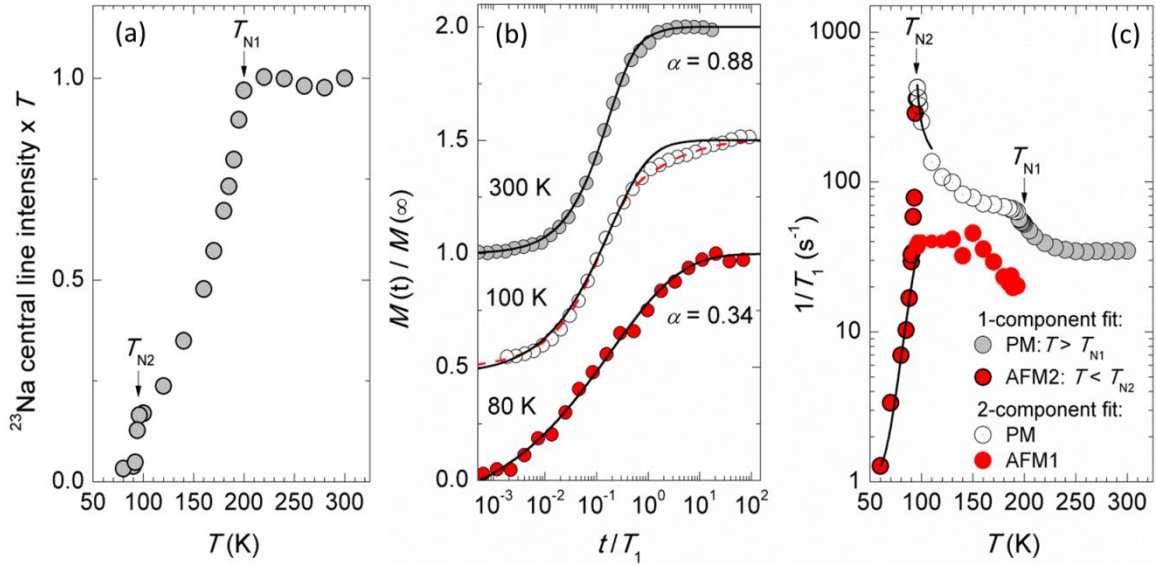


Figure 4-13 (a) The temperature dependence of the  $^{23}\text{Na}$  NMR central line intensity multiplied by temperature for  $\beta$ -NaMnO<sub>2</sub>. The arrows indicate the two transition temperatures  $T_{N1}$  and  $T_{N2}$ . (b) Normalized magnetization-recovery curves at selected temperatures. The datasets are shifted vertically for clarity. The solid lines are fits of a stretched single-component magnetic-relaxation model for  $I = 3/2$  (Eq. 4-3; see text), while the dashed line corresponds to the fit with two such components, AFM1 and PM. (c) The temperature dependence of the spin-lattice relaxation rate for  $\beta$ -NaMnO<sub>2</sub>. The arrows indicate the two transition temperatures. A double-component fit is needed in the intermediate temperature regime  $T_{N2} < T < T_{N1}$ . The solid lines indicate a critical type of behavior for  $T > T_{N2}$  and an activated one for  $T < T_{N2}$  (see text for details).

In the high-temperature paramagnetic (PM) regime,  $1/T_1$  is nearly temperature independent,  $1/T_1 = 35(1) \text{ s}^{-1}$  (Figure 4-13c). Such temperature independence is in fact anticipated for an exchange-coupled antiferromagnetic (AFM) insulator in the paramagnetic phase. The stretching exponent here is  $\alpha = 0.88$  (Figure 4-13b); a value slightly below 1 implying a small distribution of relaxation rates expected in experiments on powder samples. The transition to the magnetic state at  $T_{N1}$  is accompanied by a sizeable step-like increase in the  $1/T_1$  value to  $1/T_1 = 66(5) \text{ s}^{-1}$  and a gradual reduction of the stretching exponent (Figure 4-13b). The latter indicates that the distribution of the spin-lattice relaxation times suddenly starts increasing below  $T_{N1}$  thus indicating growing magnetic inhomogeneity between  $T_{N1}$  and  $T_{N2}$  which is in accord with the line shape changes (Figure 4-12). In fact, as two-step magnetization-recovery curves are clearly observed below  $T_{N1}$  (e.g., measurement taken at 100 K shown in Figure 4-13b), the fit of the magnetization recovery curves in the  $T_1$  experiment is significantly improved if two relaxation components are included. These are named AFM1 and PM. The relative



intensity of the component AFM1 increases at the expense of the second PM component, resembling to the wipeout effect of the narrow central line (Figure 4-12c).

No obvious critical fluctuations leading to diverging  $1/T_1$  could be detected at  $T_{N1}$ . The likely reason is the nature of magnetic fluctuations, which according to the expression,

$$\frac{1}{T_1} = \frac{2\gamma_n^2 k_B T}{(\gamma_e \eta)^2} \sum_{q\rho} A_q^\rho A_{-q}^\rho \frac{\chi''_\perp(q^\rho, \omega)}{\omega} \quad (4-4)$$

(where  $A_q$  denotes the hyperfine coupling of the <sup>23</sup>Na nuclei with the electronic magnetic moments,  $\chi''$  is the imaginary part of the dynamical susceptibility and  $\omega$  is the Larmor frequency), could be filtered out at highly symmetric Na octahedral sites. On the other hand, on approaching the lower transition temperature at  $T_{N2}$ , the  $1/T_1$  of the paramagnetic PM component is rapidly enhanced, suggesting the onset of critical fluctuations. A phenomenological fit of the critical model  $1/T_1 = A + B(T - T_{N2})^{-p}$  to the PM data in the temperature range between  $T_{N2}$  and 110 K, yields the critical exponent  $p = 0.45(10)$  for  $A = 66(5) \text{ s}^{-1}$  and  $T_{N2} = 95.0(5) \text{ K}$  (Figure 4-13c). Such critical enhancement demonstrates that the magnetic fluctuations that govern the transition at  $T_{N2}$  cannot be filtered out anymore at the Na site. This comes in full agreement with the observed <sup>23</sup>Na NMR line shape changes (Figure 4-12).

Finally, at  $T < T_{N2}$ ,  $1/T_1$  is strongly suppressed and exhibits an activated type of dependence ( $1/T_1 \propto T^2 \exp(-\Delta/T)$ , Figure 4-13c), indicating the opening of an excitation gap,  $\Delta$ , in the low-temperature phase.

## 4.5 Crystal structure evolution- Neutron powder diffraction study

### 4.5.1 Experiment and sample preparation

The arrangement of the magnetic ions in the underlying crystal structure is critical to understanding transformations as the ones witnessed by the aforementioned macroscopic studies. For this reason high quality neutron powder diffraction data have been used for the analysis of the crystallographic structure of  $\beta$ -NaMnO<sub>2</sub>. Neutron powder diffraction data were collected on the WISH diffractometer, [110] operating at the second target station (TS2) at the ISIS pulsed neutron source in the UK. WISH, with its high-brilliance, is particularly optimized for providing high resolution at long d-spacing required also for magnetic studies. For this purpose, a 2.7 g polycrystalline sample was loaded in a 8 mm V-can, which was then sealed with indium wire inside a high-quality, He-circulating anaerobic glove box. An Oxford Instrument liquid helium cryostat was used for the



temperature dependent diffraction experiments. Data analysis was performed by using the Jana2006 software [151] for the Rietveld refinements, whereas the group theory analysis was performed with the help of the ISODISTORT software[152] by Dr F. Orlandi. [147]

#### 4.5.2 Determination of crystallographic structure[147]

The main observed reflections of the neutron powder diffraction (NPD) pattern are consistent with the *Pmmn* space group, with cell parameters  $a_0 = 4.7851(2)$  Å,  $b_0 = 2.8570(8)$  Å,  $c_0 = 6.3287(4)$  Å, at 300 K. The Rietveld refinement of the main nuclear reflections (300 K), with the *Pmmn* model [131] (Mn1 in 2b position  $z = 0.617(5)$ , Na1 in 2b  $z = 0.125(4)$ , O1 in 2a  $z = 0.365(6)$  and O2 in 2a  $z = 0.872(6)$ ), suggests a significant degree of “anti-site” defects between the Mn and Na sites that leads to an average occupation of ~80:20 (Figure 4-14 bottom panel). Moreover, the refinement points to an unexpectedly large-value for the oxygen thermal parameter ( $U_{\text{iso}} \sim 0.038(2)$  Å<sup>2</sup>). The refinement of anisotropic temperature factors results in a clear elongation of the thermal ellipsoids along the c-direction (Figure 4-9 top panel) <sup>27</sup> indicating strong positional disorder. Following this suggestion we split the two oxygen positions along the c-axis and the refinement converged to a splitting of ~0.5 Å and ~70:30 occupancy of the resultant sites, with normal isotropic thermal parameters ( $U_{\text{iso}} \sim 0.015(2)$  Å<sup>2</sup>). Here it is noted that the split and especially the occupancy of O1 and O2 resemble the anti-site occupancy of the Mn and Na atoms; in particular, as shown in Figure 4-14 this distortion is needed to satisfy the coordination requirements of the Na and Mn cations.

The NPD pattern at 300 K, in association with the above analysis, reveals a remarkable feature. This is the observation of additional reflections that could be ascribed to a nuclear modulation (Figure 4-15). In support to this comes earlier transmission electron microscopy (TEM) work on  $\beta$ -NaMnO<sub>2</sub>[126] where it was pointed out that formation of planar defects establishes short-ranged ordered regions that locally (i.e. on the length scale of a few unit cells) follow the stacking sequence of NaMnO<sub>2</sub> layers characteristic of either the  $\alpha$ - or the  $\beta$ - phases.



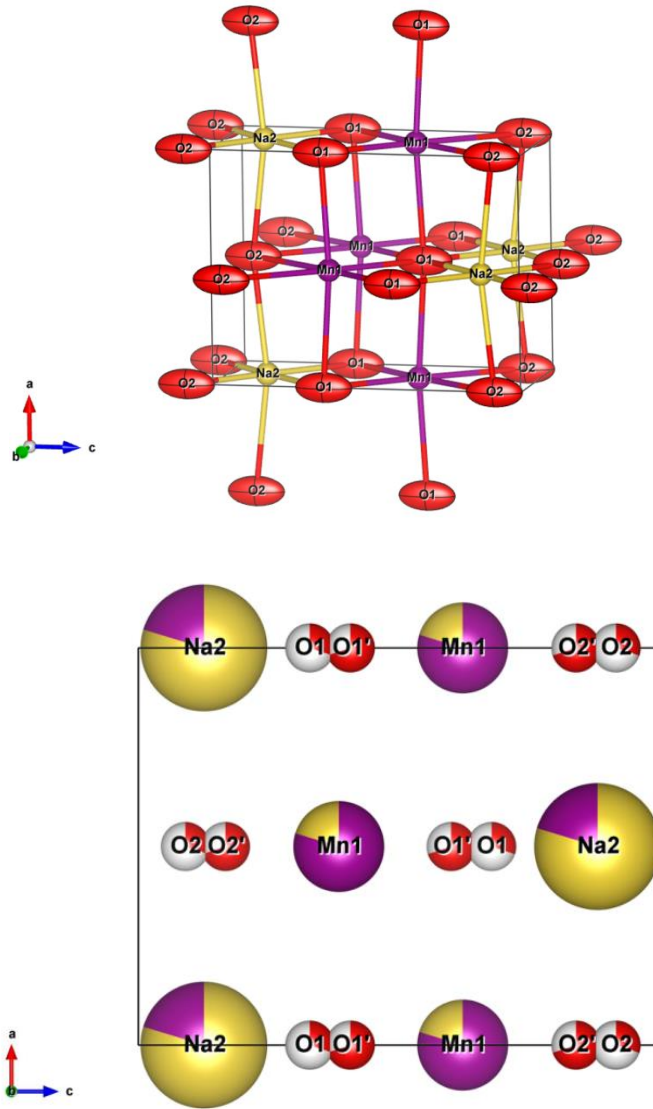


Figure 4-14 Model of the average nuclear structure ( $Pm\bar{m}n$  space group) of  $\beta$ -NaMnO<sub>2</sub> obtained from the Rietveld refinement of the main reflections of the WISH powder patterns (see main text): top, highlighting the unusually large anisotropic thermal parameter elongated along the  $c$  direction for the oxygen atoms; bottom, the splitting of the oxygen-site position, suggested from the anisotropic thermal parameters. Reprinted from reference 19.

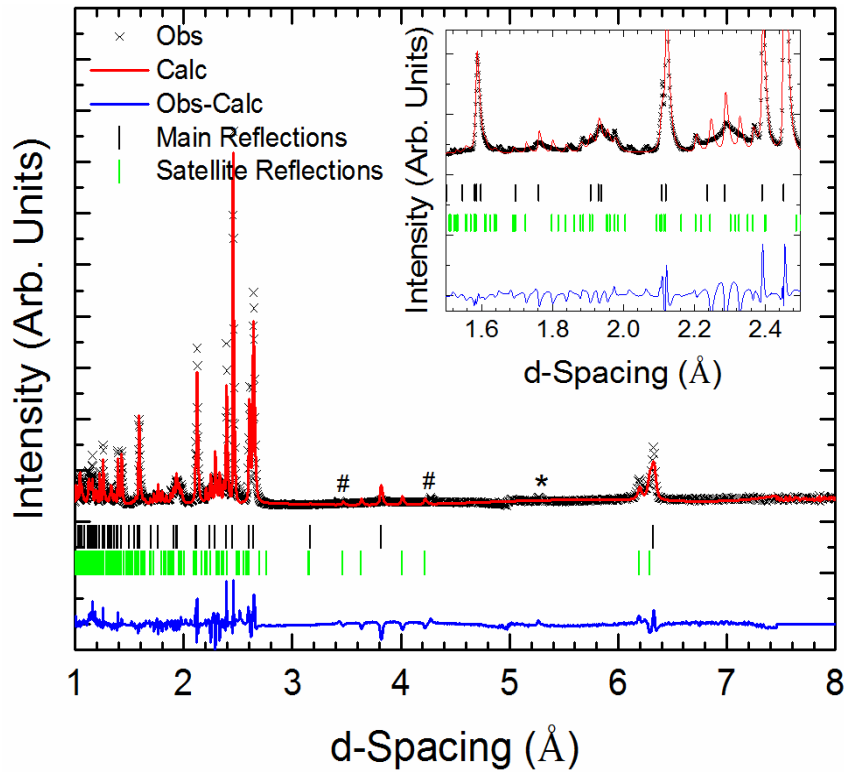


Figure 4-15 Rietveld plot at 300 K for the  $\beta$ -NaMnO<sub>2</sub> structure in the  $Pm\bar{m}n(a00)000$  superspace group. Inset: zoom of the low  $d$ -spacing region inferring that stacking faults and defects give rise to a peculiarly broadened profile function. In both panels observed (black crosses), calculated (red line) and difference (blue line) pattern are shown. The tick marks indicate the calculated position of the main (black ticks) and satellite reflections (green ticks). The asterisk marks the main reflection of the  $\alpha$ -NaMnO<sub>2</sub> impurity, whereas the hash-tags indicate, for example, two satellite peaks that are slightly off with respect to the calculated Bragg position indicating the possibility of the other two components of the modulation vector to be different from zero (see text for details). Reprinted from reference 19

From the LeBail fit of the WISH data we obtained an optimal modulation vector  $\mathbf{q} = (0.077(1), 0, 0)$ , accounting for satellites up to the second order in the NPD pattern. Some small satellite reflections, however, are sliding off the calculated position (Figure 4-15), suggesting that the other two components of the modulation vector may be slightly different from zero. Refinements where the other two components of  $\mathbf{q}$  were allowed to vary proved unstable and did not lead to reasonable results. The obtained value of  $\mathbf{q}$  is near the commensurate  $1/13$  position, which explains why the  $1/6$  value used before in the synchrotron X-ray diffraction patterns[126] indexed well a large number of satellite peaks. The fact that satellite reflections have been also met in earlier TEM measurements together with the refinement of the average nuclear structure from the NPD pattern, indicate the possibility of a compositional modulation in the structure. Such modulations have been



previously met in literature where they have been studied using superspace formalism. [153], [154] Therefore, In order to understand the NPD pattern of WISH a (3+1)-dimensional superspace approach has been used considering an occupational modulation for all the sites in the average nuclear structure. The possible superspace groups have been derived by group symmetry analysis with the help of the ISODISTORT Software Suite starting from the refined average structure and the propagation vector  $q=(\alpha 00)$ . Having taken into account the observed reflection conditions and the symmetry properties of the modulation vector, the symmetry analysis led to the  $Pmmn(\alpha 00)000$  superspace group as the best solution.

The optimization of such analysis proved to be difficult due to broad, asymmetric reflections throughout the NPD pattern, mainly due to defects (e.g. stacking faults) and strain, raising the agreement factors and making a quantitative refinement difficult. The Rietveld plot, over a wide  $d$ -spacing range, is shown in Figure 4-15 and the associated reliability factors are,  $R_p= 8.81\%$ ,  $R_{wp}= 12.73\%$ ,  $R_{main}= 9.96\%$ ,  $R_{sat\pm 1}= 15.41\%$ ,  $R_{sat\pm 2}= 14.79\%$ . Despite the apparent reflection broadening, the suggested model shows good agreement for the modulated parts of the profile, especially obvious in the relatively short  $d$ -spacing region of the pattern (inset in Figure 4-15). The crystallographic parameters of the compositionally modulated  $\beta$ -NaMnO<sub>2</sub> at 300 K, on the basis of a (3+1)D Rietveld analysis with the  $Pmmn(\alpha 00)000$  superspace group ( $a= 4.7852(4)$  Å,  $b= 2.85701(8)$  Å,  $c= 6.3288(4)$  Å,  $\alpha=0.077$  (1)) are compiled in Appendix B, table I.

This single-phase structural model, despite the presence of low intensity reflections ascribable to a small amount of the  $\alpha$ -phase and MnO (Fig. 4-15), takes into account almost all the satellites present in the NPD pattern of the  $\beta$ -phase, as compared to the two-phase description on the basis of the  $B2/m(\alpha\beta 0)00$  superspace group derived before from the analysis of the synchrotron X-ray powder diffraction data[126]. The approach that has been followed, demonstrates that having taken advantage of the superspace formalism to describe the compositional modulation of the Mn and Na sites in a single-phase atomic configuration, the incommensurate  $\beta$ -NaMnO<sub>2</sub> structure can be depicted as a coherent intergrowth of two types of NaMnO<sub>2</sub> layers, reflecting the  $\alpha$ - and  $\beta$ - polytype oxygen coordinations (Fig. 4-16). The nuclear structure model obtained is consistent with the one proposed by Abakumov *et al.*,[126] entailing coherent intergrowth of stacking sequences of NaMnO<sub>2</sub> layers along the  $\mathbf{a}_0$ -axis, characteristic of the  $\alpha$ - and  $\beta$ - polytypes.



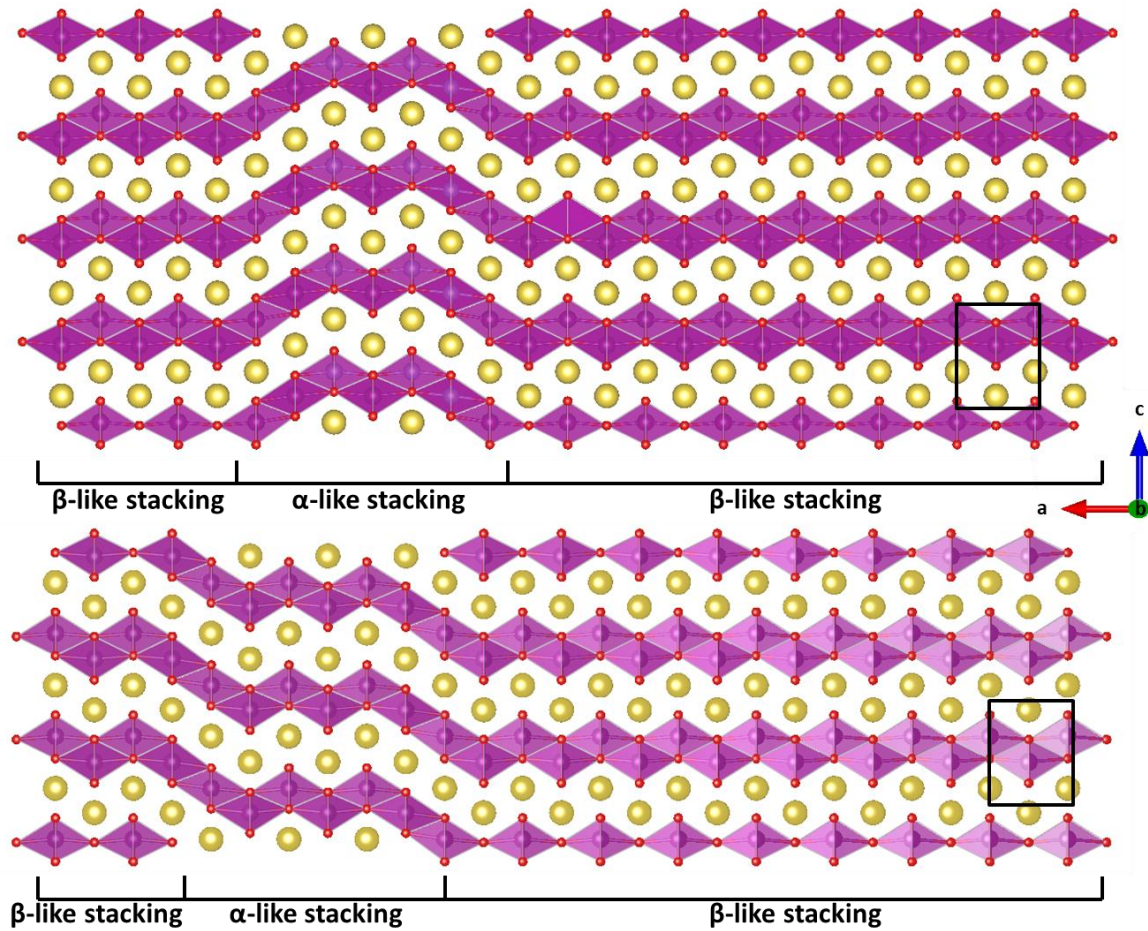


Figure 4-16 Projection of the structure in the  $ac$ -plane, depicting the refined incommensurate compositional modulated structure; two types of stacking changing between the NaMnO<sub>2</sub> polymorphs are shown. The violet atoms represent the Mn, the yellow ones the Na, and the red spheres the oxygen atoms. The small rectangle indicates the unit cell of the average  $Pmmn$  structure (Appendix B, Figure I). Reprinted from reference 19

In an effort to visualize the degree of compositional modulation in the  $\beta$ -NaMnO<sub>2</sub> structure, Fourier maps of the observed structure factor (Figure 4-17) involving the atomic sites in the  $zx_4$ -plane were computed on the basis of the observed NPD intensities and the calculated phases. Figure 4-17a shows the complementary occupation of the cation sites without any particular modulation of the  $z$  coordinate. On the contrary, from the Fourier maps centered at the oxygen positions (Figure 4-17b) it is inferred that the site-splitting observed in the average structure is needed in order to satisfy the coordination requirement of the Mn<sup>3+</sup> Jahn-Teller active cation. In fact, it is noted that when the Na and Mn swap sites (cf. compositional modulation), the same happens in the oxygen split positions so that the bonding requirements are restored as depicted in Figure 4-14b.

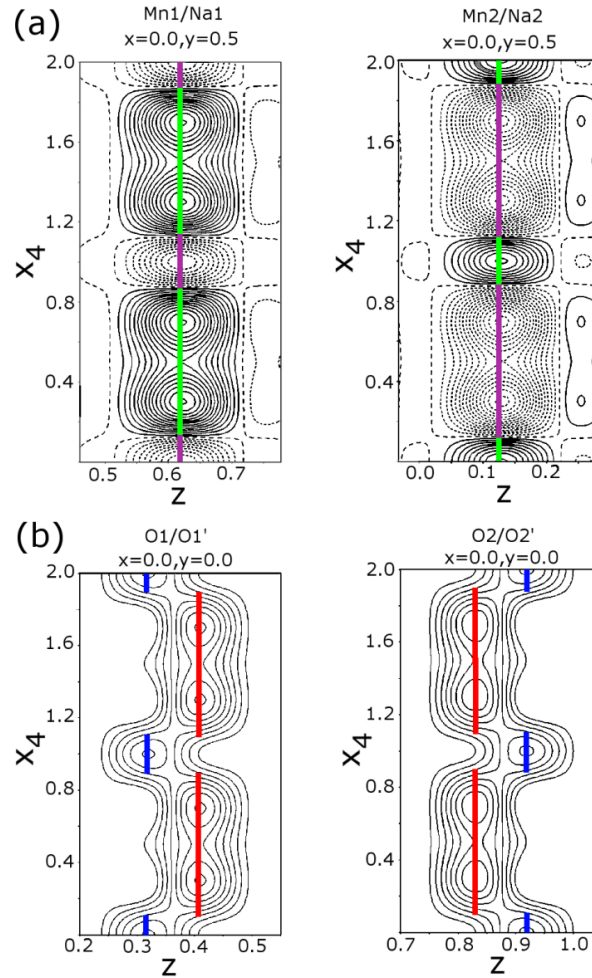


Figure 4-17 Fourier maps of the observed structure factor ( $F_{obs}$ ) depicting the crystallographic cation sites (a) and oxygen positions (b). The solid colored lines represent the calculated position of the atoms showing no positional modulation along the  $x_4$  for the Mn/Na but its presence for the oxygen sites (violet Mn, green Na, red oxygen and blue the primed oxygen position). The black continuous lines indicate the positive density iso-surface and the dashed lines the negative iso-surface (the neutron scattering length for the Mn atoms is negative). The iso-surface contours correspond to 2 scattering density units ( $\text{\AA}^{-2}$ ) in all the plots. Reprinted from reference 19

## 4.6 Magnetic Structure evolution topologically correlated to defected lattice[147]

### 4.6.1 CM and IC magnetic structures

The nuclear modulated structure observed in the NPD profiles of  $\beta$ -NaMnO<sub>2</sub> triggered the investigation of the possible correlation between the crystal and magnetic structure. The temperature evolution of the diffraction pattern demonstrates the presence of two magnetic transitions (Figure 4-18).



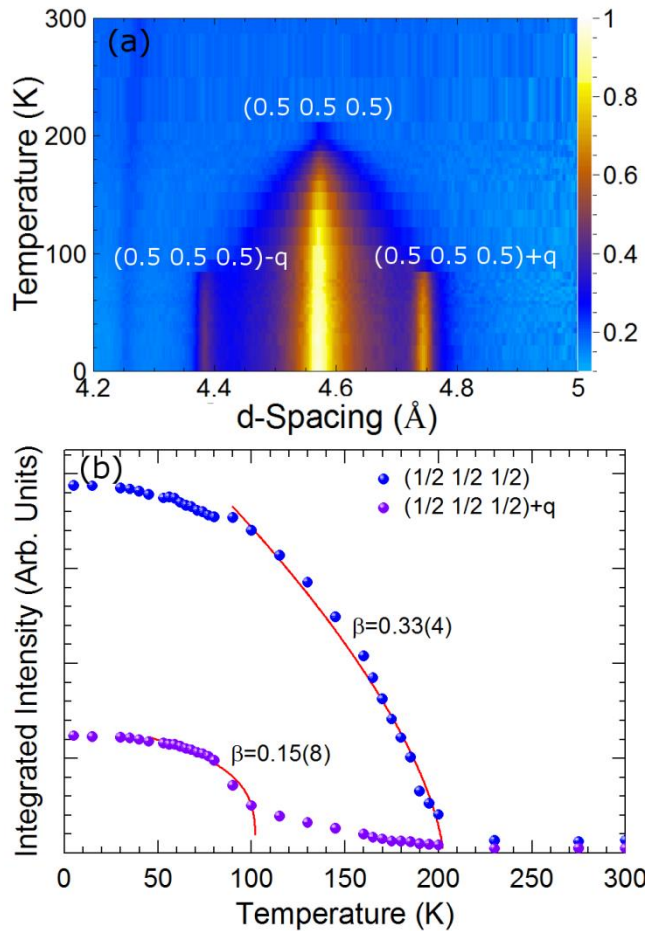


Figure 4-18 (a) A long  $d$ -spacing section of the neutron powder diffraction patterns as a function of temperature, showing the complex nature of the magnetic contribution to the pattern. Color map: the neutron scattering intensity. (b) Integrated intensity versus temperature for the main magnetic reflections with propagation vector  $\mathbf{k} = (\frac{1}{2}, \frac{1}{2}, \frac{1}{2})$ , and for the satellites with propagation vector  $\mathbf{k} + \mathbf{q}$ , where  $\mathbf{q} = (0.077(1), 0, 0)$ . The lines over the data points depict the fit to the critical region (details in text). Reprinted from reference 19

The first observation, as the system cools below  $T_{N1} \sim 200$  K, is an intensity increase at magnetic Bragg peak positions corresponding to a propagation vector  $\mathbf{k} = (\frac{1}{2}, \frac{1}{2}, \frac{1}{2})$  with respect to the  $Pmmn$  orthorhombic average structure. The observed reflections grow quickly below the magnetic transition temperature while their broad Lorentzian-like profile is an indication that the magnetic domain is sensitive to the strain and defects present in the nuclear structure (Figure 4-16), complying with the broadening of  $^{23}\text{Na}$  NMR spectra (Figure 4-12). Cooling further down, about 100 K, the development of additional reflections is observed in the diffraction patterns (Figure 4-18a). This new set of peaks can be indexed assuming the combination of the magnetic propagation vector  $\mathbf{k}$  and the nuclear

one  $\mathbf{q}$ , giving magnetic intensity at the positions  $hkl \pm [\mathbf{k} \pm \mathbf{q}]$ . The temperature dependence of the integrated intensity (Figure 4-18b) of the aforementioned two sets of reflections has been calculated in order to investigate the critical behavior of the two magnetic orders. Power law  $I = I_0 [1 - (T/T_N)]^{2\beta}$  fits of each reflection indicates that they possess different critical behavior, suggesting that the two magnetic orders likely fall into different universality classes. More specifically, the fit of the  $\frac{1}{2}\frac{1}{2}\frac{1}{2}$  reflection gives a critical exponent of  $\beta = 0.33(4)$ , indicating interactions of a 3D nature, while on the other hand, the  $\mathbf{k} \pm \mathbf{q}$  satellites allows an exponent of  $\beta = 0.15(8)$ , which is more consistent with 2D interactions (Figure 4-18b). Careful analysis of the diffraction pattern reveals the presence of some additional low intensity reflections that are not indexed with the previous propagation vectors. These extra reflections are ascribed to a small-content of MnO impurity and the  $\alpha$ -polymorph (as already commented in the XRPD study in section 4.2).

#### 4.6.2 Magnetic Spin configurations

In order to establish the possible magnetic space group, magnetic symmetry analysis has been used with the help of the ISODISTORT software.[152]

In the temperature range just below 200 K, the NPD patterns show that no clear magnetic intensity is observed on the nuclear satellite reflections, therefore pointing that the magnetic structure is not strongly related to the nuclear modulation at least in the  $100 < T < 200$  K temperature range. For this reason, magnetic symmetry analysis was initiated on the basis of parent average  $Pmmn$  nuclear structure (Appendix B, Figure II, Table I) and the propagation vector  $\mathbf{k} = (\frac{1}{2} \frac{1}{2} \frac{1}{2})$ . The results of the symmetry analysis are reported in Table 4-2. The best agreement between observed and calculated patterns was obtained for the mR1 representation, with order parameter direction (OPD)  $PI(a,0)$ , corresponding to the magnetic space group  $C_{a2}/c$ , with a change in the unit cell with respect to the parent structure described by the transformation matrix  $\{(0,-2,0), (0,0,2), (-1,1,0)\}$ . A reasonably good result gives the choice of the  $C_{a2}$  space group, but with an increased number of refinable variables, thus suggesting the higher symmetry option  $C_{a2}/c$  as the best solution. Combining the mR1  $PI(a,0)$  IRs with the compositional modulated structure, the  $C_{a2}'/c'(a0\gamma)00$  magnetic superspace group is obtained.



Table 4-2 The symmetry-allowed magnetic space groups are generated by means of the representation analysis technique, where IRs, the irreducible representations of the translational group made up of the symmetry operations of the nuclear cell and the order parameter direction (OPD) (see text). The components of the cell transformation matrix are given with respect to the  $Pmmn$  space group, with nuclear cell parameters  $a_0=4.7851(2)$  Å,  $b_0=2.85699(8)$  Å,  $c_0=6.3287(4)$  Å

IRs	OPD	Magnetic space group	Cell transformation	Origin	$R_{B\_mag}$ , average nuclear structure only
mR1	$PI(a,0)$	$C_{a2/c}$	$\{(0,-2,0),(0,0,2),(-1,1,0)\}$	$(-1/4,1/4,1/2)$	24 %
mR1	$P3(a,a)$	$F_{smm2}$	$\{(-2,0,0),(0,2,0),(0,0,-2)\}$	$(-1/2,1/2,-1)$	28 % (half Mn paramagnetic)
mR1	$CI(a,b)$	$C_{a2}$	$\{(0,-2,0),(0,0,2),(-1,1,0)\}$	$(0,0,0)$	25 %
mR2	$PI(a,0)$	$C_{a2/c}$	$\{(0,-2,0),(0,0,2),(-1,1,0)\}$	$(-1/4,3/4,1)$	37 %
mR2	$P3(a,a)$	$F_{smm2}$	$\{(-2,0,0),(0,2,0),(0,0,-2)\}$	$(-1/2,0,-1/2)$	35 % (half Mn paramagnetic)
mR2	$CI(a,b)$	$C_{a2}$	$\{(0,-2,0),(0,0,2),(-1,1,0)\}$	$(0,-1/2,1/2)$	32 %

The later superspace group was used for a Rietveld refinement of the 100K profile (Figure 4-19a). The associated reliability factors are  $R_{Fobs} = 8.46\%$  for the nuclear reflections,  $R_{Fmag} = 12.50\%$  for the magnetic ones and  $R_p = 13.88\%$  while the refined parameters are summed in table 4-3. The pronounced  $hkl$ -dependent broadening likely arising from the presence of planar defects rather affects the reliability factors. The consequent magnetic structure is drawn in Figure 4-19b, projected in the same plane as the nuclear one (Figure 4-16, top panel). It entails antiferromagnetically coupled Mn-chains running down the  $b_0$ -axis ( $a_0$ ,  $b_0$  and  $c_0$  setting is with respect to the orthorhombic  $Pmmn$  unit cell), stacked in a zig-zag fashion when viewed in an  $a_0c_0$ -plane projection (Figure 4-19b) that gives rise to antiferromagnetically coupled, corrugated MnO<sub>2</sub> layers (Figure 4-19c).



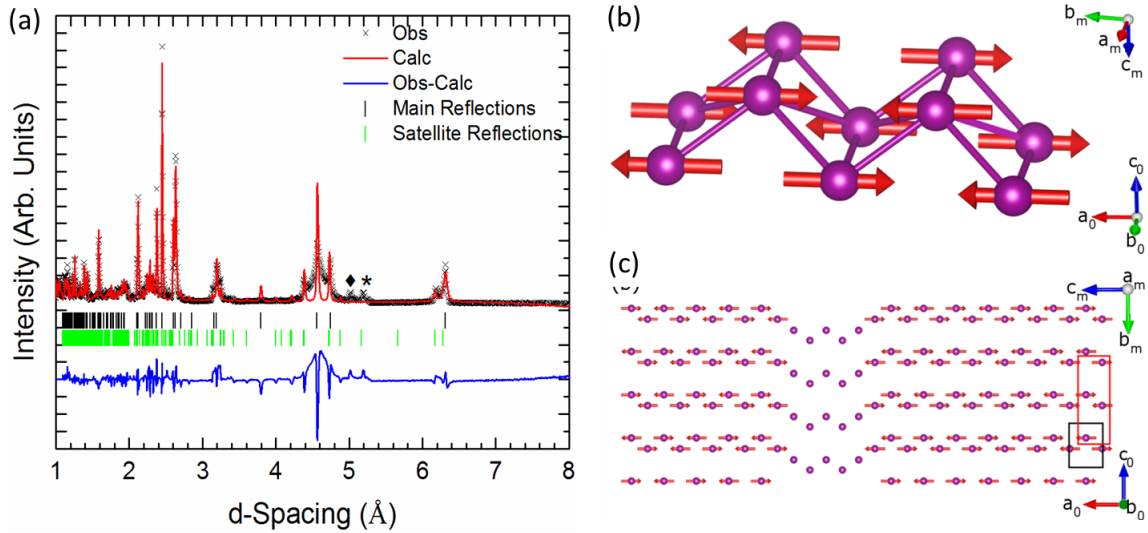


Figure 4-19 (a) Rietveld plot at 100 K of the  $\beta$ -NaMnO<sub>2</sub> structure in  $C_a2'/c'(a0\gamma)00$  superspace group, with cell parameters  $a= 5.7108(2)$  Å,  $b= 12.6394(9)$  Å,  $c= 5.5397(4)$  Å,  $\beta= 120.96(7)^\circ$ , and  $q= (0,0, 0.078(1))$ . Observed (black crosses), calculated (red line) and difference (blue line) patterns are reported. The tick marks indicate the calculated position of the main (black ticks) and satellite reflections (green ticks). The asterisk marks the main nuclear and magnetic reflections from the  $\alpha$ -NaMnO<sub>2</sub> impurity phase, whereas the diamond indicates the main MnO magnetic reflection. (b-c) Sketch of the magnetic structure below 200 K, (a) along the Mn zig-zag chain typical of the  $\beta$ - polymorph ( $a_0$  direction) and (b) in the same projection as for Figure 4-11 (top panel). The black rectangle depicts the unit cell of the average Pmmn structure ( $a_0= 4.7851(2)$  Å,  $b_0= 2.85699(8)$  Å,  $c_0= 6.3287(4)$  Å), while the red rectangle indicates the unit cell of the average low temperature monoclinic structure ( $a_m= 5.7112(2)$  Å,  $b_m= 12.6388(9)$  Å,  $c_m= 5.5365(4)$  Å,  $\beta= 120.97(7)^\circ$ ); please note that the  $c_m$ -axis is inclined by  $\sim 60^\circ$  out of the plane. Reprinted from reference 19

When temperature is lowered below  $T_{N2} \sim 100$  K, the incommensurate-like magnetic ordering appears to be described with a combination of the magnetic,  $\mathbf{k}$ , and nuclear,  $\mathbf{q}$ , propagation vectors suggesting that the second transition takes place because longer-range magnetic correlations are established in the alpha-like stacking sequence(s). Assuming that the same superspace group used for describing the nuclear structure defines also the magnetic order at  $T < 100$  K and taking into account a Mn1-site spin-configuration similar to that of the Mn2-site, magnetic scattering is calculated only for the  $\mathbf{k}+\mathbf{q}$  satellite positions. However, its relative intensity failed to match the experimentally observed one, pointing out that additional spin modulation of the existing structure is required in order to adequately reproduce the observed magnetic NPD pattern.

Table 4-3 Crystallographic atomic fractional coordinates and magnetic phase parameters for the  $\beta$ -NaMnO<sub>2</sub> structure at 100 K, as derived from a (3+1)D Rietveld refinement of neutron powder diffraction data in the  $C_{a2'/c'}(\alpha 0 \gamma)00$  ( $\gamma = 0.078(1)$ ) superspace group, with unit cell dimensions  $a = 5.7108(18)$  Å,  $b = 12.639(9)$  Å,  $c = 5.5398(4)$  Å  $\beta = 120.968(6)^\circ$ .

Atom	$x_1$	$x_2$	$x_3$	Uiso / Å <sup>2</sup>	$\Delta$	$x_4^0$	$M_x0$	$M_y0$	$M_z0$	$M_{Tot}$
Mn1	0.75	0.5536(19)	0.75	0.0129(10)	0.204	0	-	-	-	
Na1	0.75	0.5536(19)	0.75	0.0129(10)	0.699	0.5				
Na2	0.75	0.8128(19)	0.75	0.0129(10)	0.204	0				
Mn2	0.75	0.8128(19)	0.75	0.0129(10)	0.796	0.5	1.68(9)	0	2.76 (4)	2.38(10)
O1	0	0.9155(6)	0.75	0.0129(10)	0.699	0.5				
O1'	0	-0.053(2)	0.75	0.0129(10)	0.301	0				
O2	0	0.7084(7)	0.75	0.0129(10)	0.699	0.5				
O2'	0	0.6615(13)	0.75	0.0129(10)	0.301	0				

Rietveld refinements of the magnetic structure confirmed that the magnetic phase below  $T_{N2}$  can be described by a proper screw component, with propagation vector  $\mathbf{k}+\mathbf{q}$  for both Mn1 and Mn2 sites, while refinements assuming a spin-density wave type of structure produced worse agreement factors and unphysical moment size for the Mn1 site. The corresponding Rietveld refined 5 K NPD profile is shown in Figure 4-15a, with the refined magnetic parameters compiled in Table 4-4 [90]. The associated reliability parameters are,  $R_{Fobs} = 8.41\%$  for the nuclear reflections and  $R_{Fmag} = 9.4\%$  for the magnetic ones, while the  $R_p = 16.6\%$  is relatively poor again due to the extreme peak broadening. The magnetic structure below  $T_{N2}$  is depicted in Figure 4-20b-c.



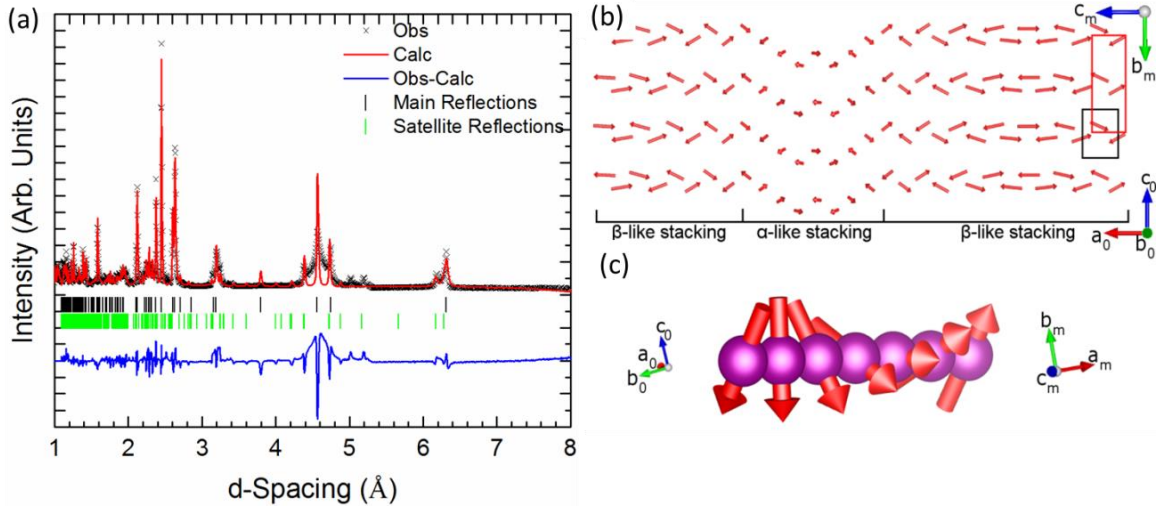


Figure 4-20 (a) Rietveld plot at 5 K for the  $\beta$ -NaMnO<sub>2</sub> structure in  $C_a2'/c'(\alpha0\gamma)00$  superspace group, with cell parameters  $a= 5.7112(2)$  Å,  $b= 12.6388(9)$  Å,  $c= 5.5365(4)$  Å,  $\beta= 120.97(7)^\circ$ , and  $q=(0, 0, 0.081(1))$ . Observed (black crosses), calculated (red line) and difference (blue line) patterns are shown. The tick marks indicate the calculated position of the main (black ticks) and satellite reflections (green ticks). (b) Schematic of the  $\beta$ -NaMnO<sub>2</sub> modulated magnetic structure at 5 K, projected at the same plane as the nuclear structure shown in Figure 6 (top panel). (c) Sketch of the incommensurate part of the magnetic structure depicting a proper screw order propagating along the  $(-110)$  direction with respect to the average  $Pm\bar{m}n$  unit cell. In both panels the axes directions with subscript '0' indicate the average orthorhombic  $Pm\bar{m}n$  cell (black rectangle), whereas the axes with subscript 'm' indicate the direction of the low-temperature monoclinic structure (red rectangle).

Table 4-4 Crystallographic atomic fractional coordinates and magnetic phase parameters for the  $\beta$ -NaMnO<sub>2</sub> structure at 1.5 K, derived from a  $(3+1)D$  Rietveld refinement of neutron powder diffraction data in the  $C_a2'/c'(\alpha0\gamma)00$  ( $\gamma= 0.081(1)$ ) superspace group, with unit cell dimensions  $a= 5.7111(2)$  Å,  $b= 12.639(9)$  Å,  $c= 5.53698(4)$  Å,  $\beta= 120.979(6)^\circ$ .

Atom	$x_1$	$x_2$	$x_3$	Uiso / Å <sup>2</sup>	$\Delta$	$x_4\mathbf{0}$
Mn1	0.75	0.5510(16)	0.75	0.0123(6)	0.204	0
Na1	0.75	0.5510(16)	0.75	0.0123(6)	0.699	0.5
Na2	0.75	0.8141(16)	0.75	0.0123(6)	0.204	0
Mn2	0.75	0.8141(16)	0.75	0.0123(6)	0.796	0.5
O1	0	0.9163(6)	0.75	0.0123(6)	0.699	0.5
O1'	0	-0.059(2)	0.75	0.0123(6)	0.301	0
O2	0	0.7095(7)	0.75	0.0123(6)	0.699	0.5
O2'	0	0.6591(14)	0.75	0.0123(6)	0.301	0
Magnetic parameters						
	$M_x\mathbf{0}$	$M_y\mathbf{0}$	$M_z\mathbf{0}$	$M_x\cos\mathbf{1}$	$M_y\sin\mathbf{1}$	$M_z\cos\mathbf{1}$
Mn1				1.5(3)	-1.5(3)	1.5(3)
Mn2	1.18(9)		2.48(4)	-1.37(3)	1.37(3)	-1.31(3)



## 4.7 Parameterization of Magnetic excitations-INS study [147]

### 4.7.1 Experiment and sample preparation

Inelastic neutron scattering work was performed on the MARI direct geometry chopper spectrometer (ISIS, UK) and also on the DCS spectrometer (NIST, USA). Experiments on MARI used incident energies  $E_i=85$  and  $150$  meV, with a Gd Fermi chopper spun at  $300$  and  $450$  Hz, respectively. Measurements on DCS were done with an incident energy of  $E_i=14.2$  meV. A powder sample of  $m=7.3$  g was loaded in an annular aluminum sachet that was placed inside a cylindrical Al-can for the ISIS experiment, while a  $5$  g sample was loaded in V-can for the NIST experiment. In either case the cans were sealed with indium wire and they were cooled at low temperatures with a top-loaded closed-cycle refrigerator. All data has been corrected for background and also phonons from the structural lattice. For the MARI data, the background plus phonon contribution to the scattering at each energy transfer was estimated from the high angle detector banks where magnetic scattering is suppressed owing to the  $Mn^{3+}$  form factor. The fit of the high angle and high momentum detectors was done at a fixed energy transfer to the form  $L(Q)=L_0+L_1\times Q^2$ , with  $L_0$  capturing the background and  $L_1$  providing an estimate of the phonon scattering.  $L(Q)$  was then used to estimate the background and phonon scattering at low momentum transfers and then it was subtracted. For data taken on DCS, the background was estimated by using the requirement for detailed balance as discussed in literature. [155]

### 4.7.2 Spin gap and dimensionality of magnetic interactions

An overview of the measured INS response, well within the magnetically ordered state ( $5$  K), is shown in Figure 4-21a for experiments on the MARI spectrometer. A complementary insight on the low energy magnetic dynamics was offered with higher resolution through the DCS spectrometer (Figure 4-22). At low temperatures ( $1.5$  K and  $75$  K) the DCS spectra show clearly the presence of a spin-gap in the excitation spectrum, with little change in the gap energy,  $\Delta\sim 5$  meV. A pronounced change is observed at  $100$  K with a filling of the gap.

To our knowledge, a full theoretical study on magnetic exchange interactions on the  $\beta$ -NaMnO<sub>2</sub> polymorph was missing along with the lack of single crystal data. For this reason, a parameterization of the dispersion  $E(\vec{Q})$  with a phenomenological expression which



satisfies the periodicity of the lattice and hence Bloch's theorem has been attempted following the method described in 2.5.1.5.

One possible form of the dispersion, consistent with lattice periodicity can be written as a Fourier series  $E^2(\vec{Q}) = \Delta + \sum_d B_d \sin^2(\vec{Q} \cdot \vec{d})$ , where  $\vec{d}$  is a bond vector connecting nearest-neighbor (NN) spins and  $B_d$  are coefficients in this series expansion, and  $\Delta$  is the magnitude of the spin-gap. Since the magnetic excitations appear sharp in energy (Figures 4-21, 4-22), the single mode approximation (SMA) is utilized. This approximation states that the structure factor, which is proportional to the neutron cross section, is dominated by a single resonant mode.

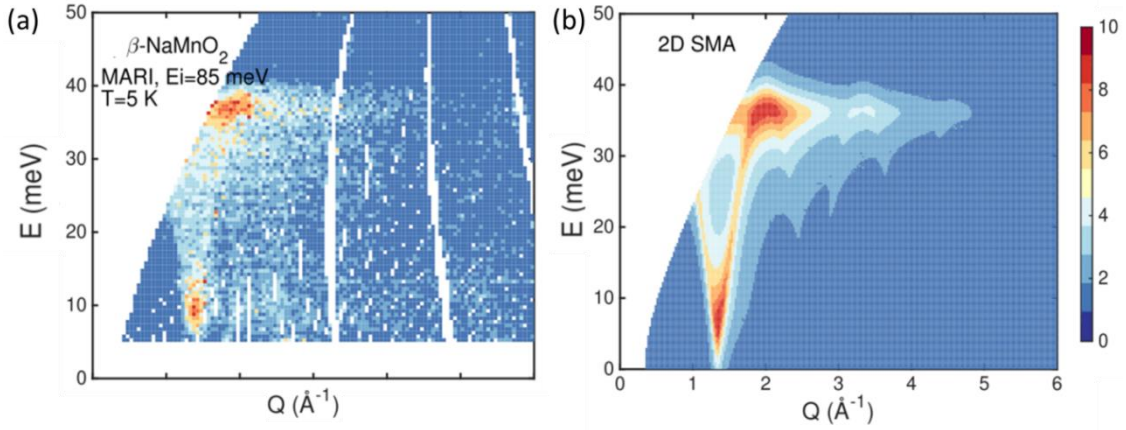


Figure 4-21 (a) The powdered averaged magnetic scattering in  $\beta$ -NaMnO<sub>2</sub> and (b) the corresponding Single Mode Approximation (SMA) heuristic model, with two-dimensional (2D) interactions. Color map: indicates the powder average scattering intensity  $\bar{I}(\vec{Q}, \hbar\omega)$ . Reprinted from reference 19

In order to derive a parameterization of the neutron cross section,  $S^{aa}(\vec{Q}, \hbar\omega) = S(\vec{Q}) \delta(\hbar\omega - E(\vec{Q}))$  (delta function being numerically approximated by a Lorentzian with the energy resolution width), an expression for  $S(\vec{Q})$  should be found. For this, the Hohenberg-Brinkmann first moment sum rule has been applied. [156] This is valid for the case of isotropic exchange and is closely related to the ground state magnetic energy. Effectively the first moment sum relates  $S(\vec{Q})$  to the dispersion  $E(\vec{Q})$  through the following expression:

$$S(\vec{Q}) = \frac{\hbar \langle \omega \rangle}{E(\vec{Q})} = -\frac{1}{3} \frac{1}{E(\vec{Q})} \sum_d J_d \langle \vec{S}_0 \cdot \vec{S}_d \rangle (1 - \cos(\vec{Q} \cdot \vec{d})) \quad (4-5)$$

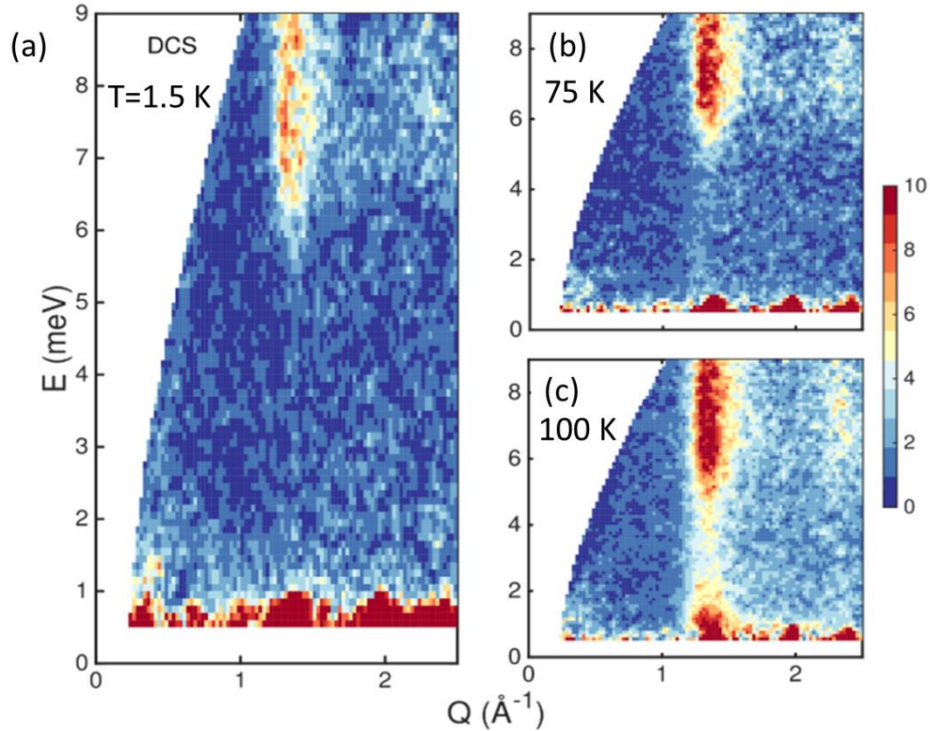


Figure 4-22 The temperature dependence of the low-energy magnetic fluctuations in  $\beta$ -NaMnO<sub>2</sub>, measured on the high-resolution DCS spectrometer. All data has been corrected for a temperature independent background using the detailed balance relation. Color map: indicates the powder average scattering intensity. Reprinted from reference 19

With this, the single-mode approximation and parameterization of the dispersion,  $E(\vec{Q})$ , helps determine the dimensionality of the excitations and the significance of correlations. In particular, the energy gap in a powder averaged constant- $Q$  scan is sensitive to the dimensionality of the interactions. This fact will be further discussed in the 4.9 section of the present chapter.

## 4.8 Magneto-electric response

The structural complexity of the  $\beta$ -NaMnO<sub>2</sub> was found to be strongly correlated to the long-range magnetic order revealed by the neutron experiments. As complex physical properties might result from the interplay of charge, spin, orbital degrees of freedom over the lattice, a key question here is if the compositionally modulated nuclear structure and magnetic order in  $\beta$ -NaMnO<sub>2</sub> might induce some degree of coupling between magnetic and electric degrees of freedom and whether this could be “engineered” when one goes from one polymorph to another.

Preliminary evidence for such a type of behavior in  $\beta$ -NaMnO<sub>2</sub> was first reported by Bakaimi et al. who demonstrated that the temperature-dependent dielectric permittivity,  $\epsilon'(T)$ , displays two small anomalies, near the  $T_{N1}$  and  $T_{N2}$  transitions discussed here.[146] Since the explanation of possible magnetoelectric coupling needs the understanding of the crystal and magnetic symmetries, these early findings remained unexplored. Now that these structures are known, through the current work, it is worth revisiting the coupling of the afore-mentioned properties.

In view of this, a series of dielectric and magnetodielectric measurements have been performed on  $\beta$ -NaMnO<sub>2</sub> system.

#### 4.8.1 Experiment and sample preparation

The dielectric and magnetodielectric measurements of  $\beta$ -NaMnO<sub>2</sub> along with the rest of the specimens of Na-Mn-O system examined in this study have been held in two different set ups:

1) The one has been the custom made, in-house MD station which has been modified as a part of the present thesis. In this station the temperature range allowed measurements down to 79 K due to the use of liquid Nitrogen (N<sub>2</sub>) as cryogenic and under the range of an external dc magnetic field up to 7 T. The frequency of the Ac voltage applied on the sample would vary from 111 Hz – 1 M Hz employing 2 different instruments for low and high frequency areas, the AH 2700A Ultra-precision Capacitance Bridge, for relatively low-frequencies (50 Hz - 20 kHz) and an Agilent LCR, for the high-frequency region up to 1 MHz.

2) The second set up has been a commercial 14 T PPMS platform located in Laboratory for Magnetic Measurements (LaMMB - MagLab) at the Helmholtz-Zentrum Berlin which allowed temperature ramps down to 10 K and served as a reference set up for the modifications made in the local MD station. Instead of an LCR meter, a Solatron 1260 Impedance/Gain Phase Analyser has been employed which is being used together with a 1296A Dielectric Interface System in order to cope with ultra-low capacitance levels. Both set ups had been tailored for dielectric constant measurements in a capacitor-like topology. In this section the studies of dielectric permittivity are presented as an expanded study to the previously published work by Bakaimi et. al. [146]

The dielectric permittivity of  $\varnothing$  5 mm pellets of pressed polycrystalline powder of  $\beta$ -NaMnO<sub>2</sub> has been studied under different external stimuli (test signal AC voltage, DC



voltage (DC bias), DC magnetic field) and in a range of temperatures 10 K- 320 K depending on the used set up. The characterization protocol that has been followed for each sample includes the following steps: measuring the temperature dependence of the dielectric permittivity  $\epsilon'_r(T)$  under zero magnetic field in different frequencies of the AC electric field applied through the test signal and followed by measurements under the application of a dc magnetic field in selected frequencies. Changes on the AC electric stimuli (test signal voltage) as well as applying a DC bias across the sample appeared not to cause an effect on the observed features of the dielectric permittivity  $\epsilon'_r(T)$ .

For the dielectric and magnetoelectric characterization the  $\beta$ -NaMnO<sub>2</sub> powders have been pelletized again using a handheld press in smaller pellets of  $\varnothing$  5 mm. The powders of beta have been hard to be prepared as firm pellets. The pelletizing conditions have been found to be best for  $m \approx 87$  mg, pelletized under 22 Nm for 60 min. These conditions resulted in pellets of 75 mg and thickness of  $\sim 1$  mm. There were prepared specimens with or without electrodes. As electrodes, have been used conductive pastes such as silver paste, carbon paste and in some cases sputtered gold. The measurements have been held on both “as made” specimens synthesized following the protocol described in section 3.2.1.2 and also on specimens that suffered an extra annealing at 300 °C under O<sub>2</sub> atmosphere after being pelletized.

As mentioned in experimental section of chapter 2 the determination of the dielectric permittivity was made by measuring the capacitance of the sample. The selected function on the LCR meter has been the Cp-D function which is appropriate for low capacitance measurements (Appendix A). [157] The protocol followed for each measurement of the capacitance has been cooling the sample under zero electric and magnetic field (ZFC) down to 10 K (or the lowest possible temperature below a known magnetic transition point). Then, measure capacitance upon heating with 2K/min rate up to 220K or above, while measurement points were taken every 0.05 K by applying an AC voltage across the sample during the warm up. Knowing the dimensions of the pellet ( $\varnothing$  5 mm, and thickness  $\approx 1$  mm) the dielectric permittivity  $\epsilon'_r(T)$  was calculated from the equation (2-8)

$$\epsilon'_r = \frac{C \cdot d}{\epsilon_0 \cdot A}, \quad D = \tan\delta = \frac{\epsilon''_r}{\epsilon'_r} \quad (4-6)$$

while the dissipation factor has been directly measured by the instrumentation in mode Cp-D.



Compared to the study of Dr Bakaimi, the present project studied the behavior of the  $\epsilon'_r$  (T) in a temperature range down to 10 K with faster point selection rate due to improvements on the in-house MD station and the employment of a Helium cooled PPMS standard system. This fact gave the advantage of observing for the first time a feature developed below 45 K which is the temperature of the transition to a AFM state of the  $\alpha$ -NaMnO<sub>2</sub>. Apart from that, the improved temperature control allowed for a better repeatability of results and the detection of artifacts caused by a non-linear temperature ramp. In the present project, the feature that is mainly discussed in the work of Dr Bakaimi at 95 K, is only detected in samples annealed in O<sub>2</sub> and not in as synthesized  $\beta$ -NaMnO<sub>2</sub> samples. Although our findings in respect with the origin of the mutually observed features are in agreement with the previous study, the application of an external magnetic field was found to cause no effect on the feature observed in 95 K but only in the low temperature (45 K) effect which is attributed to the percentage of alpha phase in samples synthesized as  $\beta$ -NaMnO<sub>2</sub>.

#### 4.8.2 Dielectric permittivity of $\beta$ -NaMnO<sub>2</sub> “as made”

In figure 4-23 the T-dependency of the dielectric permittivity  $\epsilon'_r$  (T) is measured from 10 K to 220 K. This is the first time that dielectric measurements have been held down to 10 K allowing the observation of effects while being well in the magnetically ordered state of the  $\beta$ -NaMnO<sub>2</sub> as the later has been defined by the neutron diffraction study. The protocol that has been followed is the one described earlier starting with a ZFC down to 0 K while a test signal level of  $V_{rms} = 714$  V and  $f = 111$  Hz is applied upon heating. The general trend that is observed is the increase of the value of the dielectric constant  $\epsilon'_r$  (T) with the increase of temperature. The shape of the  $\epsilon'_r$  (T) curve points out two features: A weak feature in the low temperature area  $\sim 50$  K and a broader hump in the high temperature area  $< 200$  K. Both are more pronounced in the Dielectric Loss curve as presented on the right axis of the graph. The Dielectric Loss “G” in this case is expressed in nanosiemens ( $nS = 10^{-9} S$ ). The Dissipation factor used in the Cp-D mode which is equal to the dimensionless  $\tan\delta$  is connected to the “G” Dielectric Loss through the following formula  $G = 2 \pi C_p D$ . [158]



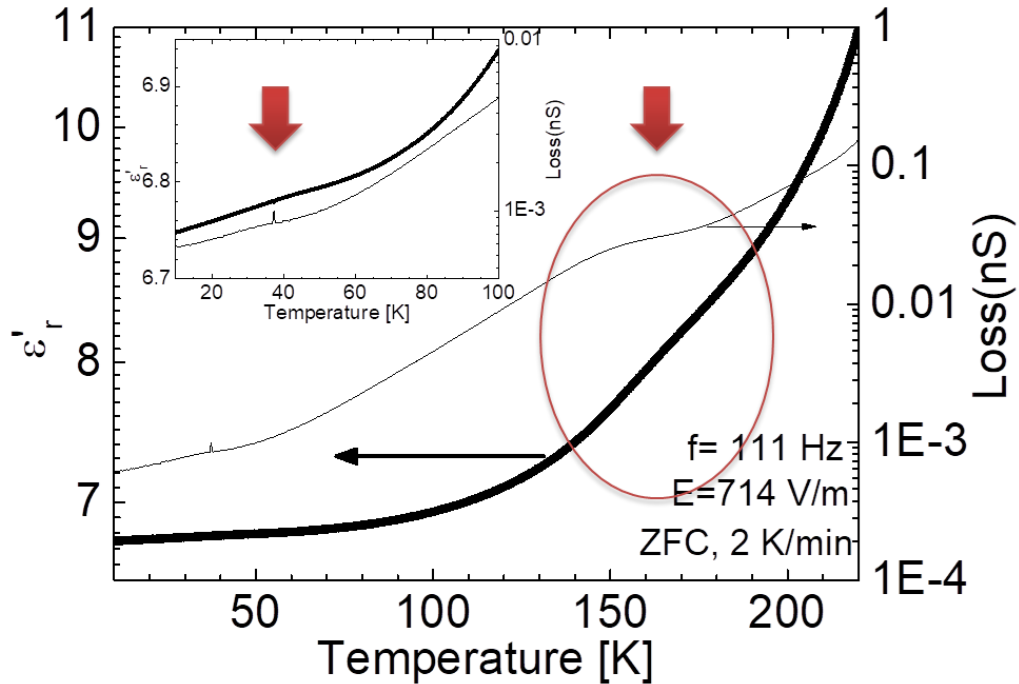


Figure 4-23 Dielectric constant ( $\epsilon'_r$ ) (black symbol-left Y-axis) and dielectric loss (black thin line-right Y-axis) of  $\beta$ -NaMnO<sub>2</sub> measured with a ZFC protocol at 111 Hz, applying 714 V/m upon heating. The inset on the  $\epsilon'_r$  (T) shows the weak feature observed below 50 K assigned to the  $\alpha$ -phase.

The magnitude of the measured dielectric constant is about  $\sim 6$ -7 at low temperature area for both low and high frequencies (figure 4-24) while the magnitude near room temperature varies depending on the frequency. However the values of the dielectric constant may vary slightly on different samples under test which is mostly because of poor electrical contact between the sample and electrodes either due to the chosen contacting paste or due to the topology chosen for the measurement (wired or capacitor topology, section 2.4.3.2). The value of dielectric constant of  $\beta$ -NaMnO<sub>2</sub> is rather small compared to other multiferroics systems of the ABO<sub>2</sub> family where the transition metal is Fe. In these cases the dielectric constant values vary from  $\epsilon'_r \sim 27$ -28 for AgFeO<sub>2</sub> [72] and  $\epsilon'_r \sim 20$  for CuFeO<sub>2</sub> [75] to  $\epsilon'_r \sim 8$  for NaFeO<sub>2</sub> [74]. On the other hand for the triangular lattice antiferromagnets ACrO<sub>2</sub> (A=Cu, Ag, Li, Na) the magnitude of the  $\epsilon'_r$  varies between  $\epsilon'_r \sim 6$ -8.

Talking about the Loss, in this case it is presented in nanosiemnes by measuring conductance “G”. conductance is related to the intrinsic property of conductivity with the following relation:

$$\sigma = G \frac{l}{A} \quad (4-7)$$

Where,  $l$  is the distance between the two flat surfaces of the sample and  $A$  the area of the surface. Generally, when  $\frac{\sigma}{\omega \epsilon'} \ll 1$  (4-8) we consider the compound to be a low-loss dielectric. In the present case at 200K in  $f=1$  kHz, we measure a  $\epsilon' = 11$ , and  $G=0.1$  nS which gives combining equations 4-7 and 4-8:

$$\frac{\sigma}{\omega \epsilon'} = 1.5 \times 10^{-12} \ll 1$$

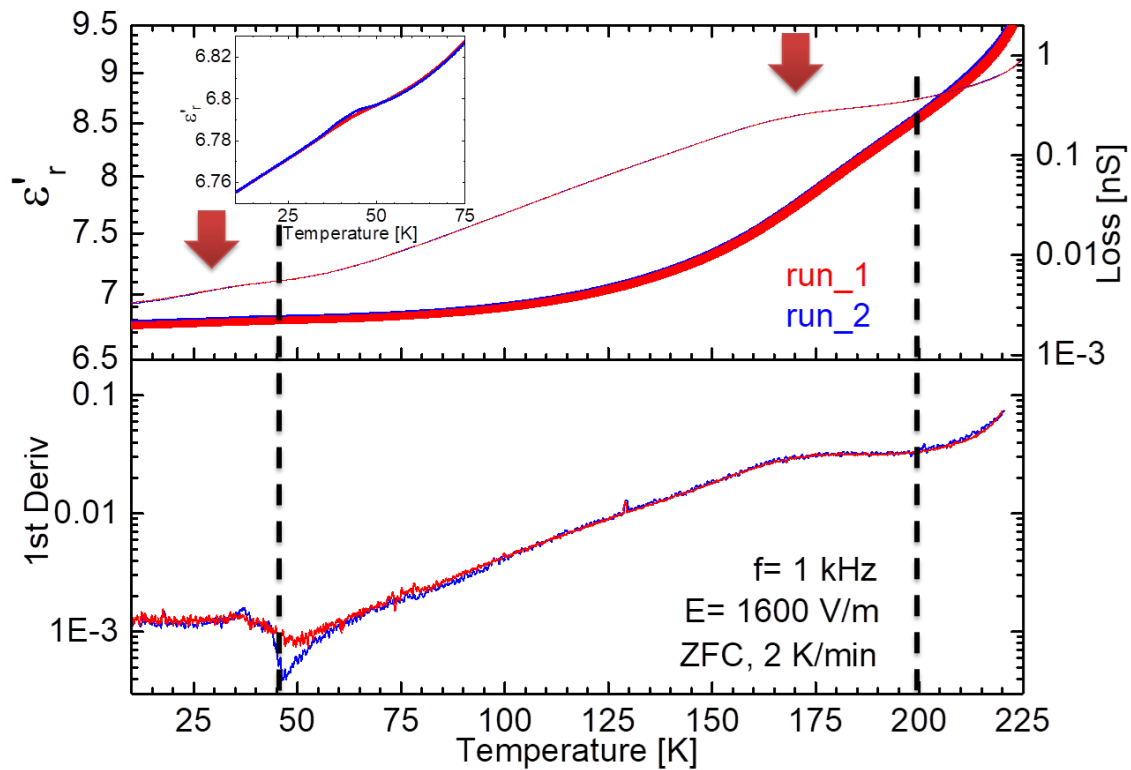


Figure 4-24 Two different runs of Dielectric constant measured at 1 kHz with  $V_{rms} = 1600$  V/m. (Top panel) The two different runs are taken with 7 hours distance while measurements in other frequencies were taken. Inset- low temperature effect is almost not changed. (Bottom panel) 1<sup>st</sup> derivative curves calculated from dielectric constant against temperature for run1 (red) and run2 (blue).

In order to test repeatability of the results each frequency was taken more than once. In figure 4-24 the run 2 (in blue) is taken 7 hours after run 1 (in red) and after several runs in higher frequencies. It is worth noting that the feature in high temperature is not affected at all while the one in the lowest temperature range seems slightly enhanced (figure 4-24 inset). The origin of this may be polarization of the sample by the intermediate runs. The



difference is more pronounced in the calculated 1<sup>st</sup> derivative of  $\epsilon'_r(T)$  over temperature (figure 4-24 bottom panel).

The calculation of the 1<sup>st</sup> derivative presented in figure 4-24 (bottom panel) allows the determination of the exact temperatures where the features start to evolve. In the case of the high temperature range the temperature coincides with the  $T_{N1}$  temperature of the magnetic transition to the AFM commensurate phase of  $\beta$ -NaMnO<sub>2</sub> as defined by the NPD work. This broad hump decays smoothly until 45 K. There, a clear dip in the 1<sup>st</sup> derivative supports the appearance of the weak hump indicated in the main  $\epsilon'_r(T)$  curve. As described earlier in this chapter, the complex structural model that has been adopted for the description of the neutron profile of  $\beta$ -NaMnO<sub>2</sub> comprises of  $\alpha$ -NaMnO<sub>2</sub> regions that are entailed inside the average Pmmn phase. The existence of a percentage of alpha phase in the form of stacking faults [126], [147] which was already witnessed as an impurity in the bulk XRPD pattern, justifies the presence of a feature in 45 K, the AFM transition temperature of the bulk  $\alpha$ -NaMnO<sub>2</sub>. Consequently, both features observed, appear to be correlated to changes in the magnetic structure and are possibly spin driven.

#### 4.8.2.1 *Effect of frequency on the dielectric permittivity*

The effect of frequency on the magnitude of the capacitance and thus of the dielectric constant has been explored with a series of measurements in both low and high frequency areas. The frequency of the Ac test signal that is applied on the specimen under test is expected to have an effect on the value of the dielectric constant since it is connected with the capacitance through the following formula:

$$C = \frac{1}{2\pi f X_c} \quad (4-7)$$

where  $C$  is the Capacitance (F),  $f$  is the frequency (Hz) of the applied ac voltage and  $X_c$  ( $\Omega$ ) is the reactance. Figure 4-25 shows the  $\epsilon'_r(T)$  of  $\beta$ -NaMnO<sub>2</sub> sample measured at  $f=$  111 Hz, 1 kHz, 20 k Hz, 100 kHz, 500 k Hz and 700 k Hz. As the frequency increases, the  $\epsilon'_r(T)$  is expected to decrease according to the aforementioned equation. However the decrease in the frequency range up to 10<sup>6</sup> Hz is not expected to be significant for a capacitance of low magnitude since such a small “capacitor” is quickly charged. In particular, for frequencies up to 10<sup>4</sup> Hz the  $\epsilon'_r(T)$  appears to decrease as a whole. It is worth noting that the feature on the high temperature range is being smeared out to completely disappear in frequencies up to 800 kHz (figure 4-19, see area in gray dotted circle). A similar behavior has been seen in the relaxor ferroelectric Sr<sub>0.8</sub> B<sub>0.2</sub>NbO<sub>6</sub> [159] where strong shifts of the broad features were



found to obey the Vogel-Fulcher law while being softened. In several transition metal oxide systems the frequency dependence of effects in the dielectric permittivity is often correlated to contact effects[103], [160] or interface phenomena caused by the grain size.[160] In such systems colossal dielectric permittivity is observed. [161] As already commented in chapter 2 during the measurements different conductive pastes and topologies have been used giving rise to such artifacts. However measurements on samples with no conductive paste proved the intrinsic character of the effect in the area below 200 K. On the same side, in CdCr<sub>2</sub>S<sub>4</sub> [162] the flank of the hump in the high temperature area which follows a Curie-Weiss like law is claimed to be an intrinsic effect.

Moving in lower temperature, the feature developed at 45 K which is attributed to the alpha phase intergrowth is not affected by the frequency.

The patterns presented in figure 4-26 show clearly the trend of a decreasing magnitude of dielectric constant with the increase of frequency for the  $\beta$ -NaMnO<sub>2</sub>. The “offset” that is observed between the set of the low frequencies on the left panel (a, c) to the high frequency set on the right panel (b, d) is because of the change in the used instrumentation and the different cabling. The same offset is to be observed also in figure 4-25 for the  $\epsilon'_r(T)$  curve measured in 100 kHz, 500 kHz and 800 kHz.



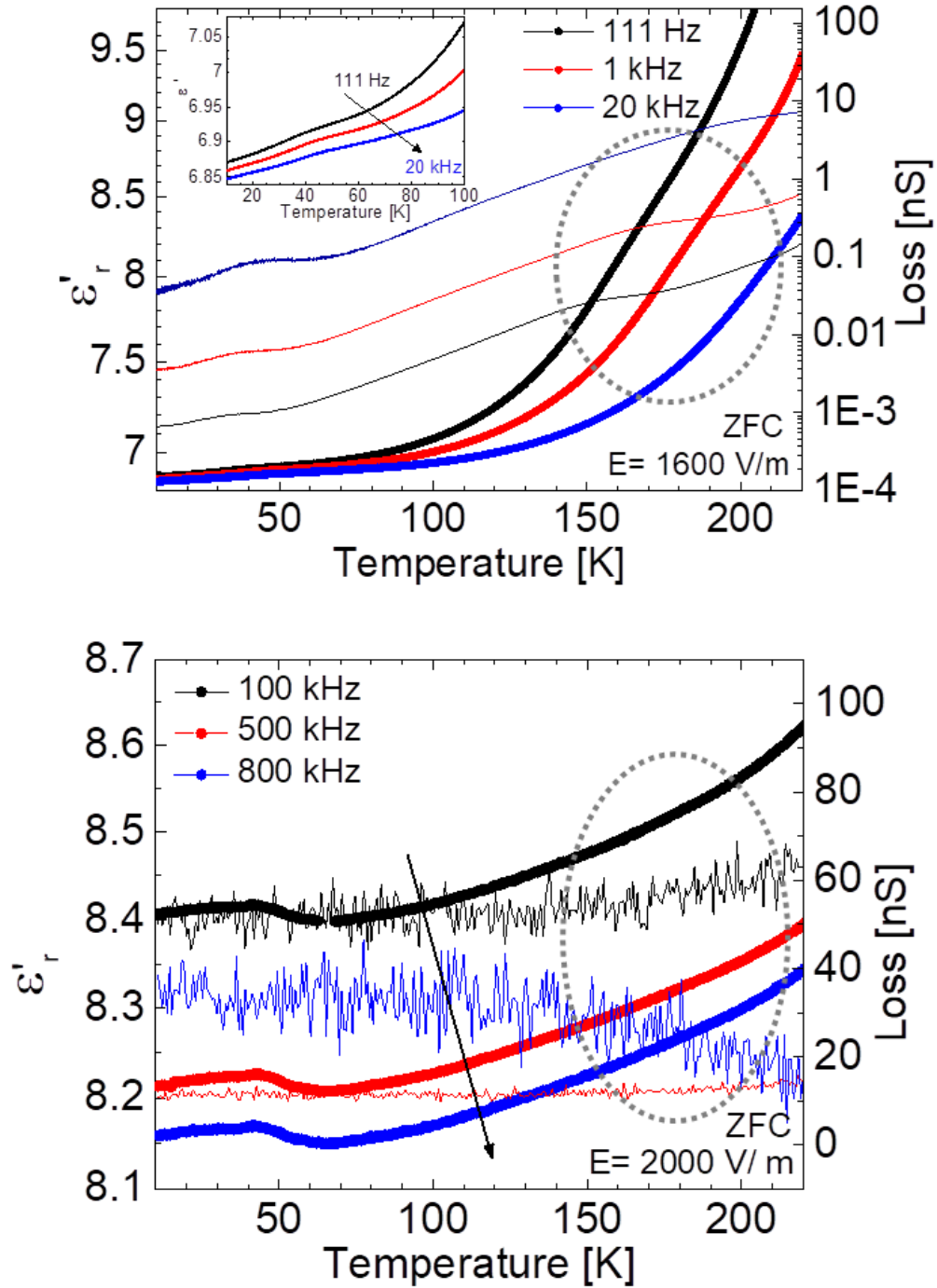


Figure 4-25 Dielectric constant and dielectric loss of  $\beta$ -NaMnO<sub>2</sub> measured at low and high frequency area. (Top panel) Low frequencies measured are 111 Hz, 1 kHz, 20 kHz and (bottom panel) high frequencies are 100 kHz, 500 kHz and 800 kHz. Inset shows the low temperature feature. The two different frequency ranges were measured using different instrumentation.

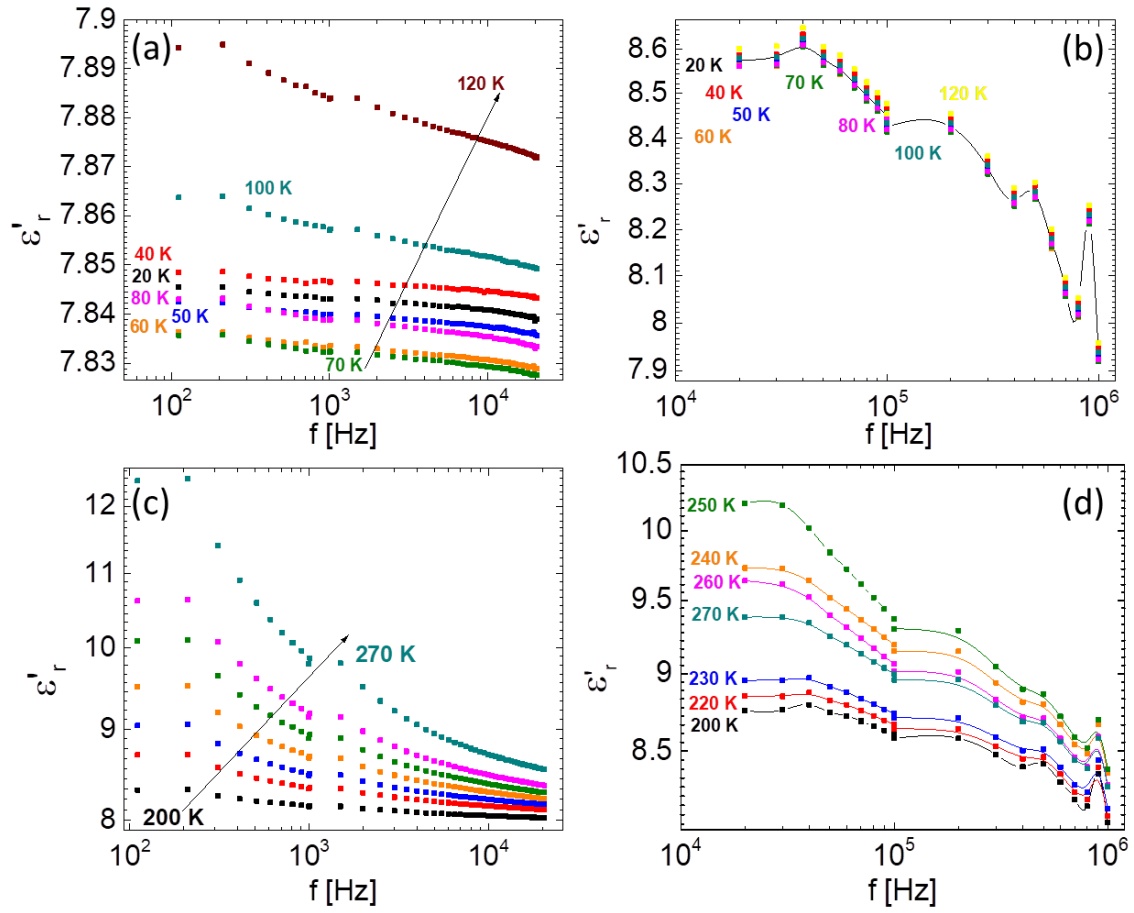


Figure 4-26  $f$ -scan of  $\epsilon'_r(T)$  from 111Hz up to 1 MHz. (a-b)  $f$ -scan for low temperatures (a) 111Hz- 20 kHz and on the right panel from (b) 30 kHz- 1 MHz are presented. (c-d)  $f$ -scan for high temperatures. The two frequency ranges were taken using different instrumentation and this is reason of the offset on the value of the dielectric constant. Nevertheless, the trend is that the magnitude of the  $\epsilon'_r(T)$  is decreasing with the increase of frequency.

#### 4.8.2.2 Ac-electric field effect

The Vrms value of the ac test signal applied by the LCR is known to affect the efficiency of the final result for capacitance values of  $\geq 100$  pF measured in frequencies above 1 kHz. This is because many LCR meters don't have the capability of supplying enough current to the sample under test at 1KHz and 1 Vac. This could be corrected by using the ALC (Automatic level correction) function that raises the applied voltage to the set value. However, for capacitance values as the ones measured in the present project that are  $\leq 100$  pF, the supplied current is usually sufficient and the applied Ac voltage could affect the value of the dielectric constant. The mechanism behind is the displacement of the electron cloud (polarization) of the dielectric due to the voltage applied. For higher permittivity

materials the charges are more easily displaced (more easily polarized). In the case of low permittivity as in the case examined very high voltage is necessary in order to cause sufficient polarization unless the thickness of the dielectric is very small. However the ALC function has been used to be on the safe side. It is worth noting, that minor changes in the actual magnitude of the  $\epsilon'_r(T)$  and no effect of enhancement or suppression on the effects has been observed (figure 4-27) in the tested samples.

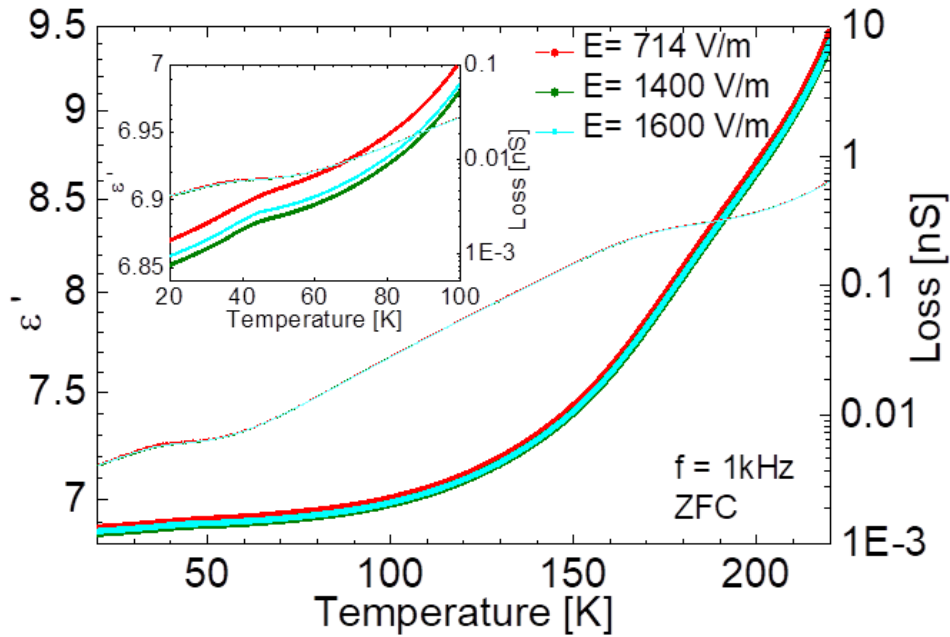


Figure 4-27 The  $\epsilon'_r(T)$  of a  $\beta$ -NaMnO<sub>2</sub> sample measured at 1 kHz under increasing  $V_{rms}$  of the ac test signal. No significant enhancement of the feature has been observed.

#### 4.8.2.3 Effect of magnetic field

In the present study the feature in the temperature area below 100 K that is detected in the work of Dr Bakaimi is not observed in the as made (or as synthesized) samples and it is worth mentioning that all effects on the  $\epsilon'_r(T)$  profile are “qualitatively” different (less sharp) probably because of the different temperature control during the ramp and the fastest point selection. Nevertheless, the dielectric behavior of the compound has been studied in the presence of magnetic field. The application of several magnetic fields up to 14 T seems to leave the feature hump below 200 K unaffected while the effect in the 45 K seems to be weakly enhanced and slightly shifted to higher temperature.



The whole trend of the  $\epsilon'_r(T)$  curve is presented in figure 4-28 top panel while a close up to the low temperature area is presented in the bottom panel.

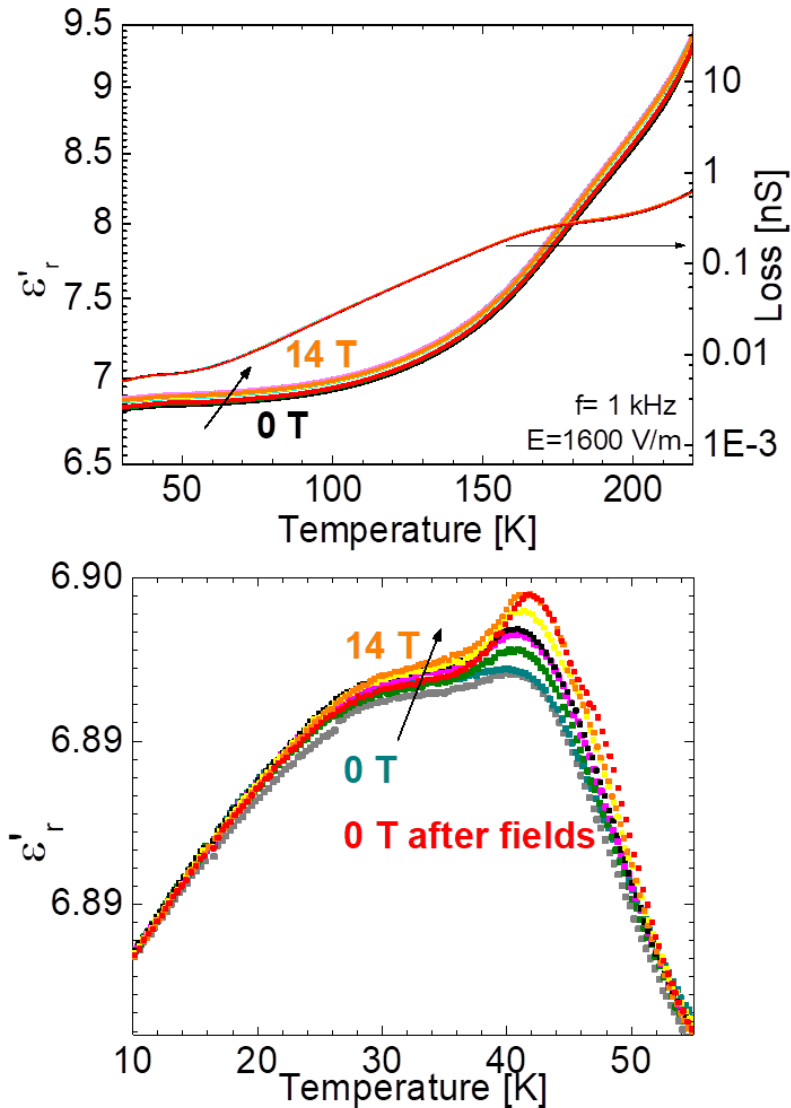


Figure 4-28 Dielectric constant of  $\epsilon'_r(T)$  of  $\beta$ -NaMnO<sub>2</sub>, measured upon heating at 1 kHz under applied magnetic fields from 0 T- 14 T. Top panel: The whole temperature range. Bottom panel: low temperature area of the same measurement zoomed in. The measurement under zero (0 T) magnetic field was carried out twice: first before the application of the magnetic fields, represented with the turquoise and second in red, after the magnetic fields have been applied.

The change of the  $\epsilon'_r(T)$  response under the application of magnetic field below 45 K indicates the presence of a weak magneto-electric effect (MDE) just below the AFM magnetic transition of the  $\alpha$ -NaMnO<sub>2</sub>. The relative dielectric response ( $\Delta\epsilon'$ (%)) has been calculated for  $H=14$  T at  $T=20, 25, 30, 35, 37, 39, 41, 43, 45, 50,$  and  $55$  K and is plotted in figure 4-24 (black axis-left) for  $f=1$  kHz. The  $\Delta\epsilon'$  (%) is defined as:



$$\Delta\varepsilon'(\%) = \frac{\varepsilon'(H) - \varepsilon'(0)}{\varepsilon'(H)} 100 \quad (4-8)$$

and is plotted against temperature to show the temperature dependence of the maximum change of the dielectric constant caused by the applied field of 14 T. According to this the MDE is about 0.033 % at 43 K.

The slight shift of the maximum value of the  $\varepsilon'_r(T)$  with the applied magnetic field is shown in the right-top axes (in red) of the figure 4-29. The general trend shows a shift towards higher temperatures which is not linear. This does not allow any safe conclusion since the increase of the magnetic field has not been taken using equal steps from 0-14 T.

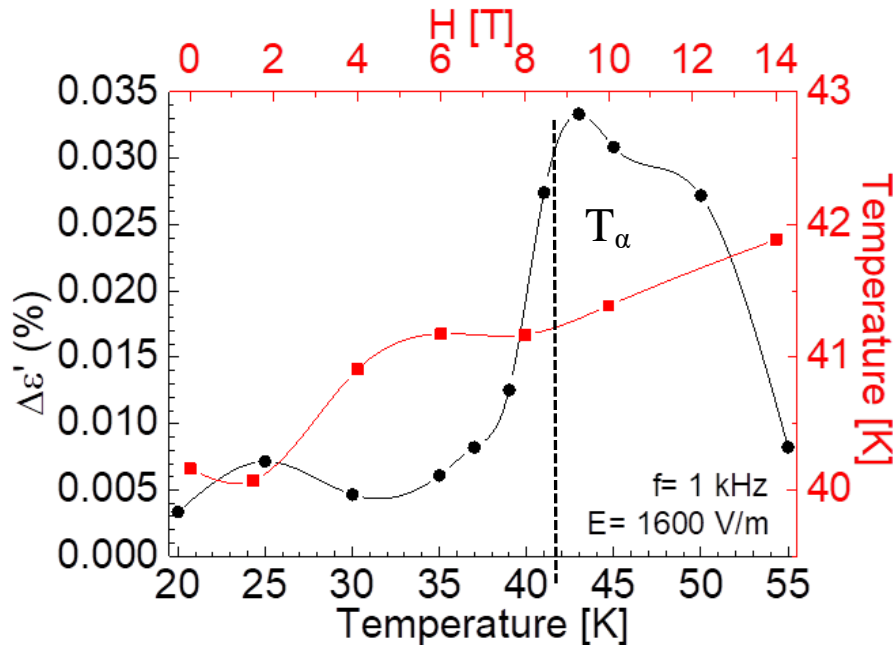


Figure 4-29 Left-bottom axes (black):  $\Delta\varepsilon'$  (%) calculation against Temperature for  $H= 14$  T showing the maximum change in the values of dielectric constant with the application of the external magnetic field. The MDE is of 0.03 % at 43 K. Right-top axes: shift of the critical temperatures  $T_\alpha$  with respect to the applied magnetic fields.  $T_\alpha$  refer to the temperature where the dielectric constant is maximum.

#### 4.8.3 Dielectric permittivity of $\beta$ -NaMnO<sub>2</sub> “annealed in O<sub>2</sub>”

In an attempt to remove internal stresses and make the final specimens more firm, some of the as synthesized or “as made”  $\beta$ -NaMnO<sub>2</sub>  $\varnothing$  5 mm pellets have been annealed at 300°C under O<sub>2</sub> flow. The resulting specimens were found to have an increased percentage of secondary phases of  $\alpha$ -NaMnO<sub>2</sub> and  $\alpha$ -Na<sub>0.7</sub>MnO<sub>2</sub> in comparison to the “as made” ones



which have already been commented in section 4.1. This enriched annealed  $\beta$ -NaMnO<sub>2</sub> specimens were found to present a different profile of dielectric constant  $\epsilon'_r(T)$ . In figure 4-30 the  $\epsilon'_r(T)$  curve of an annealed sample is presented in three different frequencies: 111 Hz, 1 kHz and 20 kHz. The main features observed are the hump below 200 K and a second one developed below 100 K. Both of them are more pronounced in 1<sup>st</sup> the derivative curves (right-axis pointed out with red arrows). The frequency dependence resembles to that of the “as made” samples having the magnitude of the dielectric constant decreased with the increasing frequency and also a slight shift of the maxima in lower temperatures as it is now easily seen through the derivative curves.

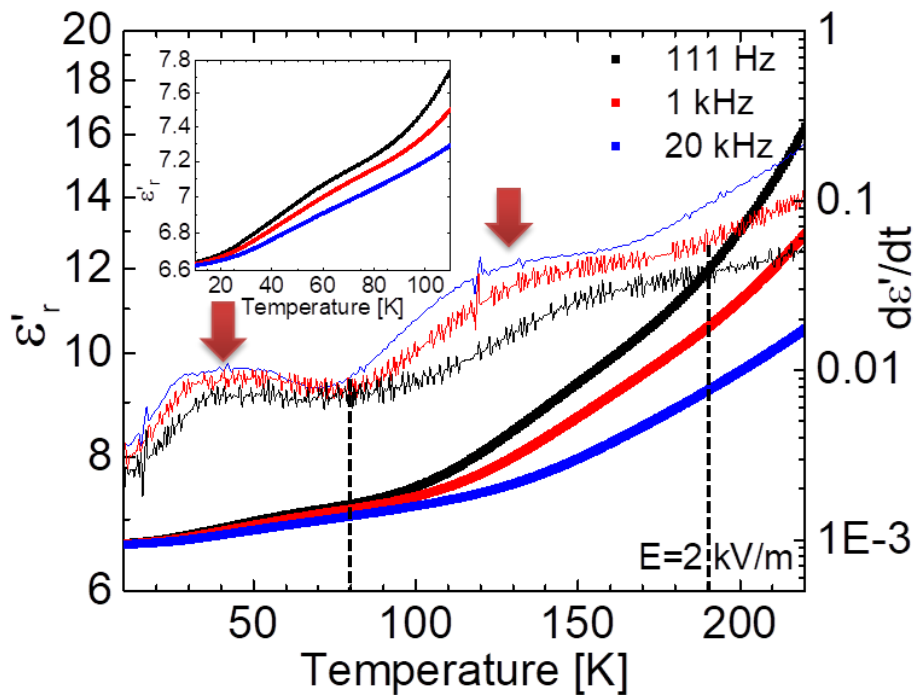


Figure 4-30 right axis: Dielectric constant and dielectric loss of annealed in O<sub>2</sub>  $\beta$ -NaMnO<sub>2</sub> measured at 111 Hz, 1 kHz, 20 kHz. Left axis: 1<sup>st</sup> derivatives of the  $\epsilon'_r(T)$  against T of the same frequencies. The red arrows point the maxima of the features while the dotted vertical lines are a guide to the eye for the Temperature of the change of slope.

In the annealed samples both features seem to soften with the increase of frequency. The general trend of a decreasing dielectric constant against increasing frequency remains the same. In figure 4-31 this trend is presented for temperatures from 10 K up to 120 K with a corrected offset for the different instrumentation (see section 4.8.2.1).



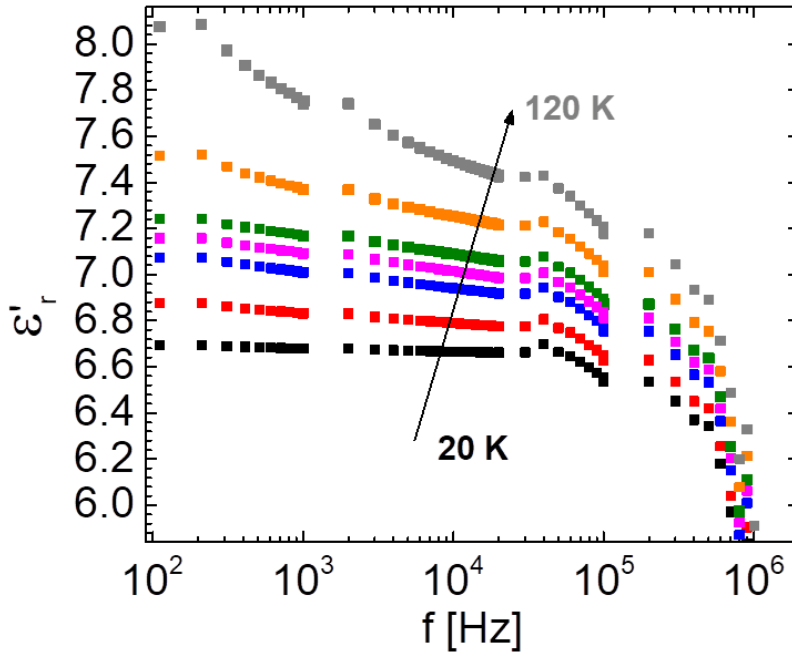


Figure 4-31  $f$ -scan of  $\epsilon'_r(T)$  from 111 Hz up to 1 MHz for low temperatures 20-120 K. The two frequency ranges (111-20000 Hz and 30 kHz to 1 MHz) were taken using different instrumentation. In this case the offset on the value of the dielectric constant has been corrected.

#### 4.8.3.1 Effect of magnetic field

After understanding the evolution of the crystal and magnetic symmetries in  $\beta$ -NaMnO<sub>2</sub>, the magnetocapacitance of  $\beta$ -NaMnO<sub>2</sub> has been revisited after the published work of Dr Bakaimi.[146] In the aforementioned study the two main features detected were observed in the temperatures where, as stated earlier, the collinear commensurate AFM state ( $T_{N1}=200$  K) and a cooperative proper-screw magnetic state ( $T_{N2}=95$  K) were established. Such complex spin configurations could be the reason for the emergence of coupling that may lead to magnetoelectricity in frustrated magnets, through competing interactions developed in the nuclear and magnetic lattice interface. [163], [164]

The present findings in the annealed  $\beta$ -NaMnO<sub>2</sub> specimens are in agreement with both features that have been detected earlier. However, the small enhancement in the feature observed below 95K under the application of magnetic field didn't come to our attention. The data presented in figure 4-32 are free of noise and it is crystal clear that there is no evidence of an effect of the applied magnetic field on the value of the dielectric constant or the shape of the features detected. It is worth noting that the applied field has been of 1.5 T and 4 T to be compared with the previous study.



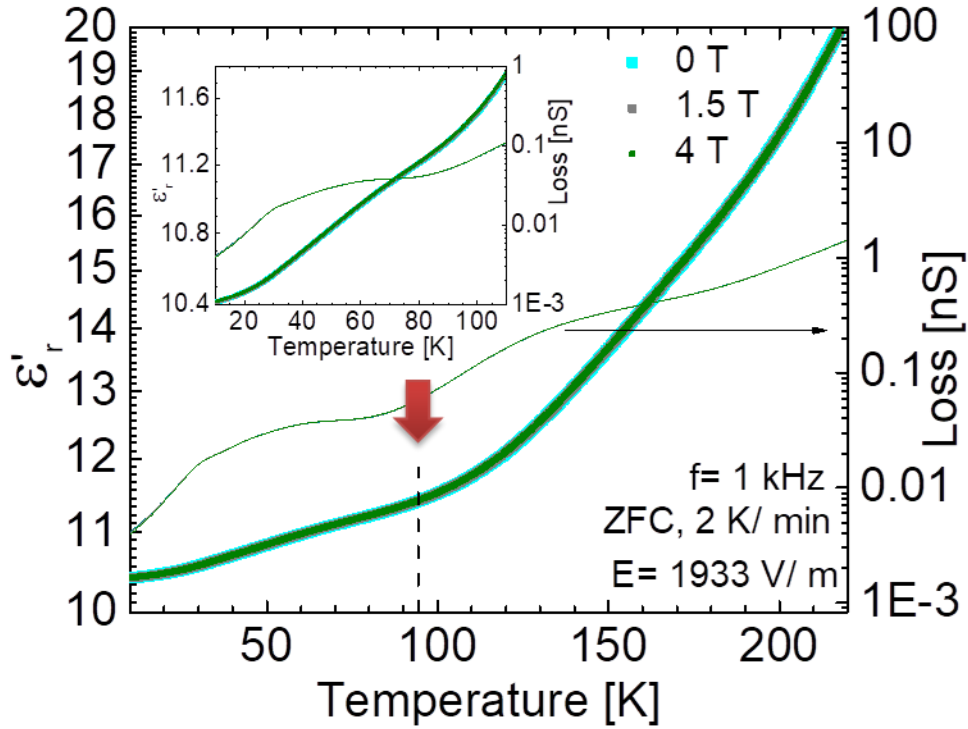


Figure 4-32 Dielectric constant of  $\epsilon'(T)$  of annealed  $\beta$ -NaMnO<sub>2</sub> measured upon heating at 1 kHz under applied magnetic fields from 0-4 T. Inset shows a close up to the low are feature developed below 100 K.

Taking a look at the origins of coupling, it is well accepted that the coupling between electric polarization (P) and magnetization (M) is governed by the symmetries of these two order parameters. [63] For a magneto-electric material [165] the Ginzburg-Landau thermodynamic potential, can take the general form:

$$F(\vec{E}, \vec{H}) \approx \epsilon_{ij}(T) \vec{E}_i \cdot \vec{E}_j + \mu_{ij}(T) \vec{H}_i \cdot \vec{H}_j + \alpha_{ij} \vec{E}_i \cdot \vec{H}_j + \frac{1}{2} \beta_{ijk} \vec{E}_i \cdot \vec{H}_j \cdot \vec{H}_k + \frac{1}{2} \gamma_{ijk} \vec{H}_i \cdot \vec{E}_j \cdot \vec{E}_k + \frac{1}{2} \delta_{ijkl} \vec{E}_i \cdot \vec{E}_j \cdot \vec{H}_k \cdot \vec{H}_l \quad (4-9)$$

This can be re-written for the specific case of the  $\alpha$ - and  $\beta$ -NaMnO<sub>2</sub> by taking into consideration symmetry-controlled rules, and in particular the constraint arising from their magnetic point groups,  $-1$  and  $2'/m'$ , respectively. As the magnetic ground states of both  $\alpha$ - and  $\beta$ - phases are centrosymmetric spatial inversion symmetry is not violated and therefore, spontaneous electrical polarization is not anticipated in their magnetically ordered states. However, the present T-dependent dielectric permittivity experiments,

$\varepsilon'_r(T)$ , have identified small, resolvable features in both zero- and field- dependent measurements. These occur at temperatures where the magnetic phase transitions take place, namely, below about  $T_{N3}= 45$  K in the case of  $\alpha$  (found also in “as made” samples of  $\beta$ -NaMnO<sub>2</sub>, figure 4-28), below about  $T_{N2}= 95$  K and below  $T_{N1}= 200$  K in the case of  $\beta$ -phase (annealed samples of  $\beta$ -NaMnO<sub>2</sub>, figure 4-32). The maxima in  $\varepsilon'_r(T)$  infer that they are driven by the onset of antiferromagnetic order taking place in each polymorph and the proper screw spin configuration developed below 95 K as a relief of the magnetic frustration in the  $\alpha$ -like sheets that in turn influences the ordering in the  $\beta$ -like stacking. In addition to that, they also point to weak magnetocapacitance effects in the case of the feature in  $T_{N3}=45$  K, as the peaks change very little despite the strength of the externally applied magnetic field (figure 4-28).

Considering the symmetry-constrained free energy for  $\alpha$ - and  $\beta$ - phases, namely:

$$F(\vec{E}, \vec{H}) \approx \varepsilon_{ij}(T) \vec{E}_i \cdot \vec{E}_j + \mu_{ij}(T) \vec{H}_i \cdot \vec{H}_j + \frac{1}{2} \gamma_{ijk} \vec{H}_i \cdot \vec{E}_j \cdot \vec{E}_k + \frac{1}{2} \delta_{ijkl} \vec{E}_i \cdot \vec{E}_j \cdot \vec{H}_k \cdot \vec{H}_l \quad (4-10)$$

it is postulated that the observed features in the dielectric constant and the magnetic field dependence is likely to be related to the non-linear [163] quadratic and bi-quadratic terms. This claim is based on the magnetic point group and indicates which coupling tensors are allowed by symmetry to be different from zero and would be valid for both homogenous and inhomogeneous states. Regarding the interface between the two sequences this may break the inversion symmetry but since the superspace point group maintain the inversion symmetry another interface in the system will have opposite polarity and the material will be non-polar.

Such higher-order magneto-electric couplings are operative in planar magnets, as for example the NiSO<sub>4</sub> · 6H<sub>2</sub>O [84] and the fluorite compound BaMnF<sub>4</sub>, [166] where the linear quadratic term is dominant even well above their Néel ordering transitions. It is also worth noting that the bi-quadratic term as in the case of EuZnO<sub>3</sub> [167], which is not limited by symmetry, gives rise to small anomalies in the dielectric constant, as in the cases of the YMnO<sub>3</sub> [66] and BiMnO<sub>3</sub> [168] magnetoelectric perovskites. This behavior, is remarkably similar to the  $\varepsilon'_r(T)$  cusps (Figures 4-28, 4-32) and its correlation to the magnetic ordering in the NaMnO<sub>2</sub> polymorphs.



## 4.9 Discussion

Already from the early in house XRPD experiments the orthorhombic *Pmmn* average structure of the  $\beta$ -NaMnO<sub>2</sub> has been found to host secondary phases of Na-Mn-O system with proven energy proximity. [6], [126], [145] The crystal chemistry of AMeO<sub>2</sub> allows for polymorphism due to oxygen-layer gliding processes[169] that lead to structural transitions and the formation of structural defects between various crystal domains. On the same side extraction of Na through a process of intercalation could lead to structural rearrangements that could extend the hosting domains formed inside the major  $\beta$ -NaMnO<sub>2</sub> phase. In such way it is possible that the annealing process of the as made samples could work. The presence of peaks of secondary phases of  $\alpha$ -Na<sub>0.7</sub>MnO<sub>2</sub> and  $\alpha$ -NaMnO<sub>2</sub> with comparable intensity to  $\beta$ -NaMnO<sub>2</sub> could be a result of structural rearrangements that further modify the expression of macroscopic properties like the dielectric permittivity and magnetocapacitance.

Neutron powder diffraction of  $\beta$ -NaMnO<sub>2</sub> gave a complex profile that could only be modeled through the superspace formalism. [153] The theory of (3 + D) superspace groups, introduced by de Wolff (1974, 1977), [170], [171] is widely used to describe the symmetry of commensurate and incommensurate modulated structures. The results presented in section 4.5 using a single phase superspace symmetry description with a modulated vector  $\mathbf{q} = (0.077(1), 0, 0)$  are in agreement with the previously employed model (modulation vector  $\mathbf{q} = (\alpha 00)$   $\alpha \approx 0.1$ ) which was used for indexing the additional satellite peaks observed in both electron and synchrotron X-ray diffraction data. [126]

However for the determination of the spin configurations in the  $\beta$ -NaMnO<sub>2</sub> the utilization of the modulated structure formalism has only been necessary for the description of the incommensurate-like magnetic ordering that is established below  $T_{N2} \sim 95$  K. In the temperature area below  $T_{N2} \sim 200$  K the magnetic symmetry analysis was well described on the basis of parent average *Pmmn* nuclear. The suggested magnetic structure entails antiferromagnetically coupled Mn-chains running down the  $\mathbf{b}_0$ -axis stacked in a zig-zag pattern when viewed in an  $a_0c_0$ -plane projection that gives rise to antiferromagnetically coupled, corrugated MnO<sub>2</sub> layers (section 4.6). A similar collinear spin-model has been utilized before for the description of the magnetic state in the isomorphous  $\beta$ -LiMnO<sub>2</sub>, where three-dimensional long-range order is established at  $T_N \sim 260$  K. [172]



The derived spin-configuration for  $\beta$ -NaMnO<sub>2</sub>, though, indicates a commensurate ordering only for the Mn2-site, as a similar ordering on the Mn1 site would have generated strong magnetic intensity at the nuclear satellite reflections, a case that is not supported by the NPD data. In this compositionally modulated nuclear structure, between  $100 < T < 200$  K only the NaMnO<sub>2</sub> layer stacking sequences characteristic of the  $\beta$ - polytype carry a net magnetic moment. Such a magnetically inhomogeneous state is consistent with the wipeout of the central <sup>23</sup>Na-NMR line (figure 4-10) and the two-component nuclear spin-lattice relaxation in the same temperature range. The magnetic moment of Mn2 sites has been computed as  $\mu \cong 2.38(10) \mu_B$  at 100 K, but as the observed NPD profile shows fairly broad magnetic peaks, the attained staggered moment may be an underestimate (cf. the full moment for spin-2 Mn<sup>3+</sup> is expected to be  $4 \mu_B$ ).

On the other hand, the incommensurate magnetic structure that is developed below  $T_{N2} \sim 95$  K could be seen as similar to the commensurate one that develops below  $T_{N1}$ , but at the “boundary” of the  $\alpha$ - and  $\beta$ - like stacking sequences (Figure 4-14), as the ordering at the Mn1-site ( $\alpha$ -NaMnO<sub>2</sub> layer stacking sequence) acts as a perturbation to the Mn2-site, the Mn-spins start to rotate away from the commensurate structure type (Figure 4-18). Within this modulated behavior, the Mn<sup>3+</sup> magnetic moment takes the lowest values within the NaMnO<sub>2</sub> layers characteristic of the  $\alpha$ -polytype (likely due to their higher degree of spin-frustration), while it grows in magnitude as we move within the  $\beta$ -like stacking sequences, reaching a maximum,  $\mu \cong 3.5(10) \mu_B$ , at their mid-point. Such a non-trivial magnetic order is in line with very broad distribution of spin-lattice relaxation times found by NMR below  $T_{N2}$ , implying a broad distribution of local environments. This complexity might be an outcome of the system’s effort to relieve competing interactions amongst neighboring spins in the  $\beta$ -NaMnO<sub>2</sub> modulated nuclear structure, therefore requiring further insights on the role of geometric frustration.

Looking for a way to determine the dimensionality of the magnetic excitations and unravel which correlations are of most importance, single-mode approximation and parameterization of the dispersion,  $E(\vec{Q})$  was chosen as a tool. The results presented in section 4.7 reveal the existence of an energy gap of  $\Delta \sim 5$  meV. The fact that the energy gap in a powder averaged constant- $Q$  scan is sensitive to the dimensionality of the interactions was previously used to show that  $\alpha$ -NaMnO<sub>2</sub> is dominated by one-dimensional magnetic correlations.[38]



Comparison of the powder averaged spectra for  $\beta$ -NaMnO<sub>2</sub> against its closely related  $\alpha$ -NaMnO<sub>2</sub> system (Figure 4-33) points to several key differences.

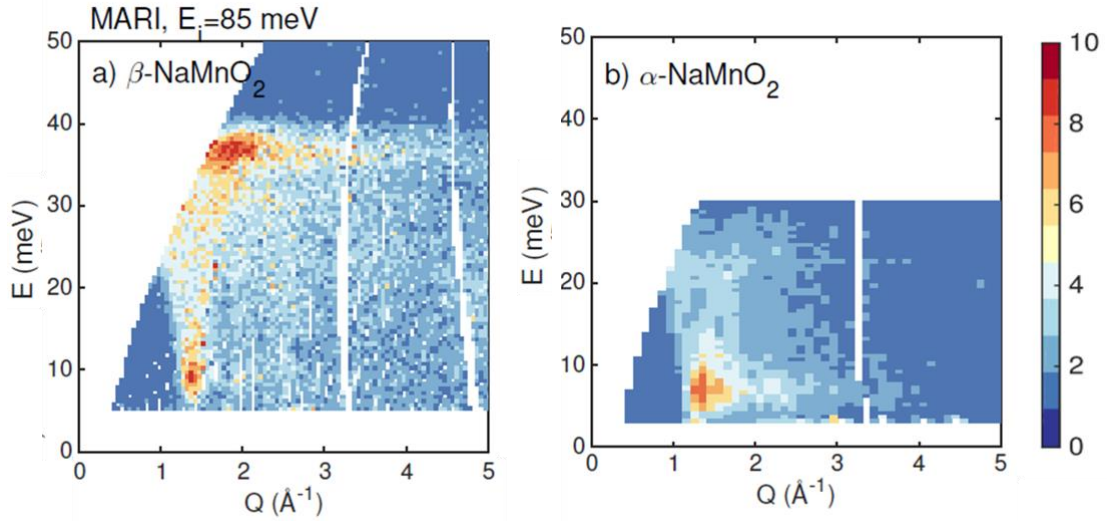


Figure 4-33 The powdered averaged magnetic scattering in (a)  $\beta$ -NaMnO<sub>2</sub> and (b)  $\alpha$ -NaMnO<sub>2</sub>. The background subtraction method to remove phonon scattering and instrument back-ground is described in the main text. Both datasets were taken on MARI with  $E_i = 85$  meV at  $T = 5$  K. Color map: indicates the powder average scattering intensity

First, the spectral weight in  $\alpha$ -NaMnO<sub>2</sub> is concentrated at low energies near the energy gap edge, while it is much more evenly distributed in energy in the case of the  $\beta$ -NaMnO<sub>2</sub> variant. The scattering is also much more strongly peaked in momentum for  $\beta$ -NaMnO<sub>2</sub>, which is indicative of the higher (cf. than the quasi-1D of the  $\alpha$ -phase) dimensionality of the associated spin correlations. In addition, considerable spectral weight is located at the top of the excitation band and the scattering is much more well-defined in momentum than in the  $\alpha$ -polytype. Such qualitative observations, suggest that  $\beta$ -NaMnO<sub>2</sub> may be more two-dimensional than the  $\alpha$ -phase.

In order to simulate the powder averaged spectra by considering the case of the two-dimensional spin-exchange, with dominant correlations along the  $\mathbf{b}_0$ -crystal axis, the dispersion relation in the following phenomenological expression has been used:

$$E^2(\vec{Q}) = B_0 + B_1 \sin^2(\pi K) + B_2 \sin^2(\pi H) + \dots + B_3 [\sin^2(\pi(K + H)) + \sin^2(\pi(K - H))] \quad (4-10)$$

This is consistent with the periodicity of the lattice ( $Pm\bar{m}n$  symmetry) and gives a minimum at half integer positions relating the observed magnetic Bragg peaks. The values

chosen are:  $B_0 = 25 \text{ meV}^2$  to account for the spin-gap ( $\Delta$ ),  $B_1 = B_2 = 625 \text{ meV}^2$  and  $B_3 = 400 \text{ meV}^2$ . To extract an estimate for the exchange constants, the inelastic magnetic response was expressed on an absolute scale using the internal incoherent elastic line as a reference. The absolute calibration combined with the first moment sum rule afforded an estimate of  $J_d \langle S_0 \cdot S_d \rangle$ . Combined with the collinear magnetic structure, we have estimated a strong exchange along the  $\mathbf{b}_0$ ,  $J_1 = 5.0 \pm 1.0 \text{ meV}$  and a weaker one along  $\mathbf{a}_0$ ,  $J_3 = 1.5 \pm 1.0 \text{ meV}$  (Figure 4-1a).

The total integrated spectral weight (elastic and inelastic) is constrained by the zero<sup>th</sup> moment sum rule which can be summarized as follows:

$$\frac{\int d^3q S(\vec{Q}, \hbar\omega)}{\int d^3q} = S(S + 1) \quad (4-11)$$

Integrating the INS data by using the elastic incoherent scattering of the vanadium as an internal standard gives the inelastic contribution to the above integral being 1.8(3). Including the ordered moment in the elastic channel and noting that there are two Mn<sup>3+</sup> ions per unit cell gives a total integral of 4.7(4) for this sum. Given the expected value for  $S = 2$  is 12, this indicates that more than half of total moment resides elsewhere in momentum and energy. One possibility is for a large fraction residing in diffuse scattering, which maybe resulting in a low-energy contribution that is beyond the resolution of the spectrometer. This stays in agreement with the broad shape of the magnetic reflections in the diffraction data and with the high density of structural defects present in the material.

The highly defected nuclear structure of the  $\beta$ -NaMnO<sub>2</sub> polymorph especially when enhanced with the extra annealing under O<sub>2</sub> atmosphere is proven to drive the emergence of coupling effects. If we take a glance through the dielectric response of  $\beta$ -NaMnO<sub>2</sub> and compare it to that of  $\alpha$ -NaMnO<sub>2</sub> as further discussed in chapter 6, the effects on the dielectric constant profile were observed in temperature areas where magnetic orders are established for both alpha and beta polymorph. Bearing in mind that the magnitude of the dielectric permittivity features in  $\beta$ -NaMnO<sub>2</sub> becomes larger with the application of an intense electric field,[146] in the present study we utilized a progressively stronger external magnetic field instead, hoping for enhanced changes in the  $\epsilon'(T)$ . Our dielectric permittivity experiments, however, identified only small anomalies in  $\epsilon'(T, H)$  curves that coincide with the onset of antiferromagnetic orders taking place in the bulk  $\alpha$ - ( $T_N = 45 \text{ K}$ ) and  $\beta$ - ( $T_{N1} = 200 \text{ K}$ ,  $T_{N2} = 95 \text{ K}$ ) phases. The feature hump just below the  $T_N = 45 \text{ K}$  in  $\epsilon'(T, H)$  of  $\beta$ -NaMnO<sub>2</sub> is a signature for contributions from  $\alpha$ - and  $\beta$ - type structural



domains, as local probes have resolved before. [145] The existence of stacking sequences implies the existence of interdomain boundaries or else domain walls as the regions in which the the ordering at the Mn1-site ( $\alpha$ -NaMnO<sub>2</sub> layer stacking sequence) acts as a perturbation to the Mn2-site and the Mn-spins start to rotate away from the commensurate structure type. Studies on delafossites of  $A\text{CrO}_2$  ( $A=\text{Cu, Ag, Li, Na}$ ) prove a correlation between proper screw spin configuration with emergence of multiferroicity. In a so-called “proper screw” the spins rotate in a plane perpendicular to  $\mathbf{Q}$ . Here the inversion symmetry is broken, but most often it does not produce polarization, although in certain cases it might. [49], [164] To our understanding, the magnetoelectric coupling must be weak in both stoichiometric NaMnO<sub>2</sub> materials, as very little changes are brought about despite the strength of the externally applied magnetic field. This arise further thinking of correlation to the complex spin configurations as well as the magnetic inhomogeneities met in the two compounds.

#### 4.10 Summary and Conclusions

The present work entails a thorough study of the crystallographic and dynamical properties of the  $\beta$ -NaMnO<sub>2</sub>. The proposed single-phase nuclear structure model, takes advantage of the superspace formalism to describe the incommensurate compositional modulation (propagation vector,  $\mathbf{q}=(0.077(1), 0, 0)$ ) of the Mn and Na sites that can be depicted as an intergrowth  $\alpha$ - and  $\beta$ - like oxygen coordinations. This peculiar topology strongly influences the physical and chemical properties of the material and underlines the role of the nearly degenerate in energy  $\alpha$  and  $\beta$  layer stacking sequences. The remarkable flexibility of  $\beta$ -NaMnO<sub>2</sub> to adapt its lattice topology is likely at the basis of the particular high charge capacity of the system as a Na-ion cathode material,[129] but also may corroborate to the stability of the various non-stoichiometric phases [145] accessible through its electrochemical Na-intercalation/removal. [120]

Moreover, the magnetic structure of  $\beta$ -NaMnO<sub>2</sub> was solved on the basis of time-of-flight neutron powder diffraction data and found to be strongly mediated by the material’s inherent lattice topology. First, below  $T_{N1}$  (200 K), a collinear commensurate antiferromagnetic state, involving only the  $\beta$ -like stacking sequences, develops with a propagation vector  $\mathbf{k}=(\frac{1}{2} \frac{1}{2} \frac{1}{2})$ . Then, a second magnetic transition is observed at  $T_{N2}$  (95 K), marked by new satellite reflections ascribed to the interaction of  $\mathbf{k}$  with the compositional modulation vector  $\mathbf{q}$ . The new magnetic ordering is due to the relief of the



magnetic frustration in the  $\alpha$ -like sheets that in turn influences the ordering in the  $\beta$ -like stacking sequences, and instigates a cooperative proper-screw magnetic state. Here, the lattice topology of the Jahn-Teller active Mn<sup>3+</sup> cation drives the original 3D spin correlations ( $T < T_{N1}$ ) to become 2D in character. Inelastic neutron scattering and <sup>23</sup>Na NMR provide evidence that a spin-gap ( $\Delta = 5$  meV) opens in the excitation spectra, in line with the 2D nature of the magnetic interactions at  $T < T_{N2}$ .

Overall, structure and dynamics point that the incommensurate  $\beta$ -NaMnO<sub>2</sub> structure can relay a magnetocapacitance effect in the low-temperature magnetic state. Such a structural complexity, inquires whether controlled engineering of coherent defects may impart the material with novel technological capabilities. In view of this, it is worth considering that in the compositionally modulated  $\beta$ -NaMnO<sub>2</sub>, domain-wall (DW)-like phenomena [173] associated with the abundance of the  $\alpha$ - and  $\beta$ - interfaces, rather than extended domains themselves, may be the active element in promoting some degree of topologically correlated (related to DW), cooperative magnetic and electric dipole arrangements. The way electronic structure changes at such interfacial regions could be relevant in order to manipulate the magnetoelectric response [174] even in this class of non-perovskite compounds and warrants further exploration.



## Chapter Five:

# Quest for single crystals in 2 D Manganites:

## $\alpha$ -Na<sub>0.7</sub>MnO<sub>2</sub>

---

### 5.1 Introduction

The first systematic studies on Na<sub>x</sub>MnO<sub>2+ $\delta$</sub>  systems date back to 1970s by Fouassier *et al.* and Parant *et al.*[3], exploring the structure and energy stability of different phases. These structures are three-dimensional tunnel structures at lower x values (x= 0- 0.44) and two-dimensional layered structures at higher x values (x> 0.5). Higher sodium content,  $\alpha$ -NaMnO<sub>2</sub> and  $\beta$ -NaMnO<sub>2</sub> phases have their phase stability dependent on temperature;  $\alpha$ -NaMnO<sub>2</sub> (O'3 structure, space group: C2/m) is the low-temperature form and  $\beta$ -NaMnO<sub>2</sub> (space group: Pmmn) is the high-temperature form. However, the Na-deficient,  $\alpha$ -Na<sub>0.7</sub>MnO<sub>2</sub>, is considered as the most stable phase energetically of all layered Na-Mn-O compounds.[3] Reducing the Na content to 0.7 induces formation of a different crystal structure: P2-, P3, and orthorhombic (P'2) Na<sub>0.7</sub>MnO<sub>2</sub>. P3 is the low temperature type and P2 is the high temperature type. In support to that, Stoyanova et. al refers to orthorhombic Na<sub>0.7</sub>MnO<sub>2</sub> (space group: Cmcm) as stable at 1000 °C (Na<sub>2/3</sub>[Mn<sup>3+</sup><sub>3/2</sub>Mn<sup>4+</sup><sub>1/3</sub>]O<sub>2</sub>).[175] Since then, several Na-deficient polymorphs have been investigated in the quest for better performance cathode materials[10], [124], [125], [129], [176], [177] having P2-Na<sub>0.7</sub>MnO<sub>2</sub> and its derivatives intensively studied. An early report by Caballero et al. showed reversible capacity delivery of more than 150 A h kg<sup>-1</sup> in a voltage range of 2–3.8 V in Na



cells for the  $\text{P2-Na}_{0.6}\text{MnO}_2$  drawing the attention towards the layered NMO systems with Na stoichiometry close to  $x=0.7$ . [119] Nowadays, it is widely recognized that the rapid capacity decline for  $\text{Na}_x\text{MnO}_2$  systems is mainly related to the strong Jahn–Teller effect of  $\text{Mn}^{3+}$  and/ or the instability of the structure in the presence of moisture and doping techniques are employed to compensate the  $\text{Mn}^{3+}$  effect. [4], [119], [178]

Together with the potential application as cathodes in Na-ion batteries,  $\text{Na}_x\text{MnO}_2$  layered compounds work as great matrices for the preparation of new layered lithium manganese oxides. [179]

### 5.1.1 Crystal structure and physical properties

In the layered structures of Na-Mn-O, the transition metal is bound in an octahedral site between two layers of  $\text{MO}_6$  sheets. Reducing the Na content to 0.7 induces formation of different crystal structures: P2-, P3- and orthorhombic P'2 [10] as has been mentioned earlier. In both P2 (hexagonal) and P'2 (orthorhombic) structures the Na may occupy two different positions where the Na(1) shares faces with the  $\text{MnO}_6$  octahedra and the Na(2) shares only edges as pictured in figure 5-1. In most powder studies both 2b and 2c sites have been partially inhabited by Na. [175], [180], [181] In P2-type phases, the relative occupation of the face centered (P(2b)) and edge centered (P(2d)) prismatic Na crystallographic sites results from the interplay between the repulsive  $\text{Na}^+-\text{Na}^+$  and  $\text{Na}^+-\text{Mn}^+$  interactions, and from  $\text{Mn}^+/\text{M}^{(n+1)+}$  charge ordering on the transition metal lattice. [124], [125] Such mechanism set an interesting base for the study of interatomic interactions and the way these tailor the macroscopic physical properties.

On this site, the magnetic behavior of the  $\text{P2-Na}_{0.67}\text{MnO}_2$  as studied by Luo et.al [182], is described by a canonical spin-glass transition as a result of the competing interactions that occur between mixed valence pairs of  $\text{Mn}^{3+}/\text{Mn}^{4+}$  and the imposed strong geometrical frustration. However no further exploration has been done in terms of anisotropy in the system for which large single crystals would be required.



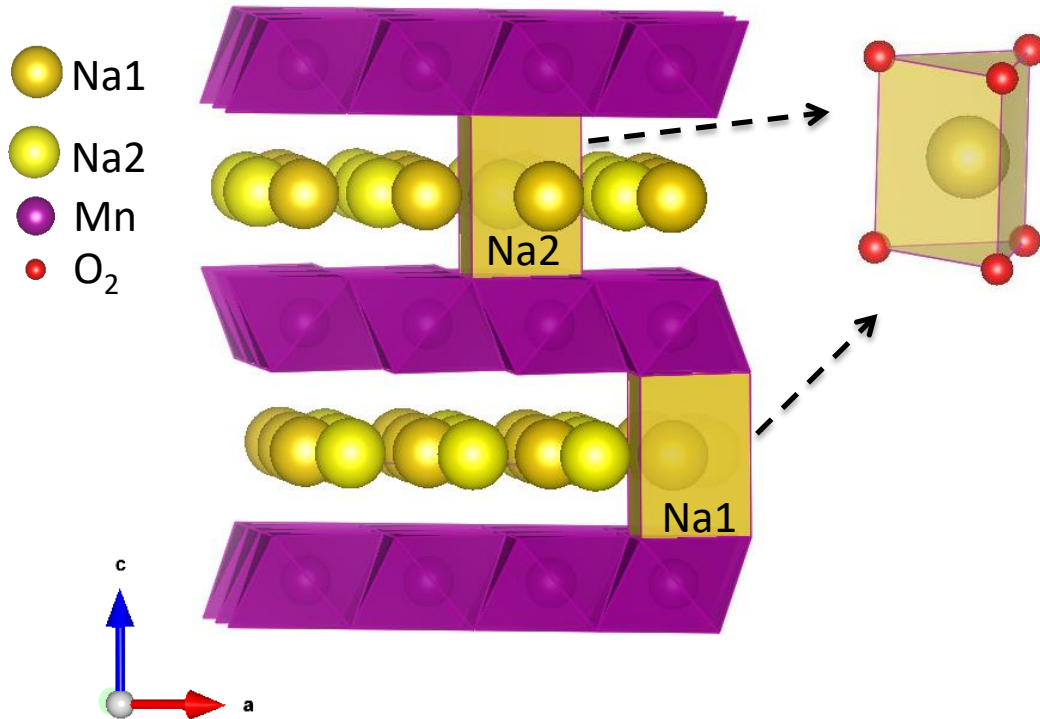


Figure 5-1 Layered P2 structure of  $\text{Na}_x\text{MnO}_2$  ( $x=0.7$ ) showing the 2 different Na sites.

### 5.1.2 Contribution of the present work

The first attempt of single crystal growth of the Na deficient NMO system was done by Hirano et al. in the 80s. [92], [122] as detailed in chapter 3. The crystallites grown adopted a hexagonal plate-like shape and a first approach of the chemical and physical properties was made presenting a semi-conducting and antiferromagnetic behavior for the  $\alpha$ - $\text{Na}_{0.7}\text{MnO}_{2.25}$ . Since then systematic study of physical properties of single crystals of this system has been lacking and thus the present study has been motivated.

In this chapter, the physical properties of the Na deficient large single-crystal  $\alpha$ - $\text{Na}_x\text{MnO}_2$  ( $x \approx 0.7$ ) samples, grown with FZ method are investigated. The chemical composition that has been studied through SEM-EDS and XPS is presented, both aiming to substantiate the structural modifications drawn by X-ray diffraction experiments (both powders and single crystal). The work quantifies the mixed Mn valence character of the crystals, while it also suggests that this electronic dis-proportionating favors a hexagonal P2 structure and the sample is crystallized in P6(3)/mmc space group. To investigate the validity of this mixed ( $\text{Mn}^{4+}/\text{Mn}^{3+}$ ) model system, DC susceptibility measurements were performed for two different crystal orientations. The glassy behavior hinted by these early studies on single

crystals comes in agreement with studies on polycrystalline  $\alpha$ -Na<sub>0.7</sub>MnO<sub>2</sub> specimens proving a canonical spin glass transition at low temperatures. The role of Mn<sup>4+</sup>/Mn<sup>3+</sup> is discussed while combined with the geometric frustration seem to play a crucial role in the formation of the spin-glass state. Finally, the effect of competing magnetic interactions on the dielectric permittivity is investigated for the first time.

## 5.2 Crystal structure

### 5.2.1 X-Ray Powder Diffraction

#### 5.2.1.1 *Experiment and sample preparation*

The purity and crystallinity of the crystal specimens has been initially checked by X-Ray diffraction on a Rigaku D/MAX-2000H rotating Cu anode diffractometer ( $\lambda=1.5406$  Å). The sample in a form of crashed crystal or crystal flake was placed on the holder and sealed with a mylar foil in the glove box, so that it was kept under Ar atmosphere and exposed if possible at all in air during the X-Rays experiment. When the use of such a holder was not feasible the pulverized crystals were mixed well with grease inside the inert atmosphere of a glove box and spread on the available Ni sample holder. All measurements have been taken with the same step of 0.02 degrees and time per step,  $t=12$  sec unless it is stated differently.

#### 5.2.1.2 *Phase purity of starting powders and grown crystals*

The growth of single crystals of the Na<sub>0.7</sub>MnO<sub>2</sub> system was performed by the floating zone (FZ) technique in O<sub>2</sub> gas atmosphere. The growths were carried out using a 2 mirror Canon Machinery SC1-MDH 11020 (University of Warwick) with standard double elliptical mirror geometry equipped with two 1.5 kW lamps while the protocols that have been followed and details on the growth conditions are presented in chapter 3.

The starting powders have been a mixture of synthesized batches of beta polymorph with an average structure that fits to the orthorhombic Pmm symmetry group ( $a=2.86$  Å,  $b=6.33$  Å,  $c=4.78$  Å,  $\alpha= \beta= \gamma= 90$  deg.). However, the appearance of secondary phases, in particular those of  $\alpha$ -NaMnO<sub>2</sub> and in smaller percentage  $\alpha$ -Na<sub>0.7</sub>MnO<sub>2</sub>, are evident by their characteristic Bragg peaks in the XRPD patterns and has been observed in some of our results.



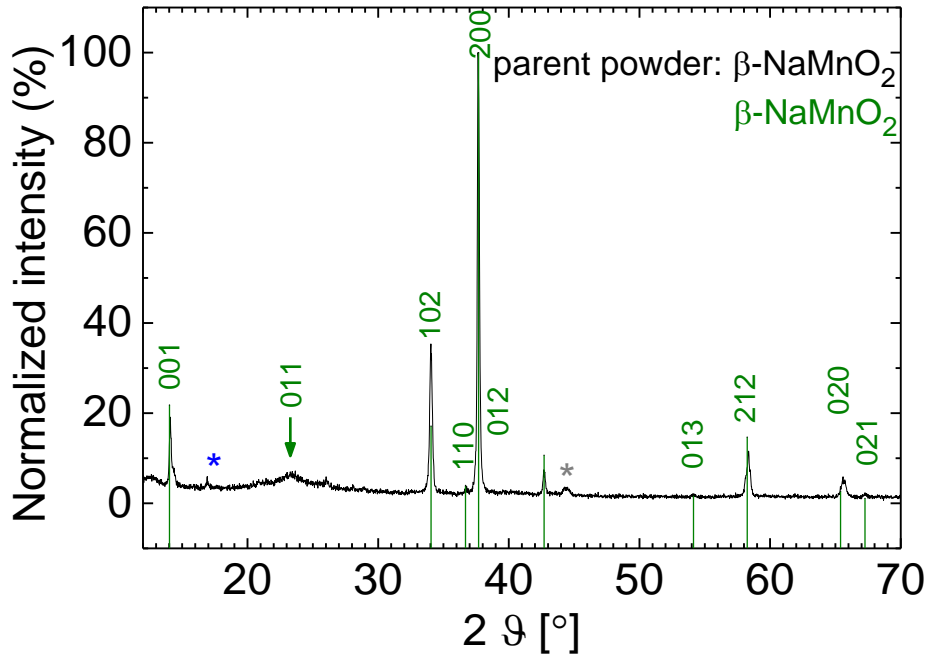


Figure 5-2 X-Ray Powder Diffraction pattern of the polycrystalline  $\beta$ - $\text{NaMnO}_2$  at room temperature. The green vertical lines correspond to the orthorhombic cell indexed according to the 16271 file of ICSD database. The blue star is attributed to the monoclinic  $C/2m$  cell of  $\alpha$ - $\text{NaMnO}_2$  (ICSD 21028). The grey star indicated a peak attributed to the sample holder (a part of the sample holder area has not been fully covered with sample powder). The green arrows represents the reflection 011 as defined by Billaud et.al [129]

Figure 5-2 shows the x-ray-diffraction pattern of a  $\beta$ - $\text{NaMnO}_2$  mixed batch synthesized according to the protocol described in chapter 3. We consider this phase a pure beta phase. The green vertical lines correspond to the beta orthorhombic cell  $Pmnm$  indexed according to ICSD 16271 cif file while the blue star is indicating the (001) reflection of the monoclinic  $C/2m$  cell of  $\alpha$ - $\text{NaMnO}_2$  as given in ICSD 21028. The gray star is attributed to the sample holder (Ni) which sometimes has not been fully covered by the powder under test. The green arrow point indicates (011) peak of  $\beta$ - $\text{NaMnO}_2$  as suggested by Billaud et. al in [129].

The beta powders after being pressed in  $\sim 7$  cm length rods (details in section 3.2.3.2), have been further sintered under  $\text{O}_2$  flow at  $950^\circ\text{C}$  following the synthesis protocol of beta polymorph. The resulting sintered rods that would be later used as feed and seed rods, were pure beta phase as shown in figure 5-3 (black line). Different sintering protocols in which the pressed rods were inserted into the tube furnace straight at  $950^\circ\text{C}$  instead of room temperature or  $100^\circ\text{C}$ , didn't make any difference in the phase of the final sintered rod (figure 3-11, table 3-5).



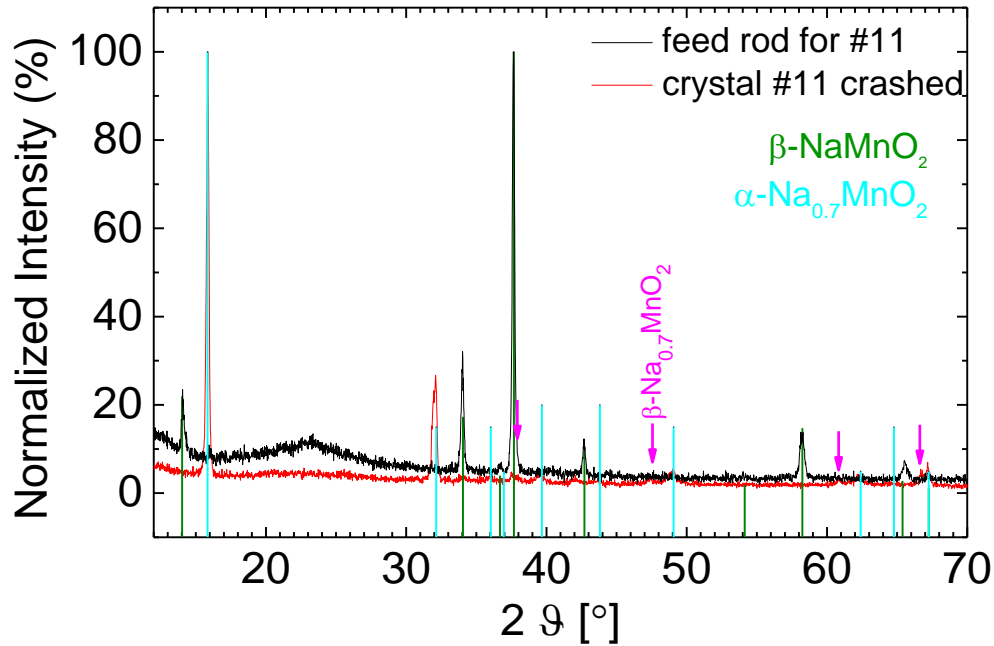


Figure 5-3 X-ray-powder diffraction pattern of the feed rod (black line) and a crashed crystal boule (red line) of #11 single crystal batch (table 3-5). Green ticks represent the 15769 card of  $\beta$ - $\text{NaMnO}_2$  and turquoise ticks are attributed to  $\alpha$ - $\text{Na}_{0.7}\text{MnO}_2$  phase. Impurities of  $\beta$ - $\text{Na}_{0.7}\text{MnO}_2$  phase (magenta arrow) are observed in the phase of the grown crystal.

In figure 5-3 a comparison of the x-ray-diffraction patterns of the feed rod (black line) and powder crashed from the final crystal boule (red line) is presented for single crystal batch #11. For the presented measurements, a part of the edge of the crystal boule grown has been ground to powder manually, using agate pestle and mortar. The crystal product of the growth adopts the hexagonal P63/mmc cell matching perfectly the  $\alpha$ - $\text{Na}_{0.7}\text{MnO}_2$  as initially presented by Parant [3] with cell parameters  $a = b = 2.876 \text{ \AA}$ ,  $c = 11.21 \text{ \AA}$  and  $\gamma = 120^\circ$ , while one can observe the existence of weak peaks of  $\beta$ - $\text{Na}_{0.7}\text{MnO}_2$  (crystallizes in orthorhombic cell Cmca). According to the aforementioned study  $\beta$ - $\text{Na}_{0.7}\text{MnO}_2$  is likely to be formed above  $700^\circ\text{C}$  together with the stoichiometric  $\beta$ - $\text{NaMnO}_2$ . The pattern however yields a preferred orientation (strongest reflections (002) and (004)) which may be due to manual pulverization of the crystal product. A single crystal flake cleaved from the main crystal boule hints the same cell and justifies the previously observed preferred orientation (figure 5-4). The crystallinity and orientation of the cleaved flakes is further confirmed by Laue method while the structure is determined by single crystal x-ray diffraction as it will be presented in the following sections.

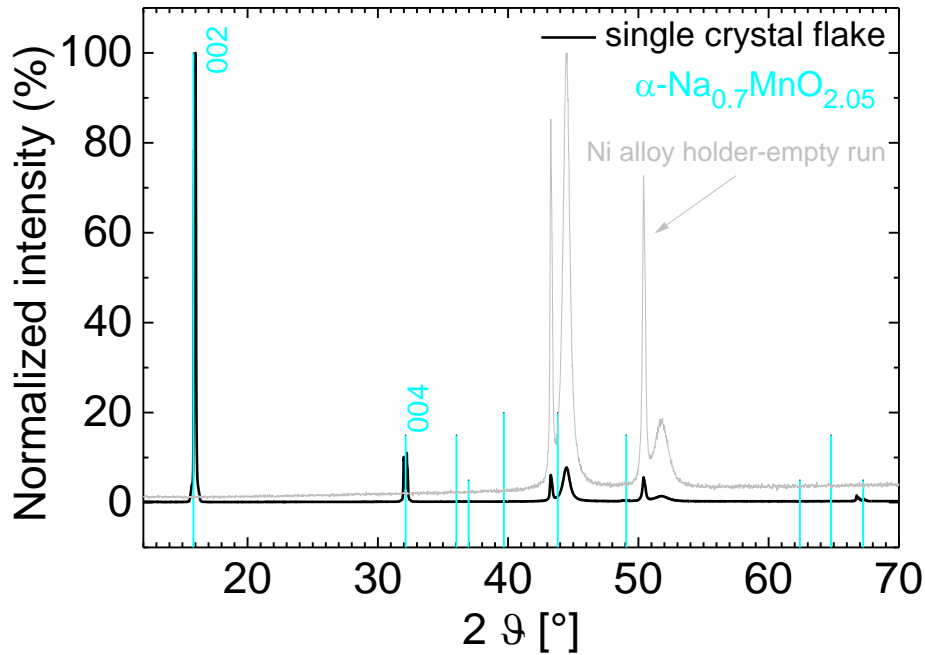


Figure 5-4 X-ray-diffraction patterns of a crystal flake of #5 batch (black line) and of the empty sample holder (gray line). Turquoise ticks represent  $\alpha\text{-Na}_{0.7}\text{MnO}_2$  as presented by Parant et. al [3].

### 5.2.2 Laue Method

Laue x-ray backscattering technique has been used in complement to the powder x-ray studies to confirm the good crystallinity of the grown crystals. Laue x-ray diffraction photographs were taken using a Photonic –Science Laue dual camera system. In the successfully grown boules we could observe a metallic shiny surface with facets (fig. 5-5a). Following the x-ray findings, we used published information [3] of the hexagonal  $P6_3/mmc$  crystal space group and simulated Laue diffraction patterns employing the Crystal Maker software. The simulated patterns seemed to match well the Laue pictures of the facets of the grown boules and the cleaved flakes (figure 5-5). In figure 5-5a, part of the crystal boule and two cleaved flakes are shown while in 5-5b the Laue photograph of one of the cleaved flakes is presented. The simulation of the  $c$  plane of  $P6_3/mmc$  cell is matched with the Laue reflections observed defining the orientation of the cleaved flake.

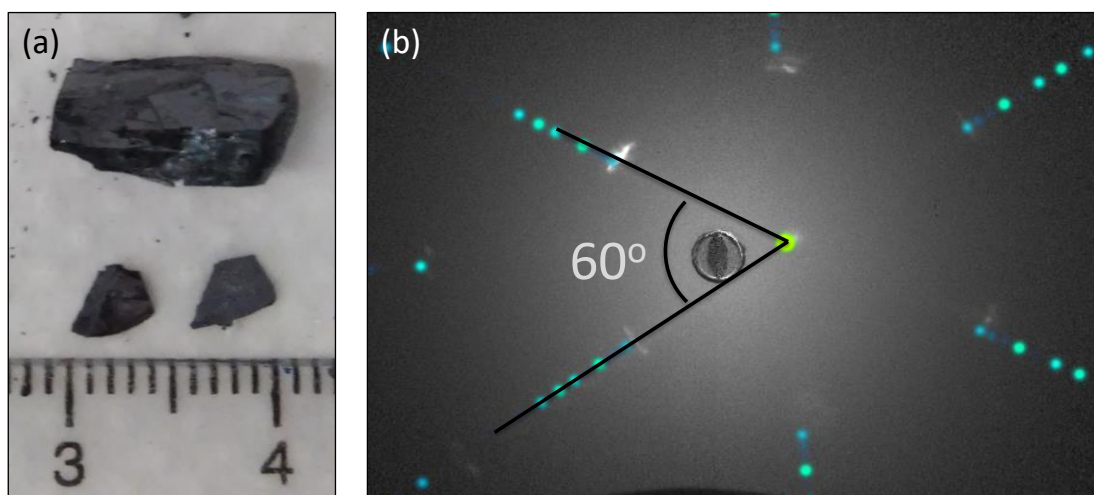


Figure 5-5 (a-b) Actual picture of boule and cleaved flakes and Laue photograph of the flat side of flake of batch #5. The Laue photograph match the simulation pattern of (001) plane of hexagonal  $P6_3/mmc$  cell.

In all successful growths ( batches #5, #11, #12) the flakes cleaved from the crystal boule following the same direction having their flat side identified as the (001) plane (fig. 5-6). Nevertheless, the cleavage has not been as easy as in the case of crystals grown from alpha powders (under Ar) as it will be described in chapter 6. Multiple spots observed in several photographs hint a stacking of single crystal flakes which is slightly misaligned giving multiple reflections for the same reflection site.

Layering implied by the Laue photographs has been further proved by SEM images while the structure of the grown crystals has been defined by single crystal x-ray diffraction study. The preferred orientation of the cleaved flakes led further investigation of the anisotropy as expressed through the study of the magnetic properties of  $\alpha\text{-Na}_{0.7}\text{MnO}_2$ .

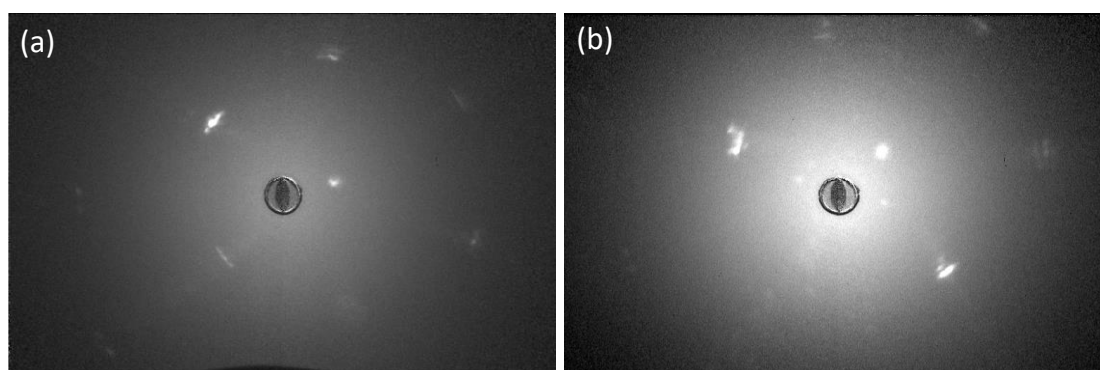


Figure 5-6 (a) Laue photograph of the flat side of a cleaved flake of batch #5 (b) Laue photograph of the flat side of a cleaved flake of batch #12. Both photographs are identical and match the simulation pattern of (001) plane of hexagonal  $P6_3/mmc$  cell.

### 5.2.3 Single Crystal x-ray Diffraction

#### 5.2.3.1 *Experiment and sample preparation*

The data collection took place both at in-house BRUKER D8 VENTURE (Cu  $K\alpha$ ,  $\lambda=1.54$  Å) diffractometer (IMBB-FORTH) under the guidance of Prof. K. Petratos and Dr R. Gessmann and at SuperNova (Mo  $K\alpha$ ,  $\lambda=0.71073$  Å) from the Rigaku Oxford Diffraction in the Laboratory of synthetic inorganic chemistry in university of Cyprus under the guidance of Prof. A. Tasiopoulos and Dr C. Papatriantafyllopoulou.

The kappa geometry of both goniometers used provides true multiplicity and better description of the absorption surface leading to an increased  $I/\sigma I$  (Average intensity / average intensity error) ratio. The PROTEUM2 [95] software has been the software tool used in order to determine the unit cell, prepare the strategy of the data collection and integrate the data collected. The crystals used for data collection in this thesis were investigated under cooled nitrogen. Showering a crystal with cold dry nitrogen during data collection reduces thermal vibrations of atoms so that better data quality is possible. The choice of crystals has been made according to size and well defined edges under a microscope. As soon as the crystal got out of the glove box they were bathed in paraffin oil to prevent any moisture absorption and then captured on the kapton loop.

#### 5.2.3.2 *Structure and stacking*

Crystal flakes taken from the successfully grown batches of #5 and #12 have been tested. The preliminary rotational images revealed multiple reflections per site indicating possible misalignment of stacked single crystals (fig.5-7). Nevertheless, the determination of the unit cell has been possible and the crystal structure has been refined according to P6<sub>3</sub>/mmc cell in agreement with previous studies on polycrystalline powders [3], [175], [183] and early single crystal work [92], [122].

In almost all cases it was feasible to collect a preliminary set of frames for determination of the unit cell. Following an auto indexing process of the reflections from the previous frames we get the reduced primitive cell and calculate the orientation matrix (which relates the unit cell to the actual crystal position within the beam). The primitive unit cell is refined using least-squares or fast fourier transformation method and then converted to the appropriate crystal system and Bravais lattice. In this step most of the times the Bravais lattice chosen was giving results that could be interpreted both using the hexagonal P and



orthorhombic C cell which encouraged further data collection. Each time the chosen cell has been refined using least-squares to determine the final orientation matrix for the sample. After the refined cell and orientation matrix have been determined, intensity data has been collected by collecting a sphere or hemisphere of data using an incremental scan method, collecting frames in 0.1° to 0.3° increments (over certain angles while others are held constant). After the data have been collected the integration process was separately done using both hexagonal and orthorhombic unit cell reducing the raw frame data to a smaller set of individual integrated intensities introducing corrections for instrumental factors, polarization effects and X-ray absorption.



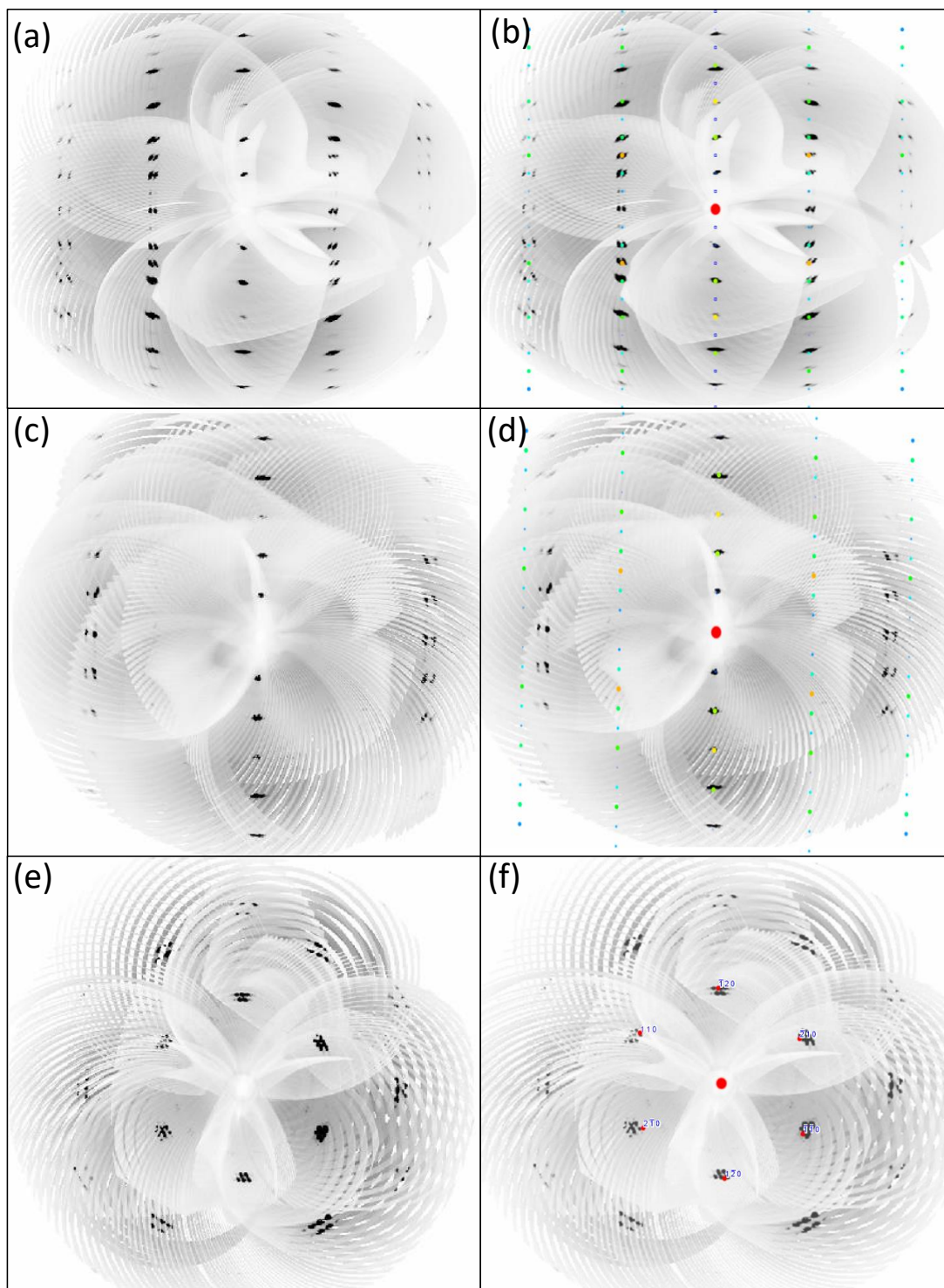


Figure 5-7 Precision picture of reflections of (a)  $0kl$  plane, (c)  $h0l$  plane and (e)  $hk0$  plane and simulation using the  $P6_3/mmc$  hexagonal cell in view direction (b)  $[001]$ , (d)  $[010]$  and (f)  $[001]$ .

In figure 5-7 the 2D reflections pattern of  $0kl$ ,  $h0l$ ,  $hk0$  planes are presented on the left panel (figure 5-7 a, c, e) together with simulated pattern indexed in the  $P6_3/mmc$  hexagonal system of  $\alpha\text{-Na}_{0.7}\text{MnO}_2$  powders on the right panel (figure 5-7 b, d, f) as it has been

determined by Parant et. al. Although the simulations match quite well the harvested reflections, multiple reflections per crystallographic site made it challenging to isolate the final phase. Finally, the retrieved *hkl* data allowed a structural interpretation which is summarized in table 5-1 and presented through the structure schematic in figure 5-8.

The derived structure is described by the hexagonal symmetry (P6<sub>3</sub>/mmc) with lattice parameters  $a = b = 2.9064 \text{ \AA}$ ,  $c = 11.1125 \text{ \AA}$ ,  $\alpha = \beta = 90^\circ$ ,  $\gamma = 120^\circ$ . The mean layered structure is confirmed to be of P2 type with no distortion of the MnO<sub>6</sub> environment (fig. 5-9). Usually the deviation of the hexagonal structure appears due to the presence of the Jahn-Teller active Mn<sup>3+</sup> ions. [175], [176] This has been the case in compositions where the presence of P2' orthorhombic (Cmcm) and O3' monoclinic (C2/n or C2/m) has been observed in XPD patterns in the cases of Na<sub>0.67</sub>MnO<sub>2</sub> [178] and Na<sub>5/8</sub>MnO<sub>2</sub> [176] powder studies. In the present study, a possible presence of Na vacancies, thus a higher concentration of Mn<sup>4+</sup>, may suppress the cooperative Jahn–Teller distortion therefore leading to the stabilization of the undistorted (ideal) P2 hexagonal crystal structure.[179]

*Table 5-1 Summary of structure parameters in P6<sub>3</sub>/mmc space group, from single crystal x-ray results taken at 100 K after the structural interpretation done with XP. The first lines of the .ins file are presented. CELL line gives the x-ray wavelength and the lattice parameters. ZERR line gives the z-factor and the errors on the lattice parameters while the fractional coordinates (x,y,z) of the atoms are found in the following lines.*

100K in P6(3)/mmc						
CELL 0.71073 2.9064 2.9064 11.1125 90.000 90.000 120.000						
ZERR 3.00 0.0038 0.0038 0.0180 0.000 0.000 0.000						
	site	x	y	z	Occ	U
<b>Mn</b>	2a	0.000000	0.000000	0.500000	10.08333	0.02110
<b>O</b>	4f	-0.666667	-0.333333	0.590500	10.16667	0.02554
<b>Na</b>	2c	0.666667	0.333333	0.750000	10.08333	0.12441



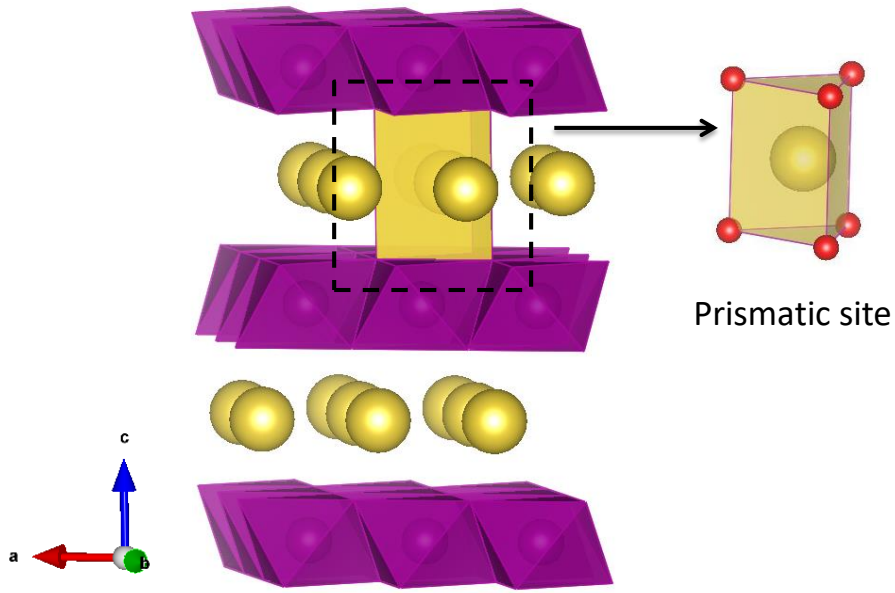


Figure 5-8 Schematic of the  $P6_3/mmc$  hexagonal structure of the crystals  $\alpha\text{-Na}_{0.7}\text{MnO}_2$ ; projections in the (a)  $ac$  plane showing the alternation of layers between the  $\text{MnO}_6$  octahedra and the Na cations in a prismatic site revealing the P2 stacking sequence.

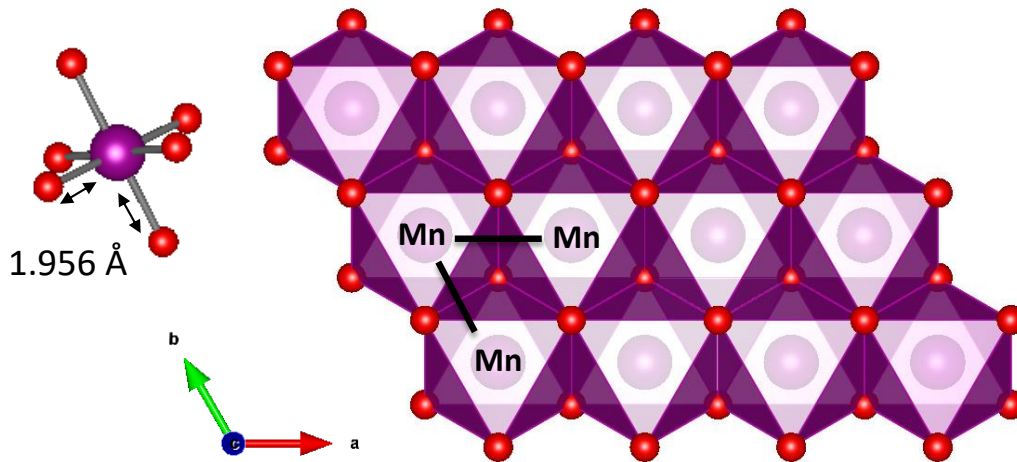


Figure 5-9 Schematic of the  $P6_3/mmc$  hexagonal structure of the crystals  $\alpha\text{-Na}_{0.7}\text{MnO}_2$ ; projections in the  $ab$  plane where the triangular topology of the Mn is clear. The  $\text{MnO}_6$  octahedra is non Jahn-Teller distorted. Mn is represented by purple spheres and Oxygen with red.

In both P2 (hexagonal) and P'2 (orthorhombic) structures the Na may occupy two different positions where the Na(1) shares faces with the  $\text{MnO}_6$  octahedra and the Na(2) shares only edges as pictured in figure 5-1. It is worth mentioning that in the present study only the occupation of 2c prismatic site is done by Na (Na(2) site) (fig.5-8, tables 5-1, 5-2) in contradiction to the powder studies where both 2b and 2c sites have been partially

inhabited by Na. [175], [180], [181] More specifically, in the study of Stoyanova et. al the refinements show that the hexagonal phase is gained against the high temperature orthorhombic when Na is displaced from the prismatic 2d (2/3, 1/3, 1/4) to 6h (2z, z, 1/4) which in the case of z=1/3 the 6h converges into 2d site.

*Table 5-2 Comparison of the Mn-Mn, Mn-O distances for the  $\alpha$ -Na<sub>x</sub>MnO<sub>2</sub> (x=0.7) powders and single crystals as derived from SC-XRD analysis. These parameters are portrayed in Figure 5-8. The powder refined parameters are taken from reference[183] for comparison purposes.*

	<b>h-NMO- crystals (present study)</b>	<b>h-NMO powders [183]</b>	<b>o-NMO powders [183]</b>
$d_{\text{Mn-Mn}} (\text{\AA})$	2.906	2.883	2.839
$d_{\text{Mn-Oap}} (\text{\AA})$	1.956	1.942	2.137
$d_{\text{Mn-Oeq}} (\text{\AA})$	1.956	1.942	1.928
$d_{\text{Na1-Mn}} (\text{\AA})$	2.778		2.805
$d_{\text{Na2-Mn}} (\text{\AA})$	3.246 (not occupied)		3.239
$d_{\text{interlayer}} (\text{\AA})$	5.556	5.575	5.575
<b>Na/Mn ratio</b>	0.71	0.65	0.64
<b>Mn oxidation state</b>	+3.62	+3.76	+3.37

In general, six oxygen ions form the nearest environment of each Na ion. In the non-distorted hexagonal structure described in the present study the Na-O distance is found to be  $d_{\text{Na(2)-O}} = 2.4407 \text{ \AA}$ . In the case of orthorhombic Cmc structure, the  $d_{\text{Na(1)-O}}$  and  $d_{\text{Na(2)-O}}$  differ establishing a more distorted environment for Na(1). At the same time, the appearance of Mn ions just above and below the Na(1) sites leads to a shorter Na(1)-Mn distance in comparison to Na(2)-Mn and the distance between identical ions (Mn-Mn, Na(1)-Na(1), Na(2)-Na(2)) inside the layers, causing significant repulsion. This fact lays the Na(1) site energetically unfavorable in comparison to the Na(2) one. A comparison of the ion distances between the present work and published work for both hexagonal and orthorhombic structures is presented in table 5-2.

Interestingly, according to the aforementioned study, the occupancy of Mn site is found to be less than 1 in the hexagonal modification. In view of that, further chemical



characterization through EDS and XPS has been pursued as discussed in the following sections.

## 5.3 Chemical characterization

### 5.3.1 SEM-EDS

#### 5.3.1.1 *Experiment and sample preparation*

Scanning electron microscopy (SEM) images were obtained using a field emission system (JEOL JSM-7000F) operating at 15 kV accelerated voltage. To acquire SEM images of crystal platelets the crystal boule was cleaved inside the glove-box with a tungsten knife by steadily pressing the boule along growth direction. We did not use spattering or polishing before the observation in order to reduce the exposure time of the crystals to ambient conditions. Quantification of the elemental ratios at the surface of the crystal flakes was carried with energy dispersive spectroscopy (EDS) by using a JEOL JSM-6390LV scanning electron microscope equipped with an Oxford INCA PentaFET-x3 detector.

#### 5.3.1.2 *Layered structure and Na:Mn ratio*

The sample flakes were taken from various sections of the grown boules in order to check consistency. The retrieved EDS spectra taken from a number of cleaved crystal flakes give an average of 0.71 for Na/ Mn, which implies the existence of non Jahn-Teller Mn<sup>4+</sup> ions. The deviation of the Na: Mn ratio ranges in between 0.68 to 0.74 (fig. 5-10a, 5-11b). In figure 5-10 a SEM picture of a crystal flake cleaved from the crystal boule #5 is shown. A close up taken close to the edge (figure 5-10 b, 5-11a) reveals well defined layered stacks of crystallites justifying the existence of multiple reflections per site in the single crystal x-ray diffraction pattern due to possibly misaligned crystallites in the stacking.



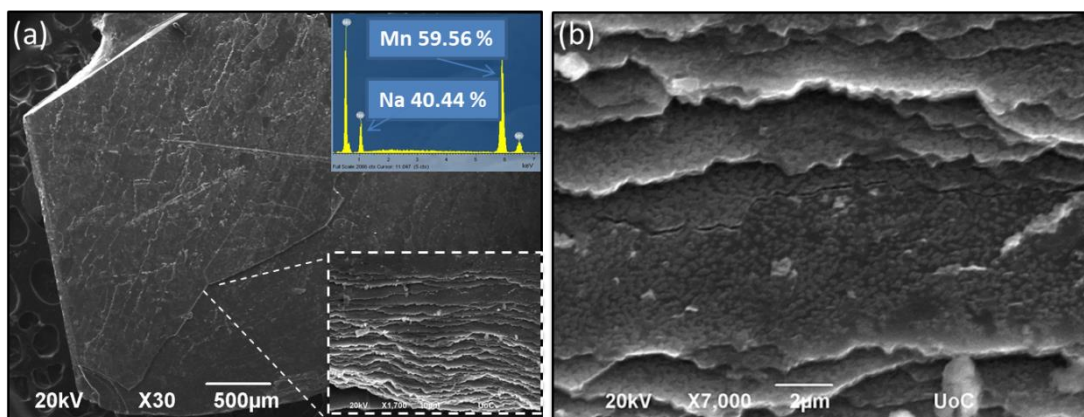


Figure 5-10 SEM image depicting (a) the layered morphology of the as-grown crystal flake of  $\alpha$ - $\text{Na}_{0.7}\text{MnO}_2$ , (b) a close-up view of the stacking layers. Inset in (a) is the EDS pattern revealing a  $\text{Na}:\text{Mn} = 0.68$ .

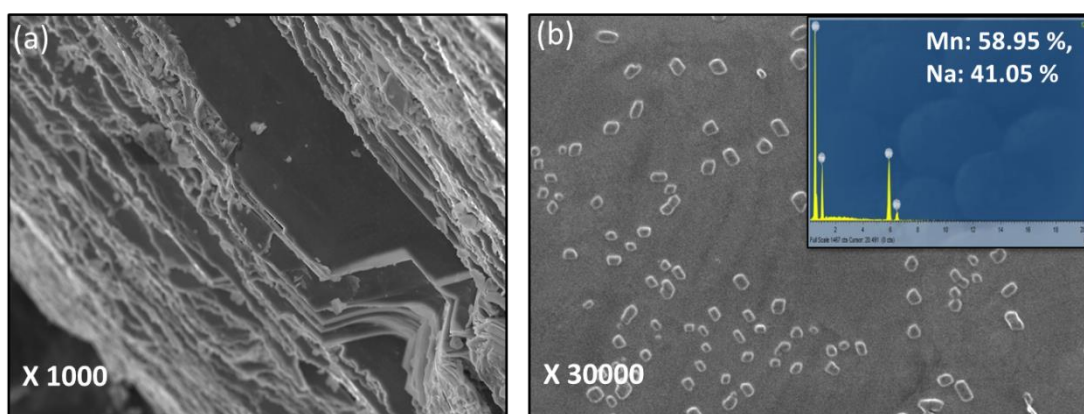


Figure 5-11 A close up of the surface of a flake with a surface stoichiometry ratio of  $\text{Na}:\text{Mn} = 0.696$

The layered structure that is observed in  $\text{Na}_x\text{MnO}_2$  compounds with  $0.6 < x < 1$  is stable and independent of the Na percentage inside the aforementioned limits. As studied by the early works of Hirano et al. [92], [122] the presence of moisture at room temperature can alternate the Na percentage and the interlayer spacing (expansion of  $c$ -parameter of the unit cell) because of oxonium ions ( $\text{H}_3\text{O}^+$ ) occupying the interlayer space. However the  $\text{MnO}_6$  layering is not collapsing and can be retrieved by immersing the crystal in NaOH solution at room temperature. The phase transitions that occur starting either from O3- or P2- type driven by sodium extraction are allowed to follow specific routes when at room temperature. The nature of these transitions should not demand breaking of the oxygen bonds as originally suggested by Delmas [9]. In the present case the  $\alpha$ - $\text{Na}_{0.7}\text{MnO}_2$  crystals

retain the P2 structure and the Na:Mn ratio as they have been kept in inert atmosphere during most procedures including preparation and experiment.

### 5.3.2 XPS

The Na deficiency that has been hinted in X-ray and EDS measurements allows for the existence of mixed Mn valence. The quantification of the Mn<sup>4+</sup>/Mn<sup>3+</sup> ratio has been pursued further using the XPS technique.

#### 5.3.2.1 *Experiment and sample preparation*

The surface analysis studies were performed in an Ultra High Vacuum (UHV) chamber ( $P < 10^{-9}$  mbar) equipped with a SPECS LHS-10 hemispherical electron analyzer at the Institute Chemical Engineering Sciences (ICE-HT, FORTH, Greece). The XPS measurements were carried out at room temperature using unmonochromatized Al K $\alpha$  radiation under conditions optimized for maximum signal (constant binding energies difference ( $\Delta E$ ) mode, with pass energy of 36 eV giving a full width at half maximum (FWHM) of 0.9 eV for the Au 4f<sub>7/2</sub> charge reference binding energy). The probed area was an ellipsoid with dimensions  $2.5 \times 4.5$  mm<sup>2</sup>. The XPS core level spectra were analyzed using a fitting routine, which allows the decomposition of each spectrum into individual mixed Gaussian-Lorentzian components after a Shirley background subtraction. Errors in our quantitative data were found in the range of ~10% (peak areas), while the accuracy for binding energy (BEs) assignments were ~0.1 eV. The pulverised Na-Mn-O crystals were deposited on a Si wafer substrate and stored in a hermetically sealed container under inert atmosphere prior to the insertion in the UHV chamber, in order to avoid oxidation.

#### 5.3.2.2 *Quantification of mixed valence ratio*

The wide spectra recorded from the sample shows the presence of elements Si, C, Na, O and Mn. In figure 5-12, the Mn 2p<sub>3/2</sub> and Na 1s peaks for one crashed crystal flake of batch # 5 are presented. The deconvoluted Mn 2p<sub>3/2</sub> core level peak (Figure 5-12a) consists of two components of binding energies 642.6 and 641.9 eV assigned to Mn<sup>4+</sup> (reference peak extracted from MnO<sub>2</sub>)[184] and Mn<sup>3+</sup> (reference peak extracted from Mn<sub>2</sub>O<sub>3</sub>)[185], respectively. The Mn<sup>4+</sup>:Mn<sup>3+</sup> ratio as estimated from the area ratio of the fits of each one of the two aforementioned components for the same crystal flake attained a value of 0.32, supporting a strong presence of Mn<sup>4+</sup>.

Moreover, the Na 1s core level peak of the same sample (Fig. 5-12 b) could be analyzed



into two components, at BEs 1071.9 eV and 1070.7 eV where the presence of the component at 1070.7 eV is assigned to Na-O bonds in  $\text{Na}_x\text{MnO}_2$  ( $x < 1$ ), [186], [187]. Since the samples are deposited on a Si wafer, the O 1s peak (not shown) is dominated by the Si-O component making further conclusions difficult at this stage.

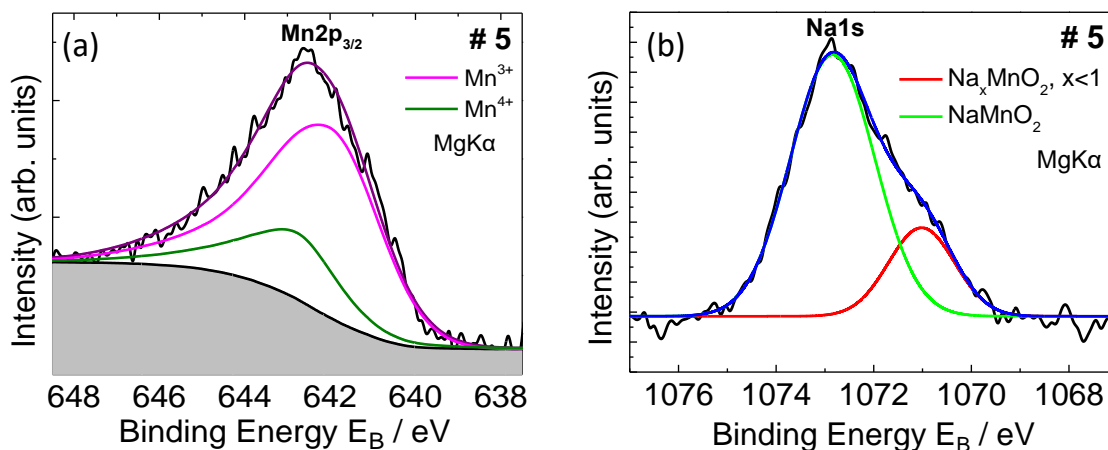


Figure 5-12 X-ray photoelectron spectra (XPS) showing the fitted deconvolution of (a) the main Mn  $2p_{3/2}$  peak, and (b) the main Na  $1s$  peak for the same crystal flake; for the component curves see main text. Comparing the area ratio of the fitted XPS data provides an estimate of the  $\text{Mn}^{4+}:\text{Mn}^{3+}$  (ca. 2.5:1) and Na:Mn (ca. 0.56:1) surface elemental ratios

Using the total peak area of both Mn  $2p_{3/2}$  and Na  $1s$  peaks and the appropriate sensitivity factors (based on Wagner's collection and adjusted to the transmission characteristics of analyser EA10), the estimated Na:Mn ratio (within experimental error  $\pm 10\%$ ) has been close to  $\sim 1$ . This value has been bigger than the maximum limit of the surface atomic Na:Mn ratio given by the EDS (Na:Mn  $\approx 0.74$ ) as discussed in the previous section. The increase of the detected sodium elemental atomic ratio seemed to be the result of Na ions moving on the surface of the crystal reacting with atmospheric  $\text{O}_2$  for the formation of  $\text{Na}_2\text{O}$  or  $\text{Na}_2\text{O}_2$ . Further reaction with the  $\text{H}_2\text{O}$  would lead to  $\text{NaOH}$  which reacting with  $\text{CO}_2$  would finally form the relatively unreactive to the atmosphere  $\text{Na}_2\text{CO}_3$  sodium carbonate. The presence of Carbon in the recorded spectra is an indication that supports a possible oxidation of the sample.

However, taking into account the Na:Mn = 0.71 average as given by the EDS studies, the  $\text{Mn}^{4+}:\text{Mn}^{3+} = 0.32$  ratio as estimated from the XPS fittings and considering no oxygen vacancies, the chemical formula has been calculated to be  $\text{Na}_{0.72}\text{Mn}_{0.76}^{3+}\text{Mn}_{0.24}^{4+}\text{O}_2^{-2}$ . However, it is worth mentioning that in hexagonal modification of  $\alpha$ - $\text{Na}_x\text{MnO}_2$  it is common that the occupancy of the Mn site is less than 1. [175] In powder studies, the



increase in the oxidation number is concomitant with oxygen uptake which acts as a compensation, while promoting vacancies in the Mn layer. [183] In the present study, the average oxidation state of Mn is +3.264 and close to the +3.14 of the  $\alpha$ -Na<sub>x</sub>MnO<sub>2</sub> (x=0.7) powders [182] that adopt the hexagonal lattice being in agreement with the average non-distorted Mn environment as presented in section 4.

Combining the information retrieved by the preliminary structural and chemical study, we will keep referring to our case of single crystals of  $\alpha$ -Na<sub>x</sub>MnO<sub>2</sub> (x  $\approx$  0.7) as h-NMO implying the hexagonal layered topology showing restricted J-T distortion in the mean structure due to the randomly distributed Mn<sup>3+</sup> and Mn<sup>4+</sup> ions (site disorder).

## 5.4 DC-magnetization study

With h-NMO single crystals in hand, the anisotropic magnetic behavior of the system has been visited for the first time since until now the only magnetic susceptibility data for Na<sub>x</sub>MnO<sub>2</sub> systems found in literature refer to polycrystalline samples.

### 5.4.1 Experiment and sample preparation

Dc magnetic susceptibility ( $\chi$ ) of h-NMO single crystals was measured on a Superconducting Quantum Interface Device (SQUID) magnetometer (MPMS-5S) under various protocols and magnetic fields (100 Oe - 50 kOe). A crystal flake of 5.287 mg cleaved with the [001] direction of the hexagonal structure being perpendicular to the flat surface, has been mounted on a kapton holder inside a straw in two different orientations. In one case, the external magnetic field (H) has been applied perpendicular to the [001] direction (or c axis) and in the second case the magnetic field has been applied in parallel to the [001] direction (c-axis) (fig. 5-13). Temperature dependent measurements in the range of 5 K to 300 K were held using the ZFC-FC protocol. Pursuing indications of magnetic transition and glassiness Thermo-Remnant magnetization measurements were held and the presence of memory effects was investigated. Field dependent hysteresis measurements in temperature below and above the transition are also presented in this section.



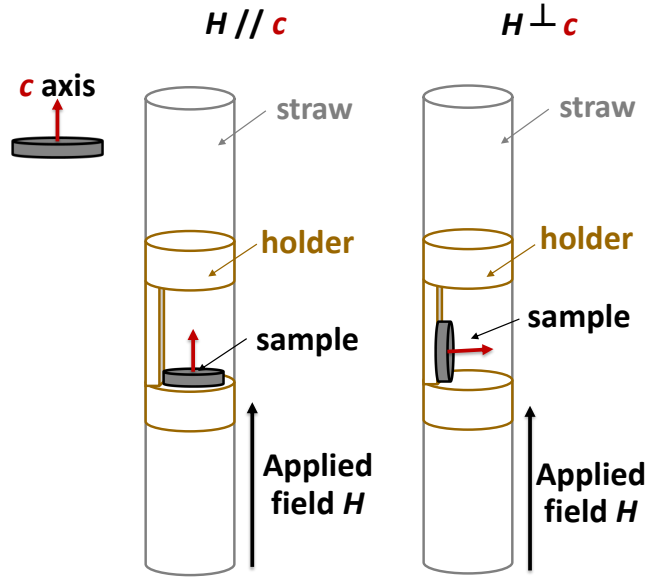


Figure 5-13 Cleaved crystal flake of  $\alpha$ - $\text{Na}_{0.7}\text{MnO}_2$  mounted in two different orientations for magnetization measurements. From left to right are presented: orientation of the flat surface of the crystal flake, mount on holder with  $H$  field in parallel with the  $[001]$  direction, mount on the holder with the  $H$  field perpendicular to the  $[001]$  direction (details in text).

#### 5.4.2 Spin-Glass behavior and magnetic anisotropy

The dc susceptibility of h-NMO single crystals has been measured in a temperature range between 1.8 K and 300 K under a magnetic field ( $H$ ) of 100 Oe and 10 kOe (fig.5-14, 5-15). The  $\chi_{\text{dc}}$  is anisotropic in the low temperature area with the measured value for  $H//c$  almost 8 times larger than the one for  $H\perp c$  (or  $H//ab$ ) in the low field measurement ( $H=100$  Oe). At first glance, the dominant characteristic of the susceptibility curve is the ZFC-FC divergence below 50 K with the appearance of a clear sharp peak in low field measurements suggesting a possible spin-glass transition and a broad feature in the high temperature area.

The magnetic susceptibility of h-NMO single crystals as presented in Figure 5-14, shows a broad hump that extends even above 200 K. This shape resembles the one observed in the  $\text{Na}_x\text{MnO}_2$  polymorphs with  $x\approx 1$  (sections 4.3.1. and 6.5.2) being indicative of low-dimensional spin-correlations. However, having a closer look at the susceptibility, as presented in the insets of figure 5-14 a, c, we can observe that the temperature where the ZFC and FC susceptibility curves start to divaricate is high ( $T_1 < 200$ - 250 K): for  $H//c$ -axis the bifurcation starts below 250 K and for  $H\perp c$ -axis below 200 K. This is also confirmed by the inspection of  $\chi^{-1}(T)$  plots as shown in figure 5-14 b, d.

Keeping this in mind, an attempt was made to apply a Curie –Weiss law  $\chi = C / (T - \theta_w)$  fit in temperature area above 240 K where the broad feature seems to get linear. The inverse ZFC susceptibility is exhibited at the inset of figure 5-14 b. From the Curie constant  $C$ , the effective magnetic moment is determined to be  $\mu_{\text{eff}} = 4.707 \mu_B$  per Mn ion which is found to be the same for both orientations. This value supports the existence of mixed Mn valence combined by  $\text{Mn}^{3+}$  ( $S = 2$ ,  $\mu_{\text{eff}} = 4.90 \mu_B$ ) and  $\text{Mn}^{4+}$  ( $S = 3/2$ ,  $\mu_{\text{eff}} = 3.87 \mu_B$ ). The Weiss temperature is found to be  $\theta = -468.385$  K which makes reasonable in the first place to expect frustrated AFM interactions of the Mn ions.

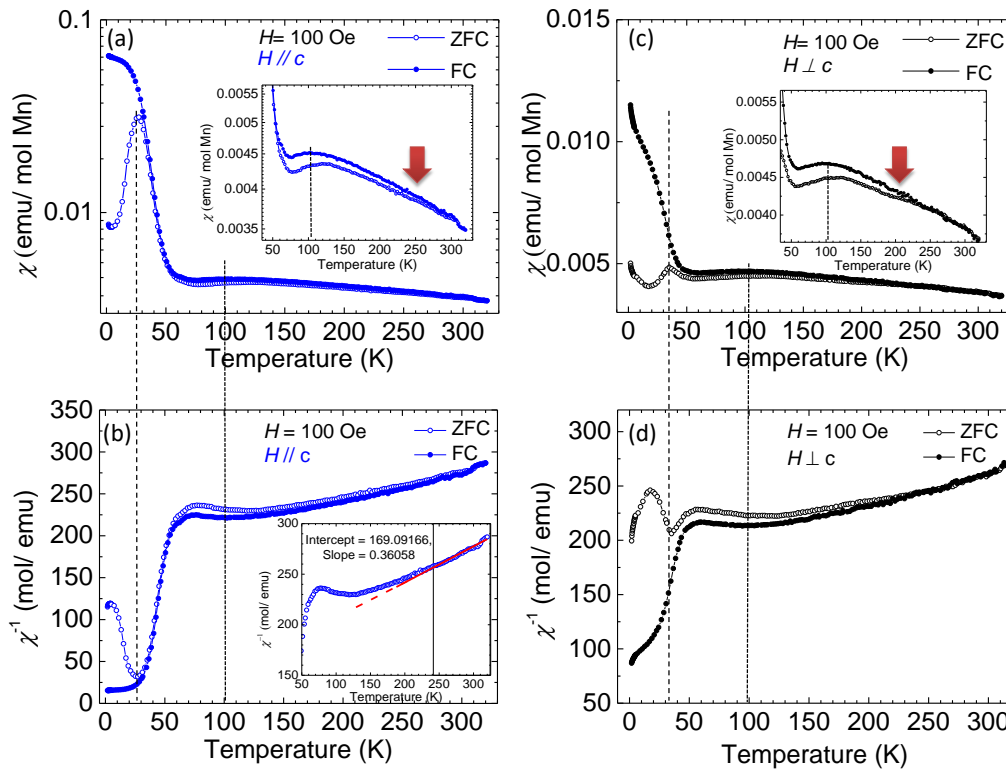


Figure 5-14 ZFC-FC susceptibility measurements of a single crystal  $\alpha$ - $\text{Na}_{0.7}\text{MnO}_2$  flake at two selected orientations ( $H//c$  left panel in blue and  $H \perp c$  right panel in black), at applied field of 100 Oe. The insets in (a), (c) present the zoomed area of susceptibility, where the start of the bifurcation and the broad feature are indicated. The dashed vertical lines from right to left, are indicative of the maxima of the broad hump ( $T_C$ ) and the sharp peak ( $T_f$ ) respectively. Red arrows point at the start of ZFC-FC bifurcation in each orientation.

Interestingly, under the application of  $H = 100$  Oe, the first splitting in the broad feature of ZFC-FC curves is followed by a clear divergence below  $T_2 = 50$  K leading to a maximum in the ZFC curve at  $\sim 27$  K when  $H//c$ -axis and  $\sim 36$  K when  $H \perp c$ -axis (fig. 5-14a, b). Such sharp features are indicative of a magnetic transition and possible establishment of a



long range magnetic order while the notable divergence indicates the existence of a net FM component. To our understanding, these 2 bifurcations may hint two distinct magnetic transitions.

Thermal irreversibility between ZFC and FC protocols may be the result of different mechanisms. It is important to stress here though, that such strong differences are met in frozen systems adopting spin-glass configuration. [44] In addition to that, the splitting of ZFC-FC profiles being persistent to temperatures above 200 K provides an evidence of history dependence to the magnetization and can be attributed to possible existence of ferromagnetic clusters in an otherwise paramagnetic state. [188]

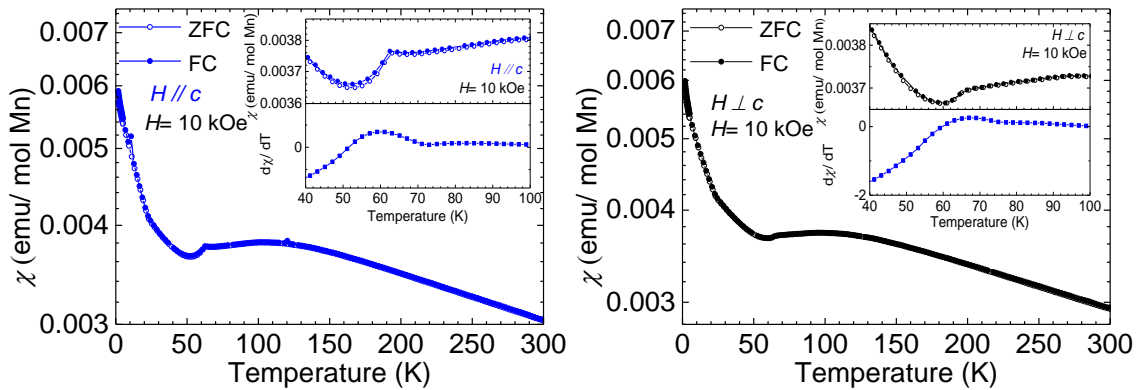


Figure 5-15 ZFC-FC susceptibility measurements of a single crystal  $\alpha\text{-Na}_{0.7}\text{MnO}_2$  flake at two selected orientations ( $H//c$  left panel and  $H\perp c$  right panel), at applied fields of 10 kOe. The insets present a zoom of the bifurcation in the low temperature area.

In the case of h-NMO crystals, the application of a higher field of 10 kOe seems to dampen the peak effect of susceptibility in the low temperature area. The dampening of the peak effect of the susceptibility observed here is in line with the powder study published earlier [182] where application of increasing magnetic fields suppresses the low-T peak while shifting it to lower temperatures. Higher magnetic fields suppressing the energy barriers and lowering the freezing temperature are consistent with a spin glass behavior.

In figure 5-15 one can see almost identical behavior for both orientations both pronouncing a shoulder around 60 K as a continuation of the broad hump feature in the high temperature area and a “dip” around 50 K. An interesting low-temperature upturn of the ZFC-FC curves which takes place in both orientations with the upturn getting sharper below 23 K, is not commented in any published results in the similarly stoichiometric NMO compounds. In addition to that, a steep rise in magnetization takes place below 5 K under



high field application in both orientations (fig. 5-15) while it is observed only for orientation  $H \perp c$  in the low field (100 Oe) measurement (fig. 5-14 c). Usually such a Curie-like upturn is indicative of magnetic impurities and is met also in some powder samples of the parent stoichiometric compounds ( $\alpha$ - and  $\beta$ -NaMnO<sub>2</sub>). However, in the case of the h-NMO grown crystals we cannot attribute it to magnetic phase impurities due to lack of impurity levels in the x-ray results. We could also exclude the possibility of saturation of free moments since it is found that the magnetization  $M(H)$  does not saturate for fields up to 50 kOe.

Investigating further the origin of the features observed in the dc susceptibility, we have measured  $M(H)$  isothermal magnetization in two selected temperatures, 70 K and 5 K in order to confirm possible hysteresis phenomena. The history dependence first implied by the insisting divergence up to 200 K, is further supported by the  $M(H)$  results. The magnetization  $M$  continues to increase with increasing magnetic field  $H$ , without any evidence of saturation until up to 50 kOe. This allows us to say that there is no ferromagnetic state established at high fields. In the high temperature measurement ( $T=70$  K) the profile is almost linear (fig. 5-17 c, d). Interestingly, a weak hysteretic behavior is observed in low temperature ( $T=5$  K) which starts to develop for fields above 10 kOe and vanishes above 30 and 35 kOe for orientations of  $H \perp c$ -axis (fig. 5-17 a) and  $H // c$ -axis respectively (fig. 5-17 b). Even if we don't have a picture of the whole loop we have a hint that it resembles a wasp-waisted like shape. The hysteretic effect is rather weak but still the width of the magnetization branch narrows as the magnetization goes to zero and opens up above a specific magnetic field. Wasp-waisting usually arises as a result of the co-existence of different magnetic grains having different coercivities [189] and can be attributed, among others, to disordered magnetic interactions [188], [190]. Mixed Mn valence introducing competing FM- AFM interactions could be the origin of such disorder. [175], [191] In general, weak hysteretic effect could be indicative of either a spin-glass behavior or existence of ferrimagnetism but further exploration of the nature of the interactions would be needed to define the driving mechanism with certainty.



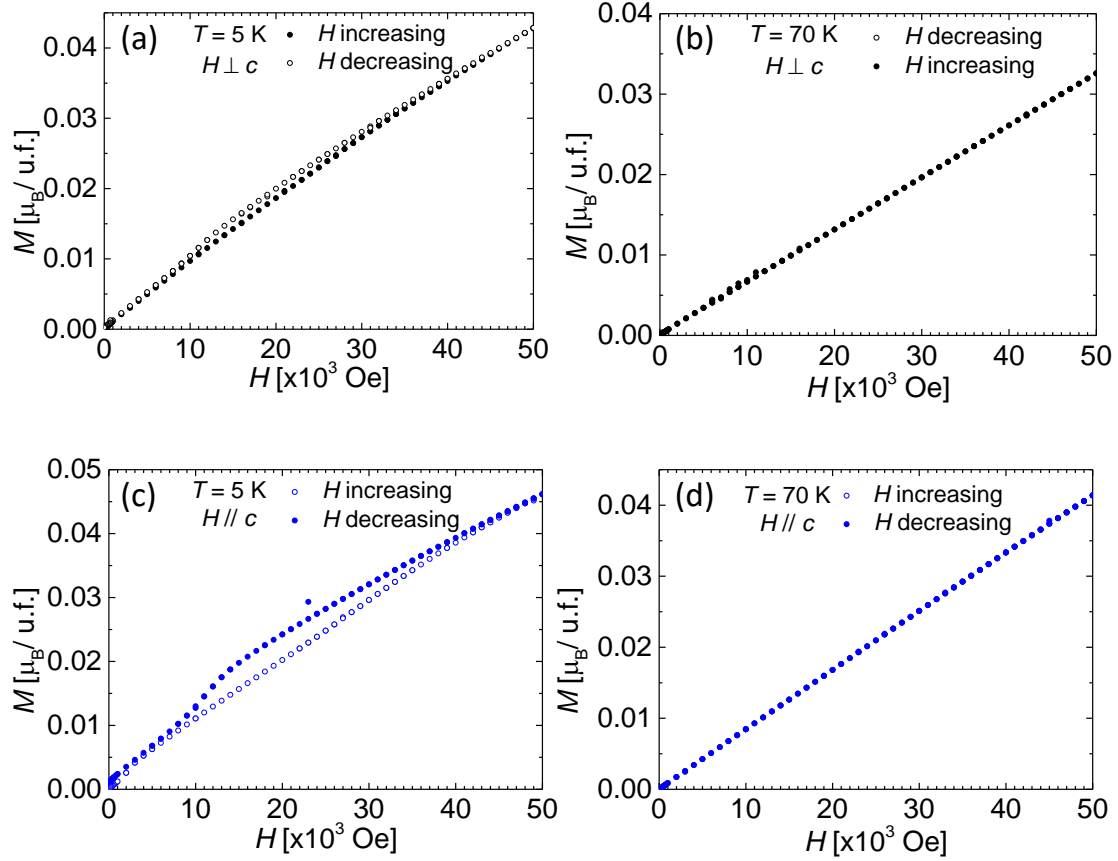


Figure 5-16 Magnetization measurements of single crystal  $\alpha\text{-Na}_{0.7}\text{MnO}_2$  flake at two selected orientations.  $M(H)$ , hysteresis loops between applied fields of  $-20 \text{ kOe} < H < +20 \text{ kOe}$ .

The glassiness implied by the dc susceptibility initiated the investigation of possible memory effects of the system. In figure 5-17 middle panel (red circles), the profile of a ZFC-FC protocol with a “waiting time” step in a temperature below the possible freezing temperature ( $\sim 27 \text{ K}$ ) of the system in  $H//c$  orientation is presented. For the  $t_w$ - protocol, the sample was cooled rapidly under zero field to a temperature  $T_w = 22 \text{ K}$  and the temperature was maintained for a waiting time  $t_w = 10^4 \text{ s}$ . Following the ageing, the sample was quenched to the lowest temperature ( $5 \text{ K}$ ) and susceptibility was measured in  $5 \text{ Oe}$  dc field in the heating run. A reference susceptibility curve was taken using again a ZFC protocol ( $H = 5 \text{ Oe}$ ) in the same panel (empty red circles). On the top panel of figure 5-17 a ZFC-Fc susceptibility measurement taken under  $H = 100 \text{ Oe}$  is put for comparison. We do observe 2 weak dips in the “aging” curve presented in the bottom panel (blue squares) which are a signature of frustrated magnetic behavior that is met below  $50 \text{ K}$  in support with the leading hypothesis of a possible glassy ground state.



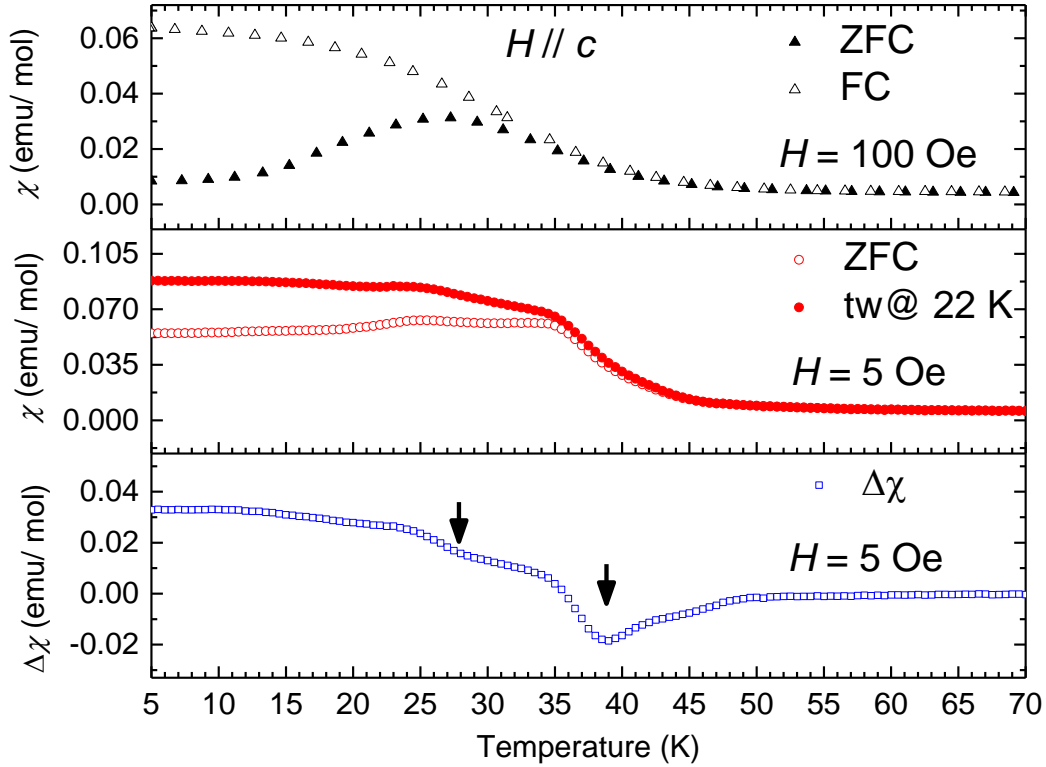


Figure 5-17 Top panel: ZFC-FC dc susceptibility measured at 100 Oe in  $H//c$  orientation. Middle panel: ZFC-reference and ZFC- $t_w$  curves measured at 5 Oe with the  $T_w = 22$  K, Bottom panel: “Ageing” or “memory” curve which is the subtraction of ZFC-reference curve from ZFC- $t_w$  curve.

## 5.5 Dielectric response of h-NMO crystals

### 5.5.1 Experiment and sample preparation

The dielectric measurements of h-NMO crystals examined in this study have been held mainly in a commercial 14 T PPMS platform located in Laboratory for Magnetic Measurements (LaMMB - MagLab) at the Helmholtz-Zentrum Berlin which allowed temperature ramps down to 10 K. A Solatron 1260 Impedance/Gain Phase analyzer has been employed which is being used together with a 1296A Dielectric Interface System in order to cope with ultra-low capacitance levels. The setup had been tailored for dielectric constant measurements in a capacitor-like topology with the sample getting in contact with the electrodes mechanically.

In the presented measurements, an AC electric stimuli of 1600 -2000 V/m was applied on the sample under test.



The crystal flakes have been measured as they have been cleaved from the crystal boule. Their shape has been roughly rectangular with dimensions  $2 \times 2.5$  mm and the thickness was measured approximately  $\sim 0.15$  mm. In this preliminary test the electric field has been applied in parallel to the  $c$  axis ( and so perpendicular to the flat surface of the cleaved flake).

The protocol followed for each measurement of the capacitance has been cooling the sample under zero electric and magnetic field (ZFC) down to 10 K (or the lowest possible temperature below a known magnetic transition point). Then, measure capacitance upon heating with 2 K/min rate up to 220 K or above, while measurement points were taken every 0.05 K by applying an AC voltage across the sample during the warm up.

### 5.5.2 Effects on the dielectric permittivity

Preliminary dielectric measurements have been held on the h-NMO crystals and for the first time the dielectric behavior of the  $\text{Na}_x\text{MnO}_2$  ( $x \approx 0.7$ ) compound has been visited. For these tests no conductive paste has been used and the electrodes of the dielectric stick were in touch with the crystal surface.

In figure 5-20 the T-dependency of dielectric permittivity  $\epsilon'_r$  (T) is presented being measured from 10 K to 220 K. The protocol that has been followed is the one described earlier starting with a ZFC down to 0 K while a test signal level of  $E = 9$  kV/m and  $f = 100$  kHz is applied upon heating. The general trend that is observed is the increase of the value of the dielectric constant  $\epsilon'_r$  (T) with the increase of temperature as in the case of beta polymorph. The shape of the  $\epsilon'_r$  (T) curve has a pronounced feature in the low temperature area  $\sim 50$  K, which is not evident in the Dielectric Loss curve. The low temperature effect appears at the temperature where the bifurcation in the ZFC-FC dc susceptibility curves is observed suggesting the onset of a glassy state. The effect persists till 10 K.

A noticeable change in the curvature of the dielectric profile is observed when the sample is cooled under the application of electric stimuli. This broad hump goes up to 240 K implying a relation to the high temperature divarication of ZFC-FC curves at 100 Oe. A straight comparison of the ZFC and FC  $\epsilon'_r$  (T) measurements is shown in figure 5-21 where the 1<sup>st</sup> derivative points out the exact point where the inclination changes presenting and the broad effect in the high-T area is more evident.



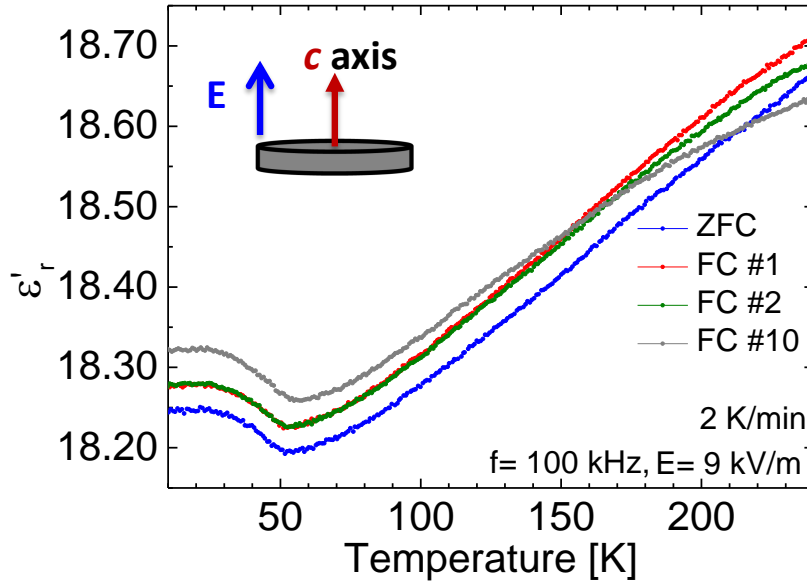


Figure 5-18 Dielectric permittivity of the  $\alpha\text{-Na}_{0.7}\text{MnO}_2$  crystals measured with the stimulating ac field in parallel to [001] direction (schematic) at frequency of 100 kHz. Several runs were taken starting from a ZFC protocol and a series of FC protocols.

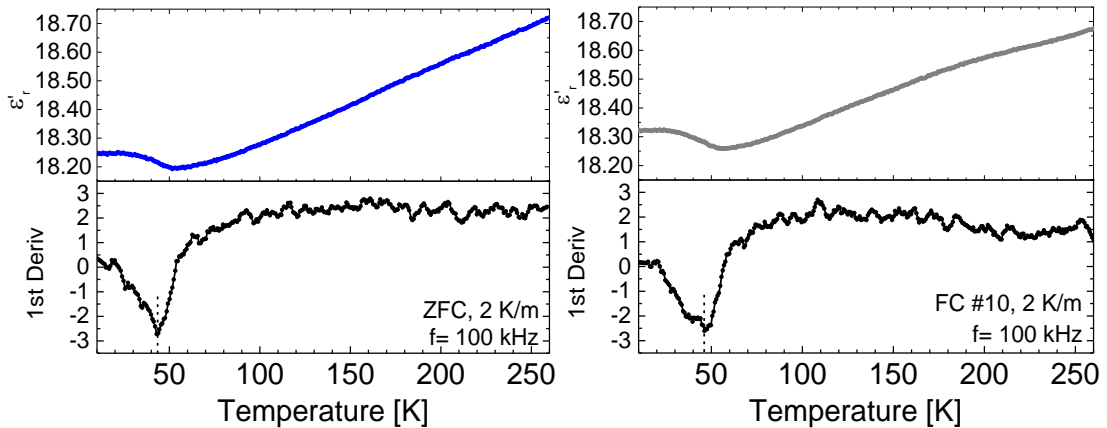


Figure 5-19 Dielectric permittivity of the  $\alpha\text{-Na}_{0.7}\text{MnO}_2$  crystals measured with the stimulating ac field in parallel to [001] direction (schematic) at frequency of 100 kHz. Left panel: ZFC run and 1<sup>st</sup> derivative, Right panel: FC 10<sup>th</sup> run and 1<sup>st</sup> derivative.

The flakes tested show a loss of only 20-30 nS which shouts out a good insulator.

## 5.6 Results and Discussion

The capability of  $\alpha\text{-Na}_{0.7}\text{MnO}_2$  to accommodate different percentage of  $\text{Mn}^{4+}$  has been mentioned as consequence of the cooling process [175] and so variations in the average

Mn valence are expected when we compare polycrystalline specimens coming from different synthetic procedures as well as when we move to single crystals. Comparing the average oxidation state of undistorted P2-type h-NMO, distorted P'2-type o-NMO powders and P2-type h-NMO single crystals as prepared for the present study, we realize that both undistorted hexagonal systems share an average oxidation number closer to 4 (table 5-2). The high percentage of Mn<sup>4+</sup> increases the percentage of competing FM-AFM interactions that enhances magnetic disorder that may be the origin of unconventional shape of the  $M(H)$  profile like the wasp-waisted observed in the present case.

Disorder is also driven by the triangular topology of the Mn ions in the layered P6<sub>3</sub>/mmc structure as a source of geometrical frustration. The degree of this frustration may be expressed empirically by the ratio  $f = |\theta_w| / T_f^2$  with  $\theta_w$  (Weiss temperature) and  $T_f$  (freezing temperature) being related to the AFM coupling in the paramagnetic state and the energy barrier height in the freezing state. The calculated value in the present case is  $f = 17.67$  in the case of  $H // c$ -axis and  $f = 13.01$  in the case of  $H \perp c$ -axis. The values of  $f > 1$  imply a strong magnetic frustration which is comparable to the value of  $f = 12.1$  met in Na<sub>x</sub>MnO<sub>2</sub> ( $x = 0.7$ ) powders. [182]

Apart from the interactions among Mn ions, in the rock-salt layered structured derivatives the role of interlayer ion is proved to control the set of the Neel state as investigated for AMnO<sub>2</sub> (A = Na, Cu) depending on the orbital overlap between the A-cation and Mn. For the stoichiometric compounds, the Neel state sets at 65 K for Cu and at 45 K for Na accompanied by different Mn-Mn interplane couplings. The different interplane distances are modified by the hosted motifs in each case, tailoring the magnetic properties of the layered compound. In the present case of h-NMO crystals, the interplane distance regulated by the Na deficiency is 5.556 Å (close to that of the powder samples of same stoichiometry 5.559 Å) which in comparison to the 5.79 Å of the stoichiometric  $\alpha$ -NaMnO<sub>2</sub> could explain the lowering of the critical temperature below 35 K. In the case of the similarly structured Na-birnessite with formula Na<sub>0.3</sub>MnO<sub>2</sub>·H<sub>2</sub>O the critical temperature below which the divergence of ZFC and FC curves happen is at ~29 K. [192]. It is worth mentioning here that in both cases of  $\alpha$ -Na<sub>0.7</sub>MnO<sub>2</sub> [182] and Na<sub>0.3</sub>MnO<sub>2</sub>·H<sub>2</sub>O [192] the critical temperature is a freezing temperature setting the onset for a glassy ground state. The static (dc) susceptibility of polycrystalline  $\alpha$ -Na<sub>0.7</sub>MnO<sub>2</sub> adopting the hexagonal cell, as published by Luo et. al [182] shares more or less the same behavior for low field application ( $10 \text{ Oe} < H < 5 \text{ kOe}$ ) as the h-NMO crystals under study. In this case, a peak in



the ZFC susceptibility curve is observed at  $T_f \approx 35$  K under the application of 25 Oe which becomes broader and shifts to lower temperatures with the application of increasing magnetic field. If we would get a mean value of the  $T_f$  of the two orientation of the crystal under field of  $H=100$  Oe this would be  $T_{f\text{average}}=31$  K while in the powder samples for the same field the critical temperature takes the value of  $T_f \approx 26$  K. Such a deviation is probably due to small differences in stoichiometry and Mn average valence as described earlier. It is worth noticing that in the study of the polycrystalline hexagonal  $\alpha$ - $\text{Na}_{0.7}\text{MnO}_2$  or Na-birnessite (fig.5-22) no broad feature is observed in the high temperature area neither any ZFC-FC bifurcation in the area around 200 K.

Studies of the similar structured  $\text{Na}_x\text{CoO}_2$  in both powder and single crystal form also point out similar differences in the shape of the magnetic susceptibility. [193] The Na ordering between the two possible sites may cause irreversibility in the magnetization in the high temperature area (200 K) as it would distort the oxygen environment of Mn locally. Such cation “ordering” may condition the electrostatic potential which further affects the magnetic properties in a strongly correlated electron system, encouraging the development of cluster like glassiness.

h-NMO crystals exhibit a complex type of magnetic behavior that is commonly observed in reentrant spin-glasses (RSGs). Upon cooling in a reentrant spin-glass there is an initial onset of partial order at  $T_1$  where ferromagnetic/ ferrimagnetic clusters are formed in the otherwise paramagnetic state. The size of these clusters grows upon cooling until the systems re-enters a spin glass state at a  $T_2$ . In the case of the h-NMO crystals  $T_1 \sim 200$  K is indicated by the divarication of ZFC-FC implying the existence of a weak ferromagnetic component that supports the hints of short-range ferromagnetic order indicated by specific heat measurements done in the polycrystalline powders. The pronounced divergence of ZFC-FC curves below  $T_2 \sim 50$  K and the cusp at 27 K ( $H//c$ ) and 36 K ( $H \perp c$ ), sets the picture of a low temperature glassy ground state. Nevertheless, such a rich magnetic behavior needs further exploration with frequency dependent (ac) susceptibility measurements in order to confirm the existence of a spin-glass (or reentrant spin-glass) state while the origin of the driving mechanisms demand investigations such as neutron diffraction experiments.



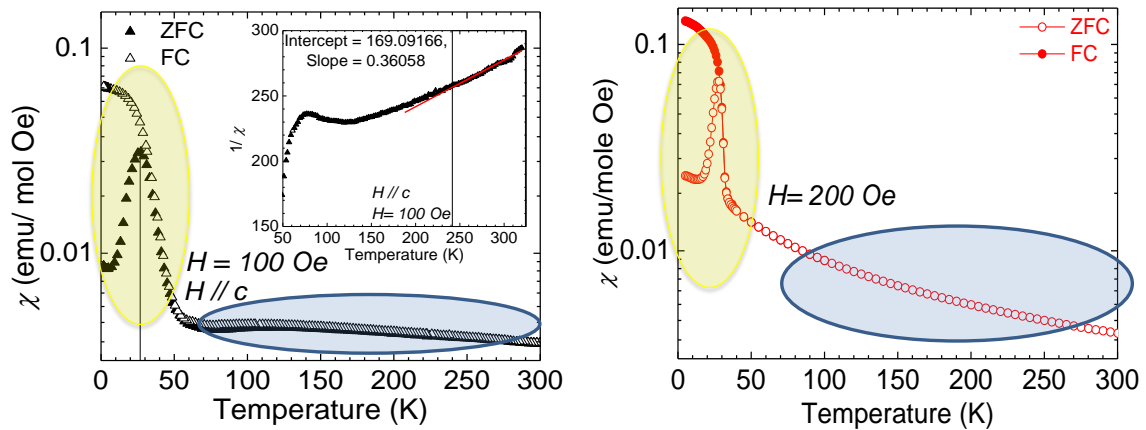


Figure 5-20 ZFC-FC susceptibility measurements of a) a single crystal  $\alpha\text{-Na}_{0.7}\text{MnO}_2$  flake at  $H//c$  left panel and b) of polycrystalline powder of Birnessite  $\text{Na}_{0.3}\text{MnO}_2 \times 0.2 \text{H}_2\text{O}$  right panel, at applied fields of 100 Oe and 200 Oe respectively. The insets present the inverse susceptibility in the case of the crystal  $H//c$  orientation.

## 5.7 Summary and Conclusions

Na deficient large single-crystal samples of  $\alpha\text{-Na}_x\text{MnO}_2$  ( $x \approx 0.7$ ) have been grown for the first time using FZ method and their structurally mediated physical properties have been investigated. X-ray diffraction experiments (both powders and single crystal) present a cell described by the hexagonal symmetry ( $P6_3/mmc$ ) with lattice parameters  $a = b = 2.9064 \text{ \AA}$ ,  $c = 11.1125 \text{ \AA}$ ,  $\alpha = \beta = 90^\circ$ ,  $\gamma = 120^\circ$ . The mean layered structure is confirmed to be of P2 type with no distortion of the  $\text{MnO}_6$  environment. The chemical composition that has been studied through SEM-EDS and XPS and quantifies the mixed Mn valence character of the crystals, while it also suggests that this electronic dis-proportionating favors a hexagonal non distorted P2 structure with  $\text{Mn}^{4+}/\text{Mn}^{3+} = 0.32$  and average Mn valence of +3.62 which is in agreement with literature [182], [183]. To investigate the validity of this mixed ( $\text{Mn}^{4+}/\text{Mn}^{3+}$ ) model system, DC susceptibility measurements were performed for two different crystal orientations revealing magnetic anisotropy with  $c$  as the magnetization easy-axis. A complex set of transitions in the dc magnetic susceptibility have been observed implying a possible reentrant spin-glass ground state. The weak FM component developing in high temperature area ( $< 200 \text{ K}$ ) seems to evolve into a glassy state in low temperatures ( $T < 50 \text{ K}$ ). The glassy behavior hinted by these early studies on single crystals comes in agreement with studies on polycrystalline  $\alpha\text{-Na}_{0.7}\text{MnO}_2$  specimens. The random distribution of  $\text{Mn}^{4+}/\text{Mn}^{3+}$  and the lack of  $\text{Na}^+$  ion ordering is believed to be in the



origin of the magnetic instability while combined with the geometric frustration seem to play a crucial role in the formation of the spin-glass state.

Finally, the effect of competing magnetic interactions on the dielectric permittivity is evident for the first time as broad effects in the preliminary dielectric permittivity measurements develop in the same temperature where the magnetic transitions occur. Further exploration in order to clarify the mechanism behind a possible ME coupling and confirm the re-entrant spin-glass profile is necessary employing frequency dependent magnetic and magnetoelectric measurements. In addition to that, neutron diffraction would be a key in order to define the nature of the magnetic interactions that are projected in the macroscopic physical properties.



## Chapter Six:

# Study of the triangular Antiferromagnet $\alpha$ -NaMnO<sub>2</sub> – from powders to single crystals

---

### 6.1 Introduction- The $\alpha$ -NaMnO<sub>2</sub> system

Non-perovskite, two-dimensional (2D) Na-Mn-O oxides are notably challenging as they are an experimental realization of a two-dimensional spin-2, spatially anisotropic triangular lattice, where the interplay of temperature and strong conflicting interactions, stimulates a remarkable inhomogeneous magnetic ground state. [194] As they are likely to exhibit strong geometrical frustration at the ground state this further leads to the development of non collinear phenomena like spin canting antiferromagnetism (AFM), absence of long range ordering (LRO) or coexistence of magnetic phases. [195], [196] Being motivated by the puzzling relief of geometrical frustration and the establishment of magnetic long-range order (LRO) which may allow emerging magnetoelectric (ME) response, we revisited the  $\alpha$ -NaMnO<sub>2</sub> polymorph as a good candidate for studying magnetoelectricity in the still frustrated ground state. [36]

The afore-mentioned  $\alpha$ -NaMnO<sub>2</sub> polymorph [3], a rock-salt derivative of the family of A<sup>+</sup>B<sup>3+</sup>O<sub>2</sub> delafossites, has also attracted a lot of interest due to its wide range of novel electronic and functional properties. Its potential use as substitute to layered Li-Mn-O compounds [10], [141], [178], [197], [198] for utilization as energy storage material has



been widely studied due to its remarkable cycling performance and operating potential. [120], [127]

The  $\alpha$ -NaMnO<sub>2</sub> compound in polycrystalline form has been synthesized for the first time in the 1970 [3] while the first attempt for single crystal specimens was done using hydrothermal and sealed crucible techniques [92], [199] as it is detailed in chapter 3. Until recently, all studies related to the system's rich behavior have been entailed in polycrystalline powder samples. Keeping in mind that successful synthesis of large volume single crystals allowed deeper insights in materials of the same ABO<sub>2</sub> family [132], [133], [200],  $\alpha$ -Na-Mn-O has been revisited in this project using single crystals grown with the floating zone method (growth details in chapter 3) for exploring interplay between the structural and magnetic degrees of freedom. It is worth to address that during the evolution of the present project a parallel work by Dally et.al on the same polymorph has been initiated and the findings [201], [202] will be discussed in this chapter.

### 6.1.1 Structure and polymorphism

Among all compounds of the series,  $\alpha$ -NaMnO<sub>2</sub> is particularly interesting because the electronic configuration promotes an active Jahn-Teller state that results in a monoclinic distortion of the rhombohedral  $\alpha$ -NaFeO<sub>2</sub> polytype (R-3m), supporting orbital-ordering of the Mn<sup>3+</sup>-dz<sup>2</sup> ( $t_{2g}^3 e_g^1$ ; S= 2;  $\mu_{\text{eff}} \cong 4.9 \mu_B$ ) already at 300 K[41]. The average crystal structure of  $\alpha$ -NaMnO<sub>2</sub> is shown in figure 6-1a. It crystallizes in the monoclinic C2/m spacegroup with cell parameters: a= 5.67 Å, b= 2.86 Å, c= 5.80 Å,  $\beta=113.14$  deg [126] and is composed by alternating layers of edge sharing MnO<sub>6</sub> octahedra separated by sodium sheets. As pictured in figure 6-1a the Mn ions are located at the center of edge-sharing octahedra, forming a topology of isosceles triangles (figure 6-1b), which maps out a two-dimensional (2D) anisotropic triangular lattice.

Na-Mn-O oxides exhibit a tailored polymorphism in particular between the stoichiometric  $\alpha$ - and  $\beta$ - polytypes. Electron diffraction patterns supported by HRTEM images of the as synthesized  $\alpha$ -NaMnO<sub>2</sub>, reveal the existence of coherent mirror twins which are randomly spaced in the lattice. Depending on their density they may create sequences of either twin or antiphase boundaries which further lead to the formation of intermediate phases that can modulate the magnetic behavior of the final material.[126] The energy cost for such coherent boundaries is very low since it only affects the distribution of Na and Mn, leaving



the close-packed arrangement of the oxygen atoms as it is. So the energy difference between  $\alpha$ - and  $\beta$ - polymorphs is on the scale of the typical thermal energies that results in a high degree of stacking disorder in these compounds. [125] Such stacking disorder can work as a structure- directing mechanism which can gradually transform the monoclinic and orthorhombic structures of the  $\alpha$ - and  $\beta$ - phases of NaMnO<sub>2</sub> into each other engineering the physical properties of the final compound.

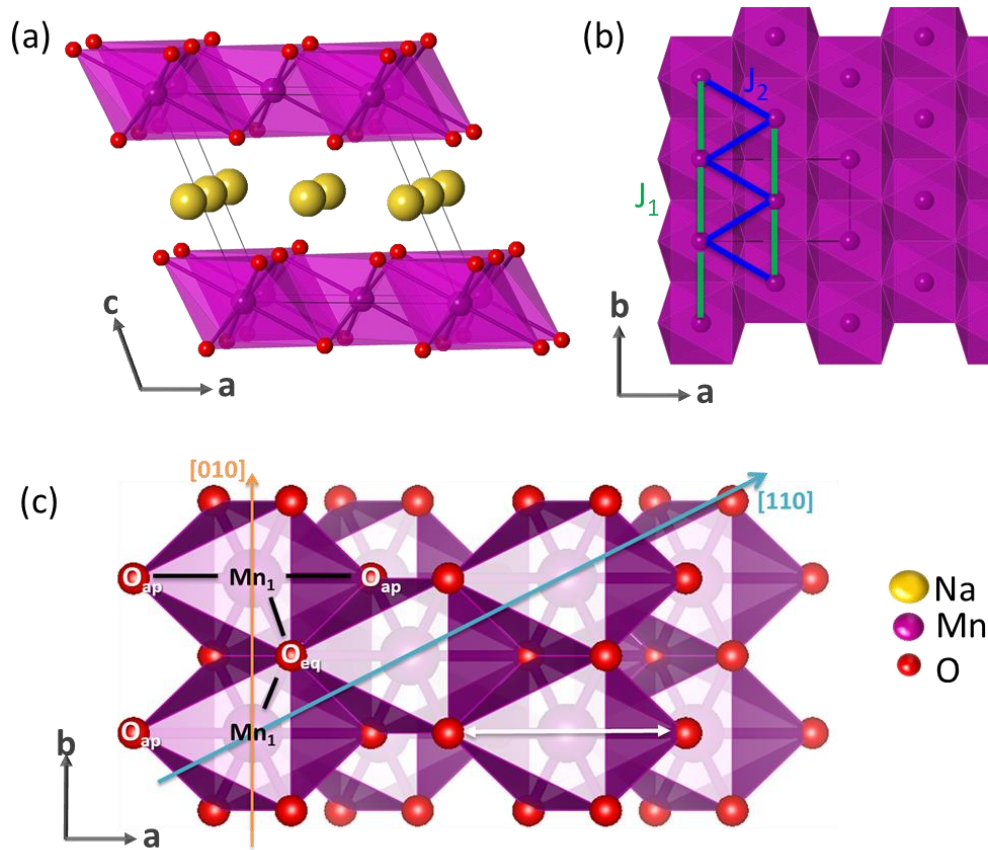


Figure 6-1 Schematic of the  $C2/m$  monoclinic structure in the stoichiometric  $\alpha$ -NaMnO<sub>2</sub>; projections in the (a)  $ac$  plane showing the alternation of layers between the MnO<sub>6</sub> octahedra and the Na cations and (b)  $ab$  plane where the triangular topology of the Mn is clear. The green and blue lines show inequivalent ( $J_1$ ,  $J_2$ ) magnetic interactions along  $bm$  and  $[110]m$  (subscript  $m$  for monoclinic). Mn is represented by purple spheres, Na with yellow and Oxygen with red.

### 6.1.2 Magnetic structure and interactions

The crystal and magnetic structure has been first studied in 2007 by Giot et. al [41]. According to this study, monoclinic  $\alpha$ -NaMnO<sub>2</sub> ( $Mn^{+3}$ ,  $3d^4$ ,  $S=2$ ) is a frustrated system of competing anisotropic magnetic interactions ( $J_1 \gg J_2$ ) (figure 6-1b). The magnetic

frustration is lifted through a magneto-elastic coupling mechanism at  $T_N=45$  K where a structural distortion to triclinic cell takes place and results in long range antiferromagnetic ordering. In particular, neutron powder diffraction (NPD) experiments reveal that upon cooling below 200 K, diffuse scattering emerged around the  $\frac{1}{2}\frac{1}{2}0$  Bragg position, with a typical Warren profile indicating strong 2D magnetic ordering. The intensity of this broad asymmetric feature ( $Q \sim 1.25 \text{ \AA}^{-1}$ ) increases upon cooling and progressively reduces below  $T_N=45$  K at the expense of sharp 3D magnetic Bragg reflections indexed by the propagation vector  $\mathbf{k} = (\frac{1}{2} \frac{1}{2} 0)$  confirming a Néel ordered state[41]. The schematic representation of the magnetic structure is depicted in figure 6-2. AFM chains run along the monoclinic  $b_m$  axis. In the  $a_m b_m$  plane, the chains are stacked ferromagnetically along the  $[1-10]_m$  direction and antiferromagnetically along  $[110]_m$  while the coupling between adjacent  $\text{MnO}_2$  layers along the  $c_m$  direction is FM.

With this symmetry breaking, a spin-gap due to leading quasi-one dimensional interactions ( $J_1 \sim 72$  K) describes the excitations observed [38], [203]. The coexistence of long and short range order below the Neel temperature proved by the NPD measurements, hints a inhomogeneous ground state and initiated further investigation. Zorko et al, in 2014, proposed a peculiar magnetostructural inhomogeneity that emerges as a consequence of the system's tendency to remove magnetic degeneracy due to spin frustration [139], [194]. In the later, the monoclinic phase is disrupted by magnetically short-range-ordered nanoscale triclinic regions, thus revealing a novel complex ground state.

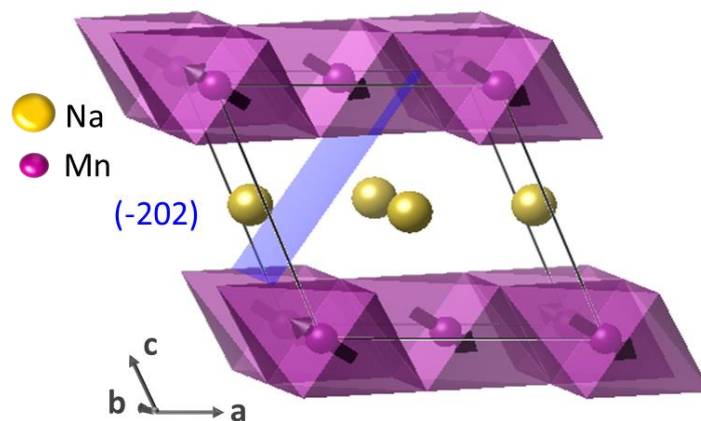


Figure 6-2 AFM spin configuration represented in the  $C2/m$  monoclinic cell of  $\alpha$ - $\text{NaMnO}_2$ . The spin arrangement consists of AFM chains running along the monoclinic  $b_m$  axis. In the  $a_m b_m$  plane, the chains are stacked ferromagnetically along the  $[1-10]_m$  direction and

*antiferromagnetically along  $[110]_m$ . Coupling between adjacent MnO<sub>2</sub> layers along the  $cm$  direction is FM.*

### 6.1.3 Deviations from stoichiometry and competing interactions

Several Na-deficient polymorphs have been investigated in the quest for better performance cathode materials.[10], [124], [125], [129], [176], [177] In contrary, less is known about the role of mixed Mn valence ( $Mn^{4+} / Mn^{3+}$ ), fostered by Na vacancies in the structure, and the consequent modification of the cooperative nature of the electronic/magnetic properties. In this respect, first principle studies, along with theoretical analysis on the Jahn-Teller distortion of the octahedra in  $\alpha$ -NaMnO<sub>2</sub> confirm that the AFM state is more stable compared to FM one due to the relatively small Mn-Mn distances, which allow direct overlap of the half-filled orbitals in the  $Mn^{3+}$  ions. Moreover, nn-interactions between the MnO<sub>6</sub> octahedra seem to be favored through the super-superexchange (SSE) path Mn-O···O-Mn, rather than the ordinary superexchange (SE) one. [204]–[206] Interestingly, Ouyang et al. predict that by increasing the hole-doping in Na<sub>x</sub>MnO<sub>2</sub> the magnetic behavior evolves from that of a striped AFM to a FM ground state, as the AFM moments become progressively canted. [207] Experimentally, it has been shown that in the  $\alpha$ -Na<sub>0.7</sub>MnO<sub>2</sub>, the mixture of  $Mn^{3+} / Mn^{4+}$  ions in the geometrically frustrated hexagonal structure creates significant site-disorder that fosters a spin-glass behavior.[182] However, in the case of the monoclinic  $\alpha$ -Na<sub>5/8</sub>MnO<sub>2</sub>, the Na-cation and Na-vacancy orderings are connected by the cooperative Jahn-Teller effect (CJTE) to the  $Mn^{3+}$  and  $Mn^{4+}$  sites in a remarkable way. The probed superstructure highlights the important role of structural details in altering the magnetic nn-interactions between  $Mn^{3+}$ (Jahn-Teller), that forms AFM atomic stripes and  $Mn^{4+}$  (non Jahn-Teller) that forms FM or AFM nn-couplings depending on the competition of various direct and indirect exchange mechanisms.[208]In the latter, the authors note the necessity for single-crystal studies, but due to the materials' air-sensitive nature that has been hard to accomplish until recently.

### 6.1.4 The quest for single crystal and contribution of the present work

Single crystals are very desirable for experiments that require large volumes or areas of samples, such as neutron diffraction and anisotropic property measurements. Single



crystals of  $\alpha$ -Na-Mn-O have been grown using the floating zone method for the first time as a part of this project. Details about the growth are described in chapter 3.

In this chapter, the evolution of the magnetic behaviour of single-crystal  $\alpha$ -Na<sub>x</sub>MnO<sub>2</sub> ( $x \approx 0.96$ ) samples, grown with a modified FZ method protocol is investigated. The chemical composition has been studied through SEM-EDS, ICPMS and XPS, is presented, both aiming to substantiate the structural modifications drawn by synchrotron X-ray powder diffraction. The work quantifies the mixed Mn valence character of the crystals, while it also suggests that this electronic dis-proportionation favors a monoclinic structure, involving two non-equivalent TM octahedral sites. To investigate the validity of this mixed (Mn<sup>4+</sup>/Mn<sup>3+</sup>) model system, susceptibility measurements were performed for different crystal orientations and complemented by single-crystal neutron diffraction data. The interplay of persistent short-range two-dimensional spin correlations with coexisting weak FM and AFM long-range spin-orderings at low-temperatures is uncovered while the geometric frustration is relieved by electronic-driven lattice distortions. Finally, the effect of competing magnetic interactions on the dielectric permittivity is investigated and presented for both polycrystalline samples and single crystal specimens.

## 6.2 Phase purity and Crystallinity

### 6.2.1 X-Ray Powder Diffraction

#### 6.2.1.1 *Experiment and sample preparation*

The polycrystalline specimens of  $\alpha$ -NaMnO<sub>2</sub> have been synthesized following the protocol presented in chapter 3 (section 3.2.1.1). A part of these batches has been used for magnetodielectric measurements prepared in pellet form while almost 76 gr have been used as starting powders for the single crystal growth as detailed in section 3.2.3.1. The purity and crystallinity of the  $\alpha$ -NaMnO<sub>2</sub> specimens has been initially checked by X-Ray diffraction on a Rigaku D/MAX-2000H rotating Cu anode diffractometer ( $\lambda=1.5406 \text{ \AA}$ ). The sample in a form of powder or crashed crystal was placed on the holder and sealed with a mylar foil in the glove box, so that it was kept under Ar atmosphere and exposed if possible at all in air during the X-Rays experiment. When the use of such a holder was not feasible the powder or crystals were mixed well with grease inside the inert atmosphere of a glove box and spread on the available Ni sample holder. All measurements have been



taken with the same step of 0.02 degrees and time per step,  $t=12$  sec unless it is stated differently.

### 6.2.1.2 Polycrystalline specimens of $\alpha$ -Na-Mn-O

The graph obtained by the XRPD is shown in Figure 6-3. The Bragg reflections obtained from the  $\alpha$ -NaMnO<sub>2</sub> show match well with the reflections obtained from the ICSD database (cif file: 21028). Therefore, the room temperature structure of the  $\alpha$ -NaMnO<sub>2</sub> can be successfully indexed upon the monoclinic structure (C2/m) with cell parameters:  $a=5.67$  Å,  $b=2.85$  Å,  $c=5.80$  Å,  $\beta=113.2$  deg.

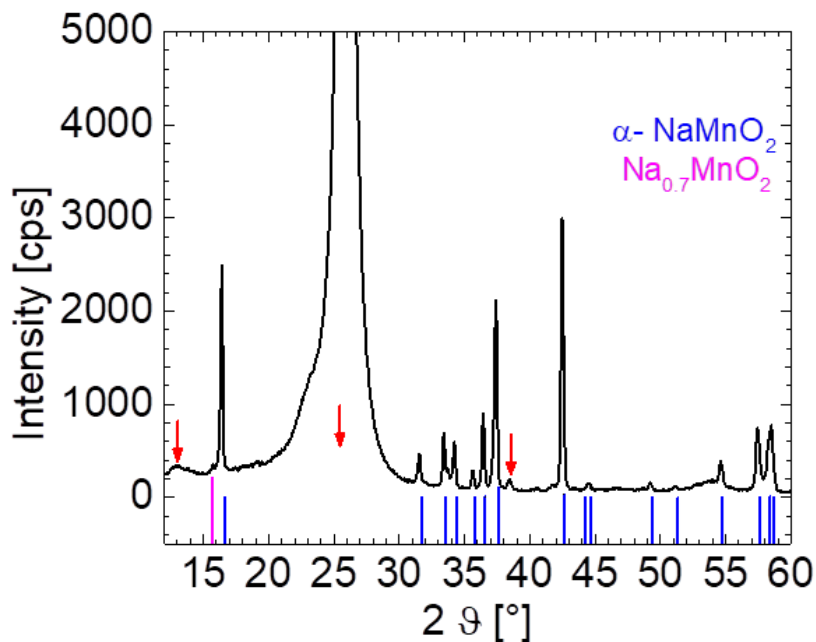


Figure 6-3 X-ray powder diffraction pattern of a polycrystalline sample of  $\alpha$ -NaMnO<sub>2</sub> (black continuous line). The indexing of the Bragg reflections has been done according to the 21028 cif file of the ICSD data base, which corresponds to the blue vertical lines. The magenta vertical line at 15.7 deg correspond to the 002 peak of the sodium deficient Na<sub>0.7</sub>MnO<sub>2</sub>. The red arrows are attributed to reflections of the mylar film.

The one reflection at 15.7 deg pointed with a vertical magenta line in the pattern corresponds to 002 reflection of the Na<sub>0.7</sub>MnO<sub>2</sub>. The  $\alpha$ -Na<sub>0.7</sub>MnO<sub>2+y</sub> Na-deficient polymorph is found to be the most stable phase energetically of the Na-Mn-O system [3] and is luckily to be formed in a lower temperature during the heating process (~600 °C). However, according to Parant et. al in temperatures above 700°C  $\alpha$ -NaMnO<sub>2</sub> is likely to be formed and coexist with the  $\beta$ -Na<sub>0.7</sub>MnO<sub>2</sub> which crystallizes in orthorhombic cell Cmc2

and with Na<sub>3</sub>MnO<sub>4</sub> (Pmnb) which we did observe in some batches (figure 6-4). In the figure 6-4 a detailed focus in the low angle area allows the observation of the main Bragg peaks of minority phases that are likely to form together with  $\alpha$ -NaMnO<sub>2</sub>. The detection of a minority phase of  $\beta$ -NaMnO<sub>2</sub> which would agree with the findings of HPTEM showing intergrowth of  $\beta$ - stacking sequences inside the  $\alpha$ - structure, is only observed in “scaled up” batches of 4gr that were mainly used for the single crystal growth.

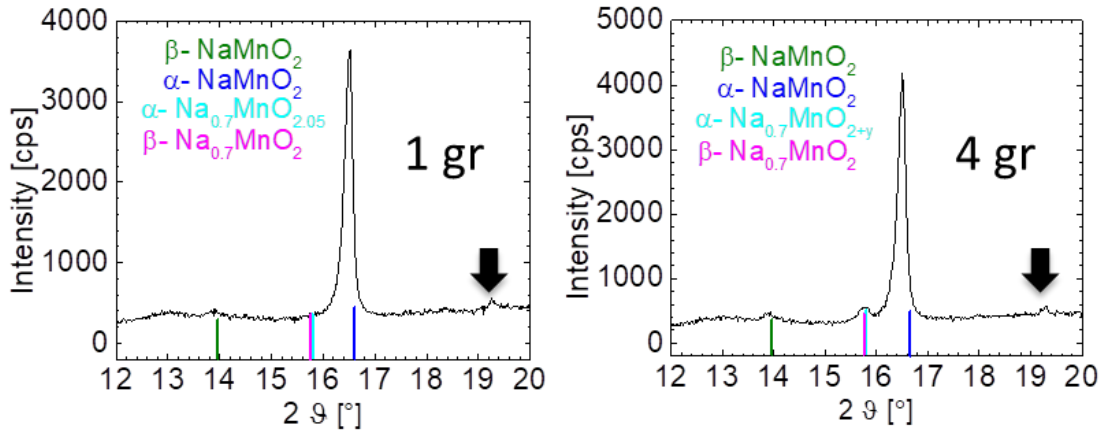


Figure 6-4 Examples of 2 different batches. Left panel batch of 1 gr. Right panel batch of 4 gr (scale up). Bragg peaks of  $\beta$ -NaMnO<sub>2</sub> (001),  $\alpha$ -Na<sub>0.7</sub>MnO<sub>2+y</sub> (002) and  $\beta$ -Na<sub>0.7</sub>MnO<sub>2</sub> (002) are detected and represented with green, turquoise and magenta lines respectively. The black arrow point the peak of Na<sub>3</sub>MnO<sub>4</sub>.

### 6.2.1.3 Single crystals of $\alpha$ -Na-Mn-O

The growth of single crystals of the Na-Mn-O system was performed by the floating zone (FZ) technique in Ar gas atmosphere. The growths were carried out using a 2 mirror Canon Machinery SC1-MDH 11020 (University of Warwick) with standard double elliptical mirror geometry equipped with two 1.5 kW lamps, which can reach a maximum operating temperature of 2000 degrees Centigrade. Several attempts were performed using different growth conditions. The protocols that have been followed and details on the growth conditions are presented in chapter 3. The starting powders have been mixture of synthesized batches that might include secondary phases. An example of a mixed batch that has been used as starting powder is given in figure 6-5.



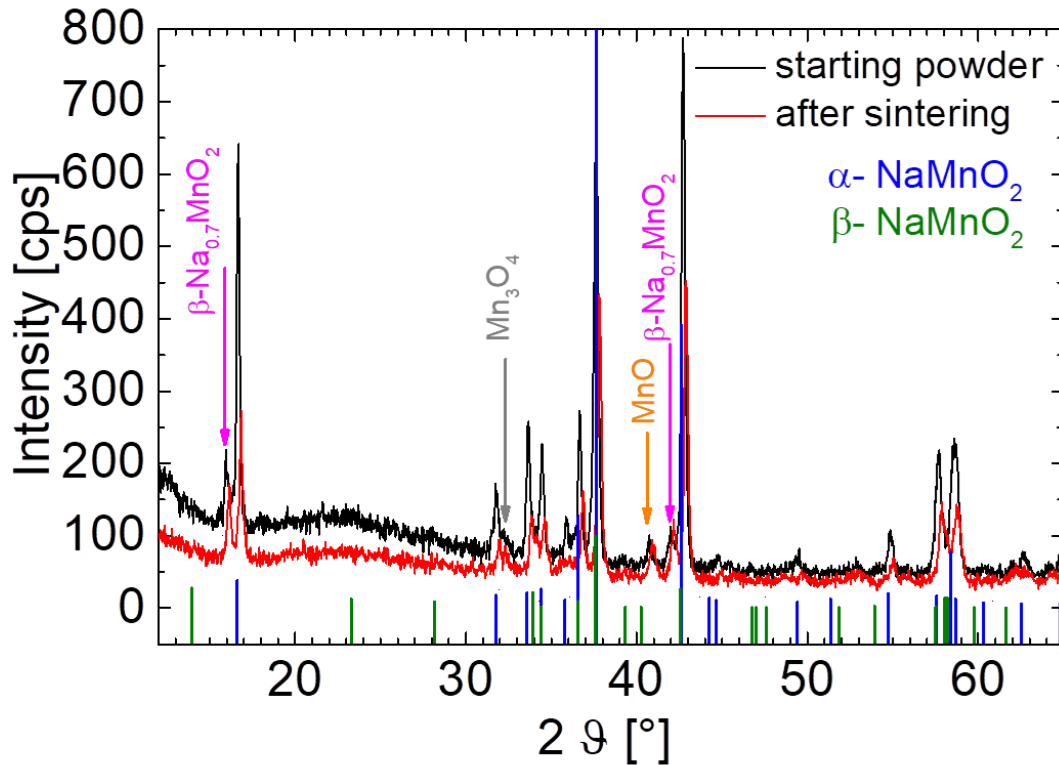


Figure 6-5 XRPD pattern of a mixed batch of  $\alpha$ -NaMnO<sub>2</sub> used as starting powders (black line) and the same batch sintered (refer to batch #3 in table 3-4) shown in red line. Blue ticks represent the 21028 card of  $\alpha$ -NaMnO<sub>2</sub> and green ticks the 15769 card of  $\beta$ -NaMnO<sub>2</sub>. Impurities of  $\beta$ -Na<sub>0.7</sub>MnO<sub>2</sub> (magenta), MnO (orange) and Mn<sub>3</sub>O<sub>4</sub> (grey) are observed both starting powders and sintered rod. The high background in low angles is the contribution of grease which was mixed with the powder as a protective media against moisture and oxygen.

After the powder has been pressed into rod it was further sintered in order to achieve a firm feed rod that could be easily mounted in the optical furnace. We should address here that in all cases the sintered rod is comprised by a majority of alpha phase, the same as the starting powder. This has been achieved by using the same temperature and inert atmosphere for sintering, as the one used for the synthesis of the starting powders (refer to chapter 3). The alpha polymorph is known to be the low temperature phase of the Na-rich phases of Na-Mn-O system composed in 750 °C [3] and so keeping the same low temperature gave as an alpha starting feed rod. Sintering protocols of 48h duration starting from room temperature ( $T_{\text{start}} = 25$  °C) gave an xrd pattern with both MnO and Mn<sub>3</sub>O<sub>4</sub> impurities (figure 6-5). The optimum sintering conditions that led to successful growths entailed a  $T_{\text{start}} = 750$  °C and a duration of 16 hours. Following the later sintering protocol, X-ray diffraction of the rods shows that the main  $\alpha$ -NaMnO<sub>2</sub> phase coexists with minority  $\alpha$ -Na<sub>0.7</sub>MnO<sub>2</sub> and  $\beta$ -NaMnO<sub>2</sub> phases, mainly at the surface. Interestingly, the majority phase of the sintered rod in similar

study was found to be of the  $\beta$ -NaMnO<sub>2</sub> crystal polytype. [136]

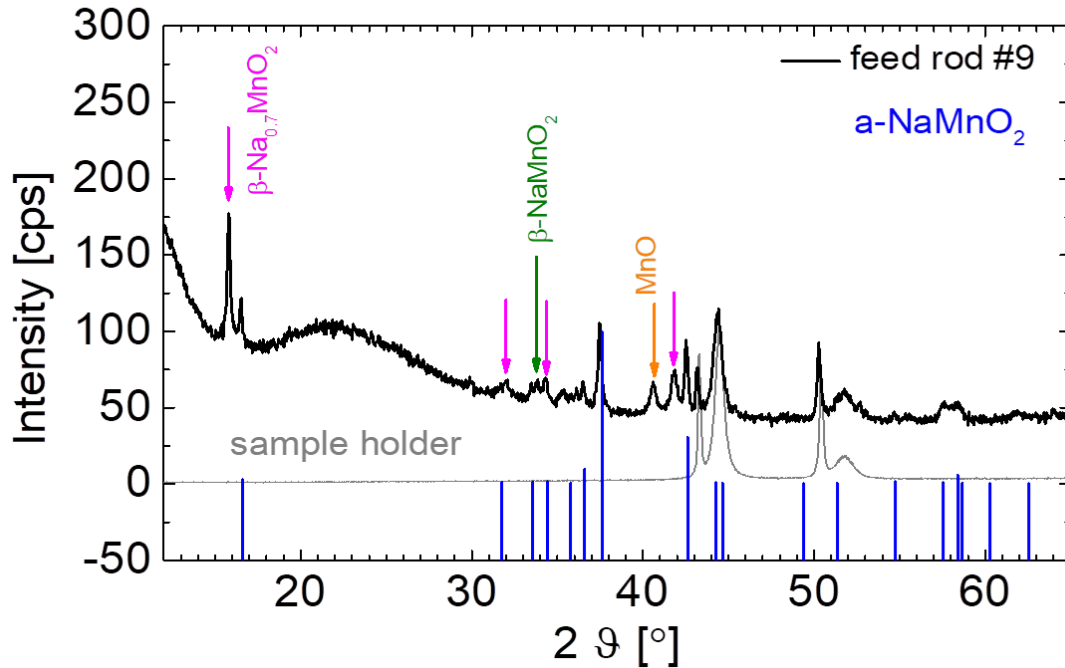


Figure 6-6 XRPD pattern of a sintered feed rod used for successful growth (black line) (refer to batch #9 in table 3-4). Blue ticks represent the 21028 card of  $\alpha$ -NaMnO<sub>2</sub>. Impurities of  $\beta$ -NaMnO<sub>2</sub> (green arrow),  $\beta$ -Na<sub>0.7</sub>MnO<sub>2</sub> (magenta arrow), MnO (orange arrow) are observed. The high background in low angles is the contribution of grease which was mixed with the powder as a protective media against moisture and oxygen when there was not available sample holder for air-sensitive samples

In figure 6-6 the XRPD pattern of the scrubbed surface of the sintered rod used for a successful growth is presented. The starting powder of this batch has been free of Mn<sub>3</sub>O<sub>4</sub> and so has been the sintered rod preserving the majority of alpha phase. Minority phase of MnO seems to disappear during the growth as it is shown in the pattern of a crashed crystal flake (figure 6-7).

The coexistence of alpha and beta phases in the XRPD pattern of the grown crystals represented in figure 6-7, shows that the single crystals grown with the floating zone method might be also prone to the structural defects that have been observed in the polycrystalline  $\alpha$ -NaMnO<sub>2</sub> specimens. For this reason, further investigation for the good crystallinity and exact determination of the nuclear structure of the grown crystals has been pursued employing single crystal X-ray diffraction and synchrotron X-ray powder diffraction, performed at the National Synchrotron Light Source (NSLS-II, BNL, USA).



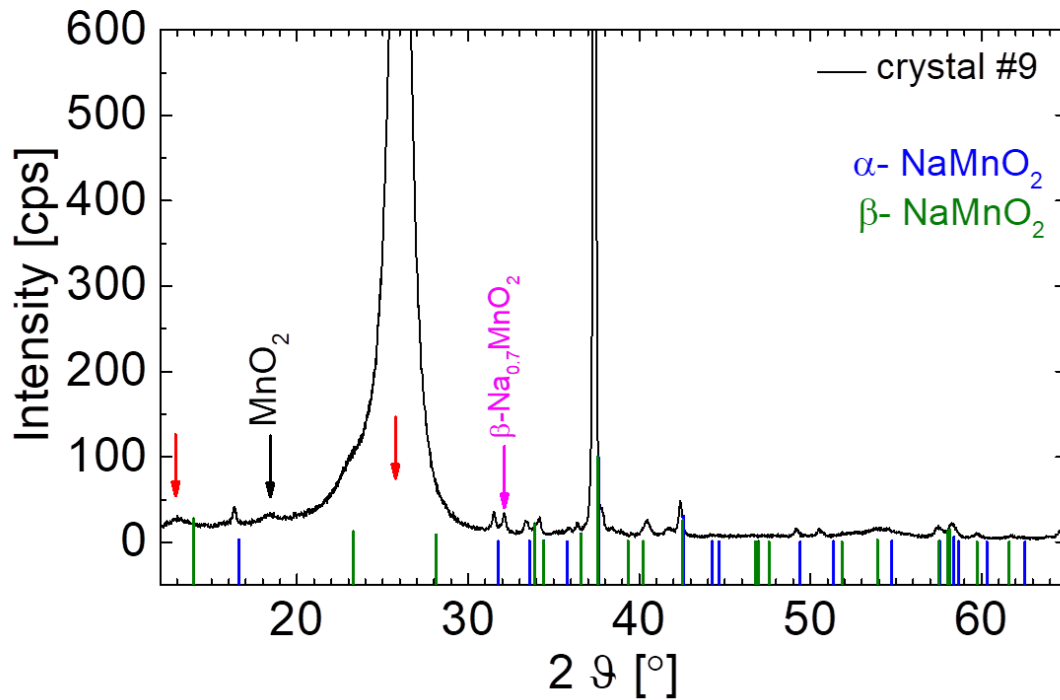


Figure 6-7 XRPD pattern of a crashed crystal boule of #9. Blue ticks represent the 21028 card of  $\alpha$ -NaMnO<sub>2</sub> and green ticks the 15769 card of  $\beta$ -NaMnO<sub>2</sub>. Impurities  $\beta$ -Na<sub>0.7</sub>MnO<sub>2</sub> (magenta arrow), MnO<sub>2</sub> (black arrow) are observed. Red arrows point out the mylar contribution of the sample holder.

### 6.2.2 Laue Method

Crystal quality and orientation of the as grown crystals was determined using Laue x-ray back reflection technique. Laue x-ray diffraction photographs were taken using a Photonic –Science Laue dual camera system. In the successfully grown boules we could observe a metallic shiny surface with facets. Using published information [3], [126] on the monoclinic crystal space group C2/m of the starting powders together with the lattice parameters we could simulate Laue Patterns employing the Crystal Maker software which would match well with the Laue pictures of the facets of the grown boules and the cleaved flakes (figure 6-9).

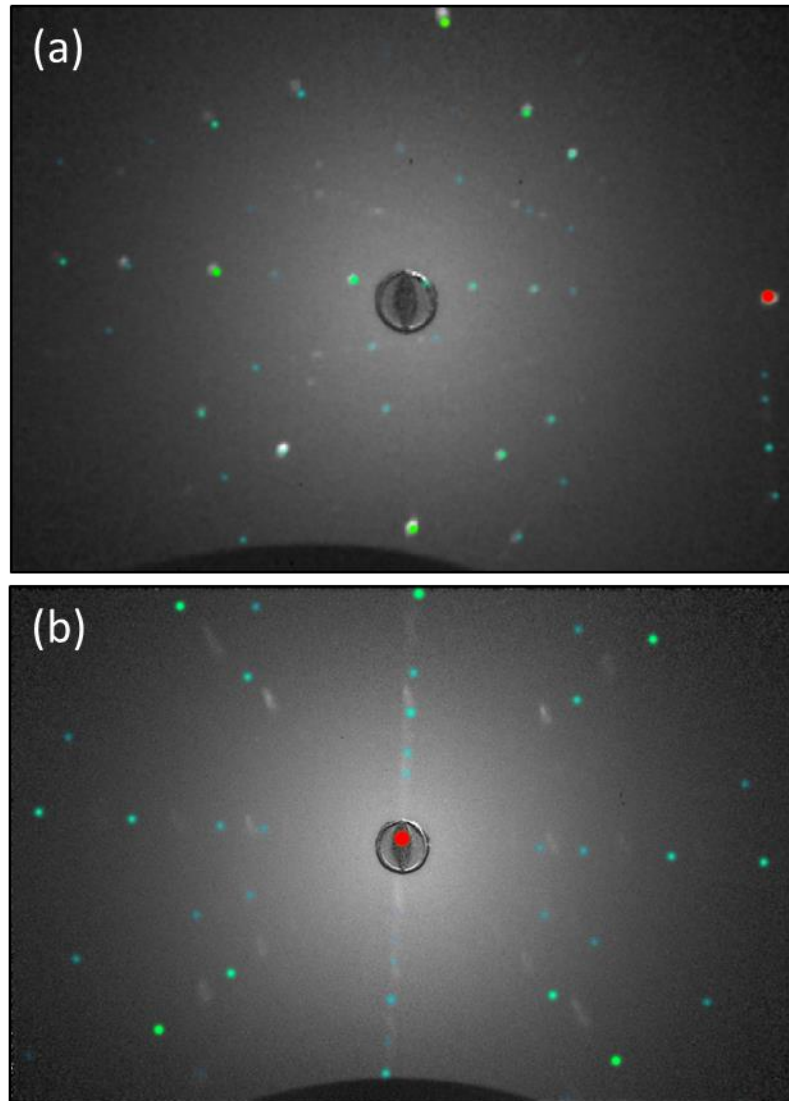


Figure 6-8 a) Laue photograph of the boule facet and b) Laue photo of the flat side of a cleaved flake, both matched with the simulation pattern of (-202) plane of monoclinic C2/m produced with Crystal Maker.

For growth #9, the Laue patterns taken from the facets of the crystal boule (Fig.6-9 a) were indexed well in the (-202) plane of the monoclinic C2/m system of  $\alpha$ -NaMnO<sub>2</sub>, confirming the good quality of the crystal flakes. Observation of multiple spots per reflection in some Laue patterns suggests a stacked layered structure (figure 6-9b), which is also evident in the SEM images (Fig. ...). The crystal boules cleave easily in the preferred (-202) plane and Laue pictures of several crystal flakes prove that (Figure 6-9 and figure 6-10). Since the flakes were cleaving naturally with a flat surface of (-202) further anisotropy characterization was planned according to that.

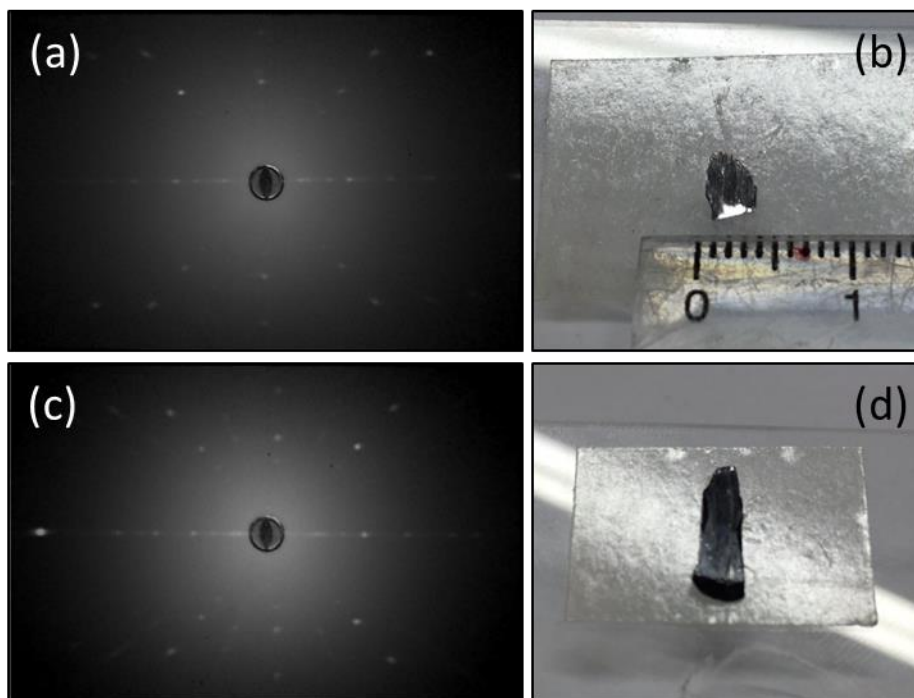


Figure 6-9 (a-b) Laue photograph of the flat side of a cleaved flake of batch#9 and the actual picture of the flake. (c-d) Laue photograph of the flat side of a cleaved flake of batch #8 and the actual picture of the flake. Both photographs are identical and match the simulation pattern of  $(-202)$  plane of monoclinic  $C2/m$  cell.

### 6.2.3 Single crystal X-ray diffraction

#### 6.2.3.1 Experiment and sample preparation

The data collection took place at in-house BRUKER D8 VENTURE (Cu  $K\alpha$ ,  $\lambda=1.54$  Å) diffractometer (IMBB-FORTH) under the guidance of Prof. K. Petratos and Dr R. Gessmann. The kappa geometry of the goniometer provides true multiplicity and better description of the absorption surface leading to an increased  $I/\sigma I$  (Average intensity / average intensity error) ratio. The PROTEUM2 [95] software has been the software tool used in order to determine the unit cell, prepare the strategy of the data collection and integrate the data collected. The crystals used for data collection in this thesis were investigated under cooled nitrogen. Showering a crystal with cold dry nitrogen during data collection reduces thermal vibrations of atoms so that better data quality is possible. The choice of crystals has been done according to size and well defined edges under a microscope. As soon as the crystal got out of the glove box they were bathed in paraffin oil to prevent any moisture absorption and then captured on the kapton loop.

### 6.2.3.2 *Results and issues*

About 10 crystal flakes cleaved from the successfully grown batches have been tested. The majority of them seemed to adopt a monoclinic unit cell but in all cases the finally integrated data didn't allow further structure determination due to the multi-crystallinity that have been observed.

The preliminary rotational image collected to screen the sample quality was most of the times indicating multiple reflections. However in almost all cases it was feasible to collect a preliminary set of frames for determination of the unit cell. Following an auto indexing process of the reflections from the previous frames we get the reduced primitive cell and calculate the orientation matrix (which relates the unit cell to the actual crystal position within the beam). The primitive unit cell is refined using least-squares or fast fourier transformation method and then converted to the appropriate crystal system and Bravais lattice. In this step most of the times the Bravais lattice chosen was giving unreasonable cell parameters and only in three cases we got a monoclinic P cell that encouraged further data collection. In these cases, the chosen cell has been refined using least-squares to determine the final orientation matrix for the sample. After the refined cell and orientation matrix have been determined, intensity data has been collected by collecting a sphere or hemisphere of data using an incremental scan method, collecting frames in 0.1° to 0.3° increments (over certain angles while others are held constant). After the data have been collected the integration process reduced the raw frame data to a smaller set of individual integrated intensities introducing corrections for instrumental factors, polarization effects and X-ray absorption.



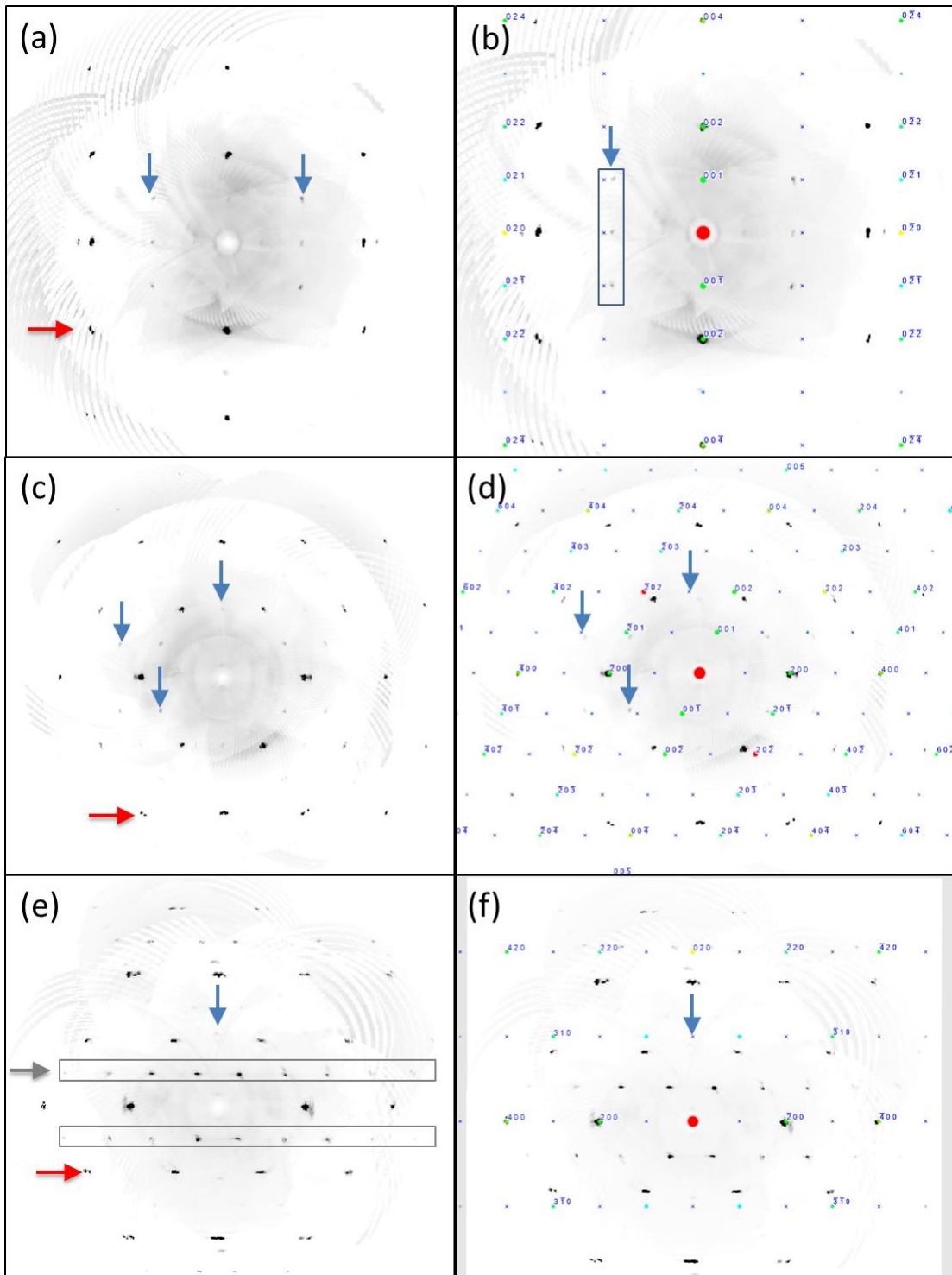


Figure 6-10 Precision picture of reflections of (a)  $0kl$  plane , (c)  $h0l$  plane and (e)  $hk0$  plane and simulation using the  $C2/m$  monoclinic cell in view direction (b)  $[001]$ , (d)  $[010]$  and (f)  $[001]$ . The gray arrows point out reflections of weaker intensity that could not be indexed by the  $C2/m$  cell, the light blue arrows point systematic absences of the  $C$ -centered unit cell while the red arrows point at examples of multiple reflections per site.

The hkl data would not allow the determination of a unique set of phases that would lead to the determination of the crystal structure. This was mainly attributed to the multiple reflections observed that could be the contribution of twin planes or stacking crystallites. In addition to that, a second crystal domain of weaker intensity that could not be fitted by the monoclinic system has been detected in the 2D precision pictures of hkl planes. In figure 6-10 the 2D reflections pattern of 0kl, h0l, hk0 planes are presented on the left panel (figure 6-10 a, c, e) together with simulated pattern indexed in the C2/m monoclinic system of  $\alpha$ -NaMnO<sub>2</sub> powders on the right panel (figure 6-10 b, d, f) as it has been determined by Abakumov et. al [126]. The red arrows point at examples of multiple reflections per site while the gray arrows point out the existence of a secondary structural domain. The weaker intensity peaks seem to form a crystallographic domain that could be attributed either to the systematic absences forced by the c-centering or by a secondary phase existing as an intergrowth in the alpha. In figure 6-11 a simulation of both alpha C2/m (fig.6-11 a) and Pmmn beta [126] phases (fig. 6-11 b) compared with the observed pattern is presented showing that the second crystal domain could be attributed either to beta phase generated by stacking faults producing a “crimped” structure or a monoclinic P cell free from absences imposed by the c-centering. All simulations have been done using the SINGLE CRYSTAL DIFFRACTION module of the CRYSTAL MAKER platform[209]. The handling of such demanding structures would need much effort and gain of expertise in the specific technique and was not possible to be pursued in the frame of the present project. In view of that, high resolution XPD data were the sole way to define the structure of the grown crystals of alpha phase.



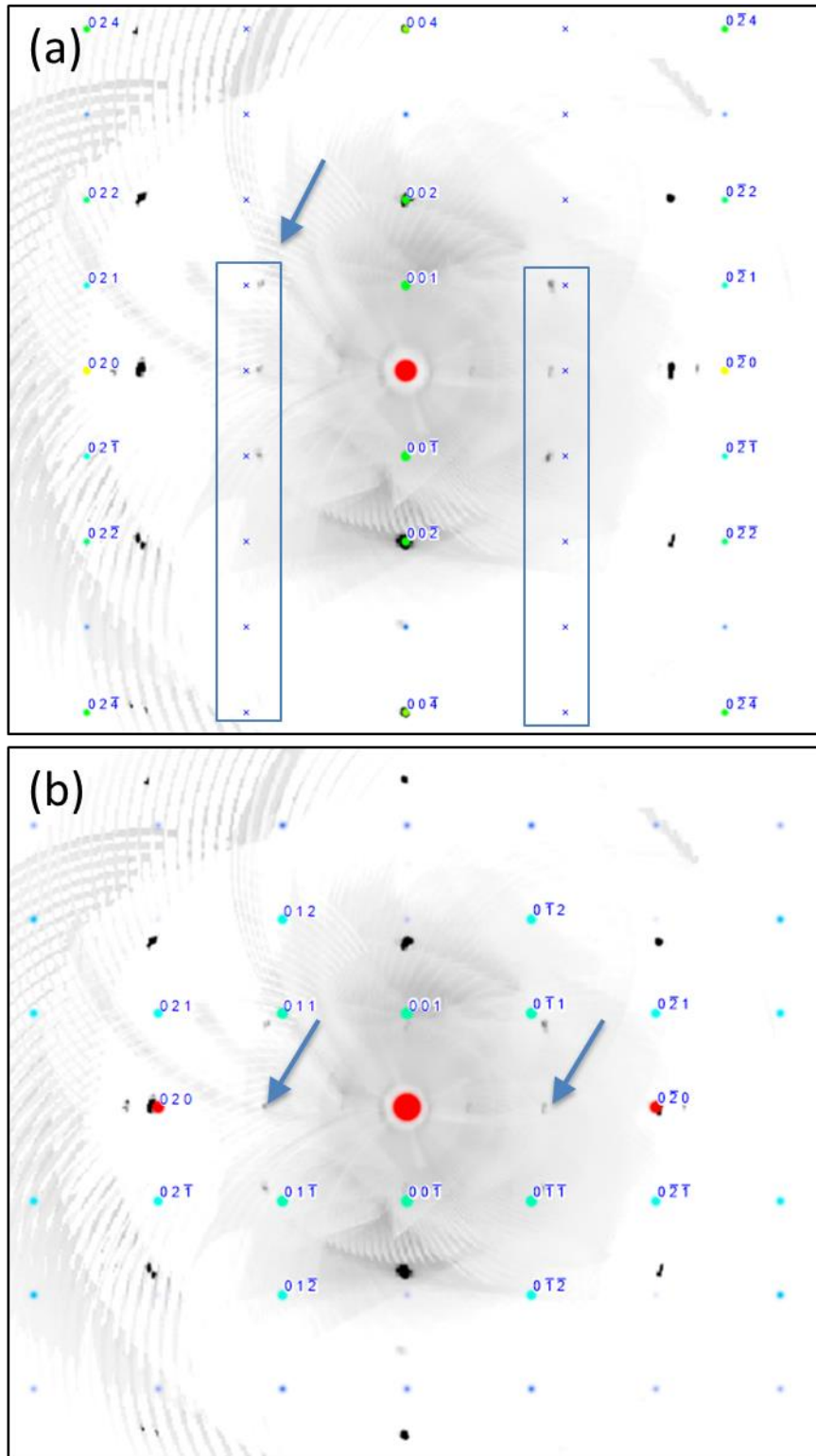


Figure 6-11 Precision picture of reflections of  $0kl$  plane and simulation using the (a)  $C2/m$  monoclinic cell and (b)  $Pmmn$  orthorhombic cell in view direction  $[100]$ . The light blue arrows point out reflections of weaker intensity that would either belong to another lattice and have been well indexed with  $Pmmn$  or were indexed as systematic absences with a blue  $x$ .

### 6.3 Chemical characterization

The nuclear structure and physical properties of Na<sub>x</sub>MnO<sub>2</sub> system are highly sensitive to the exact level of sodium within the system. So an accurate determination of x for the crystals under study is imperative for solving the nuclear structure and interpreting the magnetic findings. The Na percentage in the Na-Mn-O formula is a key factor that rules the Mn<sup>3+</sup>/Mn<sup>4+</sup> ratio and as a consequence the Jahn-Teller effect having an immediate impact on the magnetism as well as the structural stability of each phase and rule the potential applications.

For the determination of the sodium percentage and the quantification of the Mn valence several techniques have been employed with results generally in good agreement with one another.

#### 6.3.1 ICP-MS

##### 6.3.1.1 *Experiment and sample preparation*

Only 3 samples, 2 polycrystalline (p1, p2) and 1 single crystal (c1), were sent for analysis in NTNU, Department of Chemistry, in order to determine the Na level in comparison with the Mn level on alpha system. The samples have been stoichiometric  $\alpha$ -NaMnO<sub>2</sub> powders that have been used as starting powders for the single crystal growth and the crystal has been taken of the successful growth #9. They all have been dissolved in HCL to produce 3 different solutions, before being introduced into the core of an inductively coupled plasma (usually argon at >8000°C).

##### 6.3.1.2 *Results and drawbacks*

The results are summed in table 6-1.

Table 6-1

Sample	M [mg]	Volume (after dilution) [l]	Na [ug/ g]	Mn [ug/ g]	Na/ Mn
$\alpha$ -NaMnO <sub>2</sub> -p1	4	378.4	142362	398602	0.85/1
$\alpha$ -NaMnO <sub>2</sub> -p2	4	378.4	142403	395559	0.86/1
$\alpha$ -NaMnO <sub>2</sub> -c1	3.4	382.4	217995	502478	1/1
Average of all			167587	432213	0.93/1
Rsd %			26	14.1	



The quantities in ug/g have been calculated by the measured ug/L quantities following the formula:

$$\text{Concentration } \left[ \frac{\text{ug}}{\text{g}} \right] = \frac{\text{concentration in volume of sample } \left[ \frac{\text{ug}}{\text{L}} \right] * \text{Volume of Sample after dilution [L]}}{\text{Sample weight [g]}}$$

The low level of Na detected in the case of powders has been a surprise especially when compared to the stoichiometric within error c1. Due to limited time only one test sample from each batch (p1, p2, c1) was measured and so the results cannot be fully trusted.

In general the process suffers from several drawbacks. Although the technique is relatively precise (with an error in x of just 5%) the absolute accuracy depends on a calibration to a standard sample. During the powder reaction processes, an unknown quantity of sodium is lost, and so the production of a standard to calibrate the other measurements against is difficult. In addition to that the preparation of the solution itself can introduce errors to the measurement especially when the samples handled are air and moisture sensitive (as in the case of the powders). That should be taken into consideration as a possible reason of the low Na level measured in the powders. It is worth mentioning that ICP-OES measurements of past samples determined a Na/ Mn = 0.826/ 1 according to studies by Dr Bakaimi.

### 6.3.2 SEM-EDS

#### 6.3.2.1 *Experiment and sample preparation*

Scanning electron microscopy (SEM) images were obtained using a field emission system (JEOL JSM-7000F) operating at 15 kV accelerated voltage. To acquire SEM images of crystal platelets the crystal boule was cleaved inside the glove-box with a tungsten knife by steadily pressing the boule along growth direction. We did not use spattering or polishing before the observation in order to reduce the exposure time of the crystals to ambient conditions. Quantification of the elemental ratios at the surface of the crystal flakes was carried with energy dispersive spectroscopy (EDS) by using a JEOL JSM-6390LV scanning electron microscope equipped with an Oxford INCA PentaFET-x3 detector.

#### 6.3.2.2 *Layered crystals and off stoichiometry*

Despite the inevitable (under the present conditions) Na and Mn evaporation, the Na: Mn ratio in the crystals was found to be near the fully stoichiometric (1:1)  $\alpha$ -NaMnO<sub>2</sub> parent



powders. EDS spectra taken from a number of cleaved crystal flakes gives an average of 0.96: 1 for Na: Mn stoichiometry, which allows the existence of a small amount of Mn<sup>4+</sup> ions due to Na vacancies. The sample flakes were taken from various sections of the grown boule in order to check consistency.

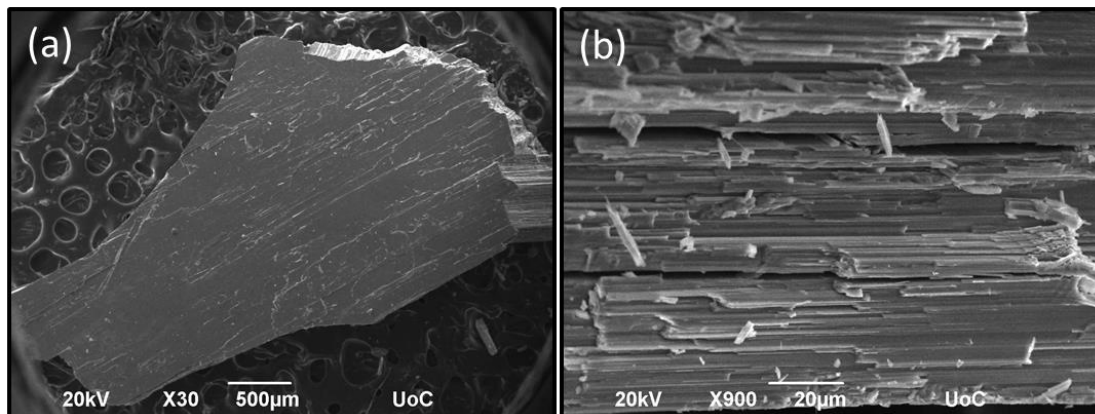


Figure 6-12 SEM image depicting (a) the layered morphology of the as-grown crystal flake of  $\alpha$ -Na<sub>0.96</sub>MnO<sub>2</sub>, (b) a close-up view of the stacking layers

In figure 6-12 a SEM picture of a crystal flake cleaved from the crystal boule #9 is shown. A close up taken close to the edge (figure 6-12 b) reveals well defined layered stacks of crystallites explaining the easy cleavage of the flakes towards a specific direction. A misalignment of these stacks is possibly the source of multiple reflections per site in the single crystal xrd pattern and later on in the single crystal neutron diffraction pattern. The really thin layers ( $\sim 0.667 \mu\text{m}$ ) make it impossible to split them by hand.

EDS spectra taken on several flakes show a deviation of the Na/ Mn ratio from the stoichiometric Na/ Mn= 1/ 1 to the Na/ Mn= 0.88/ 1. Such a deviation has been attributed to the sensitivity of the Na-Mn-O system to air and moisture allowing a fast oxidation of the surface. In order to confirm the effect of exposure to ambient conditions a chosen flake with initial surface Na/ Mn ratio of 0.96/ 1 ( same as the average ratio) was left exposed and measured a) fresh out of the glove box, b) after one day of exposure and c) after one month of exposure in ambient conditions. The result is presented in the three frames of figure 6-13. The initial Na/ Mn= 0.96/ 1 ratio has been changed to Na/ Mn= 1.01/ 1 in only one day. The surface of the crystal changed from smooth (fig.6-13 a) to one covered by a whiter layer of grains (fig.6-13 b). The increase of the detected sodium elemental atomic ratio seemed to be the result of Na ions moving on the surface of the crystal reacting with atmospheric O<sub>2</sub> for the formation of Na<sub>2</sub>O or Na<sub>2</sub>O<sub>2</sub>. Further reaction with the H<sub>2</sub>O would

lead to NaOH which reacting with CO<sub>2</sub> would finally form the relatively unreactive to the atmosphere Na<sub>2</sub>CO<sub>3</sub> sodium carbonate (white in color). The suggested mechanism of the chemical transformation that happens on the surface of the crystal follows the sequence of the reactions presented below:

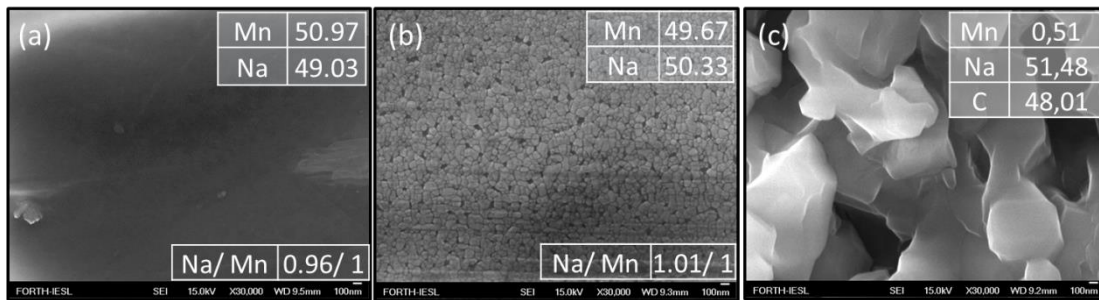
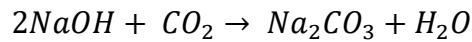
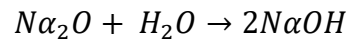
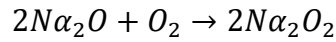
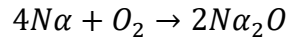


Figure 6-13 A close up of the surface of a flake that initially had a surface stoichiometry ratio of Na/Mn = 0.96/1 taken on 3 different dates having the flake exposed at ambient conditions. (a) 26<sup>th</sup> April, (b) 27<sup>th</sup> April, (c) 24<sup>th</sup> May of the same year. The tables on the top right corners present the EDS results for Na and Mn relative proportions (Atomic %)

The assumption made here is that the highly reactive sodium abandons the interlayer position and forms the aforementioned salt on the surface of the crystal. This is supported by the observation that the electron beam is burning the white surface while trying to focus on the surface as well as the detection of carbon on the surface after a longer exposure to air. In figure 6-14, a crack of the crystal formed after 1 month of its exposure into air, allows EDS analysis of the area inside the crystal (fig.6-14 b) which comes in agreement with the scenario that wants Mn to stay in the layered structure while Na in the form of Na<sub>2</sub>CO<sub>3</sub> has covered the surface of the crystal as shown in figure 6-13 c. According to Sherbini et. al [210] In presence of both O<sub>2</sub> and H<sub>2</sub>O, oxidation and hydration occur simultaneously while hydrolysis of  $\alpha$ -NaMnO<sub>2</sub> shows continuous salting out of Na as we could also witness in the SEM images.

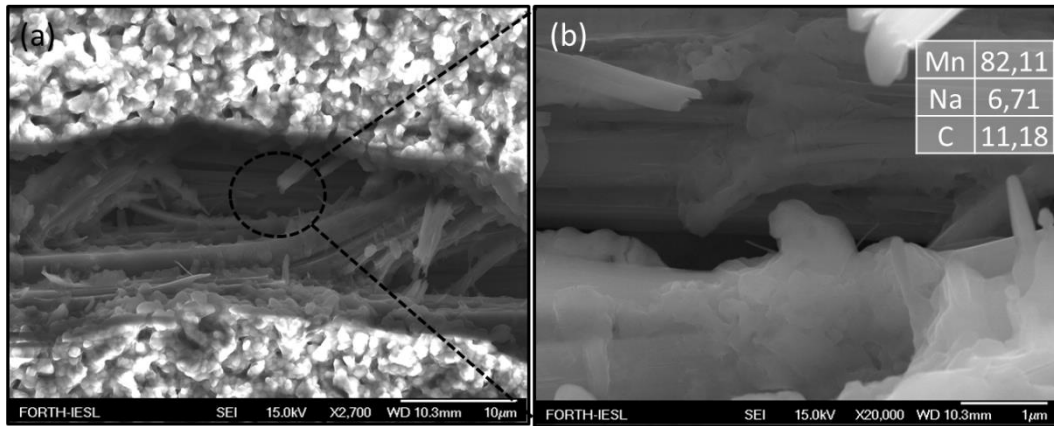


Figure 6-14 SEM picture through a developed cracked after 1 month of exposure at ambient conditions of the flake with initial Na/Mn = 0.96/ 1 ratio. (a) x2700 zoom and (b) x20000 zoom in the inner part of the crack. EDS spectra reveals reduced amount of Na in the interior of the crack (Atomic %: Mn= 82.11, Na= 6.71, C= 11.18).

### 6.3.3 XPS

The reduced Na level to  $x=0.96$ , hints for a mixed Mn valence in the  $\alpha$ -Na<sub>0.96</sub>MnO<sub>2</sub> chemical formula. As a further step in the exploration of the mixed Mn valence, XPS study of several chosen flakes allowed a more precise quantification of the Mn<sup>3+</sup>/Mn<sup>4+</sup> ratio.

#### 6.3.3.1 Experiment and sample preparation

The surface analysis studies were performed in an Ultra High Vacuum (UHV) chamber ( $P < 10^{-9}$  mbar) equipped with a SPECS LHS-10 hemispherical electron analyzer at the Institute Chemical Engineering Sciences (ICE-HT, FORTH, Greece). The XPS measurements were carried out at room temperature using unmonochromatized Al K $\alpha$  radiation under conditions optimized for maximum signal (constant binding energies difference ( $\Delta E$ ) mode, with pass energy of 36 eV giving a full width at half maximum (FWHM) of 0.9 eV for the Au 4f<sub>7/2</sub> charge reference binding energy). The probed area was an ellipsoid with dimensions  $2.5 \times 4.5$  mm<sup>2</sup>. The XPS core level spectra were analyzed using a fitting routine, which allows the decomposition of each spectrum into individual mixed Gaussian-Lorentzian components after a Shirley background subtraction. Errors in our quantitative data were found in the range of  $\sim 10\%$  (peak areas), while the accuracy for binding energy (BEs) assignments were  $\sim 0.1$  eV. The pulverised Na-Mn-O crystals were deposited on a Si wafer substrate and stored in a hermetically sealed container under inert atmosphere prior insertion in the UHV chamber, in order to avoid oxidation.

### 6.3.3.2 *Quantification of mixed valence ratio*

As it is depicted in Figure 6-15 c-d, using the total peak area of Mn 2p<sub>3/2</sub>, Na 1s and the appropriate sensitivity factors (based on Wagner's collection and adjusted to the transmission characteristics of analyser EA10), we estimate that the surface atomic ratio Na:Mn (within experimental error  $\pm 10\%$ ) is 0.96:1. The deconvoluted Mn 2p<sub>3/2</sub> core level peak is presented in Figure 6-15c. The peak consists of two components of binding energies 642.6 and 641.9 eV assigned to Mn<sup>4+</sup> (reference peak extracted from MnO<sub>2</sub>) [40] and Mn<sup>3+</sup> (reference peak extracted from Mn<sub>2</sub>O<sub>3</sub>) [185], respectively. The Mn<sup>4+</sup>:Mn<sup>3+</sup> ratio as estimated from the area ratio of the fits of each one of the two aforementioned components for the same crystal flake attained a value of 0.14:1, showing a clear majority presence of Mn<sup>3+</sup>.

Taking into account the Mn<sup>4+</sup>:Mn<sup>3+</sup> = 0.14:1 ratio and considering no oxygen vacancies, the chemical formula has been calculated to be  $Na_{0.964}Mn_{1.004}^{+3.145}O_2^{-2}$  which is in agreement with the EDS result that is mentioned in the previous section. Mn<sup>4+</sup>:Mn<sup>3+</sup> ratio and Na:Mn atomic ratio at the surface of three representative crystal flakes are compiled in Table 6-2 and the analysis is also presented in Figure 6-16. Moreover, the Na 1s core level peak of the same samples (Fig. 6-16 d-f) could be analyzed into two components, at BEs 1071.9 eV and 1070.7 eV. Although the presence of a component at 1070.7 eV could be assigned to Na-O bonds in Na<sub>x</sub>MnO<sub>2</sub> (x<1), [186], [187] since the samples are deposited on a Si wafer, the O 1s peak (not shown) is dominated by the Si-O component making further conclusions difficult at this stage.



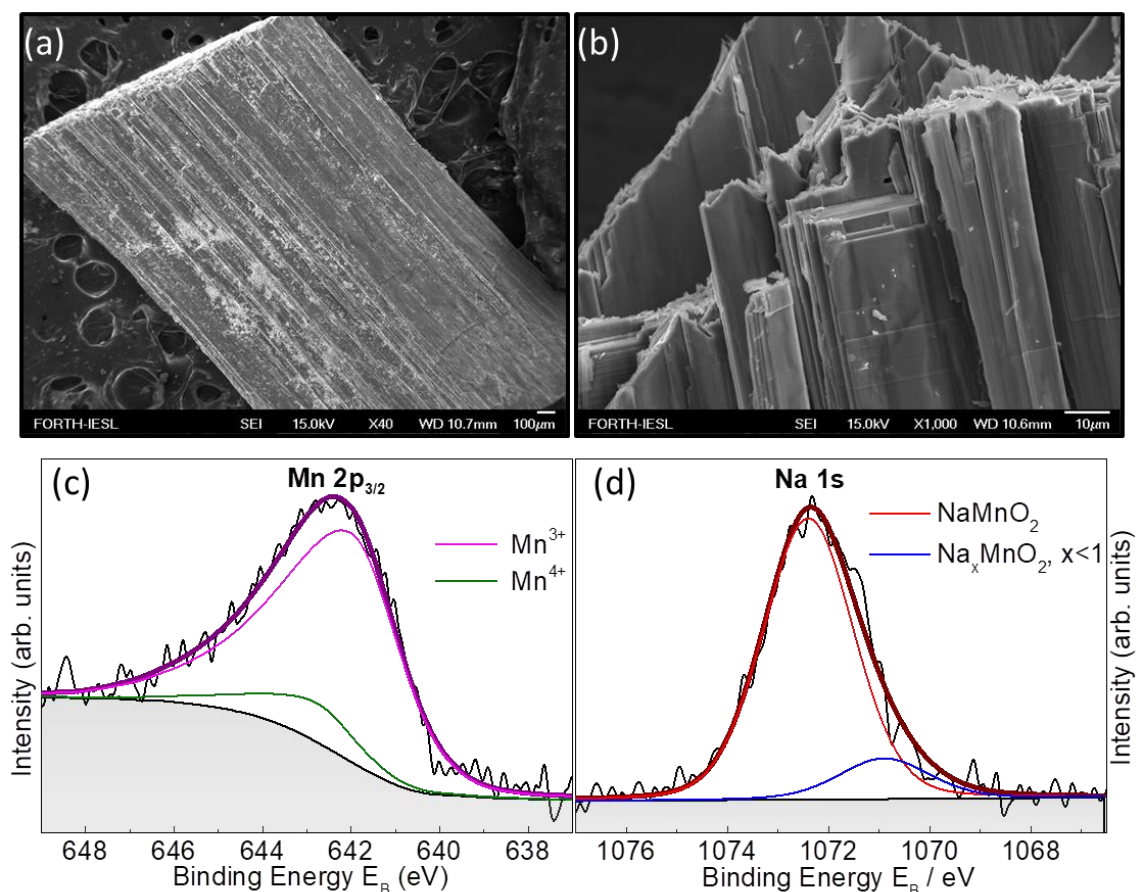


Figure 6-15 SEM image depicting (a) the layered morphology of the as-grown crystal flake of  $\alpha$ -Na<sub>0.96</sub>MnO<sub>2</sub>, (b) a close-up view. X-ray photoelectron spectra (XPS) showing the fitted deconvolution of (c) the main Mn 2p<sub>3/2</sub> peak, and (d) the main Na 1s peak for the same crystal flake; for the component curves see main text. Comparing the area ratio of the fitted XPS data provides an estimate of the Mn<sup>4+</sup>:Mn<sup>3+</sup> (ca. 0.14:1) and Na:Mn (ca. 0.96:1) surface elemental ratios.

Table 6-2 Mn<sup>4+</sup>:Mn<sup>3+</sup> and Na:Mn atomic ratios at the surface of the crystal as extracted from comparing the area ratio of fitted peaks in the XPS spectra (Figure 6-16). Errors in our quantitative analysis are found in the range of ~10% (peak areas), while the accuracy for the corresponding binding energy assignments was ~0.1 eV.

Samples	Mn <sup>4+</sup> :Mn <sup>3+</sup>	Na:Mn
Parent powders	n/a	1:1
$\alpha$ -NaMnO <sub>2</sub>		
Flake-1	0.14	0.96(9):1
Flake-2	0.42	0.93(9):1
Flake-3	0.096	1.00(9):1



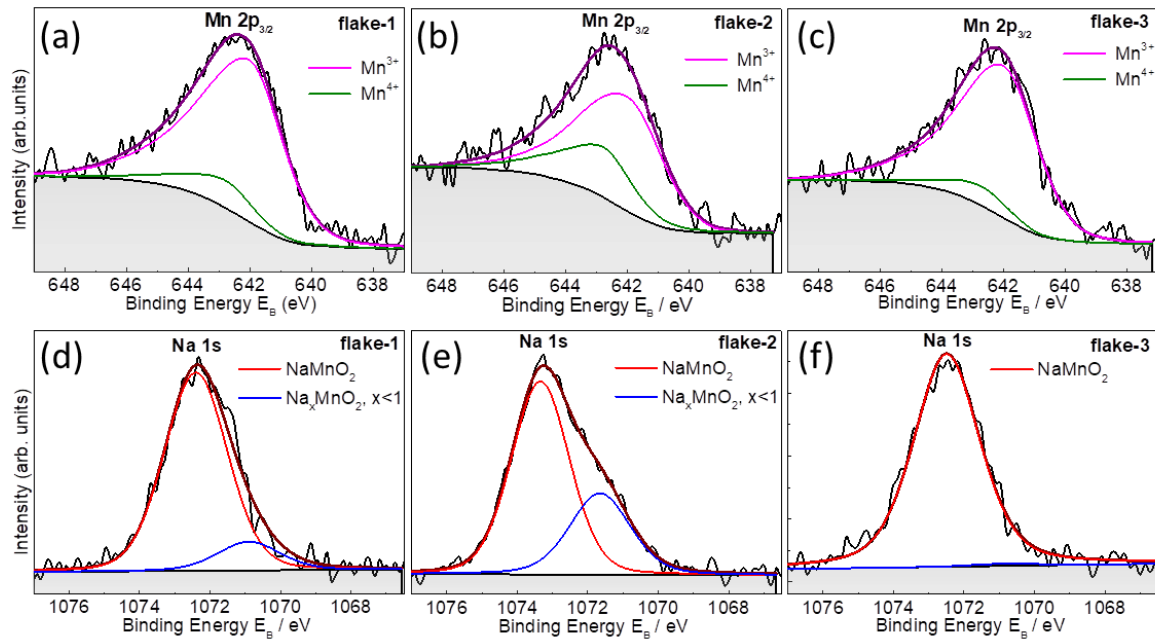


Figure 6-16 X-ray photoelectron spectra of three as-grown specimens (Table 6-2), showing the fitted deconvolution of (a-c) the main Mn  $2p_{3/2}$  peak for the three chosen crystal flakes and (d-f) the corresponding Na  $1s$  peak for the same crystal flakes.

## 6.4 Synchrotron X-ray Powder Diffraction (XPD)

Off-stoichiometry in such two-dimensional materials, is a key feature as it may trigger transformations[211] within structural groups (e.g.  $R\bar{3}m$ , rhombohedral to  $P6_3/mmc$ , hexagonal symmetries, known as O3 and P3 structures, respectively), while together with polymorphism it is commonly met due to metal-oxygen layered gliding.[212] Therefore, structural data offer an important complementary view.

### 6.4.1 Experiment and sample preparation

The phase purity of pulverised Na-Mn-O crystals was studied by synchrotron X-ray powder diffraction, performed at the National Synchrotron Light Source (NSLS-II, BNL, USA). The specific measurements were performed at room temperature employing the 28-ID-2 (XPD) beam line at NSLS-II, equipped with an image plate detector and  $\lambda = 0.2354 \text{ \AA}$ . Two small Na-Mn-O crystal flakes (growth batch #9) were ground in fine powder, loaded in  $\varnothing 1 \text{ mm}$  glass capillaries, which were then flame-sealed and studied at XPD as two separate specimens. The data were analyzed by using both the Le Bail and Rietveld refinement options available within the FullProf suite of programs.[106]



### 6.4.2 Structural considerations

The lack of adequate resolution from measurements of pulverized crystals using the in-house Rigaku D/MAX-2000H rotating Cu anode diffractometer ( $\lambda=1.5406$  Å) and the observation of mixed crystal domains observed through the SCXRD measurements, created the need for a synchrotron powder study. Through the XPD patterns it was revealed that the majority of  $\alpha$ -Na<sub>0.96</sub>MnO<sub>2</sub> Bragg reflections could be indexed in the P2/m monoclinic system at 300K. Moreover, a two-phase Le Bail refinement, using the orthorhombic Pnmm  $\beta$ -NaMnO<sub>2</sub> as a secondary, minority phase, fitted all the observed peaks (Fig. 6-17), with good reliability factors  $R_p=7.88\%$ ,  $R_{wp}=10.1\%$  and  $\chi^2=3.322$  (Table 6-3).

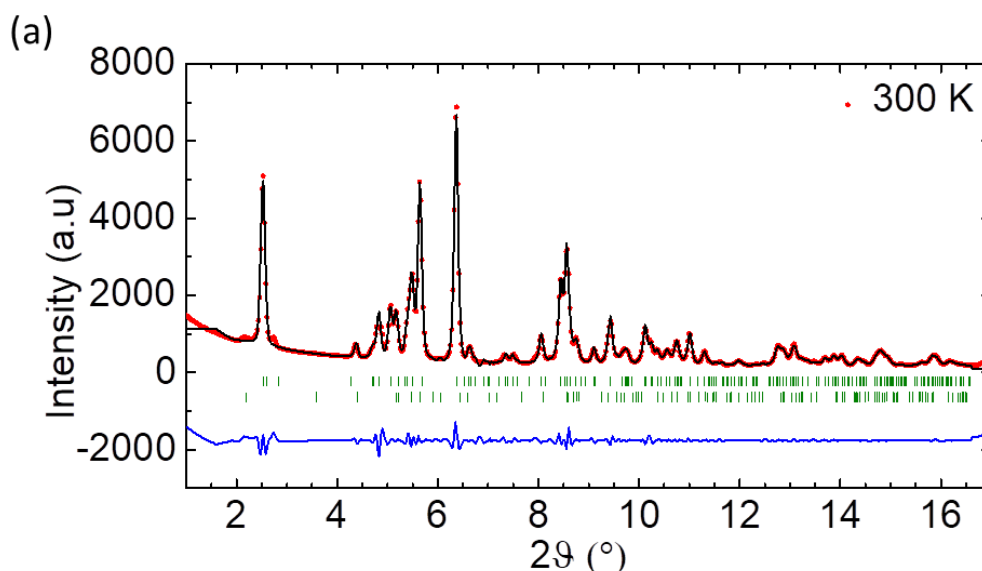


Figure 6-17 (a) Two-phase Le Bail refinement of the synchrotron X-ray diffraction data (300 K) from a pulverized  $\alpha$ -Na<sub>0.96</sub>MnO<sub>2</sub> single crystal; observed (circles), calculated (black line) and difference (bottom) profiles are shown. Vertical ticks indicate the predicted reflection positions in the monoclinic P2/m (top set) and orthorhombic Pnmm cell settings (bottom set).

Surprisingly, utilisation of the C2/m symmetry, commonly employed to describe the  $\alpha$ -NaMnO<sub>2</sub> [18] properties was of inferior quality. In that, Le Bail analysis based on a combination of C2/m and Pnmm symmetries, corresponding to Na-Mn-O stoichiometric ‘alpha’ and ‘beta’ type polymorphs, resulted in  $R_p=18.5$ ,  $R_{wp}=20.6\%$  and  $\chi^2=8.63$  (Table 6-3, Fig. 6-18 a). The possibility of having an impurity of Mn<sub>3</sub>O<sub>4</sub> intergrowth as recently studied by Dally et al. [201] has been also examined using a two phase compilation of



$C2/m$  and  $I41/amd$  for a Le Bail refinement resulting in  $R_p = 17\%$ ,  $R_{wp} = 20\%$  and  $\chi^2 = 8.81$  (Fig. 6-18 b, Table 6-3).

A two-phase analysis where the majority  $P2/m$  phase was treated by the Rietveld method (Fig. 6-19 a) instead, gave lattice constants of  $a = 5.657977(4) \text{ \AA}$ ,  $b = 2.857402(4) \text{ \AA}$ ,  $c = 5.793074(4) \text{ \AA}$ ,  $\beta = 113.071907(3)^\circ$ , indicating a small compression of the  $a$ -axis as compared to the stoichiometric ‘alpha’ that crystallizes in  $C2/m$ . [126] Further fitting attempts assuming a phase mixture with minority phase the most energetically stable, hexagonal derivative of  $\alpha$ - $\text{Na}_{0.7}\text{MnO}_2$  ( $P6_3/mmc$ ), [24] didn’t improve the quality of the fit [3] (Fig. 6-19 b, Table 6-3).

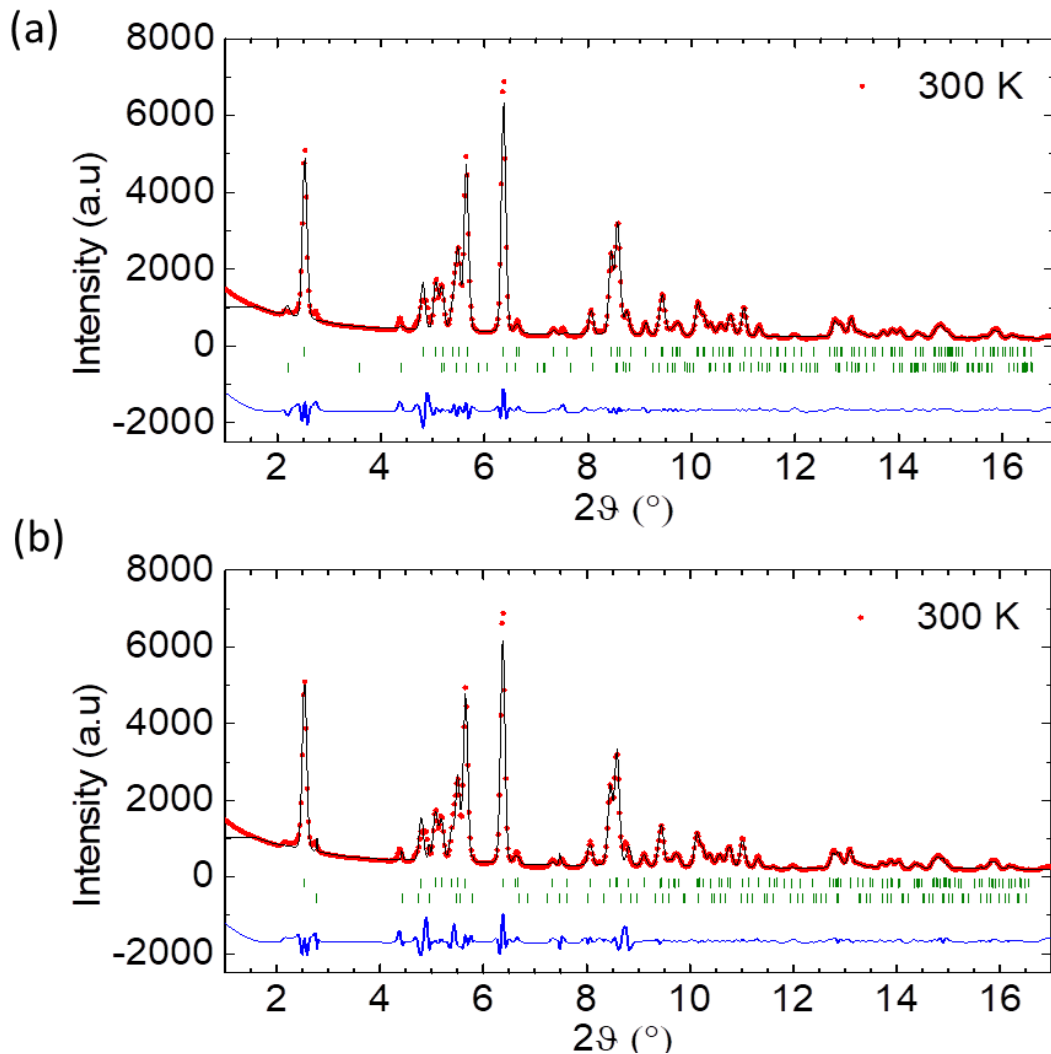


Figure 6-18 Multi-phase refinements of the synchrotron X-ray diffraction data (300 K) collected on a pulverized single crystal of  $\alpha$ - $\text{Na}_{0.96}\text{MnO}_2$ ; observed (circles), calculated (black line) and difference (thick line at the bottom) profiles are shown. Vertical ticks indicate the predicted reflection positions in (a) two-phase Le Bail model assuming the monoclinic  $C2/m$  (top set) and orthorhombic  $Pnmm$  cell settings (bottom set) (b) two-phase Le Bail model assuming the monoclinic  $C2/m$  (top set) and tetragonal  $I41/amd$  of  $\text{Mn}_3\text{O}_4$  cell settings (bottom set).

The P2/m crystal structure, obtained by using the Rietveld refined structural details (Table 6-4) is sketched in Figure 6-20 a, b. The small Na off-stoichiometry suggested by the XPS analysis has been the starting point. According to this, the Na-site occupancy was set to 0.96 allowing both Na- and Mn- site occupancies to be refined, while constrained per element (Na<sub>1</sub> site constrained together with Na<sub>2</sub> site and Mn<sub>1</sub> site constrained together with Mn<sub>2</sub> site). Refinement of both Na and Mn sites gave the same R-factors with the case where the Na-site occupancy was constrained to 0.96 in complete agreement with the XPS results. The occupancy of the Mn-site was found stoichiometric within the experimental error.

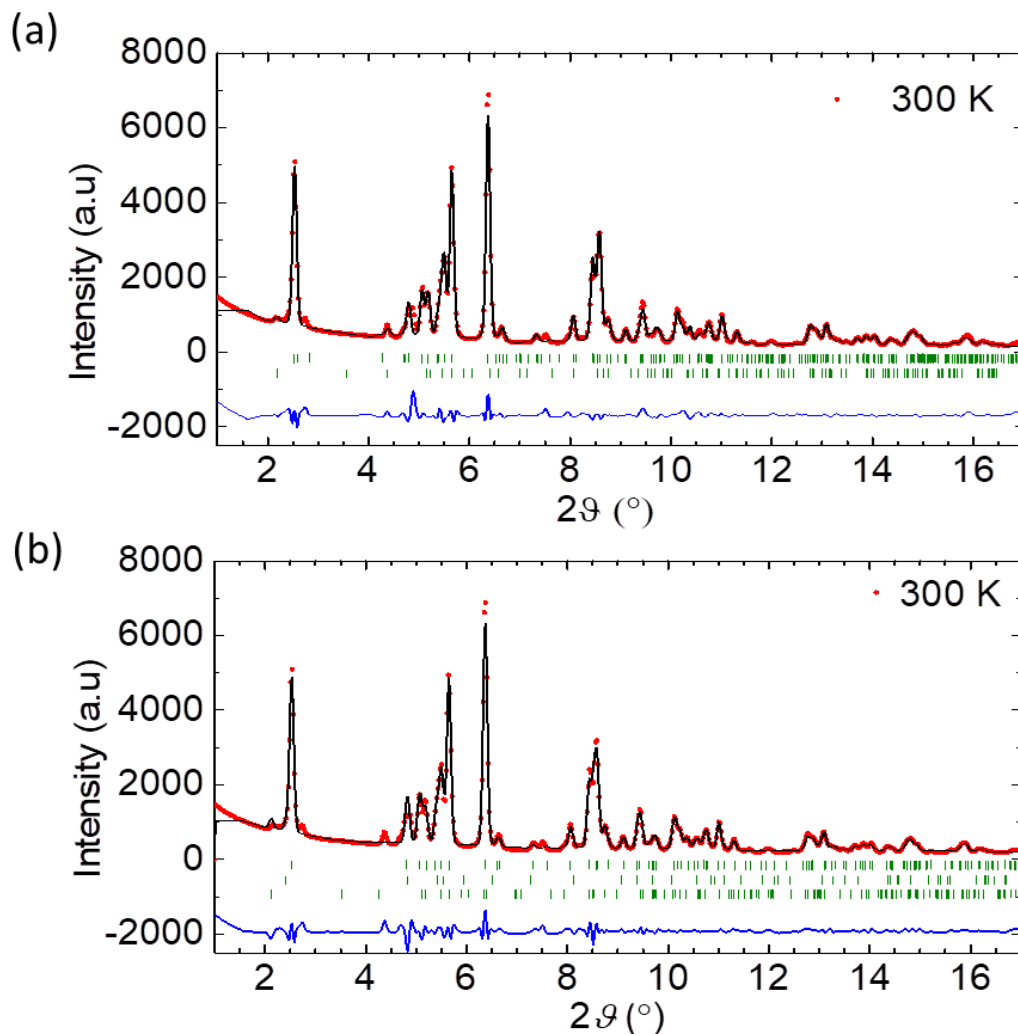


Figure 6-19 (a) Two-phase model where the monoclinic P2/m (top set) phase is treated by the Rietveld method and the minority orthorhombic Pnmm phase (bottom set) by the Le Bail approach; (b) three-phase Le Bail model assuming a majority, monoclinic C2/m (top row), hexagonal  $\alpha$ -Na<sub>0.7</sub>MnO<sub>2</sub> (P6<sub>3</sub>/mmc; middle row) and orthorhombic  $\beta$ -NaMnO<sub>2</sub> (Pnmm; bottom row) type of polymorphs. Quality of fit factors and lattice parameters are compiled in Table 6.1.

The slight Na sub-stoichiometry, infers that vacancies lead to partial oxidation of the manganese sublattice. In effect, Mn-Mn and Mn-O pathways would be influenced through distortions of the octahedral Mn-O coordination (Fig. 6-20 a, b) arising from the presence of the non Jahn-Teller active Mn<sup>4+</sup> sites. As a result of the broken C centering and the realization of P2/m symmetry, two crystallographically inequivalent Mn-sites establish differing MnO<sub>6</sub> octahedra chains perpendicular to the [100] direction (Fig. 6-20 a).

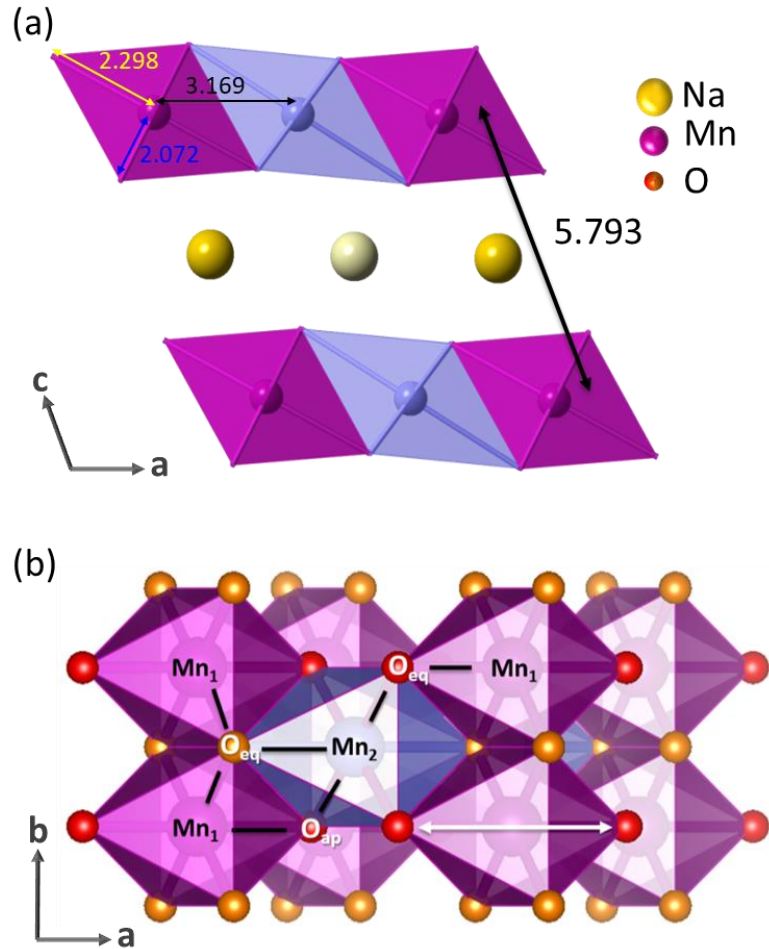


Figure 6-20 Schematic of the refined P2/m monoclinic structure in  $\alpha$ -Na<sub>0.96</sub>MnO<sub>2</sub>, projected in the *ac*- (a) and *ab*- (b) planes. The distorted oxygen coordination environment for neighboring Mn-sites is depicted by alternating color-shading of the MnO<sub>6</sub> octahedra in the [010] direction, while intercalated Na-cations are represented by gold/yellow-colored spheres. The interlayer Mn-Mn separation is marked (a), and the differing Mn-oxygen apical (O<sub>ap</sub>) and equatorial (O<sub>eq</sub>) bonds of the in-plane spatially anisotropic triangular lattice are portrayed (b).

The varying length of apical (Mn-O<sub>ap</sub>) and equatorial (Mn-O<sub>eq</sub>) bonds of the MnO<sub>6</sub> octahedra correlates with the modification of Mn- $\hat{O}$ -Mn angle (Table 6-5), which differs from the stoichiometric  $\alpha$ -NaMnO<sub>2</sub> (Fig. 6-1) to the  $\alpha$ -Na<sub>0.96</sub>MnO<sub>2</sub> (Fig. 6-20). The

induced layer corrugation likely introduces extra lattice strain to a system that already has a tendency to be inhomogeneous in the nanoscale.[126], [194] In a related study of the isostructural CuMnO<sub>2</sub> against the off-stoichiometric Cu<sub>1.04</sub>Mn<sub>0.96</sub>O<sub>2</sub>, the strain in the lattice caused by the subtle inter-site substitution in the latter, seems to disturb the balance between competing interactions, giving-rise to a nanostructural state with modified properties. [42], [213]



Table 6-3 (a) Lattice parameters and quality of fit R-factors obtained from exploratory Le Bail refinement of synchrotron X-ray powder diffraction data of a pulverized  $\alpha$ - $\text{Na}_{0.96}\text{MnO}_2$  crystal. Combination of models rest on common phase transition processes induced by Na off-stoichiometry in  $\text{Na}_x\text{MnO}_2$  ( $x < 1$ ). (b) Crystallographic atomic fractional coordinates of  $\alpha$ - $\text{Na}_{0.96}\text{MnO}_2$  nuclear structure (300 K) derived from a two-phase refinement, where the monoclinic P2/m phase was treated with the Rietveld method and the secondary orthorhombic Pnmm phase by the Le Bail approach.

	C2/m (O'3)	C2/m & Pnmm		C2/m & P6 <sub>3</sub> /mmc (O'3) & (P2)		C2/m & I 4 <sub>1</sub> /amd (Mn <sub>3</sub> O <sub>4</sub> )		C2/m & P6 <sub>3</sub> /mmc & Pnmm			P2/m & Pnmm		P2/m (O'3)
<b>a</b>	5.6591(8)	5.6366(9)	6.134(1)	5.6648(7)	2.8737(8)	5.6546(6)	5.7002(6)	5.6472(9)	2.8764(9)	6.344(1)	5.6179(8)	6.133(1)	5.6179(8)
<b>b</b>	2.8588(4)	2.8588(3)	2.8832(7)	2.8595(3)	2.8737(8)	2.8573(3)	5.7002(6)	2.8632(7)	2.8764(9)	2.8605(8)	2.8616(3)	2.8752(7)	2.8616(3)
<b>c</b>	5.7938(9)	5.7907(2)	4.7850(7)	5.7948(9)	11.062(3)	5.7846(8)	9.309 (1)	5.803(1)	11.138(4)	4.7766(9)	5.7877(7)	4.7752(9)	5.7877(7)
<b><math>\alpha</math></b>	90	90	90	90	90	90	90	90	90	90	90	90	90
<b><math>\beta</math></b>	113.102(8)	112.964(9)	90	113.102(7)	90	113.137(8)	90	113.18 (1)	90	90	112.834(6)	90	112.834(6)
<b><math>\gamma</math></b>	90	90	90	90	120	90	90	90	120	90	90	90	90
<b>R<sub>wp</sub></b>	20.6	16.4		16.4		20		17.5			10.1		16.1
<b>R<sub>p</sub></b>	18.5	14.7		13.8		17		16.5			7.88		12.3
<b>R<sub>e</sub></b>	7.01	6.97		6.74		6.74		6.9			5.54		6.5
<b><math>\chi^2</math></b>	<b>8.63</b>	<b>5.55</b>		<b>5.897</b>		<b>8.809</b>		<b>6.283</b>			<b>3.322</b>		<b>6.178</b>

Table 6-4 Crystallographic atomic fractional coordinates of  $\alpha$ -NaO<sub>0.96</sub>MnO<sub>2</sub> nuclear structure (300 K) derived from a two-phase refinement, where the monoclinic P2/m phase was treated with the Rietveld method and the secondary orthorhombic Pnmm phase by the Le Bail approach.

Atom	Mult	Wyckoff letter	x	y	z	occ.	Uiso	
Mn1	1	a	0.00000	0.00000	0.00000	0.999	0.75985(2)	
Mn2	1	d	0.50000	0.50000	0.00000	0.999	0.75985(2)	
Na1	1	e	0.00000	0.50000	0.50000	0.9600(2)	0.54524(3)	
Na2	1	f	0.50000	0.00000	0.50000	0.9600(2)	0.54524(3)	
O1	2	m	0.2802(5)	0.0000	0.7991(5)	1	0.50104(3)	
O2	2	n	0.7797(5)	0.5000	0.7535(5)	1	0.50104(3)	
Bov			1.0046					

$\mathbf{a}= 5.657977(4) \text{ \AA}$ ,  $\mathbf{b}= 2.857402(4) \text{ \AA}$ ,  $\mathbf{c}= 5.793074(4) \text{ \AA}$ ,  $\beta= 113.071907(3)^\circ$   
 $R_{wp}= 14.7$ ,  $R_p= 12.2$ ,  $R_e= 6.59$ ,  $\chi^2= 4.988$

In earlier work, Wu et al. explored the correlation between almost 90° Mn- $\hat{O}$ -Mn angles and the Mn-O $\cdots$ O-Mn pathway with anisotropic intra-chain ( $J_1$ ) and inter-chain ( $J_2$ ) Mn<sup>3+</sup>-Mn<sup>3+</sup> interactions (driven by J-T distortion) proving the dominant role of the super-super-exchange pathway (SSE) over the common AFM Mn-O-Mn super-exchange (SE) one.[206] Moreover, studies in diverse structural types, such as the mixed-valence Mn-perovskites, corroborate that the Mn- $\hat{O}$ -Mn angle has an important impact on the magnetic and transport properties of manganites. [45] This was claimed to be associated with the value of the  $e_g$  electronic bandwidth,  $W$ , favoring double exchange interaction (DE) between the carriers, which results in ferromagnetic coupling between the nearest-neighbor (nn) Mn sites, thus suppressing AFM ordering. [46,47] Learning by the mixed-valence manganite example, mixing Mn<sup>3+</sup> (Jahn-Teller) with Mn<sup>4+</sup> (non Jahn-Teller) offers a ground state that combines AFM super-exchange and FM DE nn couplings [48], the final nature of which depends on the relative number and strength of various direct or indirect coupling mechanisms. [49] However, DE is also met in mixed Mn valence systems where Mn- $\hat{O}$ -Mn is near 90°, [217], [218] while theoretical work by Ouyang et al. predicts the growth of FM couplings due to DE interaction in Na<sub>x</sub>MnO<sub>2</sub>. [207] In view of such knowledge, the small percentage of Mn<sup>4+</sup>, combined with the intrinsic (nano)structural defected nature of the Na-Mn-O compounds, [126] motivate a quest as of how the subtle interplay of emerging short and long-range interactions implicate deviations from the pathway known to relief frustration in an otherwise AFM triangular lattice. [41], [139], [203]



Table 6-5 Comparison of the Mn-Mn, Mn-O distances and Mn- $\hat{O}$ -Mn angles in ab-plane for the C2/m unit cell of the parent  $\alpha$ -NaMnO<sub>2</sub> powders and the P2/m setting of the  $\alpha$ -Na<sub>0.96</sub>MnO<sub>2</sub> crystals as derived from Rietveld analysis of diffraction dat. These parameters are extracted from the refined structure design which is portrayed in Figure 6-20 and Figure 6-1. They are measured through VESTA software and so no errors are presented. DFT calculated parameters in the C2/m space group, for both ferromagnetic and antiferromagnetic spin orderings, are taken from reference[204] for comparison purposes.

	$\alpha$ -NaMnO <sub>2</sub>	$\alpha$ -Na <sub>0.96</sub> MnO <sub>2</sub>	$\alpha$ -NaMnO <sub>2</sub>
	C2/m – powders [126]	P2/m- crystals	DFT- C2/m [204]
$d_{\text{Mn-Mn [010]}}$ (Å)	2.8600	2.8574	
$d_{\text{Mn-Mn [110]}}$ (Å)	3.1707	3.1693	
$d_{\text{Mn1- Oap}}$ (Å)	2.4078	2.2976	2.41 (AF), 2.48 (FM)
$d_{\text{Mn2- Oap}}$ (Å)		2.5144	
$d_{\text{Mn1- Oeq}}$ (Å)	1.9401	2.0728	1.95 (AF), 1.94 (FM)
$d_{\text{Mn2- Oeq}}$ (Å)		1.9385	
$\theta_{\text{Mn1- Oeq- Mn2}}$ [110]	93.02	86.842	
$\theta_{\text{Mn1- Oeq- Mn1}}$ [010]	94.96	87.145	
$\theta_{\text{Mn1- Oap- Mn2}}$ [110]		96.494	
$\theta_{\text{Mn2- Oeq- Mn1}}$ [110]		96.494	
$a$ (Å)	5.6614(3)	5.6569	
$b$ (Å)	2.8553(1)	2.8589	
$c$ (Å)	5.7947(2)	5.7943	
$\beta$ (°)	113.143(2)	113.0858	

## 6.5 DC-magnetization study

DC magnetization measurements often present a good indicator of the sample quality and initiate a discussion over the nature of the likely microscopic mechanisms that mediate the



bulk system behavior. At present, the only magnetic susceptibility data for Na-Mn-O system found in literature consists of measurements on polycrystalline samples.

### 6.5.1 Experiment and sample preparation

A Quantum Design Superconducting Quantum Interference Device (SQUID) magnetometer (Quantum Design MPMS) was used to measure *dc* magnetic susceptibility as a function of temperature  $\chi(T)$  ( $5 \leq T \leq 300$  K with 2 K step) and field dependent magnetization for three different orientations of the single crystal flakes (mass of about 2-3 mg). Temperature dependent susceptibility was measured under zero field-cooled (ZFC) and field-cooled (FC) conditions with the measuring field (low-field of 100 Oe and a moderate field of 10 kOe) applied either parallel or perpendicular to *b* crystal axis, while field-dependent magnetization measurements were carried out at several temperatures below and above the observed characteristic transition temperatures.

### 6.5.2 Canting behavior witnessed in magnetization measurements of $\alpha$ -Na<sub>0.96</sub>MnO<sub>2</sub> single crystals

In the present study, DC susceptibility measurements were performed with the crystal flakes oriented at three unique directions (a- b- c-) with respect to the externally applied magnetic field ( $H= 100$  Oe and 10 kOe; Fig. 6-21). It is worth to remind that the flat surface of each flake is always the (-202) plane. Broadly speaking, two main features were witnessed (Fig. 6-21), namely: a kink at  $T_{N1} \approx 45$  K, which is consistent with previously reported AFM LRO in  $\alpha$ -NaMnO<sub>2</sub> powders[41], [194] and a surprising subtle feature around  $T_{N2} \approx 26$  K. The first order derivative of the susceptibility,  $d\chi/dT$  (Fig. 6-21 a-, c-directions inset), marks the existence of the latter for orientations where the applied field is perpendicular to [010] direction. These findings motivated further single-crystal neutron diffraction experiments (vide-infra) aiming to corroborate their origins.

The ZFC DC-susceptibility of the crystals shows a broad feature in the high-temperature area (cf. 100-300 K), which is followed by a clear maximum below 45 K in all chosen directions (Fig. 6-21). The broad maximum in the high temperature regime suggests the built-up of low-dimensional spin-correlations which comes in agreement with the powder measurements of  $\chi(T)$  and a large negative Curie-Weiss temperature, whose exact magnitude would necessitate experiments at elevated temperatures. The similarities in the DC-magnetization behavior between alpha powders and the single crystals will be further



discussed in section 6.5.2. However, distinct ZFC/FC divergence around 45 K detected in the crystals is not one of them and requires additional clarifications. This is because a number of processes (cf. domain effects, spin-glass freezing, magnetic moment canting etc) may give rise to thermal irreversibility between ZFC and FC  $\chi(T)$  protocols. The  $\chi(T)$  is measured under fields of 100 Oe and 10 kOe (Fig. 6-21). At low- field, the bifurcation of ZFC and FC data is large suggesting large magnetic anisotropy and freezing of domains in low field. However this bifurcation is profoundly decreased with increasing the applied magnetic field (see Fig. 6-21 b-, c- directions) which indicates a reduction of the magnetic anisotropy in the system. This phenomenon together with the reduced susceptibility that is observed at the highest applied field could be associated with a weak FM component that competing interactions amongst magnetic sites may generate. The field of 1 T almost saturated the magnetic dipoles (so the value of the susceptibility below 45 K is lower under 10 kOe than under the 100 Oe field) while the assumption of a weak FM component requires probing by isothermal magnetization measurements,  $M(H)$ . Moreover, another characteristic observed in the high field measurements is an upturn/ downturn in FC/ZFC susceptibility develop below 5 K (figure 6-22). The effect seems to be more pronounced in the (b) direction. Such a hint of a possible spin flop transition seems to be related with a canted AFM which also allows the existence of FM component.

Left panel of figure 6-23 presents the  $M(H)$  loops at  $T < 60$  K for the crystals addressed in this study. Hysteretic behavior is observed for the crystal orientations (b) and (c). In the former ( $H// b^*$  and  $H \perp [-202]$ ) the effect is more pronounced as the temperature is lowered below 45 K. In effect, the coercive field ( $H_c$ ) is increased from 0.152 kOe at 45 K to 5.15 kOe at 5 K and likewise the saturation magnetization ( $M_{sat}$ ) raises from 0.016  $\mu_B/$  u.f. to 0.073  $\mu_B/$  u.f. at the corresponding temperatures (Fig. 6-23). Nevertheless, the magnetization seems not to reach full saturation at the maximum applied field, but has a remnant of 0.058  $\mu_B/$  u.f.. The small ferromagnetic moment observed along the  $b^*$  direction, combined with the AFM-like susceptibility observed in the  $ac$  plane are in favor of a canted AFM state below 45 K or the response of an almost compensated ferrimagnet.[219] Further insight on the validity of the spin canting and the suggested general magnetic moment direction is derived from the single crystal neutron diffraction work on this specimen (see section 6.6).



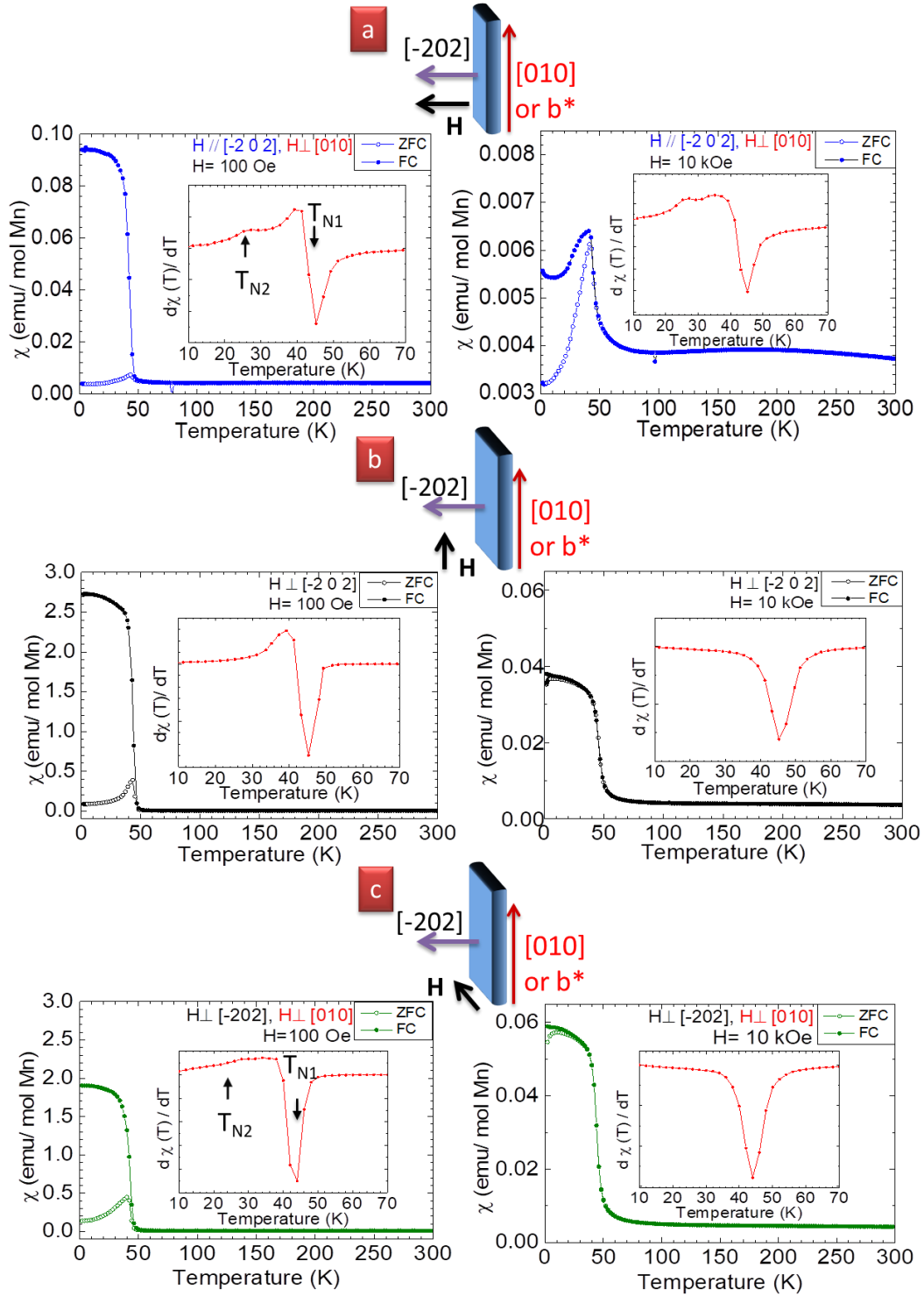


Figure 6-21 ZFC-FC susceptibility measurements of a single crystal  $\alpha$ - $\text{Na}_{0.96}\text{MnO}_2$  flake at three selected orientations (a- b- c; top row of sketches), at applied fields of 100 Oe (left panel) and 10 kOe (right panel). The insets present the 1<sup>st</sup> order derivative of the ZFC susceptibility.

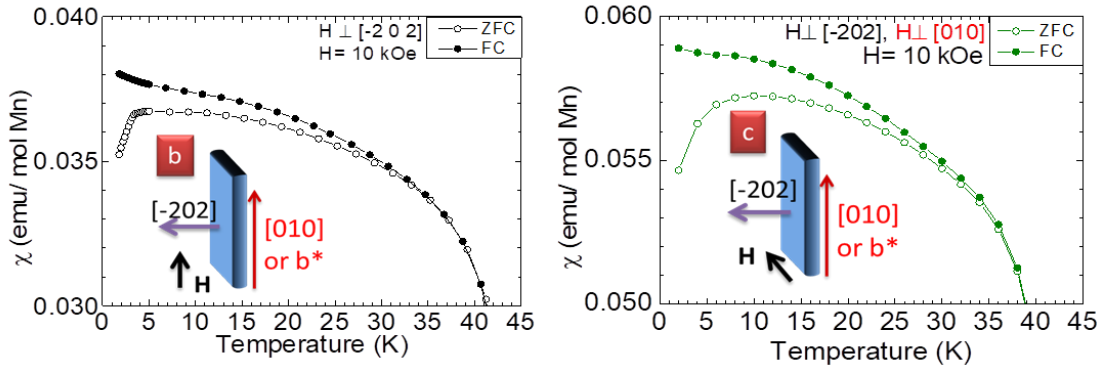


Figure 6-22 Indication of a spin-flop transition in dc-susceptibility of  $\alpha$ -Na<sub>0.96</sub>MnO<sub>2</sub> crystals measured in b and c directions as shown in the inserts.

In support of the spin-canted magnetism, as a consequence of competition between double exchange (DE; favoring FM) and superexchange (SE; supporting AFM) interactions come the mixed-valence manganites. [46] In these, doping-induced metallic ferromagnetism has been attributed to spin-configuration distortions imposed by DE between pairs of Mn<sup>3+</sup> ( $t_{2g}^3 e_g^1$ ) and Mn<sup>4+</sup> ( $t_{2g}^3$ ) ions, [2] which are capable to provoke canting of the AFM ground state even in the single impurity limit.[220] By analogy, the small Na-deficiency of the  $\alpha$ -Na<sub>0.96</sub>MnO<sub>2</sub> crystals could result in subtle DE-mediated lattice distortions. These could in turn distort the AFM spin arrangement, resulting in non-zero spontaneous magnetization at low-temperatures, while they also implicate average crystal structure modifications, bringing into play the aforementioned broken C-lattice centering.

Indication of a spin flop transition under the application of high magnetic field in a canted AFM system is also met in AFM Cr<sub>2</sub>O<sub>3</sub> nanocrystals [221] and spin-1 system SrNi<sub>2</sub>(PO<sub>4</sub>)<sub>2</sub>. [222] According to the later, for a canted AF system, the total magnetization  $M$  below  $T_N$  can be considered as a sum of the weak ferromagnetic term “ $M_{WF}$ ” and the linear AF term “ $\chi H$ ”. This is expressed as follows:  $M = M_{WF} + \chi H$ , where “ $M_{WF}$ ” arises from canted spins and  $\chi H$  from AF interactions. Therefore, the weak ferromagnetic term  $M_{WF}$  is dominative at a lower applied field  $H$  and the linear AF term becomes gradually dominative with increasing field  $H$ .



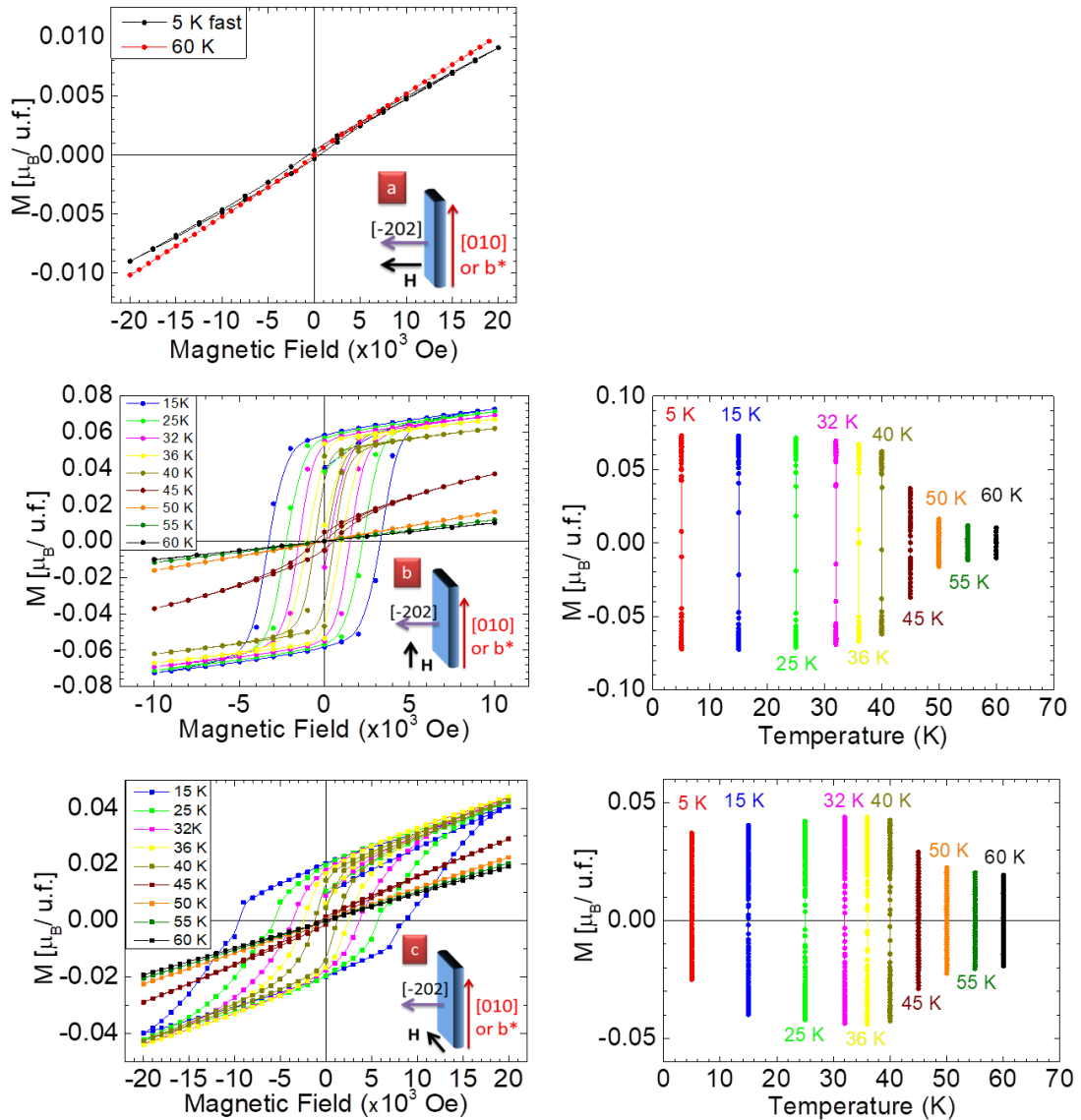


Figure 6-23 Magnetization measurements of single crystal  $\alpha$ - $\text{Na}_{0.96}\text{MnO}_2$  flake at three selected orientations.  $M(H)$ , hysteresis loops between applied fields of  $-20 \text{ kOe} < H < +20 \text{ kOe}$ . The small decrease in the saturation magnetization in panel (f) (small red arrow) indicates the evolution of a subtle competing process.

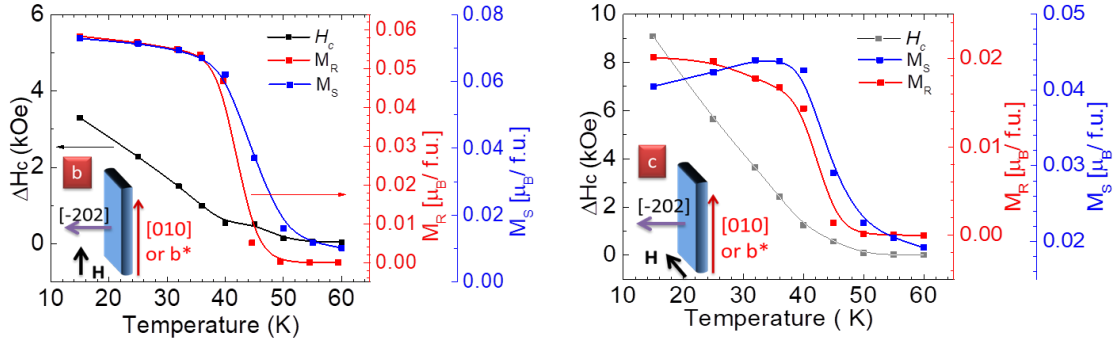


Figure 6-24 Temperature evolution of the hysteresis loops' parameters for a single crystal  $\alpha$ -Na<sub>0.96</sub>MnO<sub>2</sub> flake. The saturation magnetization ( $M_S$ ), remnant magnetization ( $M_R$ ) and coercive field ( $H_C$ ) at selected orientations, *b* (inset, left panel) and *c* (inset, right panel). The small decrease of the  $M_S$  for *c* orientation (bottom panel) is an indication for the development of competing processes below 26 K.

### 6.5.3 Powders versus single crystals

Similar measurements on polycrystalline samples of  $\alpha$ -NaMnO<sub>2</sub> (Fig. 6-25 h) are featured by a broad maximum around 200 K which is characteristic of spin-correlations built-up in low-dimensional antiferromagnets (AFM). The continuous decrease of susceptibility upon cooling is interrupted by a small anomaly around 45 K while the drop of the susceptibility below 40 K is a clear indication of enhanced AFM correlations and 3-D ordering. The susceptibility behavior changes below 20 K showing a minimum plateau (Fig. 6-25 d) which increases upon cooling. Since this increase is much slower than the one described by the Curie law, the plateau like behavior could be attributed to intrinsic behavior of the system[41], [203].

In Na-Mn-O crystals' study we observe a magnetic behavior consistent to the polycrystalline samples. The ZFC dc-susceptibility of the crystals shows a broad effect in the high temperature area, between 100-300 K, which evolves to a clear maximum below 45 K in all chosen orientations (Fig. 6-25 (a)- (c)). Following the temperature decrease, we also observe a minimum plateau below 20 K. Comparing the susceptibility values (same order of magnitude-  $10^{-3}$  emu/mol Mn) (Fig. 6-25) in the high temperature area with the powders we can confirm the realization of high spin state for Mn[203]. The broad maximum in the high temperature regime hints to low-dimensional antiferromagnetic interactions and a large negative Curie-Weiss temperature. However, in order to determine

the exact Curie-Weiss temperature measurements at higher temperatures have to be performed.

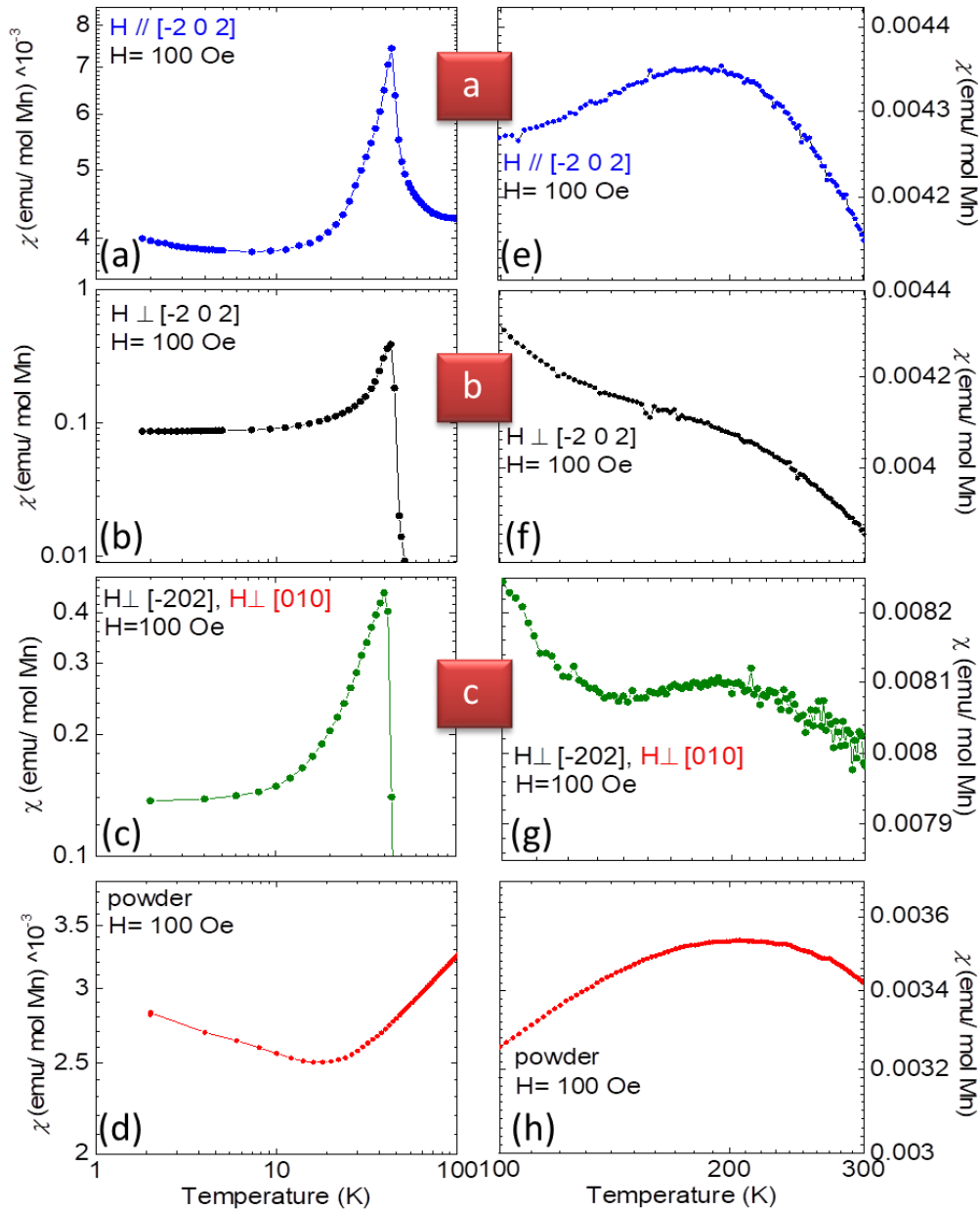


Figure 6-25 Susceptibility measurements of parent powders and single crystal flake in 3 selected orientations (a), (b) & (c). (a- d) Low temperature plateau (e- h) broad bump around 200 K related to low-dimensional AFM interactions.

## 6.6 Single crystal neutron diffraction

### 6.6.1 Experiment and sample preparation

Single-crystal neutron diffraction measurements were performed on the WISH



diffractometer [38] operating at the second target station (TS2) of the ISIS Facility (RAL, UK). WISH is equipped with a continuous array of position sensitive <sup>3</sup>He detectors that cover an angular range of  $10^\circ < 2\theta < 170^\circ$  providing the substantial Q-space coverage required for single crystal experiments, while high-brilliance and resolution at low-Q offer optimal conditions for magnetic studies. The measurements were conducted between 1.5 and 300 K and in applied field up to 8 T with an Oxford Instruments cryomagnet (nominal upper field 13.5 T). The single crystal flake was fixed in specially designed Al-holder which was hermitically sealed under He atmosphere in a He-circulating anaerobic glove-box. The crystal (m= 12 mg) was aligned with the c\*-direction ( $c^* \perp$  a-b plane or  $c^* = d_{001}^*$  direction) vertically (the direction which contains the local gravity direction at that point), allowing to collect reciprocal space intensity maps from the (hk0) scattering plane, while the external magnetic field was applied perpendicular to the latter (i.e. along the c\*-direction).

In order to derive the one-dimensional intensity patterns, the neutron diffraction data are getting reduced, which is the transformation of the dataset collected from the instrument into a dataset of physical units. Data reduction together with the analysis of the neutron scattering data has been handled out using algorithms and scripts developed within the framework of Mandid project. [224] The observed peaks have been chosen and masked in order to get the Intensity of the presented peaks. For the integrated intensity the mathematical area that is defined by each reflection peak has been calculated.

### 6.6.2 Evaluation of Single Crystal Neutron Diffraction

When the temperature is lowered for the  $\alpha$ -Na<sub>0.96</sub>MnO<sub>2</sub> crystal, two long-range-ordered magnetic regimes evolve in the neutron diffraction patterns, offering a way to compare the crystal's magnetic behavior to that probed by macroscopic magnetization. But before discussing the particulars of the magnetic scattering, a key observation is that when the crystal is still in the paramagnetic state ( $T > T_{N1} \sim 45$  K), nuclear intensity is observed at the (010) Bragg position (Fig. 6-26). This nuclear reflection is consistent with the synchrotron X-ray diffraction findings, which pointed before the violation of the C-lattice centering and favored a P2/m model for the average crystal structure (section 6.4). Accordingly, the propagation vectors that have been used to index the magnetic reflections in this study are defined with respect to the P2/m monoclinic cell.



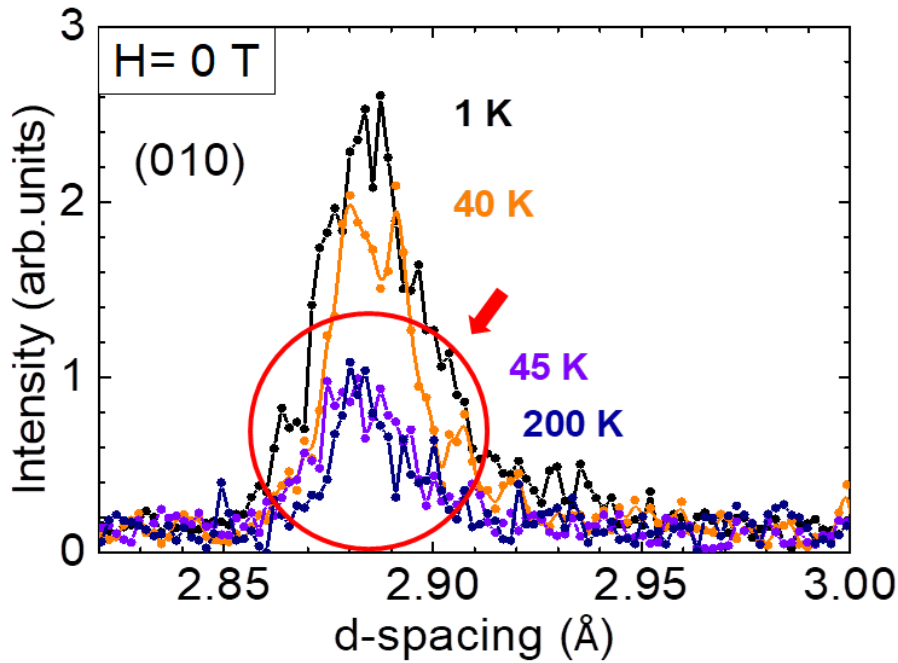


Figure 6-26 The red arrow and circle corroborate that the non-zero scattering at  $d \sim 2.87 \text{ \AA}$ , while  $\alpha\text{-Na}_{0.96}\text{MnO}_2$  is still in the paramagnetic state ( $T > 45 \text{ K}$ ), originates from the nuclear structure; it is indexed as 010 on the basis of the  $P2/m$  monoclinic cell.

When the crystal was taken at temperatures below  $T_{N1} \sim 45 \text{ K}$ , a clear increase in the intensity at the (010) nuclear reflection is observed ( $d \sim 2.857 \text{ \AA}$ ). This suggests the development of scattering of magnetic nature (Fig. 6-27a) that arises from a spin configuration with a propagation vector  $\mathbf{k}_1 = (000)$ . The profile shape of this reflection (inset, Fig. 6-27a) is similar to that adopted by the nuclear peaks, thus indicates ordering of long-range type, which complies with the development of a weak-FM moment, in agreement with the bulk magnetization measurement findings.

Below 30 K, a diffuse scattering feature at  $d \sim 5.02 \text{ \AA}$  evolves to a Bragg peak (Fig. 6-27b) which can be indexed with propagation vector  $\mathbf{k}_2 = (\frac{1}{2} \frac{1}{2} 0)$ . The shape of the associated  $(\frac{1}{2} \frac{1}{2} 0)$  reflection is broader than the regular nuclear ones, even down to 1.5 K, indicating a finite length of the magnetic domains. It is worth noting that the broad asymmetric scattering around the  $(\frac{1}{2} \frac{1}{2} 0)$  lattice position (Fig. 6-27c) precedes the Bragg scattering.

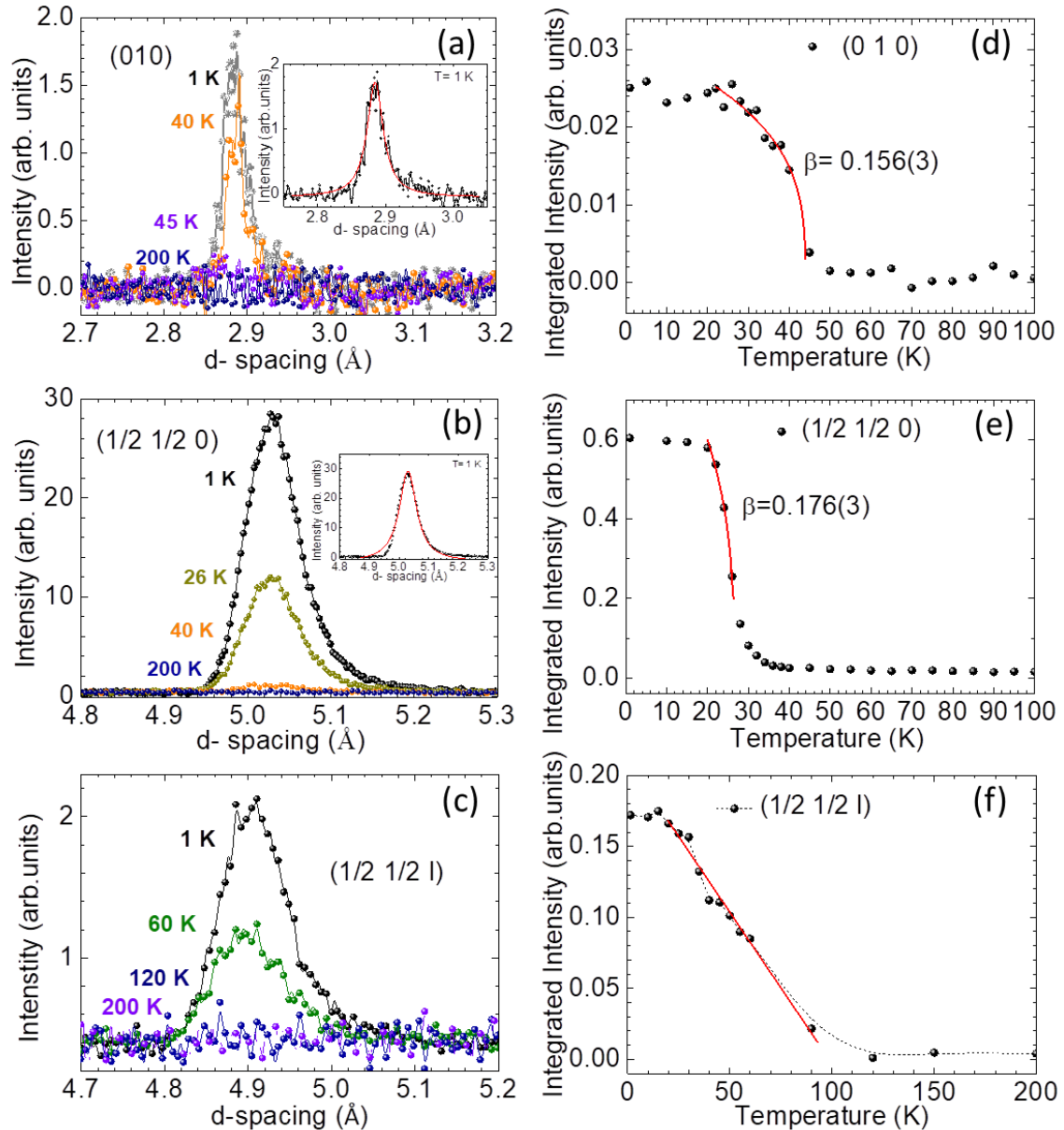


Figure 6-27 Temperature evolution of the intensity of the  $\alpha$ - $\text{Na}_{0.96}\text{MnO}_2$  neutron diffraction peaks in a limited  $d$ -spacing section (left panel) and the integrated intensity versus temperature (right panel) for the main scattering features of magnetic origin. (a), (d): Bragg peak at the (010) lattice position. The intensity of the nuclear reflection is subtracted and only the magnetic contribution is presented. (b), (e): Bragg peak at the  $(\frac{1}{2} \frac{1}{2} 0)$  lattice position. (c), (f): The broad asymmetric scattering (diffuse) around the  $(\frac{1}{2} \frac{1}{2} 0)$  lattice point indexed as  $(\frac{1}{2} \frac{1}{2} l)$ . Red lines represent the fit to the data (see text).

Careful inspection of the reciprocal space intensity maps (Fig. 6-28) uncover more on the nature of this type of scattering, which is found to persist in a wide-range of temperatures at  $T < 100$  K (Fig. 6-27 f). Namely, it is sharper in the  $HK0$  plane, while it presents an elongation along the  $L$  direction signifying a finite correlation length. The diffuse

scattering remains centered while its “rod-like” shape of is indicative of scattering from a two-dimensional (2D) lattice. Indeed the observation of a sharp scattering shape in the HK0 plane and the elongation in the L direction (Fig. 6-28) are in support of a longer correlation length within the triangular Mn layer, instead of an inter-layer one. It is worth noting that a similar diffuse signal, at the same  $\mathbf{k}_2 = (\frac{1}{2} \frac{1}{2} 0)$  was also observed in powder samples and was then described by a characteristic Warren type profile inferring analogous 2D order.[41] The persistence of the diffuse signal up to high temperature correlated to low dimension interactions agrees with the susceptibility findings that indicate low dimensionality of interactions already from high temperature.

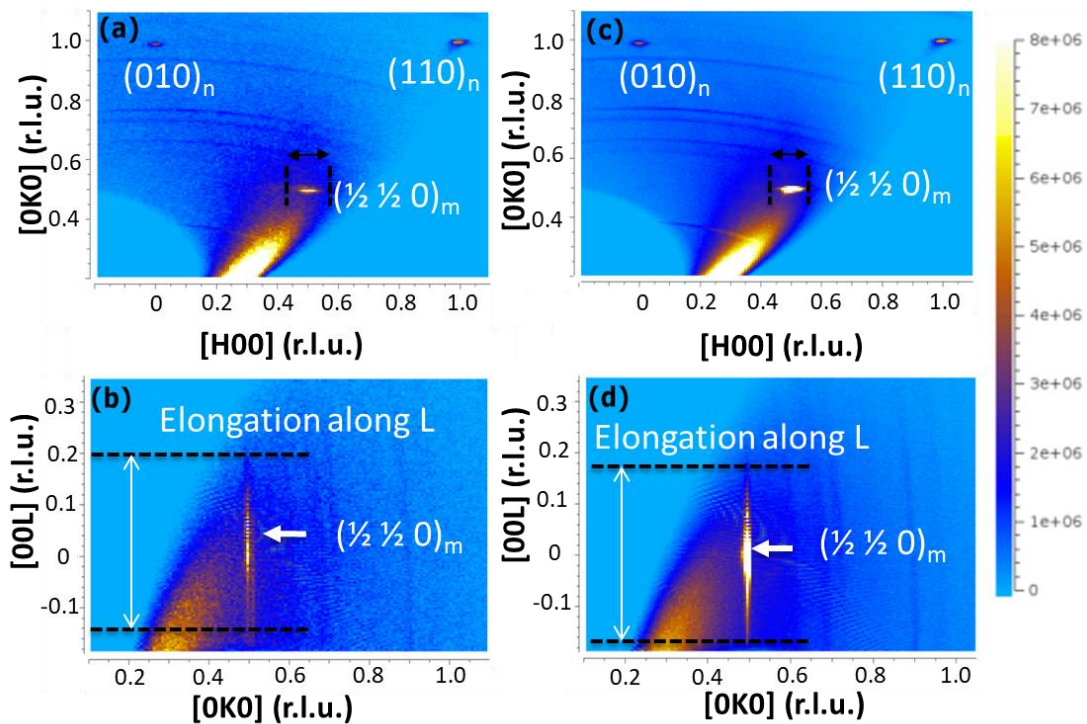


Figure 6-28 Reciprocal space intensity maps of  $\alpha$ -Na<sub>0.96</sub>MnO<sub>2</sub> in the HK0 (a, c) and in the  $\frac{1}{2}$  KL (b, d) lattice planes at (a, b), 35 K (c, d) and 1.5 K; x and y axes are presented in reciprocal lattice units (r.l.u.). The 2D character of the coexisting magnetic scattering is depicted by means of the elongation of the diffuse component along the L direction. At the base temperature (b, d), the strong increase in intensity at the L= 0 position indicates the increase of the spin-correlation length. The subscripts of the Miller indices at the scattering features of the maps, point to either nuclear (n) or magnetic (m) peak contributions.

The temperature dependence of the integrated intensities for the 010 and  $\frac{1}{2}\frac{1}{2}0$  reflections as well as that for the diffuse scattering around the  $\frac{1}{2}\frac{1}{2}0$  reciprocal lattice position are

conveyed in Figure 6-27 (d-f). The simple fitting with a power-law,  $I = I_0 [1 - (T/T_N)]^{2\beta}$ , suggests a transition temperature of  $T_{N1} = 45.033(3)$  K and  $T_{N2} = 26.48(2)$  K, for the  $\mathbf{k}_1$  and  $\mathbf{k}_2$  components, respectively, while the critical exponent assumes values of  $\beta = 0.156(2)$  and  $0.175(3)$  in each case. Despite the apparent proximity of these values to the theoretically expected  $\beta = 1/8$ , [225] for Ising-like interactions amongst neighboring spins, additional experiments may be required for its verification. However, the Ising-like behavior in an otherwise 2D spatially anisotropic Heisenberg AFM, is discussed in the early neutron powder diffraction study of the  $\alpha$ -NaMnO<sub>2</sub>, [41] suggesting that the system rests in the Ising limit due to lack of reorientation of the Mn-spins in both 2D and 3D ordered regimes. Neutron inelastic scattering on the other hand, has pointed out that either in  $\alpha$ -NaMnO<sub>2</sub> powders [20] or in recently grown  $\alpha$ -Na<sub>0.9</sub>MnO<sub>2</sub> single crystals [202], the subtle balance of degeneracy introduced through the lattice topology, results in the effective lowering of the dimensionality of spin excitations and the two-dimensional network of moments can be described by strongly coupled one-dimensional AFM spin-chains.

However, the intensity of the diffuse scattering seems that it cannot be discussed simply as critical scattering, as it rises somewhat linearly below 100 K and reaches saturation around 30 K. Bearing in mind that frustrated spin interactions are known to exhibit remarkable sensitivity to small perturbations that could favor certain states among their degenerate ground-state manifold, we resorted in the utilization of the external stimulus to shed more light in the nature of this diffuse scattering. Diffuse incommensurate signal may shift to a commensurate lattice position and the spin-structure may consequently re-configure in cases where structural inhomogeneities occur. [201] Interestingly, in related low-dimensional AFM triangular lattices, such as the LuFe<sub>2</sub>O<sub>4+ $\delta$</sub>  Ising system, with coexisting long- and short- range correlations, where the application of an external magnetic field (or oxygen deficiency) is able to manipulate the length of the interlayer correlations. [51]

Toward this direction, magnetic-field ( $H \perp c^*$ -direction) dependent single-crystal neutron diffraction experiments were carried out, at 1.5 K ( $< T_N$ ) and 50 K ( $> T_N$ ). The intensity at the (010) reflection (Fig. 6-29 a-b) increases linearly with the applied field and reaches saturation at  $\sim 4$  Tesla, as expected from the coupling of the weak-FM component with the external field. However, neither for the AFM  $\frac{1}{2}\frac{1}{2}0$  Bragg reflection (Fig. 6-30 a,b) nor for the diffuse scattering (Fig. 6-30 c,d) around this lattice point an intensity re-distribution has been resolved at fields up to 8 Tesla.



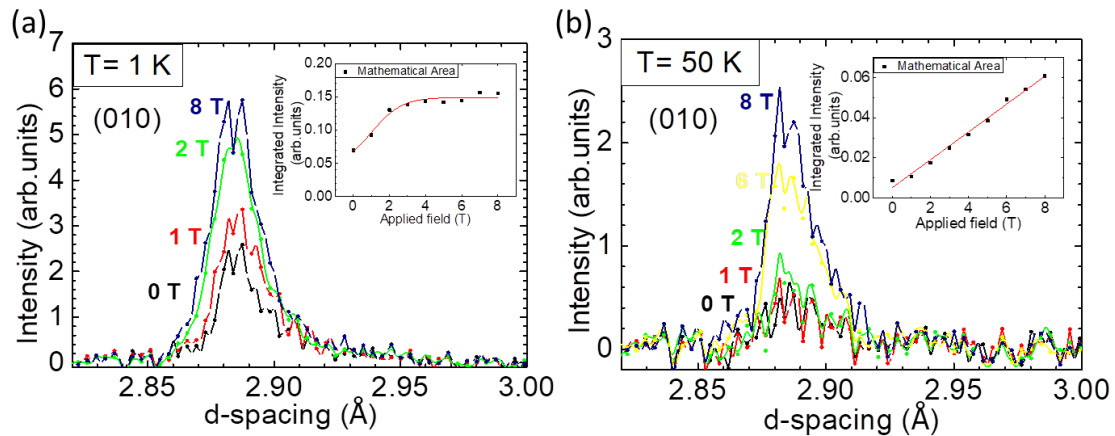


Figure 6-29 Magnetic-field dependence of the (010) reflection at 1 K (a) and 50 K (b) respectively. The progressive intensity saturation at 1 K is in line with the weak-ferromagnetic character of the ordered state.

The present experiment showed that the effect of the magnetic field on the neutron scattering patterns arising from the AFM correlations (both Bragg peak at  $(\frac{1}{2} \frac{1}{2} 0)$  and diffuse scattering) is negligible while the FM component is enhanced. This gives us the information of the coexistence of two types of magnetic correlations that could be realized either as FM and AFM clusters coexisting separately in the ground state or magnetic clusters having a canted AFM structure that allows the existence of a FM component. The simultaneous presence of the aforementioned magnetic phases below  $T_{N2} \sim 26$  K is clearly presented in in Figure 6-31.



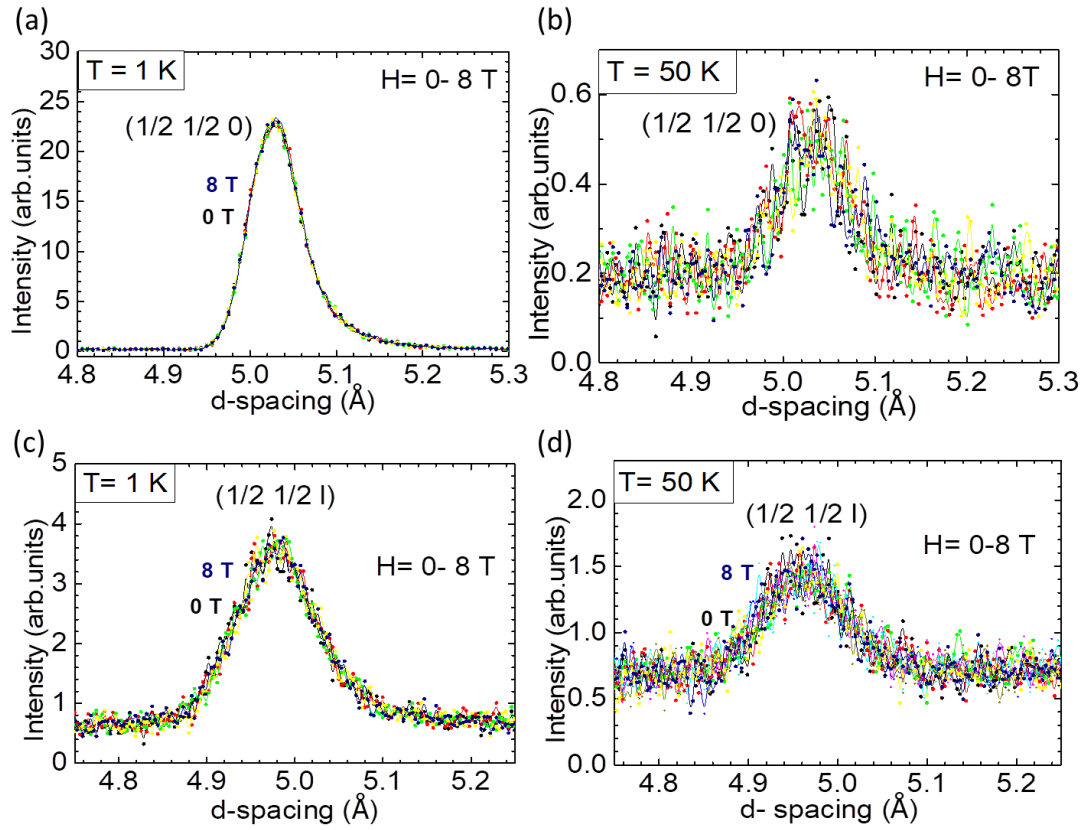


Figure 6-30 Magnetic field dependence of the scattering features at 1 K and 50 K, for (a, b) a well-shaped sharp peak indexed at the  $(1/2 \ 1/2 \ 0)$  lattice position in  $P2/m$  cell system and (c, d) a diffuse scattering contribution in the vicinity of  $(1/2 \ 1/2 \ 0)$  Bragg position, described as  $(1/2 \ 1/2 \ 1)$ .

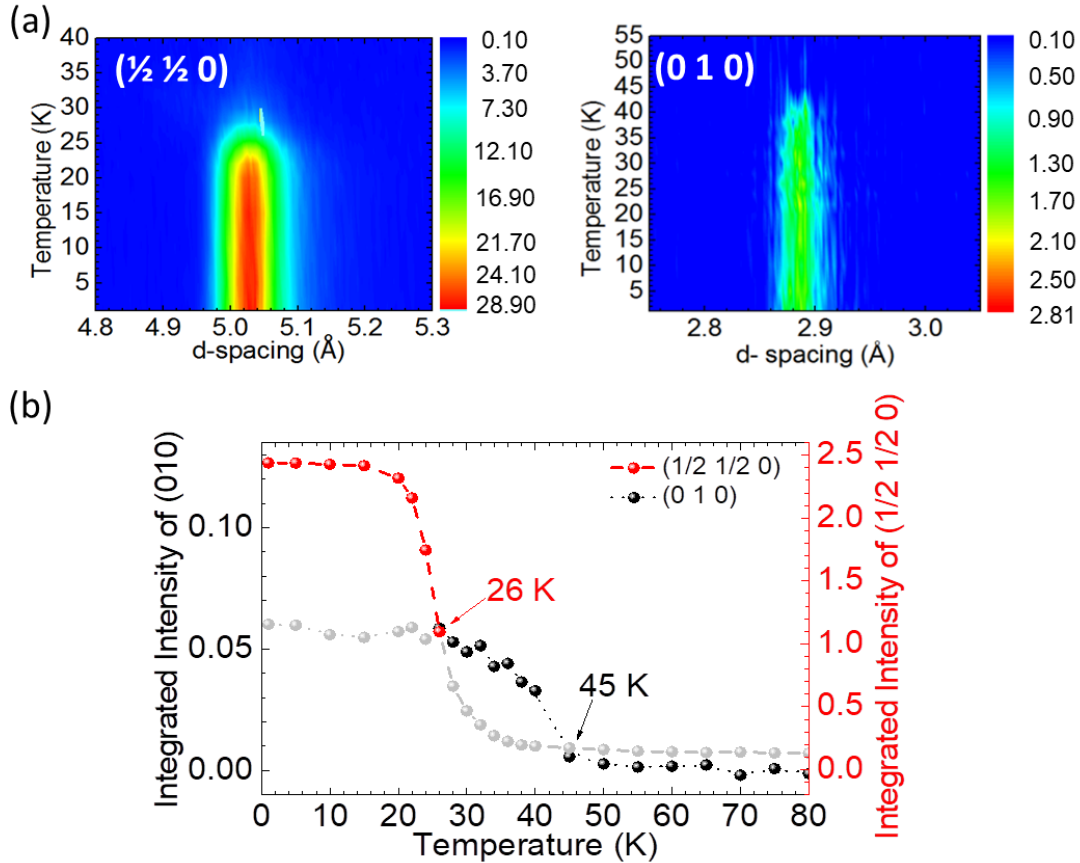


Figure 6-31 (a) A  $d$ -spacing section of the single crystal neutron diffraction patterns as a function of temperature. Intensity of AFM peak with propagation vector  $\mathbf{k} = \frac{1}{2} \frac{1}{2} 0$  (contour plot on the left) being at least 1 order of magnitude more intense than the FM peak described by propagation vector  $\mathbf{k}_1 = 0 0 0$  (contour plot on the right). Both contributions are indexed in  $P2/m$  monoclinic system (b) Temperature evolution of the integrated intensity of the two different magnetic regimes indexed in  $\mathbf{k}_1 = 000$  (FM- black spheres) and  $\mathbf{k} = \frac{1}{2} \frac{1}{2} 0$  (AFM- red spheres) suggesting a coexistence of both FM and AFM orders as temperature goes below 26 K. The existence of the plateau of the weak FM contribution (gray spheres below 26 K) confirms that only a fraction of the magnetic moments order AFM.

### 6.6.3 Possible Spin configuration

The constraints imposed by the fixed magnet geometry, utilized both for zero-field and field-dependent measurements, restricted the out-of-plane lattice coverage and did not allow the collection of adequate number of magnetic reflections to perform a complete quantitative refinement of the magnetic structure. Nevertheless, thanks to the combination of the macroscopic magnetization measurements and symmetry arguments, we can draw some clues on the possible spin configurations giving rise to the detected scattering.

With respect to the propagation vector  $\mathbf{k}_1$ , the observation of magnetic intensity at the 010

reflection indicates the presence of a spin component perpendicular to b- direction. This information combined with the clear observation of a weak FM component along the b- direction as suggested by the Dc susceptibility measurements (Fig. 6-23 b) let us conclude that the magnetic moments are likely to lie slightly out of the ac plane of the monoclinic cell in collation to the parent  $\alpha$ -NaMnO<sub>2</sub> powders allowing in that way a component of the magnetic moment along b-direction. [41] Magnetic symmetry analysis, performed with the help of the ISODISTORT software [54], using as parent symmetry the P2/m nuclear cell, indicates two irreducible representations (IRREPS),  $m\Gamma_1^+$  and  $m\Gamma_2^+$ , which allow further discussion on the data. The former allows only an ordering along the b-direction, corresponding to the P2/m magnetic space group, while the latter allows an ordered structure with the spins confined in the monoclinic ac-plane, corresponding to the P2'/m' magnetic space group. Each one of the two aforementioned IRREPS, when considered independently, cannot interpret both neutron and macroscopic magnetic measurements. Indeed, the P2'/m' magnetic space group can explain the observation of magnetic intensity at the 010 reflection (which demands a component perpendicular to b-direction), whereas the P2/m space group allows a FM moment along the b-direction, as observed in the magnetization measurements (Fig. 6-23 b). For these reasons, it is necessary to take the direct sum of the two IRREPS, namely  $m\Gamma_1^+ \oplus m\Gamma_2^+$  that results in the P-1 magnetic space group.



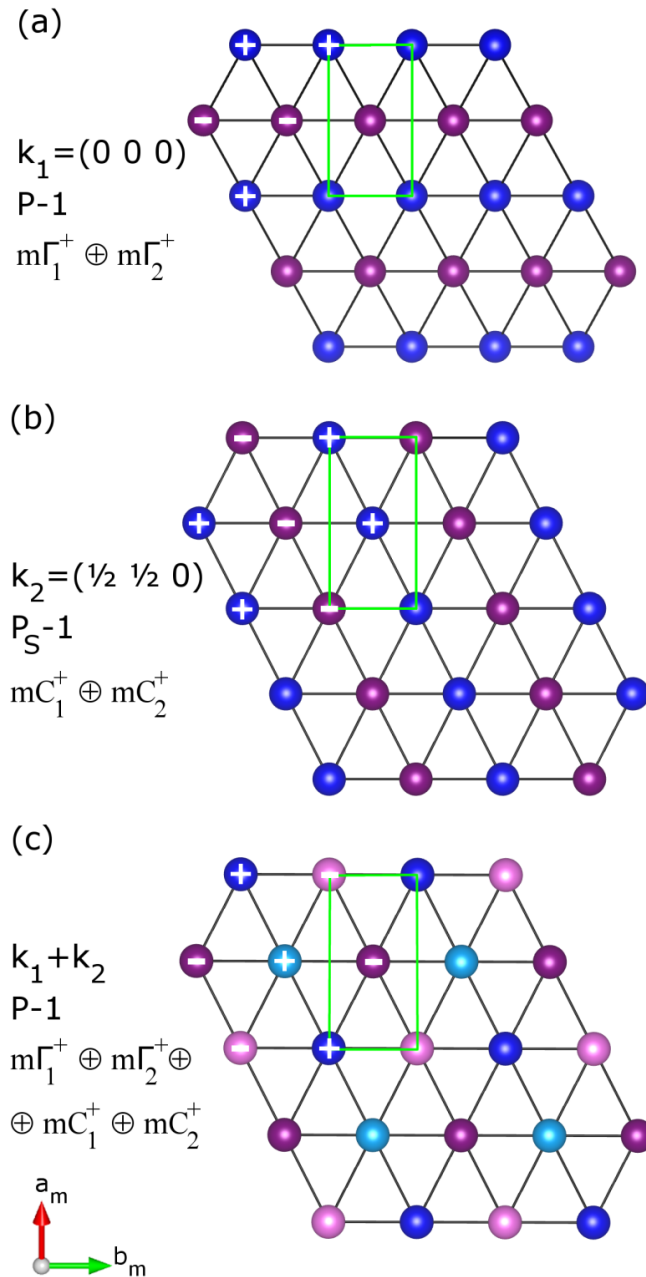


Figure 6-32 Proposed magnetic models for (a) the  $k_1 = (000)$  component, (b) the antiferromagnetic  $k_2 = (\frac{1}{2} \ \frac{1}{2} \ 0)$  state, and (c) a likely low-temperature ferrimagnetic stripe-like structure; plus and minus signs indicate the spin-orientation at adjacent Mn-sites, while the different colors indicate the symmetry inequivalent magnetic sites. For clarity only one triangular Mn-layer is shown, assuming a ferromagnetic stacking sequence along the  $c$ -axis, for both propagation vectors. The magnetic space group and the associated irreducible representations are also given for each spin configuration.

Despite the lack of a complete set of reflection, it is still possible to gain some knowledge on the relative spin-orientation of the two independent manganese sites of the  $P2/m$  nuclear model. Calculation of the magnetic structure factor of the 010 reflection in the  $P-1$

magnetic symmetry shows that in order to obtain a non-zero contribution, the spins of the two independent Mn sites need to be oriented anti-parallel to each other, at least for their x and z components. The spin arrangement is schematically shown in Figure 6-32(a) for one triangular layer. Since the AFM structure is composed of two symmetry independent lattice positions and the magnetic space group allows for a FM component in all three directions, the weak FM contribution can be ascribed to the unbalance between the two independent sub-lattices or to a canting of the AFM structure. None of the two possibilities can be excluded solely on the basis of the present neutron diffraction data, as both seem consistent with the small presence of Mn<sup>4+</sup> in the structure (fostering DE) due to the Na-vacancies, as highlighted in the previous sections (6.3-4).

The second magnetic component, with propagation vector  $\mathbf{k}_2$ , is fully consistent with the spin-ordering reported before from neutron powder diffraction data of the stoichiometric  $\alpha$ -NaMnO<sub>2</sub>. [41] On the grounds of a P2/m nuclear structure, the AFM spin-ordering is due to the common action of the  $mC_1^+$  and  $mC_2^+$  irreducible representations, resulting in the P-1 magnetic symmetry. A schematic view of the relative spin arrangement is shown in Figure 6-32(b). If we assume that the sample is magnetically homogeneous at the ground state, the two components then belong to the same magnetically ordered phase, resulting in a ferrimagnetic stripe-like structure which is schematically depicted in Figure 6-32(c). However we cannot exclude the possibility that the system is magnetically inhomogeneous and undergoes phase-separation at low temperature, but with the current neutron data and the macroscopic physical characterization, this scenario is indistinguishable from the former.

## 6.7 Magneto- electric response

The coexistence of two magnetic regimes, long-range commensurate and short-range magnetic structures, is present at low temperatures as presented by the neutron diffraction experiments in both  $\alpha$ -NaMnO<sub>2</sub> powders and the grown  $\alpha$ -Na<sub>0.96</sub>MnO<sub>2</sub> crystals. Interestingly in the second, a possible emerging of canted magnetic moments when a moderate field (1 Tesla) is directed perpendicular to the (-202) lattice plane occurs, allowing a FM component to coexist with the aforementioned magnetic regimes down to base temperature (1.5 K). Competing interactions, arisen in the present case from the mixed Mn valence, between spins and their complex magnetic orders are known to motivate spectacular cross-coupling effects that lead to improper ferroelectricity and



multiferroicity in frustrated magnets. [76], [163] In view of that, we investigate the possible magnetodielectric coupling in the  $\alpha$ -Na-Mn-O system with measurements of the dielectric constant ( $\epsilon'$ ) and dielectric loss ( $\epsilon''$  or  $\tan\delta$ ) versus temperature and under various magnetic fields.

In the early exploration of the magnetodielectric behavior of  $\alpha$ -NaMnO<sub>2</sub> the effects on dielectric permittivity could be observed in a limited Temperature area (not below 78-80 K). The only feature that has been observed at that time was at  $T= 93-97$  K and was attributed to the intergrowth of beta phase stacking sequences inside the alpha main structure. In continuity to these findings, measurements in a wider temperature range allowed us to display the contribution of the existence of the trade-off between the  $\alpha$ -type nanodomains and those of the  $\beta$ -type as created by the dense existence of stacking faults in the dielectric permittivity by going down to 5 K. This fact gave the advantage of observing for the first time a feature developed below 45 K which is the temperature of the magnetoelastic transition to the AFM state of the bulk  $\alpha$ -NaMnO<sub>2</sub>. Apart from that, the improved temperature control allowed for a better repeatability of results and the detection of artifacts caused by a non-linear temperature ramp.

### 6.7.1 Experiment and sample preparation

The dielectric and magnetodielectric measurements of  $\alpha$ -NaMnO<sub>2</sub> powders and crystals examined in this study have been held mainly in a commercial 14 T PPMS platform located in Laboratory for Magnetic Measurements (LaMMB - MagLab) at the Helmholtz-Zentrum Berlin which allowed temperature ramps down to 10 K. A Solatron 1260 Impedance/Gain Phase analyzer has been employed which is being used together with a 1296A Dielectric Interface System in order to cope with ultra-low capacitance levels. The setup had been tailored for dielectric constant measurements in a capacitor-like topology with the sample getting in contact with the electrodes mechanically.

In the presented measurements, an AC electric stimuli of 1600 -2000 V/m was applied on the sample under test. Changes in the applied electric stimuli didn't show any changes to the observed values of the dielectric permittivity in contrary to afore mentioned values while they both lay in the same order of magnitude with small differences that could be attributed to the use of different quality and thickness of electrodes.

For the dielectric and magnetolectric characterization of the  $\alpha$ -NaMnO<sub>2</sub> powders the same pelletizing process as in the case of  $\beta$ -polymorph had been followed. The final pellets had



diameter of  $\varnothing$  5 mm and thickness of approximately  $\sim$  1 mm and the pelletizing conditions have been found to be best for  $m \approx$  89 mg, pelletized under 22 Nm for 60 min. These conditions resulted in pellets of 85 mg. As electrodes, have been used conductive pastes such as silver paste, carbon paste and in some cases sputtered gold. The crystal flakes have been measured as they have been cleaved from the crystal boule. Their shape has been roughly rectangular with dimensions 2x 2.5 mm and the thickness was measured approximately  $\sim$  0.15 mm.

The protocol followed for each measurement of the capacitance has been cooling the sample under zero electric and magnetic field (ZFC) down to 10 K (or the lowest possible temperature below a known magnetic transition point). Then, measure capacitance upon heating with 2 K/min rate up to 220 K or above, while measurement points were taken every 0.05 K by applying an Ac voltage across the sample during the warm up. Knowing the dimensions of the sample the dielectric permittivity  $\epsilon'_r$  (T) was calculated from the equation (2-8)

$$\epsilon'_r = \frac{C \cdot d}{\epsilon_0 \cdot A}, \quad D = \tan\delta = \frac{\epsilon''_r}{\epsilon'_r}$$

while the dissipation factor has been directly measured by the instrumentation in mode Cp-D.

### 6.7.2 Studies on $\alpha$ -NaMnO<sub>2</sub> powders

The samples that have been measured here are of batches that have been synthesized 2-4 years before the DE measurement took place following all the same protocol. The xrd patterns of the powders have been taken again before the dielectric measurements in order to reassure the purity of the phase and the good condition of the samples.

In figure 6-33 the T-dependency of the dielectric permittivity  $\epsilon'_r$  (T) is measured from 10 K to 220 K. This is the first time that dielectric measurements have been held down to 10 K allowing the observation of effects while being well in the magnetically ordered state of the  $\alpha$ -NaMnO<sub>2</sub> as the later has been defined by the neutron diffraction study. The protocol that has been followed is the one described earlier starting with a ZFC down to 0 K while a test signal level of  $E = 1600$  V/m and  $f = 1$  kHz is applied upon heating. The general trend that is observed is the increase of the value of the dielectric constant  $\epsilon'_r$  (T) with the increase of temperature as in the case of beta polymorph. The shape of the  $\epsilon'_r$  (T) curve



points out a weak feature in the low temperature area  $\sim 50$  K which is not evident in the Dielectric Loss curve as presented on the right axis of the graph.

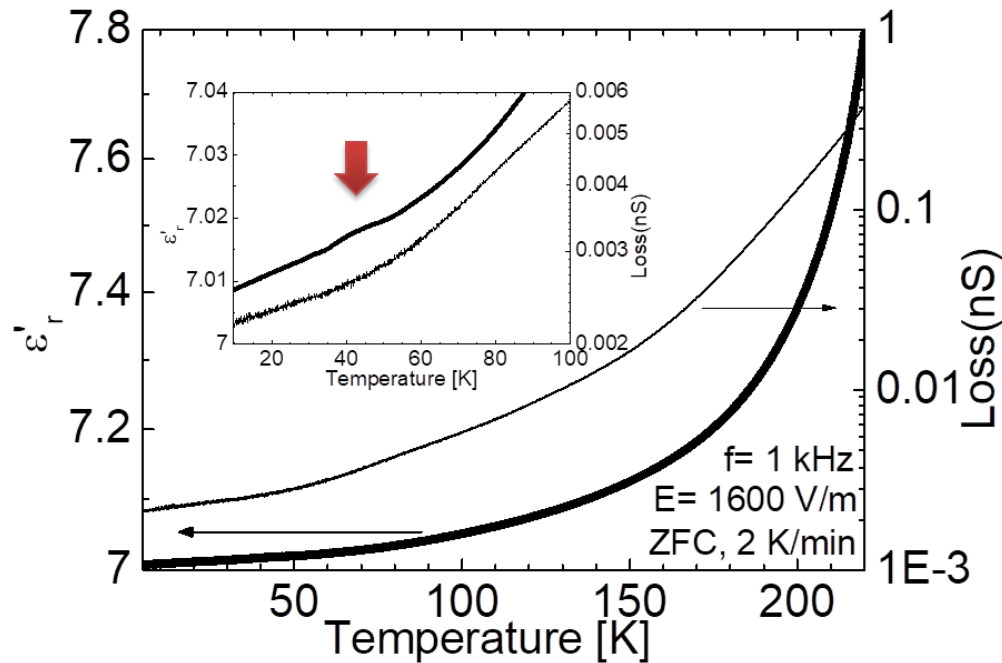


Figure 6-33 Dielectric constant ( $\epsilon'_r$ ) (black symbol-left Y-axis) and dielectric loss (black thin line-right Y-axis) of  $\alpha$ -NaMnO<sub>2</sub> measured with a ZFC protocol at 1 kHz, applying 1600 V/m upon heating. The inset on the  $\epsilon'_r(T)$  shows the weak feature observed below 50 K.

The magnitude of the measured dielectric constant is about  $\sim 7$  at low temperature area for both low and high frequencies (figure 6-34) while the magnitude near room temperature varies depending on the frequency. This value is close to the value observed in the beta powders ( $\sim 6$ -7) and so the comparison with other ABO<sub>2</sub> systems has been already presented in chapter 4. However the value of susceptibility at room temperature is lower in the  $\alpha$ -NaMnO<sub>2</sub> polymorph comparing to the  $\beta$ -NaMnO<sub>2</sub> showing a dielectric of better quality. The proof that  $\alpha$ -NaMnO<sub>2</sub> is a low-loss dielectric is also confirmed by the dielectric loss giving  $\frac{\sigma}{\omega\epsilon'} \ll 1$  where  $\sigma$  is the conductivity of the material. The dielectric loss is expressed in nanosiemens through measuring the conductance “G” related to the conductivity with the following equation:  $\sigma = G \frac{l}{A}$  where,  $l$  is the distance between the two flat surfaces of the sample and  $A$  the area of the surface.

The measurements have shown a good repeatability on several runs of the same sample for the effect in the low temperature area. The high temperature area (250-300 K) has been



affected by humidity as absorbed by silver paste contacts and has been further commented in chapter 2. The polymorphism that is met in the Na-Mn-O system proved to engineer the physical properties of the final defected system in the case of  $\beta$ -NaMnO<sub>2</sub>. [126] The appearance of high density areas occupied by alpha-like stacking sequences seems to drive the dielectric behavior as proved by the detection of an effect in the temperature area (~45 K) of the AFM transition of the bulk  $\alpha$ -NaMnO<sub>2</sub>. However, in the case of  $\alpha$ -NaMnO<sub>2</sub> powders, the density of the beta-like stacking sequences in the mean alpha structure was found to be smaller compared to  $\beta$ -NaMnO<sub>2</sub>. We support that this is the reason that in the alpha powders, no effect is present in the temperature area of 100 K where the commensurate AFM transition occurs in  $\beta$ -NaMnO<sub>2</sub>. In the end, in alpha powders the feature observed below 50 K is believed to be correlated to the magnetic transition to the commensurate AFM transition.

#### 6.7.2.1 Effect of frequency on the dielectric permittivity

Figure 6-34 shows the  $\epsilon'_r(T)$  of a  $\alpha$ -NaMnO<sub>2</sub> powder sample measured as a pellet at  $f=$  111 Hz, 1 kHz and 20 kHz. As the frequency increases, the value of the  $\epsilon'_r(T)$  is expected to decrease according to the  $C = \frac{1}{2\pi f X_c}$  which is confirmed by our observations.

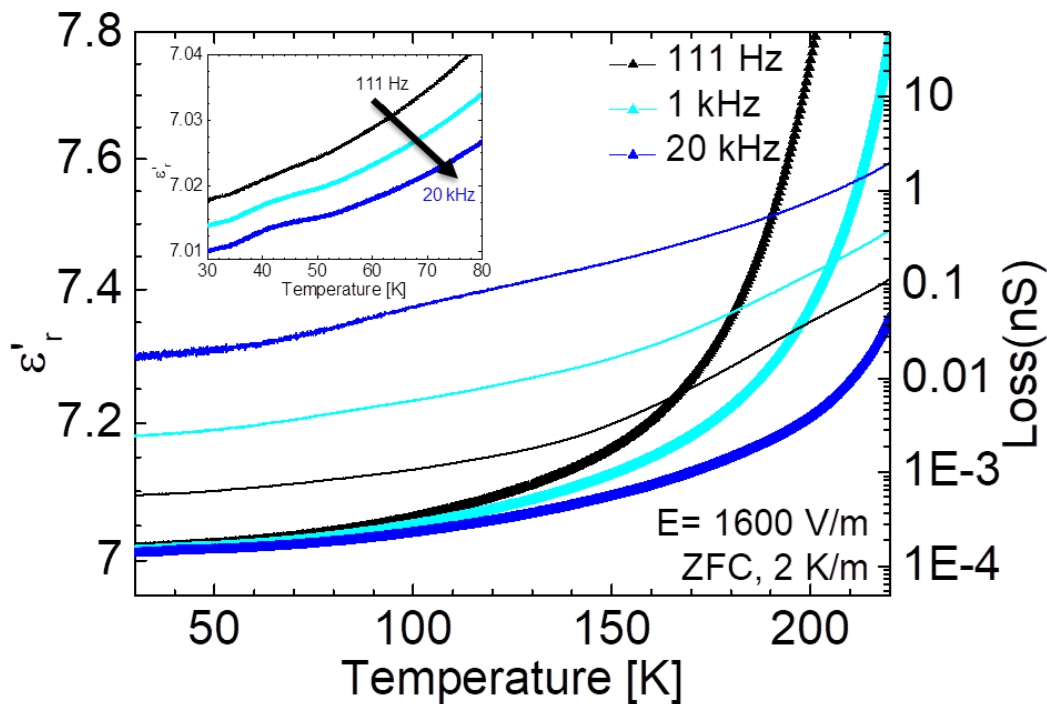


Figure 6-34 Dielectric constant and dielectric loss of  $\alpha$ -NaMnO<sub>2</sub> measured at low frequency area: 111 Hz, 1 kHz, 20 kHz. Inset shows the low temperature feature.



Interestingly, the feature developed at 45 K seems to be slightly enhanced by the increasing frequency. However it is more reasonable that this enhancement arises by the continuous “runs” as the sample gets more polarized and is not dependent on the frequency. The comparison of the bump between two different frequencies is presented in figure 6-35. The shape and “height” of the bump don’t seem to be affected by the different frequencies. However what is clearly observed through the first derivative is the slight shift of the bump to higher temperatures when the frequency increases. Similar behavior has been observed in erbium iron garnet ceramic[227] while this shift has not been further investigated.

The frequency dispersion of the effect cannot be attributed to a conventional ferroelectric phase transition. The magnetic long-range order established below  $T_N=45$  K as provided by the magnetic studies probably gives rise to the dielectric anomaly via third-order magnetoelectric (ME) contribution to the free energy,  $\delta F = -(\delta/4)P^2M^2$  (“bimagneto-bielectric effect”, [228]). This exists under all symmetries. In Debye approximation the induced *ac* permittivity follows resonant dispersion,  $\delta\varepsilon = \Delta\varepsilon / (1 + i2\pi f\tau)$  with  $\Delta\varepsilon = \varepsilon_{stat} - \varepsilon_\infty$ . It maximizes for the relaxation time  $\tau = (2\pi f)^{-1}$ , which is probably correlated with local homogeneous magnetic ordering due to magnetostatic restoring forces. Large values of  $\tau$  are expected for large magnetic correlation lengths, hence, low temperatures. This complies with the low temperature shift of the peak as the frequency decreases (figure 6-35).

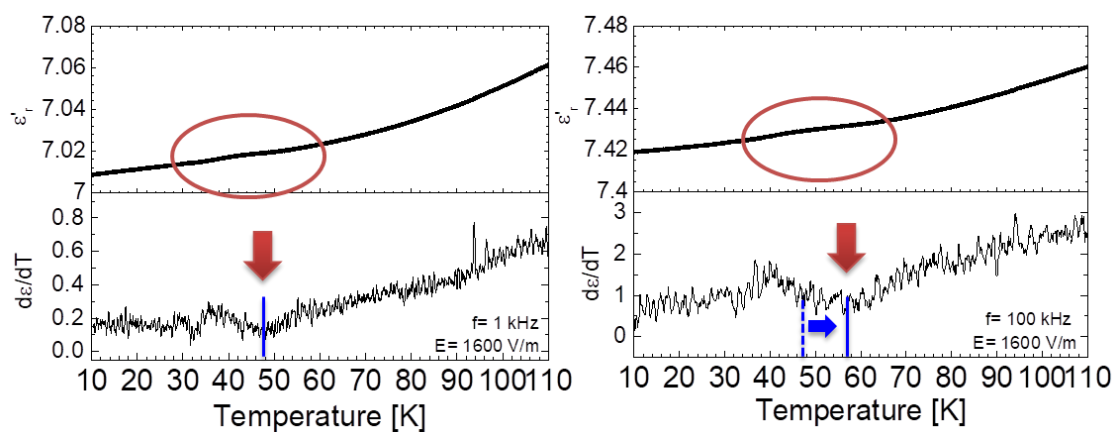


Figure 6-35 Two different runs of Dielectric constant measured at 1 kHz (left panel) and 100 kHz (right panel) with  $V_{rms} = 1600$  V/m. (Top panel) Dielectric constant against temperature. (Bottom panel) 1<sup>st</sup> derivative curves calculated from dielectric constant against temperature.



6.7.2.2 *Effect of magnetic field*

The application of several magnetic fields up to 14 T seems to have only a weak effect in the anomaly observed around 45 K. The bump seems slightly enhanced and shifted to higher temperature. The observed behavior resembles to the behavior met in  $\beta$ -phase in the same temperature range strengthening the hypothesis that both effects are correlated to the magneto elastic transition of the  $\alpha$ -phase.

The whole trend of the  $\epsilon'_r(T)$  curve is presented in figure 6-36 top panel while a close-up to the low temperature area is presented in the bottom panel.

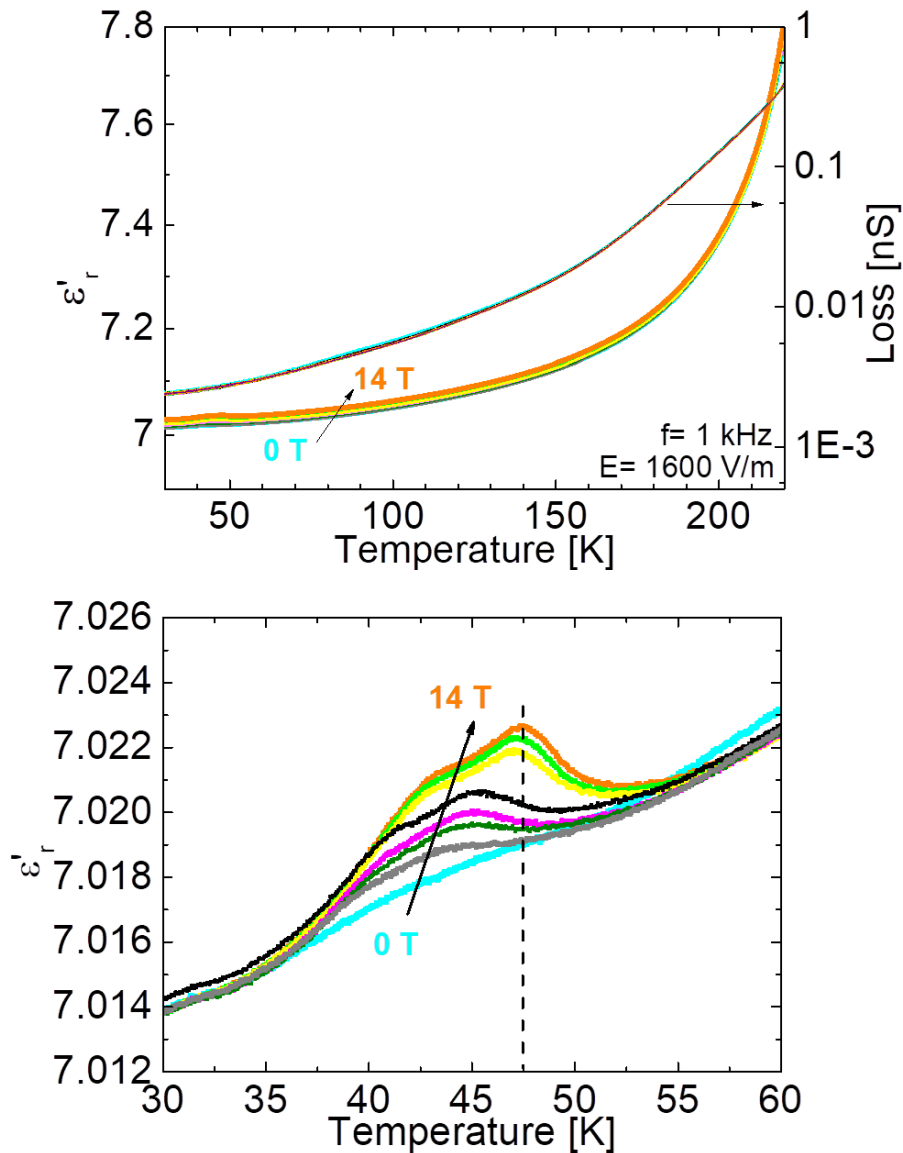


Figure 6-36 Dielectric constant of  $\epsilon'(T)$  of  $\alpha$ -NaMnO<sub>2</sub>, measured upon heating at 1 kHz under applied magnetic fields from 0 T- 14 T. Top panel: The whole temperature range. Bottom panel: low temperature area of the same measurement zoomed in. The measurement under zero (0 T) magnetic field was carried out twice: first before the application of the magnetic fields, represented with the turquoise and second in red, after the magnetic fields have been applied.



The change of the  $\epsilon'_r(T)$  response under the application of magnetic field below 45 K indicates the presence of a weak magneto-electric effect (MDE) driven by the AFM magnetic transition of the  $\alpha$ -NaMnO<sub>2</sub>. The relative dielectric response ( $\Delta\epsilon'$ (%)) has been calculated for  $H= 14$  T at  $T=35, 40, 42, 44, 45, 46, 47, 48, 50$  and  $55$  K and is plotted in figure 6-37 (black axis-left) for  $f= 1$  kHz. The  $\Delta\epsilon'$  (%) is defined as:

$$\Delta\epsilon'(\%) = \frac{\epsilon'(H) - \epsilon'(0)}{\epsilon'(H)} 100 \quad (4-8)$$

and is plotted against temperature to show the temperature dependence of the maximum change of the dielectric constant caused by the applied field of 14 T. According to this the MDE is about 0.05 % at 47 K which is slightly higher than the 0.033% value we got from samples of the beta phase. However, considering the huge magnetic field of 14 T that has been applied on the sample, the enhancement is truly weak.

The slight shift of the maximum value of the  $\epsilon'_r(T)$  with the applied magnetic field is shown in the right-top axes (in red) of the figure 6-37. The general trend shows non-linear shift towards higher temperatures.

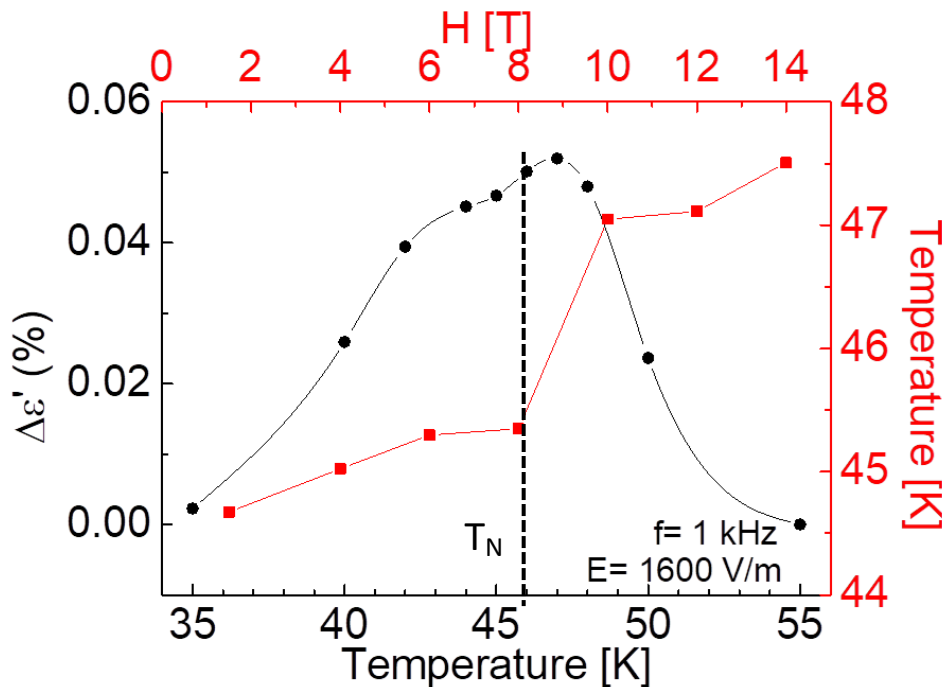


Figure 6-37 Left-bottom axes (black):  $\Delta\epsilon'$  (%) calculation against Temperature for  $H= 14$  T showing the maximum change in the values of dielectric constant with the application of the external magnetic field. The MDE is of 0.05 % at 47 K. Right-top axes: shift of the critical



temperature  $T_N$  with respect to the applied magnetic fields.  $T_N$  refers to the temperature where the dielectric constant is maximum.

In the case of  $\alpha$ -NaMnO<sub>2</sub>, possible second-order MDE coupling via so-called by Cardwell magnetodielectric effect[85] of the free energy may become active. This applies to systems with broken time-inversion due to field-induced magnetic ordering but persistent spatial inversion symmetry. Considering the symmetry-constrained, by the -1 magnetic point group, free energy for  $\alpha$ -phase which can be written as:

$$F(\mathbf{E}, \mathbf{H}) \approx \varepsilon_{ij}(\mathbf{T}) E_i E_j + \mu_{ij}(\mathbf{T}) H_i H_j + \frac{1}{2} \gamma_{ijk} H_i E_j E_k + \frac{1}{2} \delta_{ijkl} E_i E_j H_k H_l + \dots \quad (4-9)$$

it is suggested that the observed feature in the dielectric constant and the magnetic field dependence is likely to be related to the non-linear [163] quadratic and bi-quadratic terms as has already been stated in chapter 4 (beta polymorph). Here, an enhancement of the dielectric anomaly  $\delta\varepsilon = -\varepsilon_0^{-2} \left( \frac{\partial^2 F}{\partial E^2} \right) = \gamma M \propto H$  is added to the as observed (Fig. 6-36). Again, this contribution may map the density of spatial regions with dielectric relaxation times  $\tau \approx (2\pi f)^{-1}$ . Since the field-induced increase of homogeneously magnetized regions counteracts thermal disorder, the permittivity peak is shifted to higher temperatures.

Enhancement of the bump effect in the dielectric permittivity has been observed also in the structurally similar triangular antiferromagnet  $\alpha$ -NaFeO<sub>2</sub>. In that case though, the effect takes place at the onset of incommensurate (ICM2) cycloidal magnetic order and is significantly enhanced with the application of the external magnetic field while in the ICM1 phase the absence of polarization comes in agreement with the restriction of the centrosymmetric 2/m1' group. [74]

On the other hand, similar to  $\alpha$ -NaMnO<sub>2</sub> case, the “magnetocapacitance” effect has been attribute to the non-linear coupling with dominating higher ordered terms in systems where magnetostriction has been observed as in the cases of BiMnO<sub>3</sub> [168] and piezoelectric paramagnet NiSO<sub>4</sub>·6H<sub>2</sub>O[84].



### 6.7.3 Studies on $\alpha$ -Na<sub>0.96</sub>MnO<sub>2</sub> crystals

The magnetoelectric (MDE) coupling is determined by the structure and magnetic symmetry of a crystal. As a consequence, small modifications might alter, eliminate or permit MDE effect. In the case of the crystals of  $\alpha$ -Na<sub>0.96</sub>MnO<sub>2</sub> the small sodium deficiency and the resulting mixed Mn valence reduced symmetry from C2/m to P2/m tailoring the magnetic behavior in the low temperatures. Due to limited time we only had the chance to perform preliminary dielectric measurements over some crystal flakes in order to investigate possible changes in the dielectric permittivity in comparison to the parent alpha powders. The general trend remains the same while the low temperature effect appears at the onset of the as suggested canted AFM phase but persists till base temperature in opposition to the stoichiometric powders.

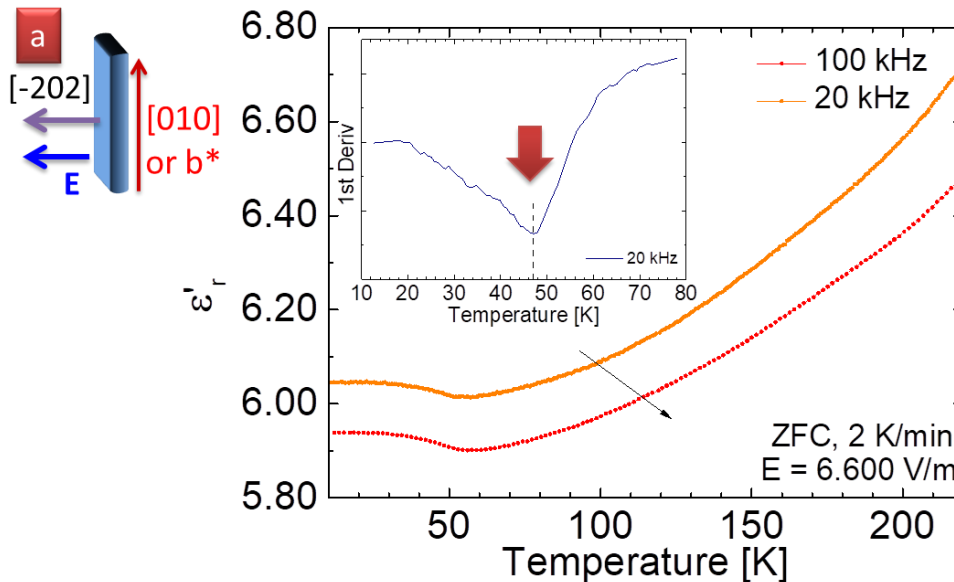


Figure 6-38 Dielectric permittivity of the  $\alpha$ -Na<sub>0.96</sub>MnO<sub>2</sub> crystals measured parallel to [-202] direction (schematic) at 2 different frequencies of 20 kHz (orange) and 100 kHz (red). The inset show the 1<sup>st</sup> derivative of the dielectric permittivity measured at 20 kHz.

In figure 6-38 the dielectric permittivity is presented as measured under  $E = 6600$  V/m ac stimuli applied parallel to [-202] as presented in the schematic. The frequency dependence follows the predictable trend of a decreasing permittivity value as the frequency increases, as commented in all previous cases. No further frequency dependency of the effect is observed while the value is at the same order of magnitude with the parent powders of alpha. What is worth noting here is that the development of the bump coincides with the

ZFC-FC divergence in the low field (100 Oe) measurements. A similar divergence of the zfc and fc  $\nu(T)$  curves at the temperature, where the MD effect begins, was reported for  $\text{Dy}_3\text{Fe}_5\text{O}_{12}$ . [229] In this work, the evidence for a MD effect below that temperature was interpreted as the setting of the non-collinear magnetic structure.

In addition to that, the effect appears at the onset of the canted AFM regime as suggested by the neutron single crystal study and shows a plateau down to 10 K where the AFM order is established. Interestingly no effect is observed in higher temperatures where the diffuse scattering takes place confirming once more that all effects on the dielectric permittivity are correlated to magnetic long range orders.

A different batch grown on the same protocol showed an alternate behavior of the dielectric permittivity but lack of detailed structural and magnetic characterization does not allow safe conclusions.

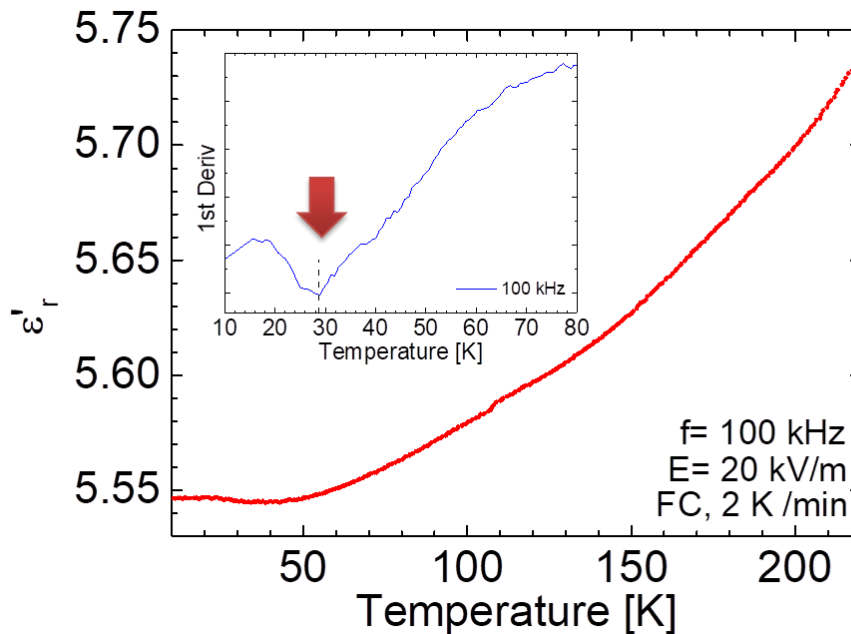


Figure 6-39 Dielectric permittivity of the  $\alpha$ - $\text{Na}_{0.96}\text{MnO}_2$  crystals measured parallel to  $[-202]$  direction at  $f= 100$  kHz (red). The inset show the 1<sup>st</sup> derivative of the dielectric permittivity measured at 100 kHz.

The general trend seems to be the same along the whole temperature range but in this case the effect is less pronounced and appears below 30 K. Talking about the same crystal this would refer to the onset of the AFM phase. However, all amplitudes seem reduced. In this case a chemical transformation by oxidation and transfer  $\text{Mn}^{3+} \rightarrow \text{Mn}^{4+}$  might partially destroy the underlying spin structure and further affect the anomaly. The inevitable

chemical inhomogeneity makes the details of the effect dependable on the volume fractions of intergrowths and so slightly depends on sample. For further understanding this phenomenon, systematic investigations of the defected microstructure and extensive dielectric and electric studies are necessary.

## 6.8 Effects of deviation from stoichiometry- discussion

To our understanding, this single crystal neutron scattering experiment suggests that long-range order (LRO) in  $\alpha$ -Na<sub>0.96</sub>MnO<sub>2</sub> develops below 45 K, as studies on powders have originally suggested. This is described by a  $\mathbf{k}_1 = (000)$  component, which coexists with a diffuse scattering contribution in the (hk0) plane that precedes the LRO (Fig. 6-40). Lowering the temperature further, a  $\mathbf{k}_2 = (\frac{1}{2} \frac{1}{2} 0)$  related intense scattering part develops below ~26 K, inferring simultaneous occurrence of both distinct LRO orders with the (hk0) rod-like diffuse scattering, which remains strong all the way down to the base-temperature, with no change in relative intensity ratios of all three components down to 1.5 K. The outcomes of the study indicate that the relief of frustration by means of spin-order in the triangular topology of these manganites is a complicated process where additional interactions may be of relevance. This is especially important in view of the sensitivity of the materials' degenerate ground state to all kinds of perturbations.[202], [230]

In the general case, with structural disorder being absent, a magnetically-driven structural phase transition is established when the energy gain in the spin system outweighs the cost in the elastic energy. However, when disorder-induced exchange randomness comes into play, fluctuations in nearest-neighbour interactions are anticipated to control the disorder-averaged ground-state energy.[231] Theory predicts that additional interactions measured by the magnitude of the quenched disorder (cf. vacancies, Mn<sup>3+</sup>:Mn<sup>4+</sup>, Jahn-Teller favored crystallographic twinings etc) may allow a frustrated system to enter a LRO Néel state either by lowering its lattice symmetry or even by avoiding to do so.[232] Such a complexity, with analogies to the observations in  $\alpha$ -Na<sub>0.96</sub>MnO<sub>2</sub>, is met in the isostructural Cu(Mn<sub>1-x</sub>Cu<sub>x</sub>)O<sub>2</sub> system. In the latter, variable Cu-doping requires creation of Mn<sup>4+</sup> ions for charge neutrality, as Na-vacancies in the former would create similar impurity-state ions. As such, the lattice strain induced by the associated structural defects in Cu(Mn<sub>1-x</sub>Cu<sub>x</sub>)O<sub>2</sub> disturbs the balance of competing interactions, allowing FM interlayer coupling in an otherwise antiferromagnetically ordered system.[213] Moreover, as the Mn magnetic lattice gets randomly diluted by Cu<sup>2+</sup>/Mn<sup>4+</sup> ions, the emerging magnetic scattering at



intermediate doping (3% Cu) is indexed by two propagation vectors. [233] When Cu doping is raised to 7%, the anticipated structural phase transition that relieves frustration in the parent CuMnO<sub>2</sub> is no more developed, but the competition between short-range (diffuse) and 3D long-range (Bragg) orderings, with the latter being addressed by a single propagation vector, is observed down to the base temperature.

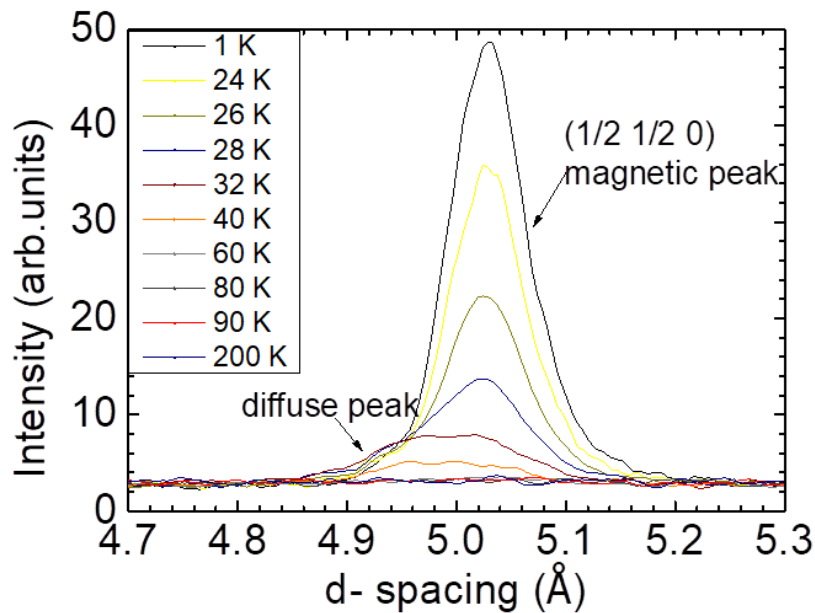


Figure 6-40 The thermal evolution of the magnetic scattering at  $d \sim 5.05 \text{ \AA}$ ; the diffuse component precedes the growth of the Bragg contribution at the  $(\frac{1}{2} \frac{1}{2} 0)$  commensurate lattice position.

We should also note that in both works of Garlea et al. and Dally et al. substoichiometry is a key in the lowering of dimensionality of the magnetic lattice. Inelastic neutron experiments in the case of the recent  $\alpha$ -Na<sub>0.9</sub>MnO<sub>2</sub> single crystal study [234], assign single-ion anisotropy, favored by a disordered ground regime, responsible for fluctuation effects that lead to a long-lived amplitude mode. In the case of  $\alpha$ -Na<sub>0.9</sub>MnO<sub>2</sub> crystals, intergrowth defects of beta seem to be avoided [136] but still high density twinings are considered as different spin domains that attribute to create a coherent model. However, it is admitted that cation vacancies and mixed Mn valence together with twin-defects could create random magnetic impurities in the lattice which in cases of Cu<sub>1+x</sub>Mn<sub>1-x</sub>O<sub>2</sub> [42], [213], [233] or  $\alpha$ -Na<sub>1-x</sub>MnO<sub>2</sub> [176], [182], [192], [207] has been proved to disturb the magnetic lattice.

Therefore in the limit of weak disorder, in which exchange randomness acts as a perturbation, ground state instability may be generated. However, in A<sub>x</sub>Mn<sub>1-y</sub>O<sub>2</sub> (A= Na,



Cu), additional interactions, such as the evolution of the  $\text{Mn}^{3+}$  Jahn-Teller distortion, may compete with the effective couplings and lead the distorted ground state to a particular nature (cf. AFM, FM etc). In view of this, a theoretical work[207] has investigated how the Jahn-Teller distortion in  $\text{Na}_x\text{MnO}_2$  system is modified upon hole doping ( $x>0$ ). As Zener explained,[235], [236] holes' hopping between Mn  $e_g$ -orbitals gives rise to FM coupling between local spins due to the DE interaction. With this argument in hand, Ouyang et al.[207] has pointed out that for very small doping concentration  $n$ ,  $\cos\theta$  (where,  $\theta$  is the canting angle between local spins along the z-axis and  $2\theta$  is the angle between two neighboring spins) increases linearly with the doping level (Fig. 6-41). The outcome is that manganese spins in  $\text{Na}_x\text{MnO}_2$  can transform from a canted striped AFM state to a FM long-range ordered one. Such an electron-complexity, in an otherwise chemically homogeneous system, has been suggested earlier by de Gennes, for compounds with mixed-valency, as a consequence of carriers which are responsible for DE as well.[196] In his theory electrons (or holes) would give rise to a distorted ground state spin arrangement, but when they fall into bound states (cf. impurity ions of opposite charge) may give rise to local in-homogeneities in the spin-distortion that relay diffuse magnetic peaks in the neutron diffraction patterns. Our experimental observations in  $\alpha$ - $\text{Na}_{0.96}\text{MnO}_2$  crystals confirm a weak FM contribution that could be due to small canting of AFM moments, and a diffuse scattering component which may infer bound states, without being able to waive out microscopic spatial in-homogeneities.

The existence of the diffuse scattering well above the first transition temperature ( $T_{N1}=45$  K and the diffuse starts developing below 90 K) is met also in  $\text{TbMnO}_3$  multiferroic. In that case it is attributed to fluctuations of both Mn and Tb contributions that could be observed in an ordered SPW phase. [237] The diffuse is said to arise out of strong magnetic frustration in the ab plane between competing FM nearest neighbor and AFM next nearest neighbor interactions.



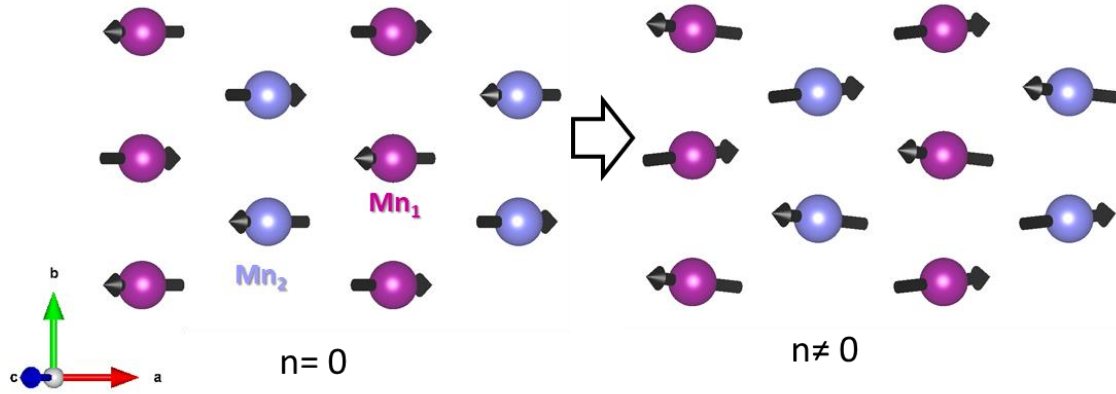


Figure 6-41 Schematic of Mn-spin canting ( $ab$ -plane view), a possibility due to non-negligible hole-concentration ( $n$ ) in the off-stoichiometric  $\alpha$ - $\text{Na}_x\text{MnO}_2$  ( $n \approx 1-x$ ). According to Ouyang et al [207] a weak ferromagnetic component is expected to develop along the  $b$ -axis of the monoclinic cell.

## 6.9 Summary and Conclusions

Large volume single crystals of  $\alpha$ - $\text{Na}_x\text{MnO}_2$  ( $x = 0.96$ ) grown by the floating zone method have been employed to examine the magnetic properties of the system for the first time. The crystals possess a monoclinic  $P2/m$  structure with  $a = 5.6579$  (4) Å,  $b = 2.8574$  (4) Å,  $c = 5.7931$  (4) Å and  $\beta = 113.0719$  (3) deg. A well-established long range antiferromagnetic order vanishes rapidly above 26 K, while a coexistent canted antiferromagnetic state persists up to 45 K. That appears as double feature in magnetic susceptibility measurements that is obvious only when the magnetic field is perpendicular to the growth direction [010] of the crystal. In high temperature area, low-dimensional, short-range correlations are inferred by the broad maximum in the susceptibility data. Magnetic scattering in the  $(hk0)_m$  plane, from single-crystal neutron diffraction data, allows us to see the two distinct magnetic regimes arise as Bragg peaks indexed with the  $k_1 = (0 \ 0 \ 0)$  propagation vector, which appears below  $T_c \approx 45$  K and the  $k_2 = (\frac{1}{2} \ \frac{1}{2} \ 0)$  that evolves below  $T_N \approx 26$  K. Critical behavior for both describes a two dimensional Ising system. A diffuse scattering in the vicinity of the  $\frac{1}{2}\frac{1}{2}0$  Bragg peak confirms the short range interactions that coexist with the aforementioned long range ordered magnetic states, persist up to almost 100 K.

It is presented that the substitution of  $\text{Mn}^{4+}$  in  $\text{Mn}^{3+}$  positions due to Na volatility in  $\alpha$ - $\text{Na}_{0.96}\text{MnO}_2$  crystals, confirmed by the XPS and EDS analysis, is at the basis of the observed magnetic properties. Competing FM ( $\text{Mn}^{3+}$ - $\text{Mn}^{4+}$ ) and AFM ( $\text{Mn}^{3+}$ - $\text{Mn}^{3+}$ )

interactions may be the root of the anisotropic magnetic properties witnessed, having a weak-FM contribution observed for the first time.

The chemical transformation by oxidation of manganese  $\text{Mn}^{3+} \rightarrow \text{Mn}^{4+}$  that is met in  $\alpha$ -Na<sub>0.96</sub>MnO<sub>2</sub> single crystals seems to alternate the underlying spin structure in comparison to the parent  $\alpha$ -NaMnO<sub>2</sub> powders. This has an impact on the dielectric behavior of the system regulating the shape and temperature range of the effect. However in both cases effects in the dielectric permittivity suggest the onset of the commensurate magnetic long range order ( $T \sim 45$  K) which in the case of the powders allows a magnetocapacitance effect of 0.05 %. Since symmetry restrictions don't permit the onset of any polarization the magneto-dielectric behavior is attributed to non-linear terms of the free energy.

The ways in which the Mn cations map out on a corrugated 2D triangular lattice, is still an open theme as studies on the evolution of the average structure and magnetism are scarce. Further understanding of the mechanisms that dictate if frustrated interactions are relieved and magnetic order is established will help us to resolve whether other coupled electron degrees of freedom are likely to be generated in this family of oxides.



## Chapter Seven:

# Wake & Perspectives

---

Simultaneously active electron degrees of freedom and their unfolding under restrictions imposed by the underlying crystal lattice has been the root of complexity met in transition metal oxides. Furthermore, competing interactions that arise from compositional modulations pertaining to magnetic frustration seem to set the ground for emergence of coexisting magnetic and ferroelectric order that can be mutually coupled arousing technological interest. Engineering the materials' structure in order to accommodate unusual neighbor interactions gives rise to the highly desired era of 'materials by design'. [64] Fostered by the better understanding of the chemistry/structure/property relationships it leads the way to technological innovations while motivating further fundamental research.

The present study wished to be a part of this progress by providing a further insight of the underline mechanisms that dictate why frustrated interactions are relieved in favor of establishment of long range magnetic order and how magnetic and electric degrees of freedom may be coupled. Layered rock-salt-type of oxides ( $AMnO_2$ ,  $A= Na, Cu$ ) are appealing in this respect, as they provide a paradigm where polymorphism and triangular lattice topology have profound implications on their spin-dependent properties. The 2D triangular Na-Mn-O system apart from the Mn triangular topology imposing magnetic frustration offers also a great playground as far as competing interactions are concerned. This happens due to structural inhomogeneities created by local intergrowth of the alpha



and beta phases into each other while the Jahn-Teller distortion of  $\text{Mn}^{3+}$  is smoothed out by the existence of  $\text{Mn}^{4+}$  as an attempt for chemical counterbalance to  $\text{Na}^+$  vacancies resulting from different synthetic routes. Na-Mn-O oxides have been revisited in the form of polycrystalline samples and for the first time as large single crystals allowing the study of the anisotropy in magnetic properties and offering the opportunity to employ techniques that require large surfaces and volumes such as neutron scattering.

A summary of the findings and conclusions will be summarized below setting some perspectives and suggested future work as initiated by the present study.

Synthesis protocols and processes for all  $\alpha\text{-NaMnO}_2$ ,  $\beta\text{-NaMnO}_2$  powders and single crystals of  $\alpha\text{-Na}_{0.96}\text{MnO}_2$  and  $\alpha\text{-Na}_{0.7}\text{MnO}_2$  (h-NMO) grown with the Floating zone technique in Ar and  $\text{O}_2$  respectively have been detailed in chapter 3. Different quenching approaches and crystal growth conditions have been explored. The result in polycrystalline specimens has been a pure main phase of the stoichiometric alpha or beta with most of the times secondary phases of the sister polymorph and /or the  $\beta\text{-Na}_{0.7}\text{MnO}_2$ . The first successful attempts of the crystal growth could work as a starting base for exploring the conditions for a successful growth of a single crystal of the beta polymorph though it proved to be extra challenging.

In chapter 4 the highly defected nuclear structure of  $\beta\text{-NaMnO}_2$  polymorph has been explored in detail through neutron powder diffraction. The intergrowth of alpha- areas into the mean beta structure has been confirmed and further modeled as one phase employing superspace formalism. The flexibility of  $\beta\text{-NaMnO}_2$  to alternate its lattice topology is at the basis of chemical and physical properties underlining the role of the energetically degenerated  $\alpha$ - and  $\beta$ - layer stacking sequences. A non-collinear spin arrangement has been found to develop as a perturbation in the boundary of the  $\alpha$ - and  $\beta$ - like stacking sequences setting a cooperative proper-screw magnetic state below  $T_2=95$  K while a second collinear commensurate AFM state sets at  $T_1= 200$  K. The lattice topology of the Jahn Teller  $\text{Mn}^{3+}$  ions drives the original 3D spin correlations ( $T < T_{N1}$ ) to become 2D in character. Inelastic neutron scattering and  $^{23}\text{Na}$  NMR provide evidence that a spin-gap ( $\Delta= 5$  meV) opens in the excitation spectra, supporting the 2D nature of the magnetic interactions at  $T < T_{N2}$ . The structural complexity of beta actually sets a new picture over the dielectric permittivity studies which have been done extensively in powder samples both as synthesized and extra annealed. In the as synthesized samples effects in dielectric permittivity have been observed in the setting of the commensurate ordered state ( $T_1= 200$  K) and the set of



commensurate state of alpha ( $T_N = 45$  K). Although weak, the magnetoelectric coupling of about 0.033% is believed to be connected to the relief of frustration of the alpha domains. The fact that in the annealed samples there is an extra effect in the setting of the proper screw magnetic state, promote the thinking of the phenomono being connected to the domain-wall like phenomena. Origin of the weak magnetocapacitance has been attributed to the high order terms of the free energy formula and should be further explored in the context of domain walls. Since the superspace point group maintains the inversion symmetry no polarization is expected. Nevertheless, pursuing measurements of polarization would shed some light in the mechanism of this weak coupling.

h-NMO crystals have been grown for the first time with the floating zone technique and in chapter 5 a study over their structure and chemically related physical properties is discussed. The crystal structure has been solved confirming a P2 type described by hexagonal  $P6_3/mmc$  cell with no distortion of the  $MnO_6$  environment. In line with this is the average Mn valence of +3.62 which is closer to 4. Dc susceptibility measurements show a complex set of transitions hinting for a reentrant spin glass state emerging at low temperatures. The glassy ground state agrees with the observations for a canonical spin glass state in the  $\alpha$ - $Na_{0.7}MnO_2$  powders. However, further investigation to detangle the glassy behavior observed in the  $Na_{0.7}MnO_2$  crystals could be initiated. For instance, ac-susceptibility measurements could be employed in order to explore the relaxation effects in spin glasses which together with thermoremanent magnetization are signature measurements for the determination of a spin glass phase and would offer a useful insight. In addition to that, neutron scattering would clarify the picture of the temperature evolution of magnetism in  $\alpha$ - $Na_{0.7}MnO_2$ . The presence of a diffuse scattering or the existence of sharp Bragg peaks indicating an ordered state would definitely add to the understanding of the distorted ground state of  $Na_{0.7}MnO_2$ . Along with that, the effect observed for the first time on the dielectric permittivity seems to originate from the competing magnetic interactions since it develops at the setting of the so-called 'spin glass order'. Further exploration of the dielectric and magneto dielectric response taking advantage the single crystal anisotropy as triggered by this preliminary dielectric study, would allow to better understand the role of competing interactions and their performance in relation to the glassy ground state.

In chapter 6 the growth of  $a$ - $Na_xMnO_2$  ( $x = 0.96$ ) single crystals by the floating zone method allowed us to see a different evolution of the magnetic system in comparison to the



alpha powders. The  $\alpha$ - $\text{Na}_{0.96}\text{MnO}_2$  crystallizes in P2/m monoclinic cell allowing the existence of two independent Mn sites. The small percentage of  $\text{Mn}^{4+}$  seems to play a role in the behavior of the system initiating FM-AFM competing interactions being the root of anisotropic magnetic properties. Single-crystal neutron diffraction data, allows us to see the two distinct magnetic regimes arise as Bragg peaks indexed with the  $k_1=(0\ 0\ 0)$  propagation vector, which appears below  $T_C \approx 45$  K and the  $k_2=(\frac{1}{2}\ \frac{1}{2}\ 0)$  that evolves below  $T_N \approx 26$  K. Critical behavior for both describes a two dimensional Ising system. A diffuse scattering in the vicinity of the  $\frac{1}{2}\frac{1}{2}0$  Bragg peak confirms the short range interactions that coexist with the aforementioned long range ordered magnetic states, persist up to almost 100 K.

The chemical transformation by oxidation of manganese  $\text{Mn}^{3+} \rightarrow \text{Mn}^{4+}$  that is met in  $\alpha$ - $\text{Na}_{0.96}\text{MnO}_2$  single crystals seems to alternate the underlying spin structure in comparison to the parent  $\alpha$ - $\text{NaMnO}_2$  powders. This has an impact on the dielectric behavior of the system regulating the shape and temperature range of the effect. However, in both cases (crystals and powders) effects in the dielectric permittivity suggest the onset of the commensurate magnetic long range order ( $T \sim 45$  K) which in the case of the powders allows a magnetocapacitance effect of 0.05 %. Origin of the weak magnetocapacitance should be further explored in the context of domain walls due to the inherent structural polymorphism of the system especially in the powders samples. A way to quantify the number of defects in the powders and in the grown crystals could be by  $^{23}\text{Na}$  NMR. Knowing the percentage of the structure faults would allow the safer conclusions as far as the origin of the magneto electric coupling is concerned.

In the same context, pursuit of more detailed and well organized experimental dielectric/magnetodielectric sequences taking advantage of the anisotropic properties of the grown single crystals would allow precise comparison with the powders and further commenting on the possible anisotropy. For this preliminary measurements on the crystals, electric field has been applied only perpendicular to the flat surface which has been the (-202) plan for  $\alpha$ - $\text{NaMnO}_2$  crystals and ab plane for  $\alpha$ - $\text{Na}_{0.7}\text{MnO}_2$ . Application of the magnetic field in parallel and perpendicular to the electric field (and so the flat surfaces) would allow the realization of an anisotropy in the observed effects.

The work presented in this thesis has furthered the existing knowledge on the structure, magnetic, dielectric and dynamical properties of the  $\text{Na}_x\text{MnO}_2$  ( $0.7 < x < 1$ ) system offering an insight on the structure imposed spin arrangements and the setting of ordered distorted



ground states. However, time limitations have not allowed us to respond to all questions arose so it is still worth to be further pursuit.

Polarization measurements or Pyro current hasn't been performed in the systems under study since this kind of measurement needs a standardization in order to have repeatable and trustworthy results. This would demand testing of the station using with a material that exhibits known polarization and working towards the way of fixing a safe measurement process. [238], [239] The proof of the existence of a ferroelectric or polar order would allow safer conclusions towards the emergence of magnetoelectric effect in the studied systems.

Proposed theories of magnetoelectricity are not only addressing the field of multiferroics, but are also widely applicable to the broader field of correlated electronic systems. [238], [239] In this sense, the development of magnetoelectric theories is one of the core physical topics of focus within Condensed Matter Physics in recent times. Certainly additional efforts are much needed to further push forward the physical understanding of this subject and be closer to real applications of these fascinating multiferroic materials.

## 7.1 Literature Studied

- [1] W. Eerenstein, N. D. Mathur, and J. F. Scott, "Multiferroic and magnetoelectric materials," *Nature*, vol. 442, no. 7104, pp. 759–765, Aug. 2006.
- [2] J. F. Scott, "Applications of magnetoelectrics," *Journal of Materials Chemistry*, vol. 22, no. 11, p. 4567, 2012.
- [3] J.-P. Parant, R. Olazcuaga, M. Devalette, C. Fouassier, and P. Hagenmuller, "Sur quelques nouvelles phases de formule  $\text{NaxMnO}_2$  ( $x \leq 1$ )," *Journal of Solid State Chemistry*, vol. 3, no. 1, pp. 1–11, Feb. 1971.
- [4] P.-F. Wang, Y. You, Y.-X. Yin, and Y.-G. Guo, "Layered Oxide Cathodes for Sodium-Ion Batteries: Phase Transition, Air Stability, and Performance," *Advanced Energy Materials*, vol. 8, no. 8, p. 1701912, Mar. 2018.
- [5] Q. Bai, L. Yang, H. Chen, and Y. Mo, "Computational Studies of Electrode Materials in Sodium-Ion Batteries," *Advanced Energy Materials*, vol. 8, no. 17, p. 1702998, Jun. 2018.



- [6] R. J. Clément, P. G. Bruce, and C. P. Grey, “Review—manganese-based P2-type transition metal oxides as sodium-ion battery cathode materials,” *Journal of The Electrochemical Society*, vol. 162, no. 14, pp. A2589–A2604, 2015.
- [7] J. Billaud *et al.*, “ $\beta$ -NaMnO<sub>2</sub>: A High-Performance Cathode for Sodium-Ion Batteries,” *Journal of the American Chemical Society*, vol. 136, no. 49, pp. 17243–17248, Dec. 2014.
- [8] Y. Cheng, B. Peng, Z. Hu, Z. Zhou, and M. Liu, “Recent development and status of magnetoelectric materials and devices,” *Physics Letters A*, vol. 382, no. 41, pp. 3018–3025, Oct. 2018.
- [9] C. Delmas, C. Fouassier, and P. Hagemuller, “Structural classification and properties of the layered oxides,” *Physica B+C*, vol. 99, no. 1, pp. 81–85, Jan. 1980.
- [10] J.-Y. Hwang, S.-T. Myung, and Y.-K. Sun, “Sodium-ion batteries: present and future,” *Chem. Soc. Rev.*, vol. 46, no. 12, pp. 3529–3614, 2017.
- [11] S. Blundell, *Magnetism in Condensed Matter*. OUP Oxford, 2001.
- [12] J. Singleton, *Band Theory and Electronic Properties of Solids*. Oxford, New York: Oxford University Press, 2001.
- [13] N. Yabuuchi and S. Komaba, “Recent research progress on iron- and manganese-based positive electrode materials for rechargeable sodium batteries,” *Science and Technology of Advanced Materials*, vol. 15, no. 4, p. 043501, Aug. 2014.
- [14] C. Delmas, J.-J. Braconnier, and P. Hagemuller, “A new variety of LiCoO<sub>2</sub> with an unusual oxygen packing obtained by exchange reaction,” *Materials Research Bulletin*, vol. 17, no. 1, pp. 117–123, Jan. 1982.
- [15] C. Delmas, J. Braconnier, C. Fouassier, and P. Hagemuller, “Electrochemical intercalation of sodium in Na<sub>x</sub>CoO<sub>2</sub> bronzes,” *Solid State Ionics*, vol. 3–4, pp. 165–169, Aug. 1981.
- [16] Z. Lu and J. R. Dahn, “Effects of Stacking Fault Defects on the X-ray Diffraction Patterns of T<sub>2</sub>, O<sub>2</sub>, and O<sub>6</sub> Structure Li<sub>2/3</sub>[Co<sub>x</sub>Ni<sub>1/3-x</sub>Mn<sub>2/3</sub>]O<sub>2</sub>,” *Chemistry of Materials*, vol. 13, no. 6, pp. 2078–2083, Jun. 2001.
- [17] Aristotle and A. Press, *On the Soul*. Aeterna Press, 2015.
- [18] N. Terada, “Spin and orbital orderings behind multiferroicity in delafossite and related compounds,” *J. Phys.: Condens. Matter*, vol. 26, no. 45, p. 453202, Nov. 2014.



- [19] Y. Tokura, S. Seki, and N. Nagaosa, “Multiferroics of spin origin,” *Rep. Prog. Phys.*, vol. 77, no. 7, p. 076501, Jul. 2014.
- [20] J. Kanamori, “Superexchange interaction and symmetry properties of electron orbitals,” *Journal of Physics and Chemistry of Solids*, vol. 10, no. 2–3, pp. 87–98, Jul. 1959.
- [21] J. B. Goodenough, “Theory of the Role of Covalence in the Perovskite-Type Manganites [  $\text{La}, \text{M}(\text{II})$  ]  $\text{MnO}_3$ ,” *Phys. Rev.*, vol. 100, no. 2, pp. 564–573, Oct. 1955.
- [22] F. D. M. Haldane, “Continuum dynamics of the 1-D Heisenberg antiferromagnet: Identification with the  $O(3)$  nonlinear sigma model,” *Physics Letters A*, vol. 93, no. 9, pp. 464–468, Feb. 1983.
- [23] F. D. M. Haldane, “Nonlinear Field Theory of Large-Spin Heisenberg Antiferromagnets: Semiclassically Quantized Solitons of the One-Dimensional Easy-Axis Néel State,” *Phys. Rev. Lett.*, vol. 50, no. 15, pp. 1153–1156, Apr. 1983.
- [24] C. K. Majumdar and D. K. Ghosh, “On Next-Nearest-Neighbor Interaction in Linear Chain. I,” *Journal of Mathematical Physics*, vol. 10, no. 8, pp. 1388–1398, Aug. 1969.
- [25] B. Kumar, “Quantum spin models with exact dimer ground states,” *Phys. Rev. B*, vol. 66, no. 2, p. 024406, Jun. 2002.
- [26] L. Limot *et al.*, “Susceptibility and dilution effects of the kagomé bilayer geometrically frustrated network: A Ga NMR study of  $\text{SrCr}_9\text{pGa}_{12-9\text{p}}\text{O}_{19}$ ,” *Physical Review B*, vol. 65, no. 14, Apr. 2002.
- [27] B. Sriram Shastry and B. Sutherland, “Exact ground state of a quantum mechanical antiferromagnet,” *Physica B+C*, vol. 108, no. 1–3, pp. 1069–1070, Aug. 1981.
- [28] S. Miyahara and K. Ueda, “Exact Dimer Ground State of the Two Dimensional Heisenberg Spin System  $\text{SrCu}_2(\text{BO}_3)_2$ ,” *Phys. Rev. Lett.*, vol. 82, no. 18, pp. 3701–3704, May 1999.
- [29] “Laboratoire National des Champs Magnétiques Intenses - Grenoble - Quantum spin systems.” [Online]. Available: <http://lncmi-grenoble.cnrs.fr/spip.php?article515&lang=en>. [Accessed: 23-May-2019].
- [30] F. Schwabl, *Statistische Mechanik: mit 26 Tabellen und 186 Aufgaben*, 3., aktualisierte Aufl. Berlin: Springer, 2006.



- [31] R. Moessner and A. P. Ramirez, “Geometrical frustration,” *Physics Today*, vol. 59, no. 2, pp. 24–29, Feb. 2006.
- [32] L. Balents, “Spin liquids in frustrated magnets,” *Nature*, vol. 464, no. 7286, pp. 199–208, Mar. 2010.
- [33] S.-H. Lee *et al.*, “Frustrated Magnetism and Cooperative Phase Transitions in Spinels,” *J. Phys. Soc. Jpn.*, vol. 79, no. 1, p. 011004, Jan. 2010.
- [34] A. P. Ramirez, “Strongly geometrically frustrated magnets,” *Annual Review of Materials Science*, vol. 24, no. 1, pp. 453–480, 1994.
- [35] R. Higashinaka, H. Fukazawa, K. Deguchi, and Y. Maeno, “Low Temperature Specific Heat of  $\text{Dy}_2\text{Ti}_2\text{O}_7$  in the Kagome Ice State,” *Journal of the Physical Society of Japan*, vol. 73, no. 10, pp. 2845–2850, Oct. 2004.
- [36] T. Jia, G. Zhang, X. Zhang, Y. Guo, Z. Zeng, and H. Q. Lin, “Magnetic frustration in  $\alpha\text{-NaMnO}_2$  and  $\text{CuMnO}_2$ ,” *Journal of Applied Physics*, vol. 109, no. 7, p. 07E102, Apr. 2011.
- [37] A. J. W. Reitsma, L. F. Feiner, and A. M. Oleś, “Orbital and spin physics in  $\text{LiNiO}_2$  and  $\text{NaNiO}_2$ ,” *New Journal of Physics*, vol. 7, pp. 121–121, May 2005.
- [38] C. Stock *et al.*, “One-Dimensional Magnetic Fluctuations in the Spin-2 Triangular Lattice  $\alpha\text{-NaMnO}_2$ ,” *Physical Review Letters*, vol. 103, no. 7, Aug. 2009.
- [39] B. A. Frandsen *et al.*, “Order, Disorder, and Nanoscale Degeneracy Lifting in a Geometrically Frustrated Antiferromagnet,” p. 8.
- [40] K. Binder and A. P. Young, “Spin glasses: Experimental facts, theoretical concepts, and open questions,” *Reviews of Modern physics*, vol. 58, no. 4, p. 801, 1986.
- [41] M. Giot, L. C. Chapon, J. Androulakis, M. A. Green, P. G. Radaelli, and A. Lappas, “Magnetoelastic Coupling and Symmetry Breaking in the Frustrated Antiferromagnet  $\alpha\text{-NaMnO}_2$ ,” *Physical Review Letters*, vol. 99, no. 24, Dec. 2007.
- [42] F. Damay *et al.*, “Spin-lattice coupling induced phase transition in the  $S = 2$  frustrated antiferromagnet  $\text{CuMnO}_2$ ,” *Physical Review B*, vol. 80, no. 9, Sep. 2009.
- [43] B. D. Gaulin, “The texture of frustrated magnets,” *Nature Mater*, vol. 4, no. 4, pp. 269–270, Apr. 2005.
- [44] J. A. Mydosh, *Spin Glasses: An Experimental Introduction*. Taylor & Francis, 1993.
- [45] K. Jonason, J. Mattsson, and P. Nordblad, “Chaos in the Ferromagnetic Phase of a Reentrant Ferromagnet,” *Phys. Rev. Lett.*, vol. 77, no. 12, pp. 2562–2565, Sep. 1996.



- [46] R. Mathieu, P. Svedlindh, and P. Nordblad, “Re-entrant spin glass transition in La<sub>0.96</sub>-yNd<sub>y</sub>K<sub>0.04</sub>MnO<sub>3</sub>: Origin and effects on the colossal magnetoresistivity,” *EPL (Europhysics Letters)*, vol. 52, no. 4, p. 441, 2000.
- [47] K. Jonason and P. Nordblad, “Sensitivity to temperature perturbations of the ageing states in a re-entrant ferromagnet,” *Eur. Phys. J. B*, vol. 10, no. 1, pp. 23–28, Jul. 1999.
- [48] H. Schmid, “Multi-ferroic magnetoelectrics,” *Ferroelectrics*, vol. 162, no. 1, pp. 317–338, Jan. 1994.
- [49] D. Khomskii, “Classifying multiferroics: Mechanisms and effects,” *Physics*, vol. 2, Mar. 2009.
- [50] N. A. Hill, “Why Are There so Few Magnetic Ferroelectrics?,” *J. Phys. Chem. B*, vol. 104, no. 29, pp. 6694–6709, Jul. 2000.
- [51] Y.-H. Chu *et al.*, “Electric-field control of local ferromagnetism using a magnetoelectric multiferroic,” *Nature Mater*, vol. 7, no. 6, pp. 478–482, Jun. 2008.
- [52] G. A. Smolenskii and I. E. Chupis, “Ferroelectromagnets,” *Sov. Phys. Usp.*, vol. 25, no. 7, pp. 475–493, Jul. 1982.
- [53] J. T. Heron, D. G. Schlom, and R. Ramesh, “Electric field control of magnetism using BiFeO<sub>3</sub>-based heterostructures,” *Applied Physics Reviews*, vol. 1, no. 2, p. 021303, Jun. 2014.
- [54] J. T. Heron *et al.*, “Deterministic switching of ferromagnetism at room temperature using an electric field,” *Nature*, vol. 516, no. 7531, pp. 370–373, Dec. 2014.
- [55] M. Bibes and A. Barthélémy, “Towards a magnetoelectric memory,” *Nature Mater*, vol. 7, no. 6, pp. 425–426, Jun. 2008.
- [56] S. Manipatruni *et al.*, “Scalable energy-efficient magnetoelectric spin–orbit logic,” *Nature*, vol. 565, no. 7737, pp. 35–42, Jan. 2019.
- [57] J. P. Velev *et al.*, “Magnetic Tunnel Junctions with Ferroelectric Barriers: Prediction of Four Resistance States from First Principles,” *Nano Lett.*, vol. 9, no. 1, pp. 427–432, Jan. 2009.
- [58] M. Gajek *et al.*, “Tunnel junctions with multiferroic barriers,” *Nature Mater*, vol. 6, no. 4, pp. 296–302, Apr. 2007.
- [59] C. Binek and B. Doudin, “Magnetoelectronics with magnetoelectrics,” *J. Phys.: Condens. Matter*, vol. 17, no. 2, pp. L39–L44, Jan. 2005.



- [60] X. Chen, A. Hochstrat, P. Borisov, and W. Kleemann, “Magnetoelectric exchange bias systems in spintronics,” *Appl. Phys. Lett.*, vol. 89, no. 20, p. 202508, Nov. 2006.
- [61] V. J. Folen, G. T. Rado, and E. W. Stalder, “Anisotropy of the Magnetoelectric Effect in  $\text{Cr}_2\text{O}_3$ ,” *Phys. Rev. Lett.*, vol. 6, no. 11, pp. 607–608, Jun. 1961.
- [62] M. Bibes, J. E. Villegas, and A. Barthélémy, “Ultrathin oxide films and interfaces for electronics and spintronics,” *Advances in Physics*, vol. 60, no. 1, pp. 5–84, Feb. 2011.
- [63] M. Fiebig, “Revival of the magnetoelectric effect,” *Journal of Physics D: Applied Physics*, vol. 38, no. 8, pp. R123–R152, Apr. 2005.
- [64] N. A. Spaldin and R. Ramesh, “Advances in magnetoelectric multiferroics,” *Nature Mater*, vol. 18, no. 3, pp. 203–212, Mar. 2019.
- [65] B. B. Van Aken, T. T. M. Palstra, A. Filippetti, and N. A. Spaldin, “The origin of ferroelectricity in magnetoelectric  $\text{YMnO}_3$ ,” *Nature Materials*, vol. 3, no. 3, pp. 164–170, Mar. 2004.
- [66] T. Katsufuji, S. Mori, M. Masaki, Y. Moritomo, N. Yamamoto, and H. Takagi, “Dielectric and magnetic anomalies and spin frustration in hexagonal  $\text{R MnO}_3$  ( $\text{R} = \text{Y}, \text{Yb}, \text{and Lu}$ ),” *Physical Review B*, vol. 64, no. 10, Aug. 2001.
- [67] A. K. Singh, S. Patnaik, S. D. Kaushik, and V. Siruguri, “Dominance of magnetoelastic coupling in multiferroic hexagonal  $\text{YMnO}_3$ ,” *Physical Review B*, vol. 81, no. 18, May 2010.
- [68] A. J. C. Buurma, G. R. Blake, T. T. M. Palstra, and U. Adem, “Multiferroic Materials: Physics and Properties,” in *Reference Module in Materials Science and Materials Engineering*, Elsevier, 2016, p. B9780128035818093000.
- [69] A. M. L. Lopes, J. P. Araújo, V. S. Amaral, J. G. Correia, Y. Tomioka, and Y. Tokura, “New Phase Transition in the  $\text{Pr}_{1-x}\text{Ca}_x\text{MnO}_3$  System: Evidence for Electrical Polarization in Charge Ordered Manganites,” *Phys. Rev. Lett.*, vol. 100, no. 15, p. 155702, Apr. 2008.
- [70] T. Kimura, “Spiral Magnets as Magnetoelectrics,” *Annu. Rev. Mater. Res.*, vol. 37, no. 1, pp. 387–413, Aug. 2007.
- [71] Y. J. Choi, H. T. Yi, S. Lee, Q. Huang, V. Kiryukhin, and S.-W. Cheong, “Ferroelectricity in an Ising Chain Magnet,” *Phys. Rev. Lett.*, vol. 100, no. 4, p. 047601, Jan. 2008.



- [72] N. Terada *et al.*, “Spiral-Spin-Driven Ferroelectricity in a Multiferroic Delafossite  $\text{AgFeO}_2$ ,” *Physical Review Letters*, vol. 109, no. 9, Aug. 2012.
- [73] S. Seki, Y. Onose, and Y. Tokura, “Spin-Driven Ferroelectricity in Triangular Lattice Antiferromagnets  $\text{A CrO}_2$  (  $\text{A} = \text{Cu}$ ,  $\text{Ag}$ ,  $\text{Li}$ , or  $\text{Na}$ ),” *Physical Review Letters*, vol. 101, no. 6, Aug. 2008.
- [74] N. Terada *et al.*, “Magnetic and ferroelectric orderings in multiferroic  $\alpha$  -  $\text{NaFeO}_2$ ,” *Physical Review B*, vol. 89, no. 18, May 2014.
- [75] T. Kimura, J. C. Lashley, and A. P. Ramirez, “Inversion-symmetry breaking in the noncollinear magnetic phase of the triangular-lattice antiferromagnet  $\text{Cu Fe O}_2$ ,” *Physical Review B*, vol. 73, no. 22, Jun. 2006.
- [76] W. Kleemann, “Disordered Multiferroics,” *Solid State Phenomena*, vol. 189, pp. 41–56, Jun. 2012.
- [77] J. H. Lee *et al.*, “A strong ferroelectric ferromagnet created by means of spin–lattice coupling,” *Nature*, vol. 476, no. 7358, pp. 114–114, Aug. 2011.
- [78] P. Curie, “Sur la symétrie dans les phénomènes physiques, symétrie d’un champ électrique et d’un champ magnétique,” *Journal de Physique Théorique et Appliquée*, vol. 3, no. 1, pp. 393–415, 1894.
- [79] H. Schmid, “Some symmetry aspects of ferroics and single phase multiferroics \*,” *Journal of Physics: Condensed Matter*, vol. 20, no. 43, p. 434201, Oct. 2008.
- [80] A. Stroppa, P. Barone, P. Jain, J. M. Perez-Mato, and S. Picozzi, “Hybrid Improper Ferroelectricity in a Multiferroic and Magnetoelectric Metal-Organic Framework,” *Adv. Mater.*, vol. 25, no. 16, pp. 2284–2290, Apr. 2013.
- [81] S. Dong, H. Xiang, and E. Dagotto, “Magnetoelectricity in multiferroics: a theoretical perspective,” *National Science Review*, Feb. 2019.
- [82] S. Dong, J.-M. Liu, S.-W. Cheong, and Z. Ren, “Multiferroic materials and magnetoelectric physics: symmetry, entanglement, excitation, and topology,” *Advances in Physics*, vol. 64, no. 5–6, pp. 519–626, Nov. 2015.
- [83] J. M. Rondinelli, M. Stengel, and N. A. Spaldin, “Carrier-mediated magnetoelectricity in complex oxide heterostructures,” *Nature Nanotech*, vol. 3, no. 1, pp. 46–50, Jan. 2008.
- [84] S. L. Hou and N. Bloembergen, “Paramagnetoelectric Effects in  $\text{NiS O}_4 \cdot 6 \text{H}_2 \text{O}$ ,” *Physical Review*, vol. 138, no. 4A, pp. A1218–A1226, May 1965.



- [85] M. J. Cardwell, “Measurements of the magnetic field dependent electric susceptibility of yttrium iron garnet,” *Philosophical Magazine*, vol. 20, no. 167, pp. 1087–1089, Nov. 1969.
- [86] S. E. Dann, *Reactions and Characterization of Solids*. 2000.
- [87] D. Braga and F. Grepioni, “Reactions Between or Within Molecular Crystals,” *Angewandte Chemie International Edition*, vol. 43, no. 31, pp. 4002–4011, Aug. 2004.
- [88] A. R. West, *Solid State Chemistry and its Applications*. John Wiley & Sons, 2014.
- [89] H. L. Bhat, *Introduction to Crystal Growth: Principles and Practice*. CRC Press, 2014.
- [90] M. Jansen and R. Hoppe, “Zur Kenntnis der NaCl-Strukturfamilie Die Kristallstruktur von NaMnO<sub>2</sub>,” *Zeitschrift für anorganische und allgemeine Chemie*, vol. 399, no. 2, pp. 163–169, 1973.
- [91] R. Hoppe, G. Brachtel, and M. Jansen, “Zur Kenntnis der Oxomanganate (III):, Über LiMnO<sub>2</sub> und  $\beta$ -NaMnO<sub>2</sub> [1],” *Zeitschrift für anorganische und allgemeine Chemie*, vol. 417, no. 1, pp. 1–10, 1975.
- [92] S. Hirano, R. Narita, and S. Naka, “Hydrothermal synthesis and properties of Na<sub>x</sub>MnO<sub>2</sub> crystals,” *Journal of Crystal Growth*, vol. 54, no. 3, pp. 595–599, Sep. 1981.
- [93] V. Pecharsky and P. Zavalij, *Fundamentals of Powder Diffraction and Structural Characterization of Materials, Second Edition*, 2nd ed. Springer US, 2009.
- [94] C. Hammond, *The basics of crystallography and diffraction*, 3. ed., reprinted (with corrections). Oxford: Oxford Univ. Press [u.a.], 2010.
- [95] “Bruker (2008). PROTEUM2, SAINT and SADABS. Bruker AXS Inc., Madison, Wisconsin, USA.” .
- [96] P. G. Zamboni and E. Desimoni, “X-Ray Photoelectron Spectroscopy: Principles, Instrumentation, Data Processing and Molten Salt Applications,” in *Molten Salt Chemistry: An Introduction and Selected Applications*, G. Mamantov and R. Marassi, Eds. Dordrecht: Springer Netherlands, 1987, pp. 425–445.
- [97] L. Reimer, *Scanning Electron Microscopy: Physics of Image Formation and Microanalysis*, 2nd completely rev. and updated ed. 1998 edition. Berlin ; New York: Springer, 1998.



- [98] “Electron Microscopy for Biological Sciences | Diamond Light Source - Diamond Synchrotron Facilities for Industry - Diamond Light Source.” [Online]. Available: <https://www.diamond.ac.uk/industry/Industry-News/Latest-News/Synchrotron-Industry-News-eBIC.html#>. [Accessed: 27-May-2019].
- [99] R. L. Fagaly, T. Technologies, and S. Diego, “SQUID Instruments and Applications,” p. 89.
- [100] “Physical Property Measurement System (PPMS) | PPMS from QuantumDesign | LOT-QuantumDesign.” [Online]. Available: <https://lot-qd.de/en/products/materials-science/systems-to-measure-physical-properties/product/physical-property-measurement-system-ppms/>. [Accessed: 22-Jan-2019].
- [101] *Specific Heats at Low Temperatures*. Springer Verlag, 2014.
- [102] D. O’Flynn, M. R. Lees, and G. Balakrishnan, “Magnetic susceptibility and heat capacity measurements of single crystal  $\text{TbMnO}_3$ ,” *Journal of Physics: Condensed Matter*, vol. 26, no. 25, p. 256002, Jun. 2014.
- [103] P. Lunkenheimer, R. Fichtl, S. G. Ebbinghaus, and A. Loidl, “Nonintrinsic origin of the colossal dielectric constants in  $\text{CaCu}_3\text{Ti}_4\text{O}_{12}$ ,” *Physical Review B*, vol. 70, no. 17, Nov. 2004.
- [104] G. Catalan, “Magnetocapacitance without magnetoelectric coupling,” *Applied Physics Letters*, vol. 88, no. 10, p. 102902, Mar. 2006.
- [105] “<http://literature.cdn.keysight.com/litweb/pdf/5950-3000.pdf> - Google Search.” [Online]. Available: <https://www.google.com/search?client=firefox-b-d&q=http%3A%2F%2Fliterature.cdn.keysight.com%2Flitweb%2Fpdf%2F5950-3000.pdf>. [Accessed: 28-May-2019].
- [106] J. Rodríguez-Carvajal, “Recent advances in magnetic structure determination by neutron powder diffraction,” *Physica B: Condensed Matter*, vol. 192, no. 1, pp. 55–69, Oct. 1993.
- [107] A. Boothroyd, “Concepts of Neutron Scattering,” p. 38.
- [108] T. Chatterji, *Neutron scattering from magnetic materials*. Gulf Professional Publishing, 2005.
- [109] G. L. Squires, *Introduction to the Theory of Thermal Neutron Scattering*. Courier Corporation, 1996.
- [110] L. C. Chapon *et al.*, “Wish: The New Powder and Single Crystal Magnetic Diffractometer on the Second Target Station,” vol. 22, pp. 22–25, Apr. 2011.



- [111] K. R. Seddon and M. Zaworotko, *Crystal Engineering: The Design and Application of Functional Solids*. Springer Science & Business Media, 1999.
- [112] G. Will, *Powder diffraction: the Rietveld method and the two-stage method to determine and refine crystal structures from powder diffraction data; with 43 tables*. Berlin: Springer, 2006.
- [113] L. B. McCusker, R. B. Von Dreele, D. E. Cox, D. Louër, and P. Scardi, “Rietveld refinement guidelines,” *Journal of Applied Crystallography*, vol. 32, no. 1, pp. 36–50, Feb. 1999.
- [114] A. Le Bail, H. Duroy, and J. L. Fourquet, “Ab-initio structure determination of LiSbWO<sub>6</sub> by X-ray powder diffraction,” *Materials Research Bulletin*, vol. 23, no. 3, pp. 447–452, Mar. 1988.
- [115] J. Rodriguez-Carvajal, M. T. Fernandez-Diaz, and J. L. Martinez, “Neutron diffraction study on structural and magnetic properties of La<sub>2</sub>NiO<sub>4</sub>,” *Journal of Physics: Condensed Matter*, vol. 3, no. 19, pp. 3215–3234, May 1991.
- [116] R. Scholder and U. Protzer, “Über Alkalimanganate(III) bis (V),” *Zeitschrift für anorganische und allgemeine Chemie*, vol. 369, no. 3–6, pp. 313–326, Oct. 1969.
- [117] Y. U. Jeong and A. Manthiram, “Synthesis of Na<sub>x</sub>MnO<sub>2</sub>+ $\delta$  by a Reduction of Aqueous Sodium Permanganate with Sodium Iodide,” *Journal of Solid State Chemistry*, vol. 156, no. 2, pp. 331–338, Feb. 2001.
- [118] R. Chen, T. Chirayil, P. Zavalij, and M. S. Whittingham, “The hydrothermal synthesis of sodium manganese oxide and a lithium vanadium oxide,” *Solid State Ionics*, vol. 86–88, pp. 1–7, Jul. 1996.
- [119] A. Caballero, L. Hernán, J. Morales, L. Sánchez, J. Santos Peña, and M. A. G. Aranda, “Synthesis and characterization of high-temperature hexagonal P2-Na<sub>0.6</sub>MnO<sub>2</sub> and its electrochemical behaviour as cathode in sodium cells,” *Journal of Materials Chemistry*, vol. 12, no. 4, pp. 1142–1147, Mar. 2002.
- [120] A. Mendiboure, C. Delmas, and P. Hagenmuller, “Electrochemical intercalation and deintercalation of Na<sub>x</sub>MnO<sub>2</sub> bronzes,” *Journal of Solid State Chemistry*, vol. 57, no. 3, pp. 323–331, May 1985.
- [121] D. Sohn *et al.*, “Fabrication of Na<sub>0.7</sub>MnO<sub>2</sub>/C composite cathode material by simple heat treatment for high-power na-ion batteries,” *Electronic Materials Letters*, vol. 14, no. 1, pp. 30–36, Jan. 2018.



- [122] S. Hirano, R. Narita, and S. Naka, “Hydrothermal synthesis and properties of  $\text{Na}_{0.70}\text{MnO}_{2.25}$  layer crystal,” *Materials Research Bulletin*, vol. 19, no. 9, pp. 1229–1235, Sep. 1984.
- [123] D. Su, C. Wang, H. Ahn, and G. Wang, “Single Crystalline  $\text{Na}_{0.7}\text{MnO}_2$  Nanoplates as Cathode Materials for Sodium-Ion Batteries with Enhanced Performance,” *Chemistry - A European Journal*, vol. 19, no. 33, pp. 10884–10889, Aug. 2013.
- [124] R. J. Clément, P. G. Bruce, and C. P. Grey, “Review—manganese-based P2-type transition metal oxides as sodium-ion battery cathode materials,” *Journal of The Electrochemical Society*, vol. 162, no. 14, pp. A2589–A2604, 2015.
- [125] R. J. Clément, D. S. Middlemiss, I. D. Seymour, A. J. Ilott, and C. P. Grey, “Insights into the Nature and Evolution upon Electrochemical Cycling of Planar Defects in the  $\beta\text{-NaMnO}_2$  Na-Ion Battery Cathode: An NMR and First-Principles Density Functional Theory Approach,” *Chemistry of Materials*, vol. 28, no. 22, pp. 8228–8239, Nov. 2016.
- [126] A. M. Abakumov, A. A. Tsirlin, I. Bakaimi, G. Van Tendeloo, and A. Lippas, “Multiple Twinning As a Structure Directing Mechanism in Layered Rock-Salt-Type Oxides:  $\text{NaMnO}_2$  Polymorphism, Redox Potentials, and Magnetism,” *Chemistry of Materials*, vol. 26, no. 10, pp. 3306–3315, May 2014.
- [127] X. Ma, H. Chen, and G. Ceder, “Electrochemical properties of monoclinic  $\text{NaMnO}_2$ ,” *Journal of The Electrochemical Society*, vol. 158, no. 12, pp. A1307–A1312, 2011.
- [128] Y. Li, X. Feng, S. Cui, Q. Shi, L. Mi, and W. Chen, “From  $\alpha\text{-NaMnO}_2$  to crystal water containing Na-birnessite: enhanced cycling stability for sodium-ion batteries,” *CrystEngComm*, vol. 18, no. 17, pp. 3136–3141, 2016.
- [129] J. Billaud *et al.*, “ $\beta\text{-NaMnO}_2$ : A High-Performance Cathode for Sodium-Ion Batteries,” *Journal of the American Chemical Society*, vol. 136, no. 49, pp. 17243–17248, Dec. 2014.
- [130] M. Shishkin, S. Kumakura, S. Sato, K. Kubota, S. Komaba, and H. Sato, “Unraveling the Role of Doping in Selective Stabilization of  $\text{NaMnO}_2$  Polymorphs: Combined Theoretical and Experimental Study,” *Chemistry of Materials*, vol. 30, no. 4, pp. 1257–1264, Feb. 2018.



- [131] R. Hoppe, G. Brachtel, and M. Jansen, “Zur Kenntnis der Oxomanganate (III):, Über  $\text{LiMnO}_2$  und  $\beta\text{-NaMnO}_2$  [1],” *Zeitschrift für anorganische und allgemeine Chemie*, vol. 417, no. 1, pp. 1–10, 1975.
- [132] J. Wooldridge, D. M. Paul, G. Balakrishnan, and M. R. Lees, “Investigation of the spin density wave in  $\text{Na}_x\text{CoO}_2$ ,” *Journal of Physics: Condensed Matter*, vol. 17, no. 4, pp. 707–718, Feb. 2005.
- [133] D. Prabhakaran, A. T. Boothroyd, R. Coldea, and N. R. Charnley, “Crystal growth of  $\text{Na}_x\text{CoO}_2$  under different atmospheres,” *Journal of Crystal Growth*, vol. 271, no. 1–2, pp. 74–80, Oct. 2004.
- [134] M. Mikami, M. Yoshimura, Y. Mori, T. Sasaki, R. Funahashi, and I. Matsubara, “Crystal Growth of Thermoelectric Material  $\text{Na}_x\text{CoO}_{2-\delta}$  by a Flux Method,” *Japanese Journal of Applied Physics*, vol. 41, no. Part 2, No. 7A, pp. L777–L779, Jul. 2002.
- [135] K. Fujita, T. Mochida, and K. Nakamura, “High-Temperature Thermoelectric Properties of  $\text{Na}_{1-x}\text{CoO}$  Single Crystals,” *Japanese Journal of Applied Physics*, vol. 40, no. Part 1, No. 7, pp. 4644–4647, Jul. 2001.
- [136] R. Dally *et al.*, “Floating zone growth of  $\alpha\text{-Na}_{0.90}\text{MnO}_2$  single crystals,” *Journal of Crystal Growth*, vol. 459, pp. 203–208, Feb. 2017.
- [137] K. Kimura, H. Nakamura, K. Ohgushi, and T. Kimura, “Magnetoelectric control of spin-chiral ferroelectric domains in a triangular lattice antiferromagnet,” *Physical Review B*, vol. 78, no. 14, Oct. 2008.
- [138] K. F. Wang, J.-M. Liu, and Z. F. Ren, “Multiferroicity: the coupling between magnetic and polarization orders,” *Advances in Physics*, vol. 58, no. 4, pp. 321–448, Jul. 2009.
- [139] A. Zorko *et al.*, “Magnetic inhomogeneity on a triangular lattice: the magnetic-exchange versus the elastic energy and the role of disorder,” *Scientific Reports*, vol. 5, no. 1, Aug. 2015.
- [140] T. Shimono, D. Tanabe, W. Kobayashi, H. Nitani, and Y. Moritomo, “Electronic State of P2-Type  $\text{Na}_x\text{MO}_2$  ( $M = \text{Mn}$  and  $\text{Co}$ ) as Investigated by In situ X-ray Absorption Spectroscopy,” *Journal of the Physical Society of Japan*, vol. 82, no. 12, p. 124717, Dec. 2013.



- [141] X. Li, Y. Wang, D. Wu, L. Liu, S.-H. Bo, and G. Ceder, “Jahn–Teller Assisted Na Diffusion for High Performance Na Ion Batteries,” *Chemistry of Materials*, vol. 28, no. 18, pp. 6575–6583, Sep. 2016.
- [142] Y. Takeda, J. Akagi, A. Edagawa, M. Inagaki, and S. Naka, “A preparation and polymorphic relations of sodium iron oxide (NaFeO<sub>2</sub>),” *Materials Research Bulletin*, vol. 15, no. 8, pp. 1167–1172, Aug. 1980.
- [143] I. J. Davidson, R. S. McMillan, J. J. Murray, and J. E. Greedan, “Lithium-ion cell based on orthorhombic LiMnO<sub>2</sub>,” *Journal of Power Sources*, vol. 54, no. 2, pp. 232–235, Apr. 1995.
- [144] A. R. Armstrong and P. G. Bruce, “Synthesis of layered LiMnO<sub>2</sub> as an electrode for rechargeable lithium batteries,” *Nature*, vol. 381, no. 6582, pp. 499–500, Jun. 1996.
- [145] R. J. Clément, D. S. Middlemiss, I. D. Seymour, A. J. Ilott, and C. P. Grey, “Insights into the Nature and Evolution upon Electrochemical Cycling of Planar Defects in the  $\beta$ -NaMnO<sub>2</sub> Na-Ion Battery Cathode: An NMR and First-Principles Density Functional Theory Approach,” *Chemistry of Materials*, vol. 28, no. 22, pp. 8228–8239, Nov. 2016.
- [146] I. Bakaimi, A. Abakumov, M. A. Green, and A. Lappas, “Crystal, magnetic and dielectric studies of the 2D antiferromagnet:  $\beta$ -NaMnO<sub>2</sub>,” 2014, p. 898716.
- [147] F. Orlandi *et al.*, “Incommensurate atomic and magnetic modulations in the spin-frustrated  $\beta$  – NaMn O<sub>2</sub> triangular lattice,” *Physical Review Materials*, vol. 2, no. 7, Jul. 2018.
- [148] N. S. Kini, E. E. Kaul, and C. Geibel, “Zn<sub>2</sub>VO(PO<sub>4</sub>)<sub>2</sub>: an  $S = 1/2$  Heisenberg antiferromagnetic square lattice system,” *Journal of Physics: Condensed Matter*, vol. 18, no. 4, pp. 1303–1311, Feb. 2006.
- [149] K. M. Ranjith *et al.*, “Commensurate and incommensurate magnetic order in spin-1 chains stacked on the triangular lattice in,” *Physical Review B*, vol. 94, no. 1, Jul. 2016.
- [150] A. Suter, M. Mali, J. Roos, and D. Brinkmann, *Journal of Physics: Condensed Matter*, vol. 10, no. 26, pp. 5977–5994, Jul. 1998.
- [151] V. Petříček, M. Dušek, and L. Palatinus, “Crystallographic Computing System JANA2006: General features,” *Zeitschrift für Kristallographie - Crystalline Materials*, vol. 229, no. 5, Jan. 2014.



- [152] B. J. Campbell, H. T. Stokes, D. E. Tanner, and D. M. Hatch, "ISODISPLACE : a web-based tool for exploring structural distortions," *Journal of Applied Crystallography*, vol. 39, no. 4, pp. 607–614, Aug. 2006.
- [153] J. M. Perez-Mato, M. Zakhour-Nakhl, F. Weill, and J. Darriet, "Structure of composites  $A_{1+x}(A'_xB_{1-x})O_3$  related to the 2H hexagonal perovskite: relation between composition and modulation," *Journal of Materials Chemistry*, vol. 9, no. 11, pp. 2795–2807, 1999.
- [154] V. Petříček, A. van der Lee, and M. Evain, "On the use of crenel functions for occupationally modulated structures," *Acta Crystallographica Section A Foundations of Crystallography*, vol. 51, no. 4, pp. 529–535, Jul. 1995.
- [155] C. Stock, E. E. Rodriguez, and M. A. Green, "Spin fluctuations and superconductivity in powders of  $Fe_{1+x}Te_{0.7}Se_{0.3}$  as a function of interstitial iron concentration," *Physical Review B*, vol. 85, no. 9, Mar. 2012.
- [156] P. C. Hohenberg and W. F. Brinkman, "Sum rules for the frequency spectrum of linear magnetic chains," *Physical Review B*, vol. 10, no. 1, pp. 128–131, Jul. 1974.
- [157] Agilent, "Basics of measuring the dielectric Properties of MAterials," 2013.
- [158] "Andeen-Hagerling 2500A Bridge." [Online]. Available: <http://www.andeen-hagerling.com/ah2500a.htm#figure1>. [Accessed: 29-Jan-2019].
- [159] J. Dec, W. Kleemann, V. V. Shvartsman, D. C. Lupascu, and T. Łukasiewicz, "From mesoscopic to global polar order in the uniaxial relaxor ferroelectric  $Sr_{0.8}Ba_{0.2}Nb_2O_6$ ," *Applied Physics Letters*, vol. 100, no. 5, p. 052903, Jan. 2012.
- [160] P. Lunkenheimer, S. Krohns, S. Riegg, S. G. Ebbinghaus, A. Reller, and A. Loidl, "Colossal dielectric constants in transition-metal oxides," *The European Physical Journal Special Topics*, vol. 180, no. 1, pp. 61–89, Dec. 2009.
- [161] E. Dagotto, T. Hotta, and A. Moreo, "Colossal magnetoresistant materials: the key role of phase separation," *Physics Reports*, p. 153, 2001.
- [162] J. Hemberger, P. Lunkenheimer, R. Fichtl, H.-A. Krug von Nidda, V. Tsurkan, and A. Loidl, "Relaxor ferroelectricity and colossal magnetocapacitive coupling in ferromagnetic  $CdCr_2S_4$ ," *Nature*, vol. 434, no. 7031, pp. 364–367, Mar. 2005.
- [163] S.-W. Cheong and M. Mostovoy, "Multiferroics: a magnetic twist for ferroelectricity," *Nature materials*, vol. 6, no. 1, p. 13, 2007.
- [164] T. Arima, "Ferroelectricity Induced by Proper-Screw Type Magnetic Order," *Journal of the Physical Society of Japan*, vol. 76, no. 7, p. 073702, Jul. 2007.



- [165] G. A. Smolenskii and V. A. Bokov, “Coexistence of Magnetic and Electric Ordering in Crystals,” *Journal of Applied Physics*, vol. 35, no. 3, pp. 915–918, Mar. 1964.
- [166] G. A. Samara and J. F. Scott, “Dielectric anomalies in BaMnF<sub>4</sub> at low temperatures,” *Solid State Communications*, vol. 21, no. 2, pp. 167–170, 1977.
- [167] R. Saha *et al.*, “Neutron scattering study of the crystallographic and spin structure in antiferromagnetic EuZrO<sub>3</sub>,” *Physical Review B*, vol. 93, no. 1, Jan. 2016.
- [168] T. Kimura, S. Kawamoto, I. Yamada, M. Azuma, M. Takano, and Y. Tokura, “Magnetocapacitance effect in multiferroic BiMnO<sub>3</sub>,” *Physical Review B*, vol. 67, no. 18, May 2003.
- [169] J. M. Paulsen, R. A. Donabarger, and J. R. Dahn, “Layered T<sub>2</sub>-, O<sub>6</sub>-, O<sub>2</sub>-, and P<sub>2</sub>-Type A<sub>2/3</sub> [M'<sup>2+</sup><sub>1/3</sub> M<sup>4+</sup><sub>2/3</sub>]O<sub>2</sub> Bronzes, A = Li, Na; M' = Ni, Mg; M = Mn, Ti,” *Chemistry of Materials*, vol. 12, no. 8, pp. 2257–2267, Aug. 2000.
- [170] P. M. de Wolff, “Symmetry operations for displacively modulated structures,” *Acta Crystallographica Section A*, vol. 33, no. 3, pp. 493–497, May 1977.
- [171] P. M. de Wolff, “The Pseudo-Symmetry of Modulated Crystal Structures,” *Acta Crystallographica Section A*, vol. 30, no. 6, pp. 777–785, Nov. 1974.
- [172] J. E. Greedan, N. P. Raju, and I. J. Davidson, “Long Range and Short Range Magnetic Order in Orthorhombic LiMnO<sub>2</sub>,” *Journal of Solid State Chemistry*, vol. 128, no. 2, pp. 209–214, Feb. 1997.
- [173] M. Daraktchiev, G. Catalan, and J. F. Scott, “Landau theory of domain wall magnetoelectricity,” *Physical Review B*, vol. 81, no. 22, Jun. 2010.
- [174] G. Catalan, J. Seidel, R. Ramesh, and J. F. Scott, “Domain wall nanoelectronics,” *Reviews of Modern Physics*, vol. 84, no. 1, pp. 119–156, Feb. 2012.
- [175] R. Stoyanova *et al.*, “Stabilization of over-stoichiometric Mn<sup>4+</sup> in layered Na<sub>2/3</sub>MnO<sub>2</sub>,” *Journal of Solid State Chemistry*, vol. 183, no. 6, pp. 1372–1379, Jun. 2010.
- [176] X. Li *et al.*, “Direct visualization of the Jahn–Teller effect coupled to Na ordering in Na<sub>5/8</sub>MnO<sub>2</sub>,” *Nature Materials*, vol. 13, no. 6, pp. 586–592, May 2014.
- [177] Q. Liu *et al.*, “Multiangular Rod-Shaped Na<sub>0.44</sub>MnO<sub>2</sub> as Cathode Materials with High Rate and Long Life for Sodium-Ion Batteries,” *ACS Applied Materials & Interfaces*, vol. 9, no. 4, pp. 3644–3652, 2017.



- [178] J. Billaud *et al.*, “Na<sub>0.67</sub>Mn<sub>1-x</sub>Mg<sub>x</sub>O<sub>2</sub> (0 ≤ x ≤ 0.2): a high capacity cathode for sodium-ion batteries,” *Energy & Environmental Science*, vol. 7, no. 4, p. 1387, 2014.
- [179] J. M. Paulsen and J. R. Dahn, “Studies of the layered manganese bronzes, Na<sub>2/3</sub>[Mn<sub>1-x</sub>M<sub>x</sub>]O<sub>2</sub> with M= Co, Ni, Li, and Li<sub>2/3</sub>[Mn<sub>1-x</sub>M<sub>x</sub>]O<sub>2</sub> prepared by ion-exchange,” *Solid State Ionics*, vol. 126, no. 1, pp. 3–24, 1999.
- [180] Y. Xiao *et al.*, “A Layered-Tunnel Intergrowth Structure for High-Performance Sodium-Ion Oxide Cathode,” *Advanced Energy Materials*, vol. 8, no. 22, p. 1800492, Aug. 2018.
- [181] A. Konarov, J. U. Choi, Z. Bakenov, and S.-T. Myung, “Revisit of layered sodium manganese oxides: achievement of high energy by Ni incorporation,” *Journal of Materials Chemistry A*, vol. 6, no. 18, pp. 8558–8567, 2018.
- [182] L. B. Luo, Y. G. Zhao, G. M. Zhang, S. M. Guo, Z. Li, and J. L. Luo, “Spin-glass behavior in hexagonal Na<sub>0.70</sub>MnO<sub>2</sub>,” *Physical Review B*, vol. 75, no. 12, Mar. 2007.
- [183] S. Kumakura, Y. Tahara, K. Kubota, K. Chihara, and S. Komaba, “Sodium and Manganese Stoichiometry of P2-Type Na<sub>2/3</sub>MnO<sub>2</sub>,” *Angew. Chem. Int. Ed. Engl.*, vol. 55, no. 41, pp. 12760–12763, Oct. 2016.
- [184] M. A. Stranick, “MnO<sub>2</sub> by XPS,” *Surface Science Spectra*, vol. 6, no. 1, pp. 31–38, 1999.
- [185] M. A. Stranick, “Mn<sub>2</sub>O<sub>3</sub> by XPS,” *Surface Science Spectra*, vol. 6, no. 1, pp. 39–46, 1999.
- [186] E. Hosono, H. Matsuda, I. Honma, S. Fujihara, M. Ichihara, and H. Zhou, “Synthesis of single crystalline electro-conductive Na<sub>0.44</sub>MnO<sub>2</sub> nanowires with high aspect ratio for the fast charge–discharge Li ion battery,” *Journal of Power Sources*, vol. 182, no. 1, pp. 349–352, 2008.
- [187] K. Hemalatha, M. Jayakumar, P. Bera, and A. S. Prakash, “Improved electrochemical performance of Na<sub>0.67</sub>MnO<sub>2</sub> through Ni and Mg substitution,” *J. Mater. Chem. A*, vol. 3, no. 42, pp. 20908–20912, 2015.
- [188] R. H. Colman and A. C. McLaughlin, “IrSr<sub>2</sub>Sm<sub>1.15</sub>Ce<sub>0.85</sub>Cu<sub>2.175</sub>O<sub>10</sub>: A reentrant spin-glass material,” *Physical Review B*, vol. 85, no. 14, Apr. 2012.
- [189] A. P. Roberts, Y. Cui, and K. L. Verosub, “Wasp-waisted hysteresis loops: Mineral magnetic characteristics and discrimination of components in mixed magnetic



- systems,” *Journal of Geophysical Research: Solid Earth*, vol. 100, no. B9, pp. 17909–17924, Sep. 1995.
- [190] L. Tauxe, T. A. T. Mullender, and T. Pick, “Potbellies, wasp-waists, and superparamagnetism in magnetic hysteresis,” *J. Geophys. Res.*, vol. 101, no. B1, pp. 571–583, Jan. 1996.
- [191] T. Stoyanova-Lyubenova, A. J. Dos santos-García, E. Urones-Garrote, M. J. Torralvo, and M. Á. Alario-Franco, “High-pressure synthesis, structural and complex magnetic properties of the ordered double perovskite  $\text{Pb}_2\text{NiReO}_6$ ,” *Dalton Trans.*, vol. 43, no. 3, pp. 1117–1124, 2014.
- [192] I. Bakaimi, R. Brescia, C. M. Brown, A. A. Tsirlin, M. A. Green, and A. Lappas, “Hydration-induced spin-glass state in a frustrated Na-Mn-O triangular lattice,” *Physical Review B*, vol. 93, no. 18, May 2016.
- [193] D. Prabhakaran, A. T. Boothroyd, R. Coldea, and L. M. Helme, “Magnetic Studies of Polycrystalline and Single-Crystal  $\text{Na}_x\text{CoO}_2$ ,” p. 22.
- [194] A. Zorko, O. Adamopoulos, M. Komelj, D. Arčon, and A. Lappas, “Frustration-induced nanometre-scale inhomogeneity in a triangular antiferromagnet,” *Nature Communications*, vol. 5, Jan. 2014.
- [195] M. F. Collins and O. A. Petrenko, “Triangular antiferromagnets,” vol. 75, p. 51, 1997.
- [196] P.-G. De Gennes, “Effects of double exchange in magnetic crystals,” *Physical Review*, vol. 118, no. 1, p. 141, 1960.
- [197] R. J. Clément, P. G. Bruce, and C. P. Grey, “Review—Manganese-Based P2-Type Transition Metal Oxides as Sodium-Ion Battery Cathode Materials,” *Journal of The Electrochemical Society*, vol. 162, no. 14, pp. A2589–A2604, 2015.
- [198] N. Yabuuchi and S. Komaba, “Recent research progress on iron- and manganese-based positive electrode materials for rechargeable sodium batteries,” *Science and Technology of Advanced Materials*, vol. 15, no. 4, p. 043501, Aug. 2014.
- [199] M. Jansen and R. Hoppe, “Zur Kenntnis der NaCl-Strukturfamilie Die Kristallstruktur von  $\text{NaMnO}_2$ ,” *Zeitschrift für anorganische und allgemeine Chemie*, vol. 399, no. 2, pp. 163–169, 1973.
- [200] D. P. Chen, X. Wang, C. T. Lin, and S. X. Dou, “Single-crystal growth and anisotropic magnetic properties of nonstoichiometric three-layer sodium cobalt oxides,” *Physical Review B*, vol. 76, no. 13, Oct. 2007.



- [201] R. L. Dally, R. Chisnell, L. Harriger, Y. Liu, J. W. Lynn, and S. D. Wilson, “Thermal evolution of quasi-one-dimensional spin correlations within the anisotropic triangular lattice of  $\alpha - \text{NaMnO}_2$ ,” *Physical Review B*, vol. 98, no. 14, Oct. 2018.
- [202] R. L. Dally *et al.*, “Amplitude mode in the planar triangular antiferromagnet  $\text{Na}_{0.9}\text{MnO}_2$ ,” *Nature Communications*, vol. 9, no. 1, Dec. 2018.
- [203] A. Zorko *et al.*, “Magnetic interactions in  $\alpha - \text{Na Mn O}_2$  : Quantum spin-2 system on a spatially anisotropic two-dimensional triangular lattice,” *Physical Review B*, vol. 77, no. 2, Jan. 2008.
- [204] O. I. Velikokhatnyi, C.-C. Chang, and P. N. Kumta, “Phase Stability and Electronic Structure of  $\text{NaMnO}_2$ ,” *Journal of The Electrochemical Society*, vol. 150, no. 9, p. A1262, 2003.
- [205] G. R. Zhang, L. J. Zou, Z. Zeng, and H. Q. Lin, “Magnetic and electronic properties of  $\alpha\text{-NaMnO}_2$ ,” *Journal of Applied Physics*, vol. 105, no. 7, p. 07E512, Apr. 2009.
- [206] F. Wu, G. Yu, D. Xu, and E. Kan, “First-principles investigations on the magnetic structure of  $\alpha\text{-NaMnO}_2$ ,” *Journal of Physics: Condensed Matter*, vol. 24, no. 45, p. 456002, Nov. 2012.
- [207] S.-D. Ouyang, D.-Y. Liu, L.-J. Zou, and H.-Q. Lin, “Jahn–Teller effect and magnetic property in anisotropic triangular compound  $\text{Na}_x \text{MnO}_2$ ,” *Journal of Applied Physics*, vol. 109, no. 7, p. 07D716, Apr. 2011.
- [208] X. Li *et al.*, “Direct visualization of the Jahn–Teller effect coupled to Na ordering in  $\text{Na}_{5/8}\text{MnO}_2$ ,” *Nature Materials*, vol. 13, no. 6, pp. 586–592, May 2014.
- [209] “CrystalMaker Software: Crystal & Molecular Structures Modelling and Diffraction.” [Online]. Available: <http://crystallmaker.com/>. [Accessed: 08-Feb-2019].
- [210] Kh. S. Abou-El-Sherbini, M. H. Askar, and R. Schöllhorn, “Hydrated layered manganese dioxide: Part I. Synthesis and characterization of some hydrated layered manganese dioxides from  $\alpha\text{-NaMnO}_2$ ,” *Solid State Ionics*, vol. 150, no. 3–4, pp. 407–415, Oct. 2002.
- [211] C. Fouassier, G. Matejka, J.-M. Reau, and P. Hagenmuller, “Sur de nouveaux bronzes oxygénés de formule  $\text{Na}_x\text{CoO}_2$  ( $\chi$ 1). Le système cobalt-oxygène-sodium,” *Journal of Solid State Chemistry*, vol. 6, no. 4, pp. 532–537, Apr. 1973.



- [212] J. M. Paulsen, R. A. Donabarger, and J. R. Dahn, "Layered T2-, O6-, O2-, and P2-Type  $A_{2/3}[M^{2+}_{1/3}M^{4+}_{2/3}]O_2$  Bronzes, A = Li, Na;  $M^{\prime}$  = Ni, Mg; M = Mn, Ti," *Chem. Mater.*, vol. 12, no. 8, pp. 2257–2267, Aug. 2000.
- [213] M. Poienar *et al.*, "Substitution Effect on the Interplane Coupling in Crednerite: the  $Cu_{1.04}Mn_{0.96}O_2$  Case," *Chemistry of Materials*, vol. 23, no. 1, pp. 85–94, Jan. 2011.
- [214] H. Y. Hwang, S.-W. Cheong, P. G. Radaelli, M. Marezio, and B. Batlogg, "Lattice Effects on the Magnetoresistance in Doped  $LaMnO_3$ ," *Physical Review Letters*, vol. 75, no. 5, pp. 914–917, Jul. 1995.
- [215] Y. Moritomo, H. Kuwahara, Y. Tomioka, and Y. Tokura, "Pressure effects on charge-ordering transitions in Perovskite manganites," *Physical Review B*, vol. 55, no. 12, pp. 7549–7556, Mar. 1997.
- [216] C. Masquelier *et al.*, "Chemical and Magnetic Characterization of Spinel Materials in the  $LiMn_2O_4$ – $Li_2Mn_4O_9$ – $Li_4Mn_5O_{12}$  System," *Journal of solid state chemistry*, vol. 123, no. 2, pp. 255–266, 1996.
- [217] T. Elkhouni, M. Amami, E. K. Hlil, and A. B. Salah, "The Structural and Magnetic Properties of  $CuRh_{1-x}Mn_xO_2$  ( $0 \leq x \leq 0.1$ ) Delafossite Oxide," *Journal of Superconductivity and Novel Magnetism*, vol. 29, no. 3, pp. 547–555, Mar. 2016.
- [218] G. Dutta, A. Manthiram, J. B. Goodenough, and J.-C. Grenier, "Chemical synthesis and properties of  $Li_{1-\delta-x}Ni_{1+\delta}O_2$  and  $Li[Ni_2]O_4$ ," *Journal of Solid State Chemistry*, vol. 96, no. 1, pp. 123–131, Jan. 1992.
- [219] M. E. Jamer *et al.*, "Compensated Ferrimagnetism in the Zero-Moment Heusler Alloy  $Mn_3Al$ ," *Physical Review Applied*, vol. 7, no. 6, Jun. 2017.
- [220] G. Gavoille and J. Hubsch, "Neutron scattering in insulating semi-spin glass," *Journal of magnetism and magnetic materials*, vol. 36, no. 1, pp. 89–94, 1983.
- [221] D. Li *et al.*, "Spin canting and spin-flop transition in antiferromagnetic  $Cr_2O_3$  nanocrystals," *Journal of Applied Physics*, vol. 106, no. 5, p. 053913, Sep. 2009.
- [222] Z. He, S. C. Chen, C. S. Lue, W. Cheng, and Y. Ueda, "Two magnetic orderings and a spin-flop transition in spin-1 system  $SrNi_2(PO_4)_2$ ," *Physical Review B*, vol. 78, no. 21, Dec. 2008.
- [223] L. C. Chapon *et al.*, "Wish: The New Powder and Single Crystal Magnetic Diffractometer on the Second Target Station," vol. 22, pp. 22–25, Apr. 2011.



- [224] O. Arnold *et al.*, “Mantid—Data analysis and visualization package for neutron scattering and  $\mu$  SR experiments,” *Nuclear Instruments and Methods in Physics Research Section A: Accelerators, Spectrometers, Detectors and Associated Equipment*, vol. 764, pp. 156–166, Nov. 2014.
- [225] J. M. D. Coey, “Magnetism and Magnetic Materials by J. M. D. Coey,” *Cambridge Core*, Mar-2010. [Online]. Available: [/core/books/magnetism-and-magnetic-materials/AD3557E2D4538CAA8488A8C1057313BC](#). [Accessed: 06-Aug-2018].
- [226] B. J. Campbell, H. T. Stokes, D. E. Tanner, and D. M. Hatch, “*ISODISPLACE*: a web-based tool for exploring structural distortions,” *Journal of Applied Crystallography*, vol. 39, no. 4, pp. 607–614, Aug. 2006.
- [227] A. Maignan *et al.*, “Magnetic and magnetodielectric properties of erbium iron garnet ceramic,” *Journal of Applied Physics*, vol. 113, no. 3, p. 033905, Jan. 2013.
- [228] X. S. Gao, J.-M. Liu, X. Y. Chen, and Z. G. Liu, “Monte Carlo approach to phase transitions in ferroelectromagnets,” *Journal of Applied Physics*, vol. 88, no. 7, p. 4250, 2000.
- [229] K. M. Song *et al.*, “Magnetodielectric effect via a noncollinear-to-collinear spin reorientation in rare-earth iron garnets,” *Physical Review B*, vol. 83, no. 1, Jan. 2011.
- [230] R. Moessner, “Magnets with strong geometric frustration,” *Can. J. Phys.*, vol. 79, no. 11–12, pp. 1283–1294, Dec. 2001.
- [231] T. E. Saunders and J. T. Chalker, “Spin Freezing in Geometrically Frustrated Antiferromagnets with Weak Disorder,” *Phys. Rev. Lett.*, vol. 98, no. 15, p. 157201, Apr. 2007.
- [232] T. E. Saunders and J. T. Chalker, “Structural phase transitions in geometrically frustrated antiferromagnets,” *Phys. Rev. B*, vol. 77, no. 21, p. 214438, Jun. 2008.
- [233] V. O. Garlea, A. T. Savici, and R. Jin, “Tuning the magnetic ground state of a triangular lattice system  $\text{Cu}(\text{Mn}_{1-x}\text{Cu}_x)\text{O}_2$ ” *Phys. Rev. B*, vol. 83, no. 17, p. 172407, May 2011.
- [234] R. L. Dally *et al.*, “Amplitude mode in the planar triangular antiferromagnet  $\text{Na}_{0.9}\text{MnO}_2$ ,” *Nature Communications*, vol. 9, no. 1, Dec. 2018.
- [235] C. Zener, “Interaction Between the  $d$  Shells in the Transition Metals,” *Phys. Rev.*, vol. 81, no. 3, pp. 440–444, Feb. 1951.



- [236] C. Zener, “Interaction between the  $d$ -Shells in the Transition Metals. II. Ferromagnetic Compounds of Manganese with Perovskite Structure,” *Phys. Rev.*, vol. 82, no. 3, pp. 403–405, May 1951.
- [237] S. Holbein, “Neutron Scattering Studies on Complex Magnetic Structures in Magnetoelectric Materials,” p. 236.
- [238] S. Dong, H. Xiang, and E. Dagotto, “Magnetoelectricity in Multiferroics: a Theoretical Perspective,” p. 23.
- [239] S.-W. Cheong, D. Talbayev, V. Kiryukhin, and A. Saxena, “Broken symmetries, non-reciprocity, and multiferroicity,” *npj Quant Mater*, vol. 3, no. 1, p. 19, Dec. 2018.
- [240] “tupta\_eeteujan2011.pdf.” .
- [241] S. van Smaalen, *Incommensurate Crystallography*, Illustrated edition. Oxford University Press, USA, 2007.



# **Appendix A: MD-Station of FUNL**

---

**USER'S GUIDE  
FOR  
DIELECTRIC AND MAGNETO-ELECTRIC MEASUREMENTS**

by  
Eleni Aza  
Heraklion-Crete

**October 2017**



## INTRODUCTION –EQUIPMENT

The Home-made Magnetodielectric Station of Functional Nanocrystals Laboratory is installed and programmed to be run remotely and sequentially using a LABview designed interface through which the user can preview and control most of the parameters.

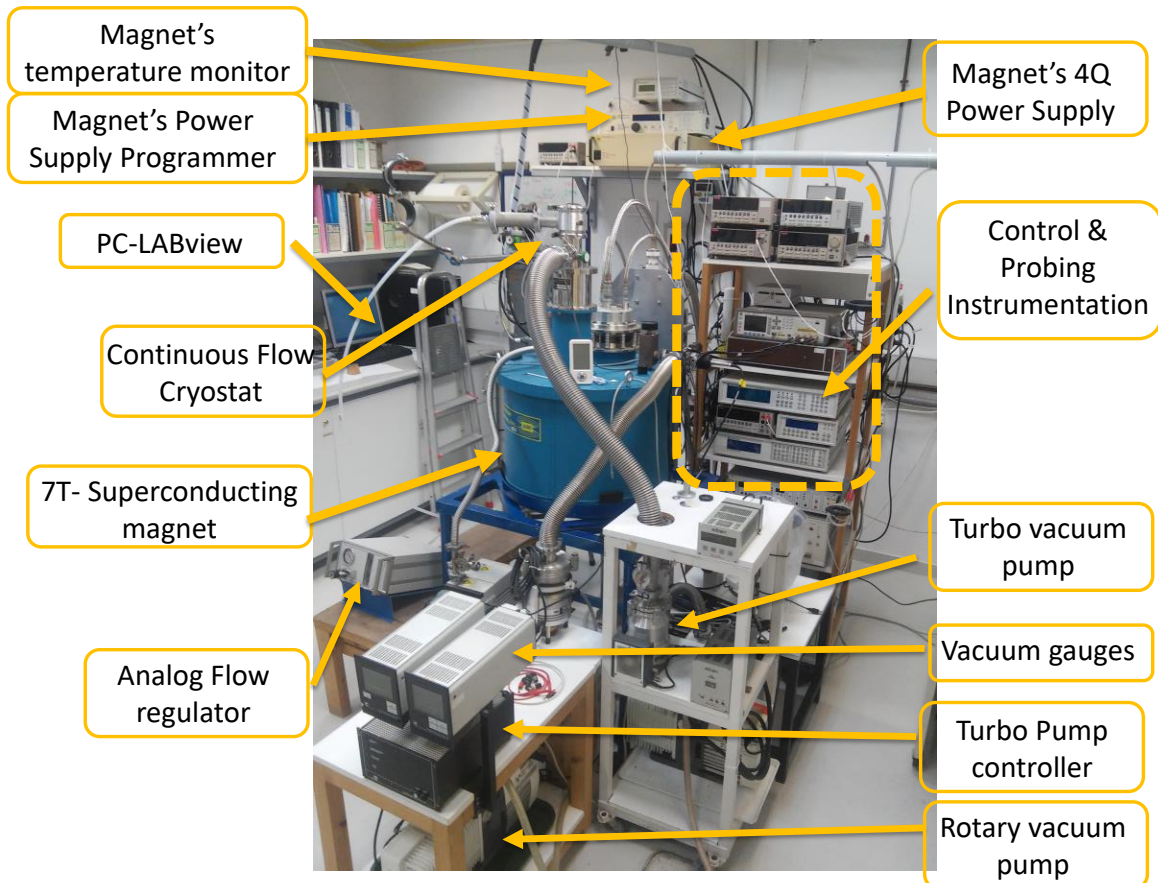


Figure 8-1 Magneto- electric Station of B009

## INSTRUMENTATION & PHYSICAL MEASUREMENTS

The system uses a continuous flow cryostat by Janis, which is placed in the center of 7 Tesla cryogen-free superconducting solenoid magnet allowing probing evolution of physical properties under specified temperature and applied magnetic field conditions. It is also equipped with electronic Instrumentation capable to probe temperature and frequency dependent phenomena with externally applied magnetic or electric stimuli and measure physical quantities like Capacitance and Dielectric Loss, Voltage, Electric DC Current and Impedance. The main Instrumentation is presented below:

## 7-TESLA CRYOGEN-FREE SUPERCONDUCTING SOLENOID MAGNET

The 7 Tesla cryogen-free superconducting solenoid Magnet is designed and manufactured for Dr. Alexandros Lappas at the Foundation for Research and Technology – Hellas by American Magnetics. The magnet system is cooled by a Cryomech pulse tube cryocooler, Model PT410 with remote motor, and Model CP2800 water cooled compressor providing 1 watt of cooling power at 4.2K. The magnet is controlled by an AMI Model 430 programmer and Model 4Q05100 bi-polar power supply and has a persistent switch heater installed with the ability to isolate the magnetic field in the coils and ensure stability of the magnetic field applied during a long lasting experiment with the main magnet leads discharged. Temperature monitoring of the magnet system is obtained using LakeShore Cernox and platinum resistor temperature sensors, and a LakeShore Model 218 temperature monitor.

## CONTINUOUS FLOW CRYOSTAT & FLOW CONTROLLER

The system uses a continuous flow cryostat by Janis, which is placed in the center of the magnet coils allowing probing properties under specified temperature and applied magnetic field conditions at the same time. The continuous flow cryostat is used in order to cool down to cryogenic temperatures (Liquid N<sub>2</sub> down to 77 K). The flow of gas into the Cryostat is maintained with the support of a diaphragm pump which is connected to the output of the cryostat and creates negative pressure. The gas is transferred into the cryostat with a cryogenic transfer line which is

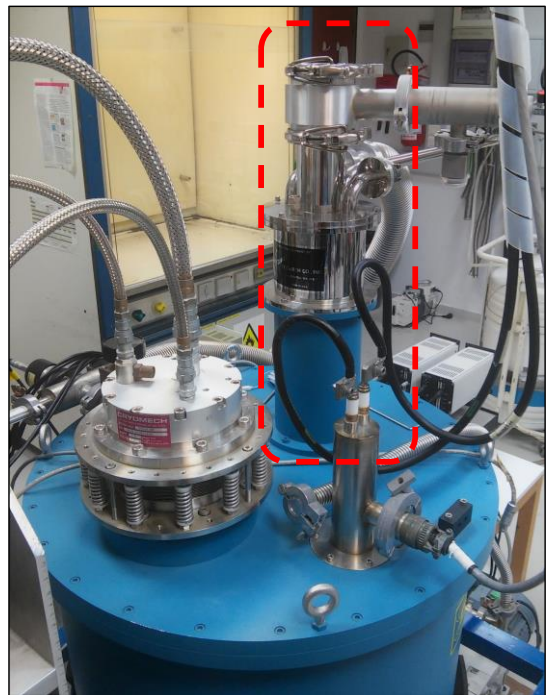


Figure 8-2 Superconducting magnet (7-Tesla) and continuous flow Cryostat

connected with a control system so that nitrogen (N<sub>2</sub>) gas is transferred in a controlled way from a Dewar of Liquid N<sub>2</sub>. On the top of the N<sub>2</sub> line there is a gear unit motor which is controlled through a parallel port from a desktop computer and is able to open/ close the

needle valve of the line and control the flow of nitrogen ( $N_2$ ) gas which is inserted in the cryostat.

### MAGNETIC FIELD CONTROLLER AND POWER SUPPLY

The AMI Model 430 Power Supply Programmer is a sophisticated digital power supply controller which controls and programs the externally connected 4-quadrant, bipolar, programmable, voltage and current stabilized d-c Power Supply 4Q06125PS (Figure 3- top left corner). The 430 Programmer allows an operator to control the current through the Persistent Switch Heater which is installed in this superconducting magnet system allowing to “trap” the magnetic field in the coils without having the main leads charged during a long duration experiment where a stable dc magnetic field is required as a stimuli. At the same time it “reads” the Voltage developed on the magnet leads ensuring electric current stabilization and as a consequence, stabilization of the magnetic field on the coils.



Figure 8-3 Instrumentation used to probe physical properties and control external stimuli

## TEMPERATURE CONTROLLERS

The Lab is equipped with a variety of temperature controllers (Figure 8-3 bottom left corner) occupied for sensing or controlling temperature. In this Station the Lakeshore 218 temperature controller is occupied with monitoring the temperature in different stages of the magnet installation in order to check normal state of operation. The main temperature control of the sample environment, both Janis Cryostat and the sample space, is in the hands of Lakeshore 332 temperature controller in which channel A is connected with the Cryostat heater of 40 Ohm and CX-1050-SD Cernox #X235263 and channel B is connected with the heater (20 Ohm) placed on the sample holder stick and CX-1050-CU Cernox #X94732. The complete temperature control is managed with the support of the controlled flow of the cryogenic liquid/gas into the cryostat by a gear unit motor, controlled through a parallel port from a desktop computer and able to open/ close the needle valve of the flexible transfer line of the cryogenic through a LABview interface which will be further described in the guide.

## CAPACITANCE BRIDGE AND LCR METERS

Impedance analyzers and LCR meters are used to measure the sample's properties at low frequencies (up to MHz). The sample is stimulated with an AC source and the actual voltage across the sample is monitored. Material test parameters are derived by knowing the dimensions of the sample and by measuring its capacitance and dissipation factor. The main instrument employed for probing Capacitance or Impedance is precision LCR meter E4980 of Agilent with a frequency range of 20 Hz- 2 MHz (or the oldest model of 4284A). Depending on the sample a 4-probe or a 2-probe connection can be established and a standard correction can be used depending on the length of the wires used. For the lower frequency range (50 Hz- 20 k Hz) an AH 2700 ultra-precision capacitance bridge is used (Figure 3- right column).

## ELECTROMETERS, NANOVOLTMETERS AND CURRENT SOURCES

For electric measurements the Keithley electrometers 6517A/ 6517B Electrometer/High Resistance Meter are used as the worldwide research laboratory standard for sensitive measurements providing reliable measurements of current levels down to 10 aA (10 x10<sup>-18</sup>A,) charge levels down to 1 fC, and the highest resistance measurements available up to



1018  $\Omega$ . The 6517B also is capable of measuring the largest voltage range - up to 200V - with an input impedance exceeding 200 T $\Omega$ . However, probing the afore mentioned values is highly dependent on the circuitry used to the sample, the quality of the contacts especially when these measurements are happening in a wide range of temperature inside a cryostat. Keithley 6221 AC & DC current source is also available and integrated into the sequential user interface together with the Keithley 2182A ideally combined for applications like Hall measurements, resistance measurements using delta mode, pulsed measurements, and differential conductance measurements.

## **PREPARE THE MD STATION**

### **SUPERCONDUCTING MAGNET- 7 TESLA**

Before energizing the Power Supply 4Q06125PS in order to charge the magnet we first need to ensure that the magnets' jacket vacuum is at least at the lowest range of  $10^{-4}$  mbar. The Magnet's Vacuum should be checked at Room Temperature.

- a) If the vacuum is lower than  $10^{-4}$  mbar then you need to pump the magnet<sup>1</sup> while at RT.
- b) If the Vacuum is at the lowest range of  $10^{-4}$  mbar then you may switch on the compressor. Switch on the Compressor by:
  - i) Switch on the "Main Breaker" ii) Switch on the Power iii) Press the button "Compressor On". Write down on the log book the Hrs of operation, the Low and High Pressure. Check the H<sub>2</sub>O flow and the H<sub>2</sub>O Temperature and write that down on the log book. iv) Switch on Lakeshore 218 (the temperature Controller above the AMI430 programmer) and note down the initial temperatures at the Compressor's Log book. v) Wait 14-15 hrs so that the temperatures will reach down close to the recommended ones: T1=45K, T2=33K, T5=4.5K, T6=5K, T7=4K.

### **CRYOSTAT:**

Check the "Janis Cryostat STPV NMR" Cryostat's Jacket Vacuum. It is recommended to have it in the range of  $10^{-5}$ . If the vacuum is lower than this range, pump it overnight before you run the experiment. Recommended to pump @ RT.

### **TRANSFER LINE:**

Check the vacuum of the transfer line, a vacuum at the range of  $10^{-4}$ - $10^{-5}$  is acceptable.



## ELECTRONIC INSTRUMENTATION:

It is advised to have switched on the instruments (LCR bridge, Lakeshore Temperature Controller332 (or340), AMI430 and the 4Q power supply) at least one hour before you start the experiment on.

<sup>1</sup> It is highly recommended to check the magnet's vacuum at least every two months. In case of low vacuum, pump up only at RT. In case of any mal function of the magnet contact: Alexandros Lappas and the American Magnetics technicians

## SAMPLE PREPARATION & PREPARATION OF THE MD- STICK

### SAMPLE PREPARATION

#### CAPACITOR TOPOLOGY

In case of Impedance or Capacitance measurements on either a single crystal or a polycrystalline sample (in a pellet form), you need to make two contacts on two flat parallel surfaces of your sample. The sample is going to be measured like a capacitor.

3. In case you are measuring a polycrystalline sample make a firm pellet. Make sure you have prepared/ cut your pellet (or crystal) with two parallel surfaces. They should be even and smooth so that a good contact with the conductive terminals can be ensured.
4. It is essential in order to calculate the dielectric permittivity to know the dimensions of your sample. Measure the thickness of the sample before putting any conductive paint on it. In case you use some conductive paint it is recommended to measure the conductive area and keep the same conductive area in both sides.
5. It is recommended to apply a conductive paint on the surfaces that are going to be used as the capacitor plates. In the lab there are available Silver<sup>2</sup> and Carbon paints but in special cases one can also deposit Gold using the Gold evaporator available in the Lab.
6. "Sample holder1- Capacitor topology" (Fig. 8-6g): In the case you use "Sample holder1" you need no wires attached to your sample. Depending on the nature of the

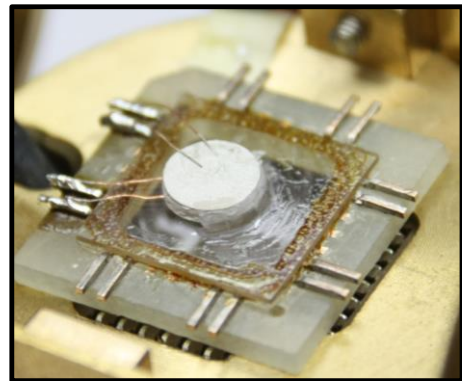


Figure 8-4 "Sample holder2" Flat carrier. The pellet is mounted with grease on the sapphire substrate. Silver paste is used on a BaTiO<sub>3</sub> pellet. Copper wires are attached with S. Paste on the sample's surfaces and soldered on the Nickel pins of the sample carrier.

sample you may use a conductive paint on the 2 flat parallel surfaces or keep them as they are if they are even and smooth.

7. “Sample holder2- Flat multi pin carrier” (Fig. 8-6h): In this case, after your sample’s surfaces are covered with a conductive paint you may attach copper or gold wire on one of the surfaces while the paint is still “wet” and let it dry before you do the same on the opposite surface. It should look like figure 8-4 (2 wires on each surface) or 8-6f, i.
8. To keep the sample mechanically stable in the case of the “Sample holder2” you may use some vacuum grease in order to keep it still on the sapphire plate while soldering the wires on Ni pins of the sample carrier. This is optional though and if you do so it is hard to remove and reuse the sample again.
9. You are prompted to check for any short between the two surfaces after the contacts are dried by measuring the resistance on the other edge of the wires (or the pins) with a multimeter.

<sup>2</sup> Check the conductivity of the silver paste. If it is not thin enough then use the silver paste solvent which is placed at the plastic drawers in lab B009. The silver paste is stored in the refrigerator of the lab B001 (and should be kept in the refrigerator! Take a small quantity in a vial for your own use)

#### STANDARD 4-PROBE TOPOLOGY

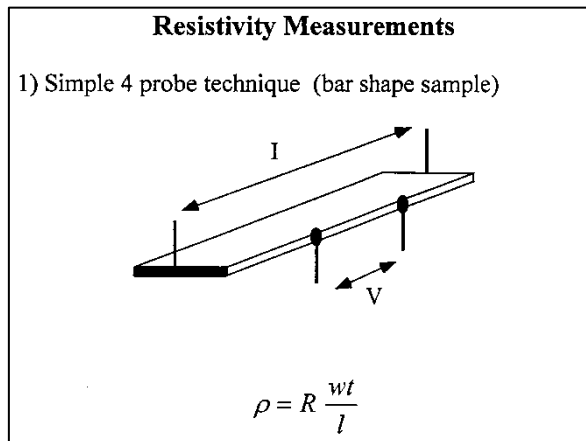


Figure 8-5 Standard 4-point topology for low resistivity measurements.

For resistivity measurements of metals or semiconductors (low resistivity) the pellet should be cut as a rectangular bar/plate and the single crystal should be chosen accordingly. You need a 4-point contact topology as the one depicted in Figure 8-5 usually done with Silver paint for both cases of polycrystalline samples and single crystals. In the case of a pellet in a pressed disc form, the Van der Paw method is suggested for contacts’ preparation.

## SHORT DESCRIPTION OF THE MD PROBE

The MD probe used in this set up is suitable for measuring dielectric properties (Capacitance or Impedance) and Pyroelectric current of non-conductive materials in both polycrystalline and single crystal forms. Two different sample holders/carriers are designed in such way so that they can be detachable from the main stick and can be prepared inside an atmosphere controlled Glove box. That makes the construction also suitable for air-sensitive samples (Fig. 8-6b). This probe is designed to be used in temperature range 2-325 K and is suitable for magnetic field up to 7 Tesla.

In order to accomplish an independent probing and control of the temperature on the sample environment we follow a dual- loop control which requires the installation of a heater and a temperature sensor on the probe apart from the ones installed inside the cryostat. The temperature sensor in the sample area is a Lakeshore CX1050-CU. The heater is a resistance of 20 Ohms constructed by Lakeshore MW-30 wire wrapped around the brass neck of the holder base (Fig.8-6e black part on the top). The electrical isolation from the brass base is succeeded with the use of the thinnest rolling paper and varnish so that there is also good temperature conductivity between the heater and the brass part. The heater is electrically isolated with a top coat of STYCAST.

The wiring allows 2-probe and 4-probe measurements depending on the physical property that is probed. The cables from the BNC connectors to the sample holder base are Lakeshore CC-C cables (solid copper center conductor drain wire and aluminized/polyester shield) since low conductor resistance is prime consideration for measuring low signals. We used the 4-Terminal-Points configuration since our main probing Instrument (LCR-Agilent) which provides 4 terminals ( $V_H$ ,  $V_L$ ,  $I_H$ ,  $I_L$ ) suggests a better probing precision in a wide range of Impedance in this configuration (Fig. 6c, d). We also use a floating GND. All 4 wires' shields are connected together on a noise shield (copper plate) which is close to the sample (or DUT) at the back side of the lower carrier socket in order to limit the stray capacitance that develops among the 4 leads (Fig. 6e). For further details on this you may want to check Mr Mouratis' Master thesis or Ms Aza PhD thesis.

The main part of the stick is chosen to be carbon fiber of diameter= 6.4 mm and its length from the bottom of the Teflon flange to the sample space calculated to bring the sample space exactly to the vertical center of the magnet coils (adjustable height from 691-716



mm) (Fig. 6a) where the magnetic field is homogeneous over a certain diameter of spherical volume (DSV) which in our case is 1 cm.

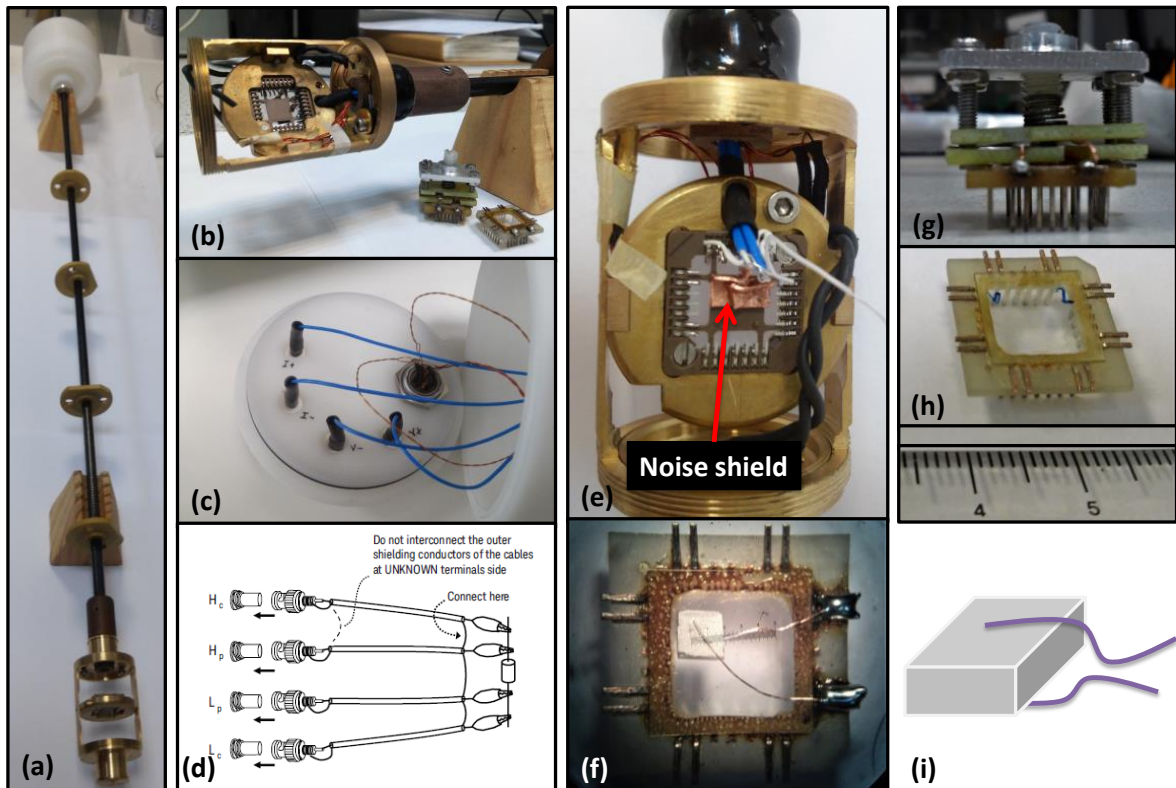


Figure 8-6 (a) MD fiber stick, (b) lower carrier socket on brass frame and 2 detachable sample holders/carriers, (c) 4 wires come down to lower carrier socket from isolated Teflon flange, (d) 4TP wiring sketch, (e) GND according to 4TP and noise shield in the lower carrier socket, (f) sample wired with 4TP as a capacitor, (g) “Sample holder1 – capacitor topology”, no wires on sample, (h) “Sample holder2- Flat multi pin carrier 2 or 4 probe wire connections to the sample, (i) sample connected as a capacitor using paste (sketch of (f)).

## MOUNTING SAMPLE

### POLYCRYSTALLINE PELLETT

If your sample is polycrystalline powder pressed in a pellet the orientation of the applied magnetic field should not affect the probing properties. So it is advised that you use the vertical orientation (flat surface of the lower carrier socket  $\perp$  to H field) during the measurement so that you do not need to mechanically stabilize your sample (Fig. 7b). You may choose between the two sample carriers/holders depending on how fragile your pellet is or how important is a fast mounting.



## SINGLE CRYSTAL

In the case of a single crystal one should take into consideration the proper orientation of mounting the sample itself on the carrier and the orientation of the carrier since the lower carrier socket can be oriented either parallel or vertical to the applied Magnetic field. The orientation of the electric field depends on the experiment and the way you are going to choose your contact areas on the sample under study.

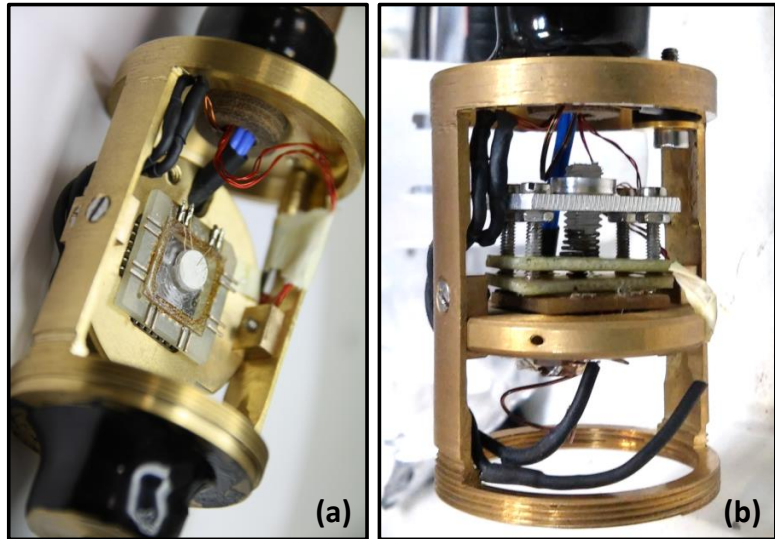


Figure 8-7 (a) Parallel to  $H$  field orientation of the sample carrier- Sample Holder2 (b) Vertical to field orientation of the sample carrier- Sample Holder1

- After connecting and stabilizing the sample on the carrier one should check continuity between the lower socket connector and the BNC sockets at the top-hat flange. In the case of the 4TP topology mentioned earlier,  $V^+$  &  $I^+$  and  $V^-$  &  $I^-$  are shorted in pairs on the sample carrier as depicted in figure 6f and only two wires (+, -) are attached on the 2 opposite surfaces of the sample.
- Mount the sample carrier on the lower carrier socket on the Brass base of the MD probe. To do this the lower carrier socket should be rotated as in Figure 7a. You can do this by loosening the side screws on the brass base. After mounting the sample carrier on the lower carrier socket you choose the final orientation of your socket.
- Open the top hat of the cryostat and place carefully the MD probe inside. ATTENTION! The cryostat should be at room temperature before opening the top hat (or at least above 285 K)!!
- Connect all four BNCs that come from the LCR bridge according to the labeled BNC sockets on the teflon Flange of the probe. Connect the LEMO connector that connects Lakeshore 332 with the temperature sensor and Heater on the sample holder to continue with temperature control.

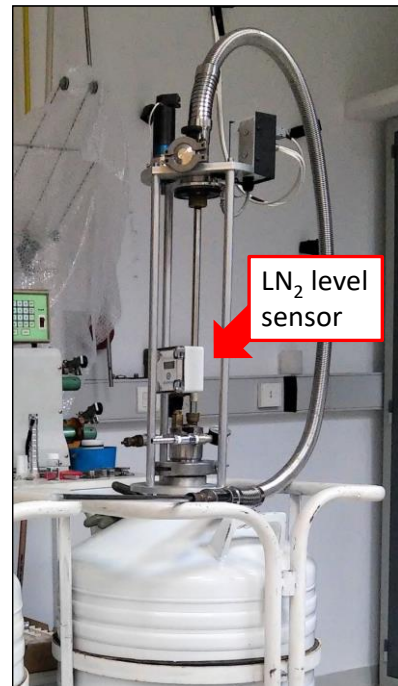


Figure 8-8 Dewar and transfer line of cryogenic liquid ( $N_2$ )

- In case our samples are air-sensitive we should have already done the process described in Section 4 for the temperature stabilization and initialization of the flow control so that there is the appropriate Gas atmosphere inside the cryostat. In such a case before inserting the probe in the cryostat we need to press the “**Auto Control**” button in order to stop the Auto Control procedure on the “*Control\_Dewar\_Valve\_ver2.vi*” and switch off the diaphragm pump temporarily. After the pressure of the system comes back to normal (The indication on the analog Gas flow controller should be back to 0) then we may open the cryostat’s top hat and insert the MD probe with the sample mounted. We switch back on the pump to ensure the gas flow and press again “**Auto Control**” button to set temperature back to our chosen Set point.

### INITIATE AN EXPERIMENT WITH TEMPERATURE CONTROL

Before starting any experimental sequence or any solo experiment even before stabilizing the temperature, it is highly recommended to open the “*Sequence\_Controller\_ver2.vi*”. By opening it, all the necessary instrument libraries for all available experiments are loaded. If the afore mentioned .vi is not opened, each time a new .vi is opened, it will force all the necessary for the experiment libraries to be reloaded and this will cause libraries to be loaded more than once which may initiate further delay to software and trash in the PC memory.

### SET THE N<sub>2</sub> LINE AND INITIATE FLOW CONTROL:

In order to set up the N<sub>2</sub> transfer line, follow the following steps:

- a) Fill up with N<sub>2</sub> (or He, depending on the temperature range of your experiment) the Liquid Nitrogen Dewar.
- b) Insert the whole system of the line in the Dewar after having placed the base neck (Fig. 9a). It should look like Figure 8.
- c) Insert the LN<sub>2</sub> level sensor (Fig. 9b). It should indicate a level above 85 %.
- d) Connect the control circuit to power and connect the cables on the black box on the Transfer Line (T.L). Turn the red switch on (on the control box on the T.L). Turn the black switch on. (Fig. 9c)
- e) Open the Labview .vi “*Control\_Dewar\_Valve\_ver2.vi*” and put it in manual mode (Fig. 10 “*Auto Control*” indicator should be OFF)





Figure 8-9 (a) Base of the cryogenic liquid transfer line, (b) Liquid N<sub>2</sub> level indicator, (c) Control circuit in box with DC motor, (d) Gear transmission system with metal stopper rod that changes the condition of the two micro switches.

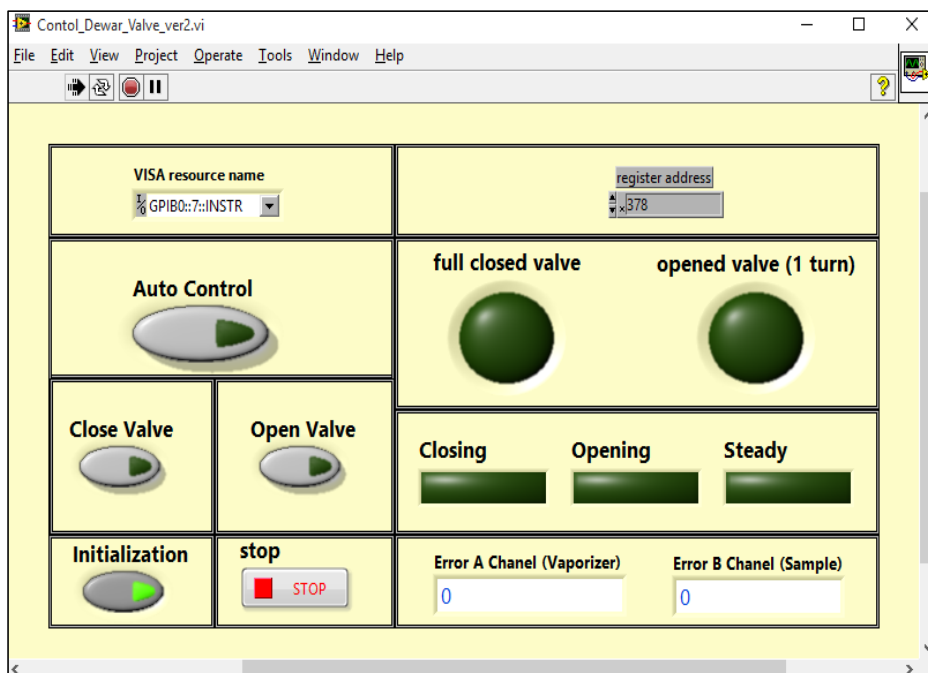


Figure 8-10 “Control\_Dewar\_Valve\_ver2.vi”

f) Rotate open the valve through software (press button “**Open Valve**” in “Control\_Dewar\_Valve\_ver2.vi”) and test if there is N<sub>2</sub> flow by placing the bayonet tip of the line in ethanol (check bubbling). Press again “**Open Valve**” button to stop rotation when the stopper rod is in the ¼ of a whole turn. Alternatively have the “**Initialization**” Button pressed before running the .vi.

g) If the flow is ok, insert the short tip of the transfer line into the cryostat input and switch on the diaphragm pump which is located in the He liquefier room (next to B009) in order to initiate flow. This pump is connected with a gas flow controller which in this set up is only used as an analog flow meter. 3-4 turns of the control valve on the flow meter should ensure sufficient flow. If you wish to evacuate the cryostat chamber before letting flow



inside, close the needle valve of the transfer line (T.L) through software let the pump work for some time (10 min) and then open the valve again.

## SET TEMPERATURE- TEMPERATURE CONTROL

After having read the steps in previous section and wish an automated control in order to reach a stable temperature point, you do the following procedure:

If you haven't executed the "Contol\_Dewar\_Valve\_ver2.vi" (Fig. 10) please run it. Before you run it make sure the "Initialization" button is activated.

As soon as the initialization button turns off (dark green) you should observe a temperature drop. If in 10 minutes time there is no temperature drop, press the "Open Valve" button in order to open the valve further than the position reached through the initialization process. If you open the valve approximately ½ turn and there is no temperature drop then one should check whether the N<sub>2</sub>

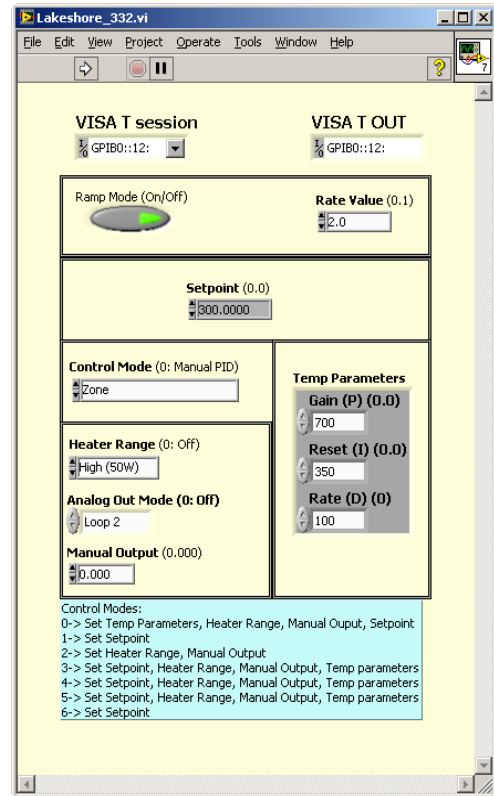


Figure 8-11- "Lakeshore 332.vi"

transfer-line is ok (we suppose that the LN<sub>2</sub> sensor is on and there is LN<sub>2</sub> in the dewar). For clean/dry the transfer line please check *Appendix C*.

When you observe a dropdown to the temperature then run the "Lakeshore\_332.vi" (Fig. 11) in order to set a specific temperature (up to 325 K). This is a single action .vi. This is set to operate the Lakeshore 332 ( temperature controller) in ramping mode and zone mode ( as defaults). After you fill in your Set Point in "Lakeshore\_332.vi" go back to "Control\_Dewar\_Valve\_ver2.vi" and press the "Auto Control" button to start the process of controlling the gas flow automatically. As mentioned earlier, in "Lakeshore\_332.vi" the default settings are the ones shown in Fig. 11 and have been programmed after several tests having in mind the temperature control using liquid N<sub>2</sub> as a cryogenic liquid. In case you use He and wish to go further down in temperature one should probably modify the control zones from the "Zone\_Tuner\_Lakeshore\_332.vi". (Find further details in MD SET UP written by Mr Mouratis Paragraphs 3.7, 3.8).



Note: When you will execute the “Contol\_Dewar\_Valve\_ver2.vi” the software will automatically open and run the “Show\_Indicators.vi”. Keep it open because all control procedures/experiments communicate with that vi.

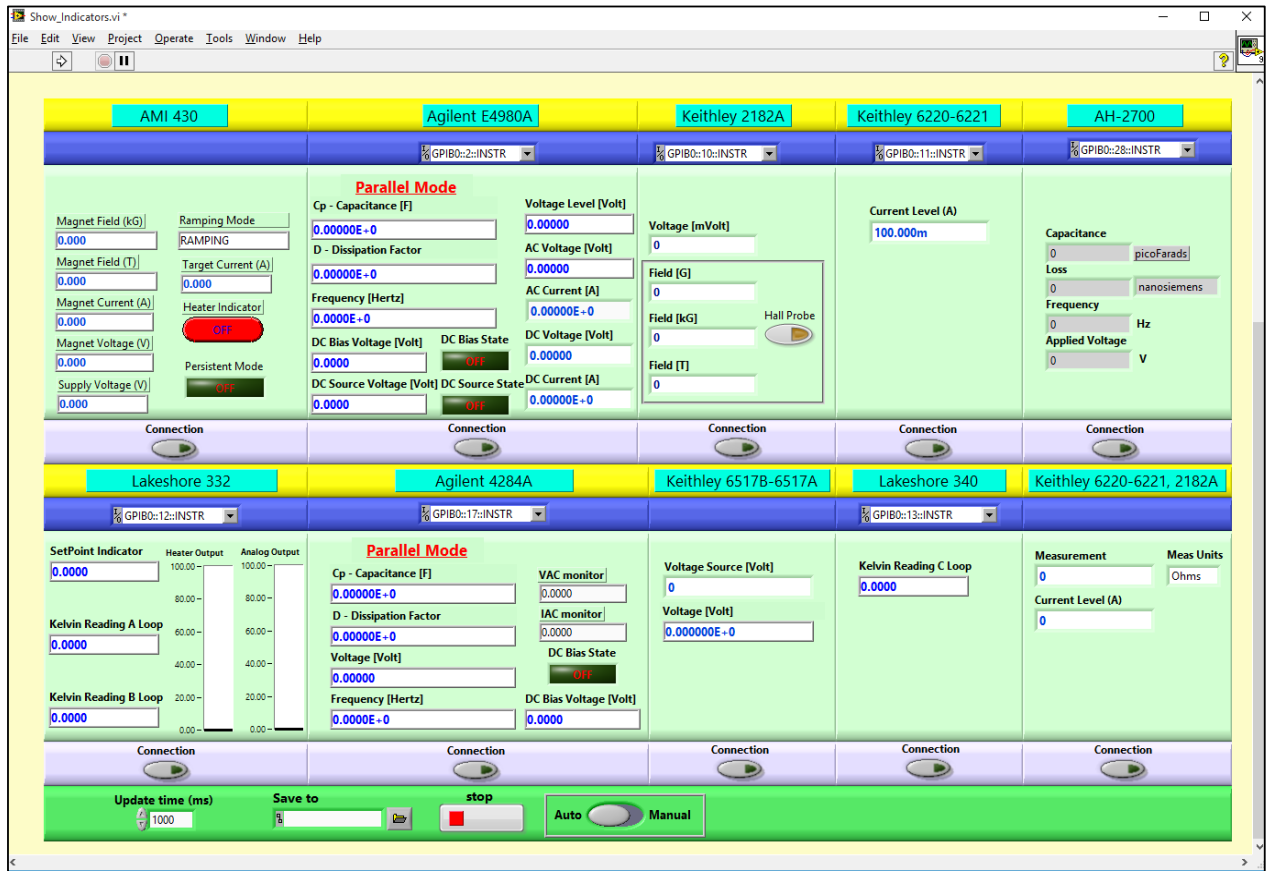


Figure 8-12 “Show\_Indicators.vi”

## DESCRIPTION OF EXPERIMENTAL PROCESSES

Before starting any experimental sequence or any solo experiment even before stabilizing the temperature, it is highly recommended to open the “Sequence\_Controller\_ver2.vi” shown in Figure 13.

One can perform an amount of single experiments with the available instrumentation arrangement on this Set Up while one can also build a sequence of experiments that use the same wiring to the sample (and the same probing instrument as well). In this chapter we will describe the main experiments that can be performed with this set up and give a user’s guide for the LabVIEW interface through which the experiments can be set, monitored and controlled.



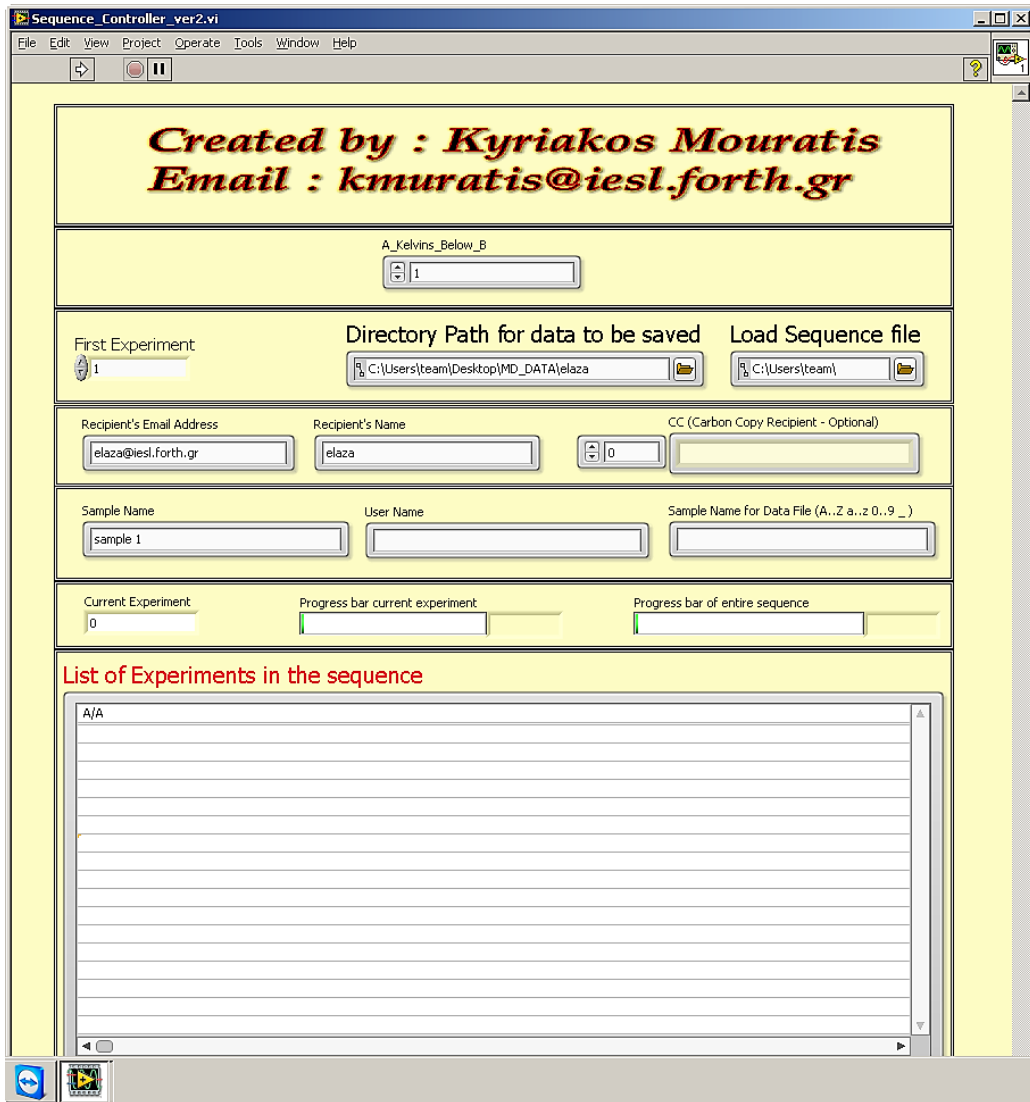


Figure 8-13 “Sequence\_Controller\_ver2.vi”

## DIELECTRIC PERMITTIVITY MEASUREMENTS

The Dielectric constant of a material “  $\kappa$  ” is a complex quantity. In a homogenous material, the dielectric constant or relative permittivity “  $\epsilon_r$ ,” is expressed as fraction of linear permittivity over the permittivity of vacuum. The definition of dielectric constant is described in equation (1).

$$\kappa = \frac{\epsilon}{\epsilon_0} = \epsilon_r = \epsilon_r' - j\epsilon_r'' \quad (1)$$

Where  $\epsilon_r'$  represents the Storage ability of the material while the imaginary part  $\epsilon_r''$  represents the Losses.



If you want to probe the dielectric permittivity of a specimen you can do it by measuring the Capacitance or the Impedance/Admittance of the sample prepared in a capacitor topology and do the calculations according to the equations that relate the afore mentioned physical quantities to each other. Since we are talking about a complex quantity we need to measure both a quantity related to the real part and a quantity related to the imaginary part of the relative permittivity. We suggest to prepare a sample in a capacitor topology as described in section 3.1 and perform AC measurements on Agilent LCR meter (or AH capacitance bridge) in a Cp-D (Capacitance-Dissipation Factor) or a  $|Y|-\theta$  (Admittance-phase angle theta) mode when small capacitance value is predicted. In order to choose the more suitable mode among the available modes on the LCR instrument, depending on the sample under test, one should check the Agilent Impedance Measurement Handbook.

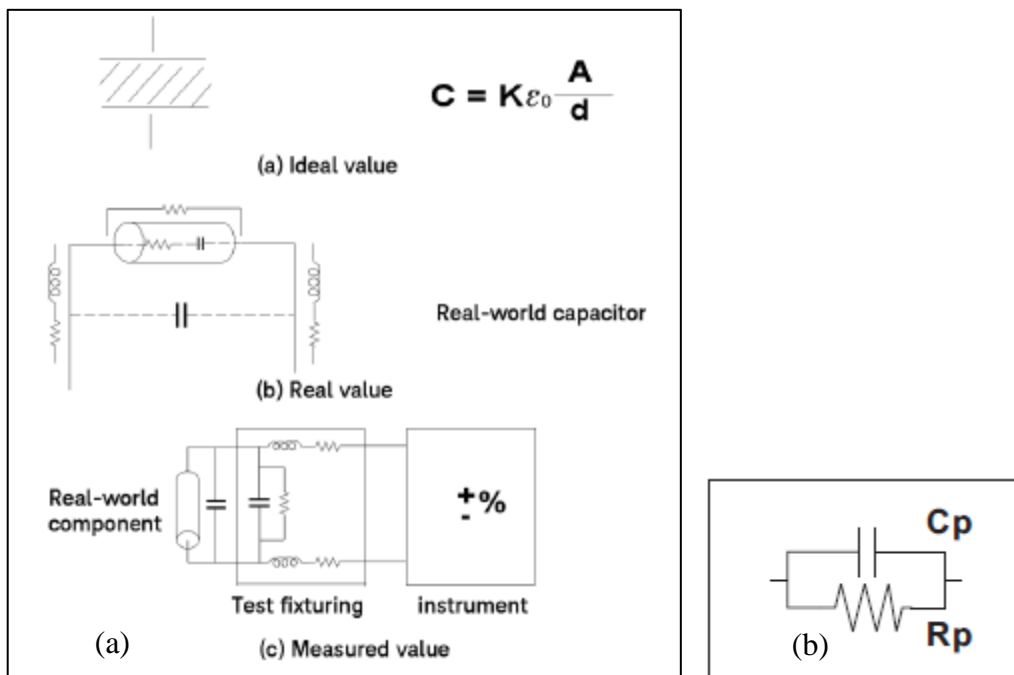


Figure 8-14 (a) Ideal, Real and Measured values in a capacitor topology, (b) parallel equivalent circuit mode for capacitor measurements

In the case you decide to measure in Cp-D mode that means you consider a parasitic Resistance in parallel with your ideal capacitor as pictured in Figure 14. In this case, you can calculate the dielectric permittivity by the following formula:

$$\epsilon_r' = \frac{C \cdot d}{\epsilon_0 \cdot S}, \quad D = \tan\delta = \frac{\epsilon_r''}{\epsilon_r'} \quad (2)$$

Where  $d$  is the distance between the capacitor plates (thickness of the sample),  $S$  is the conducting area of the plates. If we have an area covered with conductive paint this is the area we should use for our calculations. The Dissipation factor ( $D$ ) measured should be close to zero value for a good dielectric material and is related to the  $C_p$  value as following:

$$D = \frac{1}{2\pi f C_p R_p} = \frac{1}{Q} \quad (3)$$

Where  $f$  is the frequency of the  $V_{ac}$  triggering signal,  $R_p$  is the equivalent parallel resistance in the parallel equivalent model circuit (Fig. 14b) and  $Q$  is the Quality factor.  $Q$  serves as a measure of a reactance's purity (how close it is to being a pure reactance, no resistance), and is defined as the ratio of the energy stored in a component to the energy dissipated by the component and is dimensionless.

## **PROBING CAPACITANCE/IMPEDANCE AGAINST TEMPERATURE- EXAMPLE SEQUENCE**

### **MANUAL- SOLO EXPERIMENT**

When we study the behavior of a material as a function of Temperature we are usually looking for a peak or effect on the probing physical property that would indicate a transition. In order to check the temperature evolution of permittivity, in different selected frequencies of stimulant  $V_{ac}$ , we suggest the following process:

- a) Open the “*Sequence\_Controller\_ver2.vi*” in case you haven't done it already. It only serves for loading instruments' libraries for now.
- b) Execute the steps described in section 4 in order to initiate flow of cryogenic Gas and stabilize temperature before starting the experiment.
- c) Prepare the sample in a capacitor topology as described in Section 3 and mount it in an appropriate way. Insert the MD probe inside the cryostat and stabilize temperature (Section 4).



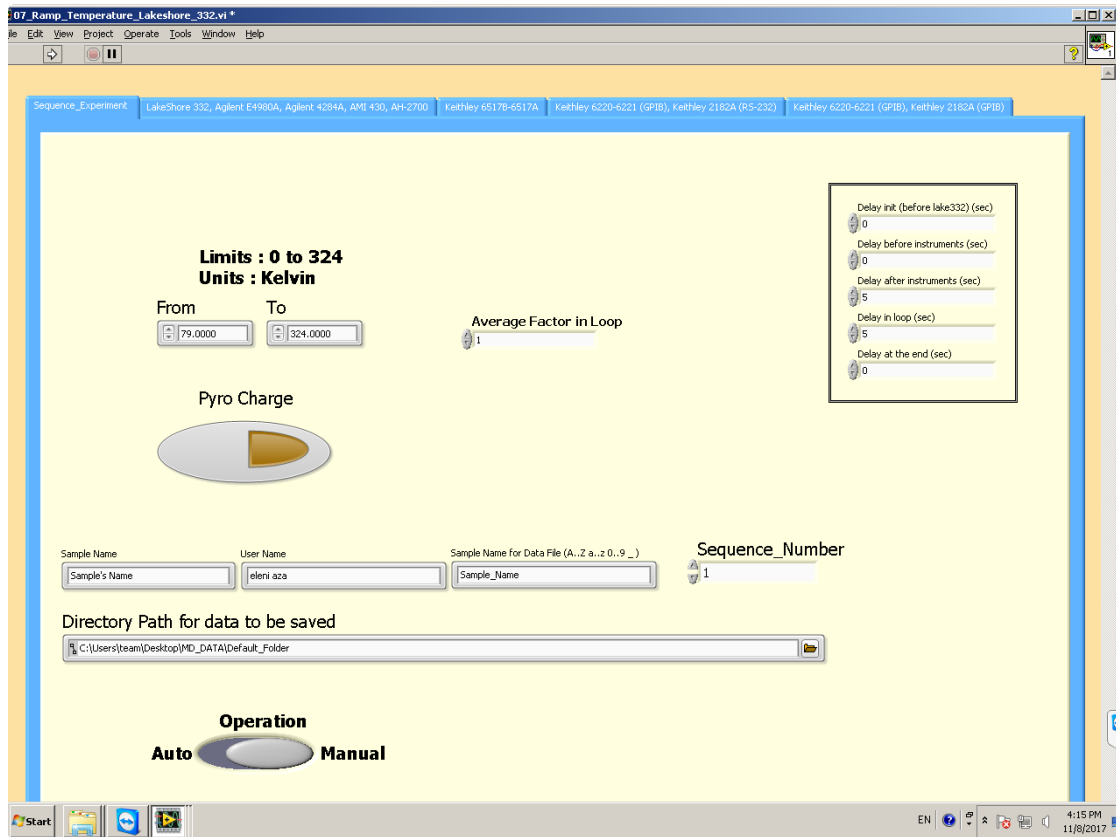


Figure 8-15 Solo experiment- “07\_Ramp\_Temperature\_Lakeshore\_332.vi”- Tab 1 Set the experiment/Save file

- d) Usually, in such experiments, we ramp to base temperature (For  $N_2$  use you can go down to 79-80 K) with zero electric field applied on our sample and measure upon heating. So once the sample is inside the cryostat at RT we cool down the system in a controlled way using “Lakeshore\_332 .vi” (Fig. 11). We recommend the default settings which should be “Ramp mode”-> ON, “Control Mode”-> Zone, “Heater Range” -> High and only change the “Setpoint” to the desired temperature (example-> 79 K) and the “Rate Value” -> 2, which represents the ramp rate of temperature to K/ min.
- e) Open the “07\_Ramp\_Temperature\_Lakeshore\_332.vi” from the Solo experiments folder (APPENDIX B). The first interface Tab (Tab 1) should look as in Figure 15.
- f) Set the starting temperature (From-> 79 K) and the final temperature (To-> 320 K) points.
- g) In the right frame of Tab 1 you may enter several delays during the measurements. We suggest a small delay in the “After Instruments” field -> after the new set values are set on the instruments and in “In Loop” which sets a delay in between each measurement loop. 5-10 sec should be enough.
- h) Set Sample name, username and select the folder in which your dataset will be saved.
- i) The Operation button should be set in Manual mode when you run a single experiment and not a sequence.



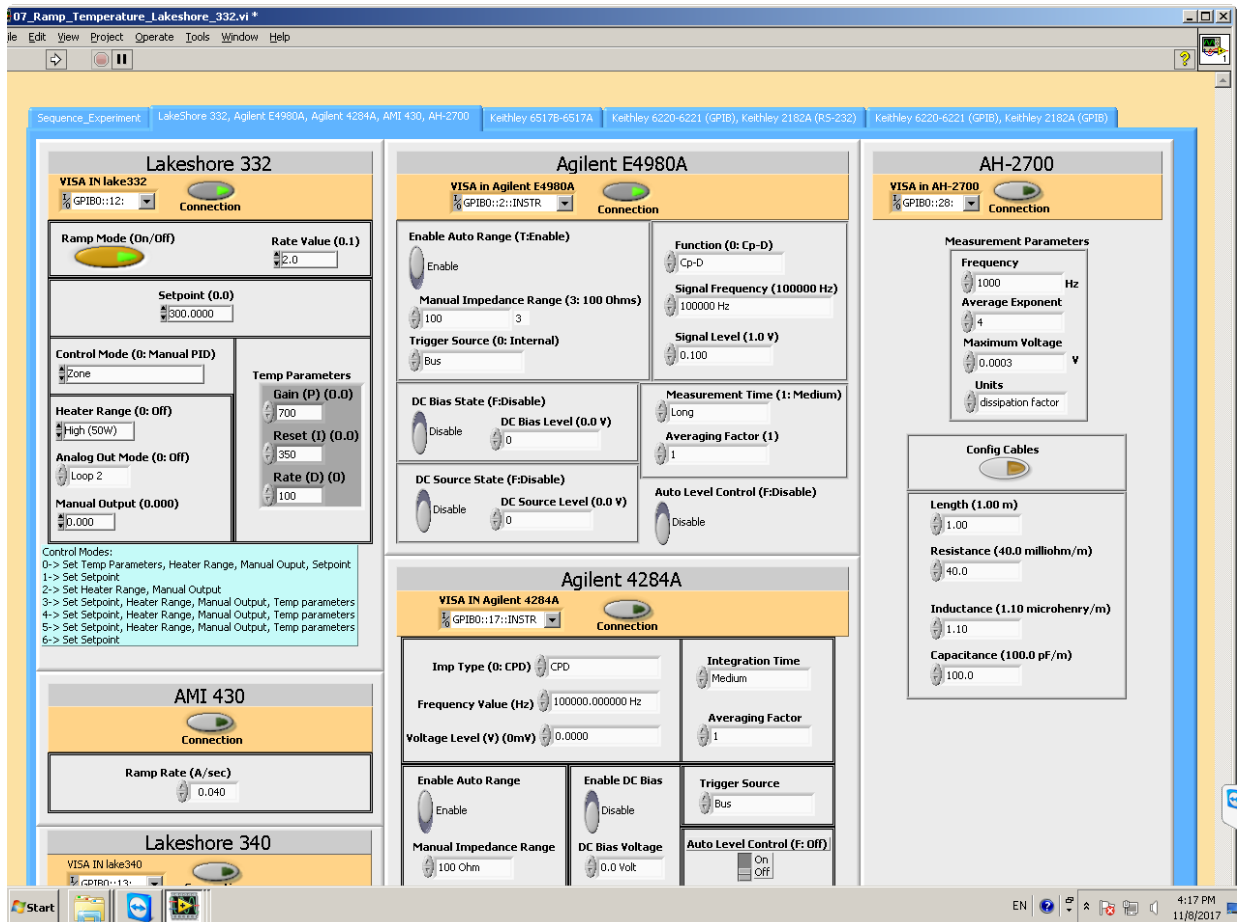


Figure 8-16 Solo experiment- “07\_Ramp\_Temperature\_Lakeshore\_332.vi”- Tab 2-Setting instruments

- j) In the second Tab of the .vi (Fig. 16) we should first connect the instruments that are used for the experiment. In all cases we would connect Lakeshore 332 that ramps and monitors temperature and we will connect one of the other 3 available probing Instruments. For accurate Low frequency measurements (50 Hz – 20 kHz) we use AH-2700 and for measurements up to 2 MHz we use the Agilent E4980A.
- k) In the Lakeshore 332 frame (Fig. 16 left) we make no changes since the main set points and ramp rate have been selected in the Tab 1 of the same .vi in the first place.
- l) In case we use Agilent E4980A, we should select the appropriate “Function”-> i.e. Cp-D, the “Frequency” of the Vac-> 100000 Hz and “Signal Level”-> 0.1 V. We may leave the rest as they are by default.
- m) If our choice is AH-2700 we can measure by Default “Capacitance” but we have a choice over the “Loss” quantity which by default is measured in Siemens (G-> conductance).
- n) We check Tabs 3-5 and ensure no other instruments are “Connected”. If we have an Instrument “Connected” but not switched ON the software will crash since it will make attempts to establish a communication that is not possible. If the Instrument is ON it will just read/save unnecessary trash.



- o) When all previous are set we are ready to go back to Tab 1 and press “Run” which is the white arrow on the top left part of the .vi.
- p) As soon as the experiment starts running, the “*Show\_Indicators.vi*” will start automatically and then the “*Graphs.vi*” will visualize the measurements after the first two points are measured (Fig. 17).

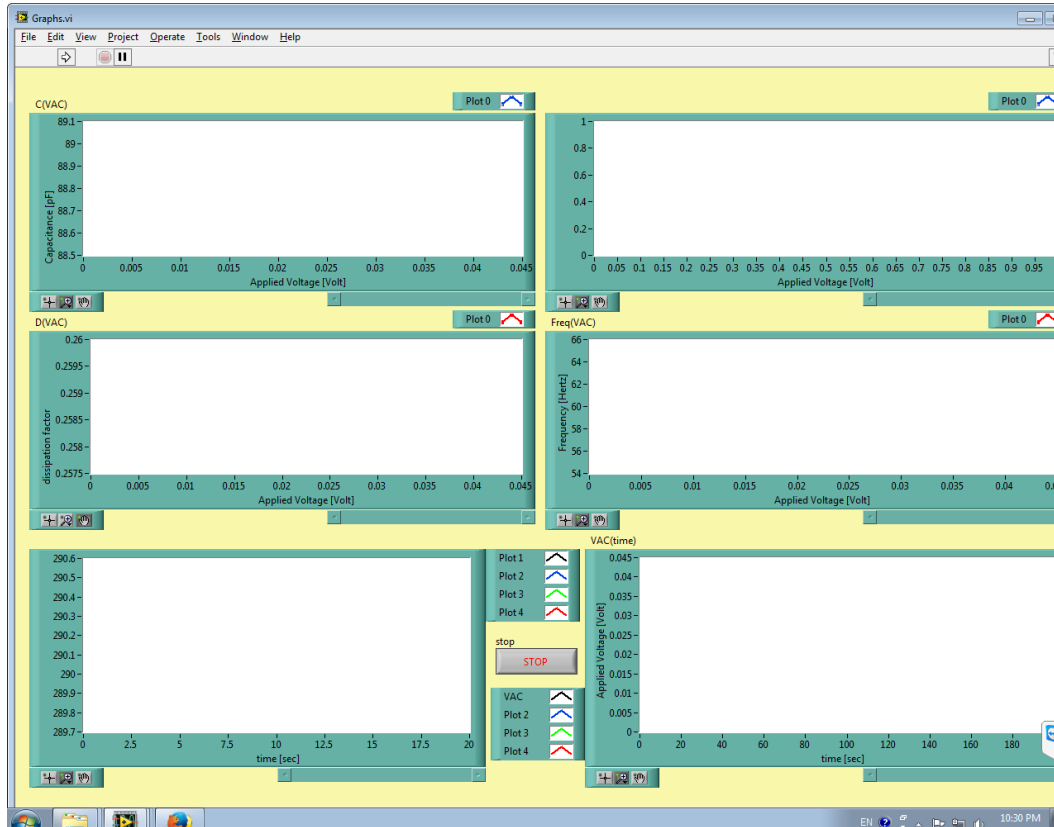


Figure 8-17 “*Graphs.vi*”

## SEQUENCE EXAMPLE

If you want to perform the ramp temperature experiment several times in different frequencies or using different settings of Vac/ Vdc you may program a sequence of experiments that will automatically run one after the other. In such case an example sequence and some tips are given below.

- a) Be sure that you have enough cryogenic liquid for several temperature ramps.
- b) You follow steps a-c from 5.2.1 section.
- c) Open “*Create\_Sequence\_ver3.vi*”



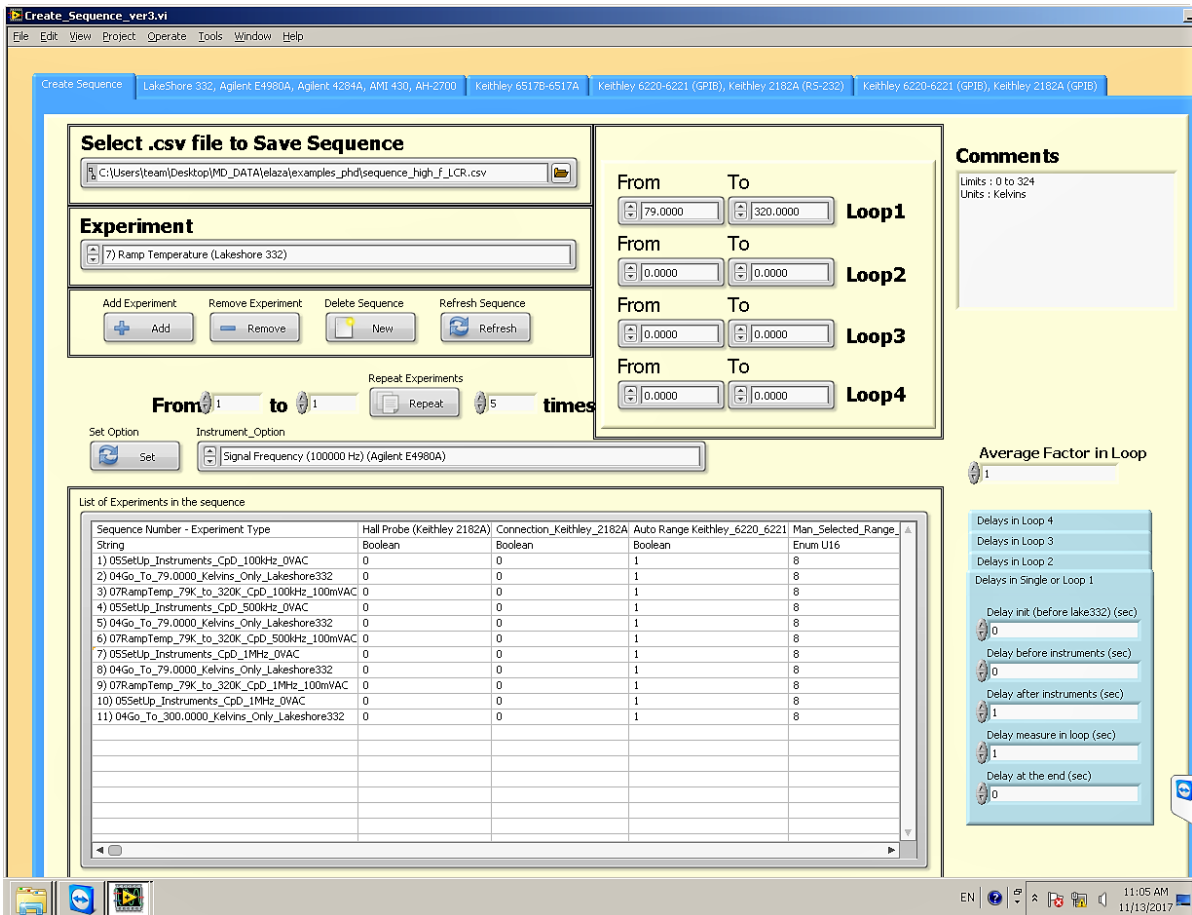


Figure 8-18 “Create\_Sequence\_ver3.vi”- Tab 1 Add experiments, Save file

- d) Select a .csv file to save the sequence. The easiest way to select a file is to copy an older file from a different folder, and afterwards paste it in the folder you specify and select that one.
- e) Press the “Delete Sequence” button if you want to clear previous data from the file and start adding experiments.
- f) Choose your first experiment from the “Experiment Type” menu. You may choose among 100 experiments. In this example we will make a sequence for several ramp Temperature measurements probing Cp-D in different frequencies.
- g) Each time you choose an experiment this is programmed to set/monitor different instruments. So depending on the experiment you should connect and Set the appropriate instrumentation. Once you select the experiment and before adding it to sequence you set the parameters in Tab 2-5. So every time you want to insert an experiment in a sequence you
  - Select Experiment
  - Set parameters/ Connect instruments (tabs2-5)
  - Press “Add experiment” button
 An example Sequence is presented in Figure 18.



- h) First experiment is “05\_SetUp\_Instruments\_Without\_Lakeshore\_332\_Lakeshore\_340\_AMI\_430.vi”. In this you need to connect one of the Capacitance probing instruments apart from the Lakeshore 332 controller (Tab 2). Although Lakeshore 332 is connected, this experiment is designed to only set up the probing Instruments. So to start the specific experiment you Set “Function”-> i.e. Cp-D, the “Frequency” of the Vac-> 100000 Hz and “Signal Level”-> 0.0 V in order to cool down in zero E field. You may double check your settings
- i) Second experiment is “04\_Go\_To\_Temperature\_Only\_Lakeshore\_332.vi”. We only need to Set the temperature in Tab 2. It is recommended to keep the probing instrument connected.
- j) Third experiment is “07\_Ramp\_Temperature\_Lakeshore\_332.vi” which is set as described in 5.2.1 section.
- k) To fill the sequence you repeat these 3 experiments as many times as desired changing the necessary parameters. In this sequence in every “07\_Ramp\_Temperature\_Lakeshore\_332.vi” we set a different frequency.
- l) In the end of each sequence it is suggested to add “05\_SetUp\_Instruments\_Without\_Lakeshore\_332\_Lakeshore\_340\_AMI\_430.vi” in order to Set the electric field to 0.0 Volts and after that add “04\_Go\_To\_Temperature\_Only\_Lakeshore\_332.vi” to go to 300 K in order to be ready to remove the sample stick.

### New feature!

For a quick temperature scan in different frequencies at the same time you may use the solo experiment “07-Ramp\_Temperature\_Lakeshore332\_multifrequencies.vi”. In tab-1 (Figure19), you may set the temperature limits. For example you start your cooling with no field @ 324 K (Start Temp), you cool down to 80 K (Cool Temp) and measure upon warming up to 324 K (Warm Temp). After the measurement is finished you may wish that the system goes back to 300 K (End Temp). In the center of the tab-1 the 2-states button allows you to choose between LCR E4980A or AH\_2700 depending on the frequency range you want to check and choose the frequencies in which you would like to take a measurement of the chosen physical property (for example Cp-D).

In Tab-2, you connect and set the instruments that are used in the experiment as described earlier (Figure 20).



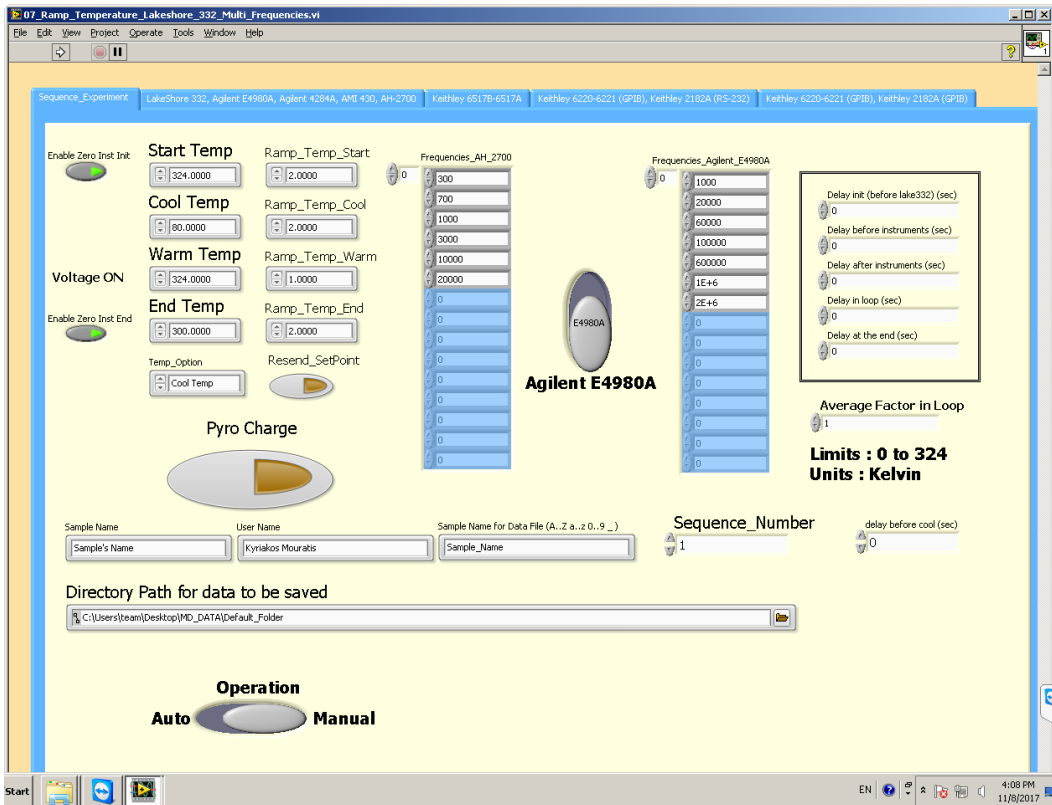


Figure 8-19 “07-Ramp\_Temperature\_Lakeshore332\_multifrequencies.vi”- Tab-1- Set temperature and select frequency range.

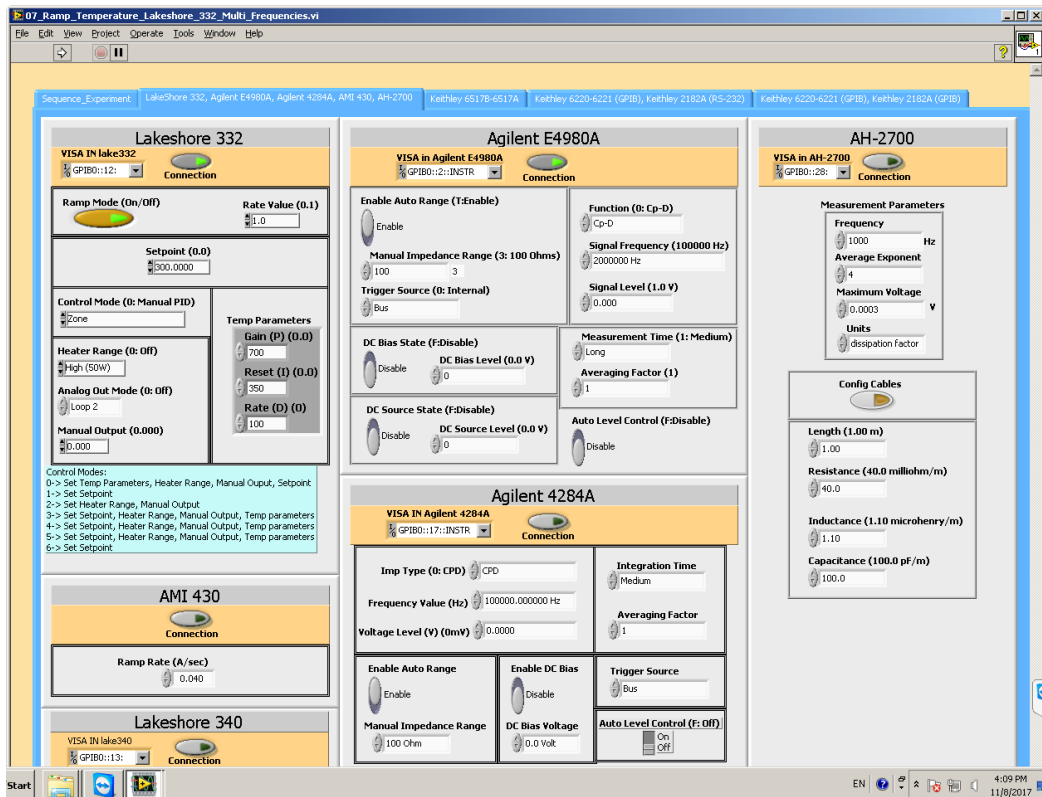


Figure 8-20 “07-Ramp\_Temperature\_Lakeshore332\_multifrequencies.vi”- Tab-2- Connect & Set Instruments



## PROBING CAPACITANCE/IMPEDANCE AGAINST FREQUENCY- EXAMPLE SEQUENCE

When we need to observe the behavior of a material as a function of frequency we are usually looking for a peak or effect on the probing physical property that would indicate a resonant or relaxation effect (Figure 8-22). In the case of piezoelectric sample for example, we expect electromechanical response when poled so we can observe several peaks in specific frequencies (piezoelectric sample: typical resonant and antiresonant frequencies) (Figure 8-21). In order to check the frequency response of permittivity, in selected temperatures we suggest the following process:

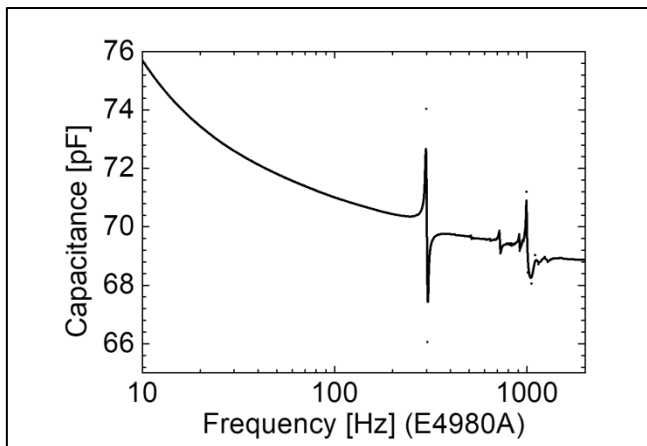


Figure 8-21 Example of resonance peaks in piezoelectric material

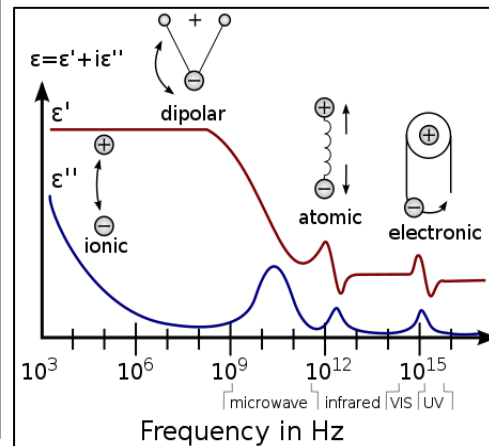


Figure 8-22 Frequency dependence of dielectric permittivity

- Follow the steps a-c from 5.2.1 section
- Depending on the case of study we may need to ramp down to a temperature below a transition and then ramp up to the temperature of interest in order to perform a frequency sweep. We handle this using “04\_Go\_To\_Temperature\_Only\_Lakeshore\_332.vi”.
- For the frequency sweep with LCR E4980A (after having stabilized the temperature to the desired point) we use “45\_Sweep\_Frequency\_From\_File\_Agilent\_E4980A.vi”. (Figure 22).
- There are some prepared .txt files of frequency points on the whole frequency range that make the measurement short and manageable. These files are in MD “C:\Users\team\Desktop\Muraza\Projects\text\_files” folder.
- After you select and load the frequency points file you select the folder where the data will be saved and go to Tab 2 to connect and set Instruments.

- f) Since the “45\_Sweep\_Frequency\_From\_File\_Agilent\_E4980A.vi” is used E4989A will be connected by default in Tab 2. One only needs to select function (Cp-D or other) and signal level (o.1 V) on this frame. Check if Lakeshore 332 is connected and set the temperature you want the frequency scan to happen. Once the temperature is stable the scan will start.

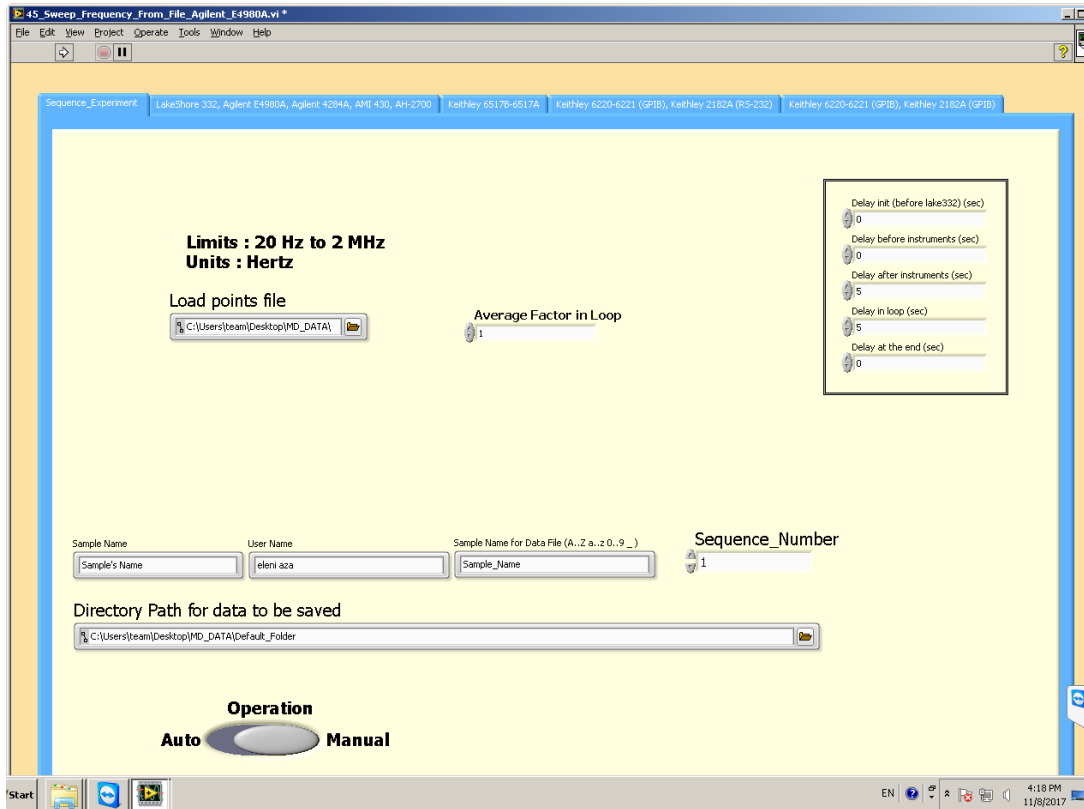


Figure 8-23 “45\_Sweep\_Frequency\_From\_File\_Agilent\_E4980A.vi”, Tab 1-Load point file and save data

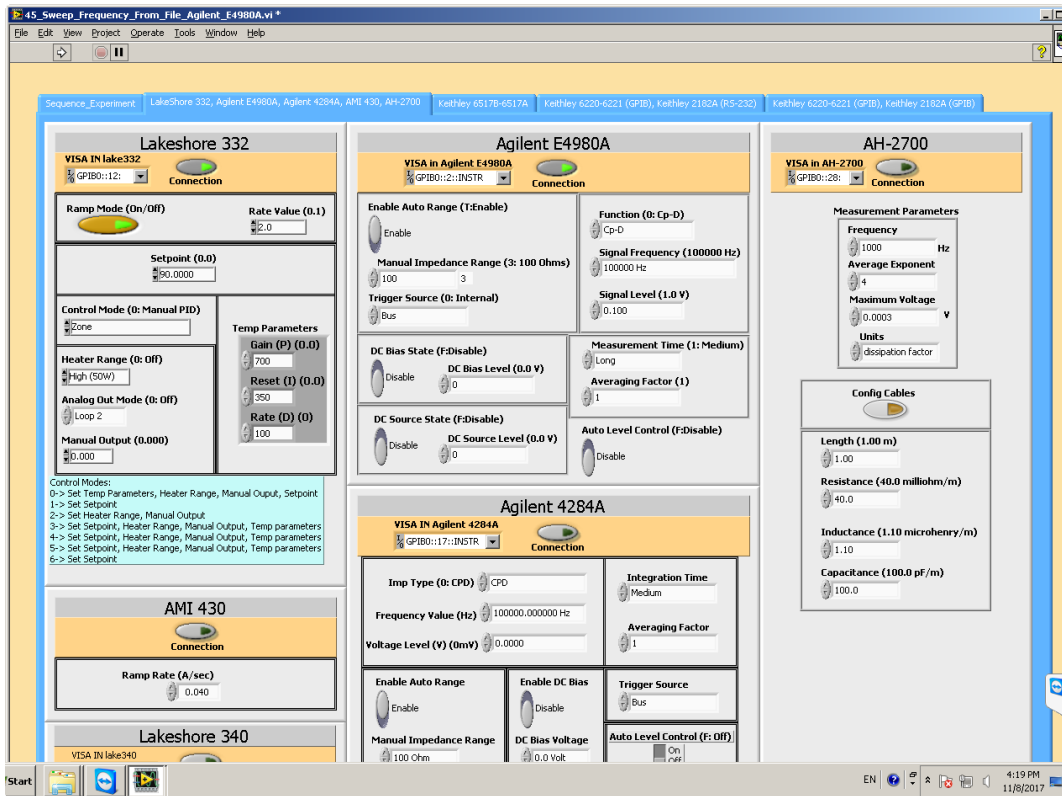


Figure 8-24 “45\_Sweep\_Frequency\_From\_File\_Agilent\_E4980A.vi”, Tab 2-Set temperature, measurement mode and signal level

- g) In case you need frequency scans in several temperatures it is recommended to create a sequence in which the main experiments will be “04\_Go\_To\_Temperature\_Only\_Lakeshore\_332.vi” and “45\_Sweep\_Frequency\_From\_File\_Agilent\_E4980A.vi”. You may follow the tips on creating a sequence as mentioned in section 5.2.2
- h) In the case you need to perform a frequency scan limited to lower frequencies you can use the AH Capacitance bridge and select “89\_Sweep\_Frequency\_From\_File\_AH\_2700.vi”.

## RESISTIVITY MEASUREMENTS

### Resistivity of conductors/semiconductors

Four-probe method is used to measure low resistivity of metals and semiconductors when contact resistance gives errors in two probe

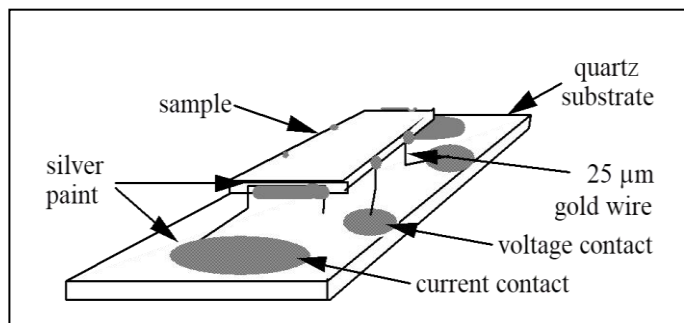


Figure 8-25 Wiring for measuring resistivity with the direct 4-probe method.

measurements. However, for high resistance measurements in kOhms and above four probe is not used. So for low-resistivity measurements the sample should be prepared in 4-point contact topology as summarized in 3.1.2 section. Depending on the sample under test it is recommended for the experimentalist to study which method would be more appropriate for the case. Four-probe (regular bar shape), Van der Pauw (for arbitrary shaped sample), Montgomery's method etc. Typically a 100 mA ac current should be used though dc measurements are also possible if the current is reversed to account for thermal emfs. Following the latest suggestion you can measure using delta mode which is programmed and available for Keithley nanovoltmeter 2182A. Find our suggestion below.

- a) Prepare sample contacts following 4-point topology and mount it in the MD-probe if measurements against temperature are your intention.
- b) Connect output of Keithley 6221 current source to I+, I- on the BNC sockets on the probe and input of Keithley Nanovoltmeter 2182A in the V+, V- sockets.
- c) Open the "*Sequence\_Controller\_ver2.vi*" in case you haven't done it already. It only serves for loading instruments' libraries for now.
- d) Execute the steps described in section 4 in order to initiate flow of cryogenic Gas and stabilize temperature before starting the experiment.
- e) For measurements against temperature we suggest again the "*07\_Ramp\_Temperature\_Lakeshore\_332.vi*". We set the first Tab as described earlier. In the next tabs we want connected only the instruments that are used in the experiment.
- f) In Tab-2 we keep Lakeshore connected but disconnect LCR. We check that nothing is connected in Tab-3.
- g) In Tab-4 we connect Keithley 6220-6221- Keithley 2128A (delta measurements) (figure 26). Current level of 1 mA dc is usually ok but it depends on the sample.



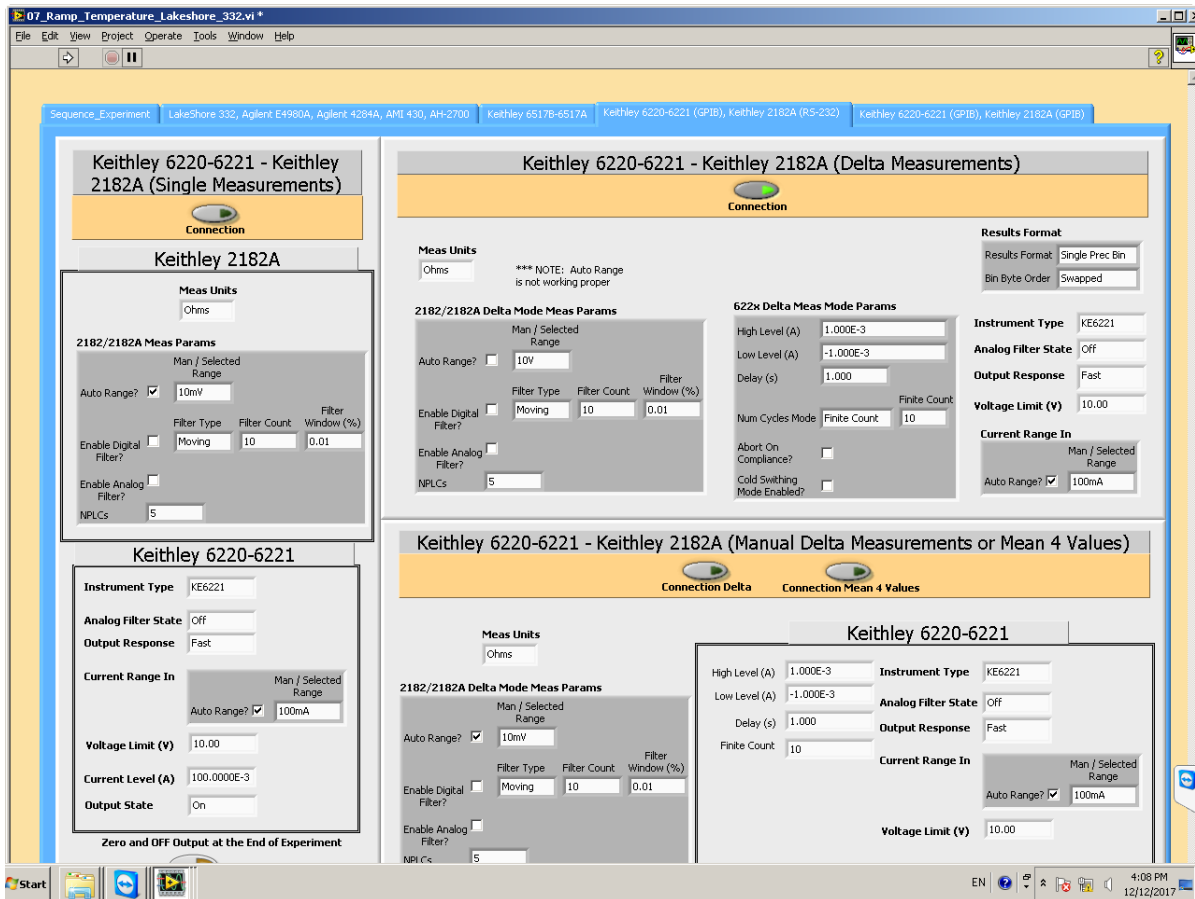


Figure 8-26 “07\_Ramp\_Temperature\_Lakeshore\_332.vi”- Tab-4 Connect and set current source and nanovoltmeter for Delta function resistivity measurements.

### Resistivity of Insulators

The resistivity of an Insulator is determined by applying a voltage to the sample for a specified period of time measuring the resulting current with an electrometer (or picoammeter) and then calculating the resistivity based on Ohm’s law and geometric considerations. In this case the sample is prepared and connected using a capacitor topology (figure 27). [240] According to the ASTM standard, a commonly used test condition is a voltage of 500 V applied for 60 seconds. According to the IEC standard, apply 100 V for 60 seconds unless another voltage is stipulated (as mentioned in Keithley’s application notes for electrometer 6517B). After the electrification period the current is measured using an ammeter

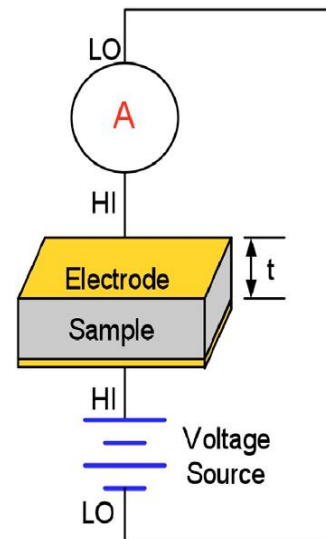


Figure 8-27 Determine the resistivity of an insulator

capable of measuring nanoamps or lower. Volume resistivity can be calculated based on the area of the electrodes and the thickness of the sample under test.

$$\rho = \frac{V A}{I t} \quad (4)$$

Keithley electrometer 6517B is available for measurements of resistivity but the sequence as described above is not programmed through software since it is a very short measurement.

### MEASURE PYRO ELECTRIC CURRENT- EXAMPLE SEQUENCE

- a) The most popular experiment in order to investigate the existence of polarization is pyro-electric current measurements. The protocol goes as follows: Apply a big DC Voltage (enough to pole your sample) and cool down to a temperature below the FE transition. Zero the voltage and wait for 60 sec. Then measure current upon warming without applying any voltage. Keithley 6517B electrometer can be also used to perform this measurement. Before doing any measurement using electrometer Keithley 6571B/A we strongly recommend to study the manual, user's guide and Keithley's application notes in order to use the appropriate and safe configuration for the measurement of choice. A suggested procedure for pyro-electric current measurement would be the following (similar to the resistivity measurement protocol of an insulator):



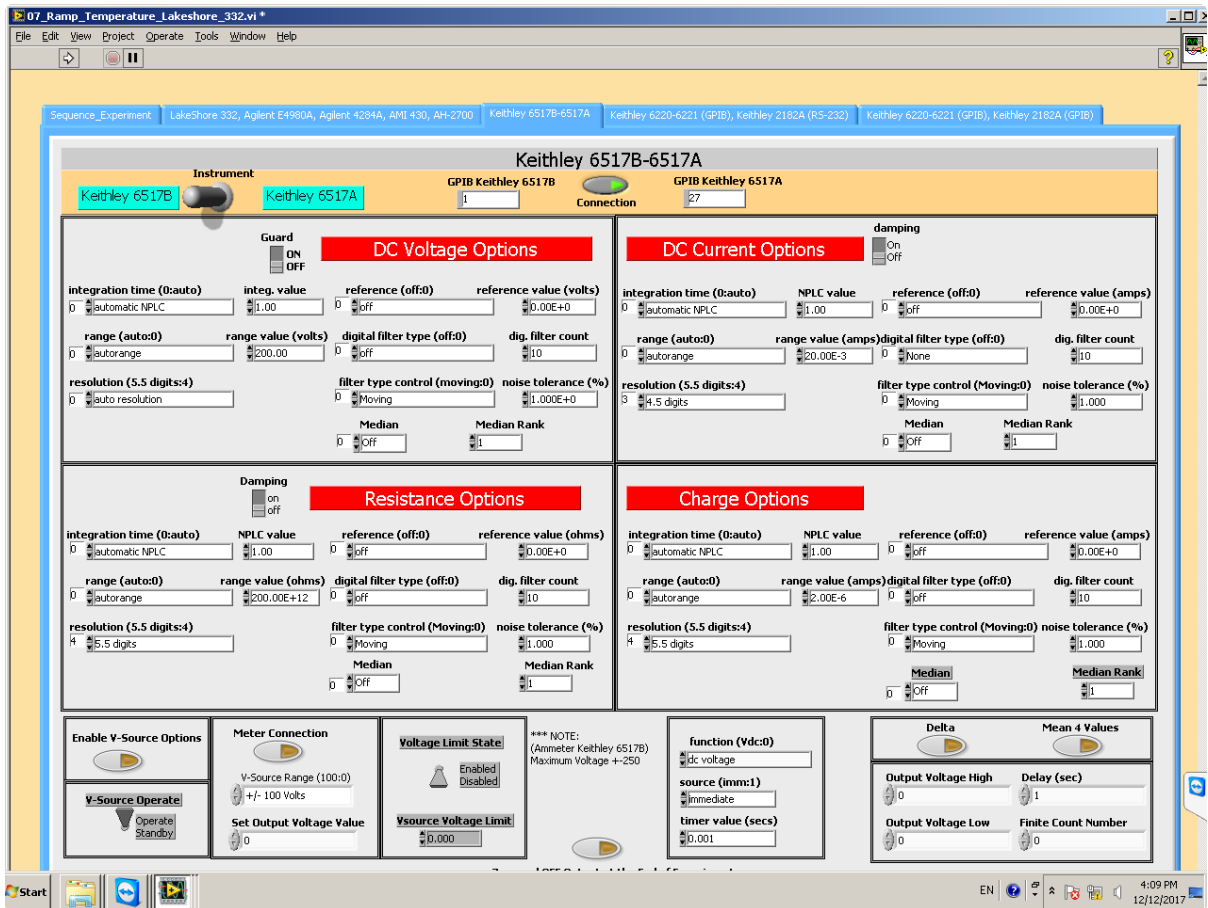


Figure 8-28 “07\_Ramp\_Temperature\_Lakeshore\_332.vi”-Tab-3 Keithley 6517B connected

- b) Prepare and mount the sample in an appropriate way. It is important to measure dimensions of the sample before mounting it. Thin samples (<1mm) are preferable for this measurements.
- c) Connect output of Keithley 6517B (V+, V-) to the V+ and V- respectively on the BNC connectors on the probe. Apply a field of 100 V on the sample using the instruments display.
- d) Cool down to a temperature below transition without zeroing the electric field. You may use the solo experiment “04\_Go\_To\_Temperature\_Only\_Lakeshore\_332.vi” to cool down.
- e) After stabilizing the temperature, zero the electric field and wait for 60 secs.
- f) At this point you should disconnect instantly the V+/V- from the BNC sockets of the probe and connect I+/I- of the triax cable of the electrometer on the I+/I- sockets on the probe.
- g) You may use “07\_Ramp\_Temperature\_Lakeshore\_332.vi” in order to start ramping up the temperature. This time the Keithley 6517B should be connected in Tab-3 (Figure28) so that you collect data of the current intensity as you warm up.



Note! We haven't managed to see a pyro-electric current on the samples tested the last 4 years using this software. The experimentalist should take into consideration possible wiring or thermal noise and even consider an instant discharge during the change of cable configuration from applying Voltage (electrifying process) to the sensing of the current. The software seems to work fine.

## USE OF MAGNETIC FIELD AS AN EXTERNAL STIMULI

All, afore mentioned, experiments can be performed under the application of magnetic field. The 7-Tesla superconducting magnet, as mentioned in section 1.4, is controlled by AMI430 Power Supply Programmer and powered by model 4Q05100 bi-polar power supply. It is also equipped with a Persistent Switch heater to ensure the stability of the magnetic field during a long lasting measurement. Using solo experiment vis we can control some functions by communicating with the AMI430 Programmer.

- a) Charge the magnet -> *"00\_Target\_Magnetic\_Field\_AMI\_430.vi"* (Figure 29). With this vi, once the magnet is cold and in good vacuum (check section 2-Prepare MD Station), you can charge up to the desired field. The limits are 7 and -7 Tesla. In a manual procedure, in order to charge up the magnet, first the heater should be warmed. This .vi does it for you so you don't need to press the persistent switch button on the Programmer. If the heater is already warm the software will check it and will move on charging the magnet.
- b) Enter Persistent mode-> *"01\_Entering\_Persistent\_Mode\_AMI\_430.vi"*. With this .vi the programmer gets the command to cool the heater and then discharge the cables. If all of these functions can be done manually with no problem then software should be trusted. Usually we use this vi in a sequence of experiments just before getting into a "ramp temperature" experiment which lasts quite long (5 hours). After our long experiment is over and we want to take control of the field again (for example discharge or change field) we need to run the next .vi.
- c) Exiting Persistent mode-> *"02\_Exiting\_Persistent\_Mode\_AMI\_430.vi"*. This .vi commands the programmer to charge the cables to the previously used magnetic field and warm up the PSheater. When the PSheater is warmed then you can run again the *"00\_Target\_Magnetic\_Field\_AMI\_430.vi"* in order to change field. In case you finish your experiment with the magnetic field application you may energize the button that is labeled as **"Close Heater and Connection when zero Output"** in *"00\_Target\_Magnetic\_Field\_AMI\_430.vi"* (Figure 29). IF YOU DO SO you need to restart the .vi to recover connection with AMI 430.
- d) When we need the magnet values and communication with the AMI430 in a ramp temperature experiment we should not forget to connect AMI430 in tab-2.(Figure30)



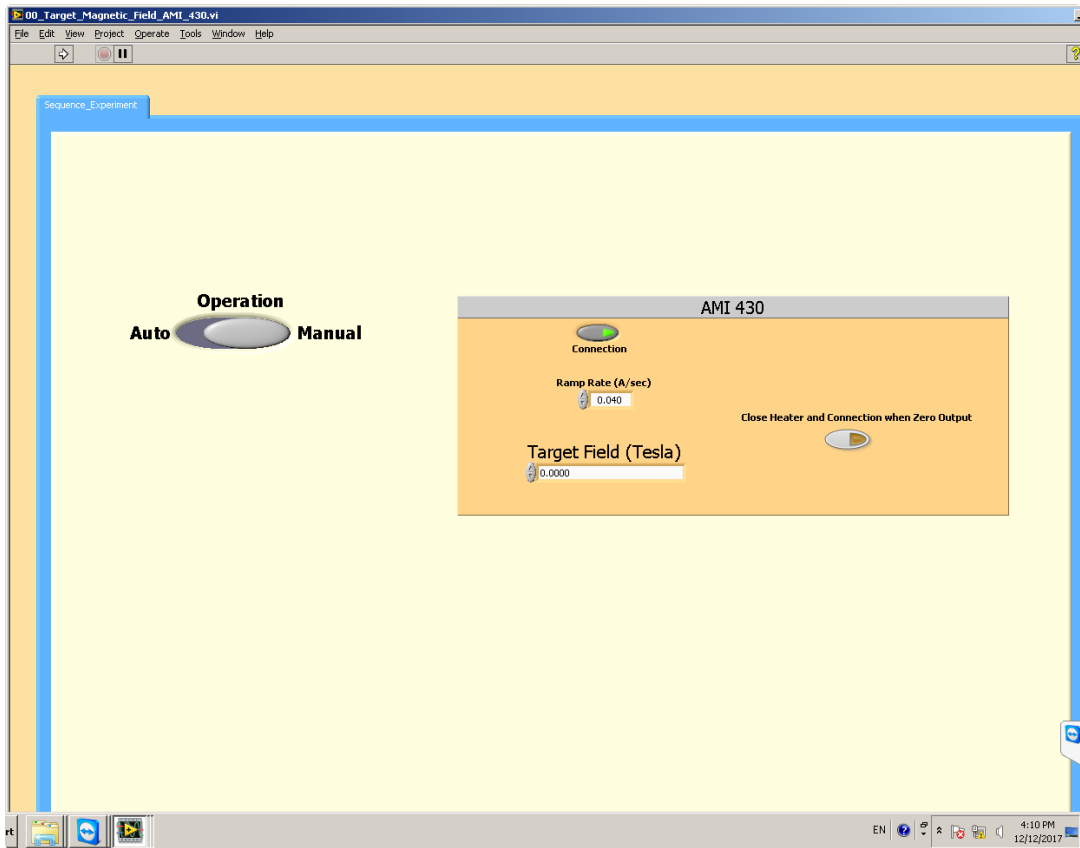


Figure 8-29 “00\_Target\_Magnetic\_Field\_AMI\_430.vi”

Ramp field experiments

If we want to perform an isothermal magnetic field ramp or sweep we may use one of the solo experiments from 16 to 24 depending on the case. They can be used solo as well as in a sequence.

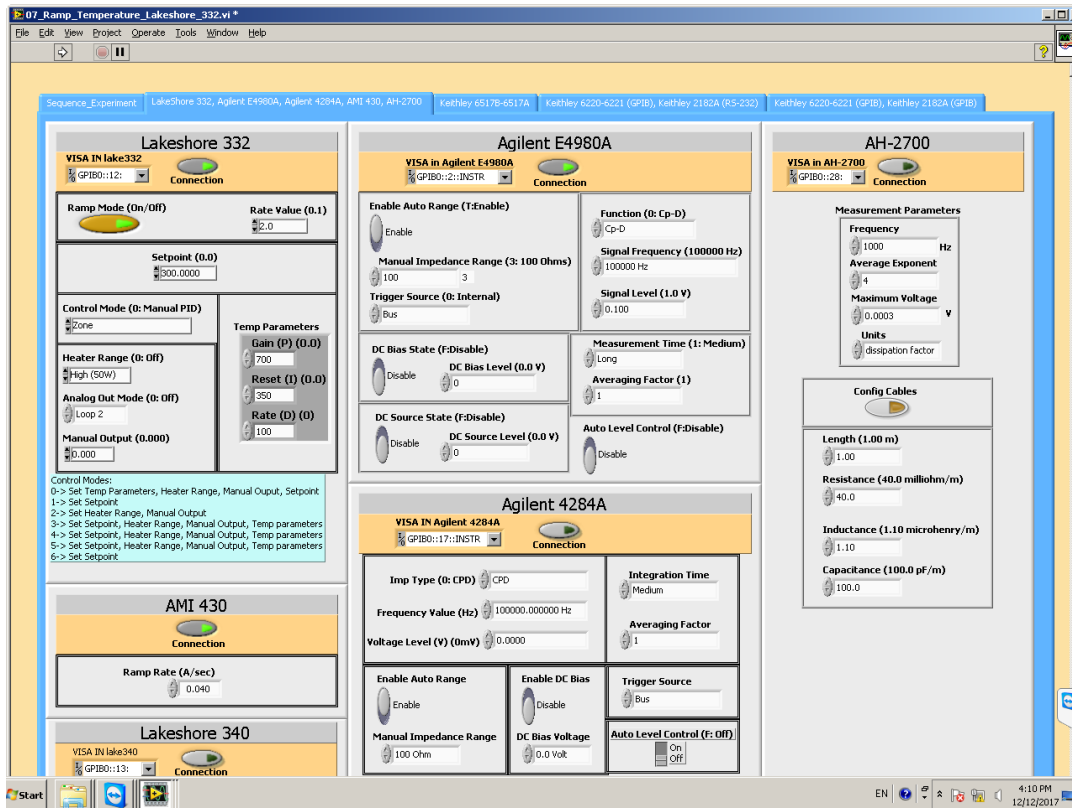


Figure 8-30 Keep AMI430 connected during an experiment that takes place under magnetic field

## CLOSE EXPERIMENT

In order to close safely an experiment check the following

- Be sure that your experiment/sequence is over.
- Be sure that you have no electric or magnetic field applied on the sample under test. If so, set zero field using the appropriate controlled instrumentation.
- Verify that you are at room temperature so that you can remove the sample from the cryostat.
- When at room temperature you may stop the N<sub>2</sub> flow (or other cryogenic in use). You do this by first of all stop the “Auto Control” of the flow from “Control\_Dewar\_Valve\_ver2.vi”. Then press Close Valve until it is completely closed.
- Observe the HEATERS level (Lakeshore 332 panel or Indicators .vi). When the heaters’ level goes below 10% you may close the heaters by using “HEATERS\_OFF.vi”. You may observe a small temperature fall after that.
- When HEATERS are OFF and there is no field applied on the sample you may unplug all connectors from the MD probe.
- Now the cryostat is in negative pressure. In order to export the stick the diaphragm pump should be switched off and wait for system to come to equilibrium.



- h) If the system (cryostat) is still above 290 K you can export the sample. If you can't take the probe out due to the pressure use the pressure relief valve of the Janis Cryostat.
- i) Place the probe to the bench and unmount the sample. Store it as usually.
- j) Remove the transfer line first from the cryostat and then from the Cryogenic Liquid Dewar. **Be Careful!** Be sure to relief the pressure inside the Dewar, before you take the Transfer Line out! Otherwise when you try to take out the transfer line, or the adaptor the pressure might cause the Cryogenic Liquid to burst out on the experimenter!!
- k) Switch off the Temperature Controller.
- l) Switch off all the instruments (first-4Q Power Supply, second- AMI430, LCR)
- m) Before you place the Transfer Line to the wall be sure you have dried it with the heat gun/ hair drier and that it is completely dry.

### **TIPS ON SOFTWARE EMERGENCIES**

For more detailed description on the function of some functional but not experimental vis you may want to study the "MD SET UP" written by Mr Mouratis in the paragraphs referred to:

**GLOBAL STOP**

**HEATERS OFF**

**Close a .vi programmatically**



## APPENDIX I. VACUUM PREPARATION

### PUMP CRYOSTAT/MAGNET-PROCESS

- a) The system should be at Room Temperature.
- b) In the case of the cryostat check that the green vacuum valve is closed. In the case of the magnet you want the black round valve on the magnet to be closed. (Fig.4)
- c) Open the water valves (red & blue) that cool the turbo pump and are located behind the magnet system. Indication of the flow meter should be 4-5 lt/min. (Fig.4)
- d) Ensure the relief valve of the rotary pump is closed before you switch on the pump (clockwise). Ensure the oil of the pump is in good condition and in the suggested by the manual level (between the two indications). Change of oils is noted on the pupms Logbook. First you switch on the rotary (Adixen Pascal 2021 SD) pump and wait for the thermovac TM21 gauge to reach  $10^{-2}$  -  $10^{-3}$  before you switch on the turbo pump (about 15-20 min ).
- e) When the indication of thermovac TM21 , pirani has reached  $10^{-3}$  then you may switch on the turbo pump TURBOVAC 150CSV through the frequency converter (TURBOTRONIC 150/360) -> START. After some seconds the indication “normal/normalbetrieb.” of TURBOTRONIC should be illuminated.
- f) Switch on the penning (Penningvac PM31) to check the vacuum level. When vacuum level is of  $10^{-4}$  open slowly the green vacuum valve on the cryostat. The range of  $10^{-5}$  is good vacuum for the cryostat.

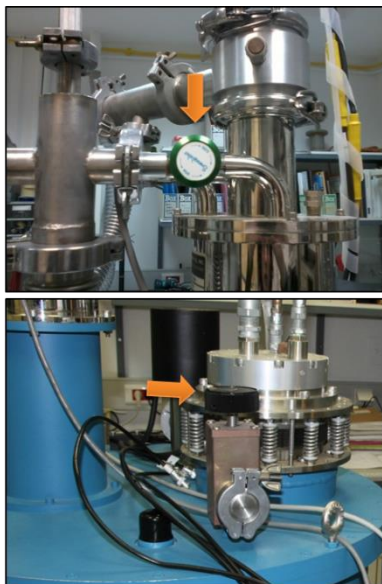


Fig.4 **top:** cryostat vacuum valve, **bottom:** magnet vacuum valve



Fig.5 **top-left:** water flow meter, **top right:** rotary vacuum pump for low vacuum **Bottom:** vacuum gauges and controller of the turbo pump

### **Reverse process**

- a) When we reach the satisfactory vacuum we first switch off the vacuum valve on the pumped equipment (green valve on the cryostat/ black valve on the magnet).
- b) Switch off the turbo pump -> STOP on TURBOTRONIC. Wait for 15-20min (up to 30 min) till it stops spinning.
- c) Then switch off the rotary pump. Important! After switching the rotary off we break the vacuum by rotating anticlockwise the relief valve (Fig. 4). This protects the turbo pump and bellow lines from rotary pump's oil.
- d) Turn off red & blue water valves on the wall behind the magnet.



**APPENDIX II. LABVIEW FOLDERS AND FILES ON PC**

The experiments that you can execute are the following:

(You can find them in the following location

C:\Users\team\Desktop\ShortCut\_JanisLab\_SubVIs\Experiments\_Solo” folder)

- 00\_Target\_Magnetic\_Field\_AMI\_430.vi
- 01\_Entering\_Persistent\_Mode\_AMI\_430.vi
- 02\_Exiting\_Persistent\_Mode\_AMI\_430.vi
- 03\_Delay\_Time\_Between\_Experiments.vi
- 04\_Go\_To\_Temperature\_Only\_Lakeshore\_332.vi
- 05\_SetUp\_Instruments\_Without\_Lakeshore\_332\_Lakeshore\_340\_AMI\_430.vi
- 06\_Time\_dependance\_in\_seconds.vi
- 06b\_Time\_dependance\_Continuous.vi
- 07\_Ramp\_Temperature\_Lakeshore\_332.vi
- 08\_Sweep\_with\_Steps\_Temperature\_Lakeshore\_332.vi
- 09\_Loop2\_Ramp\_Temperature\_Lakeshore\_332.vi
- 10\_Loop2\_Sweep\_with\_Steps\_Temperature\_Lakeshore\_332.vi
- 11\_Loop3\_Ramp\_Temperature\_Lakeshore\_332.vi
- 12\_Loop3\_Sweep\_with\_Steps\_Temperature\_Lakeshore\_332.vi
- 13\_Loop4\_Ramp\_Temperature\_Lakeshore\_332.vi
- 14\_Loop4\_Sweep\_with\_Steps\_Temperature\_Lakeshore\_332.vi
- 15\_Sweep\_Temperature\_From\_File\_Lakeshore\_332.vi
- 16\_Ramp\_Magnetic\_Field\_AMI\_430.vi
- 17\_Sweep\_with\_Steps\_Magnetic\_Field\_AMI\_430.vi
- 18\_Loop2\_Ramp\_Magnetic\_Field\_AMI\_430.vi
- 19\_Loop2\_Sweep\_with\_Steps\_Magnetic\_Field\_AMI\_430.vi
- 20\_Loop3\_Ramp\_Magnetic\_Field\_AMI\_430.vi
- 21\_Loop3\_Sweep\_with\_Steps\_Magnetic\_Field\_AMI\_430.vi
- 22\_Loop4\_Ramp\_Magnetic\_Field\_AMI\_430.vi
- 23\_Loop4\_Sweep\_with\_Steps\_Magnetic\_Field\_AMI\_430.vi
- 24\_Sweep\_Magnetic\_Field\_From\_File\_AMI\_430.vi
- 25\_Sweep\_Frequency\_From\_File\_Agilent\_4284A.vi



26\_Loop2\_Sweep\_Frequencies\_From\_Files\_Agilent\_4284A.vi  
27\_Loop3\_Sweep\_Frequencies\_From\_Files\_Agilent\_4284A.vi  
28\_Loop4\_Sweep\_Frequencies\_From\_Files\_Agilent\_4284A.vi  
29\_Sweep\_with\_Steps\_AC\_Voltage\_Agilent\_4284A.vi  
30\_Loop2\_Sweep\_with\_Steps\_AC\_Voltage\_Agilent\_4284A.vi  
31\_Loop3\_Sweep\_with\_Steps\_AC\_Voltage\_Agilent\_4284A.vi  
32\_Loop4\_Sweep\_with\_Steps\_AC\_Voltage\_Agilent\_4284A.vi  
33\_Sweep\_AC\_Voltage\_From\_File\_Agilent\_4284A.vi  
34\_Loop2\_Sweep\_AC\_Voltage\_From\_Files\_Agilent\_4284A.vi  
35\_Loop3\_Sweep\_AC\_Voltage\_From\_Files\_Agilent\_4284A.vi  
36\_Loop4\_Sweep\_AC\_Voltage\_From\_Files\_Agilent\_4284A.vi  
37\_Sweep\_with\_Steps\_DC\_Bias\_Voltage\_Agilent\_4284A.vi  
38\_Loop2\_Sweep\_with\_Steps\_DC\_Bias\_Voltage\_Agilent\_4284A.vi  
39\_Loop3\_Sweep\_with\_Steps\_DC\_Bias\_Voltage\_Agilent\_4284A.vi  
40\_Loop4\_Sweep\_with\_Steps\_DC\_Bias\_Voltage\_Agilent\_4284A.vi  
41\_Sweep\_DC\_Bias\_Voltage\_From\_File\_Agilent\_4284A.vi  
42\_Loop2\_Sweep\_DC\_Bias\_Voltage\_From\_Files\_Agilent\_4284A.vi  
43\_Loop3\_Sweep\_DC\_Bias\_Voltage\_From\_Files\_Agilent\_4284A.vi  
44\_Loop4\_Sweep\_DC\_Bias\_Voltage\_From\_Files\_Agilent\_4284A.vi  
45\_Sweep\_Frequency\_From\_File\_Agilent\_E4980A.vi  
46\_Loop2\_Sweep\_Frequencies\_From\_Files\_Agilent\_E4980A.vi  
47\_Loop3\_Sweep\_Frequencies\_From\_Files\_Agilent\_E4980A.vi  
48\_Loop4\_Sweep\_Frequencies\_From\_Files\_Agilent\_E4980A.vi  
49\_Sweep\_with\_Steps\_AC\_Voltage\_Agilent\_E4980A.vi  
50\_Loop2\_Sweep\_with\_Steps\_AC\_Voltage\_Agilent\_E4980A.vi  
51\_Loop3\_Sweep\_with\_Steps\_AC\_Voltage\_Agilent\_E4980A.vi  
52\_Loop4\_Sweep\_with\_Steps\_AC\_Voltage\_Agilent\_E4980A.vi  
53\_Sweep\_AC\_Voltage\_From\_File\_Agilent\_E4980A.vi  
54\_Loop2\_Sweep\_AC\_Voltage\_From\_Files\_Agilent\_E4980A.vi  
55\_Loop3\_Sweep\_AC\_Voltage\_From\_Files\_Agilent\_E4980A.vi  
56\_Loop4\_Sweep\_AC\_Voltage\_From\_Files\_Agilent\_E4980A.vi



57\_Sweep\_with\_Steps\_DC\_Bias\_Voltage\_Agilent\_E4980A.vi  
58\_Loop2\_Sweep\_with\_Steps\_DC\_Bias\_Voltage\_Agilent\_E4980A.vi  
59\_Loop3\_Sweep\_with\_Steps\_DC\_Bias\_Voltage\_Agilent\_E4980A.vi  
60\_Loop4\_Sweep\_with\_Steps\_DC\_Bias\_Voltage\_Agilent\_E4980A.vi  
61\_Sweep\_DC\_Bias\_Voltage\_From\_File\_Agilent\_E4980A.vi  
62\_Loop2\_Sweep\_DC\_Bias\_Voltage\_From\_Files\_Agilent\_E4980A.vi  
63\_Loop3\_Sweep\_DC\_Bias\_Voltage\_From\_Files\_Agilent\_E4980A.vi  
64\_Loop4\_Sweep\_DC\_Bias\_Voltage\_From\_Files\_Agilent\_E4980A.vi  
65\_Sweep\_with\_Steps\_DC\_Source\_Voltage\_Agilent\_E4980A.vi  
66\_Loop2\_Sweep\_with\_Steps\_DC\_Source\_Voltage\_Agilent\_E4980A.vi  
67\_Loop3\_Sweep\_with\_Steps\_DC\_Source\_Voltage\_Agilent\_E4980A.vi  
68\_Loop4\_Sweep\_with\_Steps\_DC\_Source\_Voltage\_Agilent\_E4980A.vi  
69\_Sweep\_DC\_Source\_Voltage\_From\_File\_Agilent\_E4980A.vi  
70\_Loop2\_Sweep\_DC\_Source\_Voltage\_From\_Files\_Agilent\_E4980A.vi  
71\_Loop3\_Sweep\_DC\_Source\_Voltage\_From\_Files\_Agilent\_E4980A.vi  
72\_Loop4\_Sweep\_DC\_Source\_Voltage\_From\_Files\_Agilent\_E4980A.vi  
73\_Sweep\_with\_Steps\_DC\_Voltage\_Keithley\_6517B\_6517A.vi  
74\_Loop2\_Sweep\_with\_Steps\_DC\_Voltage\_Keithley\_6517B\_6517A.vi  
75\_Loop3\_Sweep\_with\_Steps\_DC\_Voltage\_Keithley\_6517B\_6517A.vi  
76\_Loop4\_Sweep\_with\_Steps\_DC\_Voltage\_Keithley\_6517B\_6517A.vi  
77\_Sweep\_DC\_Voltage\_From\_File\_Keithley\_6517B\_6517A.vi  
78\_Loop2\_Sweep\_DC\_Voltage\_From\_Files\_Keithley\_6517B\_6517A.vi  
79\_Loop3\_Sweep\_DC\_Voltage\_From\_Files\_Keithley\_6517B\_6517A.vi  
80\_Loop4\_Sweep\_DC\_Voltage\_From\_Files\_Keithley\_6517B\_6517A.vi  
81\_Sweep\_with\_Steps\_DC\_Current\_Source\_Keithley\_6221\_6220.vi  
82\_Loop2\_Sweep\_with\_Steps\_DC\_Current\_Source\_Keithley\_6221\_6220.vi  
83\_Loop3\_Sweep\_with\_Steps\_DC\_Current\_Source\_Keithley\_6221\_6220.vi  
84\_Loop4\_Sweep\_with\_Steps\_DC\_Current\_Source\_Keithley\_6221\_6220.vi  
85\_Sweep\_DC\_Current\_Source\_From\_File\_Keithley\_6221\_6220.vi  
86\_Loop2\_Sweep\_DC\_Current\_Source\_From\_Files\_Keithley\_6221\_6220.vi  
87\_Loop3\_Sweep\_DC\_Current\_Source\_From\_Files\_Keithley\_6221\_6220.vi



- 88\_Loop4\_Sweep\_DC\_Current\_Source\_From\_Files\_Keithley\_6221\_6220.vi
- 89\_Sweep\_Frequency\_From\_File\_AH\_2700.vi
- 90\_Loop2\_Sweep\_Frequencies\_From\_Files\_AH\_2700.vi
- 91\_Loop3\_Sweep\_Frequencies\_From\_Files\_AH\_2700.vi
- 92\_Loop4\_Sweep\_Frequencies\_From\_Files\_AH\_2700.vi
- 93\_Sweep\_with\_Steps\_AC\_Voltage\_AH\_2700.vi
- 94\_Loop2\_Sweep\_with\_Steps\_AC\_Voltage\_AH\_2700.vi
- 95\_Loop3\_Sweep\_with\_Steps\_AC\_Voltage\_AH\_2700.vi
- 96\_Loop4\_Sweep\_with\_Steps\_AC\_Voltage\_AH\_2700.vi
- 97\_Sweep\_AC\_Voltage\_From\_File\_AH\_2700.vi
- 98\_Loop2\_Sweep\_AC\_Voltage\_From\_Files\_AH\_2700.vi
- 99\_Loop3\_Sweep\_AC\_Voltage\_From\_Files\_AH\_2700.vi
- 100\_Loop4\_Sweep\_AC\_Voltage\_From\_Files\_AH\_2700.vi



### **APPENDIX III. DRY THE TRANSFER LINE**

Usually it is enough to place the Transfer Line to the wall and dry it with the heat gun/ hair drier until it is completely dry. It would help to let some ethanol on the bayonette tip to remove any humidity. It is recommended once you have experienced a blocked transfer line to leave it hanging dry for a couple of days.

remove any humidity. It is recommended once you have experienced a blocked transfer line to leave it hanging dry for a couple of days.



## Appendix B:

# Study of $\beta$ -NaMnO<sub>2</sub> modulations through Superspace formalism

---

In continuation of section 4.5.2, a (3+1)-dimensional superspace approach has been used considering an occupational modulation for all the sites in the average nuclear structure derived by the NPD patterns of  $\beta$ -NaMnO<sub>2</sub>.

The symmetry analysis led to the  $Pm\bar{m}n(\alpha 00)000$  superspace group as the best solution, corresponding to the  $\Sigma_1$  irreducible representations (IRs), with order parameter direction (OPD)  $P(\sigma, 0)$  where  $\sigma$  is the allowed direction of the order parameter in the distortion vector space defined by the irreducible representations within ISODISTORT suite.

To account for the compositional modulation a step-like (Crenel) function is introduced for every site in the structure. The Crenel function is defined as:[241]

$$\begin{aligned} p(x_4) &= 1 \in \langle x_4^0 - \Delta/2, x_4^0 + \Delta/2 \rangle \\ p(x_4) &= 0 \notin \langle x_4^0 - \Delta/2, x_4^0 + \Delta/2 \rangle \end{aligned} \quad (1)$$

where  $x_4$  is the internal (fourth) coordinate in the (3+1)D approach and  $\Delta$  is the width of the occupational domain centered at  $x_4^0$  ( $\Delta$  corresponds also to the average fractional occupancy of the site). The modulation functions on the same cation site are constrained to be complementary, meaning that in every point of the crystal the site is occupied (this results in the equations  $\Delta[Mn_i] + \Delta[Na_i] = 1$  and  $x_4[Mn_i] = 1 - x_4[Na_i]$  for each cation site). For the split oxygen positions we introduce a similar constraint, imposing that in any position



in the crystal we have the superposition of the two split sites. Regarding the origin along the fourth axis, the superspace group constrains this value to two equivalent values: 0 and 0.5, thus making the choice trivial. Moreover, an additional constraint is introduced regarding the two Mn/Na sites. The electron diffraction measurements, reported by Abakumov *et al.* suggest that the quasi-periodic stacking sequences of the NaMnO<sub>2</sub> layers entail coherent stacking faults, a feature which points that their modeling can be reduced to the alternation sequence of the Na and Mn cations. We followed a similar approach for the modeling of the NPD pattern assuming that the step-like functions were constrained to have in every NaMnO<sub>2</sub> plane the right Mn/Na ordering, that is to say, when one site switches from Mn to Na the other changes from Na to Mn. The crystallographic model built in this way was employed for qualitative Rietveld refinements. Broad, asymmetric reflections throughout the NPD pattern, mainly due to defects (e.g. stacking faults) and strain make such analysis hard to optimize, raising the agreement factors and making a quantitative refinement difficult.

*Table 9-1 Crystallographic atomic fractional coordinates of the  $\beta$ -NaMnO<sub>2</sub> commensurately modulated nuclear structure (300 K), derived from a (3+1)D Rietveld refinement of neutron powder diffraction data in the  $Pm\bar{m}n(\alpha 00)000$  superspace group, with unit cell dimensions  $a=4.7852(4)$  Å,  $b=2.85701(8)$  Å,  $c=6.3288(4)$  Å,  $\alpha=0.077(1)$ . The displacive modulation is defined as a step-like Crenel function (see text).*

Atom	$x_1$	$x_2$	$x_3$	Uiso / Å <sup>2</sup>	$\Delta$	$x_4^0$
Mn1	0	0.5	0.617(5)	0.0136(12)	0.204(4)	0
Na1	0	0.5	0.617(5)	0.0136(12)	0.796	0.5
					(4)	
Na2	0	0.5	0.125(4)	0.0136(12)	0.204(4)	0
Mn2	0	0.5	0.125(4)	0.0136(12)	0.796(4)	0.5
O1	0	0	0.3268(14)	0.0136(12)	0.699(8)	0.5
O1'	0	0	0.404(3)	0.0136(12)	0.301(8)	0
O2	0	0	0.9104(16)	0.0136(12)	0.699(8)	0.5
O2'	0	0	0.834(3)	0.0136(12)	0.301(8)	0

The crystallographic parameters of the compositionally modulated  $\beta$ -NaMnO<sub>2</sub> at 300 K, on the basis of a (3+1)D Rietveld analysis with the  $Pm\bar{m}n(\alpha 00)000$  superspace group ( $a=4.7852(4)$  Å,  $b=2.85701(8)$  Å,  $c=6.3288(4)$  Å,  $\alpha=0.077(1)$ ) are compiled in Table 0-1.



It may be considered as good approximation to the real chemical phase, as planar defects, seen by electron microscopy, could violate the idealized Crenel-type function used in the present analysis of the NPD data. In this model, the MnO<sub>6</sub> octahedra throughout the structure display strong Jahn-Teller distortion (see Figure I, for oxygen-cation distances in the (3+1)D approach), with four short bonds below 2 Å and two long ones around 2.4 Å, in a fashion analogous to the  $\alpha$ -NaMnO<sub>2</sub>. [41] On the other hand, while Na is also octahedrally coordinated to oxygen, the distances involved are longer due to its larger ionic radius.

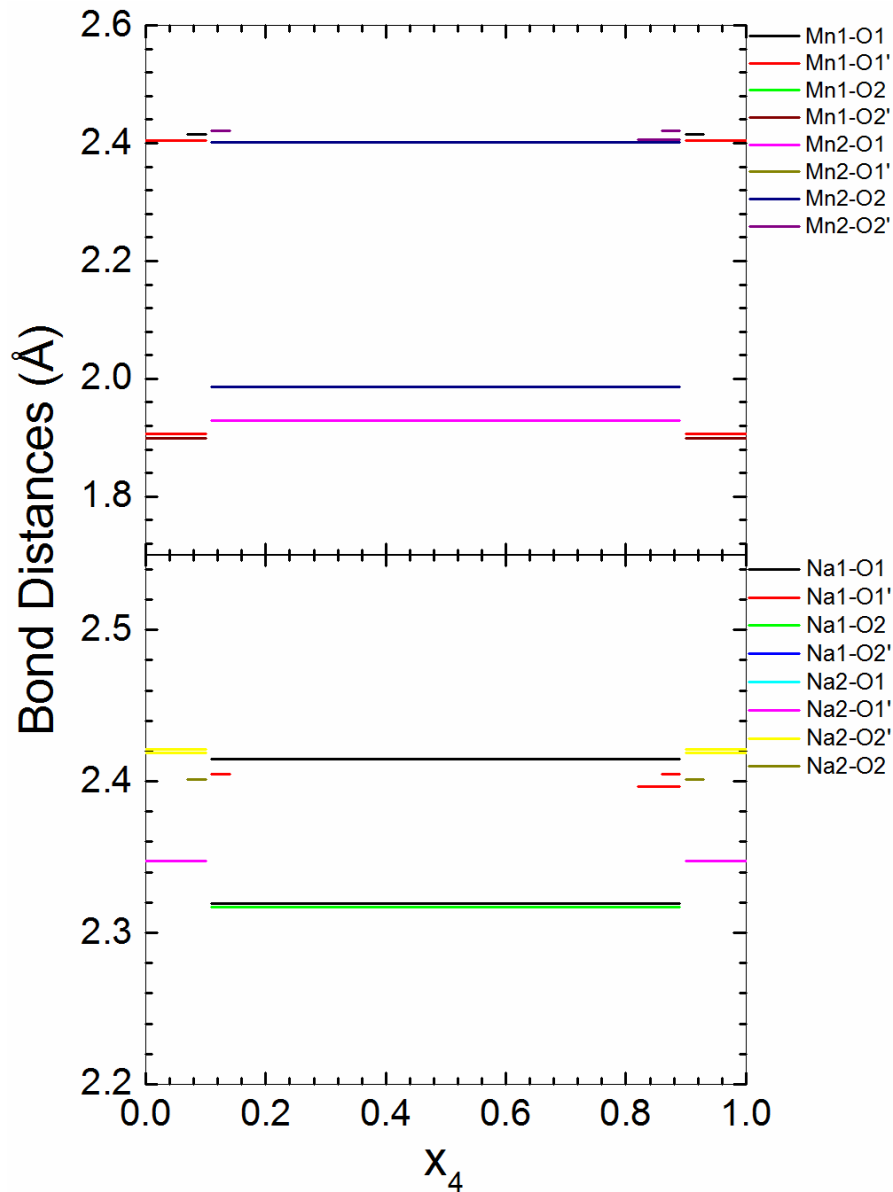


Figure 9-1 The cation-oxygen distances against the fourth coordinate ( $x_4$ ) in the (3+1)D approach ( $t$ -plot) for the room temperature crystal structure of  $\beta$ -NaMnO<sub>2</sub>.



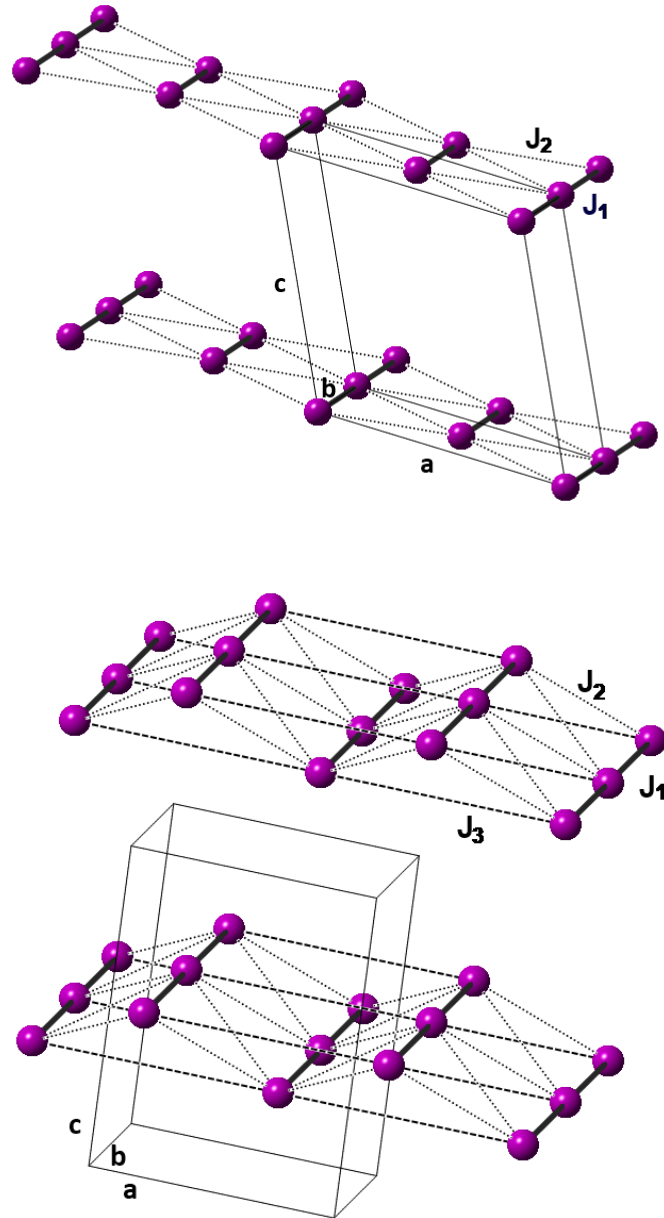


Figure 9-2 Schematic representation of the Mn sublattice topology, in top panel the monoclinic ( $C2/m$ )  $\alpha$ - $\text{NaMnO}_2$  and bottom panel the orthorhombic ( $Pmmn$ )  $\beta$ - $\text{NaMnO}_2$  polymorphs. The Mn-Mn distances drawn, depict the possible intra-layer magnetic exchange coupling pathways ( $J_1$  to  $J_3$ ).

## Appendix C:

# Single Crystal Holder for Neutron diffraction experiment

---

A striking finding of the  $\alpha$ -NaMnO<sub>2</sub> NPD experiments, believed to be an intriguing complexity of competition due to geometrical frustration, was that upon cooling below 200 K, diffuse scattering emerged around the  $(\frac{1}{2}, \frac{1}{2}, 0)$  Bragg position, with a typical Warren profile indicating strong 2D magnetic ordering. The purpose of that proposal requesting time in WISH TOF diffractometer, has been to probe the apparent inhomogeneity in the magnetostructural channel of  $\alpha$ -NaMnO<sub>2</sub> from the perspective of a single crystal specimen and provide a greater insight on the origin of the unusual diffuse scattering features.

As mentioned in section 2.3.1 when a stationary single crystal is randomly oriented and irradiated by monochromatic beam, only a few, if any points of the reciprocal lattice will coincide with the surface of the Ewald's sphere. This occurs because first, the sphere has a constant radius determined by the wavelength, and second, the distribution of the reciprocal lattice points in three dimensions is fixed by both the lattice parameters and the orientation of the crystal. The resultant diffraction pattern may reveal just a few Bragg peaks. Many more reciprocal lattice points are placed on the surface of the Ewald's sphere when the crystal is rotated around an axis.

In single crystal neutron scattering such a rotation could be achieved by a TAS (Triple Axis Spectroscopy). In triple axis spectrometry, the instrument is set up to travel through paths of reciprocal space and energy as defined by the experimentalist and therefore



requires prior knowledge of the nature of the excitations under study. Since that was the first time a single crystal has been grown we decided to proceed in a TOF experiment where the single crystal needs to be oriented properly in order to get the meaningful reflections and so the single crystal had to be oriented in multiple ways in order to get as many reflections as possible

In the specific case we were expecting Bragg peak at  $(\frac{1}{2} \frac{1}{2} 0)$  position of the monoclinic C2/m cell according to the alpha polymorph powder studies, together with the diffuse scattering observed in the vicinity of  $(\frac{1}{2} \frac{1}{2} 0)$  Bragg peak position.

The single crystal flakes as cleaved from the main crystal boule have been found to have all the same orientation as suggested by Laue (section 6.2.2). So the big flat side would be the (-202) plane while the crystal was grown towards b-axis of the monoclinic cell (fig.I).

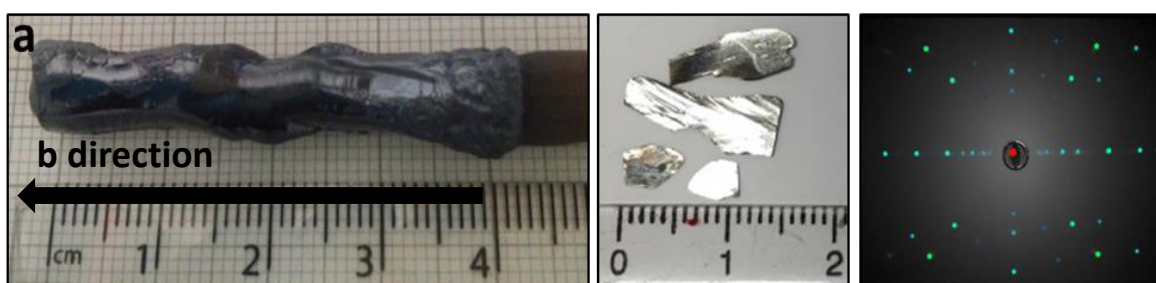


Figure 10-1 Left to right: As grown single crystal boule, cleaved flakes, Laue photograph.

In scope of. neutron experiment that was held on WISH diffractometer at ISIS, a sample holder had to be designed and made from scratch in order to keep the desired orientation during the scattering. As shown in Figure II the arc shaped holder had such an arrangement o that pin holder could be fixed in 9 positions of an arc ( $R=21.5$  mm) having a screw height regulator in order to have the crystal exactly in the center of the beam. A close up of the pin holders is shown in figure III. The crystal was kept safe with vacuum grease on the pin holder. Each one has been differently shaped to carry a different angle and serve the crystal shape.

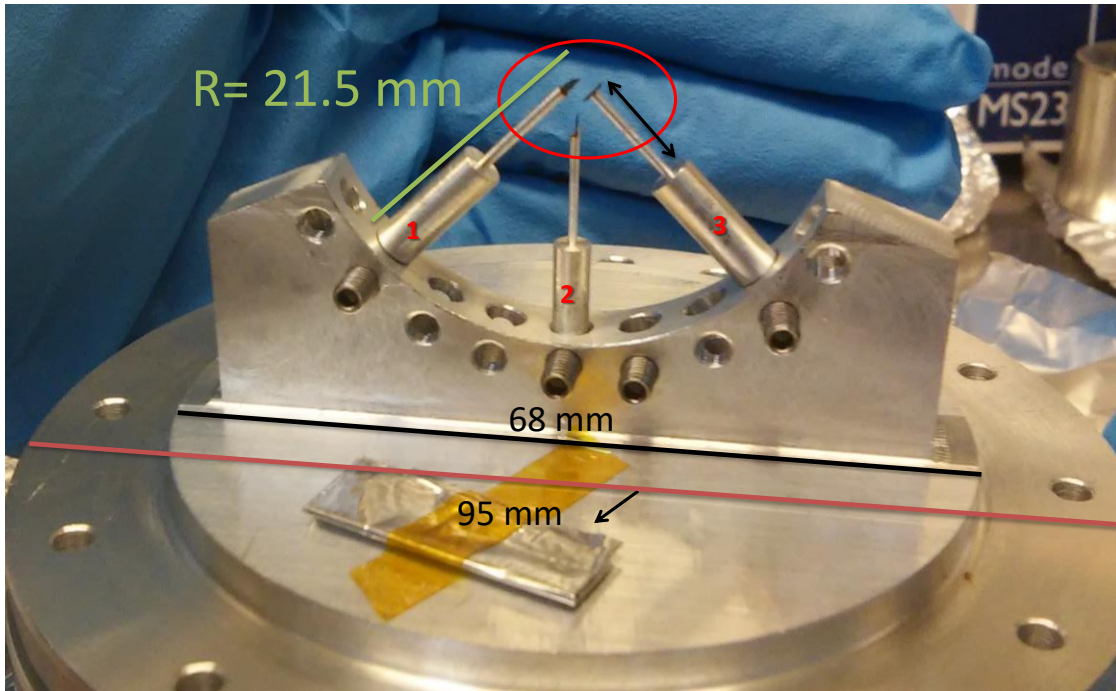


Figure 10-2 The base of the holder carrying three crystals in different orientations.

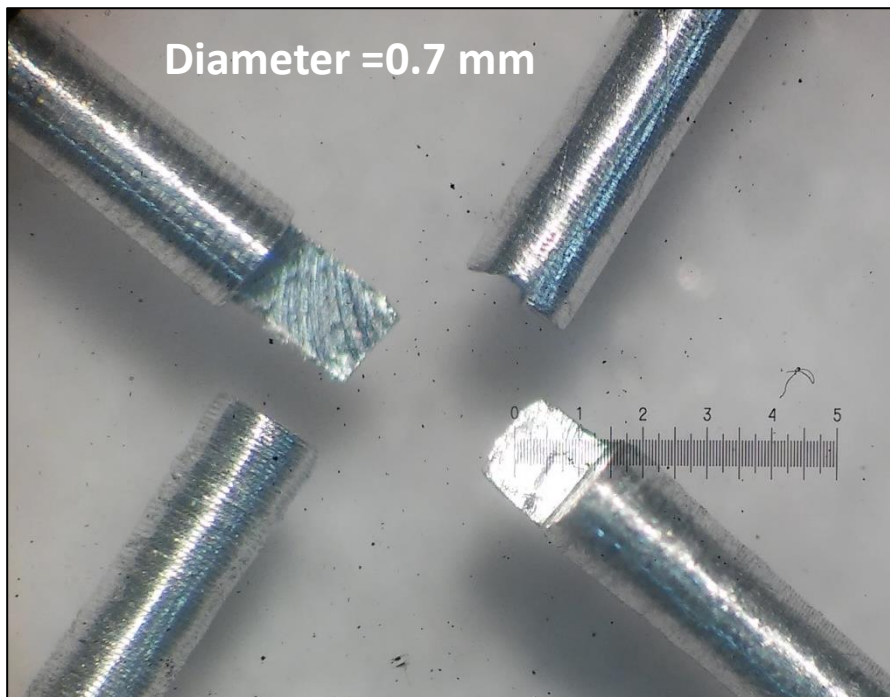


Figure 10-3 pin holders shaped in 4 different ways in order to accommodate the crystal in different angles.

However after the first discussions while being in the facility, we decided to choose only one big flake of almost 1 cm length which would sit oriented as desired in one single pin holder that would inevitable be larger in size than the ones prepared.

The puzzle of the orientation has been solved in favor of the crystal flake oriented in such way as illustrated in figure IV-right panel.

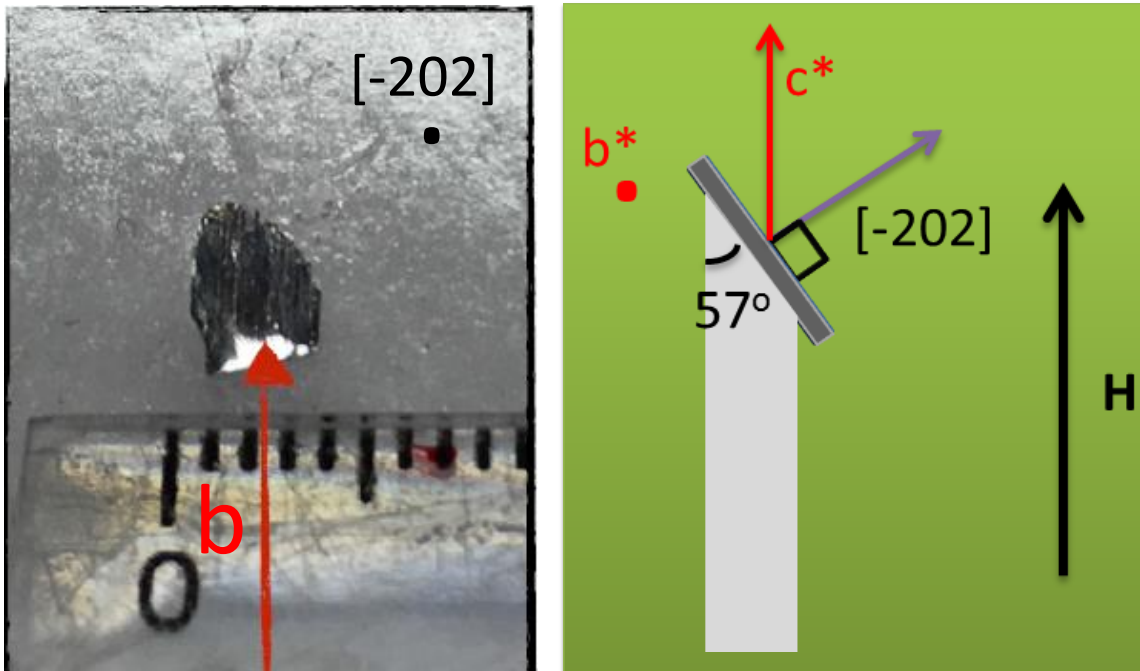


Figure 10-4 left: actual crystal flake cleaved from boule. The tiny lines on the crystal's surface are indicative  $b$ -axis while the flat surface is described by this orientation  $[-202]$ . Right: illustration of the desired orientation of the specific crystal in order to have

The single crystal flake was fixed in specially designed Al-holder which was hermitically sealed under He atmosphere in an He-circulating anaerobic glove-box. The crystal ( $m=12$  mg) was aligned with the  $c^*$ -direction ( $c^* \perp a$ - $b$  plane or  $c^* = d_{001}^*$  direction) vertically (the direction which contains the local gravity direction at that point), allowing to collect reciprocal space intensity maps from the  $(hk0)$  scattering plane, while the external magnetic field was applied perpendicular to the latter (i.e. along the  $c^*$ -direction). In order to derive the one-dimensional intensity patterns, the neutron diffraction data are getting reduced, which is the transformation of the dataset collected from the instrument into a dataset of physical units. Data reduction together with the analysis of the neutron scattering data has been handled out using algorithms and scripts developed within the framework of Mandid project. [224] The observed peaks have been chosen and masked in order to get the Intensity of the presented peaks. For the integrated intensity the mathematical area that is defined by each reflection peak has been calculated.